RESIDUAL STRESS AND DEFORMATION IN SPR JOINTS OF HIGH STRENGTH MATERIALS

REZWANUL HAQUE

A thesis in partial fulfilment of the requirements of
Swinburne University of Technology for the degree of
Doctor of Philosophy

The programme of research was carried out in Industrial
Research Institute Swinburne under Faculty of Engineering
and Industrial Science

in collaboration with

CAST CRC and Henrob (UK) Pty Ltd, Queensland, Australia

2014

To my loving parents

Abstract

The first aim of this work was to study systematically force-displacement curve of self-piercing riveting (SPR) process in conjunction with specimen characterization. Carbon steel sheet with different thicknesses and hardnesses and steel rivets with different lengths and hardness levels were used to examine the influence of material properties on the force-displacement characteristic curve. Flat dies with three specific diameters and five types of depth also have been used to observe their influence on the joint formation and force-displacement curve. This study shows that the force-displacement curve can be used to monitor the quality of a joint within the process parameters (rivet length and hardness, total stack thickness and die geometry) studied.

A simple and effective model was developed to determine rivet flaring in self-piercing riveted (SPR) joints by taking into account the effect of C-frame deflection on the force-displacement curve. Both interrupted and un-interrupted SPR experiments were performed to define the start of rivet flaring and the subsequent path of the flaring rivet tip. Two key point events of the force-displacement curves were identified, d_0 and d_{max} for start and end of rivet flaring respectively. A relationship was established for interrupted SPR samples, and was then validated for complete (un-interrupted) joints. The study shows that the characteristic force-displacement curve can be used to predict the rivet flaring inside an SPR joint without characterising the cross-section of a joint.

The study was then followed by testing the feasibility of measuring residual stresses in Self Pierce Riveted (SPR) joints by neutron diffraction technique. The main challenge involved dealing with the very small dimensions of SPR joints. Two different joints were examined: aluminium-steel and steel-steel. Even though small dimensions were involved, meaningful results were obtained. In the rivet head, a tensile stress was observed for the steel-steel specimen, whereas only compressive stress was observed for the aluminium-steel. The residual stress evaluated in the rivet head was higher in the centre and lower at the edge for both joints. Stresses in the sheet material adjacent to the rivet wall and at a distance of three times the rivet radius from the rivet axis were not significant. For the SPR joints examined, the maximum value of residual stress was found to be compressive and occurred in the rivet leg. It is evident from the residual stress profiles that the neutron diffraction technique successfully predicts the position of the rivet leg after flaring in a joint. The results are discussed according to the physical events involved during the process.

The uncertainties involved in measuring residual strain and their dependence on both the gauge volume of the neutron beam and acquisition time in self-pierce riveted (SPR) joints were also examined. The main challenge was to develop an optimum instrument configuration that allows fast and/or more accurate stress measurement in SPR while maintaining the same time resolution required for the mm-scale of the problem. Two different gauge volumes were used, 0.125 mm^3 and 1.0 mm^3, and two different measuring directions were chosen in order to examine the rotational accuracy of the sample table. Even though small sizes were involved, meaningful results were obtained and measurement errors were reduced by optimizing the instrument parameters. Typically, 240 and 900 seconds are necessary to achieve error (measurement uncertainty) within the range of ± 50 µm in sheet material for 1.0 and 0.125 mm^3 gauge volume respectively while the neutron path length is around 4.0 mm.

Applying these optimum instrument parameters, the evaluation of residual stress for a wide range of SPR joints is reported to provide guidance for the optimum design of SPR joining conditions. The effect of the ply material's hardness and thickness, and rivet hardness on the residual stress profile was analysed. It was observed that the residual stress towards the rivet leg increases up to a certain limit depending on the material's hardness and thickness, and the rivet's hardness. A zero residual stress was observed due to further increase in hardness of the materials and rivets, which indicates a crack inside the joint. The result was then verified by an extracted rivet. The study shows that a crack inside the joint can be successfully predicted by the residual stress profile of an SPR joint. The residual stress profile of a joint can be linked with the characteristic force-displacement curve.

Subsequent work was focused on the mechanical behaviour of the joint for the above different joining conditions. The static strength depending on the loading condition (cross-tension and lap-shear) and process parameter are discussed. In general, the strength of a SPR joint is highly dependent on the loading conditions: higher strength is always observed for lap-shear than cross-tension loading condition. However, in both loading conditions (lap-shear and cross-tension) the strength of a joint is greatly influenced by the hardness and thickness of sheet materials. The harder and thicker the ply materials are, the higher the strength of a joint in terms of both maximum force and energy.

The rivet flaring model was then extended to predict the joint strength directly from the characteristic force-displacement curve in cross-tension loading. Nine different cases were studied. All predictions of joint strength fall within 10% of the measured joint strength.

Finally a relationship was developed between the cross-tension and lap-shear loading conditions. The purpose was to predict the joint strength in lap-shear condition from the joint strength in cross-tension loading. An empirical equation was proposed by following the design formulae presented in Eurocode 9. The equation relates the joint strength between the two loading conditions with less than 8% error. The developed relationship between cross-tension and lap-shear condition represents a useful reference to be considered for further studies especially for different rivet and die geometry.

Acknowledgement

I am grateful to a number of people who contributed academically and professionally in my journey towards PhD. Without their constant support it would have been impossible for me to complete the project successfully.

At the beginning I would like to acknowledge my principle supervisor Dr Yvonne Durandet, who arranged everything for my scholarship and gave me the opportunity to work in this project. I appreciate her valuable guidelines throughout the project. I consider myself fortunate that I got the opportunity to work with her.

I would also like to express my sincere gratitude to my co-supervisor, Dr Yat Choy Wong for his valuable guidance and suggestions during the project. I have learned research culture and was well trained from the beginning to the final level of this degree from him.

I am grateful to Professor John Beynon, my associate supervisor. He helped me a lot to develop research skill and confidence. I have developed my ability of critical thinking that leads to a research question by his guidance.

I am also grateful to my associate supervisor, Mr Stuart Blacket from Henrob (UK) Pty Ltd. He continuously encouraged and supported me till the end of this project.

I would like to thank Henrob (UK) Pty Ltd. for supplying the materials required to produce the joints.

The support of CAST CRC is acknowledged. CAST was established under and was supported in part by the Australian Government's Co-operative Research Centre Program.

I would also like to thank Mr. Neal S. Williams from Henrob (UK) Pty Ltd. for his continuous technical support and valuable suggestions. I would also like to thank other members from Henrob.

A special thanks to Professor George Collins, CEO, CAST CRC Ltd for his continuous support and encouragement. He gave me valuable suggestions on preparing the application for beam time at ANSTO to carry out the neutron diffraction experiment. I would also like to thank Dr Mark Easton and Dr Aiden Beer from CAST CRC for their feedback on manuscript writing.

I also acknowledge the Australian Institute of Nuclear Science and Engineering (AINSE) for awarding grant Nos. 1416, 2076 and 2198 to carry out neutron diffraction studies at the Australian Nuclear Science and Technology Organisation (ANSTO). I would like to express my special thanks to instrument scientists, Dr Anna Paradowska, Dr Oliver Kirstein and Dr Vladimir Luzin from ANSTO for their technical support while running the neutron diffraction experiment at Kowari.

The technical support from Mr Brian Dempster, Mr Andrew Moore, Mr Girish Thipperudrappa and Dr William Song is highly appreciated. Without their continuous technical support it would be impossible for me to complete this project within this time frame.

I would like to thank my family members. Their unconditional love and continuous inspiration are the keys of all my achievements.

Thanks to all of my colleagues and friends from Swinburne University of Technology for their useful advice and ongoing support.

Finally, I would like to thank all of my friends for their wonderful discussions, sharing of knowledge and experiences during my course of PhD.

Declaration

The author hereby declares that this thesis:

- is candidate's own work
- contains no material which has been accepted for the award to the candidate of any other degree or diploma at any university, and
- to the best of the candidate's knowledge contains no material previously published or written by another person except where due reference is made in the text of the examinable outcome.

REZWANUL HAQUE

Content

List of Figures

List of Tables

List of Symbols

a	Crack length (mm)
b	Bottom thickness (mm)
C	Constant
C_1	Coefficient dependent on rivet hardness
C_2	Coefficient dependent on rivet length
d	Lattice spacing (μm)
d_0	Displacement of rivet before flaring (mm), Undeformed lattice spacing (μm)
d_{max}	Maximum displacement (mm)
d_r	Reference lattice spacing (μm)
Δd	Error in lattice spacing measurement (μm)
Δd_r	Error in reference lattice spacing measurement (μm)
D_0	Initial rivet diameter (mm)
D_d	Die diameter (mm)
D_h	Rivet head diameter (mm)
D_r	Diameter of rivet shank (mm)
D_t	Deformed rivet diameter (mm)
E	Young's elastic modulus (GPa)
f	Frequency (Hz)
F	Force (kN)
F^{CT}	Joint strength in cross-tension loading (kN)
F^{LS}	Joint strength in lap-shear loading (kN)
F^{T}	Joint strength (kN)
F_h^T	Joint strength for head pull-out (kN)
F_t^T	Joint strength for tail pull-out (kN)
K	Stress intensity factor
L_i	Incident neutron beam length (mm)
L_d	Diffracted neutron beam length (mm)
L_r	Rivet length (mm)
m	Constant

n	Constant
P_{max}	Maximum fatigue load (N)
P_{min}	Minimum fatigue load (N)
Q_1	Top seal
Q_2	Bottom seal
R	Load ratio (P_{max}/P_{min})
RSR	Rivet spread ratio
R_r	Rivet radius (mm)
t	Time (s), Thickness of sheet materials (mm)
Δt	Difference between time (s)
t_1	Top sheet thickness (mm)
t_2	Bottom sheet thickness (mm)
t_{eff}	Effective length of rivet in bottom sheet (mm)
u	Under-cut (mm)
W	Web thickness of rivet (mm)
x	Rivet flaring (mm)
Y	Head height (mm)
Y'	Geometrical constant
Y''	Constant
Z	Die depth (mm)
α_T	Empirical coefficient for tensile loading
α_{CT}	Empirical coefficient for cross-tension loading
α_{LS}	Empirical coefficient for lap-shear loading
β_h	Empirical coefficient of the sheet bending induced thickness for head side
β_t	Empirical coefficient of the sheet bending induced thickness for tail side
θ	Diffraction angle (°)
λ	wave length (Å)
η_h	Empirical coefficient of material degradation due to piercing for head side
η_t	Empirical coefficient of material degradation due to piercing for tail side

σ	Ultimate strength of material, Stress (MPa)
σ_t	Yield strength of material (MPa)
μ	Friction coefficient
ε	Strain
$\Delta\varepsilon$	Error in strain measurement
ϑ	Poisson’s ratio

1 INTRODUCTION

Self-Pierce Riveting (SPR) is now a well-established mechanical fastening technique for joining sheet materials. The joining method has been widely adopted by the automotive industry due to its suitability for high volume production and for use in combination with structural adhesives [1]. To reduce carbon emissions and fuel consumption, the demand for lighter, more energy efficient vehicles is increasing. This demand for a lighter car is met by using a combination of dissimilar materials such as light weight and high strength materials in the automotive industry. The SPR is found to be an effective process to join these dissimilar materials. The advantages of SPR include fast cycle time with easy automation, no need for a predrilled hole or accurate alignment with a predrilled hole, no waste material produced, high process reproducibility, and consistent joint strength [2-9].

Sheet metal joining is a very important part in the manufacturing process of automobile industries. Making of building roof, aeroplane, ship deck and oil carrying drums all involve metal joining processes. Joining technology of sheet metal includes resistance spot welding, arc welding, friction stir welding, laser welding, adhesives, nuts and bolts, screws, conventional riveting, clinching and self-piercing riveting (SPR). Resistance spot welding is very popular in the automobile industries as it is a very well known, extensively proven technology and the industries are comfortable with this technique, having considerable experience. The automotive industries are increasingly using light weight and high strength materials such as aluminium or magnesium alloys, and advanced high strength steel to improve the energy efficiency by reducing the weight of the vehicle structure [10, 11]. Direct welding of dissimilar materials is difficult and sometimes impossible as they undergo some fusion process which may lead to the production of different and unwanted phase transformation. High thermal conductivity and surface oxide layer are also crucial for welding, particularly for aluminium alloy. Hence, mechanical fasteners, clinching and adhesive bonding techniques are increasingly being considered by design engineers [12]. Nut and conventional riveting require predrilled holes which make the process slower and the clinching generally produce joints with lower strength than SPR. For all of the above reasons, SPR is increasingly used in automobile, packaging and appliance industries.

1.1 The self-pierce riveting process

The SPR technique is generally used to fasten two or more sheets of material by cold forming, as shown in Fig. 1.1.1. A semi-tubular or fully tubular rivet is driven through the top sheet by displacing material into the rivet bore and die, piercing but not perforating the bottom sheet, and flaring the legs in the bottom sheet under the guidance of a suitable die [1]. Not perforating the bottom sheet means a seal is maintained and the rivet leg is not exposed to the environment; the resulting joint is resistant to gas and liquid penetration and corrosion in the die side [1, 13].

The sheet with the rivet head is called top sheet and the sheet in the die side is called bottom sheet. Throughout the thesis this naming convention is followed.

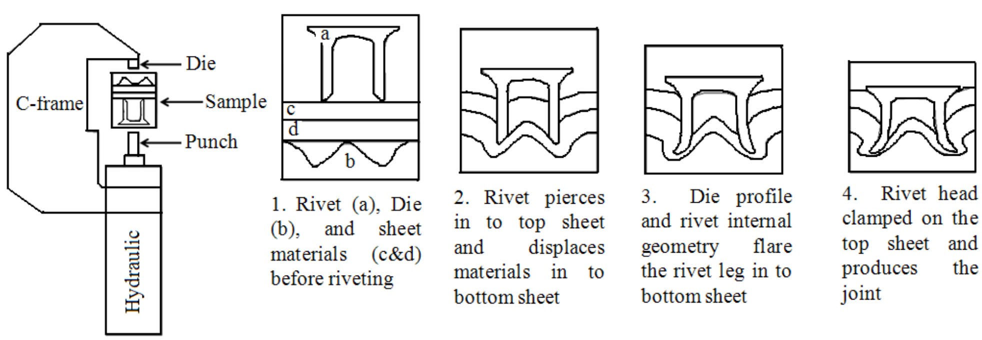

Fig. 1.1.1 Schematic diagram of the riveting process.

The SPR process originated ~50 years ago, but during the last 20 years, it progressed significantly, although limited literature has been published in this field [14]. There is, in particular, limited performance data on SPR joints. The rivet needs to satisfy two conflicting properties, hardness and ductility in order to complete the process. The rivet should have sufficient hardness to pierce the top sheet completely and to pierce the bottom sheet partially. However, the rivet should also have sufficient ductility to flare and deform in the bottom sheet without cracking in order to create mechanical interlock. The ply materials should also have sufficient ductility to deform inside the die cavity without cracking. SPR process also produces residual stress due to the plastic deformation of both the rivet and the sheet material.

1.2 Deformation behaviour

The SPR joining involves two distinct events: piercing and flaring of the rivet. However, further investigation has demonstrated that these events occur over four significant stages that can fully describe the fastening process. These four stages are named as: (i) bending of sheet materials, (ii) piercing of the top sheet, (iii) partially piercing of the bottom sheet and (iv) filling of the die cavity with the radial flow of materials, and forming of the interlock by setting of the rivet head [15-17]. The key measurable process parameters for the riveting system are identified as the rivet setting force applied by the punch and the displacement of the punch rivet as shown in Fig. 1.2.1.

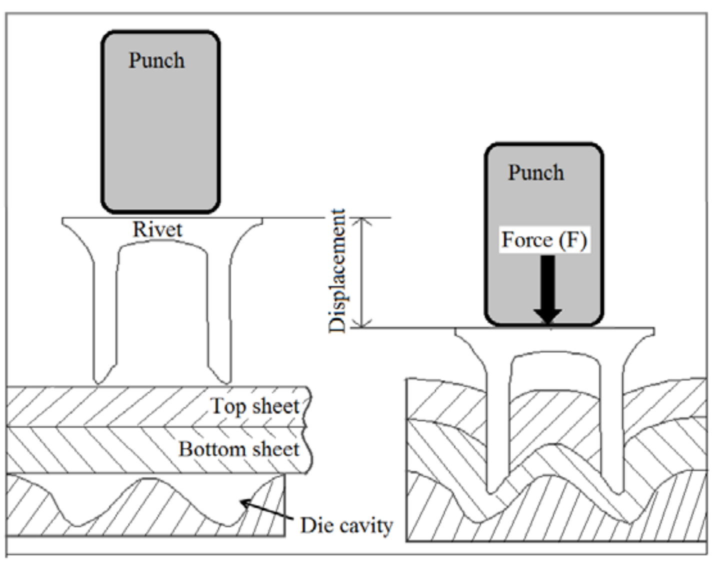

Fig. 1.2.1 Schematic of measurable process parameter.

The punch force and the displacement can be measured directly during riveting. A force-displacement curve thus can be produced as shown in Fig. 1.2.2. The deformation behaviour of the rivet and sheet material can be described fully by this force-displacement curve. It is known that any change in process parameters will make a unique change on the force-displacement curve [16].

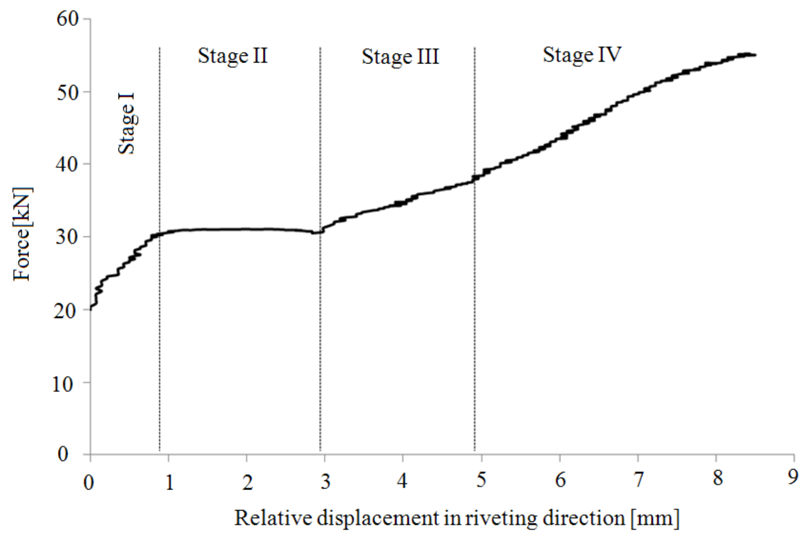

Fig. 1.2.2 A standard force-displacement curve for SPR process.

1.3 Research objectives

At present, the prediction of SPR joint performance is derived mainly from experience. There is a certain amount of literature that discussed the performance of SPR, but the actual mechanism of joint formation and deformation behaviour during the joining is not clear. The self-piercing rivet must have two conflicting properties i.e., hardness and ductility; the rivet should have sufficient hardness to pierce the top sheet and high ductility to flare in the bottom sheet. Residual stress develops in the joint due to plastic deformation of both sheets and the rivet.

The aim of this research is to understand the deformation behaviour of the rivet and sheet material during the riveting process. Another goal of this research is to study the residual stress developed during a SPR process because of plastic deformation of the rivet and sheet materials. Finally the project aims to study the mechanical behaviour of SPR joints to extend the existing knowledge which will enable the prediction of joint strength for a variety of riveted joints. The research aims will be achieved by:

- Creating a range of riveted joints by changing different parameters such as different materials, rivets and dies, interrupting the family of joints in different positions and then establishing the force-displacement curve, and determining the rivet flaring at each interrupted positions. Finally determining the C-frame deflection.
- Feasibility study of the residual stress evaluation in SPR joints by the neutron diffraction method and evaluating the residual stress in a collection of different SPR joints by the neutron diffraction technique.
- Producing a series of SPR joints for both the cross-tension and lap-shear loading condition and measuring the strength of each joint in each loading condition.

1.4 Outline of the thesis

The body of the thesis is presented in nine main chapters beginning with an introduction which provides an outline of the SPR process and states the principle objectives of the current research.

Previous research which was performed in the field of SPR is described in chapter two. Different SPR techniques, mechanics of joint formation, quality monitoring process and different factors that affect the joint quality are described. The static, dynamic and fatigue behaviour of the SPR joints are also presented in the literature review chapter. A brief comparison with SPR and other techniques is also provided.

The challenges associated with residual stress in SPR are identified in chapter three. A short literature survey on the general effect of residual stress on different structures is discussed and different measuring methods of residual stress are introduced.

In chapter four the experimental approach and procedure used to understand the deformation of the rivet and sheets by interrupting the joints are presented. The measurement technique of residual stress is fully described starting from the feasibility tests followed by optimizing parameters for meaningful measurement to the final stage of the experiment. The method to determine the mechanical behaviour, the equipment and testing procedure are fully described.

Chapter five presents the results from the interrupted tests. The characteristics of SPR process from a family of riveting conditions are analysed and the significance of different process variables is established. The chapter mainly demonstrates the deformation of the rivet and sheet material by analysing the force-displacement curve and the cross-sectional pictures of the joints interrupted at different positions. A model is also presented to determine the rivet flaring from experimentally measured force-displacement curve.

In chapter six, at first, the feasibility of evaluating residual stress in SPR joints by the neutron diffraction technique is provided. Then an optimization test is performed to determine the optimum instrument parameters that will enable faster and accurate evaluation of residual stress. The main objectives are to determine the residual stress profile in different SPR joints by using the optimum instrumental condition. Detailed residual stress profiles are presented for a variety of SPR joints consisting of sheets with several types of hardness and thickness of materials, different rivet hardness and die depth. The results are discussed with respect to the physical events occuring in the SPR process.

The mechanical behaviour of the SPR joints is discussed in chapter seven. The chapter reports the dependency of static strength on loading condition and failure modes of joints. An analytical procedure to predict the joint strength in the cross-tension loading condition is presented and the relationship of a joint strength in lap-shear and cross-tension is also demonstrated.

Finally in chapters eight and nine a guidline for the industry, summary of the conclusions and recommendation for future research are prescribed.

2 LITERATURE REVIEW

Joining of metal sheets is very important in the manufacturing industry especially in automotive industries. Self-piercing riveting is found to be advantageous among the various joining methods particularly for joining of dissimilar sheet materials [18-21]. The automotive industries are increasing the use of light weight high strength materials to reduce the total weight of a vehicle in order to improve fuel efficiency. SPR is now a widely adopted joining technology in the automotive industry due to the increasing demand of joining light materials such as magnesium and aluminium [2]. SPR is also used in other industrial sectors like building construction and packaging industries [22-25]. The process is very suitable for high volume production with and without structural adhesives [26].

SPR is a relatively new technology, having originated about 50 years ago [14, 27]. However, several car manufactures started to implement SPR as a major joining process to assemble aluminium roofs and different parts of a car body after 1990 [2, 11, 28, 29]. Audi adopted SPR in its A8 model for joining the aluminium space frame in 1994 and 70% of joints were made by SPR [2, 18]. In 1999 Audi produced the first mass aluminium car and SPR was the main method of joining [18]. A considerable amount of SPR joints are used in car chassis and doors by eliminating MIG welding by Jaguar, Ford and Mitsubishi [10, 30, 31]. As a result, SPR progressed significantly in the last 25 years. During the last decade several patents were also lodged in riveting and applications [32].

As now-a-days automotive industries are using coated, light weight and high strength materials for the manufacture of the car body, it is essential for them to re-examine the conventional joining processes such as welding [3, 4, 6, 33]. Direct welding of dissimilar metals is difficult or impossible as they undergo some fusion process which may lead to the production of a phase transformation. High thermal conductivity and surface oxide layer are also crucial for welding, especially for aluminium alloy [3, 6, 34]. For this reason, SPR has drawn increasing interest and applications in recent years. The advantages of SPR include [5, 35-40]:

- Simple process with no predrilled holes required.
- Fast cycle time and easy automation.
- No heat fumes, dust or chips
- No waste material is produced so friendly and safe to the environment.
- High strength and better fatigue properties achieved.
- Low energy requirement so relatively low cost.
- Very little or no damage to pre-coated material.
- 'Water tight' joint is formed.
- Possible to join a range of dissimilar materials such as steel, aluminium, plastic, polymer and multiple material stacks
- Very good reproducible behaviour and compatible with adhesive and lubricant

Like all other technologies, SPR also has some disadvantages, which include [41-43]

- Requires access to both sides of the joint.
- Not suitable for brittle materials.
- During the forming process high force is necessary, which requires a relatively strong and heavy C-frame.
- There are sudden increases of surface in the joints which may not be acceptable aesthetically.

This thesis provides a review of the literature on SPR process which includes 12 theses, 2 book chapters, many journal and conference papers, and reports from the open literature and private communications. Finite element modelling (FEM) of the SPR processes is also discussed with 63 references. Static and fatigue performance of the joint for different loading conditions (coach-peel, cross-tension, lap-shear and pure shear) and different specimen configurations are also discussed. The effect of process parameters such as rivet diameter, hardness and length, properties of ply materials (thickness and hardness), different types of dies, rivet setting pressure and direction of riveting on the performance of the riveted joint are also reviewed in this thesis.

2.1 SPR joining process

SPR is a cold forming process. This process is used to fasten two or more sheet materials, as shown in Fig. 2.1.1. Here a tubular rivet is driven through the top sheet and flaring the legs in the bottom sheet under the guidance of the rivet's internal geometry and a die which is positioned below the bottom sheet [1, 41, 44]. A seal is maintained as the bottom sheet is not pierced through and the resulting joint is resistant to gas and liquid penetration at the bottom sheet and therefore resistant to corrosion [2, 13, 45]. SPR is capable of joining up 2 to 6 mm of steel and 2 to 10 mm of aluminium stack thickness [2, 46]. The process is also capable of joining mixed grades of materials and multiple material stacks up to 4t (Fig. 2.1.2), and use of interlayered adhesive and sealant is also possible [46, 47].

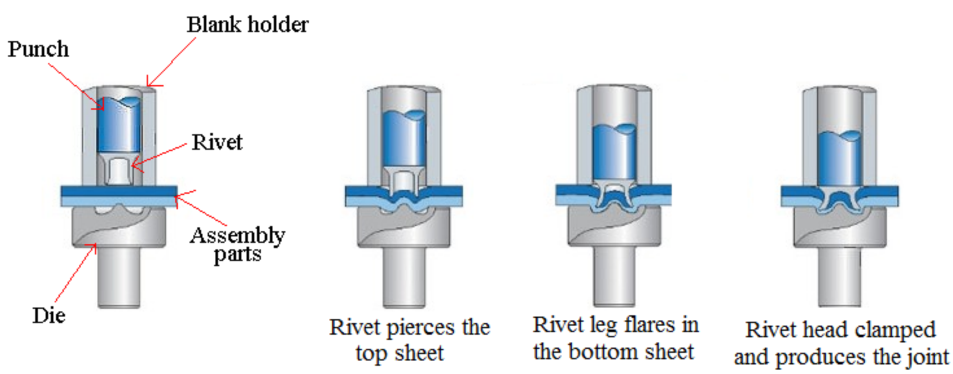

Fig. 2.1.1 Schematic illustration of SPR process [48].

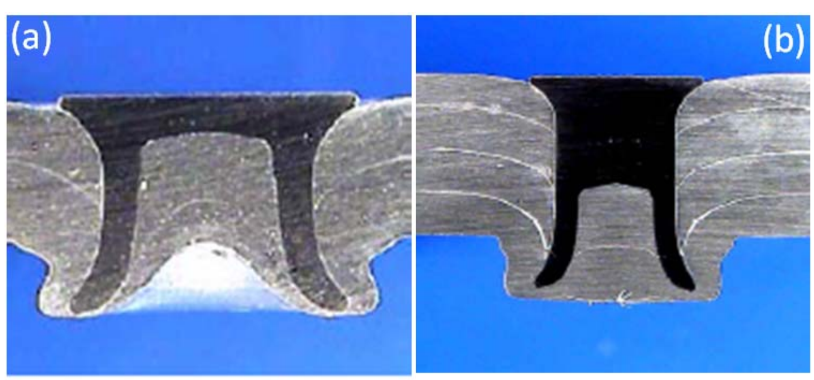

Fig. 2.1.2 Joining capability of SPR (a) 2t and (b) 4t stack-up [2].

2.2 Different SPR processes

2.2.1 Traditional SPR process

The SPR joining involves a high setting force. To supply a high force, a strong and heavy C-frame is used in the SPR process (Fig. 2.2.1). A die is mounted on one side of the C-frame, a punch is set on the other side and the specimen is positioned in between. The riveting speed is generally 10 mm/s. A range of C-frames are available to meet the different load requirements [35].

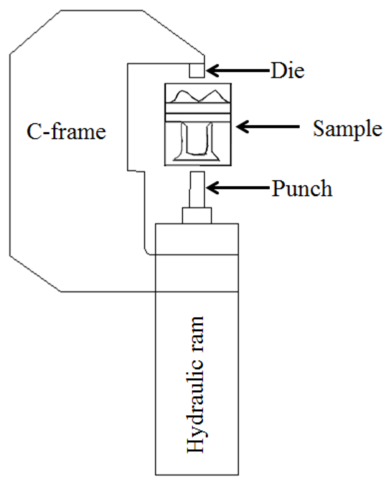

Fig. 2.2.1 Schematic of a C-frame used in traditional SPR processing.

2.2.2 Laser assisted self-piercing riveting

Plastic deformation of materials is involved in SPR joining. The bottom sheet requires sufficient ductility to deform within the die anvil without cracking. However, joining a material with low ductility such as magnesium is not possible with conventional SPR [12, 49-51]. The magnesium bottom sheet cracked during the riveting operation as shown in Fig. 2.2.2 [52-54]. The bottom sheet can be preheated by a laser beam in order to improve the ductility before riveting [55, 56]. Crack-free magnesium joint is possible by increasing the workability of magnesium when the bottom sheet is pre-heated before the joining (Fig. 2.2.2).

However, the preheat temperature depends on the material properties and to determine the optimum pre-heat temperature Zener-Hollomon parameters were employed by Wang and co-authors [49]. The optimum preheat temperature of magnesium is 180º - 210ºC [49, 54]. Within this preheat temperature the deformability of magnesium increased greatly on account of the softening of magnesium. The softening of magnesium occurred due to dynamic re-crystallization [54, 57]. It is suggested that the analytical approach to the temperature at the onset of joining can provide the basis for online process monitoring [56]. The total cycle time is increased to 5 seconds due to the time required for the preheating of magnesium alloy [52, 55]. However the process is still viable and development work is needed to decrease the cycle time and to monitor the heat absorbed from the laser and control the heat transfer between the sheets [54-56].

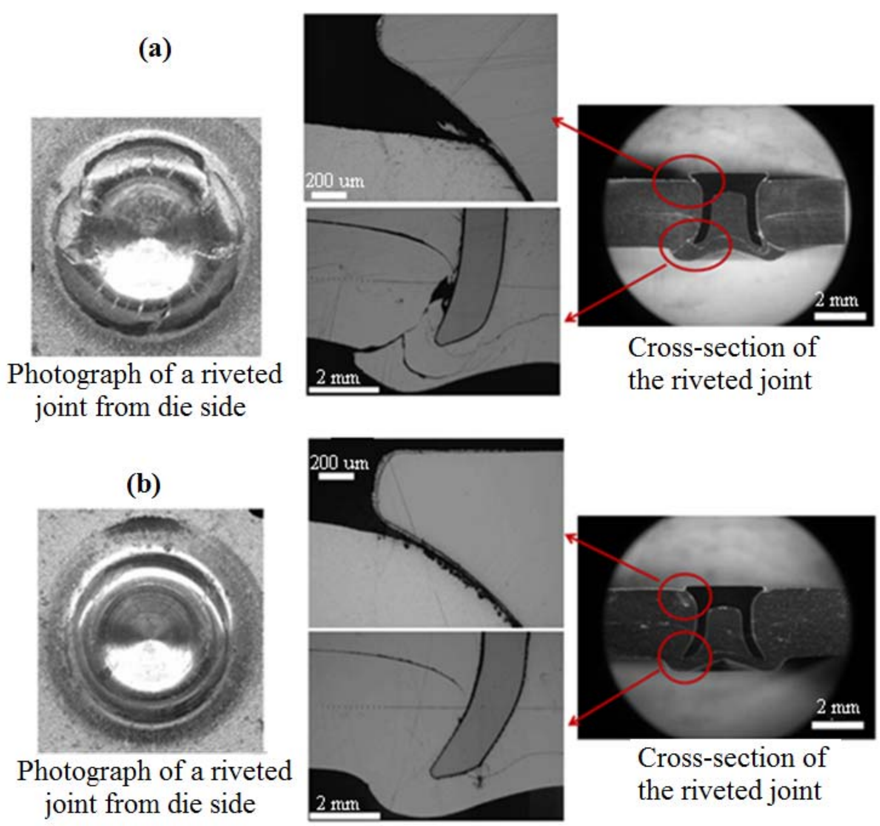

Fig. 2.2.2 The SPR joint of 3 mm + 3 mm AZ31 produced (a) without laser and (b) with laser heating [52].

2.2.3 Electro-plastic self-piercing riveting process

In this process a DC current is applied to advanced high strength steel (AHSS) to reduce the deformation resistance of DP780 steel [58]. A thin isolation plate was placed between the two sheets in order to avoid current flow in the aluminium sheet. The new technology increased the joint strength significantly when the harder material is at the bottom. Obvious effects on undercut, rivet head height, rivet flaring and bottom thickness are observed in Fig. 2.2.3 [58].

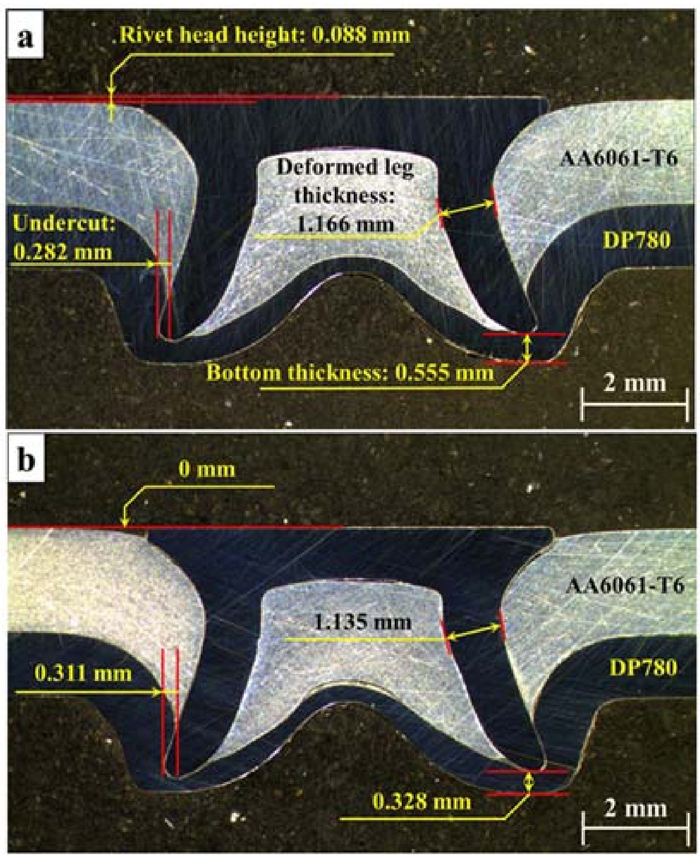

Fig. 2.2.3 The effect of DC current on riveted joints of 2 mm AA6061-T6 + 1.25 mm DP780 (a) a SPR joint and (b) an Electro-Plastic SPR joint at 1005° C [58].

2.2.4 Impulse self-piercing riveting process

This is a high speed SPR aimed to reduce distortion of the top sheet [59]. The joints are produced without a C-frame to avoid deflection and sometimes gun powder is used to achieve the high impulse [59, 60]. It is clear from Fig. 2.2.4 that the Impulse SPR cuts the top sheet at an early stage but the conventional SPR stretches the top sheet to a large extent. The top sheet is dragged down by the rivet tip in conventional riveting speed and the deformation rate is much higher in Impulse SPR and the strength was also found to be higher than that for conventional SPR because of less stretching of both the top and the bottom sheets [59]. The geometric dimension is significantly changed from the conventional speed of 10 mm/s and few differences were observed between speeds of 10 and 100 m/s [60].

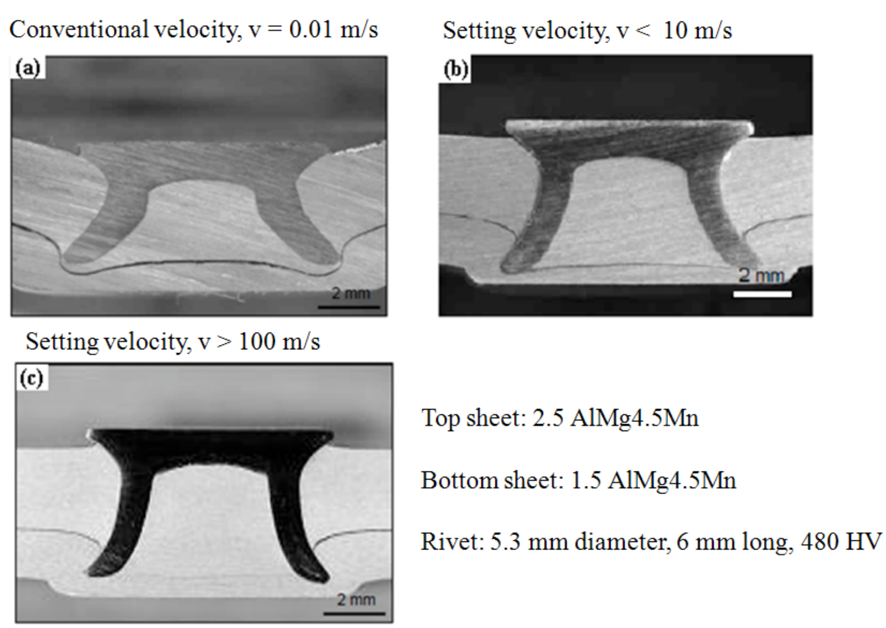

Fig. 2.2.4 The influence of the riveting speed on the quality of joints [60].

2.2.5 Hydro-formed self-piercing riveting process

In the Hydro-formed SPR high pressure fluid is used instead of the die set, as shown in Fig. 2.2.5 [61]. The high pressure fluid prevents excessive bending of hydro-formed sheet. Thus deformability of sheets is increased and the operating window can be widened by this method. The flaring mainly depends on the pressure of the fluid and the rivet's geometrical shape. A linear relationship was found between the interlock and fluid pressure [61].

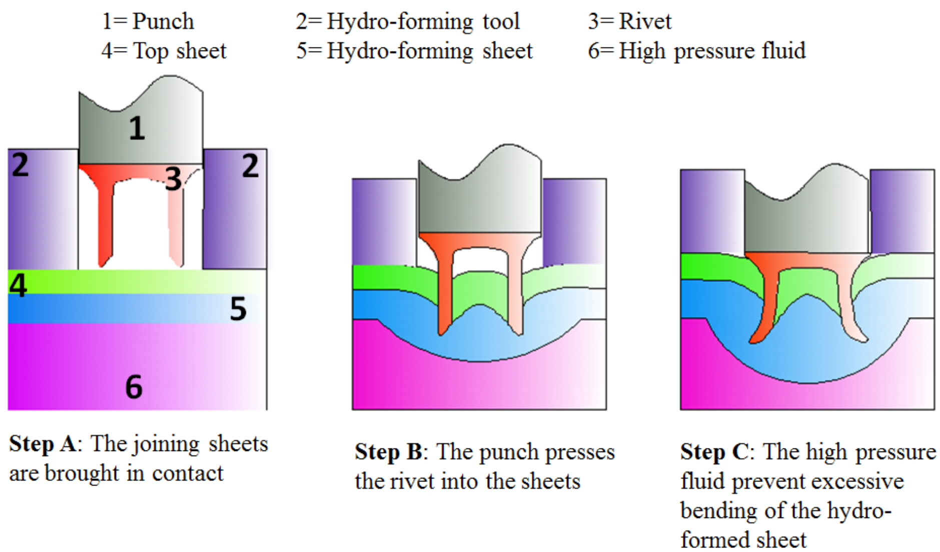

Fig. 2.2.5 Operational sequence of Hydro-Self-Pierce Riveting [61].

2.2.6 Hybrid self-piercing riveting process

To improve the performance of an SPR joint in shear loading, adhesives are used in conjunction with the SPR, which is known as Hybrid joints [62-64]. However, the use of adhesive may lead to unwanted deformation of the top and bottom sheets and create an undesired joint. A schematic of the influence of adhesives on SPR joints is drawn in Fig. 2.2.6 according to Hahn and Wibbeke [65]. They optimized the process for hybrid joining in three stages. In the first stage they increased the hardness of the rivet. In the second stage they reduced the clamping force and increased the joining speed. Finally, they applied all these together and they found an optimized joint with good interlock [65]. The effect of adhesives on the joint quality and performance will be presented in section 2.9.10.

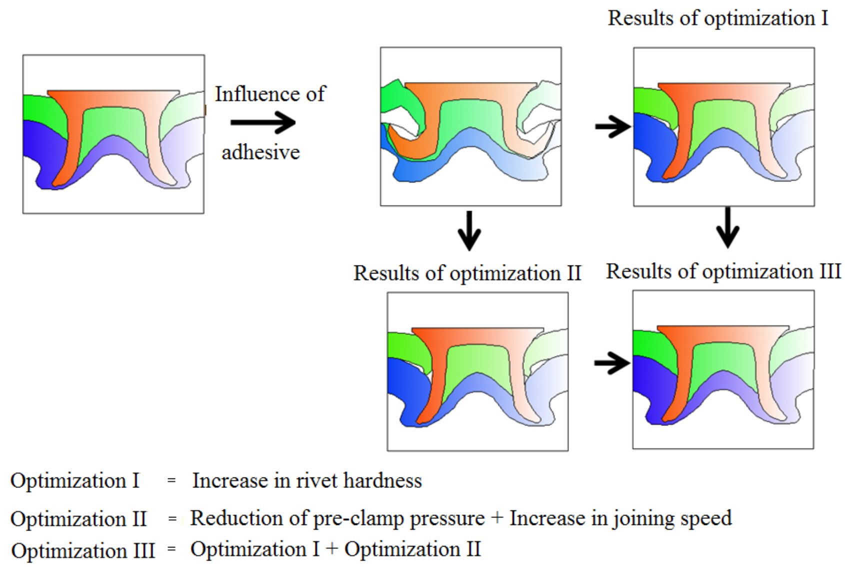

Fig. 2.2.6 Schematic optimization process of a hybrid joint.

2.2.7 Joint design modification in SPR process

Here the joint design is modified by including two flat washers; one is on the top of the top sheet and another is underneath the bottom sheet, as shown in Fig. 2.2.7 [66]. The need here is driven by carbon fibre reinforced material (CFRP), e.g. to suppress the delamination of CFRP laminates at the point of piercing. The strength of this modified SPR joint was compared with a bolted joint and it was observed that the modified SPR joint showed a better strength.

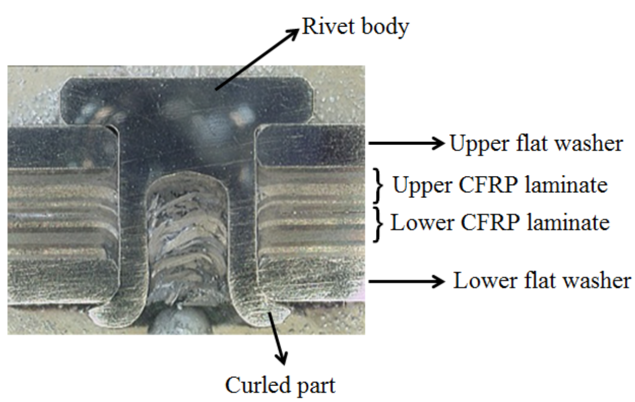

Fig. 2.2.7 Cross-section of a jointed CFRP by the modified SPR process [66].

2.3 The Quality of a SPR joint through cross-section

In general, the quality of a SPR joint is evaluated in four stages: at first by visual inspection of the joint, secondly by inspecting the cross-section of a joint, thirdly by evaluation of the static strength in different loading conditions and finally by examining the fatigue life of the joint. Fig. 2.3.1 shows the geometrical quality parameters in an SPR joint. It should be noted that the schematic is drawn by considering the following assumptions:

- No bulging or buckling of rivet column during riveting.
- The joint button completely fills the die cavity.

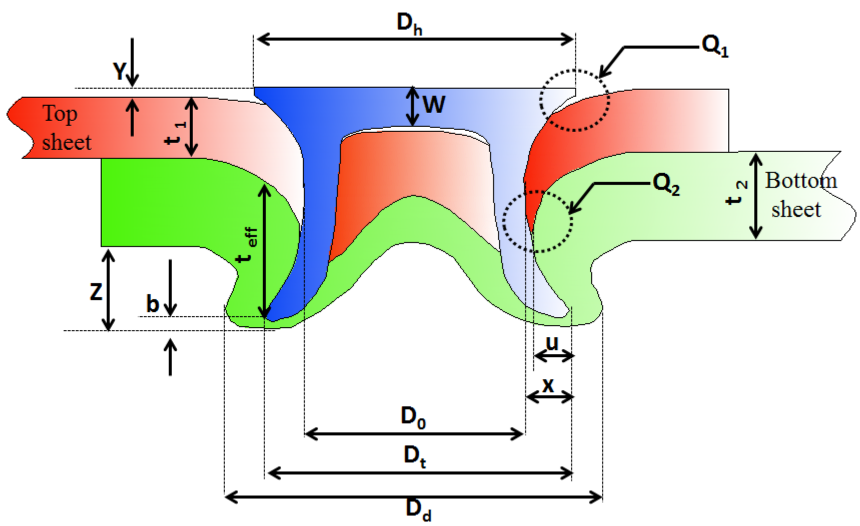

D_h = Rivet head diameter
D_0 = Initial rivet diameter
D_t = Deformed rivet diameter
D_d = Die diameter
W = Web thickness of rivet

Q_1 = Top seal
Q_2 = Bottom seal
Y = Head height
Z = Die depth
x = Rivet flaring

b = Bottom thickness
t_1= Top sheet thickness
t_2= Bottom sheet thickness
u = Under-cut
t_{eff}= Effective length of rivet in bottom sheet

Fig. 2.3.1 Schematic cross-section of a riveted joint showing the geometrical quality parameters.

A good SPR joint should have the following quality features, as shown in Fig. 2.3.1 [67-73]:

- Rivet head height (Y) should be very close to zero.
- There should be no gap between rivet head and top sheet (Q_1) and between top and bottom sheet (Q_2). This is necessary to avoid corrosion and to improve fatigue life of the joint.
- A minimum of bottom thickness (b) of 0.15 mm is necessary [68]. The risk of crack in the bottom sheet and the exposure the rivet leg in the environment will increase if the bottom thickness is reduced.
- The undercut (u) should be more than 0.1 mm [68]. The mechanical interlock heavily depends on this.
- Good interlock of rivet in the bottom sheet (t_{eff}) and rivet flaring (x). This will increase the joint strength.
- Minimum collapse or buckling of rivet leg.

2.4 Mechanics of joint formation and characteristic force-displacement curve

The mechanics of the SPR joining process can be described by the characterizing the force-displacement curve (Fig. 2.4.1) by measuring the force and displacement of the punch [16, 74, 75]. The force-displacement curve is segmented in four different stages. These stages are: Stage I- bending, Stage II- Piercing of top sheet, Stage III- Die filling and Stage IV- flaring and rivet setting [15, 16, 76].

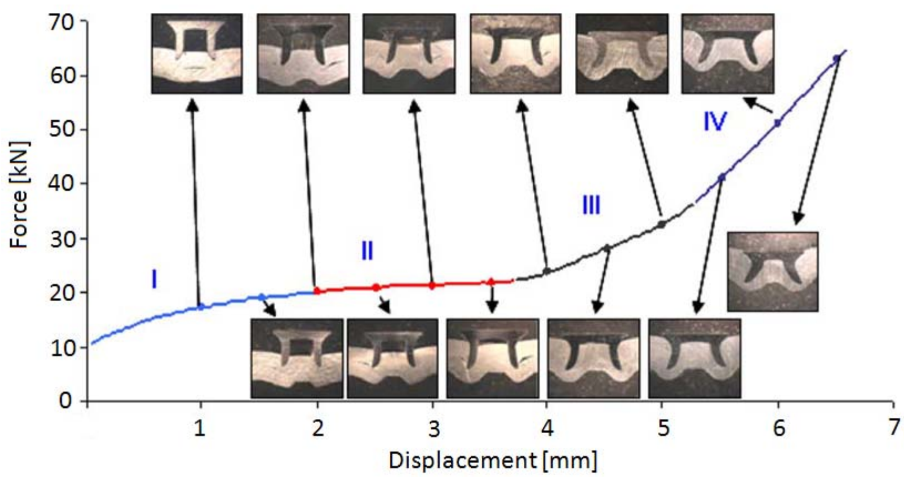

Fig. 2.4.1 Typical four stage force-displacement curve describing the joining mechanism [17].

During the first stage, the metal sheets bend, but no failure occurs as the stress generated during this period is below the ultimate strength of the material [16, 58, 77]. The thickness and hardness of ply materials play a very important role in the force developed in this stage: the thicker and harder the ply material the higher is the force [1, 78]. A 15% increase in force for a 25% increase in thickness was reported by King [1] for a joint of aluminium alloy 5251-H3. Riveting at an elevated temperature, which softens the materials, can lead to lower force during this stage [79].

During the second stage, the rivet pierces the top sheet. As soon as the force reaches the ultimate strength of the material, failure is initiated in the top sheet and piercing begins. The force is almost constant during this stage for a given total stack thickness. The thickness of the top sheet mainly influences this stage and other parameters such as bottom sheet thickness, rivet length, diameter and hardness, and die profile have negligible effect on this stage [16, 58, 77].

During stage III, the die recess volume is largely filled. As a result the die volume is the most significant parameter at this stage. The force increases roughly linearly with displacement during this period. Rivet hardness and length, and the bottom sheet's hardness are the three main factors that affect this period of the curve [77, 80-82]. The shank of the rivet remains straight during this step and rivet bulging occurs when the sheet is too hard compared to the rivet hardness, or when the rivet is too long compared to the joint stack thickness [15].

Stage IV is the most crucial part of the SPR process as mechanical interlocking takes place during this stage by rivet flaring. The mechanical interlock occurs if the rivet penetrates and flares into the bottom sheet, but if flaring occurs between the top and bottom sheets (when the length of stage III is too small) no interlock would form [16, 50]. The force increases with a high gradient, continuously pushing the cylindrical wall of the rivet to flare outwards, which gradually forms the interlock by this outward deformation of the rivet wall (rivet flaring) and compression of the sheets in the die recess and rivet bore.

A missing rivet, double rivet or other process faults can easily be identified by analysing the force-displacement curve. An axial misalignment may increase the force at stage I and II, as reported by Hou et al.[16]. A planar misalignment can lead to a significant increase in force during the third and fourth stages [16]. As a result this curve can be used for the quality monitoring of a SPR joint.

2.5 Quality monitoring of a SPR joint

The quality of a SPR joint is monitored by both destructive and non-destructive methods. A SPR joint is cross-sectioned for the destructive method and the non-destructive methods include: force-displacement curve, ultrasonic method, and visual inspection through a high speed camera.

2.5.1 Destructive method by having a cross-section

In the destructive method the joint quality is evaluated by having a cross-section of a joint. Major defects that would lead to a failure of a joint are (Fig. 2.3.1):

- Large gaps under the head of the rivet i.e. poor top seal.
- Obvious breakthrough of the rivet tail through the bottom sheet of material.
- Serious collapse of the rivet legs.
- Poor interlock of the rivet tail in the bottom sheet of material.
- Large cracks in the rivet tail.

2.5.2 Non-destructive method (NDT)

In general the quality of a SPR joint is mainly evaluated by observation of a cross-sectioned joint. However, for industrial automation a couple of non-destructive techniques for quality monitoring are developed. The following notes compare the force-displacement curve, ultrasonic measurement and visual measurement by camera.

2.5.2.1 Quality evaluation by force-displacement curve

The widely developed method is to establish a force-displacement curve for an optimum joint and then compare the force-displacement curve of each produced joint with the optimum one [16]. King [1] in his thesis proposed to study six different points (P1- P6) on the force-displacement curve of a joint for the quality monitoring, as shown in Fig. 2.5.1. Upper and lower limits of these positions can be defined and if the force-displacement curve of a joint falls within these limits, the joint may pass. An automated quality monitoring by comparing the force-displacement curve was developed by He and co-authors [83-85] and they concluded that the process is capable of monitoring the quality with high accuracy.

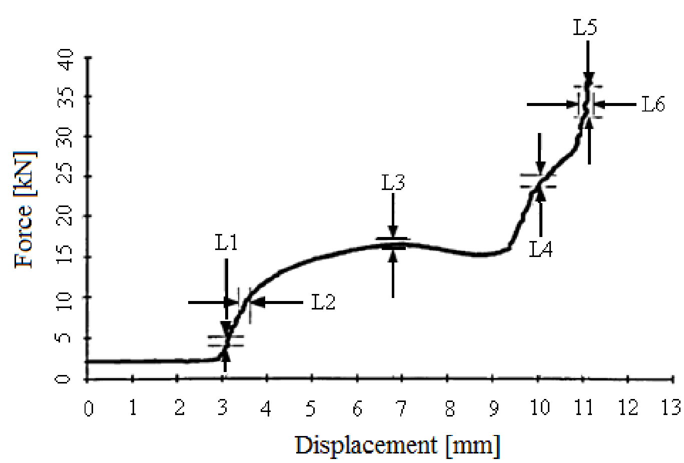

Fig. 2.5.1 Six positions of the force-displacement curve for monitoring the quality [1].

2.5.2.2 Ultrasonic and T-sonic quality monitoring

A new method for non-destructive quality assessment of SPRs using ultra-sound was developed by Stepinski [86]. The rivet inside the joint was inspected by sending an ultrasonic continuous wave at a predetermined frequency (Fig. 2.5.2). The quality of the rivet was evaluated by monitoring variations in the transducer's electrical impedance. Hewitt and co-authors [87] at Warwick University (UK) tried to apply Tsonic waves to measure the quality. However, the level of significance was not large enough to provide a confident result.

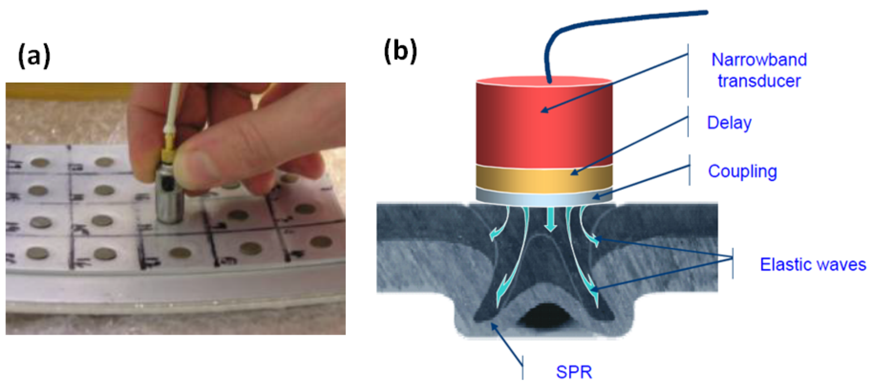

Fig. 2.5.2 Operating principle of quality monitoring (a) T-sonic [87] and (b) ultra-sonic transducer [86].

2.5.2.3 Online visual quality monitoring

A NDT method to determine the common mistakes (such as no rivet or 2 rivets in one place) was developed by using computer vision, camera and laser line generator [88, 89]. It was also possible to measure the joint thickness accurately by this method. The status of the rivet can be identified using common image processing and the common failures (which may compromise the mechanical interlock) that occurred in the industry can be avoided. Another technique based on digital image correlation (DIC) was developed by Sadowski and Knec [90] to observe the deformation behaviour of the SPR process in many applications.

2.6 Factors affecting the quality of a SPR joint

Several parameters affect the quality of a SPR joint such as rivet, die, material etc. The effect of the rivet diameter and length on rivet flaring and setting pressure was described by King, Fu and co-authors [1, 78, 91]. The rivet should have enough strength to pierce the top sheet [92-94]. The rivet coating is important to protect from corrosion [7, 8, 95]. Optimized rivet geometry is required, particularly the radius under the rivet head and the profile of the rivet leg for a good quality joint. The optimization of the rivet head radius reduces the residual stress and improves the top seal, and optimization of the rivet leg increases the piercing capability and flaring [96, 97]. However, the residual stress can be reduced by coining after the riveting operation, which would increase the fatigue life of SPR joint [98].

The blank holder is also an important process parameter of riveting [99]. The diameter and pressure of a blank holder highly influence the distortion on the global assembly of a SPR joint [100, 101]. The distortion can be greatly reduced by increasing the pre-clamp pressure [69, 102].

The hardness and thickness of sheet material are the most significant factors that affect the quality of the joint [103, 104]. Ageing, pre-straining and paint baking can change the hardness and ductility of a material, hence it can alter the quality [105, 106]. It is suggested that an increase in pre-straining can decrease the interlock and increase the head height [107, 108]. The piercing direction (riveting order) can improve the join-ability by increasing the flaring (Fig. 2.3.1) and the effective length of the rivet in the bottom sheet [109, 110]. The effect of the edge distance on the quality of the joint is shown in Fig. 2.6.1 [111]. A minimum of 11.5 mm edge distance is suggested to create a quality joint.

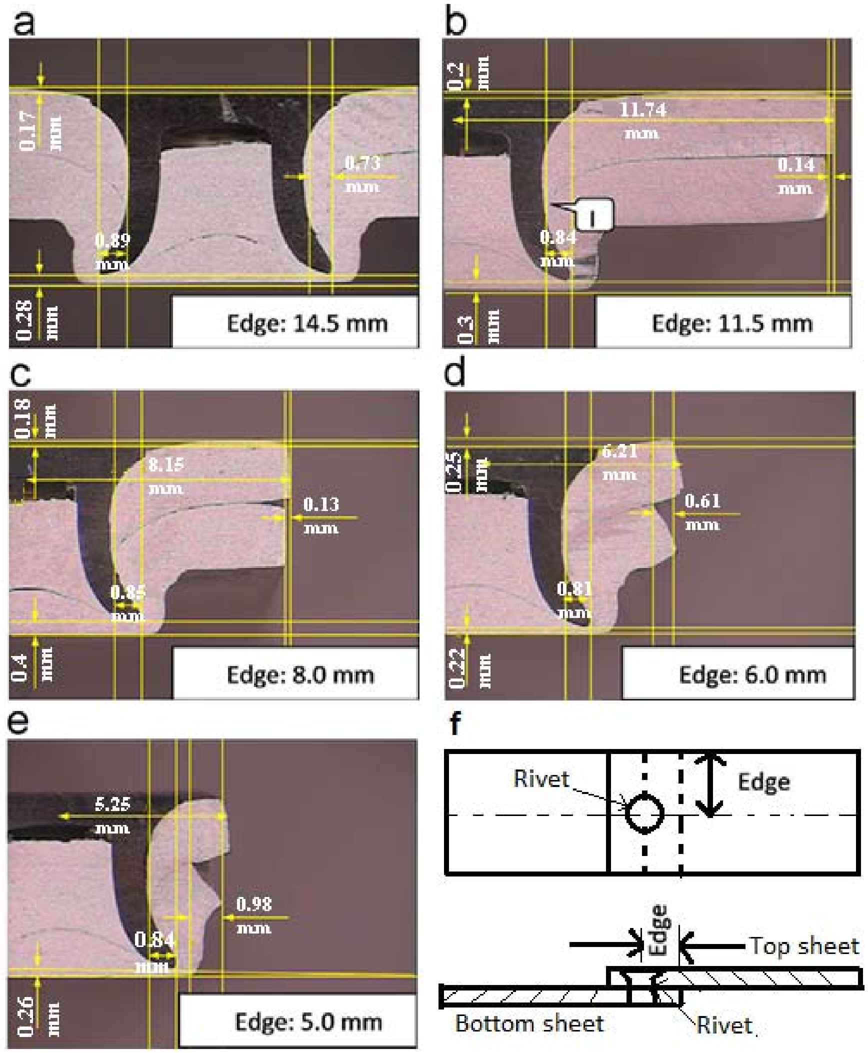

Fig. 2.6.1 Joint cross-section depending on edge distance [111].

The addition of a coating, adhesive and lubricant can effectively change a friction coefficient, and thus affect the quality [70, 112]. The effect of a coating on the quality parameters (setting pressure, head height, interlock and remaining bottom thickness, as shown in Fig. 2.3.1) of an aluminium joint are summarized in Table 2.6.1 [70]. The coating thickness can be reduced by using a polyester coating or cadmium plating and the selection of coating obviously depends on surface appearance, cost and availability [13]. In order to achieve satisfactory joint results, the SPR process needed different setting parameters for uncoated and coated sheets [113]. The presence of a lubricant coating could delay the onset of fretting damage leading to longer fatigue life [67, 114]. The addition of adhesive can greatly improve the performance of a SPR joint [115-117]. However, optimization of rivet and die geometry as well as riveting pressure is required when an adhesive is used in SPR [118].

Table 2.6.1 Measurement results for coated and un-coated specimens [70].

Condition	Top / Bottom sheet	Die diameter (mm)	Specimen	Head height (mm)	Interlock (mm)	Remaining material (mm)
1	1.8 mm NG 5754 / 1.2 mm HSLA	9	E-coated/ Un-coated	0.03/0.08	0.47/0.34	0.05/0.29
2		10	E-coated/ Un-coated	0.05/0.08	0.30/0.25	0.24/0.28
3	2 mm NG 5754 / 2.5 mm HSLA	9	Zn-plated/ Un-coated	-0.10/-0.08	1.07/0.91	0.22/0.59

In SPR two types of dies are used: flat and profiled. For a flat die, diameter and depth are considered as the process parameters [119]. However, in profiled dies, two additional parameters are considered along with diameter and depth: height of the die pip and sharpness of that pip [120]. A schematic of die parameters is shown in Fig. 2.6.2.

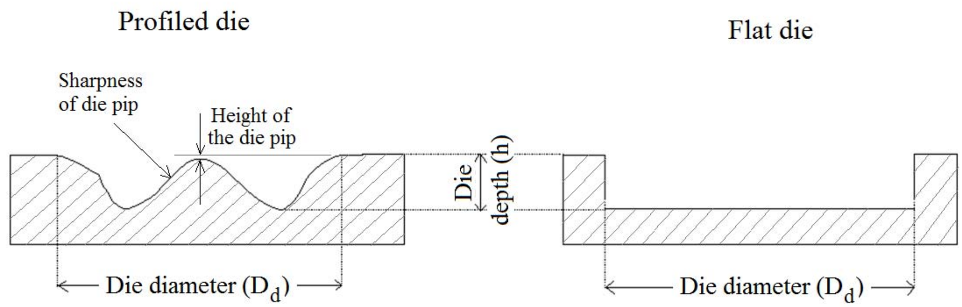

Fig. 2.6.2 A schemaric of different dies

The SPR process can be optimized by changing the die parameters [121]. A proper die can greatly increase the join-ability by increasing the rivet spread ratio (RSR) and reducing cracking in the bottom sheet [122]. RSR is defined as the ratio of deformed and initial rivet diameter ($RSR = \frac{D_t}{D_0}$ in Fig. 2.3.1). A high central pip of the die makes the specimen stiffer, thus an increase in force is observed [16, 80]. The rivet flaring increases with the central pip height but at the same time the possibility of cracking at the die side increases [123]. So it is suggested that when the height of the die pip increases a reduction of sharpness of that pip is necessary [124, 125].

The punch pressure and speed greatly influence the SPR quality. Excessive pressure may lead to a crack in the joint and too low pressure may lead to an incomplete joint [126]. The riveting pressure should be determined by several factors: die profile and depth, material hardness and thickness, rivet hardness and length, and the finished head height required [78]. The punch speed can change the geometrical shape of a joint because at high speed dragging of the top sheet is greatly reduced [59].

The parameters that can affect the quality of a joint are summarized in Fig. 2.6.3. However, the C-frame deflection also influences the quality and it is necessary to investigate the effect of C-frame deflection on joint quality [1].

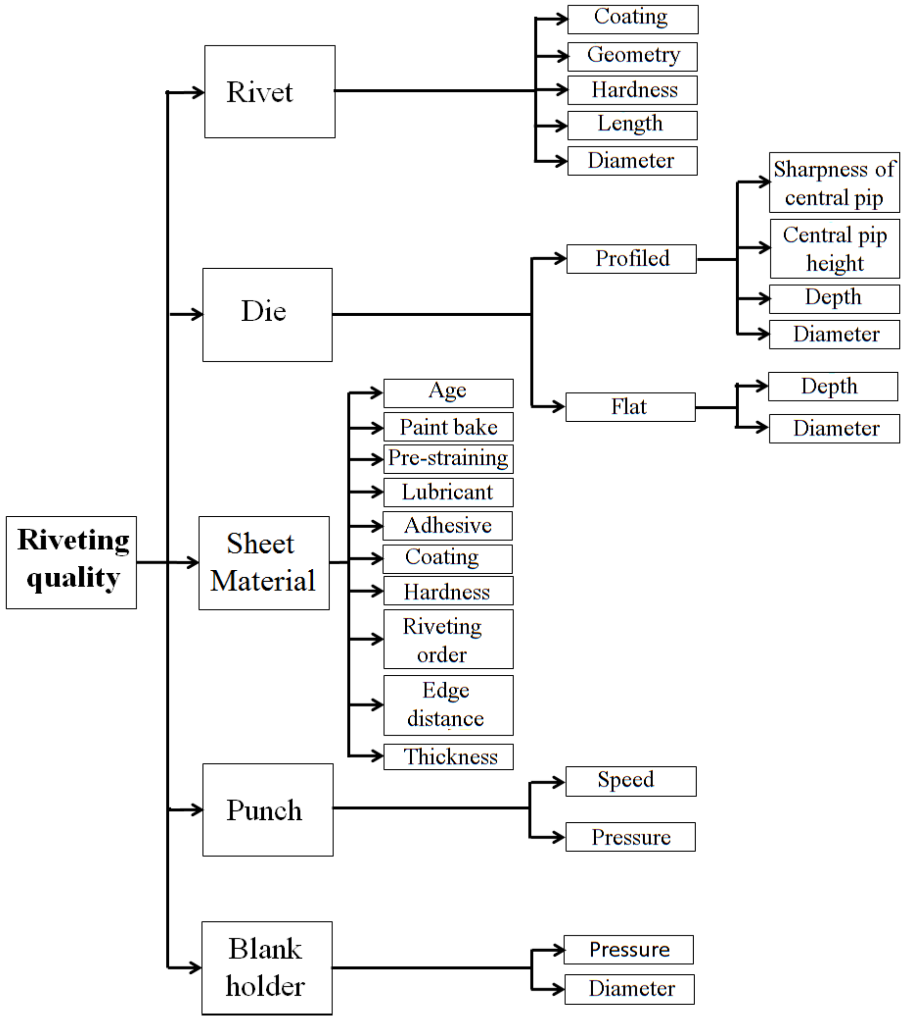

Fig. 2.6.3 Factors that can affect the quality of a SPR joint

2.7 Assembly distortion

The SPR process requires significant plastic deformation of material, especially at the bottom sheet. As a result, distortion occurs during the process. An examination by Cai et al. [17] of the assembly distortion due to a single riveted joint is shown in Fig. 2.7.1. The material was aluminium alloy AA 5754 with different thicknesses from 1 mm to 5 mm, and rivet lengths ranged from 3 mm to 9 mm. The results showed that the distortion was higher at the top sheet compared with the bottom sheet. However, the amount of distortion was negligible at a distance of 50.4 mm (2 inch) from the rivet. A semi empirical model with experimental distortion as an input during the design stage was used to predict the global distortion for an aluminium rear door sub assembly by Cai et al. [17].

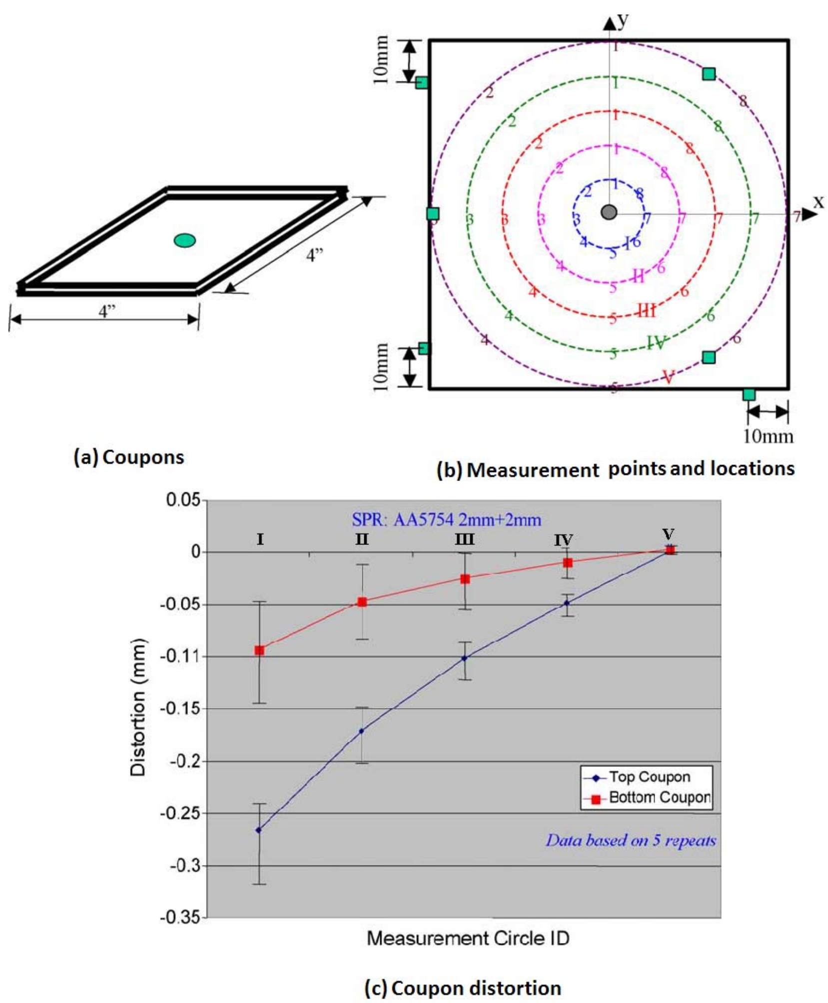

Fig. 2.7.1 Assembly dimensional prediction of a single riveted joint [17].

It was suggested that the dimensional accuracy of a global assembly due to the local distortion should be addressed [73, 127]. A finite element model was used to determine the distortion in the global assembly by Mastres et al. [128] and the direction of the distortion was predicted successfully. The distortion depends on a number of design and process factors, including die volume, rivet length and gauge combination [17]. However, clamping force (depends on the diameter and pressure of the blank holder) was found to be most influential in reducing the distortion to zero, as shown in Fig. 2.7.2, and the sheet size (width and thickness) has a minor effect [99].

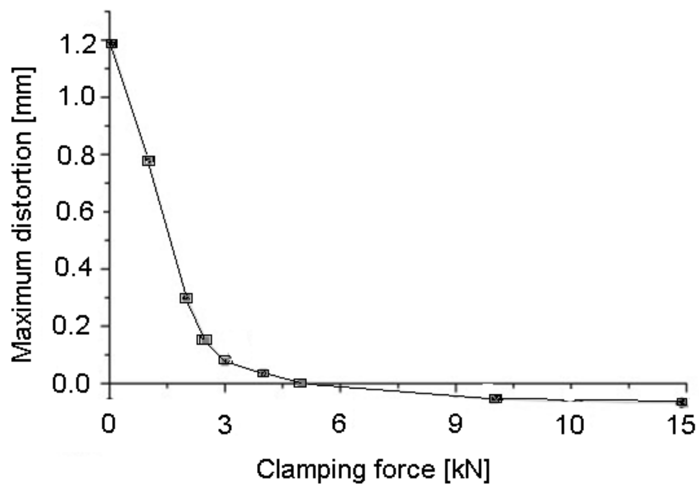

Fig. 2.7.2 Assembly distortion depending on clamping force [99].

2.8 Join-ability

SPR technology is capable of joining a vast range of dissimilar materials. SPR joining of magnesium, aluminium, mild steel, advanced high strength steel, carbon fibre reinforced polymer (CFRP), basalt fibre reinforced polymer (BFRP) and light weight polymeric cored laminate (Hylite LSS) sandwich has been investigated [62, 64, 122, 129, 130]. The definition of defects is shown in Fig. 2.8.1a and a joint is called good when the fastening does not have any of these defects [131].

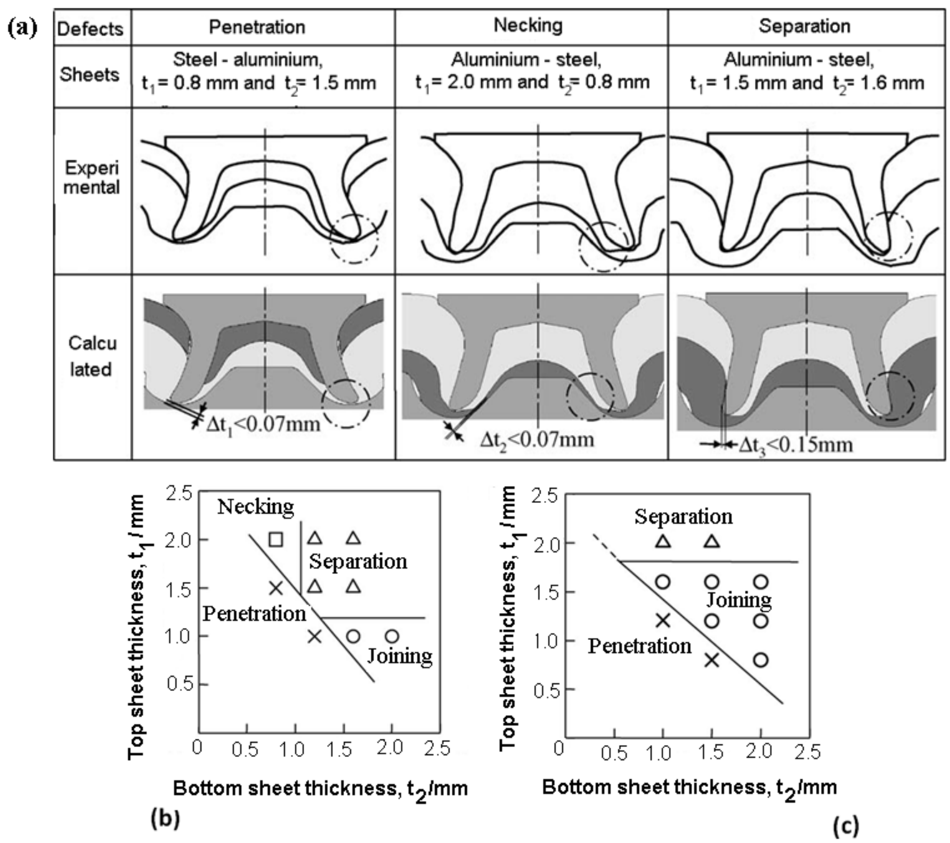

Fig. 2.8.1 (a) Definition of defects, (b) aluminium to steel and (c) steel to aluminium join-ability [131].

A join-ability experiment was conducted by Abe et al. [121, 131, 132] and the joining experiment was conducted on ultra-high strength steel with aluminium and the thickness ranged from 1 to 2.5 mm. Penetration through the bottom sheet occurred for small total thickness and long rivet, and necking of the bottom sheet occurred for thin bottom sheet [121]. The join-ability is plotted as a function of top and bottom sheet thickness in Fig. 2.8.1. It is clear that the join-ability increases when the softer sheet is placed on the die side and it is suggested that the harder sheet should be placed on the top [71, 131]. However, this suggestion is in contradiction with the industry rule of thumb [18, 46], and Bouchard [133], Chenot [134], Huang [135] and co-authors, who suggested placing the harder sheet on the die side. However, die optimization is required to improve the join-ability [121]. The join-ability and performance can also be enhanced by optimizing the rivet length [136].

2.9 Static strength

The strength of a SPR joint depends on many factors such as the width, thickness and material properties of the joining sheets and properties of the die and rivet [137-139]. The strength also depends on loading condition, joining orientation of single and double rivets, and width of the specimen [140-142]. Each of the parameters that affects the static strength is described below.

2.9.1 Loading condition

The loading condition is the first parameter that affects the strength of a SPR joint [143]. Five different loading conditions were identified for a single point riveted joint: coach-peel, cross-tension, lap-shear (also known as tensile-shear), pure shear and push-out (Fig. 2.9.1). Among these, the strength was lowest for the push out test and highest for the pure shear condition [1, 136]. In the lap-shear condition the bearing load was mainly transferred by the rivet but in cross-tension the bearing load was mainly transferred by the shearing between the rivet leg and materials [67, 136]. As a result the energy absorption and load were higher for lap-shear than cross-tension. The coach-peel strength was even lower than in cross-tension as rivet rotation occurred due to the bending moment. The same behaviour of strength is followed for a three-sheet SPR joint (Fig. 2.9.2).

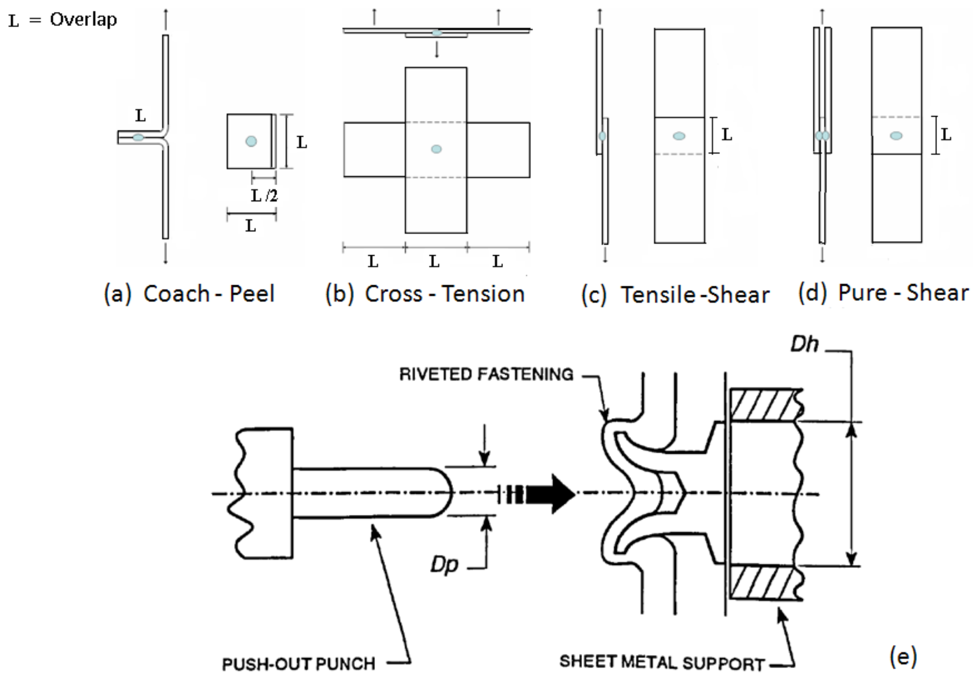

Fig. 2.9.1 All possible loading condition for static strength examination (a) coach-peel, (b) cross-tension, (c) tensile-shear, (d) pure-shear [144], (e) push out [1].

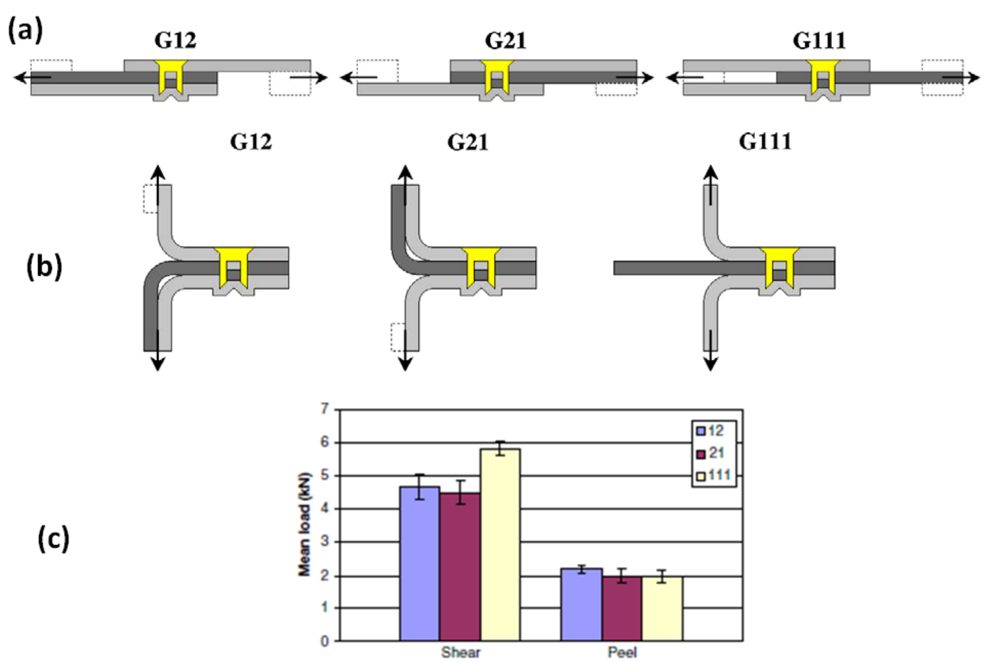

Fig. 2.9.2 (a) Lap-shear (b) Coach-peel loading condition and (c) Joint strength depending on the loading condition and joint configuration [137].

2.9.2 Joint design

All the possible joining design for single and double riveted joints are shown in Fig. 2.9.3. The strength of a double riveted joint was no better than a similar single-rivet joint for the same value of applied stress per rivet [145]. For a double riveted joint (length-wise), the highest strength is exhibited when the rivet heads are close to the loading ends, 'Type B' as shown in Fig. 2.9.3e. Rivet pitch influences the strength of a double riveted joint (both length-wise and width-wise). The strength of the joint was highest when the rivet pitch equals half of width and half of overlap for width-wise and length-wise double riveted joints, respectively [111, 140, 146]. However, these conclusions are only for the similar material (AA 5754) with or without different thicknesses. For the double riveted joints, the rivets are placed in the middle of the width in the length-wise orientation (Fig. 2.9.3d), but in the width-wise orientation (Fig. 2.9.3c) the rivet pitch was varied by changing the edge distance. The strength of the joint was highly dependent on the edge distance. An optimum edge distance of 11.5 mm (half of the pitch) was suggested to achieve a good performance and a minimum edge distance of 8 mm (outer radius of die) was required to maintain a reasonable fatigue resistance [140].

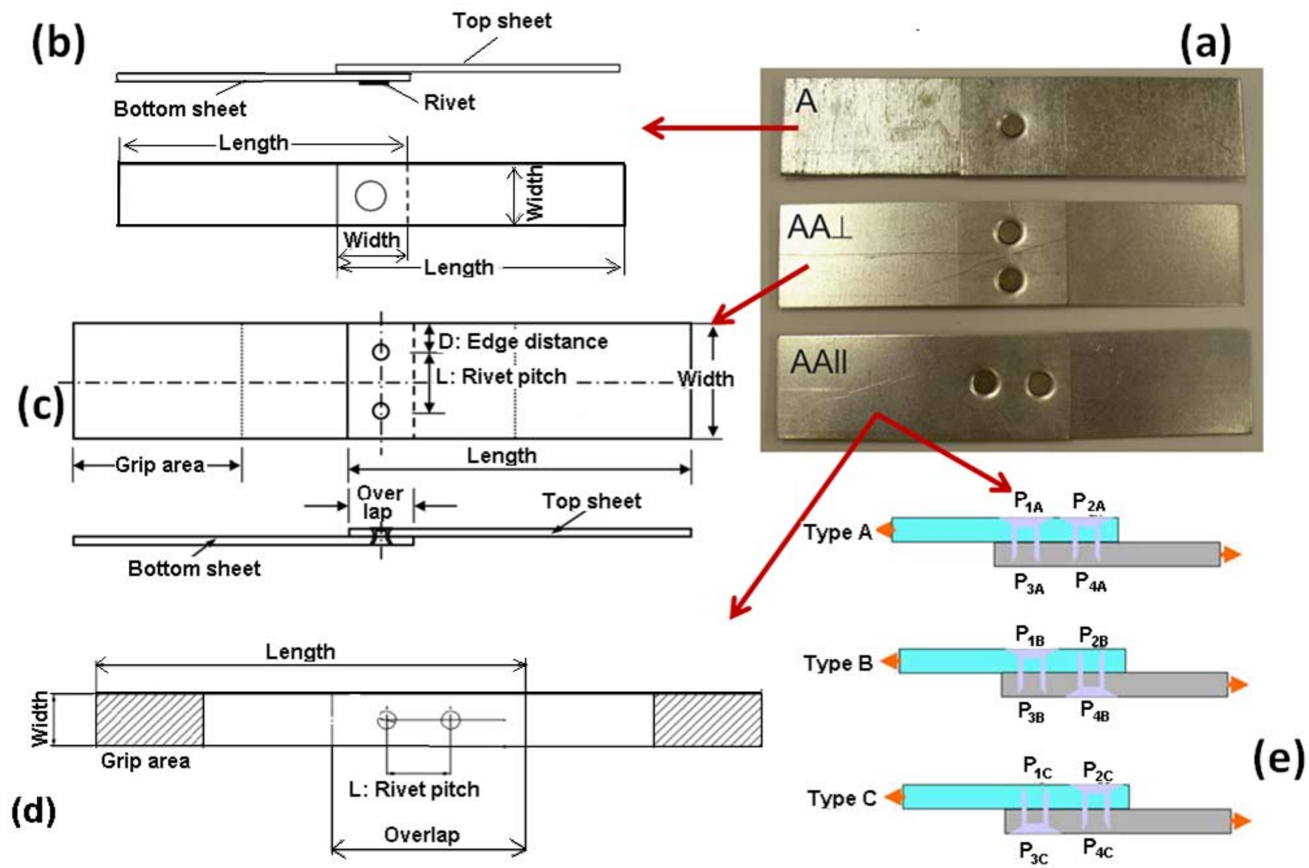

Fig. 2.9.3 All possible joining orientation for single and double rivet in lap-shear loading condition (a) experimental [141], (b) schematic of single riveted joint , (c) Schematic of double riveted joint in width-wise [111], (d) schematic of double riveted joint in length-wise [147] and (e) schematic of double riveted joint in length-wise with different piercing direction [145].

2.9.3 Width sensitivity analysis

In spot welding the failure mode depends on the width of the specimen. Zhou et al. [148] studied the width sensitivity analysis and concluded that for a fixed weld diameter the probability of getting a desired failure mode depends on the width of the specimen (Fig. 2.9.4c). A schematic of undesirable failure mode is drawn in Fig. 2.9.4b. This is undesirable because sheet fractured occurred instead of failure in the joint button [148].

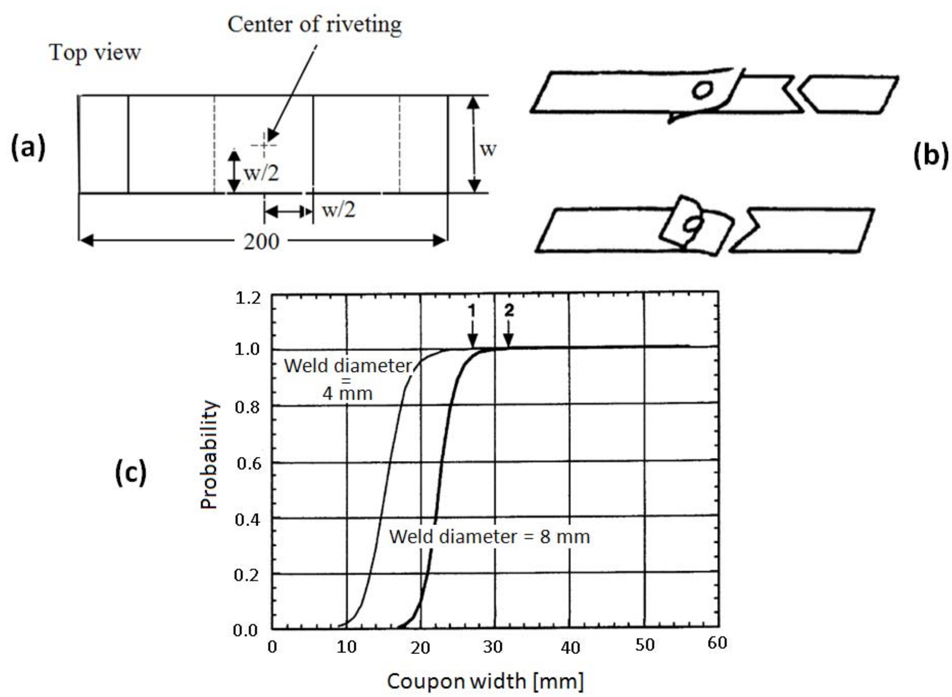

Fig. 2.9.4 (a) Width sensitivity analysis [68], (b) undesired failure mode [148] and (c) probability of getting desirable failure modes. Marks 1 and 2 indicate the (minimum) widths to achieve desirable failure modes for welds with 4 and 8mm diameters [148].

Xu [68] examined the effect of specimen width on SPR joint strength in lap-shear loading (see Fig. 2.9.4) and found that if the specimen width lies between 30 mm and 150 mm (the length of the specimen) the probability of giving a desired failure mode is 100% and in all other cases the joint would show an unexpected failure mode . If the width is too small compared with the length (150 mm) the chance of absorbing the impacted energy is less, which may lead to undesirable failure mode (see Fig. 2.9.4). The author [68] suggested an overlap equal to the width of the specimen in order to obtain a good result. A literature survey shows that different researchers used different lengths, widths and overlaps. The specimen sizes for the static strength used by different authors are summarized in Table 2.9.1. However, most of the authors maintained the overlap equal to the width.

Table 2.9.1 Specimen sizes for single point lap-shear condition

Length (mm)	Width (mm)	Overlap (mm)	Reference
200	50	80	[149]
		50	[62]
	25	90	[147]
192.5	60	45	[67, 105, 150]
152.5	29	25	[106, 151]
150	50	50	[22, 24, 25, 109, 136, 152]
135	36	36	[66]
125	40	40	[110]
122.5	60	45	[114, 153, 154]
120	30	30	[1]
114.3	25.4	31.75	[13]
111.5	48	23	[111, 140]
110	20	20	[83]
105	45	20	[100, 155]
104.78	34.93	31.76	[79]
100.2	25.4	25.4	[91, 156]
100	40	40	[81, 141]
		30	[4, 70, 137]
	30	30	[74, 75, 157]
	28	40	[58]
	25	50	[64, 146, 158, 159]
		25	[160, 161]
	20	15	[26]
90	40	30	[103]
80	38	20	[123, 162]
62.5	25	25	[163]
59	38	38	[33]
52.5	48	20	[67]

2.9.4 Failure mode

The failure mode of an SPR joint is basically pull-out of the rivet either at the top sheet or the bottom sheet [74, 136]. However, a closer look demonstrates that tilting of the rivet occurs as well with the rivet pull-out [164-167]. In some cases failure occurred in the sheet material [111, 140, 156]. Examples of different failure modes are shown in Fig. 2.9.5.

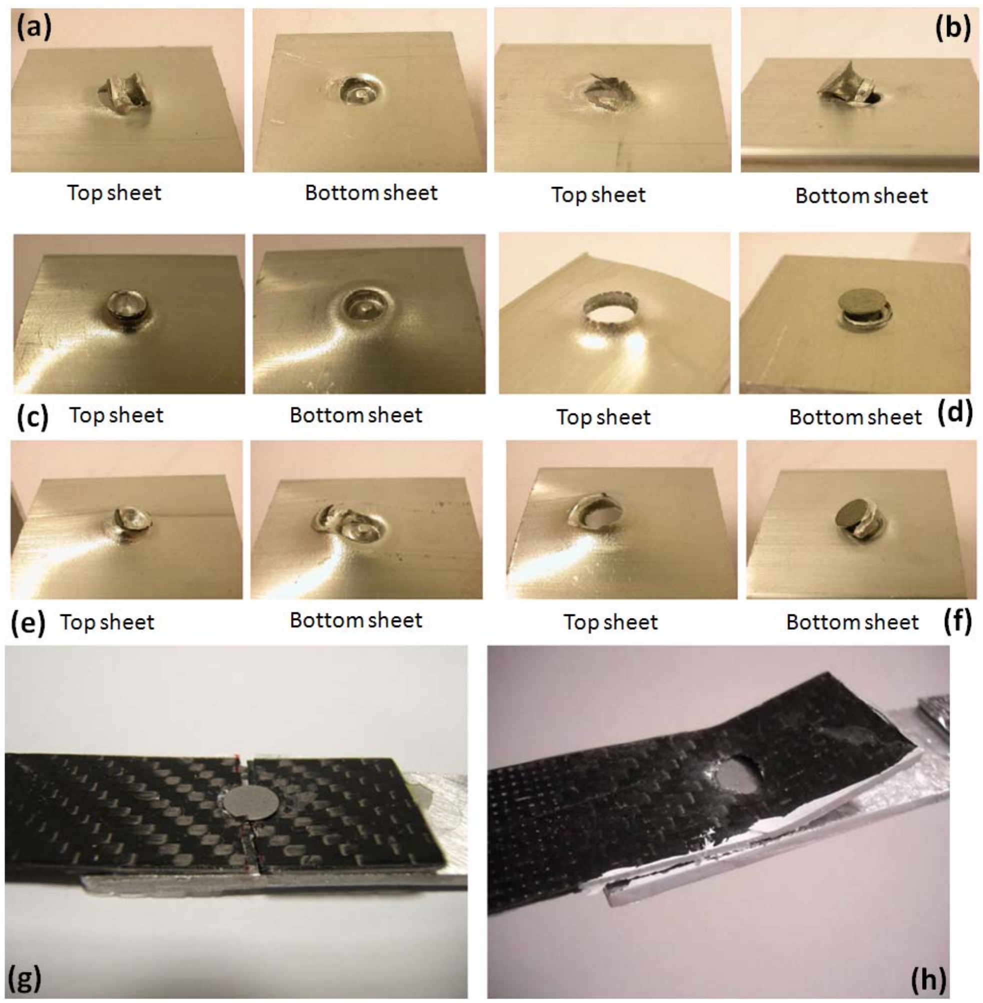

Fig. 2.9.5 Different failure modes (a) Tilting and pull-out of the rivet from the bottom sheet with additional pull out of the rivet head from the top sheet [166], (b) Tilting and pull-out of the rivet head from the top sheet [166], (c) Pull-out of the rivet from the bottom sheet [166], (d) Pull-out of the rivet from the top sheet [166], (e) mixed failure of (a + c) [166], (f) mixed failure of (b + d) [166], (g) failure in the top carbon fibre sheet [64] and (h) pull-out of the rivet from the top sheet with fracture in the sheet [64].

The failure mode changes for various reasons: static or fatigue loading [121], coating and lubricant on sheet material [113], width of the specimen [68] and sheet material properties [168]. The failure mode changes from tail pull-out to head pull-out when a fatigue load is applied instead of a static load [121] or when a very thin top sheet is used [168]. Material failure occurs instead of tail pull-out when a fatigue load is applied [146]. However, the opposite phenomenon is observed (the failure mode changes from material failure to pull-out) when heat is applied prior to riveting [49, 50]. The fibre orientation of CFRP laminate can change the failure mode: material failure occurred in cross ply fibre orientation and pull-out failure occurred for angle ply fibre orientation [64]. A failure map has been developed by Calabrese et al. [160] with respect to the top sheet thickness. Occasionally, rivet failure occurs when a very soft and long rivet is used or when the riveting pressure is too high [67, 169].

2.9.5 Joint strength prediction

Sun and Khaleel [136] have studied the rivet joint and proposed an empirical equation to estimate the static strength of the joint in cross-tension loading assuming that the rivet periphery was under perfect axisymmetric loading just before failure. They also assumed that sufficient interlock had been achieved during the riveting process. Equations (2.9.1) and (2.9.2) are their proposed equations.

$$F_h^T \approx \eta_h \beta_h t_1 \pi\, D_h \sigma_h \tag{2.9.1}$$

$$F_t^T \approx 0.7 \eta_t \beta_t t_{eff} \pi\, D_t \sigma_t \tag{2.9.2}$$

where F_h^T and F_t^T are the joint strength for head pull-out and tail pull-out failure, respectively. η_h and η_t are empirical coefficients of material degradation due to piercing process for the head and tail sides, respectively. β_h and β_t are empirical coefficients of the thickness reduction for head and tail side materials respectively (Fig. 2.3.1). Nine different cases consisting of different thicknesses and grades of aluminium and steel were examined to validate this strength estimator. The static tensile strength was determined by the lower value of F_h^T and F_t^T, which can be expressed as:

$$F^T = \min(F_h^T, F_t^T) \tag{2.9.3}$$

A different approach was taken by other researchers to estimate the joint strength [167, 170, 171]. They followed the design formulae proposed by Eurocode 9 (prEN1999-1-4) [172] based on the theoretical background of failure of joints. Their proposed equation is of the form:

$$F^T = \alpha_T \times \sigma \times \sqrt{D \times t^3} \tag{2.9.4}$$

where F^T is the joint strength, α_T is the empirical coefficient for the tensile loading, σ is the ultimate tensile strength, D is the initial undeformed rivet diameter and t is thickness of the top and bottom sheet for head and tail pull-out, respectively. Another different approach to strength estimation, depending on the head height (Y in Fig. 2.3.1) was studied by Matsumura et al. [31]. They used 1.3 mm aluminium (AA 6000 series) as the top sheet, 0.65 mm soft mild steel as the middle sheet and 1.2 mm high strength steel (yield strength 590MPa) as the bottom sheet. They concluded that for a large head height (Y) the failure mode is head pull-out and the strength is low. The strength increases with a decrease in head height to a certain limit. The strength decreases for further reduction in head height and the failure mode changes from head pull-out to tail pull-out.

2.9.6 Effect of sheet material properties

Sheet material properties play a very important role on the static strength of a riveted joint. Rivet head pull-out occurred for a thin top sheet while tail pull-out occurred when the top and bottom sheets were of same material and thickness [121, 136, 168]. A failure map is proposed by Calabrese et al. [160] focussing on the top sheet thickness, as shown in Fig. 2.9.6. They used aluminium alloy (AA6082) of four different thicknesses (1, 1.5, 2 and 3 mm). A 6.5 mm rivet (460 HV) was used to join a stack thickness of 3 and 4 mm. The specimens were aged for 60 days using an automated immersion tank. The ageing conditions were controlled at a temperature of 27ºC with a relative humidity of 45%. The materials were cyclically exposed to air for 50 minutes and then immersed in NaCl solution (3.5%) for 10 minutes. Failure in the sheet occurred for a very thin top sheet, head pull-out occurred with a thin top sheet, and tail pull-out occurred for a thick top sheet. However, the failure mode changes due to ageing of materials because of softening, which ultimately affects the magnitude of the joint strength [160]. A reduction in joint strength was observed due to the paint-baking of material [67].

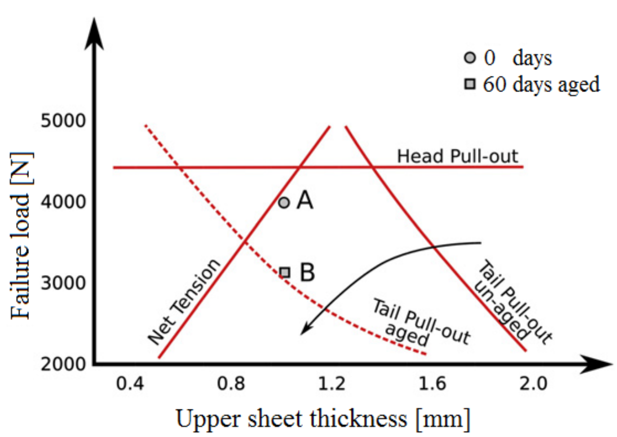

Fig. 2.9.6 Simplified failure map for net-tension and pull-out mechanisms for lap-shear loading condition: corrosion effect [160].

2.9.7 Effect of piercing direction

The joint strength can be optimized by changing the piercing direction [132, 173]. Sun and Khaleel [109, 136] have studied a joint of 2 mm Al 5182-O and 1 mm HSLA 350 with a 6 mm long rivet (480HV). The joint strength was increased from 2.9 kN to 4.9 kN when the 1 mm steel was placed on the top instead of bottom. For the same material combination and same rivet, having the harder material on the riveting side (where the rivet head is situated) gave higher strength [152, 174]. When the soft material is placed in the die side (A5052-H34 + Mild steel SPCC joint) a much better clinched structure is achieved, which improved the joint strength [121, 131]. For the same material combination (AA 5754) placing the thicker sheet on the top (2 + 1 mm joint) can absorb more energy [68]. However, the piercing direction depends on the accessibility of the riveting C-frame in the industrial environment.

2.9.8 Effect of rivet properties

Fu and Mallick [91] reported the effect of rivet hardness on the strength of a SPR joint. By analysing variance (ANOVA) they found that the contribution of the rivet hardness to the strength of the joint was only 4.53%. In their experiments they used 4 and 5 mm long rivets for joining 1 + 1 mm Al 5754-O and 6 and 6.5 mm long rivet for joining 2 + 2 mm Al 5754-O. However, they considered only three levels of hardness: normalized (rivet as produced, without any heat treatment), 410HV and 480HV. A long rivet with a large diameter can absorb more impact energy [68, 109]. Xu [68] in her thesis examined the effect of rivet parameters (diameter and length) on joint quality and strength. Aluminium alloy AA 5754 was used with four different thicknesses (1, 2, 3 and 4 mm) and a 480 HV rivet was used. A 3.3 mm diameter and 5 mm long rivet was used to join 1 + 1 mm, 1 + 2 mm, 2 + 1 mm and 2 + 2 mm joint. Again a 5.3 mm diameter rivet with two different lengths (5 and 6.5 mm) was used to fasten 1 + 1 mm, 1 + 2 mm, 2 + 1 mm and 2 + 2 mm joint. A significant increase in joint strength was observed for the larger diameter and long rivet. Sun and Khaleel [109] optimized the performance of the riveted joint by increasing the rivet length. They used a 480 HV rivet to join 2 mm AA5182-O (top sheet) + 1.6 mm DP600 (bottom sheet) with two different lengths (6 and 6.5 mm). The joint strength was increased from 3.7 to 5.3 kN for the 6.5 mm rivet. However, a longer rivet requires more volume to be displaced, which can affect the residual stress developed inside the joint and ultimately affect the joint strength [96, 97, 134].

2.9.9 Effect of die profile

Die volume and shape greatly influence the energy absorption and strength of a joint [68, 69, 81]. Rivet spread ratio increases as die diameter increases and die depth is reduced for bulk aluminium specimens, as a result, the strength increases [67, 122, 155]. A very limited amount of literature is available that investigates directly the joint strength depending on die profile. This is due to the fact that an inappropriate die can cause crack failure in the bottom sheet during the joining.

2.9.10 Effect of adhesives

The use of adhesive with SPR produces optimum joint performance and is known as a hybrid joint [3, 4, 63]. The combination of SPR with adhesive is also known as riv-bonding [4]. Typically a single-part heat-curing toughened epoxy is used as adhesive and the curing is carried out during the paint bake cycle [2]. The adhesive layer becomes dominant in shear loading and the SPR gives the interlock [4, 18]. Briskham et al. [4] studied the effect of adhesive on joint strength of 3-ply (2.0 mm 5754-O + 1.5 mm 5754-O + 2.0 mm 6111-T4P) and 4-ply (2.0 mm 5754-O + 1.5 mm 5754-O + 1.8 mm 5754-O + 2.0 mm 5754-O) SPR joints in lap-shear loading. They used single-part epoxy adhesive (Dow-Betamate 4601) and the adhesives were cured at 180ºC for 25 minutes, which represents a typical paint-bake cycle used in automotive industries. The joint strength increased significantly (more than double) due to the addition of adhesive in both cases.

Durandet et al. [54] suggested that adhesive may be used in conjunction with the laser assisted SPR because of very low radial variation of temperature from the centre to the edge of the heated spot produced by the laser beam. The adhesive improves the joint quality even when it is used in the joining of composites [62, 64].

Fiore et al. [62] presented the influence of adhesives in joining of basalt fibre reinforced polymer (BFRP) with aluminium. In their investigation, two different thicknesses of BFRP (2.12 mm when fabricated by hand-lay-up technology and 1.33 mm when fabricated by vacuum-bagging technology) was used as top sheet and 2 mm AA6082-T6 was used as a bottom sheet and a 6.5 mm long rivet was used to join them. Epoxy resin (SP 106) was used as adhesive and the curing was conducted at 25ºC with a relative humidity of 40% for 48 hours. A significant increase in joint strength was observed due to the addition of adhesive.

Similar results were obtained by Franco and co-authors [64] when joining carbon fibre reinforced polymer (CFRP) with aluminium. In their experiments they used a 6.5 mm rivet to join 1.5 mm CFRP with 2.7 mm AA2024-T6. The epoxy was I-SX10 and cured at 25ºC with a relative humidity of 30% for 24 hour.

The joint strength was increased by 64% when adhesive was used in conjunction with SPR. However, in the crushing test (velocity of 5.8 m/s), the addition of adhesive does not make any significant difference [175]. They used two part methacrylate (PLEXUS® MA822) as structural adhesive and a 5 mm long rivet was used to join 1 mm SPCEN (cold rolled coil) with 1 mm Al 5J32-T4. The curing was conducted at room temperature (25ºC) for 15-20 minutes.

Sun and Khaleel [152] concluded that the inclusion of structural adhesive dramatically increases the joint strength for both static and dynamic loading especially in the lap-shear condition. They made three different joints (2 mm Al

5182-O + 1 mm HSLA 350, 1 mm HSLA 350 + 2 mm Al 5182-O and 2 mm Al 5182-O + 1.6 mm DP 600 with 5, 5 and 6 mm long rivet respectively) with Dow Betamate 4601 as structural adhesives and the strength examination was conducted at three speeds; static (strain rate of $10^{-4}s^{-1}$), 4.47 m/s and 8.94 m/s.

The load-displacement curve of a hybrid joint showed a different shape as the failure of the adhesive layer occurred in a brittle manner [118]. However the addition of adhesive requires optimization in die and rivet geometry and rivet setting pressure [65, 176]. It is suggested that the adhesive layer should be controlled properly to 0.1 mm thickness [118]. In general, the addition of adhesive increases the joint strength of SPR in any loading direction [177, 178].

2.9.11 Dynamic behaviour

The effect of test speed on a joint's ductility and peak strength can be obtained by a dynamic joint strength test. The mechanical behaviour of metals differs from quasi-static to high strain rate loading [152, 173]. A comparison of load vs. deformation curves for static and dynamic behaviour in the lap-shear condition for a joint of 1.0 mm HSLA 350 + 2 mm AA 5182-O is shown in Fig. 2.9.7a. The joint strength increases with the increase in test speed from static to 4.47 m/s (10mph). No further increase of strength is seen from 4.47 m/s (10 mph) to 8.94 m/s (20 mph), although displacement to failure decreased with increased test speed throughout this range [152].

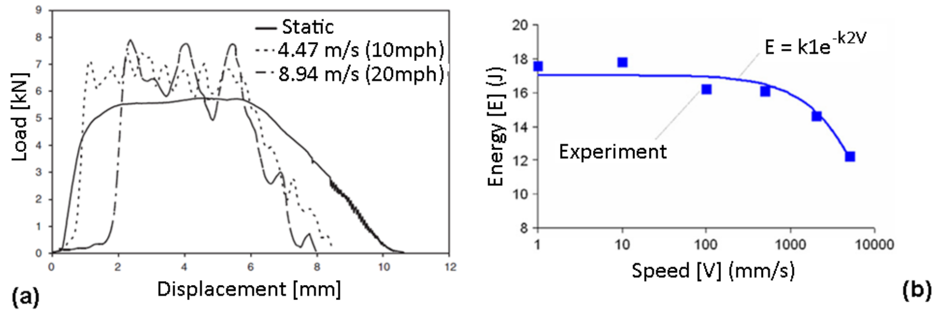

Fig. 2.9.7 (a) Dynamic behaviour of SPR joint depending on loading speed [152] and (b) relationship between energy and speed [151].

Tileli [72], Porcaro [179], Presz [180] and co-authors found that the peak load was similar in both the static and dynamic condition but the average load was reduced in the quasistatic condition. A correlation was developed between the energy absorption and the speed by Wood et al. [151] as shown in Fig. 2.9.7b. The joint was created by 2.5 + 2.5 mm aluminium alloy (A 5754) with a 7 mm long rivet having a hardness of 410 HV. The dynamic strength examination was performed at 5 different speeds (0.01, 0.1, 0.5, 2 and 5 m/s). The joint strength was practically constant below the speed of 0.5 m/s. The reduction of joint performance at high speed was attributed to the lowering of frictional force between rivet and sheet material because the friction decreases with the increase in sliding speed [151].

2.10 Fatigue strength

SPR is considered to be an alternative to spot welding. After much research in this area it is believed that SPR gives joints of comparable static strength with superior fatigue behaviour to spot welding [14, 47, 181]. All the factors that affect static strength also affect fatigue strength [161, 182]. Additionally, maximum load and load ratio ($R = \frac{P_{min}}{P_{max}}$) and fretting wear affect the fatigue life of a SPR joint [114, 154, 156]. Different aspects of fatigue life are described in the following sections.

2.10.1 Crack initiation and propagation

To understand the fatigue characteristics of a SPR joint it is necessary to identify the crack initiation and propagation path. Khanna et al. [161] examined the fatigue behaviour of the SPR joints of aluminium sheets (5754-O) of different thickness (1+1, 1 + 2, 1 + 3, 1.5 + 1.5, 2 + 2 and 2.5 + 2.5 mm) for both coach-peel and tensile shear conditions with a tensile-tensile force and testing frequency of 5 Hz with two different load ratios (0.1 and 0.3). The maximum load was 450 and 571 N for load ratios of 0.1 and 0.3, respectively. For the same stack thickness, most of the failure occurred at the top sheet (with the rivet head), but failure occurred at the bottom sheet when this sheet was thin. Two possible sites of crack initiation were observed: the interface between top sheet and rivet head and the interface between top and bottom sheets. This could be the reason for the frequent failure in the top sheet. While for a thin bottom sheet, failure occurred in the bottom sheet because of its low tensile strength. The fatigue crack propagation path is shown in Fig. 2.10.1a [161] where the crack initiated first from the location mark **X** (the interface between top sheet and the rivet), rather than from **Y** (the interface between top and bottom sheet). However, other study [156] showed that the crack initiated from the location 'Y' as shown in Fig. 2.10.1b. Li et al. [111] demonstrated that multiple crack may be initiated, as shown in Fig. 2.10.1c.

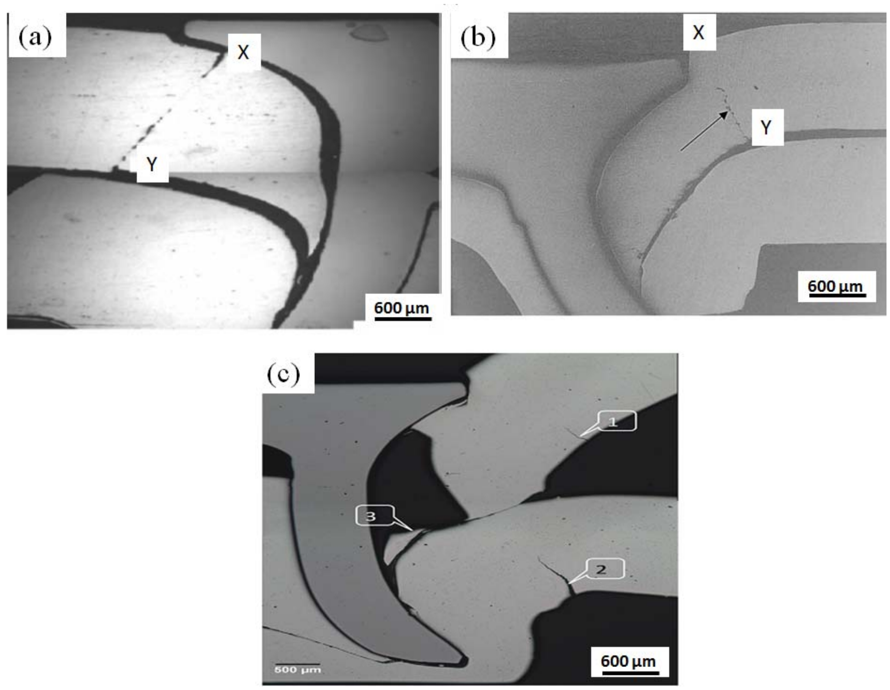

Fig. 2.10.1 Crack initiation and propagation path in fatigue with load ratio R=0.1 (a) 1 + 1 mm AA6111 joint with a load of 2000 N after 2.4 x 10^4 cycles [161], (b) 2 + 2 mm AA5754 joint with a load of 810 N after 5792 cycles [156] and (c) 1 + 1 mm AA6111 joint with a load of 1650 N after 2.91 x 10^6 cycles [111].

2.10.2 Fretting fatigue

Fretting occurs at a very low level of load in fatigue [142, 145]. According to Han and co-authors [150, 153, 154] fretting took place at the adjoining surfaces between rivet and the two sheets, and fatigue crack tends to initiate at fretting areas as shown in Fig. 2.10.2 with intimate mixing of debris occurring at critical zones. They observed flange-face fretting at the interface between the sheets and pin-bore fretting at the interface between rivet and two sheets.

Han [67] studied the effect of paint-baking on the fretting behaviour of riveted joints of aluminium alloys for different thicknesses and material grades (2 + 2 mm NG 5754, 2 mm AA6111 + 2 mm NG 5754 and 0.9 mm AA611 + 2 mm NG 5754). The NG 5754 sheet was coated with a wax based lubricant with a concentration below 1%. Three different loads (2.7, 3.6 and 4.5 kN) were considered with a minimum load of 0.5 kN and the loading frequency was 20 Hz. The paint-baking process led to removal of the wax-based surface lubricant and fretting cracks therefore initiated at an earlier stage of the fatigue test and led to debris containing oxides, which contributed to the initiation and propagation of fatigue cracks [67].

Chen et al. [154] described the mechanism involved in the fretting wear of riveted joints of aluminium alloy (AA 5754) and the alloy was coated with wax based lubricant. In their experiment, they used a 7 mm long rivet to join 2 + 2 mm thick joint. The fatigue test was performed at the same condition described by Han [67]. Fretting took place at two locations: at the interface between the top and bottom sheet, and at the interface between rivet and bottom sheet. Several mechanisms contributed to the fretting damage: a ploughing process during the initial stage, followed by oxidation and then third body abrasive wear, and finally expansion of the fretting scar during steady-state behaviour [154].

Han and co-authors [67, 107, 150] studied the work hardening of materials due to fretting with an aluminium alloy joint (2 + 2 mm AA 5754). The fatigue tests were performed at five different load levels ranging from 2.7 kN to 4.5 kN at a frequency of 20 kHz and interval stops at different periods of time. They concluded that fretting led to work hardening at the surface of the riveted sheets. The depth of work-hardened area below the fretting interface after different periods of fretting represented the damage as a result of fretting fatigue.

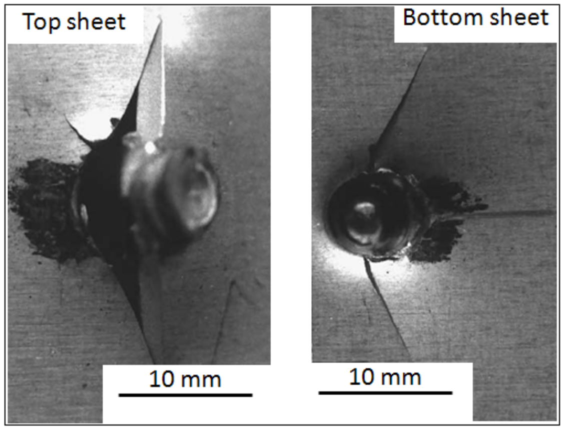

Fig. 2.10.2 Fretting scars and fracture on the interface between riveted sheets for 4.9×10^5 loading cycles at 3.6 kN in a joint of 2 + 2 mm AA 5754 [154].

The interfacial condition between the sheets influences the fretting properties. Three different interfacial conditions were examined by Han et al. [114] for the same material thickness (2 + 2 mm AA 5754 joint with 7 mm long rivet): lubricant-coated, plain surface and PTFE tape (0.2 mm) insert. A change in interfacial condition can have an effect on the friction coefficient. Friction coefficient was measured using a direct shear apparatus and the maximum friction coefficient was determined for the lubricant coated (μ=0.26) while the minimum was determined for the PTFE tape (μ=0.03), which is one order of magnitude less. On the other hand, the friction coefficient for the plain surface was found to be quite similar to that for the lubricant coated one, having a value of μ=0.24. The fatigue test was performed at five cyclic load levels ranging from 2.7 kN to 4.5 kN at 20 Hz. The result obtained from this experiment showed that, for the same maximum load, the overall fretting life increased with increasing friction co-efficient. The failure mechanisms were also examined and it was found that the lubricant coated and uncoated specimens failed in a similar way: at low load the specimen failed by fracture of the sheet, but at high load failure occurred due to rivet fracture [67, 114]. In contrast, rivet fracture was the only failure mechanism observed for the PTFE specimen. At low load levels, the energy was transferred to the sheet by the frictional force for lubricant coated and uncoated specimen, so the failure occurred in the sheets. It was proposed that for the lubricated specimen the energy was first used to remove the lubrication followed by wear of the sheets. For this reason lubricant coated gave a better fatigue life. In a joint, part of the cyclic load is transferred by friction and the rest is transferred by bearing between the rivet shank and the sheet adjacent to the rivet. When a fraction of load transferred by friction is reduced, the bearing load on the rivet increases, which leads to failure in the rivet [67, 114, 150].

2.10.3 Effect of material

The material properties have a similar effect on fatigue life as static loading: the fatigue life of a SPR joint increases with increased thickness of material, as shown in Fig. 2.10.3a [161]. The fatigue test was performed on an aluminium alloy (6111) joint with different thickness combinations (1+ 1, 1 + 2, 1+ 3, 1.5 + 1.5, 2 + 2 and 2.5 +2.5 mm) at 5 Hz with a maximum load of 571 and 450 N for load ratios of 0.3 and 0.1 respectively. For a joint of identical total thickness, the joint which had the same thickness of top and bottom sheets exhibited better fatigue performance. The load ratio ($R = \frac{P_{min}}{P_{max}}$) also influences the fatigue performance of a SPR joint. High load ratio resulted in longer fatigue life due to the joint rotation during fatigue test [161, 168]. The presence of lubricant coating could delay the onset of fretting damage leading to longer fatigue life [114].

In a cumulative fatigue test the sequence of loading is significant. Fu and Mallick [156] performed a cumulative fatigue test on an aluminium alloy (6111-T4) joint (1 +1 mm with 4 mm long rivet) at 20 Hz with 0.1 load ratio and the maximum load was either 1601.3 N or 1067.5 N. The fatigue test was interrupted at different periods (50, 75 and 90% of the fatigue life) and those specimens were tested in the static condition at a strain rate of 0.02 mm/s. When the high load level was applied first an improvement in fatigue life was observed due to the cyclic hardening of sheets [156].

Jin and Mallick [98] concluded that the fatigue life can be enhanced by coining. They conducted their experiments on aluminium alloy (5754-O) with six different thickness combinations (1 + 1, 1 + 2, 1 + 3, 2 + 2, 2 + 3 and 3 + 3 mm). The fatigue test was performed at 15 Hz and the load ratio was 0.1 with a variety of maximum fatigue stress ranges from 53.3 to 95.9 MPa. The coining was conducted by a MTS servo hydraulic machine with a circular groove having a width of 0.5 mm with two different inner diameters (10 and 12 mm).

Pre-straining of material can also improve the fatigue performance. Han et al. [107] studied a joint of 2 + 2 mm NG 5754 joint (made with a 7 mm long rivet) and the materials were pre-strained to three different levels (3, 5 and 10%). The fatigue test was performed at 20 Hz with a range of maximum load from 2.7 kN to 4.5 kN. For each condition the minimum load was kept at 0.5 kN. They concluded that increasing pre-straining led to a better fatigue performance due to the reduction in the fretting scar.

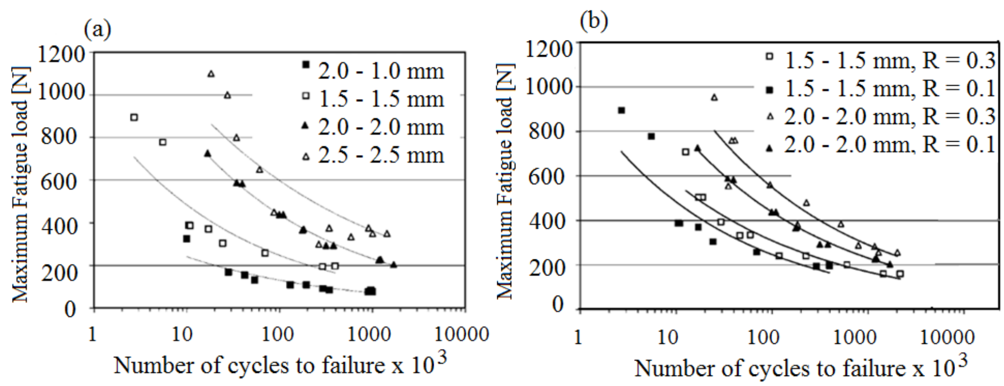

Fig. 2.10.3 Fatigue load depending on (a) material thickness and (b) load ratio [161].

Sun and Khaleel [174] studied the effect of common head/tail side materials in SPR joints. Eleven different joint populations were studied, comprising four different materials (AA 5182-O, SAE 1008, DP 600 and HSLA 350) and four different thicknesses (1, 1.4, 1.6 and 2 mm). The fatigue test was performed at a frequency of 20 Hz and the load ratio was 0.1 with a variety of loads applied until a visible crack was observed. They concluded that one can estimate the fatigue strength of an SPR joint between dissimilar metals based on the known SPR fatigue strength of known material combinations. For example, joint 1 and joint 2 (see Table 2.10.1) have the same top sheet (material A) and similar fatigue failure mode (eyebrow cracking on the head side) and both joints exhibit very similar fatigue strength. Again joint 3 and joint 4 have same bottom sheet and similar fatigue failure mode (eyebrow cracking at the tail side). Based on these observations, one can say that, joint 3 and joint 4 have very similar fatigue strength.

Table 2.10.1 Riveting parameters of different joint (for demonstration only).

	Head side material	**Tail side material**	**Fatigue failure mode**
Joint 1	A	B	Eyebrow cracking in head side material
Joint 2	A	C	Eyebrow cracking in head side material
Joint 3	D	A	Eyebrow cracking in tail side material
Joint 4	A	A	Eyebrow cracking in tail side material

2.10.4 Effect of piercing direction

Piercing direction greatly influences the fatigue strength (Fig. 2.10.4a). For the same material combination and same rivet, having a hard top sheet gave higher strength [174]. If the bottom sheet was more ductile a much better clinched structure was found on the tail side, which was verified by metallurgical examination of the joint cross section [174]. The fatigue strength of double-rivet SPR is no better than a similar single-rivet joint for the same value of applied stress per rivet. Both the fatigue and static strength of double-rivet SPR joints are dependent on the orientation combination of rivets (see Fig. 2.9.3e). In cases where the rivet heads are close to the loading ends (**Type B,** in Fig. 2.9.3e), joints exhibit the highest strength [145].

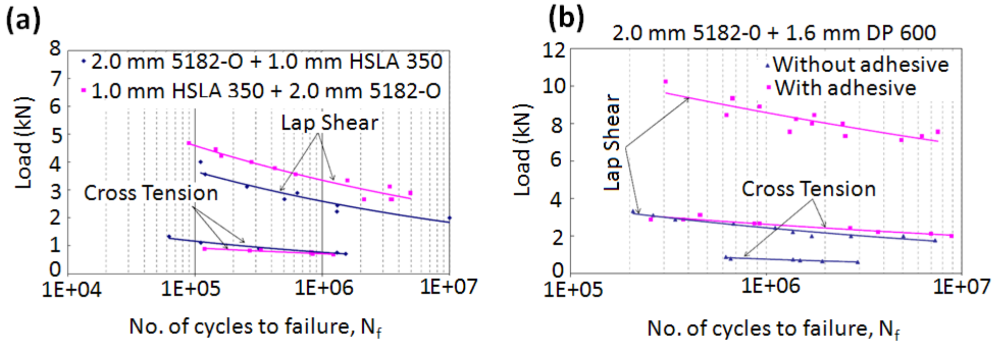

Fig. 2.10.4 Fatigue life depending on (a) piercing direction and (b) adhesive [174].

2.10.5 Effect of adhesive

Structural adhesive greatly increases the fatigue strength for both cross-tension and lap-shear loading conditions (Fig.2.10.4b). Sun and Khaleel [174] studied the effect of adhesives on three different joints of dissimilar materials (2 mm AA5182-O + 1 mm HSLA 350, 1 mm HSLA 350 + 2 mm AA5182-O and 2 mm AA5182-O + 1.6 mm DP 600) with Dow betamate 4601 as the adhesive. The fatigue test was performed at a frequency of 20 Hz with a load ratio of 0.1. For each of the conditions the addition of adhesive greatly improved the fatigue performance. For any kind of material combination adhesives increase the fatigue performance [174, 175].

2.10.6 Effect of rivet

Limited literature is available which discussed the effect of rivet hardness, diameter and geometry on fatigue behaviour of SPR joints. However Han et al. [153] reported that the fatigue strength is highly dependent on rivet and die design. A 30% increase in fatigue load by optimising the rivet design (in a joint of 2 + 2 mm NG 5754 with a 7 mm long rivet) was reported. On the other hand, Fu and Mallick [91] studied the effect of different rivet parameters on the fatigue behaviour of a SPR joint of 5754-O aluminium alloy of three different combinations (1 + 1, 1 + 2 and 2 + 2 mm). Two types of diameters (3 and 5 mm), three forms of hardness (normalized rivet as forged, 410 HV and 480 HV) and four different lengths (4, 5, 6 and 6.5 mm) of rivet were considered. An ANOVA analysis showed that only rivet diameter has a small impact (3.17%) on the fatigue strength. Rivet length and hardness have no significant impact on the fatigue strength [91]. The impact of rivet length and hardness on the fatigue strength were 0.46 and 0.86%, respectively.

2.11 Vibrational behaviour of a SPR joint

A study was conducted by He and co-authors [183-187] to understand the vibrational behaviour of a SPR jointed cantilever beam. Sheets of 2024-T3 aluminium alloy with a thickness of 2 mm, specimen size, first eight mode shape and natural frequency depending on Young's modulus of material are shown in Fig. 2.11.1.

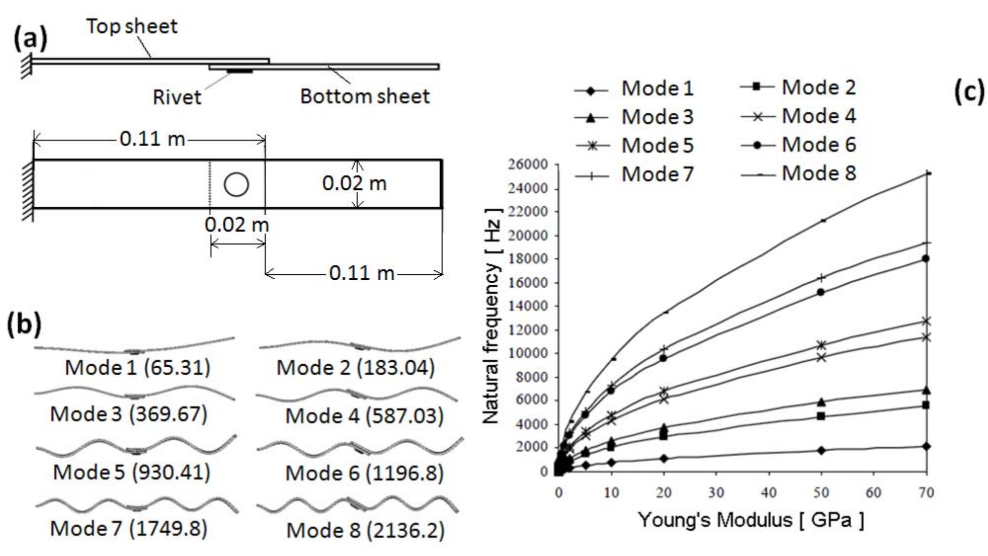

Fig. 2.11.1 (a) A single rivet lap jointed SPR cantilever beam [185], (b) first eight mode shape of vibration [186] and (c) natural frequency of each mode [184].

An exponential relationship was developed between the natural frequency and the Young's modulus as per equation (2.11.1) below:

$$f = mE^{0.5} \tag{2.11.1}$$

where, f is the natural frequency, E is the modulus of elasticity of the material and m is a constant. The density of the material also influences the natural frequency and the mode shape. Eight different densities (1000, 1500, 2000, 2500, 3000, 3500, 4000 and 4500 kg/m^3) of material were tested to examine the effect of density on the natural frequency [184] and it was found that natural frequency decreases with the increase in density of material. However, the Poisson's ratio (0.3, 0.32, 0.34, 0.36, 0.38 and 0.4) has no influence on the vibrational properties within the tested parameters. The same author also studied the effect of adhesive's properties (Poisson's ratio of 0.3, 0.35, 0.4 and 0.45, Young's modulus of 0.001, 0.01, 0.1, 0.2, 0.5, 1, 2, 5, 10, 20, 50 and 70 GPa and density was 1100 kg/m^3) on the vibrational behaviour of SPR jointed cantilever beam. The simulated results showed that adhesive's strength has a significant effect on the odd mode shape of vibration. The mode shape is more pointed when the adhesive is relatively soft, but when the adhesive is relatively stiff, the mode shape becomes flat and because of a local stiffening effect [183, 185]. The natural frequency has an exponential relationship with the Young's modulus of the adhesives but the Poisson's ratio of the adhesive has no impact on the vibrational characteristics [185, 186].

2.12 Aluminium rivet

The SPR process typically utilizes a martensitic high strength steel rivet. The possibility of replacing the steel rivet with aluminium has been studied by Hoang et al. [15]. Aluminium rivets (6 mm long) made with 3 different alloys (6082-T6, 7108-T5, 7278-T6) were considered for this study. Nine different combinations of joints comprising three different tampers of aluminium alloy (6060-W, T4 and T6) having a thickness of 2 mm were examined and it was concluded that SPR joining was only possible when the sheets were soft (6060 W) and the rivets were hard (7278-T6). Rivet fracture occurred for the same hard rivet for hard sheet material (6060 T4 and T6), and rivet compression occurred for the rivets made with soft materials (6082-T6, 7108-T5). Heating prior to riveting to soften the material can be beneficial for the rivet to avoid cracking and with a flat die it showed better performance in terms of rivet flaring than a profiled die [15]. The mechanical performance of the riveted joint for 3 different rivets is shown in Fig. 2.12.1. It is clear that the initial stiffness is similar for all joints, which means that the stiffness is not dependent on the rivet properties, though the maximum load and the energy absorption increased with the increase in hardness of the rivet [15, 188].

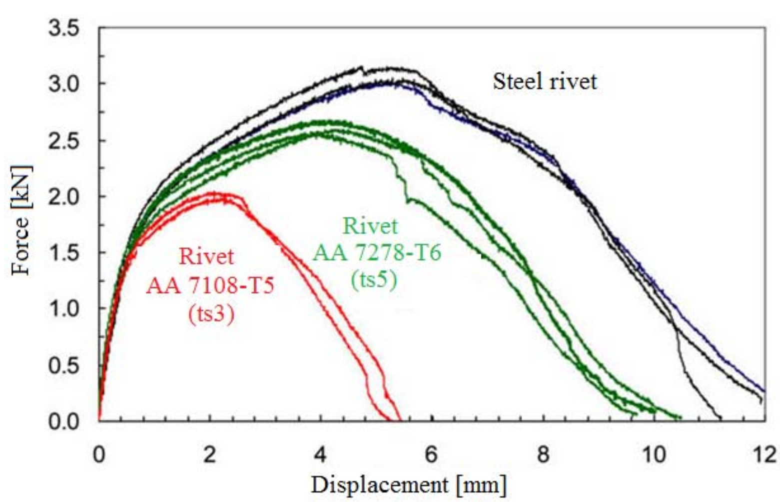

Fig. 2.12.1 Comparison of joining strength between Al rivets and steel rivet [15].

A further study on the experimentally observed failure of the aluminium rivet showed that shear fracture initiated after 85% of the maximum displacement, as shown in Fig. 2.12.2 [165]. The fracture behaviour was also examined by numerical modelling and it was concluded that the fracture was dependent on the friction coefficient and a value of μ=0.8 showed the best match between the experimental and numerical results [165]. The effect of ageing on the mechanical performance of an aluminium rivet (6 mm long and the material was AA7278-T6) joint (2 + 2 mm AA6063-W) was studied by Hoang et al. [189]. Natural ageing was conducted at room temperature for 3 and 30 days. The strength of the aluminium riveted joint had stabilized after 3 days of natural ageing [189].

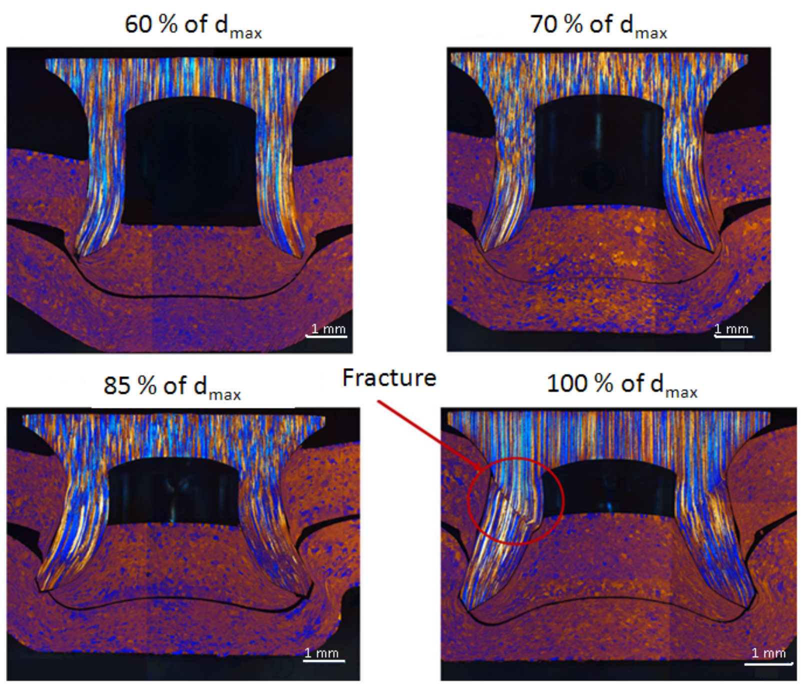

Fig. 2.12.2 Rivet fracture in a joint of 2 mm + 2mm AA6060-T4 with Aluminium (AA7278-T6) rivet [15, 165].

2.13 Finite element modelling

The formation of joints and the mechanical behaviour of the SPR joints depend on the geometrical characteristics of rivet and die and on the process parameters. It is very difficult to predict the performance of the SPR joints for the various changes in rivet, die, material and process parameters. However, numerical simulation may provide a basis to predict the performance and can help to optimize the process parameters.

Several commercial software products are used for the numerical simulation of SPR process such as LSDYNA [121], FORGE [133], EVAS [17], DEFORM-2D [146, 190], ABAQUS [74], FEMFAT SPOT SPR pre-processor [144], MSC Marc and MSC SuperForm [191], PamASSEMBLY™ and PamCRASH™ [128]. The development and optimum design of a light-weight C-frame result from a finite element simulation conducted by Westgate et al. [94]. A 2D model is sufficient for the early design of the C-frame, however a 3D model in necessary for accurate results [94].

In general, finite element modelling (FEM) was verified by experimentally obtained force-displacement curves of the riveting process [76, 131, 192]. To study the SPR process material data were used as an input to the FEM simulation [193]. The specimen size of the sheet material and the rivet is shown in Fig. 2.13.1. To determine the flow properties of the material several sheets were glued together to a total height of 12 mm and for the steel rivet a tubular specimen was obtained by removing the head and the lower part of the rivet skirt. The resulting material data are also shown in Fig. 2.13.1 [120, 166]. Plastic properties of materials can be defined by

$$\sigma = Y'' + C * \mathcal{E}^{n} * \varepsilon^{m} \qquad (2.12.1)$$

where, Y'', C, n and m are constants and $\mathcal{E}$ is the plastic strain [194]. The accuracy of the simulation depends on the flow data of the materials and rivet from the compression test [124, 194-196].

The join-ability of aluminium (AA5052-H34; thickness of 1, 1.5, 2 and 2.5 mm) with mild steel (SPCC; thickness of 0.8, 1.2, 1.8 and 2 mm) and high strength steel (SPFC 980; thickness of 1, 1.4 and 2.3 mm) was studied by Abe, Mori and co-authors using ANSYS [121, 131, 132]. This enabled identification of different faults and then optimization of the process by geometrical modification of die and rivet [195, 197, 198]. A modified rivet (diameter and edge angle) and die (flattened central pip) geometry was proposed by Khezri, Mori and co-authors [121, 125] for joining ultra-high strength steels (SPFC 980, Trip 800) with thickness ranging from 1 mm to 2.3 mm. A strong rivet (large web thickness of rivet; W in Fig. 2.3.1) with gradual increase in thickness of rivet leg was suggested to join ultra-high strength steel (EN 1.4301, HyTens 800 and HyTens 1200) with a thickness of 1 and 2 mm to avoid cracking in the rivet [130, 199].

Another join-ability experiment was conducted by Franco and co-authors [146, 159] to join carbon fibre (thickness of 1.5 mm) and basalt fibre (1.3 mm) with aluminium (2.7 mm AA2024-T6) by using a 6.5 mm long rivet, and good agreement was observed between the experimental and numerical results.

To predict the joint properties of 3-ply SPR joints of different materials (AA5754, steel XES and DP 450) and different thicknesses (1, 1.2, 1.5 and 2 mm) numerical simulation of the 2-ply joints was conducted and good agreement was found for the mechanical performance of the 3-ply joint [71, 133]. The kill-element technique was used in the commercial software DEFORM in this analysis [133, 200]. Other plasticity models known as Johnson-Cook plasticity and Rousselier material model are widely used in modelling of SPR [169, 196]. The choice of element is also crucial and the eight node brick element was used in most of the modelling of SPR [182, 193, 196].

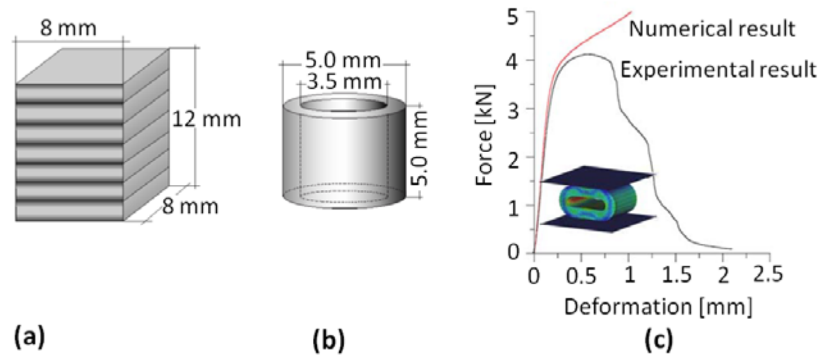

Fig. 2.13.1 (a) specimen size of sheets for material characterization [120], (b) specimen size of rivet for material characterization [120] and (c) material characterization data for numerical simulation [166].

Prediction of assembly dimension for different materials (AA 6181-T4, AA 5754-HO, AA 5182-H11, XES, HCT600XD steel) with different thicknesses (1, 1.15 1.5 and 2 mm) with different rivets (5, 6 and 6.5 mm) was conducted by Cai, Sui, Neugebauer, Masters and co-authors [17, 102, 128, 201]. The finite element code EVAS (elastic assembly variation simulation) was used to predict the global assembly due to the distortion occurring locally [17]. An experiment was conducted by Chenot et al. [134, 202] for a joint of 1 mm 5754 + 2 mm XES steel with 5 and 6 mm long rivet, and it was concluded that the inclusion of residual stress that arises from the riveting process can identify the assembly dimension more accurately.

Investigation of the failure load in shear and tensile loading condition of 2.5 + 2.5 mm aluminium alloy (yield stress of 132 MPa) with 6 mm long riveted joint was conducted by Porcaro et al. [203] to identify the modelling parameter for FEM. They identified the values constants Y, C, m and n as presented in equation 2.12.1, which provides a direct accuracy of the model.

Hahn et al. [60] conducted a numerical simulation to verify the experimental results in impact SPR joining of 2.5 +1.5 mm AlMg4.5Mn with a 6 mm long rivet (480 HV) for different speeds (0.002, 10 and 100 m/s). They found that at high speed, joining of aluminium is feasible by using a flat anvil instead of profiled die. However, they suggest a change in rivet geometry because of excessive strain.

To find the optimum rivet setting pressure for different combination of joints, FEM was used by King, Khezri and co-authors [1, 124]. The stiffness of a joint is evaluated by ABAQUS by Lim [144] for different loading conditions (coach-peel, cross-tension, lap-shear and pure shear) of 1 + 1.5 mm A5032-T4 by using a 5 mm long rivet and he concluded that the stiffness was highly dependent on the loading condition.

The vibrational behaviour of a SPR jointed cantilever beam was studied by He and Oyadiji [183]. The simulated results showed that the adhesive's strength has a significant effect on the odd mode shape of vibration. The effect of different faults in the fatigue life of SPR joints of different materials (aluminium alloy AA 5754-O, AA 4047, and steel of SAF2205, SAF2304, DP600, AISI301, AISI304 and DDQ) with different thicknesses (1, 1.2, 1.5 and 2 mm) and different rivets (5, 6 and 6.5 mm long) were investigated by Chukwuemka, Khezri and co-authors [204, 205]. They found that the stress concentration was localized near the faulty areas.

The modelling of SPR needs to define the failure criterion of the material [191]. Damage is normally introduced in the software by two different methods: uncoupled damage criterion or coupled formulation with the Lemaitre law [134, 202]. By the Lemaitre law not only the SPR process can be simulated and optimized, but also the mechanical strength can be simulated. The optimization of the riveting process can be achieved by adapting the data from other relevant processes such as sheet forming and clinching. Prediction of deformation behaviour and residual stress can be modelled successfully by FEM. The crucial step is to transfer the 2D properties into the 3D model [202]. An optimum mesh size and adaptive time interval are required to achieve the best compromise between accuracy and computational time [76, 143, 196].

Porcaro et al. [76] implemented an optimum condition (0.1 x 0.1 mesh size and 12 adaptive steps) to a FEM model for sixteen different joining conditions consisting of two different materials (AA 6064-T4 and T6), two types of thicknesses (2 and 3 mm), four different rivets (6, 6.5, 7 and 8 mm long) and two set of dies (flat and profiled) with 3 loading conditions. They obtained very good correlation between the calculated and experimental results.

The rivets are mainly produced from martensitic steel of high strength. However, the risk of fracture in a rivet is high when ultra-high-strength steels are joined or when an aluminium rivet is used to join aluminium. Gardstam [123] conducted a FEM analysis to identify residual stress and risk of fracture in the rivet while joining ultra-high-strength steels (EN 1.4301, HyTens 800 and HyTens 1200) of different thicknesses (1 and 2 mm). A modified riveting parameter (rivet geometry, die geometry and rivet setting pressure) was proposed to remove the risk of a cracking in the rivet. A finite element model was developed based on the reverse engineering approach from the analytical background of the failure mechanism by Hanssen, Hoang and co-authors [77, 188] to determine possible cracks in aluminium rivets while joining aluminium components.

FE simulations were also made to locate cracks in rivets especially under the head radius when joining ultra-high strength steel [97, 130, 206]. A vast range of simulation work was performed by Swedish Institute for Metals Research (SIMR) to determine residual stress in rivets when joining ultra-high-strength steel [120, 195, 197, 207]. Several different joining conditions consisting of ultra-high-strength steel (like Hytens 1200, Hytens 800, Trip 800) of different thickness (1 and 2 mm) were examined by SIMR where effective stress ranges from 1100 to 1800 MPa in the rivet and the setting force range from 58-80 kN were obtained. The simulation result was also used to predict the static and fatigue behaviour of the joint. The simulated results were worst when no residual stress was considered in the joint due to riveting. The following conclusions were reached by the group: similar rivet and die set can lead to large differences in residual stress depending on the setting load, a more pointed pip of the die (Fig. 2.6.2) can reduce the setting force with an increasing risk of break-through of the bottom sheet. The obtained results were then used to design new rivets to avoid cracking in the rivet due to high rivet setting pressure by Leijon, Malender and co-authors [129, 208]. New rivet geometry was proposed by them. Heat treatments of martensitic stainless steels (VAL2AV, VAL2MON, VAL2ACT and 17-7PH) were optimized for the manufacturing of self-piercing rivets using the knowledge obtained from the previous results obtained by this group [199, 209]. Best base material for martensitic rivets was found to be VAL2AV, which showed a good combination of strength and ductility [199].

The numerical simulation depends highly on the correct assumption of the friction coefficient between different mating surfaces. Six different contacts have been identified for the SPR process: punch-rivet, rivet-top sheet, rivet-bottom sheet, top-bottom sheet, bottom sheet-die and blank holder-top sheet [84, 123, 165]. The value of friction coefficient was chosen by trial and error and different authors used different values of friction coefficient between different surfaces. Malendar [208] studied the effect of friction coefficient on the result of simulation of a joint of 1.2 + 1.2 mm steel (yield strength of 700MPa) with a 5 mm rivet (480 HV). Four different friction coefficients were considered (μ= 0.01, 0.1, 0.15 and 0.2) and μ=0.1 gave the best matching result. However it should be mentioned that he considered the same coefficient of friction for all the contact surfaces. On the other hand, Atzeni, Huang and co-authors [74, 99] proposed different coefficients of friction between different contact surfaces when joining aluminium alloys (Al 6082-T4, AA 5182-H11) of different thicknesses (1.5 + 1.5 and 3 + 3 mm). The fracture behaviour of an aluminium rivet (Fig. 2.13.2) was examined for different friction coefficients and it was observed that only for the value of μ = 0.8 did the failure mechanism match with the experimental study [165]. An opportunity exists to study the effect of friction coefficient on the simulation results of the SPR process.

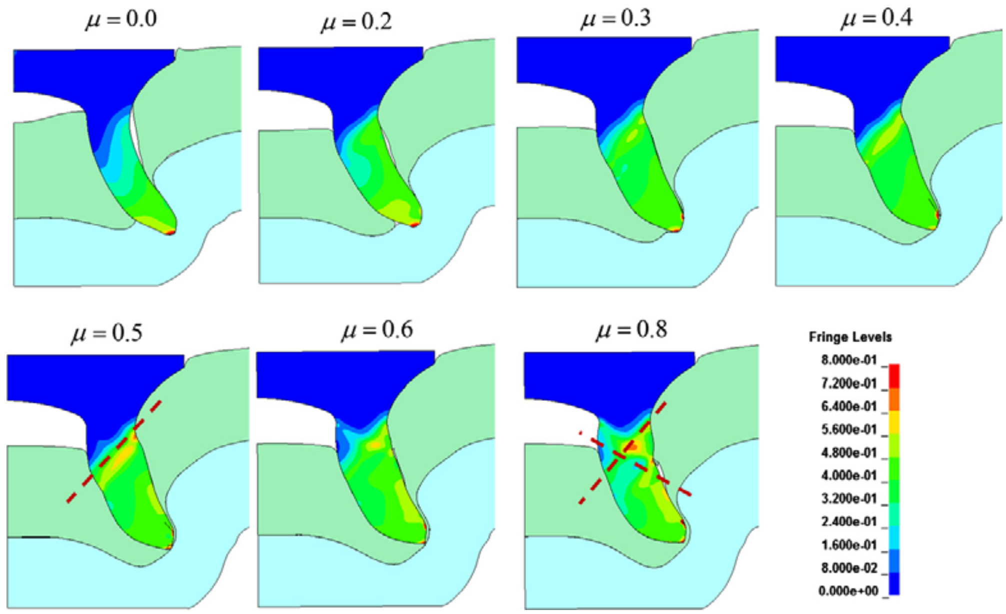

Fig. 2.13.2 Effect of friction coefficient on the numerical result; a friction coefficient of μ= 0.8 can predict the experimental failure mode properly as shown in Fig. 2.12.2 [165].

2.14 Comparison with other joining techniques

Several authors [2, 4, 9, 210] have compared the performance of joints produced by SPR and other joining methods like friction stir welding (FSW), resistance spot welding (RSW), spot friction joining (SFJ) and mechanical clinching. Blacket [2] presented a comparison of fatigue life of a 2 + 2 mm Al6000 joint between SPR and RSW and much better fatigue life was observed for SPR.

Blundell et al. [210] compared the static strength between SPR and SFJ for both lap-shear and cross-tension loading conditions. The materials were 1.8 mm NG 5754 and 2 mm AA 6111 and the rivet was 7 mm long. Two groups of joints were produced by alternating the sheets at top and bottom. The parameters for SFJ were: 4.5 s weld time, 5 kN forge pressure and 2250 rpm rotational speed. The static strength was found to be significantly higher for SPR. The strengths were 4.95 and 2.11 kN for SPR and 3.23 and 0.75 kN for SFJ in the lap-shear and cross-tension loading conditions respectively.

Lee et al. [9] studied the joint strength in an impact test on a H-type specimen of 2.5 + 2.5 mm AA 6063 for SPR and mechanical clinching joining. They obtained similar joint strengths for both conditions. However, clinching is generally intended to join thin sheet material (total thickness < 3 mm) and generally gives lower static strength than SPR [7, 8].

Lennon, Pedreschi and Sinha [149] compared the static strength of SPR with other cold-joining methods (mechanical clinching, pop rivets, press-joint and self-tapping screws). They used galvanized mild steel (yield strength of 300 MPa) of different thickness combinations (1, 1.2, 1.6 and 2 mm). The joint strength was significantly higher for SPR when compared with other techniques.

Han, Thornton and Shergold [33] compared the mechanical behaviour of SPR and RSW joint of aluminium sheets for automotive industries. They used AA 5754-O material of various thicknesses (1 + 1, 2 + 2, 2 + 3, 3 + 2 and 3 + 3 mm) and the test was performed for both lap-shear and coach-peel loadings. The joint strengths had less scatter with SPR than with RSW. They also concluded that the interlock was important for SPR, whilst the periphery of the nugget was important for RSW; and stack orientation had no effect for RWS but had a significant effect for SPR on joint strength. Static SPR joint strength was similar to FSW, RSW and SFJ, but fatigue strength was much better than a welded joint [9, 17, 211].

Lee et al. [175] described a comparative study of dissimilar materials (1 mm cold rolled coil + 1 mm Al 5J32-T4) between SPR, RSW and adhesive joining in a crushing test. A 5 mm long rivet was used in SPR and methacylate (PLEXUS® MA822) as structural adhesive. The joint strength was similar but the specific energy absorption was higher for SPR, which makes the process favourable in a crushing test [175]. A comparison of cycle time and joining strength of three different methods are shown in Fig. 2.14.1 [4]. Cycle time of SPR and clinching does not change with thickness of material, but in welding it differs. The energy consumption is significantly higher in RSW than SPR, and SPR is much more environmental friendly. On the other hand, the assembly distortion is high in SPR compared with welding [17].

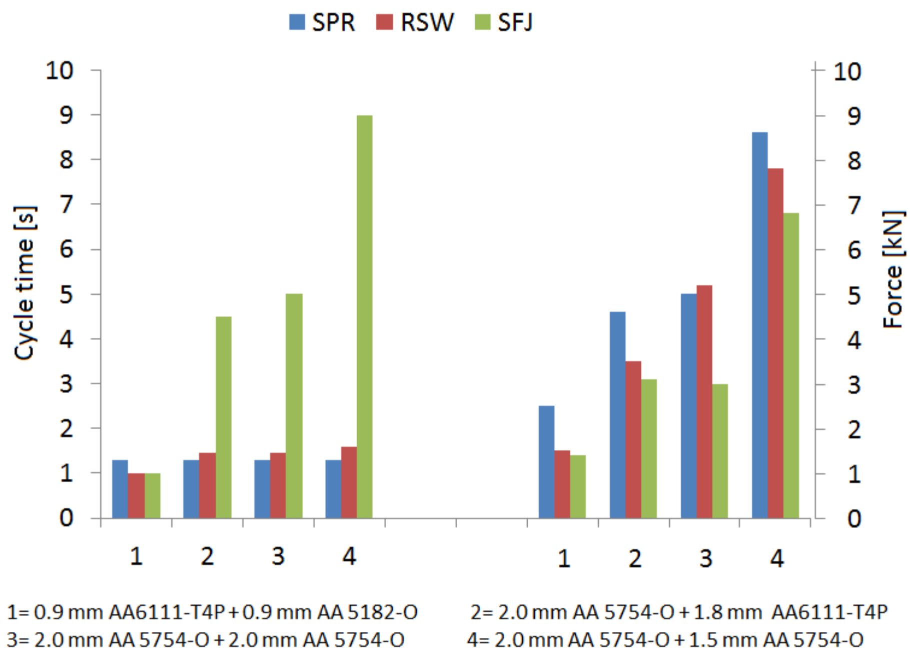

Fig. 2.14.1 Comparison of cycle time and static strength for different joining method [4].

2.14.1 Cost analysis

The frequency and cost of destructive testing, cost of maintenance and labour cost are similar in SPR, RSW and SFJ [4, 18, 212]. However, the initial equipment cost for producing 35,000 units per year is $10 million for SPR, $4 million for RSW and $11 million for SFJ [4]. The main drawback of RSW is high cost for the electricity consumption [18]. On the other hand the ongoing cost of rivets makes the process more expensive, but this may be outweighed by the enhanced joint performance [4].

Varis [7] made an economic comparison of mass production between SPR and clinching. Several points of view were discussed and calculation of marginal costs was presented. The significance of tool service life to unit cost was also introduced. A normalized total cost of SPR and clinching is presented in Fig. 2.14.2. The total costs are equal for both joining methods when the service life of the clinching tool is equal to 111,111 joints. If the tool service life is lower than this limit value (111,111) then SPR is more favourable for mass production. However, it should be noted that in this calculation the initial cost of the SPR process was ignored by assuming the cost of this process was directly related to the number of rivets.

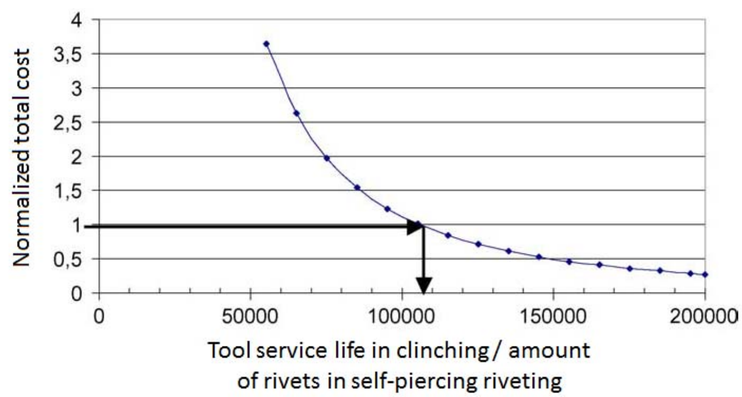

Fig. 2.14.2 Economics of SPR joint in comparison with clinching [7].

2.15 Summary

Self-piercing riveting is a metal joining technique in which a tubular rivet is inserted through two or more sheets with no need for a predrilled hole in the sheet metal. This technique has become increasingly popular as a way of joining, particularly in the fields of light metals and dissimilar metals joining, which is difficult or sometimes impossible by fusion welding.

In this chapter, the SPR process is critically reviewed from the perspectives of static and fatigue performance. For process monitoring, a typical force-displacement curve has been introduced. The mechanics of joint formation and quality of joints that may arise depending on different variables, such as: thickness and hardness of the ply materials, length and hardness of rivet, different types of rivet head and web thickness of the rivet head, rivet setting pressure and die profile are discussed.

The static strength of a joint can be obtained by an analytical strength estimator, but great care should be taken while measuring the geometry as the dimensions are very small. The factors affecting the fatigue strength of SPR joints are also discussed.

A literature survey has shown that the number of articles on SPR is increasing significantly. A comparison of published papers is shown in Fig. 2.15.1. The graph is generated using the number of articles cited in this chapter.

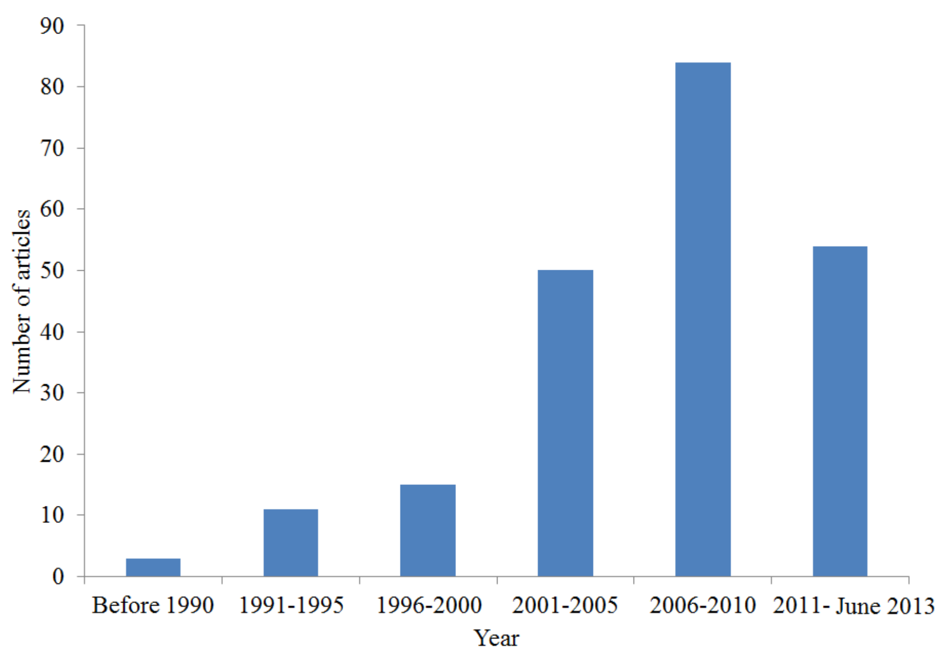

Fig. 2.15.1 Graphic illustration of the publications on SPR prior to 1990 and thereafter.

SPR is increasingly used in combinations of dissimilar materials because of the development of ultra-high strength alloys. To push the operating window of the

SPR process it is necessary to gain more understanding of the deformation characteristics of the rivet and ply materials, but no open literature was found that explained the deformation characteristics in terms of residual stress. It is a challenge to identify the residual stress distribution in order to understand the mechanics of joint formation and the mechanical performance of joints.

2.16 Research Questions

SPR is an interesting process. This process is also complex and intricate. This is essentially a joining-by-forming process. As nowadays, more and more ultra-high-strength materials and alloys are used in automotive industries, it is necessary to understand the deformation behaviour of the rivet and material during the forming process. FEA is a useful tool to gain more understanding and optimize the process in order to join new alloys and materials. A literature survey shows that most of the FEA was validated through cross-section and force-displacement curves, but many unknown assumptions were made to match model outputs with experimental cross-section and force-displacement curves. Direct match of cross-section and force-displacement curves has been achieved with interrupted tests.

However, very limited attention was paid to studying the force-displacement curve to understand the deformation behaviour of the rivet and sheets during SPR. The following are the key research questions arising from the literature review:

- Is it possible to extract more information by studying the force-displacement curve in order to characterize the riveting process?
- Is there any possibility of predicting the joint characteristics (rivet flaring) directly from the force-displacement curve?
- Is there any relationship between the force-displacement curve and the residual stress distribution?
- Is it feasible to measure residual stress in SPR joints?
- Is it possible to predict the joint performance directly from the characteristic force-displacement curve?

3 CHALLENGES ASSOCIATED WITH RESIDUAL STRESS IN SPR

SPR is increasingly used on materials and dissimilar combinations that are difficult or even impossible to join by spot welding. The materials should, however, have sufficient ductility to deform without cracking. As ply materials increase in hardness, strength or thickness, the ability of a rivet to pierce and deform in a ductile manner becomes increasingly limited, therefore the operating window in terms of joint quality and performance becomes narrower. Forces for setting the rivet are high, typically 30 to 50 kN. This high setting force may generate cracks inside the rivet. Previous studies [53, 57] show that a joint may look good externally (Fig. 3.1a), but micro-computed tomography (CT) shows cracking in the same joint (Fig. 3.1b).

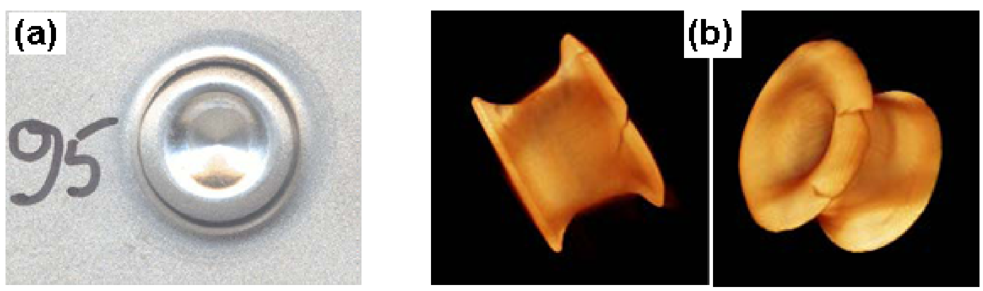

Fig. 3.1 (a) Scan of a joint on tail side [53] and (b) Micro CT scans of the same joint [57].

To understand fully the behaviour of SPR joints, one key aspect is to understand the joint formation mechanism and the sequence of material and rivet deformation during the formation of SPR joints. Another key aspect is to appreciate the residual stress distribution in the joint arising from the riveting process.

A literature survey showed that only FEA analysis work was performed to predict the residual stress inside a SPR joint. Some simulation work was executed to predict the residual stress and reported as high as 1075 MPa inside the rivet in a joint of 1 + 1 mm Trip 800 but not validated [125]. However, that simulation depended on a few assumptions such as elastic properties of material, friction coefficient between different surfaces, mesh size, simulation time, etc. No experimental approach to measure the residual stress was found in the literature. Thus, a feasibility experiment is necessary to evaluate the residual stress. The challenges also involved dealing with very small dimensions.

3.1 Residual stress

Residual stresses are defined as self-equilibrating stresses within a stationary solid body when no external forces are applied [213]. These stresses may arise from misfits in the natural shape between different regions, parts or phases [214]. Little has been reported in the open literature regarding the effect of residual stress in SPR. However, literature [215] has been found related to the residual stress in friction stir welded joints. It should be noted that residual stress developed in SPR due to high plastic deformation of the rivet and sheet. On the other hand, residual stress in welded joint developed due to thermal effect. A general overview of residual stress and its effects and different measuring techniques are described in the following sections.

3.1.1 Effect of residual stress

The effect of residual stress can be either beneficial or harmful depending on the magnitude, sign and distribution of the residual stress with respect to the load-induced stresses [216]. The static loading performance of brittle material can be improved largely by the intelligent use of beneficial residual stress by introducing compressive surface stress [213]. For ductile materials, the residual and applied stresses can be added together directly until the yield strength is reached. So, in this respect, residual stress may accelerate or decelerate the plastic deformation, which is important when failure occurs by plastic collapse. However, residual stress affects the static ductile fracture only a little, because residual elastic strains are small compared with the plastic strains generated prior to failure.

The effect of residual stress on fatigue life is discussed by Jang and co-authors [217]. Fatigue is generally divided into two types [213]: low-cycle fatigue (LCF) which involves fewer than 10,000 cycles to failure and high cycle fatigue (HCF). Generally residual stress has negligible effect on LCF as the primary residual stresses tend to be affected by the large amplitude of the oscillating strain. On the other hand, residual stress affects HCF by offsetting the mean stress of any fatigue loading. Chang et al. [218] examined the effect of residual stress in welded steel pipe and found that the life decreased 9-15% due to residual stress. Welding residual stresses, which are generally close to the yield strength of the material, cause brittle failure [216]. To improve the performance of the weldments it was suggested to reduce/eliminate the residual stress by heat treatment or to change its nature from tensile to compressive.

If a structure contains cracks, one needs to determine how many cycles it will take for one of these cracks to grow to such an extent that catastrophic fracture can occur. As the stress at the crack tip is related to the crack length and also to loading geometry, the loading of the crack tip is generally expressed as “stress intensity factor,” K, where

$$K = Y' \sigma \sqrt{\pi a} \qquad (3.1.1)$$

Here, a is the crack length, Y' is a geometrical constant approximately equal to 1 and σ is the stress. Residual stress can change the amplitude of the stress intensity factor, which indicates that it can also increase or decrease the fatigue life [213]. Fig. 3.1.1 shows how residual stress can affect the stress intensity factor.

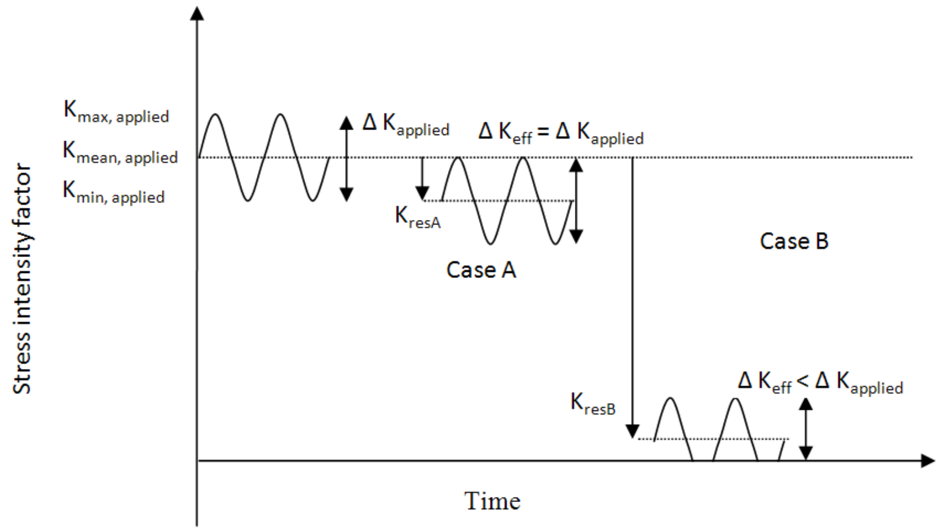

Fig. 3.1.1 Residual stress affecting the stress intensity factor for two different cases, A and B [213].

3.1.2 Measuring techniques for residual stress

Residual stress cannot be measured directly in practice. It can be obtained from a measure of the elastic strain, displacement or secondary quantity, which can be related to stress, such as the speed of sound or magnetic signature [219]. Measurement techniques for residual stress can be divided into destructive and non-destructive methods. Some well-known destructive tests are: layer removal, hole drilling, block sectioning, contour method and deep hole drilling. It may be noted that block sectioning provides single stress measurement, hole drilling provides depth profiles, and contour provides area maps of residual stress. The advantage of the hole drilling method is that it is not limited to crystalline material and this technique can be applied to plastics, composites, and coated materials [216].

On the other hand, non-destructive techniques usually measure some parameter that is related to the stress. Some non-destructive tests are: X-ray, magnetic and eddy current, ultrasonic, neutron diffraction and synchrotron diffraction techniques [220]. X-ray diffraction is limited to a depth of 5 µm, whereas neutron diffraction can measure the strain up to 50 mm depth in steel [219]. But X-ray diffraction has a high spatial resolution and consequently faster acquisition time due to a low diffraction angle compared with neutron diffraction. Synchrotron X-ray diffraction is more suitable for strain mapping experiments for finite element (FE) model validation while neutron diffraction is more suited for deep line stress profiling experiments [219].

Fig. 3.1.2 shows the approximated capabilities of various techniques for measurement of residual stress in steel. For the measurement of residual stress in SPR joints, where the materials of interest are high-strength steels, neutron diffraction and synchrotron X-ray diffraction are the most appropriate techniques among the non-destructive methods, while the contour method is appropriate among the destructive methods. These techniques are discussed in detail below.

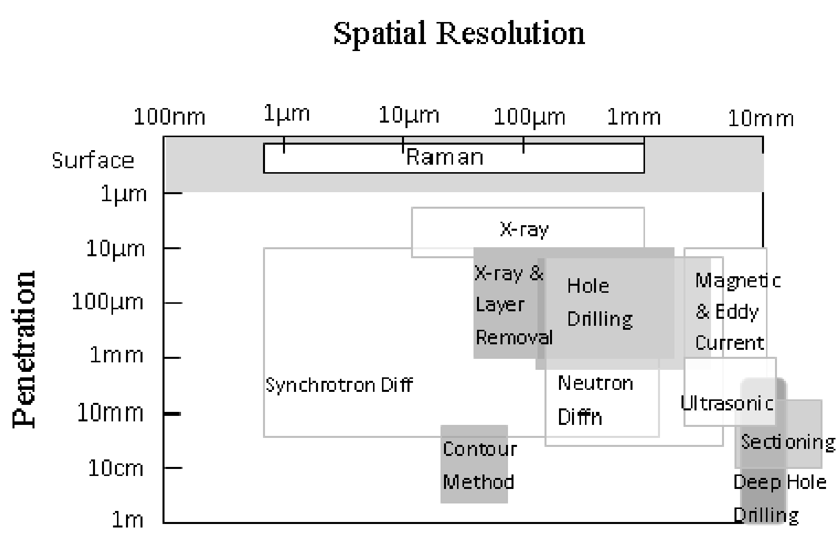

Fig. 3.1.2 Capabilities of various residual stress measurement techniques [219].

3.1.3 Neutron diffraction method

When a neutron beam of wavelength λ is incident on a crystalline material, the radiation diffracts as distinctive Bragg peaks [221, 222]. If the angle is 'θ' where the Bragg peaks occur, the lattice spacing can be determined using equation (3.1.2).

$$2d \sin\theta = \lambda \tag{3.1.2}$$

where, d is the lattice spacing and 2θ is the diffraction angle (see Fig. 3.1.3).

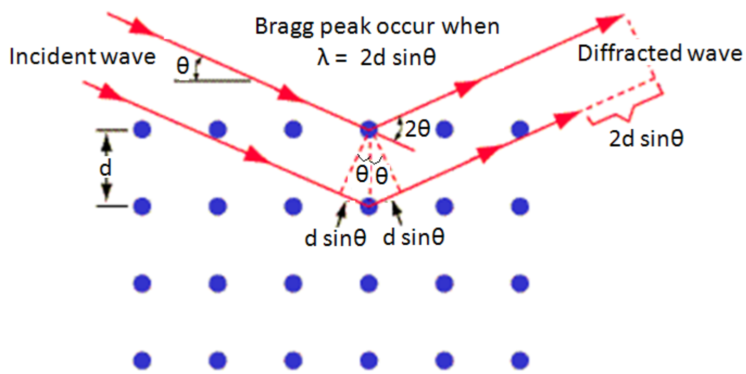

Fig. 3.1.3 Schematic Diagram of Bragg's equation.

If the lattice spacing and diffraction angle are d_0 and θ_0 respectively for a unstressed lattice, the elastic strain (ε) can be determined by,

$$\varepsilon = \frac{d-d_0}{d_0} = -(\theta - \theta_0)\cot\theta \tag{3.1.3}$$

The stress may then be determined from the stress-strain relation of the material [221]. This technique is known as $\theta/2\theta$ scanning. Care should be taken in selecting the diffracting plane because, in isotropic engineering materials, the single crystal may be anisotropic. This means that different lattice plane (h k l) reflections may exhibit different strains when subjected to same stress (Fig. 3.1.4).

So measurement should be made only for those planes which represent bulk behaviour and are not affected by plane strain. The planes (2 1 1) and (1 1 0) are suitable for ferritic steel, in which the crystal structure is body centred cubic (bcc) at room temperature, while plane (3 1 1) is suitable for aluminium and nickel alloys, as these are face-centred cubic (fcc) crystal structures [222, 223].

There is another technique of neutron diffraction available known as time of flight approach. In this case, the Bragg angle θ is kept constant (usually $2\theta = 90^0$) and the wavelength λ varied. This is done because there is a large range of neutron energies and the beam which is most energetic arrives at the specimen first and the least energetic arrives last. The energy can be deduced from the time of flight. Here, the strain is given by the following equation,

$$\varepsilon = \frac{\Delta t}{t} \tag{3.1.4}$$

where, t is the time of flight and Δt is the difference between the time of flight of an unstressed and a stressed lattice.

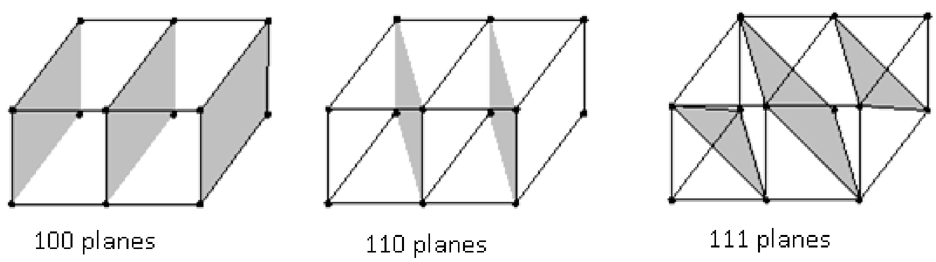

Fig. 3.1.4 Different h k l planes.

These two methods have developed depending upon the two forms in which neutron beams are available: continuous beam from a reactor source and pulsed beam from a spallation source. The continuous beam is suitable for $\theta/2\theta$ scanning and the pulsed beam is suitable for the time of flight method [220]. The neutron diffraction technique is very suitable when the thickness of the specimen is large and when it is necessary to measure the stress to a large depth [223]. This is also very popular as it can provide the full set of stress components i.e. in three directions [224, 225]. The neutron diffraction technique is only applicable to crystalline materials, which is the main limitation of this technique [216].

3.1.4 Synchrotron diffraction method

This technique follows the same rules as the neutron diffraction technique, but here the beam is made up of Synchrotron X-rays which is a million times more intense than conventional X-ray. Synchrotron (or Hard) X-rays can provide high energy photons which are a thousand times more penetrating than conventional X-rays. This is a very quick process and the spatial resolution is very high. The minimum gauge dimension is 20 μm and it is also characterized by high energy two-dimensional diffraction. The uncertainties involved in measuring peak diffraction angles are very low, so the precision is very high, which is equal to ± 10×10^{-6} strain [225]. However, this technique can measure residual stress only in two-directions.

3.1.5 Contour method

The contour method is a destructive technique for measuring residual stress. This technique was first proposed by Prime in 2000 [226-228]. This is a newly invented relaxation technique which enables one to evaluate a 2D residual stress map on a plane of intersects [229]. The theory of this technique is based on the Bueckner principle: 'if a cracked body subject to external loading or prescribed displacements at the boundary, has forces applied to the crack surfaces to close the crack together, these forces must be equivalent to the stress distribution in an uncracked body of the same geometry subject to the same external loading' [as referenced in 230]. The basic principle of Bueckner's theorem is described in Fig. 3.1.5 [230, 231]. If a specimen containing residual stress as described in Fig. 3.1.5(a) is cut, the two surfaces created by the cut deform due to stress relaxation.

The principle is that it is possible to make the cut surfaces plane again by applying identical stress of opposite direction. So it is possible to measure the residual stress by measuring the surface contour after cutting a specimen assuming that the relaxation of the residual stress occurs elastically and the cutting does not induce any further stress.

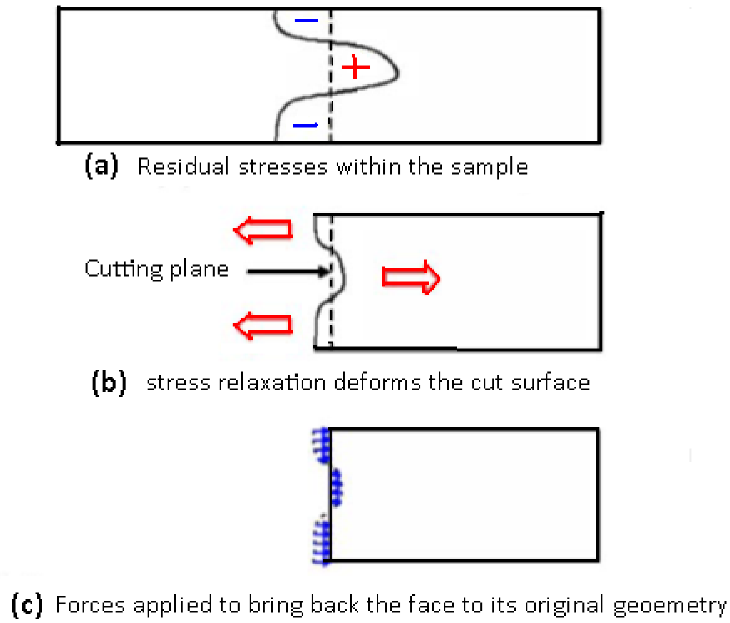

Fig. 3.1.5 Bueckner Principle of Contour method [230].

The contour method was first published in details in 2001, where the technique was verified numerically by finite element modelling using the ABAQUS software and experimentally by a known residual stress specimen which was a plastically bent beam [226]. Four main steps are involved with the application of contour method: specimen cutting, contour measurement, data reduction and stress analysis [229]. Special care should be taken for the first part of the process which is specimen cutting as the final result is influenced by this. A single flat cut is very important in order to achieve high accuracy and a constant width cut is also important which will guarantee a flat cut. Scientists identified that the electric discharge machining (EDM) is the most suitable method of cutting for the contour method because it will ensure a flat cut as well as constant width cut. The next step is contour measurement of the cut surface. A co-ordinate measuring machine (CMM) is very suitable for the accurate surface profile measurement. The third step of the contour measurement is data reduction. It is obvious that the measured data contain errors from cutting and measurement, so the first step of the data reduction is to average each pair of measurement points. The next step of the data reduction is smoothing of the measurements which is crucial to achieve an accurate stress profile. Figs. 3.1.6 and 3.1.7 show the difference between the measured contour and smoothed contour. The final step is inverse calculation of the original stress from the contour; this is generally done by FE modelling.

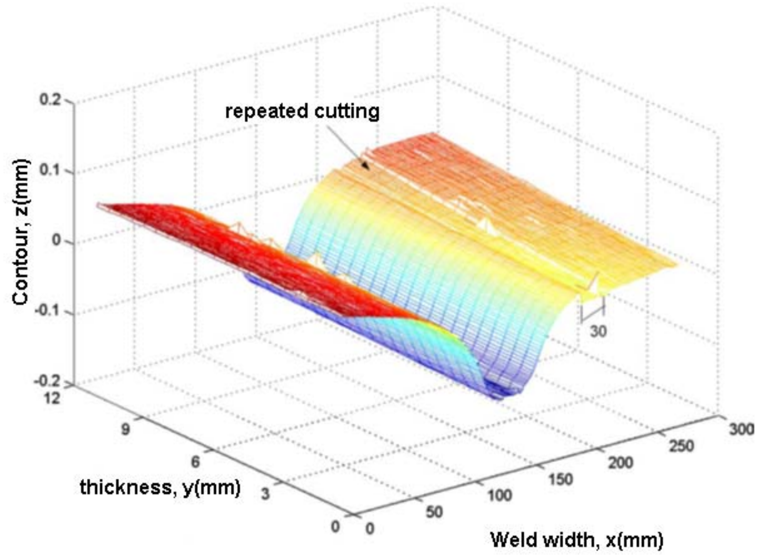

Fig. 3.1.6 Measured contour of a welded plate [229].

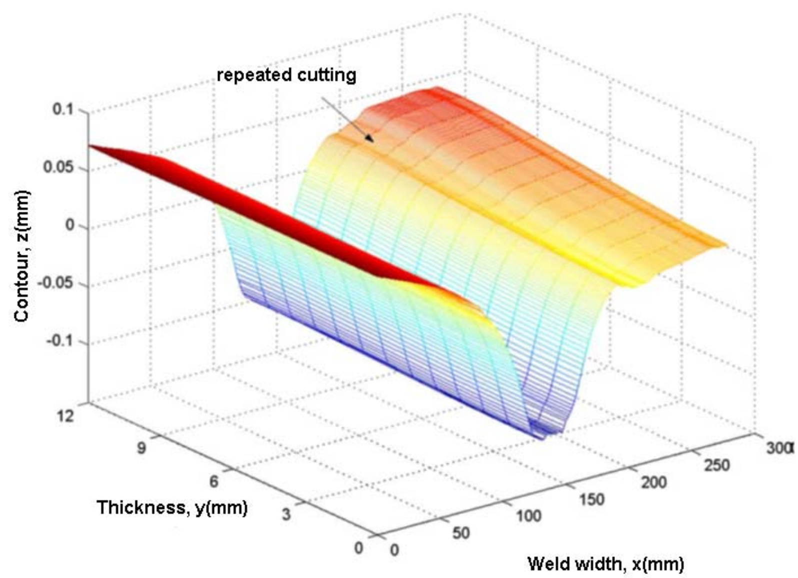

Fig. 3.1.7 Smoothed contour of Fig. 3.1.6 [229].

The contour method is a relatively simple method as it can produce residual maps directly from displacement maps with minimum time and computational cost. However, the main disadvantage with this method is that only one residual stress component can be obtained, which is normal to the cut surface.

Very recently, a method for measuring multiple residual stress components, proposed by De wald and Hill [232, 233] and verified by Kartal [234], compared the stress profile obtained by neutron diffraction and synchrotron diffraction. Computing the eigen strain from the measured displacement is the basic principle of the multi-axial contour method. Eigen strain is the permanent strain that comes from some inelastic process such as plastic deformation, thermal expansion and mismatch between different parts of an assembly. Residual stress then may be obtained from the eigen strain. The eigen strain remains constant upon residual stress distribution. A change in geometry may alter the residual stress distribution but not the eigen strain which motivates the scientist to use eigen strain to determine residual stress. Fig. 3.1.8 shows that the eigen strain remains unchanged while the residual stress distribution changed after cutting [234]. In this method Kartal et al. used the data from two additional 45° cuts by assuming a constant longitudinal stress profile. The main draw-back of this technique is that the length of the specimen must be twice as long as its width, which will ensure the cuts along their diagonals i.e. at an angle of 45°.

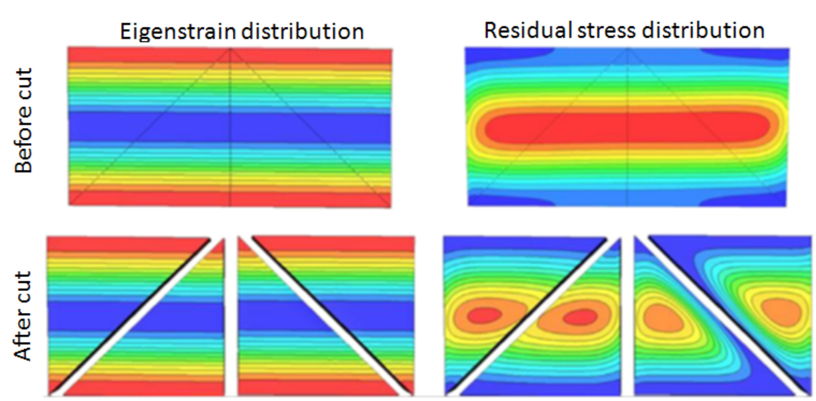

Fig. 3.1.8 Eigen strain and corresponding stress [234].

3.2 Summary

The general effects of residual stress on structures are discussed and different techniques for evaluating residual stress in SPR joints are also introduced in chapter 3. Two main challenges identified for the measurement of residual stress in SPR joints are dealing with very small dimensions and the available facilities for residual stress measurement. It was found that, when the material of interest is steel, neutron diffraction and synchrotron diffraction methods are very suitable among the non-destructive methods and the contour method is suitable among destructive methods for evaluation of residual stress.

4 EXPERIMENTAL PROCEDURE

The experimental methodology developed to understand the deformation behaviour of the sheet material and rivet during the SPR process is described in this chapter. The study examines the SPR process in three distinct phases: characterisation of riveting process, residual stress distribution and static strength. A full description of the joining conditions, experimental equipment and testing procedure is provided.

Primarily, a family of curves for a variety of fastening condition was created. Specifically, force, pressure and displacement data were monitored as a function of time (during riveting operation). Key parameters were identified and their effects on riveting operation were analysed.

To examine closely the material deformation during riveting, the formation of a group of joints was interrupted at different positions by inserting spacers between the upsetting die and die holder.

Metallographic analyses for both interrupted and completed joints were performed which enabled the measurement of the dimensional parameters relating to the material deformation during the SPR process.

A series of joints was produced to obtain the residual stress distribution inside the rivet and the top and bottom sheets.

In addition, cross-tension and lap-shear strength experiments were executed to establish the static strength of the SPR joints.

4.1 Aim of the experiment

The experiment was conducted to study three main aspects of SPR joints: the deformation behaviour of the rivet and the top and bottom sheets during riveting, the residual stress distribution in the rivet and sheet materials of a SPR joints for a variety of riveting parameters and the static strength of a joint for different loading conditions. A systematic approach was taken to study the above mentioned features of a riveted joint. The approaches are described below:

1. Study the deformation behaviour of the rivet and the top and bottom sheets during the riveting operation by;
   - Creating a range of riveted joints by changing different parameters such as different materials, rivets and dies
   - Establishing the characterization of the force-displacement curve on each joint
   - Interrupting a family of joints at different riveting positions and measuring the force and the displacement of each interruption
   - Determining the rivet flaring at each interrupted positions by metallographic experiment
   - Finally determining the C-frame deflection.

2. Study the residual stress distribution in a group of SPR joints by;
   - Feasibility study of residual stress evaluation in SPR joints by the neutron diffraction method
   - Optimizing the parameters for meaningful residual stress results
   - Lastly, evaluating residual stress in a collection of different SPR joints by the neutron diffraction technique.

3. Study the static strength of a group of SPR joints by;
   - Producing a series of SPR joints for both cross-tension and lap-shear loading condition
   - Measuring the strength of each joint in each loading condition.

4.2 Sheet materials

All the joints for this study were produced by two sheets of materials only as this is common in most industrial applications. The constituent materials were selected based on widely used materials in the industrial applications in Australia. Carbon steel of two different grades (G450 and G300 carbon steel) was selected for this study. The sheet materials have been chosen for the interest of the industry. The material properties are given in Table 4.2.1.

Table 4.2.1 Carbon steel sheet material properties.

Material designation		G300 steel	G450 steel
Mechanical properties	Young's modulus (GPa)	220	220
	Poison's ratio	0.3	0.3
	Tensile strength (MPa)	340	480
	Yield stress (MPa)	300	450
	Hardness (HV)	198	270
	Elongation (%)	18	9
Chemical properties	Carbon (%)	0.3	0.2
	Phosphorus (%)	0.1	0.04
	Manganese (%)	1.6	1.2
	Sulphur (%)	0.035	0.03

4.3 Rivets

Self-piercing rivets are produced by a cold-forming process from wire materials. The wire materials are generally Boron treated steel and rivets are heat-treated to the desired hardness level after the forging process. The external surface of a rivet is protected by a coating to protect it from galvanic corrosion. In industrial practice different types of coatings are used depending on the application. The most common coatings are mechanical zinc, zinc-tin plated and aluminium. Electro-zinc coating is also used in some applications. The basic form of a rivet is shown in Fig. 4.3.1. All the rivets for this study were supplied by Henrob (UK) Pty Ltd, Australia.

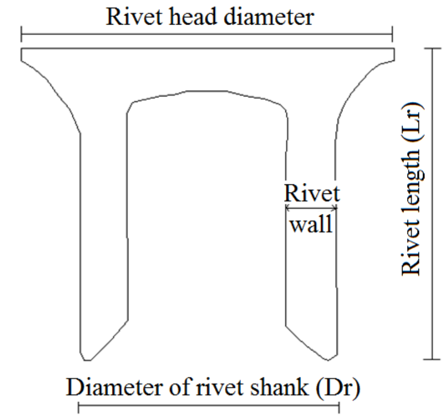

Fig. 4.3.1 A typical self-piercing rivet.

The most common rivet diameters used in SPR joining are: 3 and 5 mm. The 3 mm rivets are normally used to join thinner materials (usually less than 3 mm). However the 5 mm rivets are used to fasten a full range of material thickness. The rivet wall thickness also has a significant importance for the SPR process. A thick rivet wall is normally used in riveting of high strength materials to avoid buckling of the rivet. The length of the rivet is chosen relative to the thickness of the ply materials to be joined. The rivet length has to be increased when the joint thickness increases. During SPR, a rivet should have sufficient hardness to pierce the top sheet. However, the rivet should also have sufficient ductility to flare in the bottom sheet. Hence, the hardness of a rivet is a very important parameter in SPR joining. In this study, rivets with three different hardnesses and lengths were chosen depending on materials. The properties of the rivets considered in this study are given in Table 4.3.1.

Table 4.3.1 Properties of rivets considered for this study.

<table>
<tr><th>Rivet designation</th><th>Hardness (HV)</th><th>Length (mm)</th><th>Head diameter (mm)</th><th>Wall thickness (mm)</th><th>Shank diameter (mm)</th><th>Coatings thickness (µm)</th></tr>
<tr><td>HG 0642</td><td>410</td><td rowspan="2">6</td><td rowspan="6">7.4</td><td rowspan="6">1.1</td><td rowspan="6">5.5</td><td rowspan="6">12 (Mechanical zinc)</td></tr>
<tr><td>HG 0644</td><td>480</td></tr>
<tr><td>HG 0742</td><td>410</td><td rowspan="3">7</td></tr>
<tr><td>HG 0744</td><td>480</td></tr>
<tr><td>HG 0746</td><td rowspan="2">555</td></tr>
<tr><td>PG 0846</td><td>8</td></tr>
</table>

4.4 Die

A die is used to control the deformation of the ply materials in SPR joining. Dies are mainly of two types as shown in Fig.4.4.1: flat and profiled dies. Profiled dies are mainly used in joining of soft material and to achieve a high flaring. On the other hand flat dies are mainly used in joining of hard sheet materials. The selection of die mainly depends on the ply materials properties (hardness and thickness). A high die recess volume is required for a thick combination of joint in order to accumulate the large volume of the deformed material. In this study, a flat die is used with different diameters and depths depending on materials. The die parameters are given in Table 4.4.1.

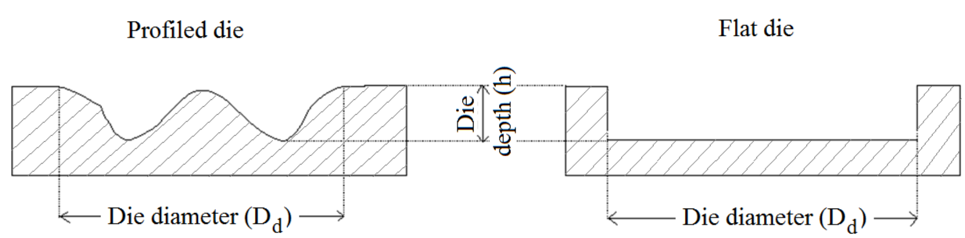

Fig. 4.4.1 Schematic of profiled and flat dies.

Table 4.4.1 Parameters of the die considered in this study.

Die designation	Diameter (mm)	Depth (mm)
DF 09200	9	2.0
DF 09230	9	2.3
DF 10210	10	2.1
DF 10250	10	2.5
DF 10300	10	3.0
DF 11235	11	2.35

4.5 Test specimens

The schematic and experimental test specimen setups are shown in Figs.4.5.1 and 2. The sheet specimens are 150 mm long by 50 mm wide. Three different thicknesses have been considered: 1.5, 2.0 and 2.5 mm. Five riveted joints were made in each test specimen at an equal spacing of 25 mm.

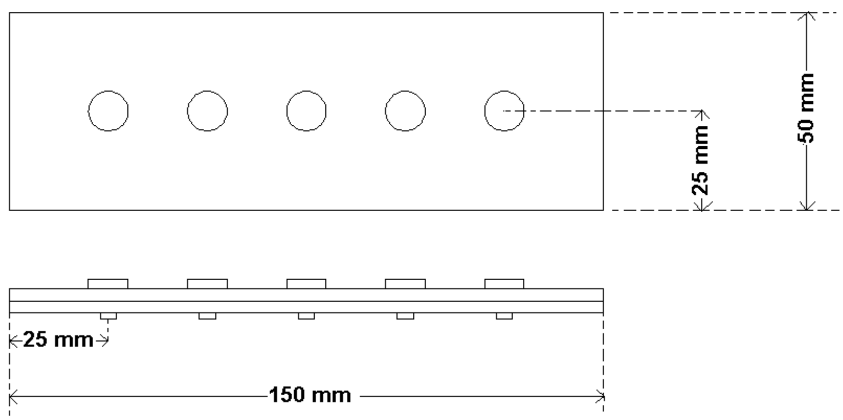

Fig. 4.5.1 Schematic of Riveting test specimens.

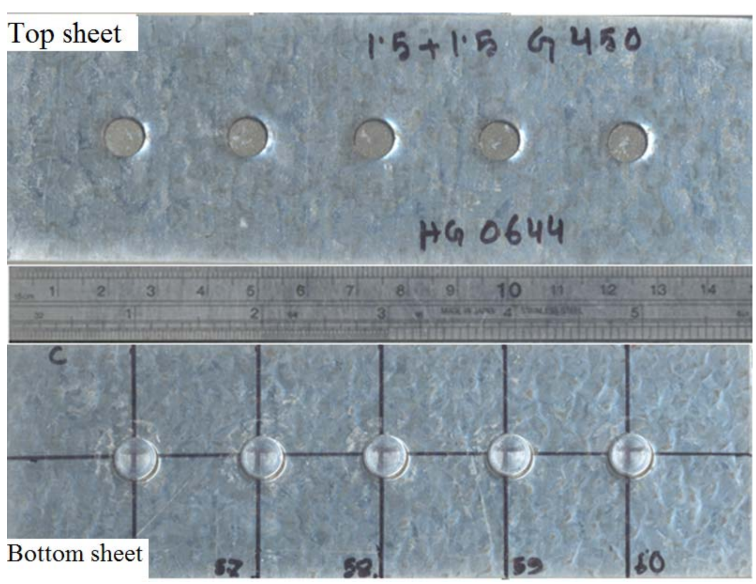

Fig. 4.5.2 Experimental setup of the test specimens.

4.6 SPR configuration

SPR trials were conducted using a Henrob hydraulic rivet setter. The laboratory setup is shown in Fig. 4.6.1. Sheet specimens were setup on a fixture table to make the joints. A load cell was mounted between the die and C-frame to measure the reaction force during riveting. A linear variable differential transformer (LVDT) was placed just beneath the riveting gun to measure the punch displacement. Two pressure transducers were positioned to measure the pre-clamp and rivet setting pressure in the SPR rig. Pre-clamp pressure was 125 bar for all of the specimens produced in this study. However, the rivet setting pressure was kept between 220-250 bar based on the ply materials' thickness and hardness.

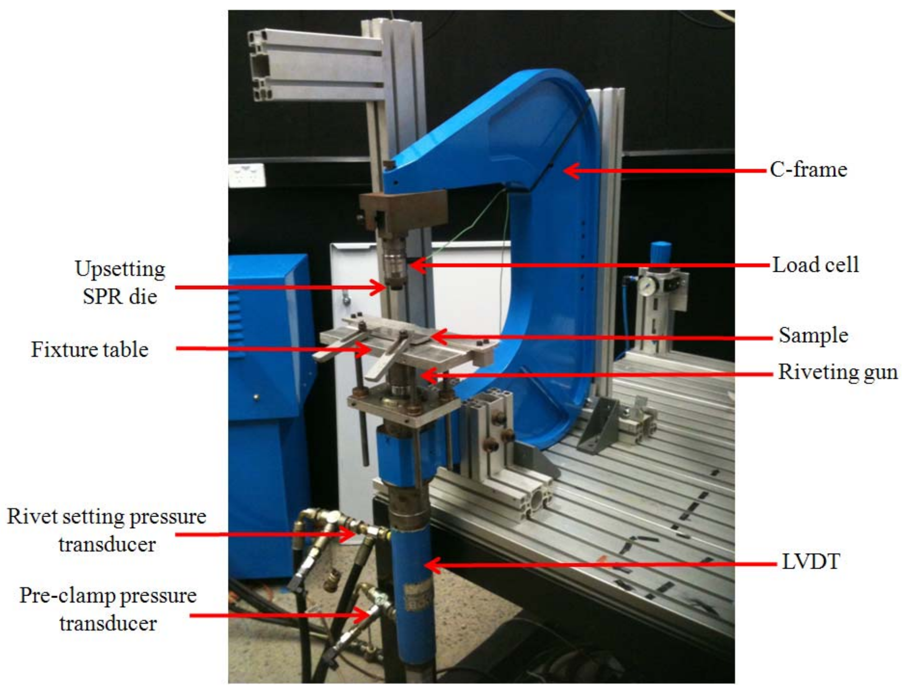

Fig. 4.6.1 Laboratory setup for self-pierce riveting (SPR) trials.

4.7 SPR process data acquisition

The data for force, displacement, pre-clamp and rivet setting pressure were recorded as a function of time at a logging rate of 1000 Hz. Experiment shows that an increase in logging rate greater than 1000 Hz did not make any difference. Force, displacement and pressure were measured by a load cell, LVDT and a pressure transducer respectively. The characteristics of the load cell, LVDT and the pressure transducer are summarized in Table 4.7.1.

Table 4.7.1 Key characteristics of equipment for data acquisition.

Characteristics	Load cell	LVDT	Pressure transduce
Range	0-70 kN	0-145 mm	0-250 bar
Signal output	0-10 V dc	0-10 V dc	0-10 V dc
Max non-linearity (% full scale output)	$\leq \pm 0.5$	$\leq \pm 0.02$	$\leq \pm 0.2$
Operating temperature (^{o}C)	-40~140	-40~85	-40~85

4.8 Joint assembly for characterization of riveting process

To characterise the riveting process a series of joints was produced and the punch displacement in the riveting direction (Fig. 4.8.1) was measured as a function of time. The force, rivet setting pressure and pre-clamp pressure were also measured as a function of time as shown in Fig. 4.8.2.

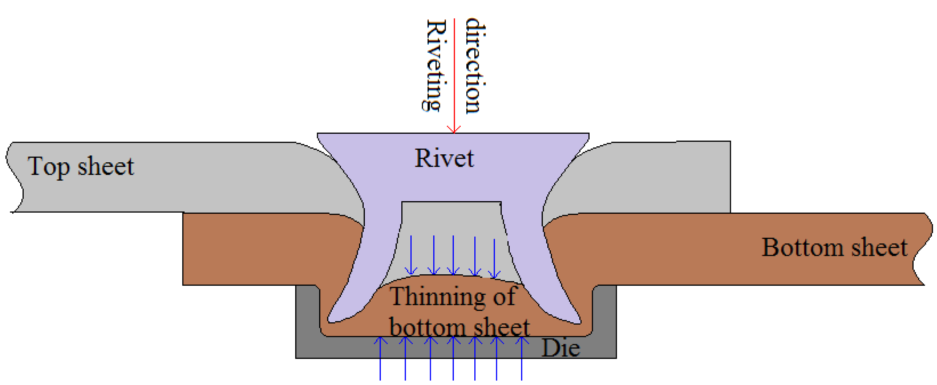

Fig. 4.8.1 Schematic diagram of a riveted joint.

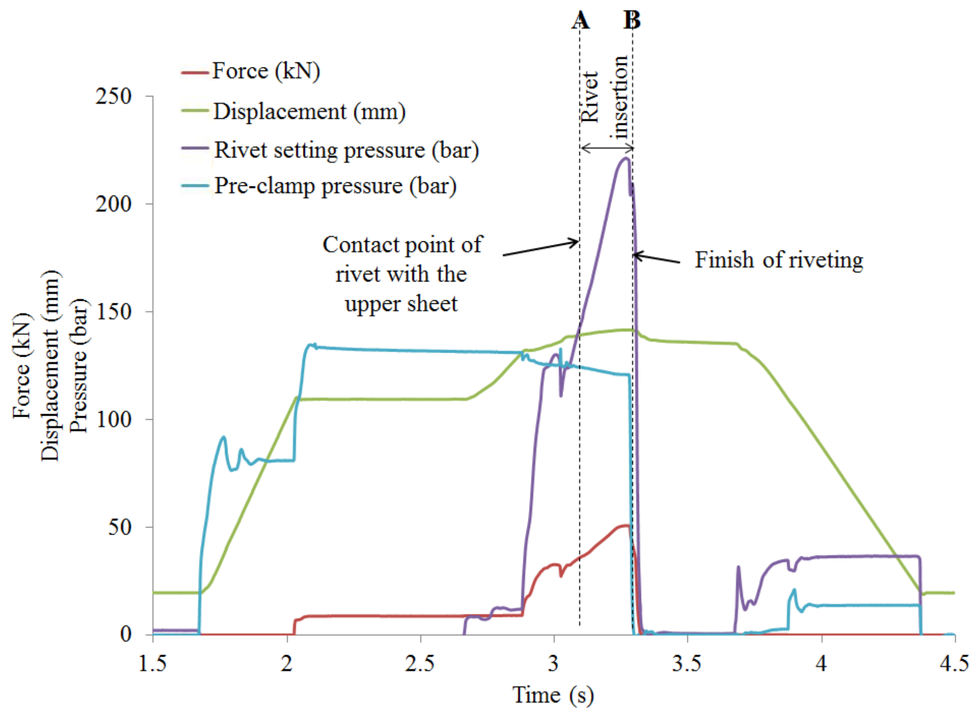

Fig. 4.8.2 Typical raw data acquired during riveting.

The data were processed to identify the time and position of the punch, where both the force and the rivet setting pressure simultaneously increased after pre-clamping, which corresponds to the event when the rivet first comes in contact with the top sheet. The punch displacement relative to that event was subsequently used to generate all force-displacement curves. An example force-displacement curve is presented in Fig. 4.8.3 from the processing of a joint of 2.5 mm G300 carbon steel top and bottom sheets using an 8 mm long rivet of hardness 555 HV.

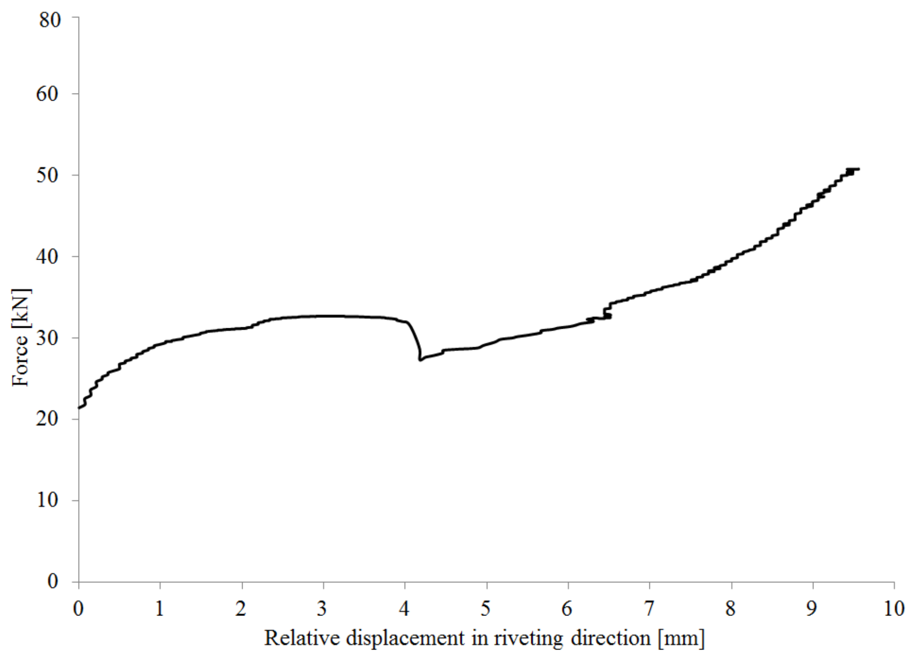

Fig. 4.8.3 Force-displacement curve after processing of 2.5 + 2.5 mm G300 steel sheet joint with an 8 mm long rivet having a hardness of 555 HV.

A family of joints was produced for a matrix of materials, rivet and die set. Table 4.8.1 shows the different combinations of joints produced to characterize the riveting process which will be analysed in chapter 5. To systematically study the effects of rivet length and thickness, material thickness and properties and die depth on characteristic force-displacement curve, 3 different thicknesses and two different hardnesses of materials were chosen. The matrix was created by the combination of these materials. However for each condition five joints were made at 25 mm spacing according to chapter 4.5 (see Figs. 4.5.1 and 2) and also the data were recorded during the riveting operation. It was observed that the riveting process showed a very good reproducibility for all joints produced in this study. Typical force-displacement curves for five joints in a test specimen of 1.5 G300 carbon steel as top and bottom sheets using 6 mm long rivets with hardnesses of 480 HV and a flat die (9 mm diameter and 2 mm depth) are shown in Fig. 4.8.4.

Table 4.8.1 Matrix of joints produced for characterizing the riveting process in chapter 5.

<table>
<tr><th rowspan="2">Joint matrix</th><th rowspan="2">Ply materials</th><th rowspan="2">Joint thickness (mm)</th><th colspan="2">Rivet</th><th colspan="2">Die (flat die profile)</th><th rowspan="2">Rivet setting pressure (bar)</th><th rowspan="2">Pre-clamp pressure (bar)</th></tr>
<tr><th>Length (mm)</th><th>Hardness (HV)</th><th>Depth (mm)</th><th>Diameter (mm)</th></tr>
<tr><td>1</td><td>G450</td><td rowspan="3">2.5 + 2.5</td><td rowspan="3">8</td><td rowspan="4">555</td><td rowspan="2">2.35</td><td rowspan="2">11</td><td rowspan="9">250</td><td rowspan="15">125</td></tr>
<tr><td>2</td><td rowspan="2">G300</td></tr>
<tr><td>3</td><td>3.0</td><td rowspan="5">10</td></tr>
<tr><td>4</td><td rowspan="2">G450</td><td rowspan="4">2.0 + 2.0</td><td rowspan="4">7</td><td rowspan="4">2.1</td></tr>
<tr><td>5</td><td>480</td></tr>
<tr><td>6</td><td rowspan="2">G300</td><td>555</td></tr>
<tr><td>7</td><td>480</td></tr>
<tr><td>8</td><td>G450</td><td rowspan="2">1.5 + 1.5</td><td rowspan="2">6</td><td rowspan="2">480</td><td rowspan="2">2.0</td><td rowspan="2">9.0</td></tr>
<tr><td>9</td><td rowspan="7">G300</td></tr>
<tr><td>10</td><td>2.5 + 2.5</td><td>8</td><td rowspan="2">555</td><td>3.0</td><td rowspan="4">10</td><td rowspan="6">220</td></tr>
<tr><td>11</td><td rowspan="3">2.0 + 2.0</td><td rowspan="3">7</td><td rowspan="3">2.5</td></tr>
<tr><td>12</td><td>480</td></tr>
<tr><td>13</td><td>410</td></tr>
<tr><td>14</td><td rowspan="2">1.5 + 1.5</td><td rowspan="2">6</td><td>480</td><td rowspan="2">2.3</td><td rowspan="2">9.0</td></tr>
<tr><td>15</td><td>410</td></tr>
</table>

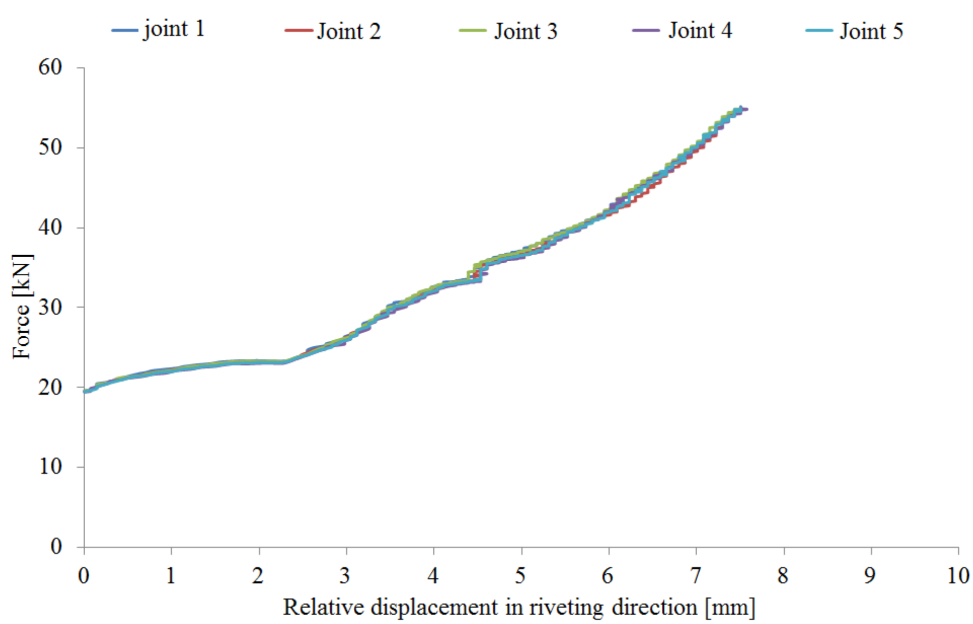

Fig. 4.8.4 Different curves of joints showing the great reproducibility of the SPR process.

4.8.1 Metallographic investigation of the riveted joints

The main objective of metallography was to analyse the cross-sectional characteristics of the collection of riveted joints. At first, specimens were sectioned by a precision cutter at a very slow speed after the joint was made. Careful attention was paid when the cutter reached the middle of the joint to avoid minimal damage to the rivet. The specimen was small so it was mounted in epoxy resin and the mounting process was a cold mount. The specimen was then polished by SiC paper (up to 1200 grit) until all the scratches polishing marks have been removed. A typical micrographic cross-section of a joint and schematic diagram showing how to achieve a cross-sectional view of the joint is shown in Fig. 4.8.5. It should be noted that eccentric and anisotropy effects may exist in some of the cross-sectional views. Rivet flaring was measured for both completed and interrupted joints from the micrographic cross-section by using a microscope. In this thesis only the rivet flaring was measured as a literature survey shows that thinning of bottom ply and head height (y in Fig. 2.3.1) can be linked with rivet flaring.

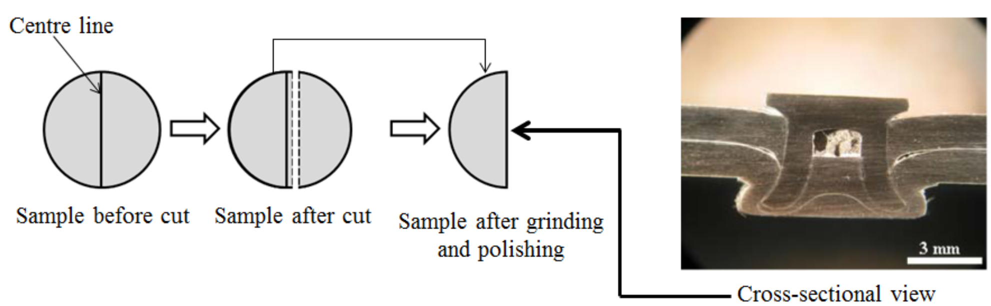

Fig. 4.8.5 Cross-section of a riveted joint and schematic diagram showing the sectioning and polishing of a rivet.

To examine the microstructure of the rivet and material; the mounted specimen was polished by using 1μm colloidal silica suspension. Finally the specimen was etched according to the ASM metals handbook volume 9 [235]. The etchant was 4% nital solution (4 mL concentrated nitric acid + 96 mL ethyl alcohol) for the sheet material and the etching time was 10s. To reveal the microstructure of the rivet 2% nital solution was used as etchant and the etching time was 5s.

The microhardness of the rivet and sheet were measured by a Buehler Micromet 2100 Series Microhardness Tester with a load of 50 gmf.

4.9 Residual stress investigation of the joints

Sample preparation for residual stress measurement follows the same procedure as described in chapter 4.5. Five joints were created in a specimen of 150 mm x 50 mm sheets comprised of different materials and thicknesses at 25 mm spacing. The residual stress examination was conducted in three different stages. For the first stage, a reproducibility and feasibility test was conducted. The next stage of the experiment was optimizing parameters for making meaningful evaluation. The final stage was to evaluate residual stress in different combinations of SPR joints using the technique developed in the first two stages. The final stage of the residual stress evaluation was made to study the residual stress profile in SPR joints of three main parameters: sheet materials' hardness, thickness and rivet hardness. The matrix of joint family for the different stages of residual stress analysis is shown in Table 4.9.1.

Table 4.9.1 Joint combination for different stages of residual stress investigation (pre-clamp pressure is 130 bar).

<table>
<tr><th rowspan="2">Experiment stage</th><th rowspan="2">Top sheet</th><th rowspan="2">Bottom sheet</th><th colspan="2">Rivet</th><th colspan="2">Die</th><th rowspan="2">Rivet setting pressure (bar)</th></tr>
<tr><th>Length (mm)</th><th>Hardness (HV)</th><th>Diameter (mm)</th><th>Depth (mm)</th></tr>
<tr><td rowspan="2">Feasibility</td><td>3.1 mm Al 6060</td><td>2.0 mm G300</td><td>8</td><td>410</td><td rowspan="3">10</td><td>3</td><td rowspan="3">215</td></tr>
<tr><td colspan="2">2.0 mm G300</td><td rowspan="2">7</td><td rowspan="2">410</td><td rowspan="2">2.5</td></tr>
<tr><td>Parameter optimization</td><td colspan="2">2.0 mm G300</td></tr>
<tr><td rowspan="9">Residual stress distribution in different SPR joints</td><td colspan="2">1.5 mm G450</td><td rowspan="2">6</td><td rowspan="2">480</td><td rowspan="2">9</td><td rowspan="2">2</td><td rowspan="9">250</td></tr>
<tr><td colspan="2">1.5 mm G300</td></tr>
<tr><td colspan="2">2.5 mm G450</td><td rowspan="2">8</td><td rowspan="2">555</td><td rowspan="2">11</td><td rowspan="2">2.35</td></tr>
<tr><td colspan="2">2.5 mm G300</td></tr>
<tr><td colspan="2">2.0 mm G300</td><td rowspan="5">7</td><td>480</td><td rowspan="5">10</td><td>2.5</td></tr>
<tr><td colspan="2" rowspan="2">2.0 mm G450</td><td>555</td><td rowspan="4">2.1</td></tr>
<tr><td>480</td></tr>
<tr><td colspan="2" rowspan="2">2.0 mm G300</td><td>555</td></tr>
<tr><td>480</td></tr>
</table>

Neutron diffraction measurements were performed on the Strain Scanner named 'Kowari' [236] at the Australian Nuclear Science and Technology Organisation (ANSTO). A monochromatic beam of thermal neutrons of wavelength 1.66 Å was used and the Feα(211) diffracting plane was chosen for the investigation. A 2D position sensitive ^{3}He detector was used to record the diffraction peak. The detector was positioned at an angle of 90° with respect to the incident beam to utilize the Feα(211) reflection. A schematic setup of the diffraction experiment is shown in Fig. 4.9.1. The laboratory setup for the neutron diffraction experiment is shown in Fig. 4.9.2.

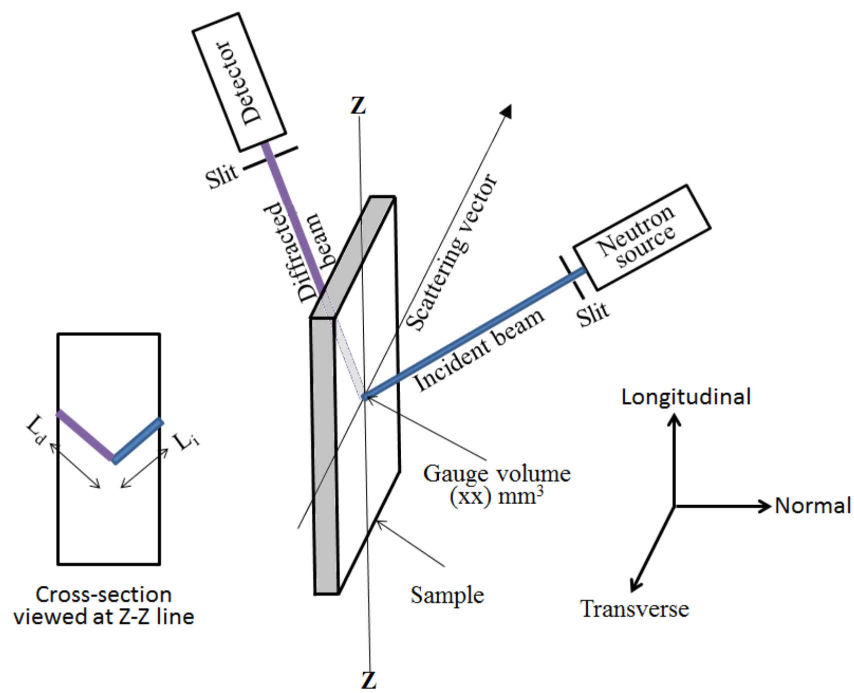

Incident neutron beam length = L_i Diffracted neutron beam length = L_d
Neutron path length = $L_i + L_d$

Fig. 4.9.1 Schematic diagram of strain scanner showing the setup for diffraction experiment.

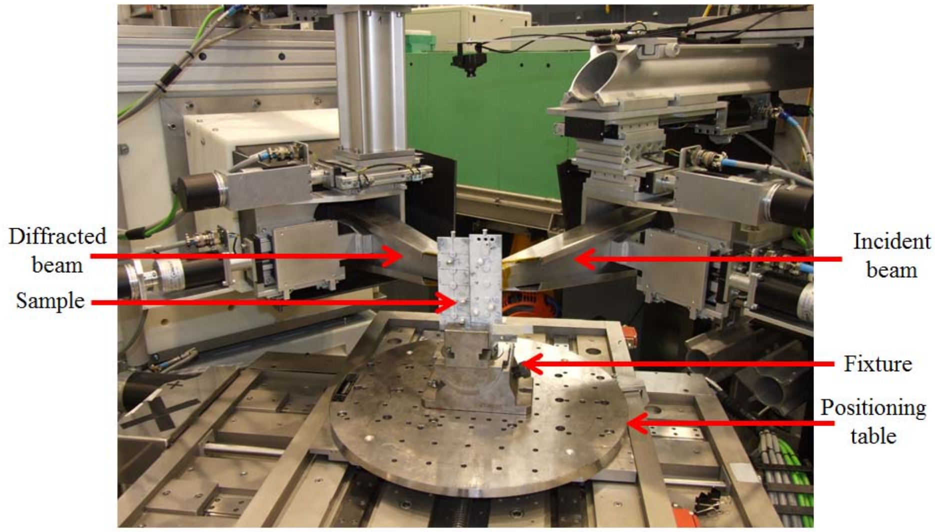

Fig. 4.9.2 Laboratory setup of the strain scanner (Kowari at ANSTO) showing the typical setup for the diffraction experiment of a normal residual strain component.

The specimen was accurately positioned (± 100 μm) on the instrument using the virtual instrument of Kowari in SScanSS [237, 238] software. The model of the Kowari strain diffractometer within the SScanSS software is shown in Fig. 4.9.3.

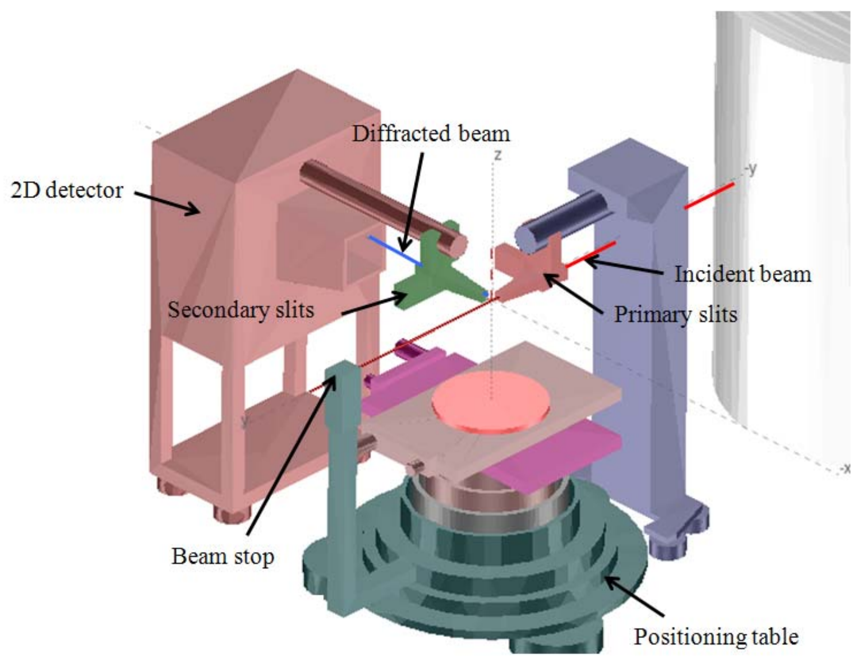

Fig. 4.9.3 Main components and layout of the Kowari strain scanning diffractometer model within the SscanSS software

The specimen was first laser scanned to obtain a 3D model, was then positioned on the experimental table and aligned using dedicated robotic arms with the touch probe. SScanSS was also used to define the measurement points (Fig. 4.9.4), based on the cross-section of the joint at the X-X line as the internal features of the joint are hidden from the laser scan, and to estimate the required counting time depending on the beam path length for a given direction of strain. To double check the alignment a line scan was conducted in order to find the wall of the specimen. Neutron measurements were conducted at 30 points and the intensity of those points was plotted in the software EC-align as shown in Fig. 4.9.5.The position of the specimen wall was obtained by analysing the intensity as shown in Fig. 4.9.5 and this position was verified by the software SScanSS.

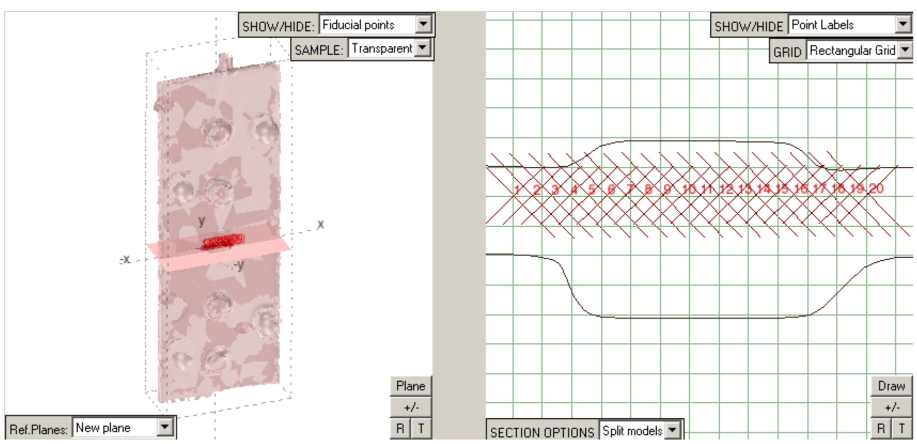

3D model of the sample Cross-section of the joint viewed at X-X line

Fig. 4.9.4 Defining the measuring points within the software SscanSS.

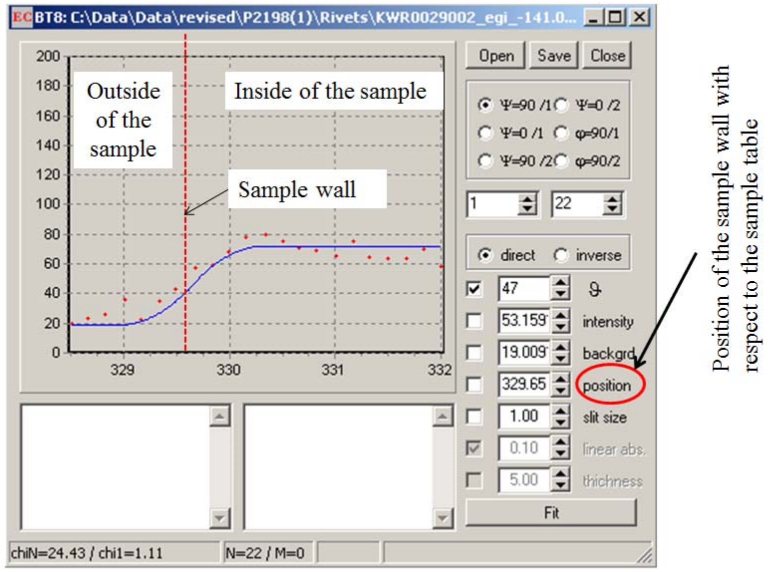

Fig. 4.9.5 Double checking the specimen alignment by a combination of neutron scanning and EC-align software at the Kowari strain scanner.

4.9.1 Feasibility test

At first, sheet specimens of aluminium and steel were chosen to ensure that all diffracted peaks could be determined easily from either the rivet or the bottom sheet, as the diffraction angles for steel and aluminium are different. A riveted joint specimen was produced, as shown in Fig. 4.9.6a, using 3.1 mm aluminium and 2.0 mm steel as the top and bottom sheets respectively. Five joints were made at 25 mm spacing using rivets and die selected according to the total ply thickness and sheet materials. Joint 68 located in the middle of the specimen shown in Fig. 4.9.6a was chosen for the residual stress evaluation.

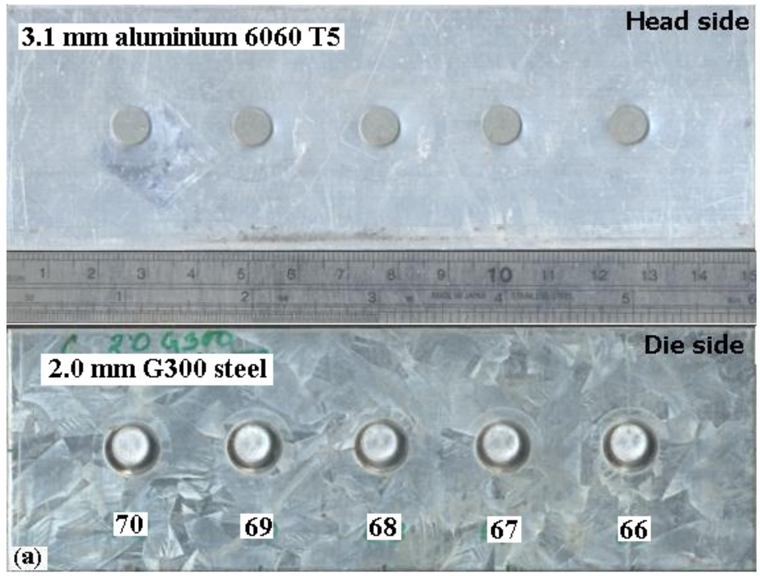

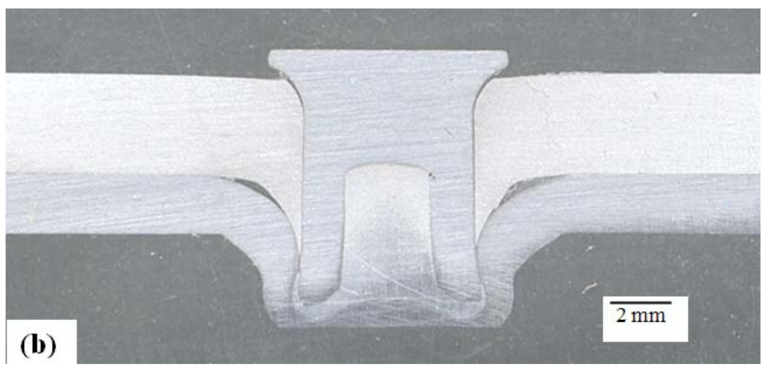

Fig. 4.9.6 (a) Aluminium- steel riveted joint under investigation (b) Cross-sectioned joint-68 after neutron diffraction evaluations were made.

In this case, the thickness was reduced to 4.0 mm (2.0 mm carbon steel as top and bottom sheet) as a result of replacing the top aluminium sheet with 2.0 mm steel sheet (Fig. 4.9.7a). Force and displacement were recorded during the riveting process and it was observed that for both conditions all five joints showed high reproducibility during the riveting operation (Fig. 4.9.8). The maximum force was 49 kN and the rivet setting pressure was 215 bar, whereas the pre-clamp pressure was 130 bar. Joint 78 located in the middle of the specimen shown in Fig. 4.9.7a, was chosen for the residual stress evaluation.

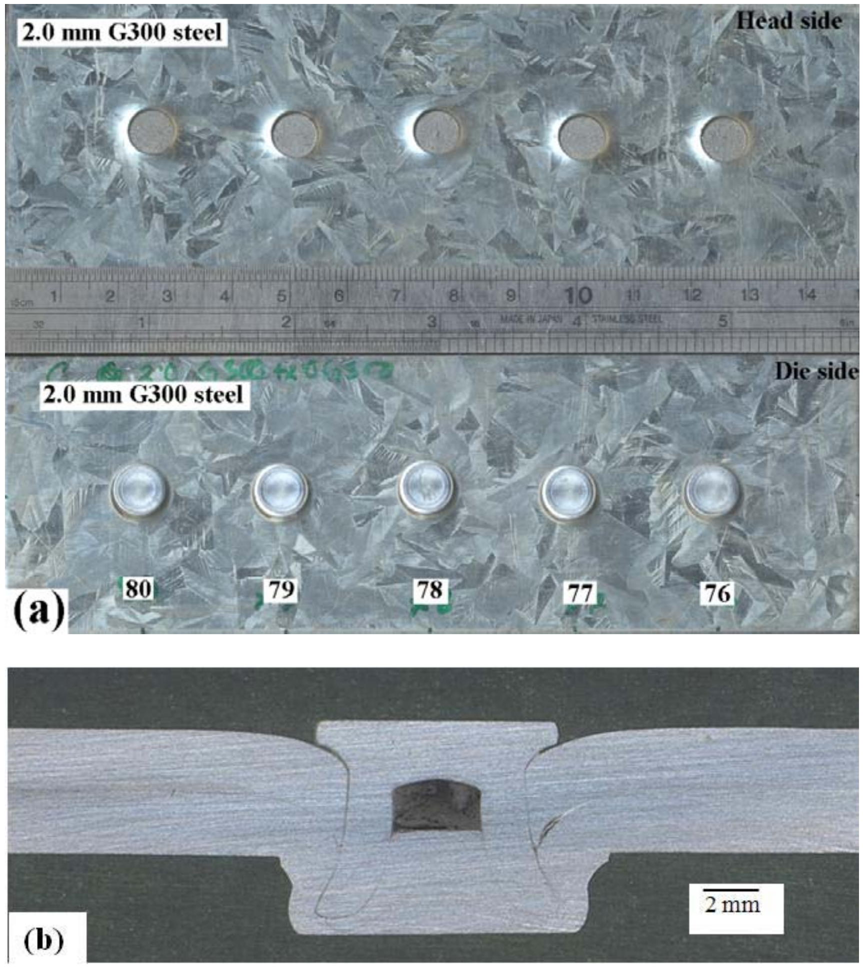

Fig. 4.9.7 (a) Steel- steel riveted joint under investigation (b) Cross-sectioned joint-78 after neutron diffraction evaluations were made.

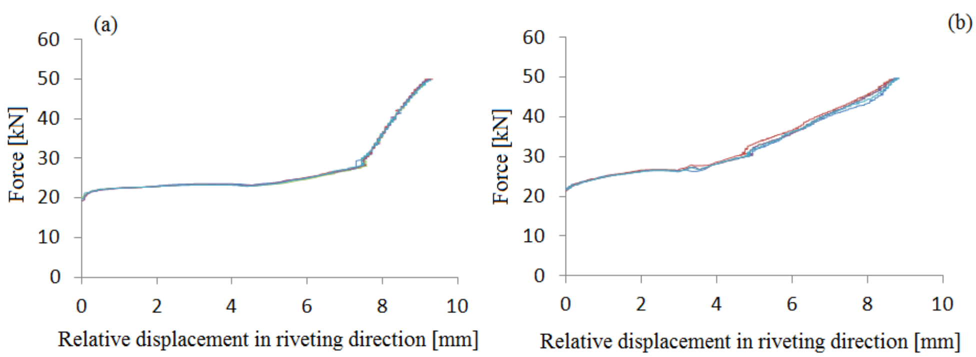

Fig. 4.9.8 Force versus displacement curves of the SPR process showing high reproducibility (a) for an aluminium-steel joint (b) for a steel-steel joint.

4.9.2 Parameter optimization for meaningful measurement

The sample size was kept the same and five joints were made at 25 mm spacing (Fig. 4.9.9a) using rivets and die selected according to the total ply thickness and sheet materials. The maximum force was 49 kN and rivet setting pressure was 215 bar, whereas the pre-clamp pressure was 130 bar. Force and displacement were recorded during SPR and it was observed that the riveting process showed high reproducibility, as shown in Fig. 4.9.8. Hence, the joint located in the middle of the specimen shown in Fig. 4.9.9a was chosen for residual stress evaluation. A cross-section of the middle joint (Fig. 4.9.9b) was taken after the neutron diffraction analysis was completed.

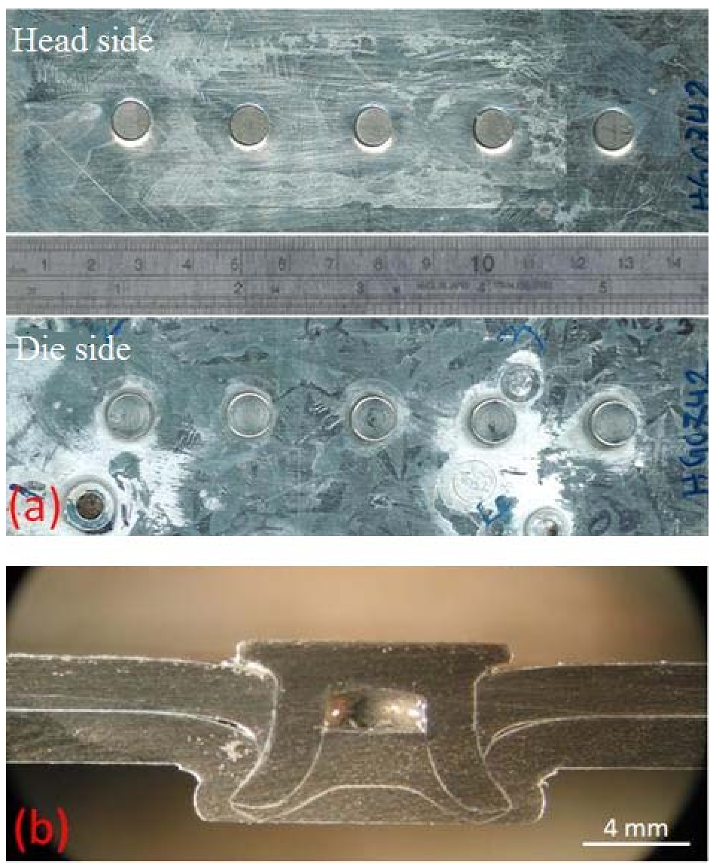

Fig. 4.9.9 (a) Steel- steel riveted joint under investigation, and (b) cross-sectioned middle joint after neutron diffraction evaluation were made.

4.9.3 Residual stress in different SPR joints

Nine different combinations of joints comprised of two different material hardnesses, three forms of rivet hardnesses and three types of material thicknesses were chosen for this study according to Table 4.9.1. In each case five joints were created in each specimen and the joint in the middle was investigated for residual stress evaluation.

4.10 Static strength tests

Static strength of the SPR joints was examined in two different loading conditions: Cross-tension and lap-shear. Nine different combinations of joints comprised of three types of thicknesses (5.0, 4.0 and 3.0 mm) and two different hardnesses of material (G300 and G450 carbon steel with hardnesses of 198 HV and 270 HV respectively), and two forms of rivet hardnesses (555 and 480 HV) were considered for both loading conditions in this study. A flat die was used for each condition with a high die recess volume for the thick joint and a low die recess volume for the thin joint.

The static test was performed in a MTS machine under displacement control at a rate of 1 mm / minute. The experiment was programmed in a way so that the process stopped automatically when the joint failed. The force and the displacement were recorded during the examination with a logging rate of 20 Hz and the force was plotted as a function of displacement. The analysis of these results is discussed in Chapter 7.

4.10.1 Cross-tension loading condition

For the purpose of good statistics, five test pieces were produced for each joint combination for cross-tension loading condition (Fig. 4.10.1) using a single rivet pierced in the middle of the sheets. It was observed that the force-displacement curve for a single riveted joint overlayed with the force-displacement curves of 5 riveted joint. To test the cross-tension strength the specimen was mounted in a MTS machine as shown in Fig. 4.10.2.

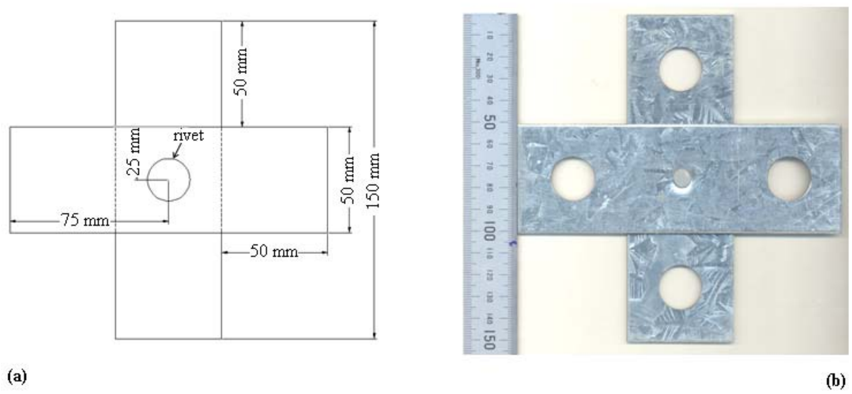

Fig. 4.10.1 Diagram of a single point cross-tension SPR joint (a) schematic and (b) experimental.

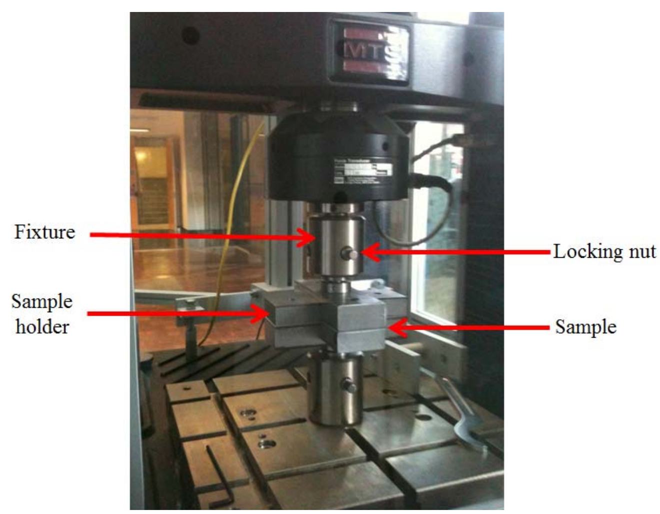

Fig. 4.10.2 Lab setup for the cross-tension test in a MTS machine.

4.10.2 Lap-shear loading condition

Like the cross-tension condition, again five test pieces were produced for each joint combination for cross-tension loading condition (Fig. 4.10.3) using a single rivet pierced in the middle of the sheets. To test the lap-shear strength the specimen was mounted in a MTS machine as shown in Fig. 4.10.4.

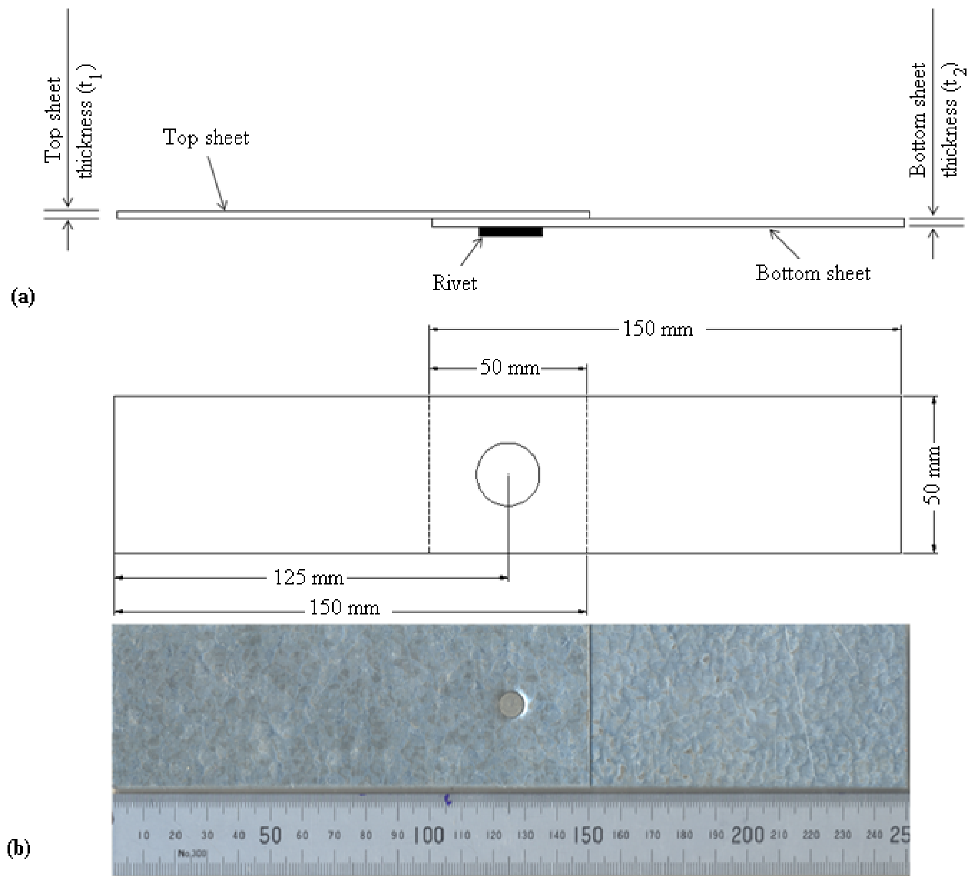

Fig. 4.10.3 Diagram of a single point lap-shear SPR joint (a) schematic and (b) experimental.

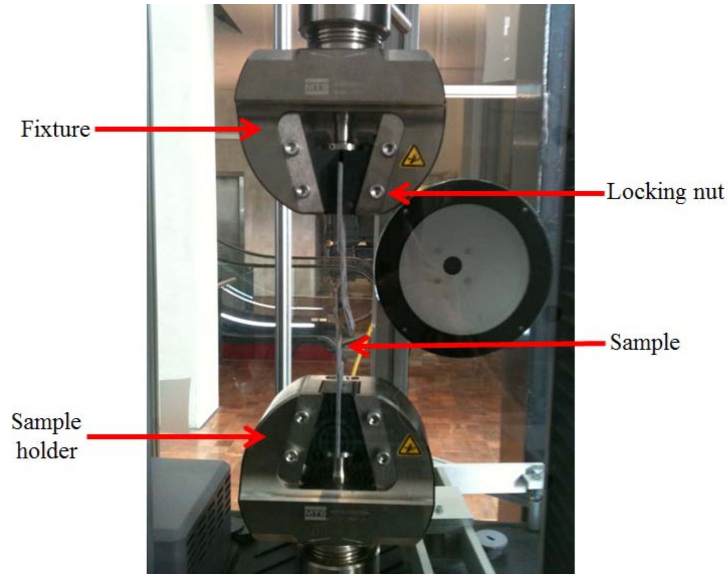

Fig. 4.10.4 Lab setup for the cross-tension test in a MTS machine.

5 CHARACTERIZATION OF RIVETING PROCESS

For process monitoring, measurable parameters should be established. A characteristic curve can be produced by measuring force and displacement directly during riveting. A typical force-displacement curve is shown in Fig. 5.1 for the SPR process. Such a curve is usually divided into four steps to describe key events occurring during SPR, namely: step I – bending of sheet and partial filling of die; step II – piercing of top sheet and sheet bending when the rivet is driven through the top sheet by shearing; step III – die filling, penetration of rivet in the bottom sheet and start of spreading of rivet; and step IV – rivet flaring, setting of the rivet head and forming of the interlock [15-17].

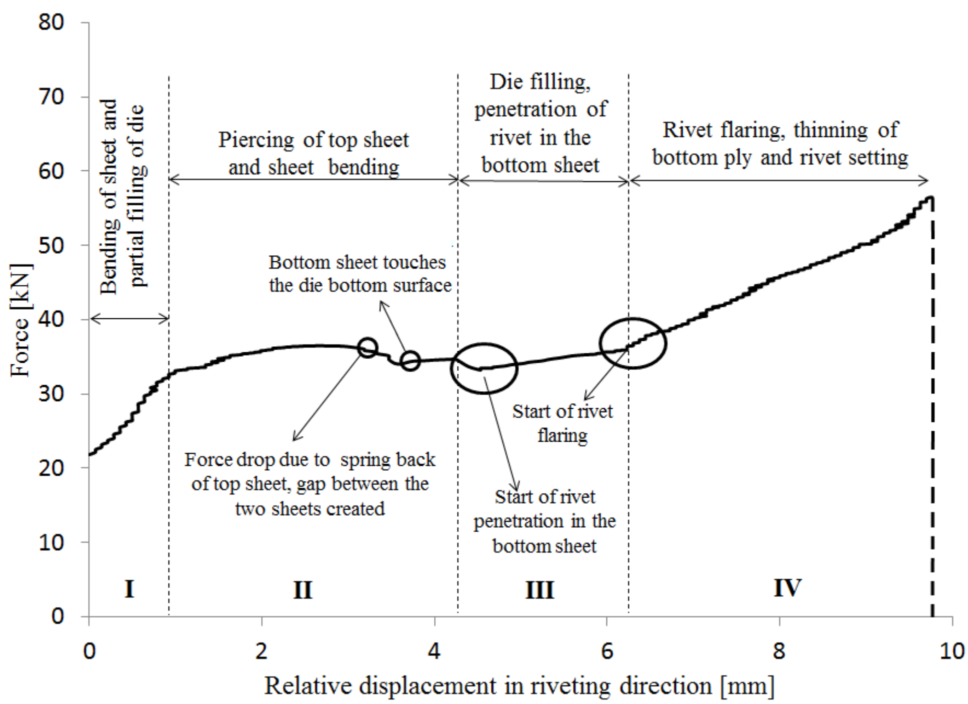

Fig. 5.1 Force-displacement curve of 2.5 mm + 2.5 mm sheets (280 HV) joint with an 8 mm long rivet having a hardness of 555 HV.

To understand the riveting process, it is necessary to fully characterize the force-displacement curve by determining the length of each step in terms of displacement and the effects of stack thickness, rivet length and hardness of ply materials and rivet on the characteristic force-displacement curve. Therefore a series of SPR experiments was conducted on steel sheets of different hardnesses, where the formation of joints was interrupted at different positions by inserting spacers between the upsetting die and die holder. In all experiments, the force and punch displacement of the punch in the riveting direction (Fig. 4.8.1) were measured directly during the riveting process using a load cell and LVDT, respectively. Chapter 5.1 describes the procedures developed from interrupted test.

Selection of a die is a very important part of the riveting process. Improper die selection may lead to cracking, resulting in an unwanted joint in the SPR process. Details of die selection are shown in chapter 5.2. In the following stage (chapter 5.3) the effect of die depth on the characteristic curve is illustrated. Chapters 5.4 and 5.5 demonstrate the influence of ply materials' hardness and thickness on the characteristic curve respectively. The force-displacement profile is also changed by rivet hardness. The dependency of the characteristic curve on rivet hardness is explained in chapter 5.6. Finally the change in characteristic curve subject to single ply and double ply is narrated in chapter 5.7. While acknowledging the multifactorial dependency on the whole process parameters, the approach used in this thesis was to conduct a systematic analysis by changing one parameter at a time in sections 5.1 to 5.7.

C-frame deflection occurs during the riveting process in the SPR rig. The measuring technique of the C-frame deflection and characterization of the force-displacement curve after deducting the C-frame deflection is reported in the subsequent sections of this chapter.

Finally, a simple and effective model has been developed to determine rivet flaring in self-piercing riveted (SPR) joints after introducing C-frame deflection in this chapter. Fourteen different conditions have been considered, comprising three types of thicknesses and two different hardnesses of ply materials, and steel rivets with three forms of hardness values. Some joints have been interrupted at different punch positions and cross-sections of those joints have been taken in order to identify the starting point of rivet flaring and to determine the flaring path of the rivet tip. The internal geometric characteristics of interrupted joints have been measured from cross-sections by quantitative metallography and have been related to the force-displacement curve obtained for each joint.

This chapter shows that the characteristic force-displacement curve can be used to predict the rivet flaring inside an SPR joint by using the mathematical relationship developed which eliminates the need for having to cross-section the joint to determine rivet flaring by quantitative metallography. Another destructive method for rivet flaring measurement is rivet extraction but information on effective rivet length on the bottom sheet may be lost.

5.1 Interrupted test

SPR joining involves mainly two distinct events (piercing and flaring) during the process. During SPR, a tubular rivet is driven through the top sheet, piercing but not perforating the bottom sheet, accompanied by flaring of the legs in the bottom sheet under the guidance of a suitable die. The rivet material should have adequate hardness to pierce the top sheet and sufficient ductility to deform in the bottom sheet without cracking, thereby providing a sound mechanical interlock between the top and bottom sheets. To characterize the force-displacement curve, a series of SPR experiments was conducted on carbon steel sheets (G300 and G450 carbon steel having hardnesses of 198 HV and 270 HV respectively), where the formation of joints was interrupted at different positions by inserting spacers between the upsetting die and die holder according to Table 5.1.1 The interrupted positions were chosen in order to obtain sufficient snapshots to understand what is happening during SPR. The length of the rivet was chosen according to the total ply thickness together with the die-set. It should be noted that all these materials and sizes are realistic for industrial conditions.

Table 5.1.1 Materials and joining parameters (pre-clamp pressure was 125 bar).

Joint parameters	Ply materials	Rivet		Die (flat die profile)		Interruption distances (mm)
		Length (mm)	Hardness (HV)	Depth (mm)	Diameter (mm)	
Condition 1	2.5 mm + 2.5 mm G450	8	555	2.35	11	3.45, 3.90, 4.20, 4.30, 4.40, 4.70, 4.90, 5.40, 6.30, 7.30, 8.20, 9.10, 9.80
Condition 2	2.5 mm + 2.5 mm G300	8	555	3.0	10	2.60, 3.25, 3.90, 4.40, 5.00, 5.60, 7.10, 7.60, 8.50, 9.50
Condition 3	2.0 mm + 2.0 mm G300	7	555	2.5	10	1.85, 2.35, 3.35, 3.55, 4.25, 5.25, 6.60, 8.50
Condition 4	2.0 mm + 2.0 mm G300	7	480	2.5	10	1.90, 2.25, 2.85, 3.30, 4.40, 5.50, 6.60, 8.70
Condition 5	2.0 mm + 2.0 mm G300	7	410	2.5	10	2.30, 3.60, 4.20, 4.90, 6.15, 8.35, 8.80
Condition 6	1.5 mm + 1.5 mm G300	6	480	2.3	9	1.85, 2.50, 2.90, 3.40, 4.10, 4.50, 6.95
Condition 7	1.5 mm + 1.5 mm G300	6	410	2.3	9	2.00, 2.50, 2.95, 3.45, 3.95, 4.45, 7.50

5.1.1 Condition # 1 (2.5 + 2.5 mm G450 carbon steel)

To thoroughly understand the SPR process, at first, a thick sheet (stack thickness of 5.0 mm) of hard material (G450 carbon steel) was chosen and interrupted at 13 different positions (condition 1 in Table 5.1.1). Force-displacement curves, photo of SPR joints from the die side and cross-sections of joints are shown in Figs. 5.1.1-26. It can be observed from these figures that during the early stage of the SPR process, bending of sheet metal occurred, and the die was filled partially by the material. The sheet deformed plastically, but no failure occurred as the stress generated during this period was below the ultimate strength of material.

Interruption distance of 3.45 mm

A photograph of a SPR joint from the die side, a cross-section of the joint and a force-displacement curve interrupted at 3.45 mm are shown in Figs. 5.1.1-2. The rivet wall remained straight (Fig. 5.1.1b). At the beginning, the force started to increase with a high gradient up to 1 mm displacement (Fig. 5.1.2). Then, the curve flattened, indicating the start point of piercing into the top sheet by the rivet.

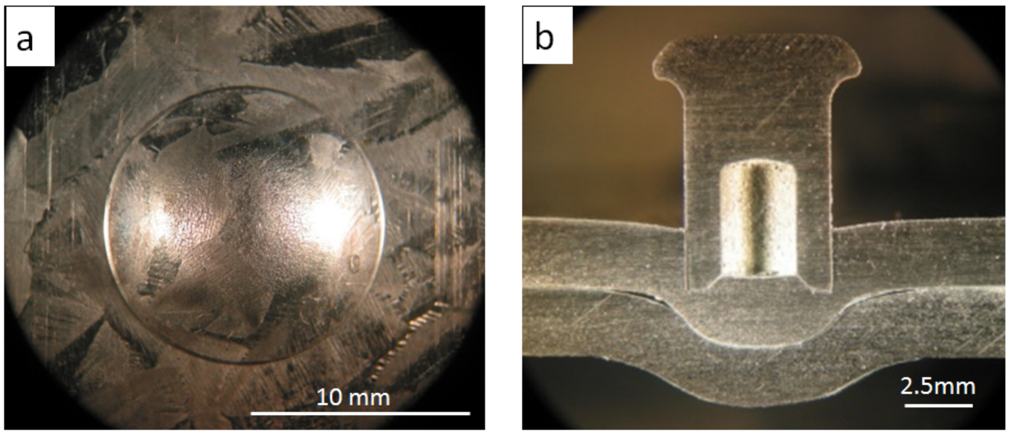

Fig. 5.1.1 (a) Photo of a SPR joint from die side and (b) cross-section of 2.5 mm + 2.5 mm G450 steel joint with 8 mm long rivet of hardness 555 HV interrupted at 3.45 mm.

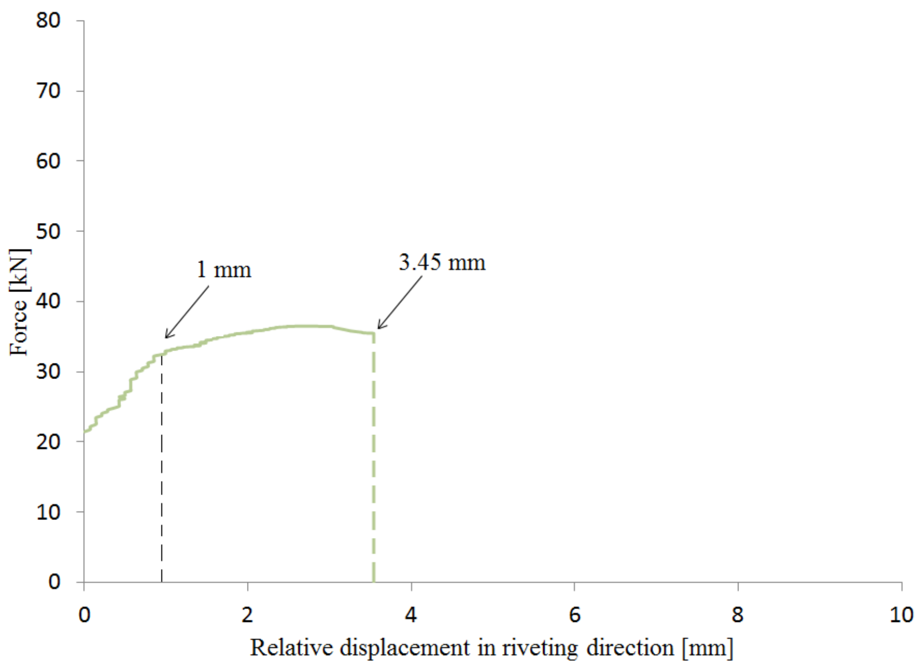

Fig. 5.1.2 Force-displacement curve of 2.5 mm + 2.5 mm G450 steel joint with 8 mm long rivet of hardness 555 HV interrupted at 3.45 mm.

Interruption distance of 3.90 mm

A photograph of a SPR joint from the die side, a cross-section of the joint and a force-displacement curve interrupted at 3.90 mm are shown in Figs. 5.1.3-4. It is noticeable from Fig. 5.1.4a that after a displacement of 3.0 mm the force dropped gradually due to the decrease in bending force, where a gap was observed between top and bottom sheet (Fig. 5.1.3b). However, it can be observed from Fig. 5.1.6 that at 3.90 mm the force started to increase. Fig. 5.1.3a shows that a flat round spot was created in the middle of the joint due to the footprint from the die bottom surface, i.e., the bottom sheet touched the die bottom surface at a displacement of 3.90 mm. The touch point of the die bottom surface depends mainly on the hardness and thickness of the materials and the die parameters (diameter and depth). It is observed from Fig. 5.1.3b that the rivet wall also remained straight.

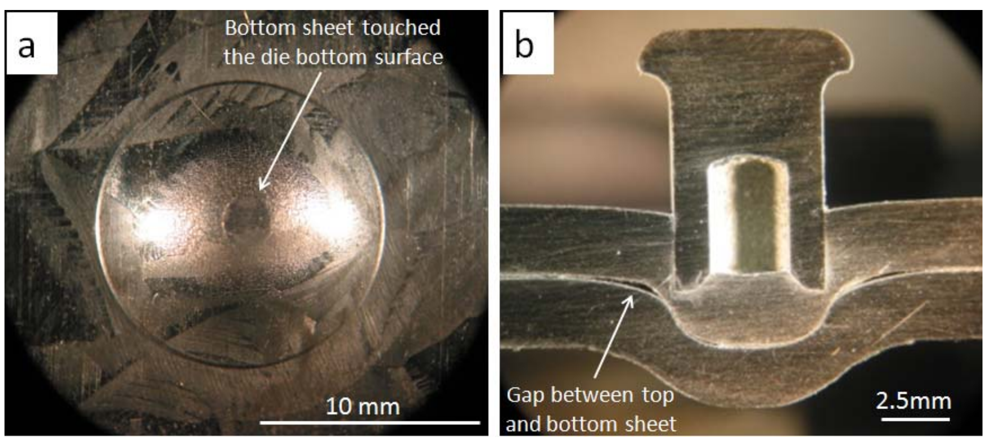

Fig. 5.1.3 (a) Photo of a SPR joint from die side and (b) cross-section of 2.5 mm + 2.5 mm G450 steel joint with 8 mm long rivet of hardness 555 HV interrupted at 3.90 mm.

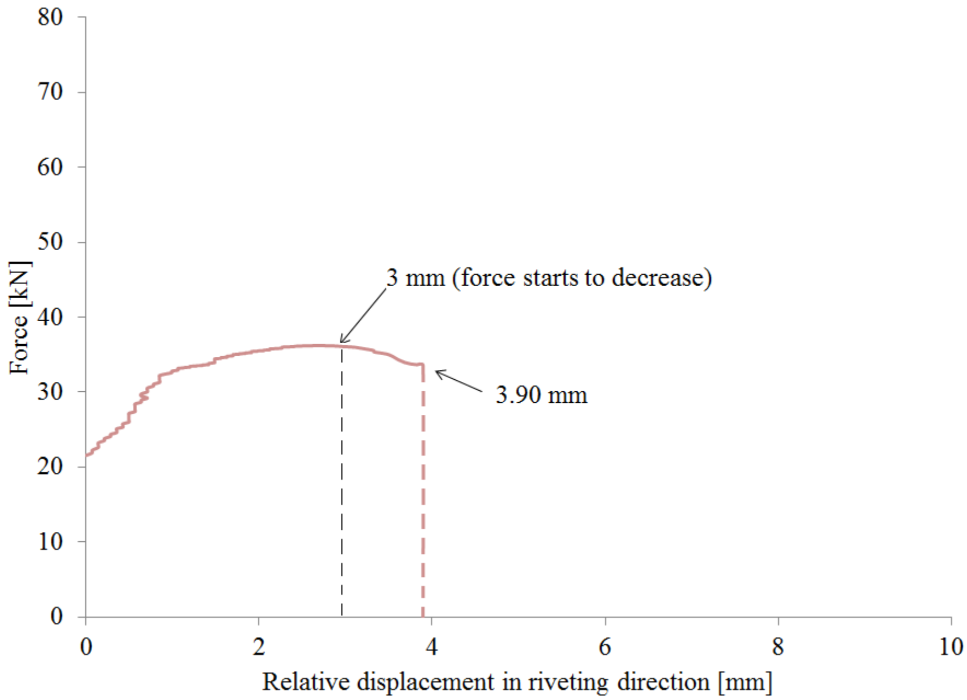

Fig. 5.1.4 Force-displacement curve of 2.5 mm + 2.5 mm G450 steel joint with 8 mm long rivet of hardness 555 HV interrupted at 3.90 mm.

Interruption distance of 4.20 mm

As soon as the bottom sheet touched the die bottom surface at a displacement of 3.90 mm (Fig. 5.1.6), the force started to increase due to the increased reaction force from the die. Before this point (3.9 mm) the flow of material towards the die cavity occurred mainly axially in the riveting direction, and then radially. For this reason, the size of the footprint from the die bottom surface of the joint increased gradually with the displacement (Fig. 5.1.5a) while the wall of the moving rivet remained straight (Fig. 5.1.5b).

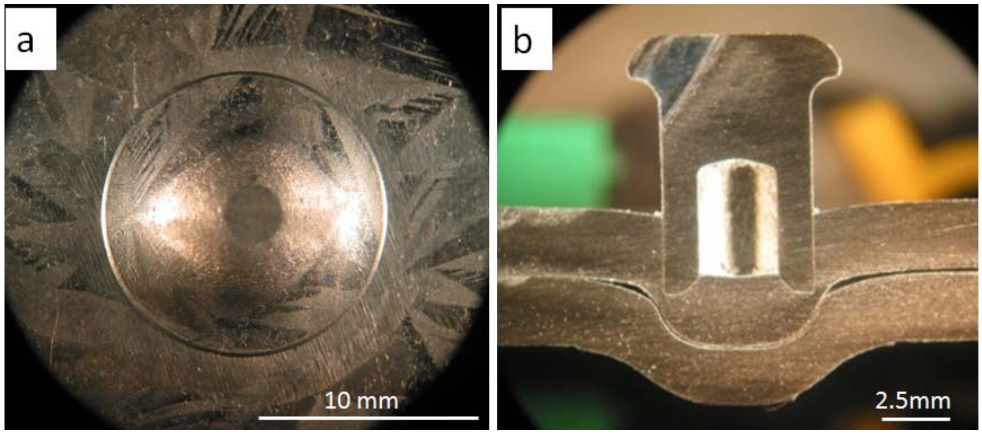

Fig. 5.1.5 (a) Photo of a SPR joint from die side and (b) cross-section of 2.5 mm + 2.5 mm G450 steel joint with 8 mm long rivet of hardness 555 HV interrupted at 4.20 mm.

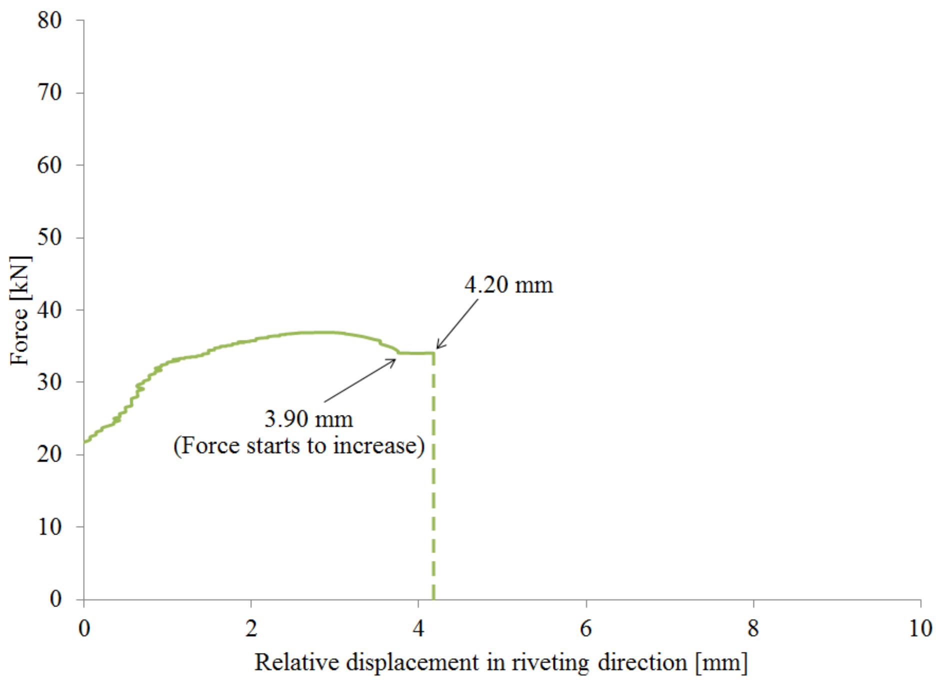

Fig. 5.1.6 Force-displacement curve of 2.5 mm + 2.5 mm G450 steel joint with 8 mm long rivet of hardness 555 HV interrupted at 4.20 mm.

Interruption distance of 4.30 mm

It is evident from Fig. 5.1.8 that the force started to increase gradually with displacement after the first drop at 3.90 mm. This increase in force was mainly related to the material flow in the radial direction characterised by the increasing size of the foot print in the bottom sheet material (Fig. 5.1.7a). It is also obvious from Figs. 5.1.7-8 that the die was filling up with the material while the rivet was piercing the top sheet. The rivet wall also remained straight (Fig. 5.1.7b).

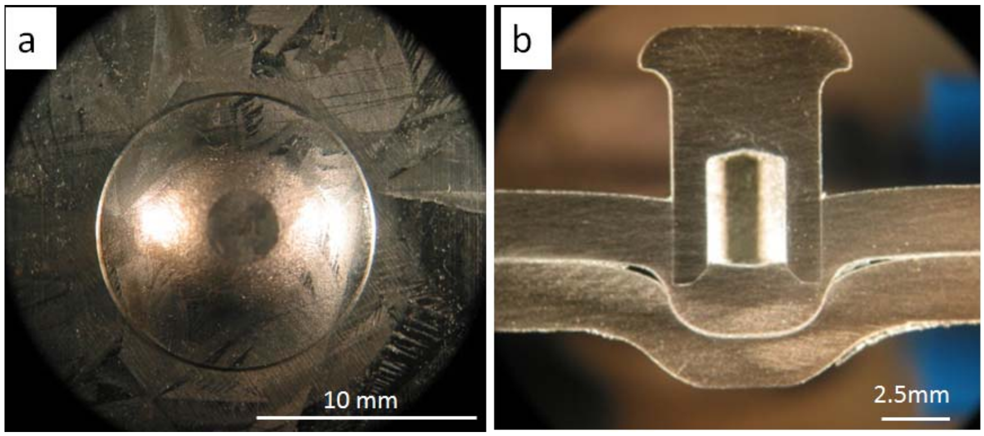

Fig. 5.1.7 (a) Photo of a SPR joint from die side and (b) cross-section of 2.5 mm + 2.5 mm G450 steel joint with 8 mm long rivet of hardness 555 HV interrupted at 4.30 mm.

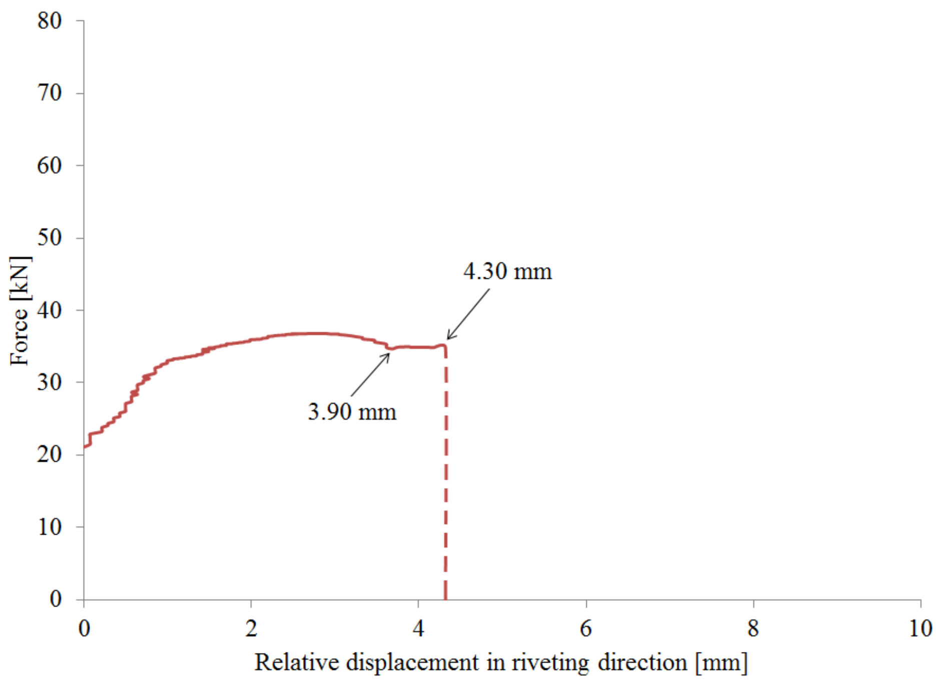

Fig. 5.1.8 Force-displacement curve of 2.5 mm + 2.5 mm G450 steel joint with 8 mm long rivet of hardness 555 HV interrupted at 4.30 mm.

Interruption distance of 4.40 mm

The size of the foot print from the die bottom surface continued to increase with displacement (Fig. 5.1.9a) and the rivet wall remained straight (Fig. 5.1.9b). The force continued to increase with a low gradient while the rivet was piercing the top sheet.

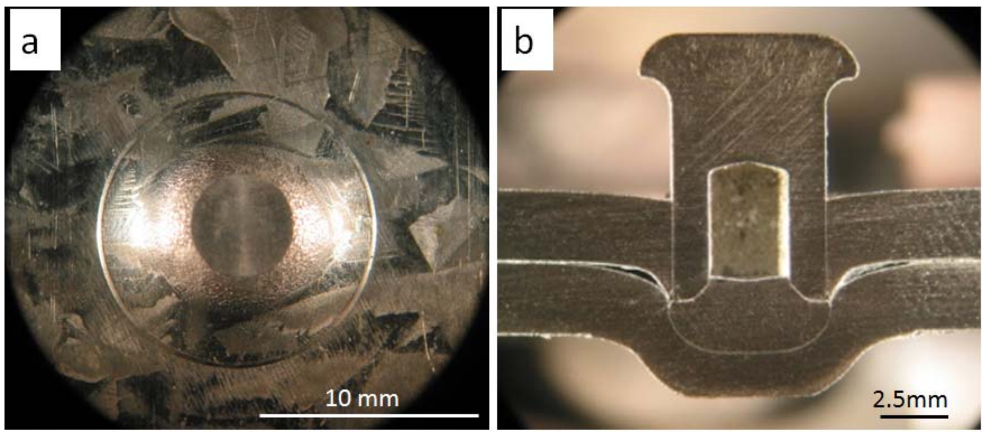

Fig. 5.1.9 (a) Photo of a SPR joint from die side and (b) cross-section of 2.5 mm + 2.5 mm G450 steel joint with 8 mm long rivet of hardness 555 HV interrupted at 4.40 mm.

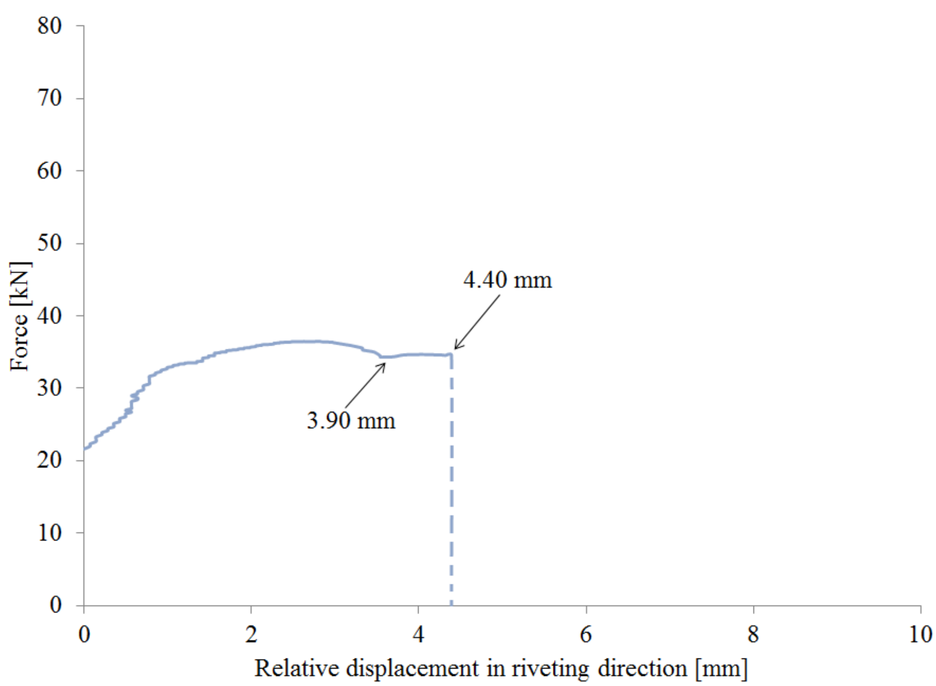

Fig. 5.1.10 Force-displacement curve of 2.5 mm + 2.5 mm G450 steel joint with 8 mm long rivet of hardness 555 HV interrupted at 4.40 mm.

Interruption distance of 4.70 mm

A second drop in force was observed at a displacement of 4.50 mm (Fig. 5.1.12). The resistance force decreased from 33 kN to 32 kN once the top sheet was perforated, the decrease thus indicating the end of piercing of the top sheet as shown clearly in Fig. 5.1.11b the rivet completed the piercing of the top sheet. The decrease in force would be more visible for a thick and hard top sheet. For a thin and soft top sheet this drop in force would be less visible.

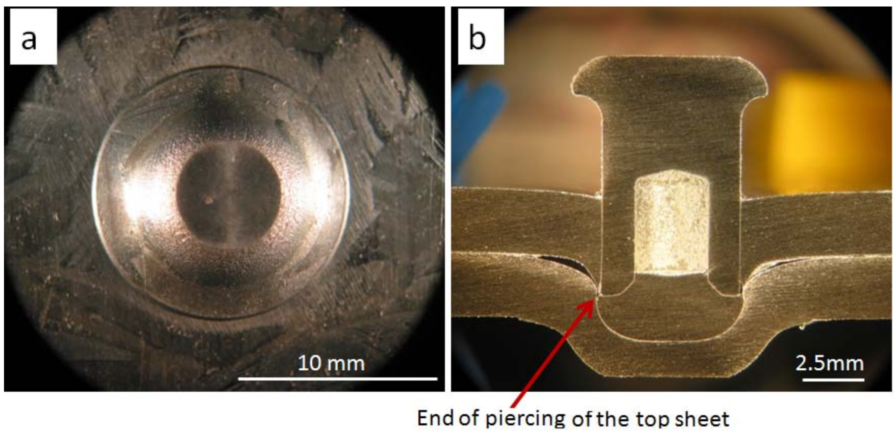

Fig. 5.1.11 (a) Photo of a SPR joint from die side and (b) cross-section of 2.5 mm + 2.5 mm G450 steel joint with 8 mm long rivet of hardness 555 HV interrupted at 4.70 mm.

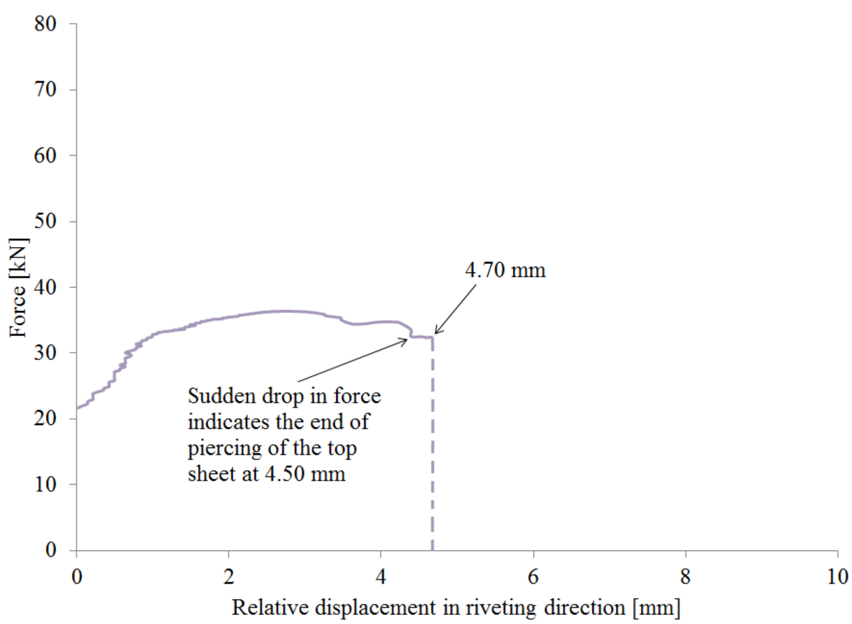

Fig. 5.1.12 Force-displacement curve of 2.5 mm + 2.5 mm G450 steel joint with 8 mm long rivet of hardness 555 HV interrupted at 4.70 mm.

Interruption distance of 4.90 mm

Once the top sheet was pierced the force rose again (Fig. 5.1.14) as more material flowed inside the die cavity. The size of the footprint continued to increase (Fig. 5.1.13a) and the rivet wall remained straight (Fig. 5.1.13b).

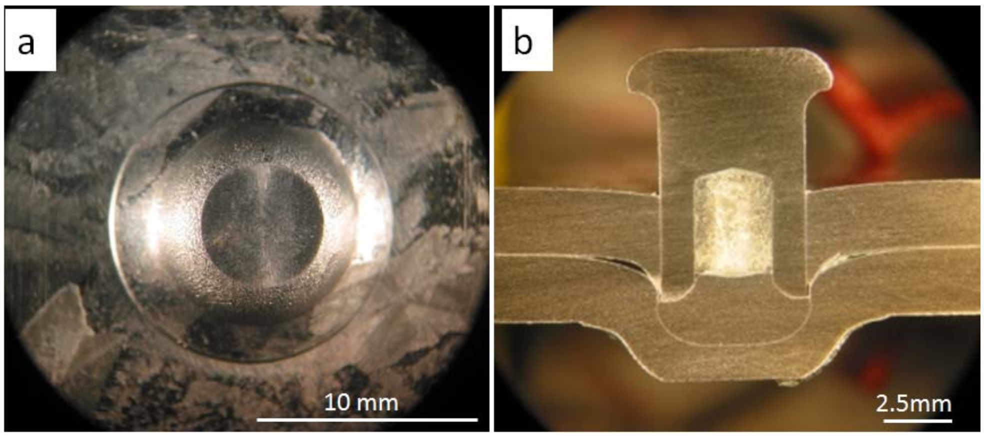

Fig. 5.1.13 (a) Photo of the SPR joint from die side and (b) cross-section of 2.5 mm + 2.5 mm G450 steel joint with 8 mm long rivet of hardness 555 HV interrupted at 4.90 mm.

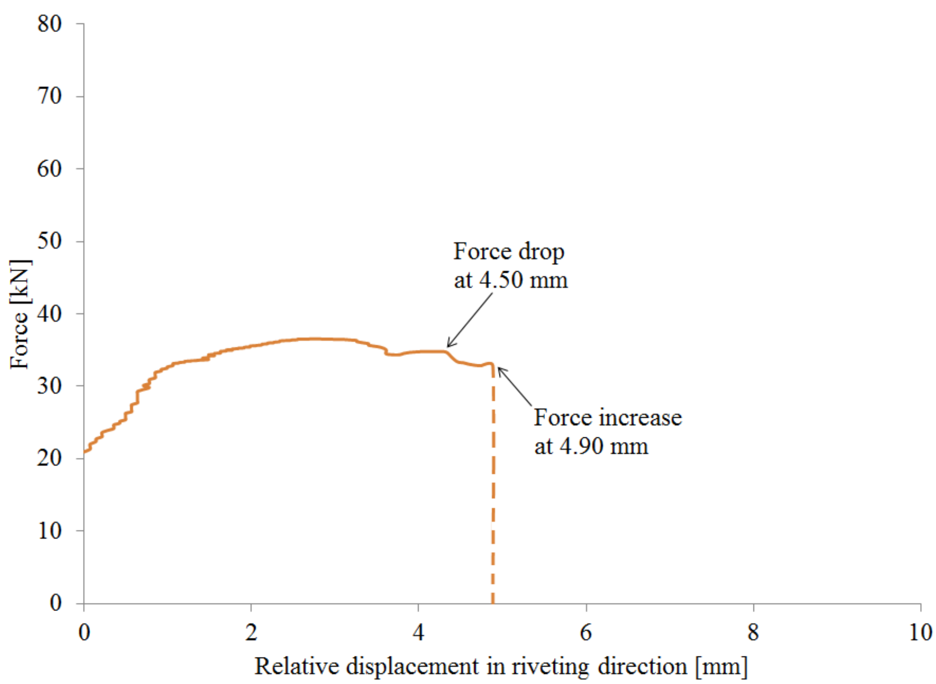

Fig. 5.1.14 Force-displacement curve of 2.5 mm + 2.5 mm G450 steel joint with 8 mm long rivet of hardness 555 HV interrupted at 4.90 mm.

Interruption distance of 5.40 mm

The force increased linearly during this period (Fig. 5.1.16). Material movement without plastic deformation in the riveting direction was no longer possible towards the die. The rivet then started to penetrate the bottom sheet (Fig. 5.1.15b). A minimum of rivet penetration in the bottom sheet is necessary before the rivet starts to flare for an effective mechanical interlock. Thus the length of this stage gives the characteristics of the penetration of the rivet into the bottom sheet (t_{eff} in chapter 7).

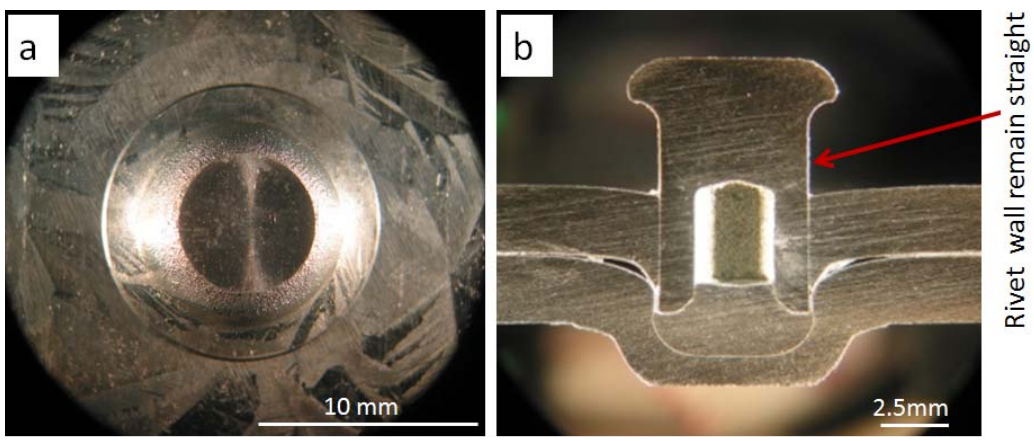

Fig. 5.1.15 (a) Photo of a SPR joint from die side and (b) cross-section of 2.5 mm + 2.5 mm G450 steel joint with 8 mm long rivet of hardness 555 HV interrupted at 5.40 mm.

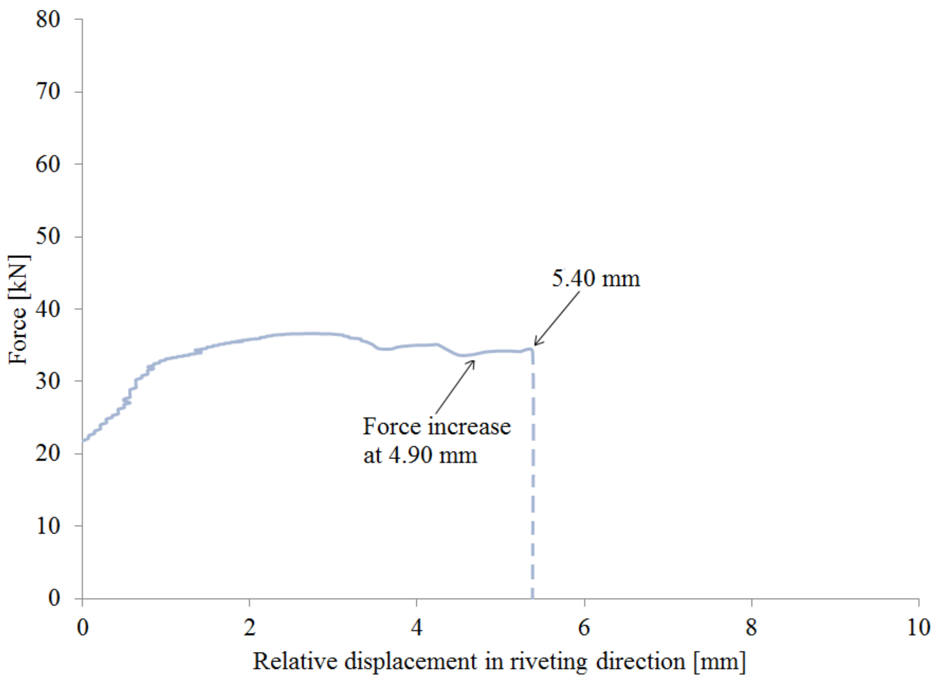

Fig. 5.1.16 Force-displacement curve of 2.5 mm + 2.5 mm G450 steel joint with 8 mm long rivet of hardness 555 HV interrupted at 5.40 mm.

Interruption distance of 6.30 mm

It is clear from Fig. 5.1.17a that the diameter of the footprint continued to increase with displacement. It is also clear from Fig. 5.1.17b that the rivet wall is no longer straight i.e. rivet flaring has started. The corresponding sudden rise in force is not visible in Fig. 5.1.18 as the SPR process was interrupted just at that point, but the step rise in force is visible with the next interrupted distance (Fig. 5.1.20). The rivet was pushed downward because the punch pressure was applied until the pre-set rivet pressure was reached. So a sudden increase in force is observed at a displacement of 6.30 mm and flaring, and in some cases bulging, of the rivet started (Fig. 5.1.20). Rivet bulging occurs when the sheet is too hard compared to the rivet hardness, or when the rivet is too long compared to the joint stack thickness.

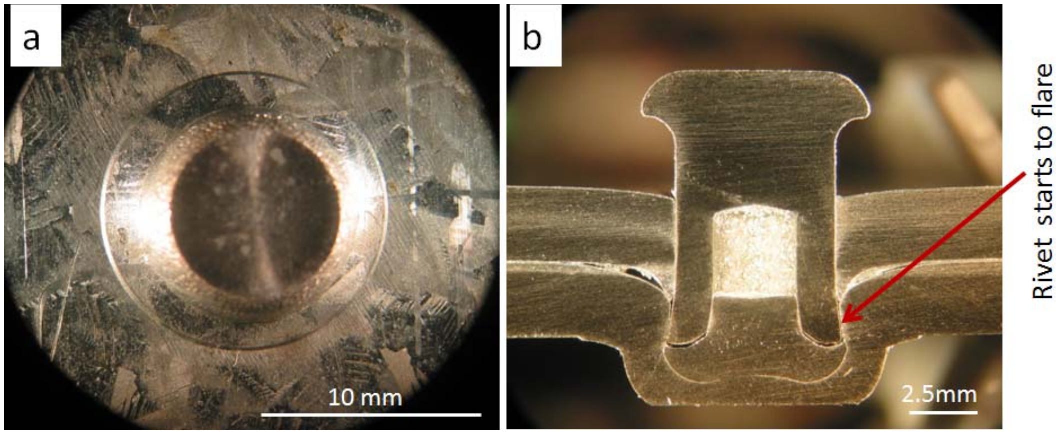

Fig. 5.1.17 (a) Photo of a SPR joint from die side and (b) cross-section of 2.5 mm + 2.5 mm G450 steel joint with 8 mm long rivet of hardness 555 HV interrupted at 6.30 mm.

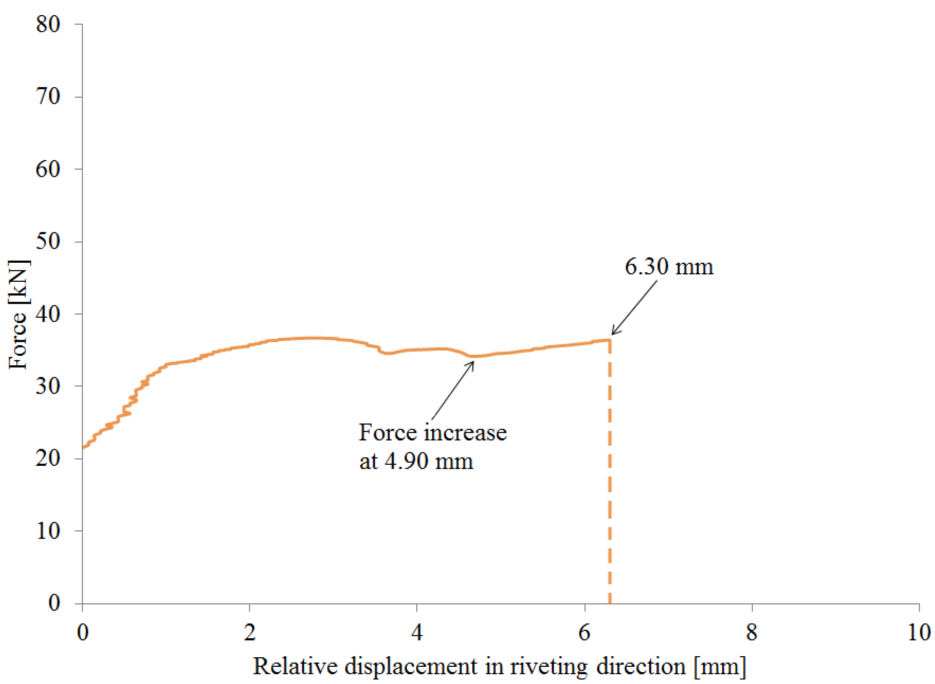

Fig. 5.1.18 Force-displacement curve of 2.5 mm + 2.5 mm G450 steel joint with 8 mm long rivet of hardness 555 HV interrupted at 6.30 mm.

Interruption distance of 7.30 mm

As the rivet started to flare, material flow in the radial direction increased. A rapid increase in the diameter of the footprint is observed in Fig. 5.1.19a due to material flow in radial directions. Thinning of bottom ply started (Fig. 5.1.19b) and the force increased linearly with a higher gradient (Fig. 5.1.20).

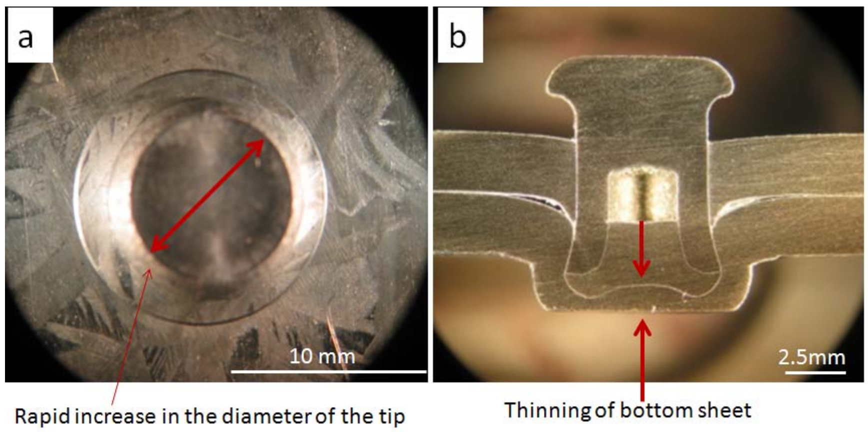

Fig. 5.1.19 (a) Photo of a SPR joint from die side and (b) cross-section of 2.5 mm + 2.5 mm G450 steel joint with 8 mm long rivet of hardness 555 HV interrupted at 7.30 mm.

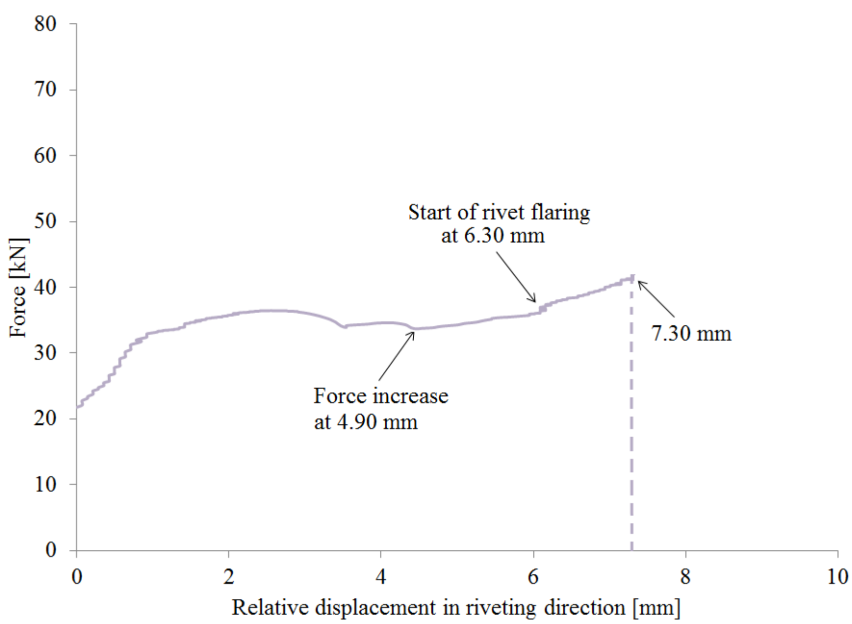

Fig. 5.1.20 Force-displacement curve of 2.5 mm + 2.5 mm G450 steel joint with 8 mm long rivet of hardness 555 HV interrupted at 7.30 mm.

Interruption distance of 8.20 mm

Thinning of bottom ply continued to occur (Fig. 5.1.21b) and the force continued to increase in a linear manner (Fig. 5.1.22). The thinning of the bottom sheet followed the rivet tip geometry.

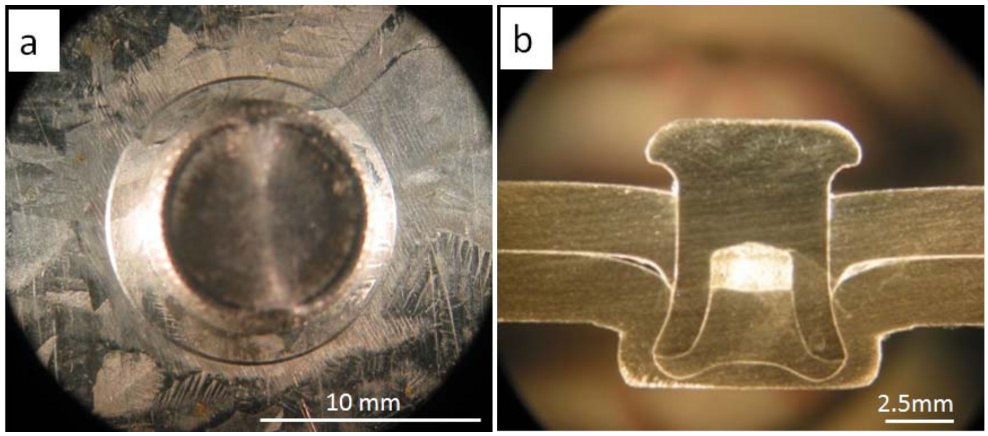

Fig. 5.1.21 (a) Photo of a SPR joint from die side and (b) cross-section of 2.5 mm + 2.5 mm G450 steel joint with 8 mm long rivet of hardness 555 HV interrupted at 8.20 mm.

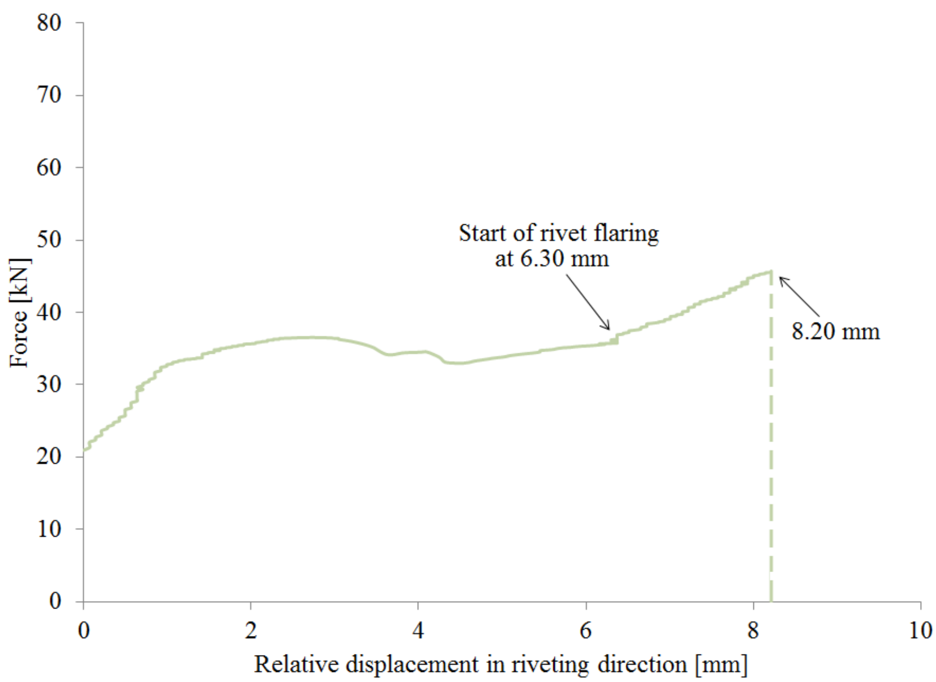

Fig. 5.1.22 Force-displacement curve of 2.5 mm + 2.5 mm G450 steel joint with 8 mm long rivet of hardness 555 HV interrupted at 8.20 mm.

Interruption distance of 9.10 mm

Thinning of the bottom ply continued to occur (Fig. 5.1.23b) and the force continued to increase in a linear manner (Fig. 5.1.24).

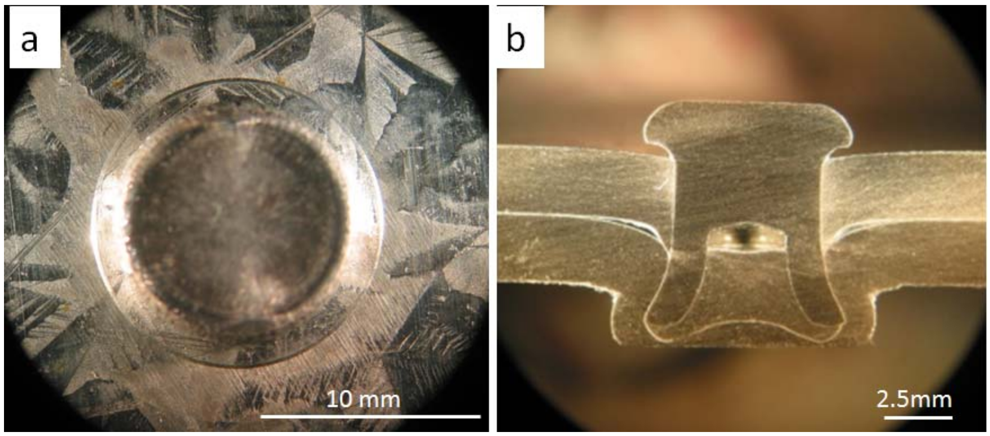

Fig. 5.1.23 (a) Photo of the SPR joint from die side and (b) cross-section of 2.5 mm + 2.5 mm G450 steel joint with 8 mm long rivet of hardness 555 HV interrupted at 9.10 mm.

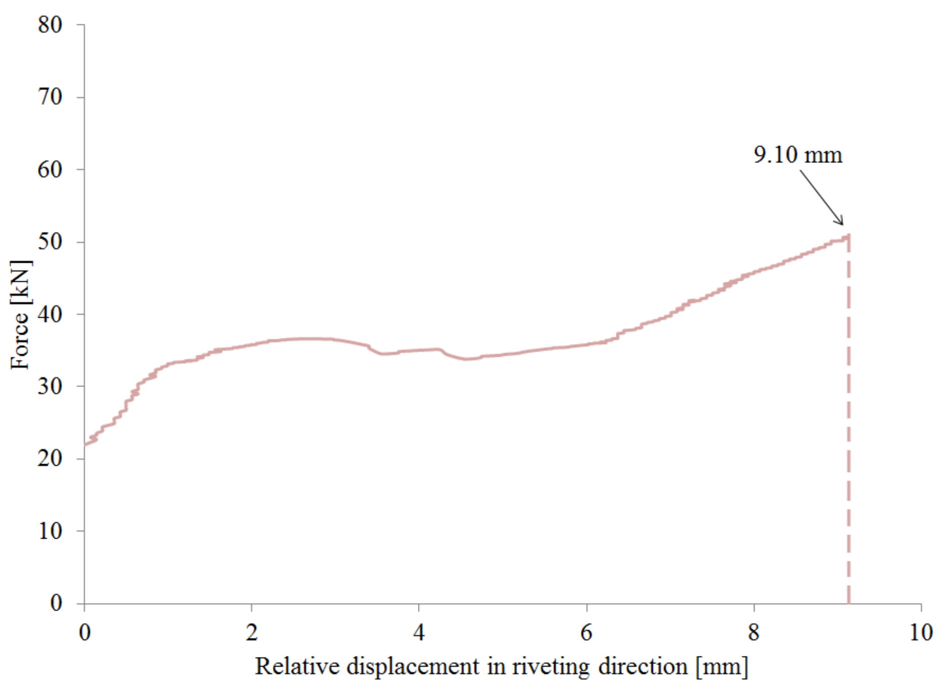

Fig. 5.1.24 Force-displacement curve of 2.5 mm + 2.5 mm G450 steel joint with 8 mm long rivet of hardness 555 HV interrupted at 9.10 mm.

SPR interrupted distance at 9.80 mm (complete joint)

It is clear from Fig. 5.1.25b that rivet flaring and thinning of bottom ply continued to occur up to the end of the riveting process. The mechanical interlock was created gradually by the rivet flaring. The mechanical interlock occurs if the rivet penetrates and flares into the bottom sheet, but if flaring occurs between the top and bottom sheets no interlock would form. The force increases with a high gradient, continuously pushing the cylindrical wall of the rivet to flare outwards, which gradually forms the interlock by this outward deformation of the rivet wall (rivet flaring) and compression of the sheets in the die recess and rivet bore.

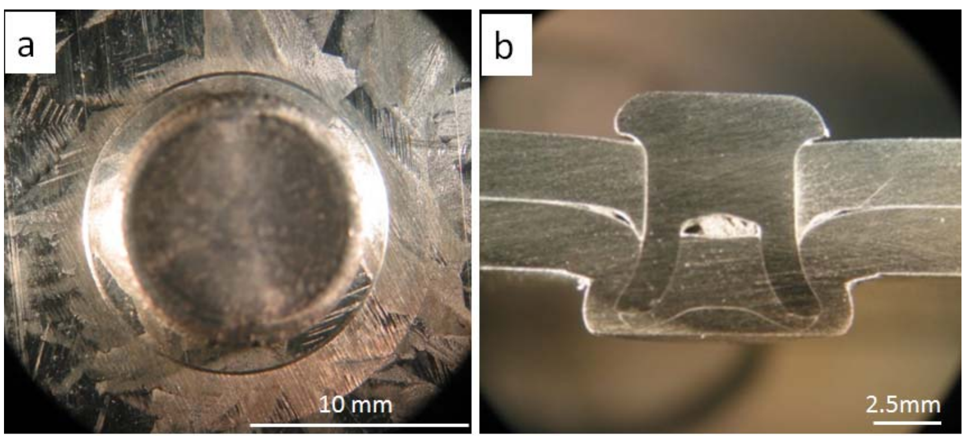

Fig. 5.1.25 (a) Photo of a SPR joint from die side and (b) cross-section of 2.5 mm + 2.5 mm G450 steel joint with 8 mm long rivet of hardness 555 HV at 9.80 mm (complete joint).

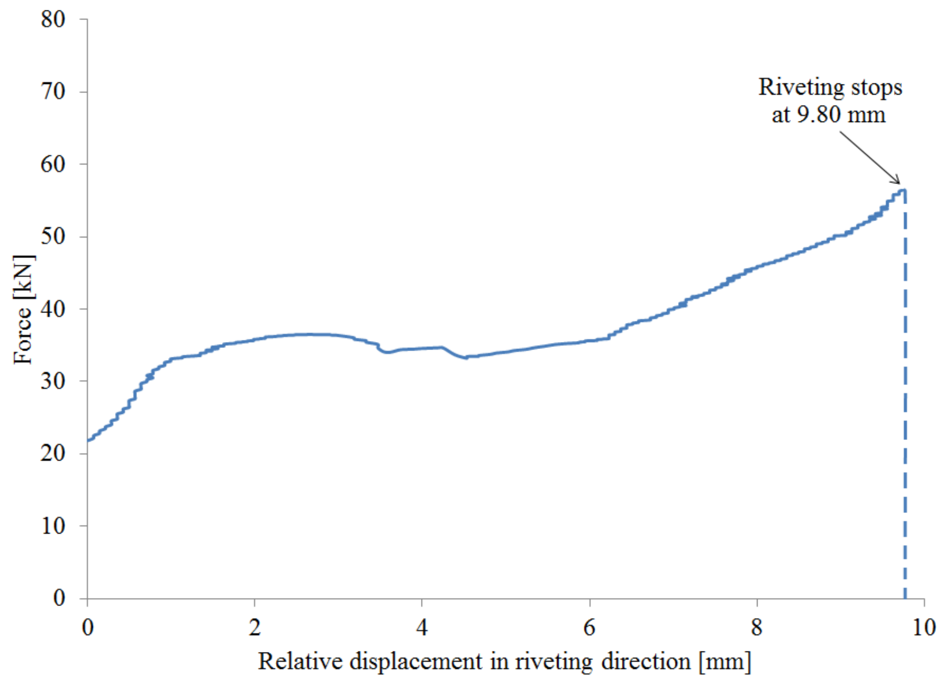

Fig. 5.1.26 Force-displacement curve of 2.5 mm + 2.5 mm G450 steel joint with 8 mm long rivet of hardness 555 HV at 9.80 mm (complete joint).

The whole sequence of interrupted force-displacement curves and associated joints' cross-sections obtained at the different stages for condition 1 in Table 5.1.1 is shown in Fig. 5.1.27. It was clear that successive interrupted curves consistently match each other and fit with the un-interrupted full SPR cycle, which demonstrated that the process had very good reproducibility and the method of interruption had not unduly affected the process conditions, aside from the incompleteness of a given cycle.

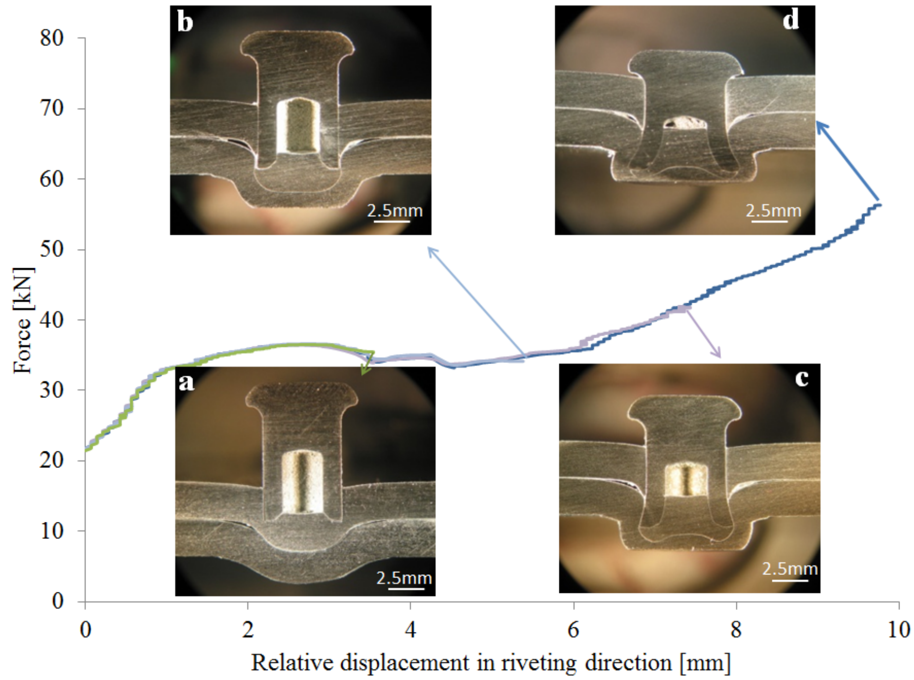

Fig. 5.1.27 Force-displacement curve for different steps of 2.5 mm + 2.5 mm G450 steel joint with 8 mm long rivet of hardness 555 HV.

5.1.2 Condition # 2 (2.5 + 2.5 G300 carbon steel)

After thoroughly studying the force-displacement curve of a thick and hard material, an understanding was developed of the riveting process. To develop the understanding further, another condition was chosen (condition 2 in Table 5.1.1). In this condition the thickness of the material was kept the same as in the previous condition but a soft material (G300 steel having a hardness of 198 HV) was chosen. However, the number of interruptions was decreased: the joint was interrupted at 10 different positions instead of 13. The whole sequence of interrupted force-displacement curves and associated joints' cross-sections obtained at different stages for condition 2 in Table 5.1.1 are shown in Fig. 5.1.28.

It is clear from Fig. 5.1.28 that the force reached a value of 32 kN was lower than the condition 1 (36 kN), due to less rigidity of a soft material which requires less bending force. The first force drop was observed after a displacement of 4.20 mm.

The magnitude of the force drop in this case was much higher (6 kN) compared with condition 1 (2 kN), because of the combination of two simultaneous processes: force drop due to bending and force drop once the rivet perforated the top sheet.

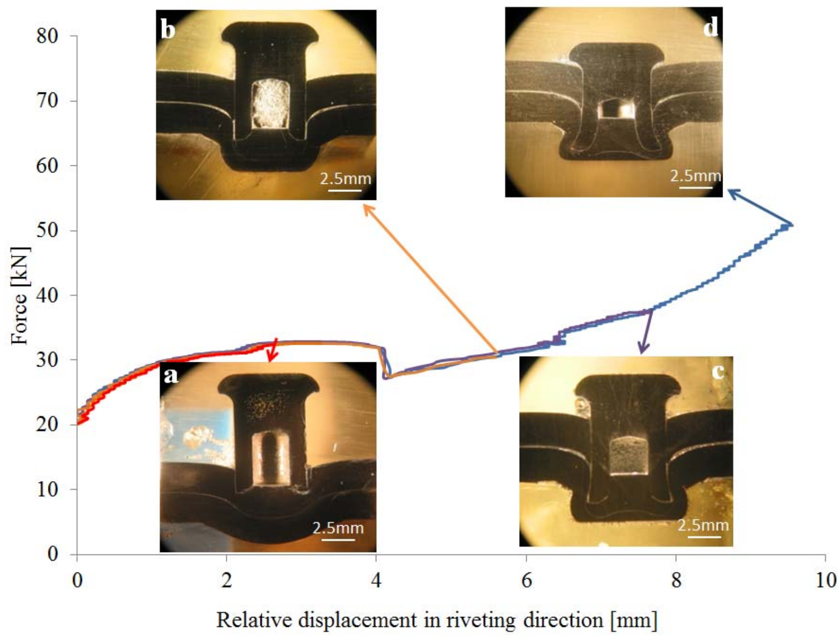

Fig. 5.1.28 Force-displacement curves for different steps of 2.5 mm + 2.5 mm G300 steel joint with 8 mm long rivet of hardness 555 HV.

Once the top sheet was pierced, the force increased gradually with displacement. This was due to material flow inside the cavity, as for condition 1 in Table 5.1.1. The force was increased linearly with the displacement. A sudden increase in force was observed at a displacement of 6.30 mm which indicated the start of rivet flaring. The rivet shank remained straight before this sudden increase in force (Fig. 5.1.28), but the shank of the rivet started bending after this step rise of force was observed. Thinning of the bottom ply continued to occur at this stage and the force increased with a high gradient. The force was due to the punch pressure continuously pushing the cylindrical wall of the rivet to flare outwards, which gradually forms the interlock.

The detailed force-displacement curve and associated cross-section of each interruption are provided in Appendix A. It is clear that successive interrupted curves consistently match each other as seen for the previous condition, and fit with the un-interrupted full SPR cycle, which demonstrated that the process had very good reproducibility and the method of interruption had not unduly affected the process conditions, aside from the incompleteness of a given cycle.

5.1.3 Condition # 3 (2.0 + 2.0 mm G300 carbon steel and 555 HV rivet)

To develop knowledge of a riveting process for thin materials combination, another condition was chosen: condition 3 in Table 5.1.1. In this condition the thickness of the material was reduced to 2.0 mm. Because of the improved familiarity, the number of interruptions was decreased further: the joint was interrupted at 8 different positions. The length of the rivet was reduced to 7 mm as total stack thickness was reduced. The die was changed in order to accommodate the reduced volume of the stack. The sequence of interrupted force-displacement curves and associated joints' cross-sections obtained at the different stages for condition 3 in Table 5.1.1 are shown in Fig. 5.1.29. Good reproducibility of the process was also observed here.

It is clear from Fig. 5.1.29 that the force reached up to 26 kN during the bending stage of the riveting process, which was lower than the previous condition. This was due to the reduced thickness of ply materials which reduces the overall stiffness. The first force drop was observed at a displacement of 3.10 mm. As the thickness of ply materials was reduced, the force drop due to bending was less visible and here the force drop occurred mainly due to the rivet piercing the top sheet completely. The force then started to increase gradually due to the reaction force when the bottom sheet touched the die bottom surface. As for the previous two conditions, a step rise in force was also observed (at a displacement of 5.0 mm in Fig. 5.1.29), indicating the start point of rivet flaring which was also confirmed by the observation of the cross-sections. Again, the force started to increase but with a higher gradient. The detailed force-displacement curve and associated cross-section of each interruption for condition 3 are provided in Appendix A.

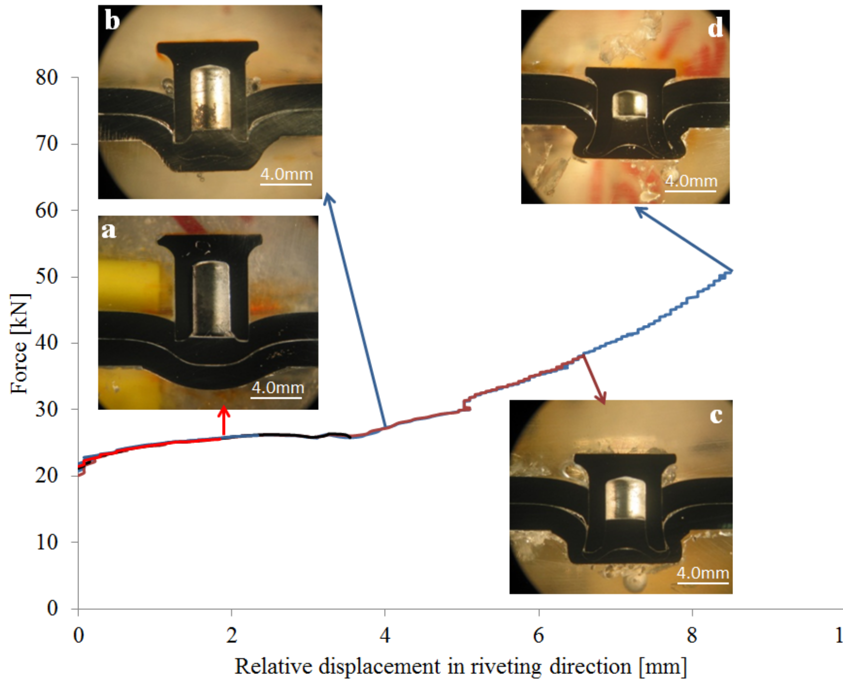

Fig. 5.1.29 Force-displacement curves for different steps of 2.0 mm + 2.0 mm G300 steel joint with 7 mm long rivet of hardness 555 HV.

5.1.4 Condition # 4 (2.0 + 2.0 mm G300 carbon steel and 480 HV rivet)

To understand the riveting process due to a change in rivet hardness another joining condition was chosen to be investigated: condition 4 in Table 5.1.1. In this case, all the joining parameters were kept the same as in condition 3 except for the rivet hardness. A rivet was chosen with a hardness of 480 HV. The sequence of interrupted force-displacement curves and associated joints' cross-sections obtained at the different stages for condition 4 in Table 5.1.1 are shown in Fig. 5.1.30. The reproducibility of the process was also found to be good. Detailed force-displacement curve and associated cross-section of each interruption for condition 4 are provided in Appendix A.

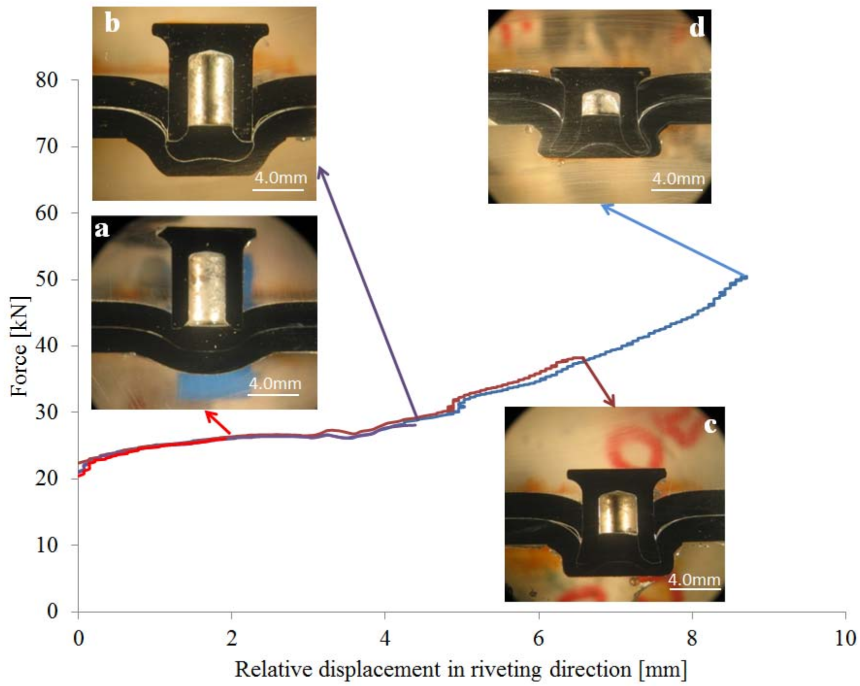

Fig. 5.1.30 Force-displacement curves for different steps of 2.0 mm + 2.0 mm G300 steel joint with 7 mm long rivet of hardness 480 HV.

Like the previous condition, the force reached a value of 26 kN at the bending stage. This demonstrated that the force due to bending was dependent on the material properties not on rivet properties. Unlike the previous three conditions, no force drop was observed in this condition, but a rise in force was observed at a displacement of 3.20 mm and then a change in slope was observed. The force drop due to the completion of piercing of the top sheet was not visible because the bottom sheet touched the die bottom surface immediately before the rivet completed piercing the top sheet. It should be noted that the rivet completed the penetration through the top sheet a bit earlier in condition 3 (at a displacement of 3.10 mm in Fig. 5.1.29) due to a hard rivet. The remaining part of the force-displacement curve behaved similarly to the previous case. A step rise in force was observed at a displacement of 4.90 mm (Fig. 5.1.30) indicating the start point of rivet flaring. Then the force started to increase with a high gradient. It should also be noted that the gradient of the force-displacement curve at this condition was less than the previous condition; the soft rivet required less force to be flared.

5.1.5 Condition # 5 (2.0 + 2.0 mm G300 carbon steel and 410 HV rivet)

Another condition was chosen with an even softer rivet (410 HV) while keeping all other parameters same as in conditions 3 and 4. The number of interruptions was reduced again (only 7 for this condition). The cross-sections and the associated force-displacement curves for this condition are shown in Fig. 5.1.31. The same good reproducible behaviour was found for this condition.

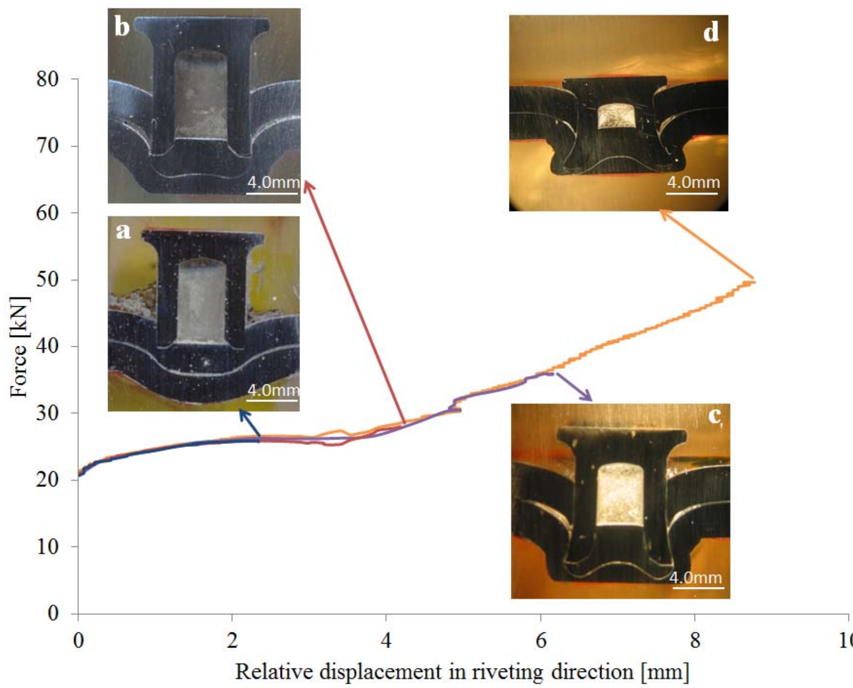

Fig. 5.1.31 Force-displacement curves for different steps of 2.0 mm + 2.0 mm G300 steel joint with 7 mm long rivet of hardness 410 HV.

The first change in slope was observed at a displacement of 3.30 mm. As the hardness of the rivet reduced, the piercing of the top sheet required more displacement (3.30 mm) compared to the hard rivet (3.20 mm). The step rise of force was observed at a displacement of 4.85 mm which was earlier than the previous two conditions because of the same reason (the soft rivet required less force to flare). Again, the gradient at which the force increased at its last stage was lower than the previous two conditions. Detailed force-displacement curves and associated cross-sections of each interruption for condition 5 are provided in Appendix A.

5.1.6 Condition # 6 (1.5 + 1.5 mm G300 carbon steel and 480 HV rivet)

The thickness of the material was reduced further in condition 6 in Table 5.1.1. The thickness of both top and bottom sheets was 1.5 mm. The length of the rivet was also reduced to 6 mm as the thickness of the total stack was reduced to 3.0 mm. The cross-sections and the associated force –displacement curve for this condition are shown in Fig. 5.1.32. Good reproducibility still exists in this condition.

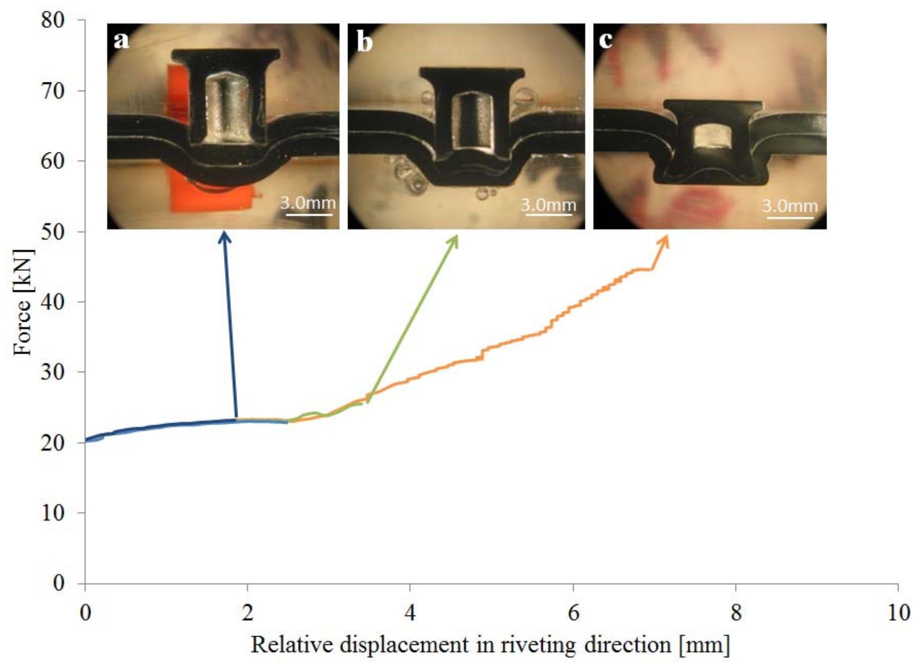

Fig. 5.1.32 Force-displacement curves for different steps of 1.5 mm + 1.5 mm G300 steel joint with 6 mm long rivet of hardness 480 HV.

Force rise due to bending at the initial stage of the SPR process decreased to 23 kN due to thin materials. The first change in slope was observed at a displacement of 2.60 mm. The step rise of force was observed at a displacement of 4.80 mm. Detailed force-displacement curves and associated cross-sections of each interruption for condition 6 are provided in Appendix A.

5.1.7 Condition # 7 (1.5 + 1.5 mm G300 carbon steel and 410 HV rivet)

Finally, another condition was chosen in order to check the effect of rivet hardness in thin ply materials: condition 7 in Table 5.1.1. In this condition, a reduced hardness of rivet (410 HV) was chosen and all other parameters were kept identical with those for condition 6. The cross-sections and the associated force-displacement curves for this condition are shown in Fig. 5.1.33. Again, good reproducibility exists in this condition.

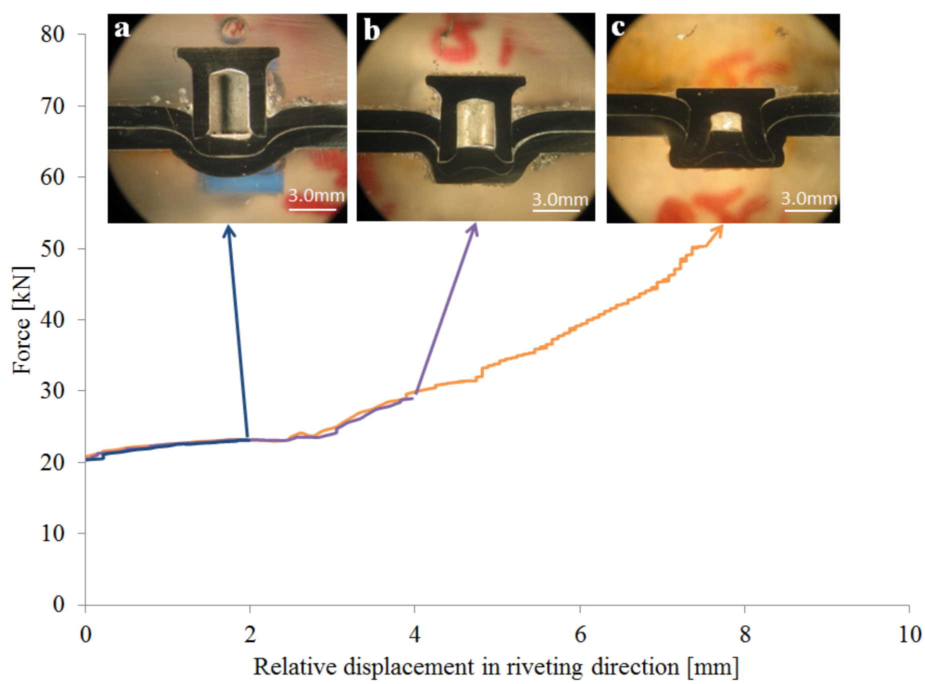

Fig. 5.1.33 Force-displacement curves for different steps of 1.5 mm + 1.5 mm G300 steel joint with 6 mm long rivet of hardness 410 HV.

Force rise due to bending at the initial stage of the process again reached 23 kN due to the same material (thickness and hardness). The first change in slope was observed at a displacement of 2.60 mm. The step rise of force was observed at a displacement of 4.75 mm which was earlier than that for the previous condition due to the soft rivet. Detailed force-displacement curves and associated cross-sections of each interruption for condition 7 are provided in Appendix A.

The interrupted tests have mainly focussed on understanding the physical events involved in the formation of SPR joints by characterizing and relating the force-displacement curve to the joint's structure. A systematic characterization study of the SPR process using force-displacement curves has been carried out by interrupting the formation of SPR joints at different rivet positions for three types of thicknesses and two different hardnesses of ply materials with three levels of rivet hardness. The understanding and knowledge gained from this study could be used for monitoring of the industrial SPR process. The same study could also be used to select the appropriate die for a given combination of ply material thickness and hardness.

5.2 Selection of die

Selection of the die is the first key point of the SPR process. A proper die is necessary to create a sound joint. The die should be chosen to accommodate the volume of material that needs to be displaced in order to produce a joint. The thickness of material is an important parameter to consider in selecting a proper die. The depth of the die should be controlled to avoid cracking in the bottom sheet.

5.2.1 5 mm (2.5 mm + 2.5 mm) stack thickness

A force-displacement curve, a cross-section and a scan from the tail of the joints for a 5.0 mm stack thickness (2.5 + 2.5 mm G450 carbon steel) and 8.0 mm long rivet (555 HV) for die depths of 2.35 and 3 mm are shown in Figs. 5.2.1 and 2. It is clear from Fig. 5.2.2 that using a wrong die can lead to severe cracking as observed in the bottom sheet. The rivet also became exposed to the environment which is not good in terms of corrosion. It can be observed from Fig. 5.2.1 that the force dropped rapidly after a displacement of 2.0 mm for the wrong die. This means the crack was initiated at a very early stage of the SPR process. As the die was too deep, there was no support for the bottom sheet while it went under bending. So, a crack was initiated due to excessive bending at the early stage of the process.

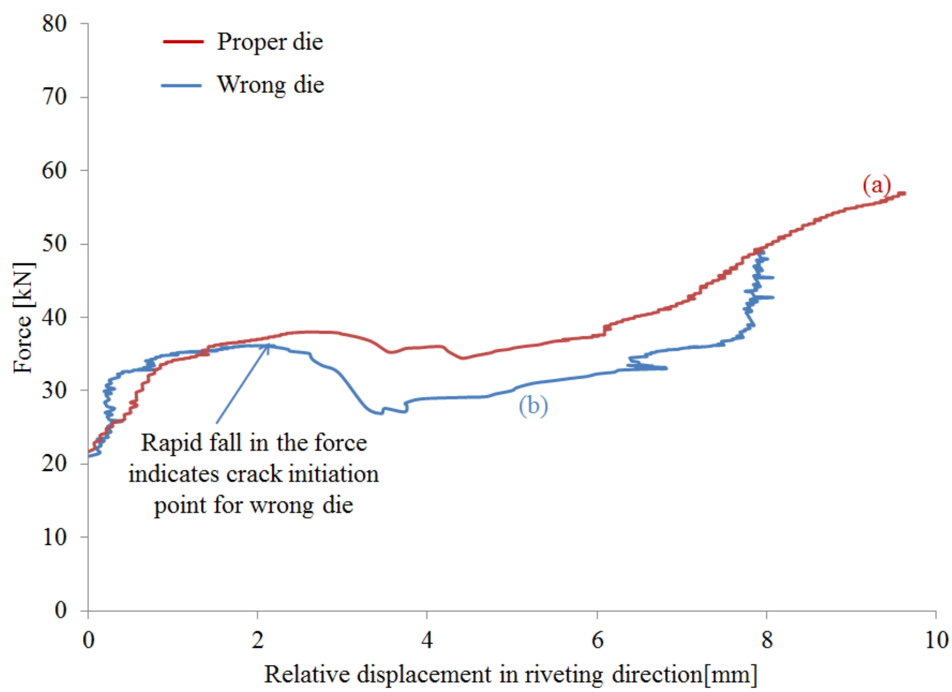

Fig. 5.2.1 Force-displacement curves for different die of 2.5 + 2.5 mm G450 carbon steel joint with an 8 mm long and 555 HV rivet (a) 2.35 mm deep die and (b) 3.0 mm deep die.

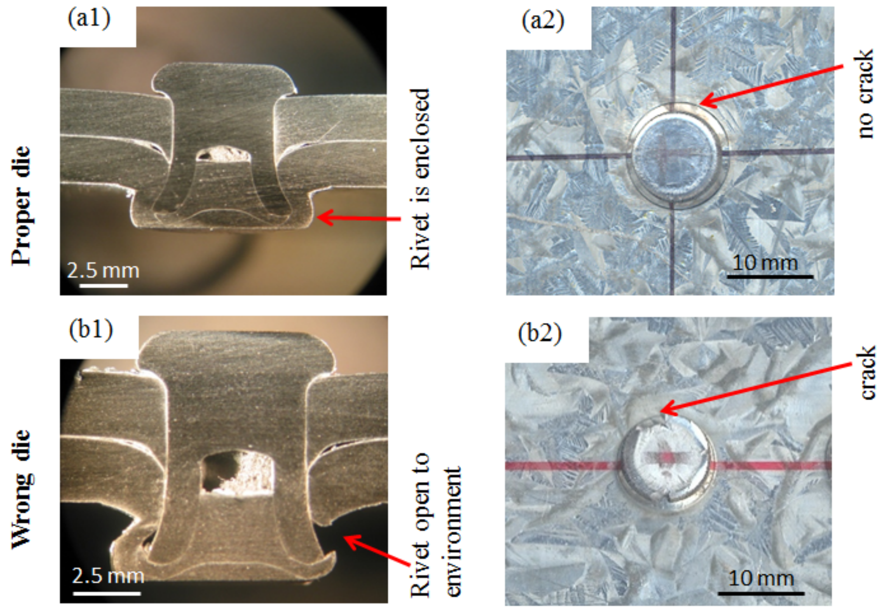

Fig. 5.2.2 Cross-sections and scans from the tail side for different die for 2.5 + 2.5 mm G450 carbon steel joints with 8 mm long and 555 HV rivets (a1, a2) 2.35 mm deep die and (b1, b2) 3.0 mm deep die.

5.2.2 4 mm (2.0 mm + 2.0 mm) stack thickness

Die selection is also important for thin ply materials combination. Force-displacement curves, cross-sections and scans from the tail of joints for 4.0 mm total stack thickness (2.0 mm G40 steel + 2.0 mm G450 steel) and 7.0 mm long rivet with different hardnesses of 555 and 480 HV are shown in Figs. 5.2.3 and 4.

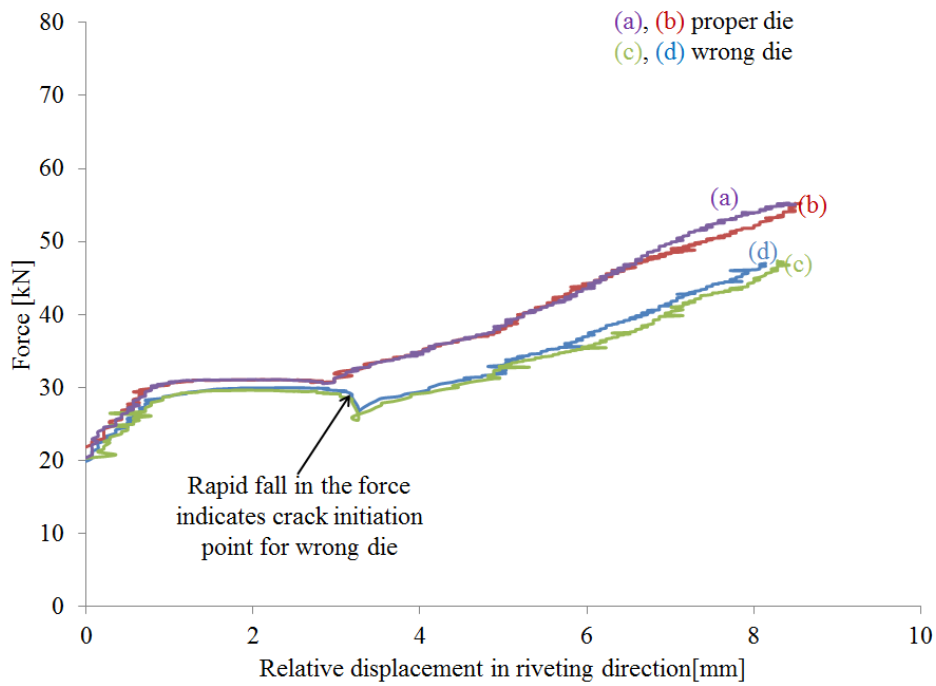

Fig. 5.2.3 Force-displacement curves depending on different dies for 2.0 mm + 2.0 mm G450 carbon steel joints with a 7 mm long rivet (a) 555 HV and (b) 480 HV rivet with 2.1 mm deep die, (c) 555 HV and (d) 480 HV rivet with 2.5 mm deep die.

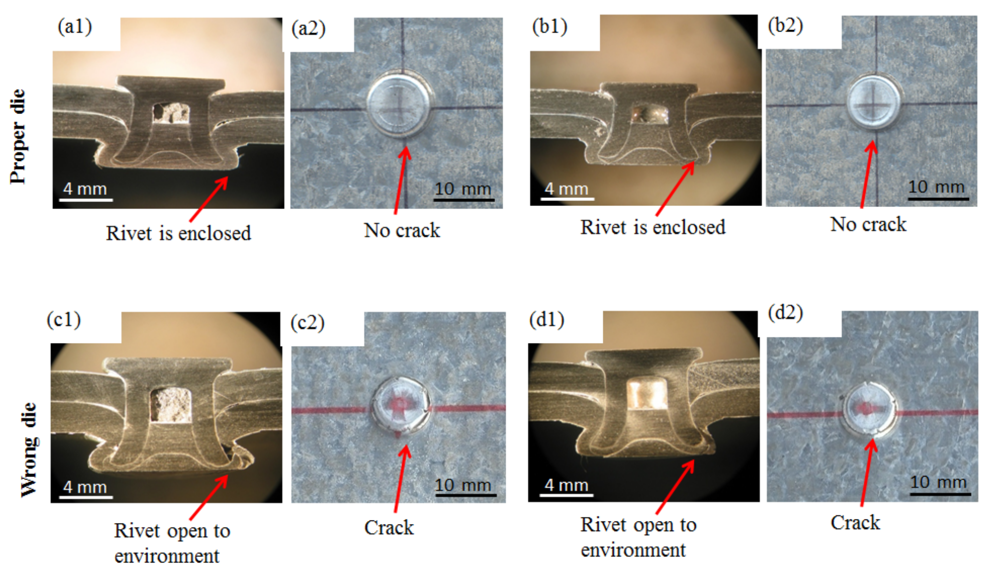

Fig. 5.2.4 Cross-sections and scans from the tail side depending on die depth for 2.0 + 2.0 mm G450 carbon steel joints with a 7 mm long rivet (a1, a2) 555 HV and (b1, b2) 480 HV rivet with 2.1 mm deep die, (c1, c2) 555 HV and (d1, d2) 480 HV rivet with 2.5 mm deep die.

It is clear from Figs. 5.2.3-4 that a very good joint as well as a good cross-section was possible by using a proper die. While using a 2.5 mm deep die, a sharp force drop was observed at a displacement 3.1 mm (Fig. 5.2.3) which was at the end of the bending stage. The bottom sheet showed cracking because of excessive bending as there was no support from the die bottom surface. The crack was created during bending and rivet hardness was not important in this case.

5.2.3 3 mm (1.5 mm + 1.5 mm) stack thickness

Another thickness (1.5 mm G40 + 1.5 mm G450) of ply materials was chosen to study the effect of material thickness. In this case, a 6 mm rivet with a hardness of 480 HV was selected. A 9.0 mm diameter die was taken with two different depths: 2.3 and 2.0 mm. Force-displacement curves, cross-sections and scans from the tail of the joints depending on die depth are shown in Figs. 5.2.5 and 6. A sharp drop in force was observed at a displacement of 2.40 mm, which indicates the point of crack creation in the bottom sheet (Fig. 5.2.5). Severe cracking in the tail side material was observed for a wrong die which was 2.3 mm deep (Fig. 5.2.6). The failure occurred for the same reason as discussed before. As the material was hard, it was not possible for this material to flow in the riveting direction without support. So the crack was initiated during the bending of the bottom sheet towards the die cavity.

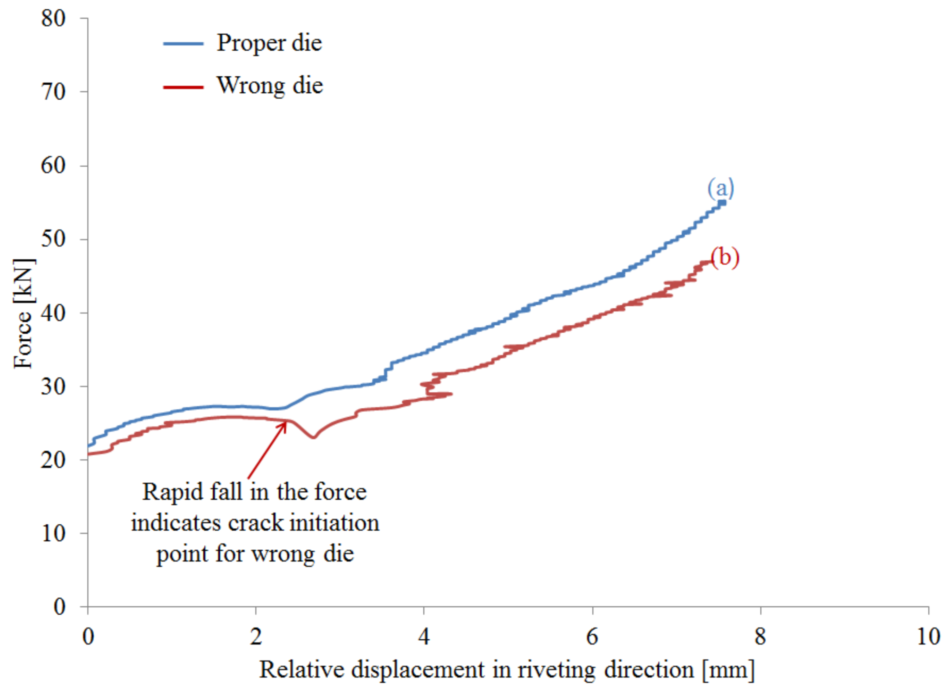

Fig. 5.2.5 Force-displacement curves of 1.5 mm + 1.5 mm G450 steel joints with 6 mm long rivets having a hardness of 480 HV for a 9mm diameter die with depth of (a) 2.0 mm and (b) 2.3 mm.

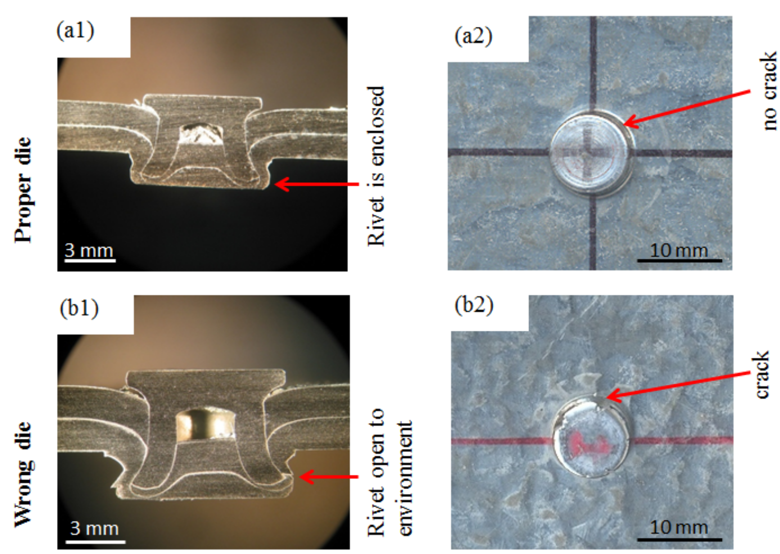

Fig. 5.2.6 Cross-sections and scans from the tail side for different dies of 1.5 + 1.5 mm G450 carbon steel joint with 6 mm long and 480 HV rivet (a1, a2) 2 and (b1, b2) 2.3 mm deep die.

5.3 Effect of die depth on the characteristic curve

As soon as an appropriate die has been chosen for a given combination of ply materials thickness it is necessary to check the effect of die depth on the force-displacement curve. To do this, sheets of G300 carbon steel with three different combinations of thicknesses were chosen. The lengths of the rivet were chosen according to the total stack thickness.

5.3.1 5 mm (2.5 mm + 2.5 mm) stack thickness

A cross-section and a force-displacement curve for two different 5.0 mm joints are shown in Fig. 5.3.1 depending on die depth. A flat die with two different depths was used: 2.35 and 3.0 mm. Both joints were good but the joint produced by the 2.35 mm deep die was better because of more flaring. A sharp drop in force was observed after a displacement of 4.2 mm for the joint created by the die depth of 3.0 mm. This sharp drop in force was due to two simultaneous processes: force drop due to bending and force drop once the rivet perforated the top sheet.

It should be noted that, no crack was found in this case as a soft material (G300 carbon steel) was used which had an elongation of 15%. If a hard material was used (G450 instead of G300 carbon steel), this amount of force drop would represent an initiation of a crack in the bottom sheet due to excessive bending.

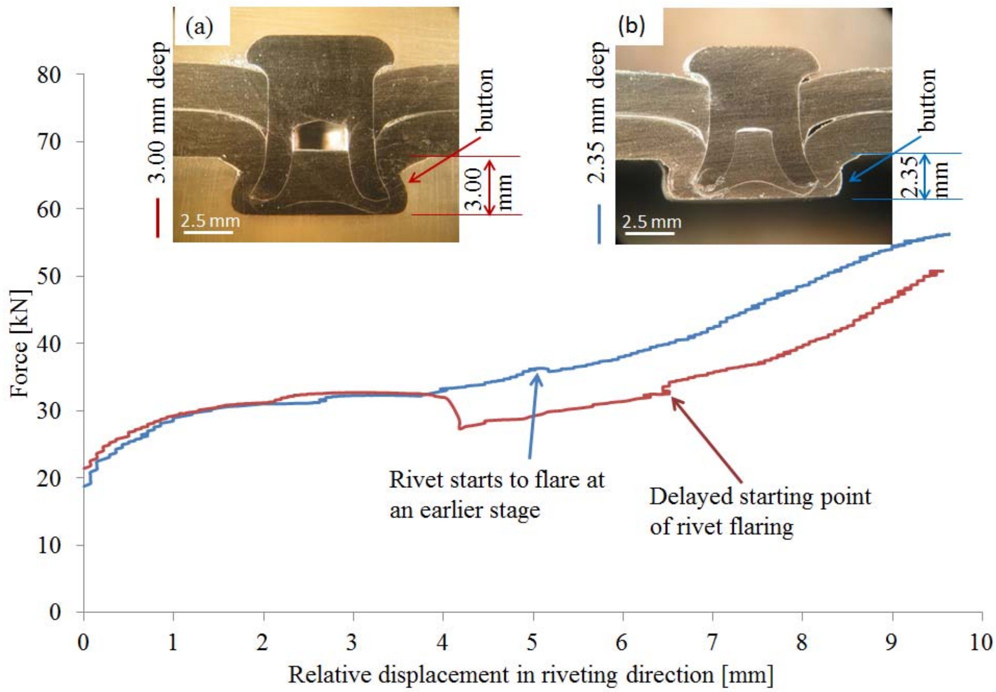

Fig. 5.3.1 Force- displacement curves and associated cross-sections depending on die depth of 2.5 + 2.5 mm G300 carbon steel joint with an 8 mm long 555 HV rivet.

A rise in force was observed at a displacement of 5.10 mm and 6.45 mm for the joint produced with 2.35 mm and 3.0 mm deep die respectively. This rise in force indicates the starting point of rivet flaring. The rivet started to flare early for the joint with the shallower die, while the overall displacement was the same. Thus, more flaring of the rivet occurred inside the joint with the shallow die. As the flaring is an important quality parameter for a riveted joint it is preferable to use a shallow die. The height of the button in the die side of the joint was big for a deep die as this height was determined by the depth of the die. The overall volume of the deep die was high, so less force was required to displace the material inside the die cavity. Due to this reason, the maximum force was lower with the deeper die than the shallower die. A gap under the rivet head was observed for the joint with the deep die, because the material that was displaced by the rivet was less than the volume of the die cavity. On the other hand, no gap under the rivet head was observed for the shallow die as the volume inside the die cavity matched the volume displaced by the rivet.

5.3.2 4 mm (2.0 mm + 2.0 mm) stack thickness

The effect of the die depth on the characteristic curve in a 4.0 mm total stack thickness (2.0 mm + 2.0 mm) for two different hardnesses of the rivet is shown in Fig. 5.3.2. Like the previous condition, a drop in force was observed at a displacement of 2.60 mm for the 2.50 mm deep die while no drop in force was observed for the 2.10 mm deep die regardless of rivet hardness. With a shallow die (2.1 mm deep) the bottom sheet touched the die bottom surface before the rivet completed the piercing of the top sheet. So no drop in force occured and the positive force due to the reaction from the die bottom surface was higher than the negative force due to completion of the piercing the top sheet. So the force started to increase without any drop. A step rise in force was observed at a displacement of 4.2 and 4.9 mm for the 2.1 mm deep and 2.5 mm deep dies respectively. As the bottom sheet touched the die bottom surface earlier and the die filled up at an earlier stage with the shallow die (2.1 mm deep), the reaction force required to flare the rivet leg was achieved prior to a displacement of 4.2 mm. However the total displacement was the same for both the shallow and deep dies. Hence, a large flaring was observed for the 2.1 mm deep die (1.11 mm and 1.01 mm for 555 HV and 480 HV respectively) compared with that for the 2.3 mm die (1.03 mm and 0.78 mm for 555 HV and 480 HV respectively).

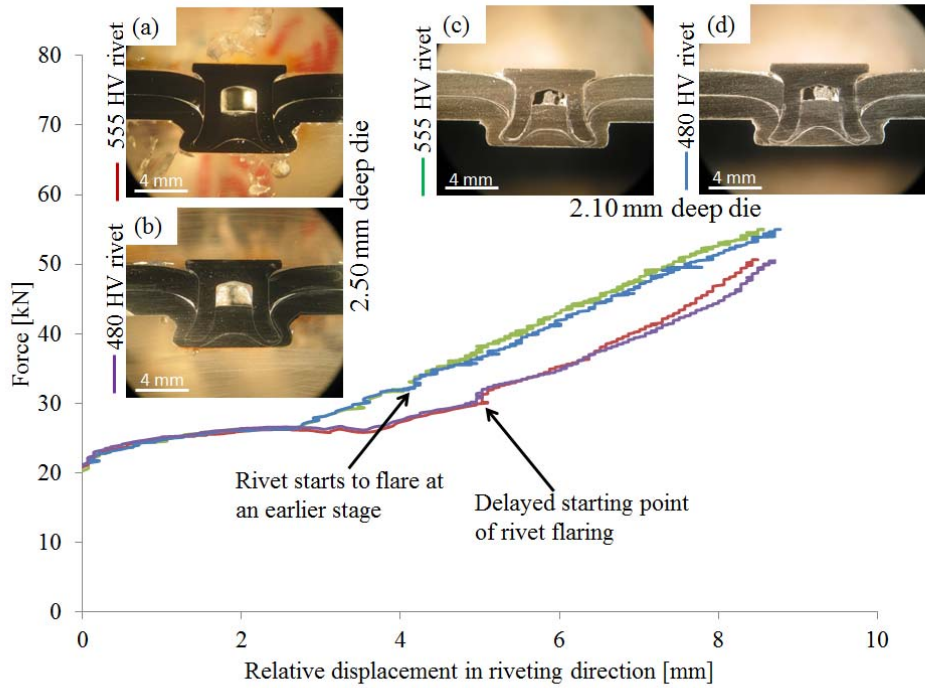

Fig. 5.3.2 Force-displacement curves and associated cross-sections depending on die depth of 2.0 mm + 2.0 mm G300 steel joint with a 7 mm long rivet.

5.3.3 3 mm (1.5 mm + 1.5 mm) stack thickness

The effect of the die depth was studied again by reducing the total stack thickness to 3.0 mm (1.5 + 1.5 mm). In this case, the length of the rivet was reduced to 6.0 mm due to the decrease in total stack thickness. A 9.0 mm diameter die with two different depths (2.3 and 2.0 mm) was used to produce the joints. The force-displacement curves are shown in Fig. 5.3.3. It can be observed that a drop in force occurred at a displacement of 2.5 mm for a shallow die according to the same principle described before. The step rise in force which indicates the start point of the rivet flaring was observed at an earlier stage for the shallow die (4.4 and 4.9 mm for 2.0 and 2.3 mm deep dies respectively). Again, the total rivet flaring (0.66 mm) was less for the die depth of 2.3 mm compared with that for the die depth of 2.0 mm (0.90 mm).

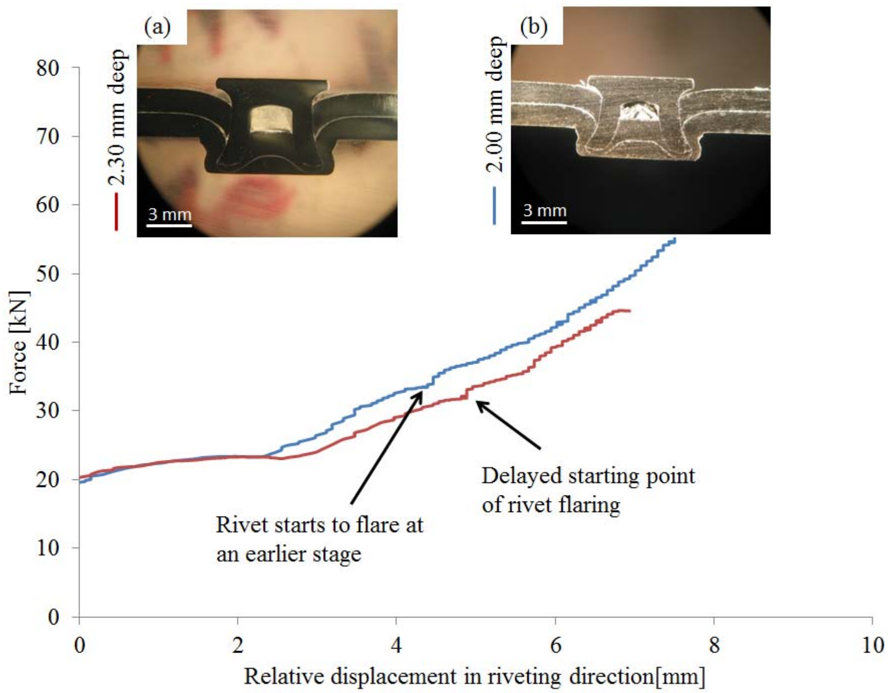

Fig. 5.3.3 Force-displacement curves and associated cross-sections depending on die depth of 1.5 mm + 1.5 mm G300 steel joint with a 6 mm long 480 HV rivet.

5.4 Effect of ply material hardness on the characteristic curve

Necessity of selecting a proper die and the effect of die depth on the characteristic curve were discussed in the previous two sections. However, it is necessary to detect the effect of ply material hardness on the characteristic force-displacement curve. Two different hardnesses of materials consisting of three types of thicknesses were chosen to investigate the effect of material's hardness on the characteristic curve.

5.4.1 5 mm (2.5 mm + 2.5 mm) stack thickness

Two riveted joints of 5.0 mm (2.5 + 2.5 mm) thickness were produced with two types of materials (G300 and G450 carbon steel with hardnesses of 198 HV and 270 HV respectively) using an 8 mm long and 555 HV rivet. A flat die with 11 mm in diameter and 2.35 mm depth was used to produce the above joints. The characteristic force-displacement curves are shown in Fig.5.4.1. It is clear that the material hardness mainly affects the bending stage of the SPR process and the effect from the material's hardness was negligible after 4.40 mm displacement. The force reached 36 kN during the bending stage for the joint made with hard material (G450 carbon steel). Hard material requires a high force to bend because of high rigidity. As a result, the force was high for the G450 carbon steel joint. The materials' response was different up to a displacement of 4.4 mm as the reaction force was mainly from the material. However, when the die was filled with materials, the reaction force was mainly from the die and the material properties were not prominent and the properties of rivet became dominant. Thus, the two joints behaved similarly after 4.4 mm as the rivet length was the same.

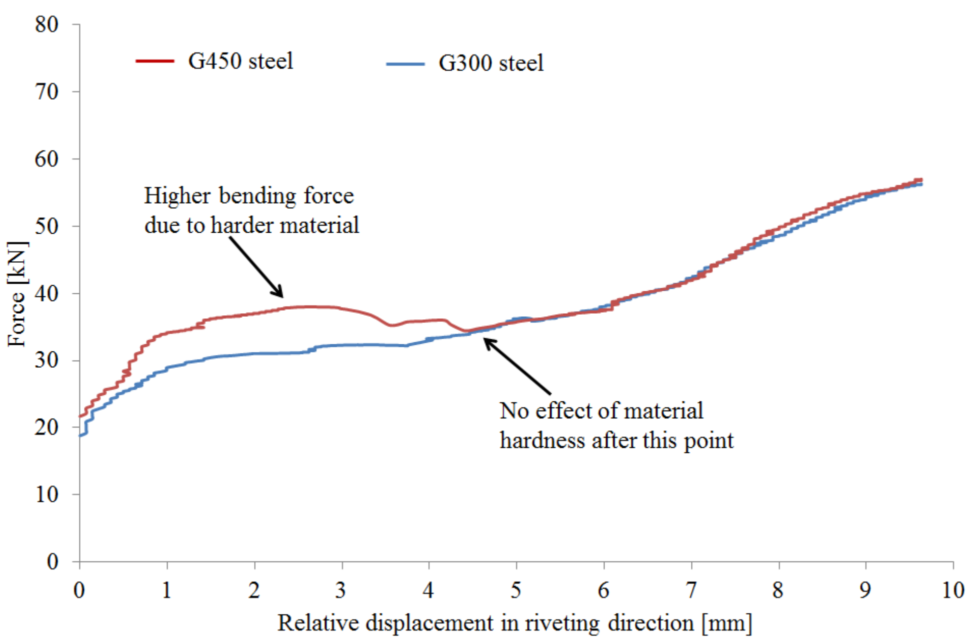

Fig. 5.4.1 Force-displacement curves depending on material hardness of 2.5 + 2.5 mm joint with an 8 mm long rivet having a hardness of 555 HV.

5.4.2 4 mm (2.0 mm + 2.0 mm) stack thickness

To study the effect of material hardness on the force-displacement curve again, four more joints were produced by decreasing the total stack thickness to 4.0 mm: two joints by G450 and another two joints by G300 carbon steel. In this case, joints were produced with a 7 mm long rivet having two different hardnesses: 555 and 480 HV. The die was chosen according to the total stack thickness; 10 mm diameter and 2.1 mm deep. The force- displacement curves depending on material hardness for a 4.0 mm stack thickness are shown in Fig. 5.4.2. During the bending stage of the SPR process, the force reached 31 kN for joints with G450 carbon steel while the force was only 26 kN for joints produced with the G300 carbon steel. The force continued to stay high for a hard material up to a displacement of 4.8 mm. After that displacement change in the gradient of the curve depends mainly on the rivet hardness rather than material properties. A step rise in the force was observed at 4.2 mm for G300 carbon steel but for G450 carbon steel, the step rise in force was observed at of 4.8 mm. The total displacement was same for all the joints, which indicates a high flaring for soft ply materials.

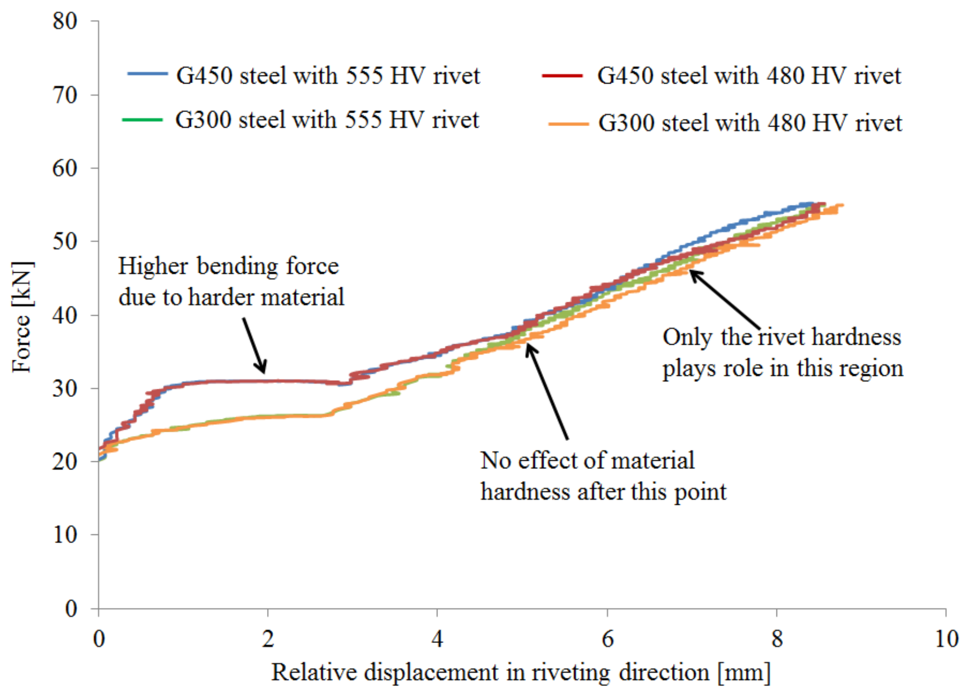

Fig. 5.4.2 Force-displacement curves depending on material hardness of 2.0 + 2.0 mm joint with a 7 mm long rivet.

5.4.3 3 mm (1.5 mm + 1.5 mm) stack thickness

In this case the same materials were used by reducing the stack thickness to 3.0 mm. The length of the rivet was also reduced to 6.0 mm and the die geometry (9.0 mm diameter and 2.0 mm deep) was changed in order to control the required volume that was needed to displace. Similar behaviour was also observed for a thin combination of ply materials (Fig. 5.4.3). The forces during the bending were 27 kN and 22 kN for joints with G450 and G300 carbon steel respectively.

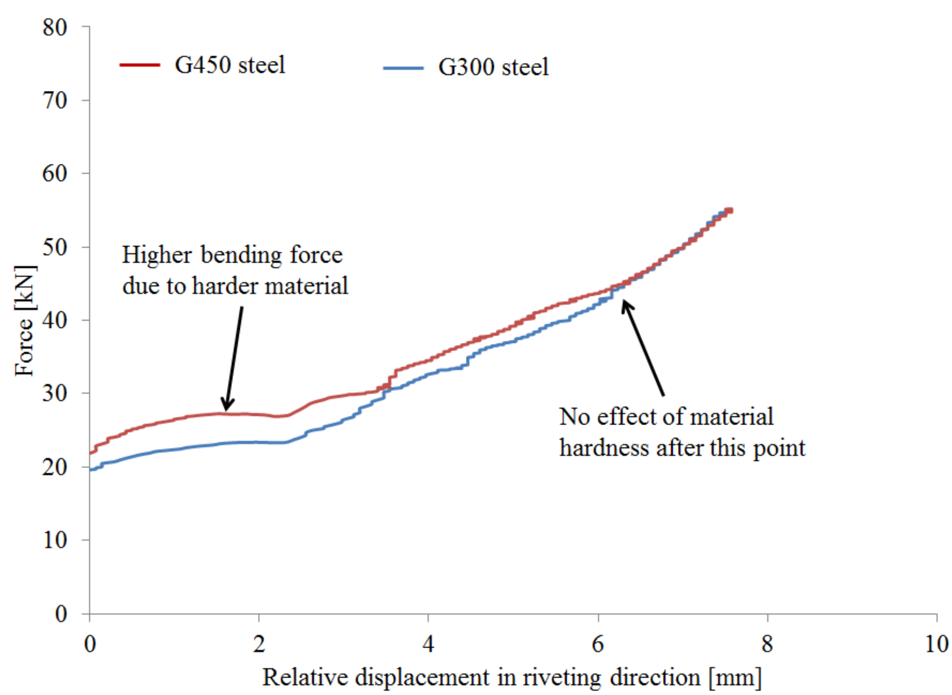

Fig. 5.4.3 Force-displacement curves depending on material hardness of 1.5 + 1.5 mm joint with a 6 mm long rivet having a hardness of 480 HV.

5.5 Effect of ply material thickness on the characteristic curve

Sheet thickness plays a very important role in the different stages of the characteristic curve. As the overall thickness of the ply material increases, a longer rivet is needed. So the first effect of stack thickness is on the overall length of the force-displacement curve. This can be seen in Figs. 5.5.1-3 where the total punch displacement were 9.6, 8.6 and 7.5 mm for a joint with G300 carbon steel having a total ply thickness of 5, 4 and 3 mm, respectively. The same increase in overall length of the force-displacement for G450 carbon steel which can be seen in Figs. 5.5.4 and 5 where the total punch displacements were 9.6, 8.5 and 7.6 mm for joints having a total ply thickness of 5, 4 and 3 mm, respectively.

5.5.1 G300 steel, 5.0 mm vs. 4.0 mm total stack thickness

The force-displacement curves depending on ply materials thickness are shown in Fig. 5.5.1. The dies chosen to accumulate the appropriate volume that was needed to displace were 11 and 10 mm in diameter, 2.35 and 2.1 mm in depth for 5.0 and 4.0 mm stack thicknesses respectively. It is clear from Fig. 5.5.1 that the force reached 32 and 26 kN during the bending and piercing stage for the joint stack-up thickness of 5 and 4 mm, respectively. This was due to an increase in the thickness of material making the structure more rigid, which restricted the sheet's capacity to bend into the die cavity while generating higher forces. The overall lengths of the curves were 9.6 and 8.6 mm for 5.0 and 4.0 mm joints respectively.

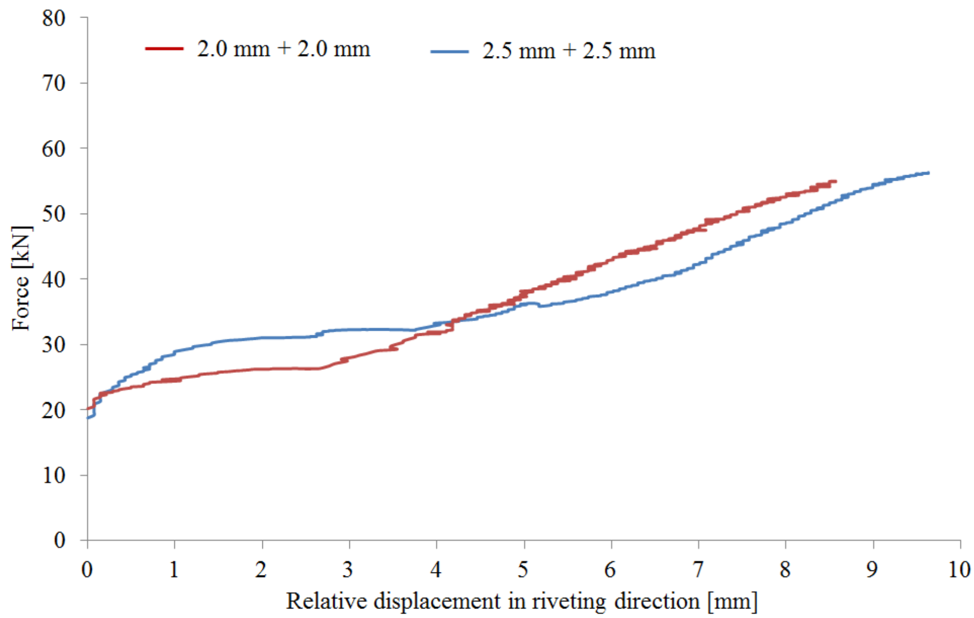

Fig. 5.5.1 Force-displacement curves depending on material thickness for G300 carbon steel using a 555 HV rivet (5.0 mm vs. 4.0 mm).

5.5.2 G300 steel, 4.0 mm vs. 3.0 mm total stack thickness

The force-displacement curves depending on ply materials thickness for two different rivet hardnesses are shown in Fig. 5.5.2. The dies chosen in order to accumulate the appropriate volume of material that needed to be displaced were 10 and 9 mm in diameter, 2.5 and 2.3 mm in depth for 4.0 and 3.0 mm stack thicknesses respectively. The force reached 26 and 22 kN for 4.0 and 3.0 mm joints respectively. This was due to the same reason as discussed previously: an increase in the thickness of material making the structure more rigid, which restricted the sheet’s capacity to bend into the die cavity while generating higher forces. It was also noticeable that the rivet hardness was not important during the beginning of the process curve, but during the last part of the curve a high force was observed for a hard rivet.

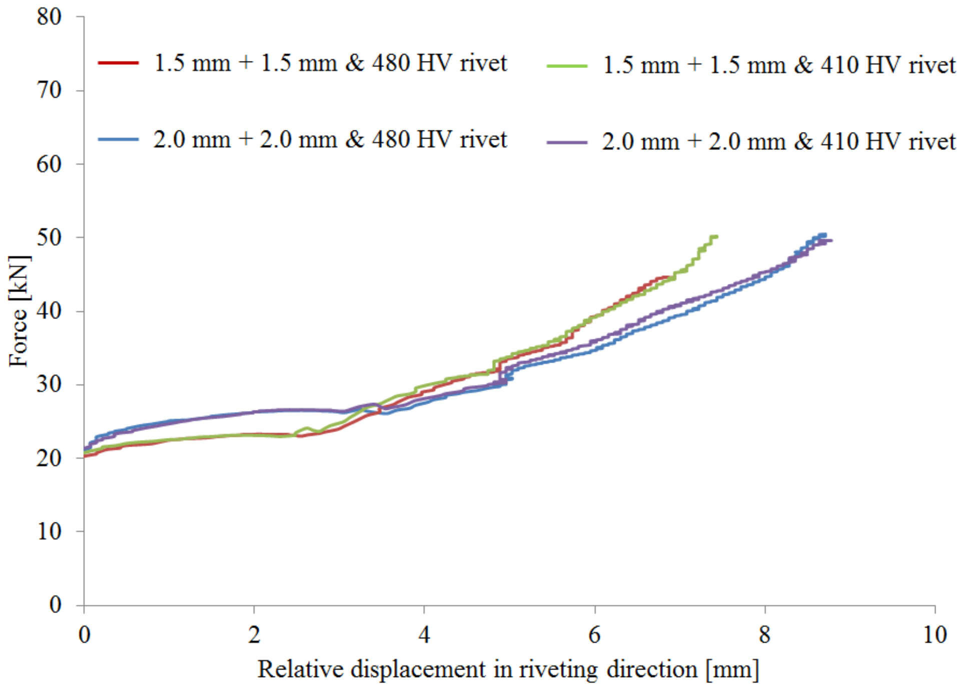

Fig. 5.5.2 Force-displacement curves depending on material thickness for G300 carbon steel (4.0 mm vs. 3.0 mm).

5.5.3 G300 steel, 4.0 mm vs. 3.0 mm total stack thickness with shallower die

The effect of sheet material thickness on the characteristic curve is further studied by changing the die depth to 2.1 and 2.0 mm for stack thicknesses of 4.0 and 3.0 mm respectively. It can be observed from Fig. 5.5.3 that the force-displacement curves showed similar behaviour as in Fig. 5.5.2. The force reached a high value for the thicker joint during the bending and piercing stage.

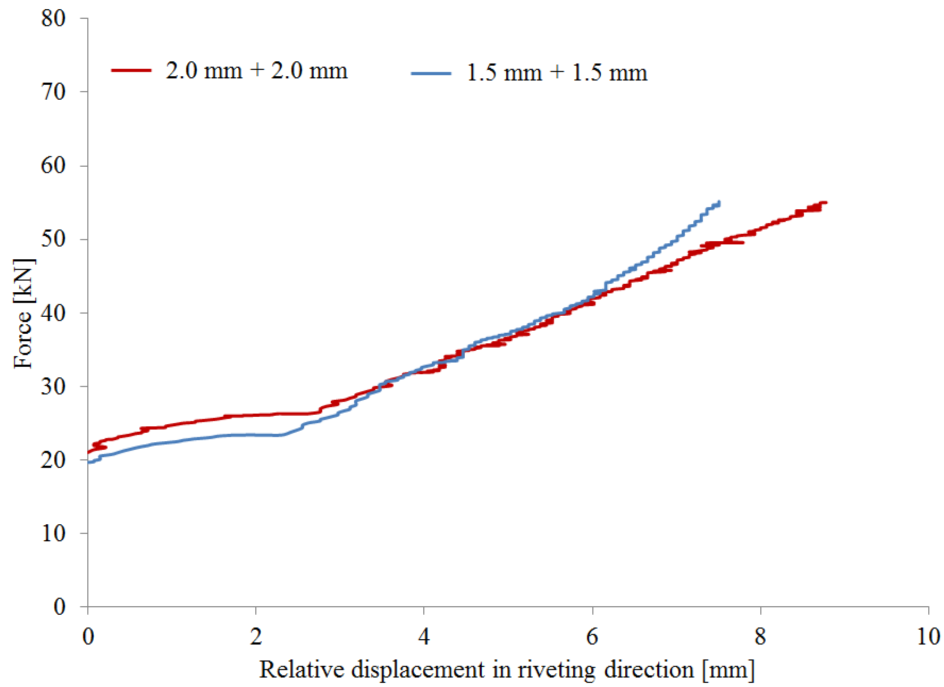

Fig. 5.5.3 Force-displacement curves depending on material thickness for G300 steel (4.0 mm vs. 3.0 mm).

5.5.4 G450 steel, 5.0 mm vs. 4.0 mm and 4.0 mm vs. 3.0 mm total stack thickness

The effect of sheet material thickness on the force-displacement curve for G300 carbon steel has been observed before. However, it is still unknown whether the characteristic curve would show the same behaviour for different materials. In order to do so at first the same stack thicknesses were chosen by changing the material (G450 instead of G300 carbon steel) while all other parameters were kept the same. It is clearly visible from Fig. 5.5.4 that the force-displacement curves showed similar behaviour as described before. A high force was observed for a thick combination during the bending and piercing stage. The force reached 40 and 32 kN for the 5.0 and 4.0 mm joints respectively. The length of the overall curve was low for a thin joint. Similar behaviour was also observed while comparing 3.0 and 4.0 mm joint (Fig. 5.5.5).

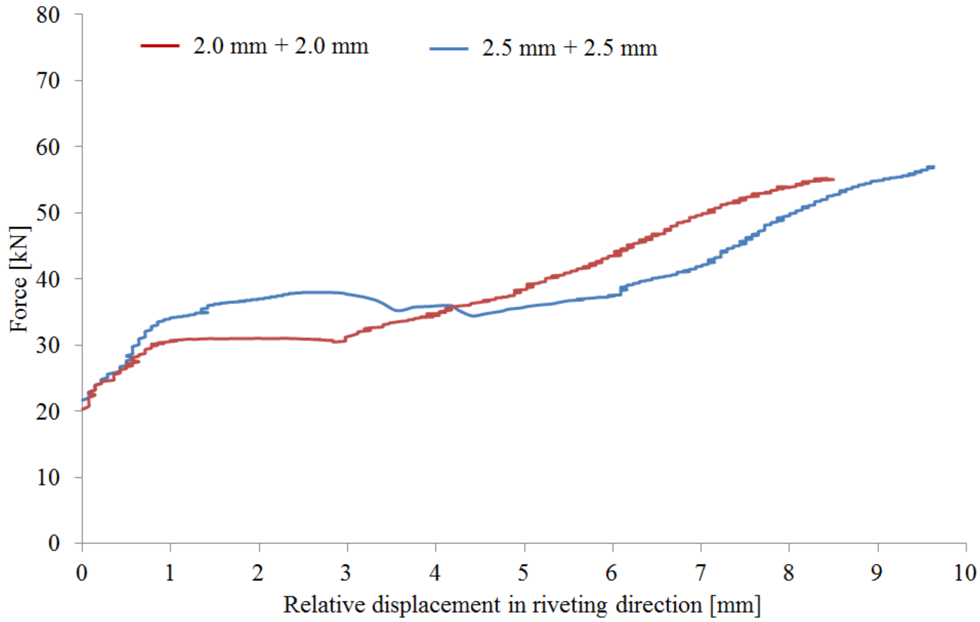

Fig. 5.5.4 Force-displacement curves depending on material thickness for G450 carbon steel (5.0 vs. 4.0 mm).

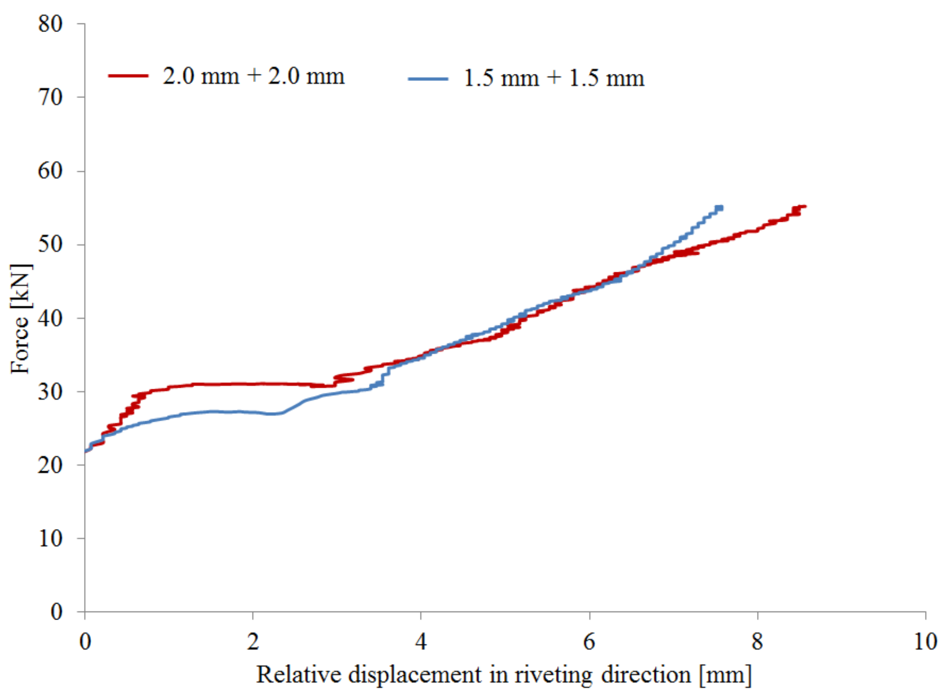

Fig. 5.5.5 Force-displacement curves depending on material thickness for G450 carbon steel (4.0 vs. 3.0 mm).

5.6 Effect of rivet hardness on the characteristic curve

The effect of sheet material's thickness on characteristic curve for different materials was discussed in the previous section. However, there are also effects of rivet hardness on the characteristic curve. The impact of rivet hardness on characteristic curve is discussed in this chapter.

5.6.1 G300 steel with 4.0 mm total stack thickness

Force-displacement curves for joints having the same total ply thickness of 4.0 mm and produced using the same die, with rivets of the same length but of different hardness are shown in Fig. 5.6.1. It was evident that the overall length of the curve decreased from 8.8 to 8.7 then 8.5 mm with increasing rivet hardness from 410 to 480 then 555 HV respectively. This decrease in overall length indicates that the extent of rivet flaring is less for a harder rivet. It is also clear from Fig. 5.6.1 that a harder rivet started piercing at an earlier stage, but started flaring later. The slope of the last stage of the characteristic curve was higher for a harder rivet. Other than this change of slope in last stage, the effect of rivet hardness was not prominent on the characteristic curve in terms of the magnitude of the force during each step of the curve.

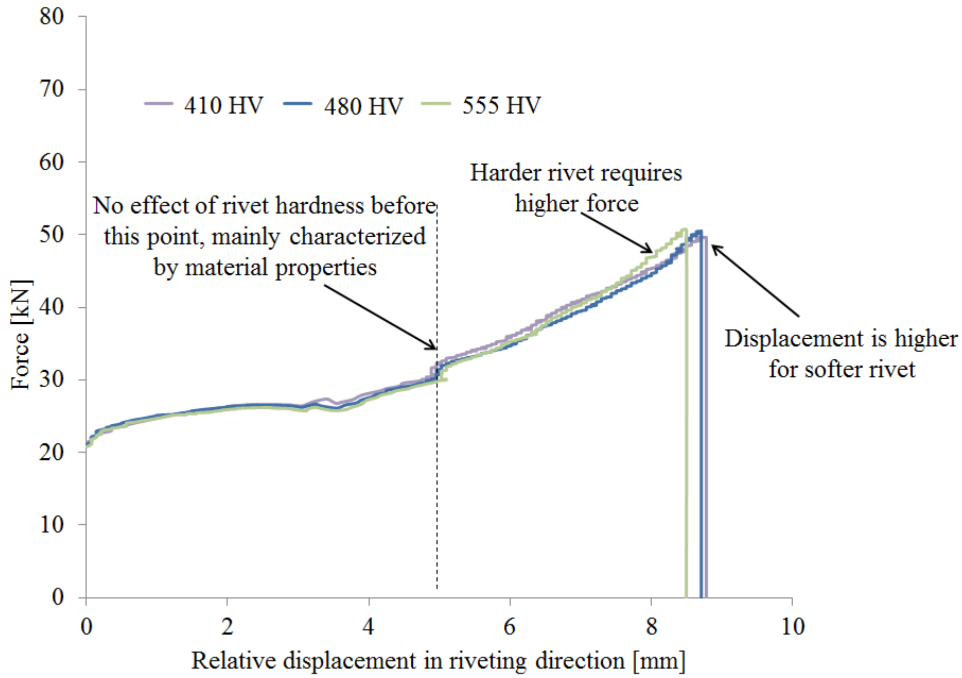

Fig. 5.6.1 Force-displacement curves depending on rivet hardness for 2.0 + 2.0 mm G300 carbon steel joint using a 2.5 mm deep die.

Similar behaviour of the force-displacement curve is found while using a shallow die. Two joints were produced with G300 carbon steel of 2.0 mm as the top sheet and the bottom sheet. The die depth was reduced to 2.1 mm by keeping the diameter constant at 10.0 mm. The force-displacement curves are shown in Fig. 5.6.2. It is clear that after the die was filled up completely, rivet hardness started to influence the force-displacement curve.

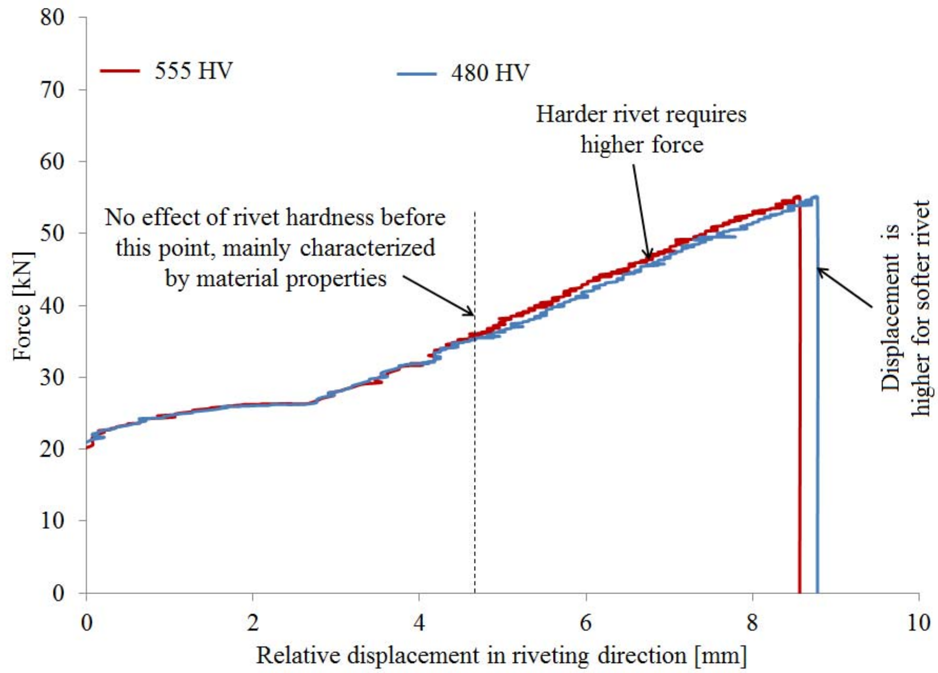

Fig. 5.6.2 Force-displacement curves depending on rivet hardness for 2.0 mm + 2.0 mm G300 steel using a 2.1 mm deep die.

5.6.2 G450 steel with 4.0 mm total stack thickness

The effect of rivet hardness on the force-displacement curve was further examined for G450 steel. Force-displacement curves are shown in Fig. 5.6.3 for joints having the same total ply thickness of 4.0 mm and produced using the same die, with rivets of the same length but of different hardnesses. It is apparent from Fig. 5.6.3 that the overall length of the curve was decreased from 8.5 mm to 8.4 mm with increasing rivet hardness from 480 to 555 HV respectively. Like previously, this decrease in overall length indicates that the extent of rivet flaring is less for a harder rivet.

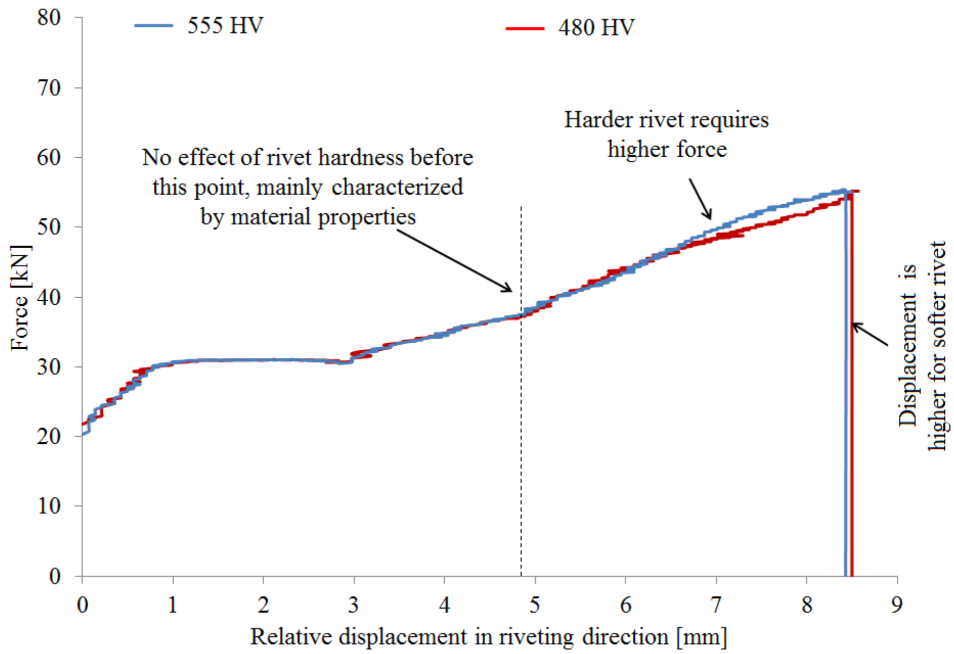

Fig. 5.6.3 Force-displacement curves depending on rivet hardness for 2.0 mm + 2.0 mm G450 steel using a 2.1 mm deep die.

To compare the overall effect of the rivet hardness for both G300 and G450 steel joints, the characteristic force-displacement curves were plotted in one graph (Fig. 5.6.4). It is obvious from Fig. 5.6.4 that the force reached a higher value during the bending and piercing stage for harder material regardless of the rivet hardness. The force started to increase in higher gradients at displacements of 4.55 and 6.45 mm due to higher rivet hardness for G300 and G450 carbon steel joints, respectively. The total length of the curve in terms of displacement was higher for the softer material (G300 carbon steel). However for the same material the length was decreased with increase in the rivet hardness. The highest length of the curve was found to be 8.8 mm for G300 carbon steel with a 480 HV rivet and the lowest length was found to be 8.4 mm for G450 carbon steel with a 555 HV rivet.

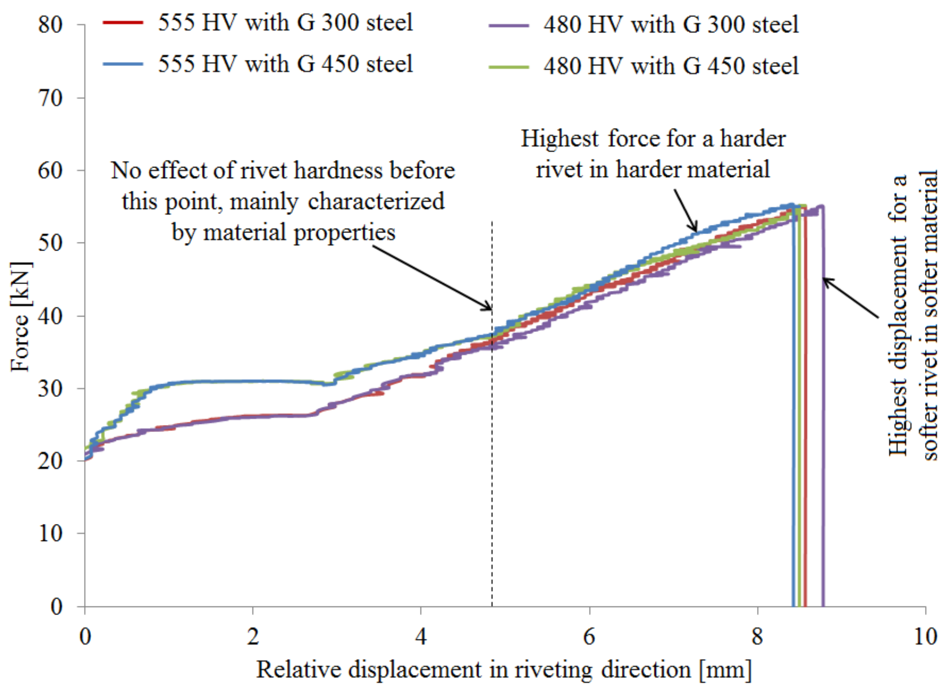

Fig. 5.6.4 Force-displacement curves depending on rivet hardness for 2.0 mm + 2.0 mm using a 2.1 mm deep die.

5.7 Change in the characteristic curve depending upon single ply vs. double ply

The effect of sheet material properties (thickness and hardness), rivet properties (hardness) and die depth on the force-displacement curve were discussed in previous four sections (Chapters 5.3 to 5.6). To complete the loop, the change in characteristic curve depending on single ply and double was examined.

5.7.1 5.0 mm total stack thickness with 555 HV rivet

Cross-sections and the associated force-displacement curves are shown in Fig. 5.7.1 and 2 for joints having the same total ply thickness of 5.0 mm using the same die (11 mm diameter and 2.35 mm deep), with rivets of the same length (8.0

mm) and hardness (555 HV) but single sheet and double sheet. A significant deviation between the two curves was observed at the initial stages of the process; during the material deformation into the die cavity. A single sheet provides a more rigid structure than two single sheets. Thus, the force was high for a single thick sheet joint. Once the material is deformed and contacts the die bottom surface there is no discrimination: the sheets behave as a single element.

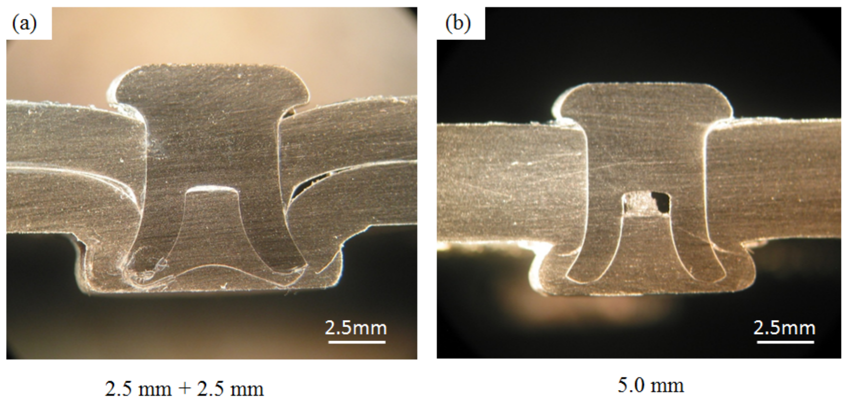

Fig. 5.7.1 Cross-sections of (a) double ply and (b) single ply of 5.0 mm joint using an 8 mm 555 HV rivet with a 2.35 mm deep die.

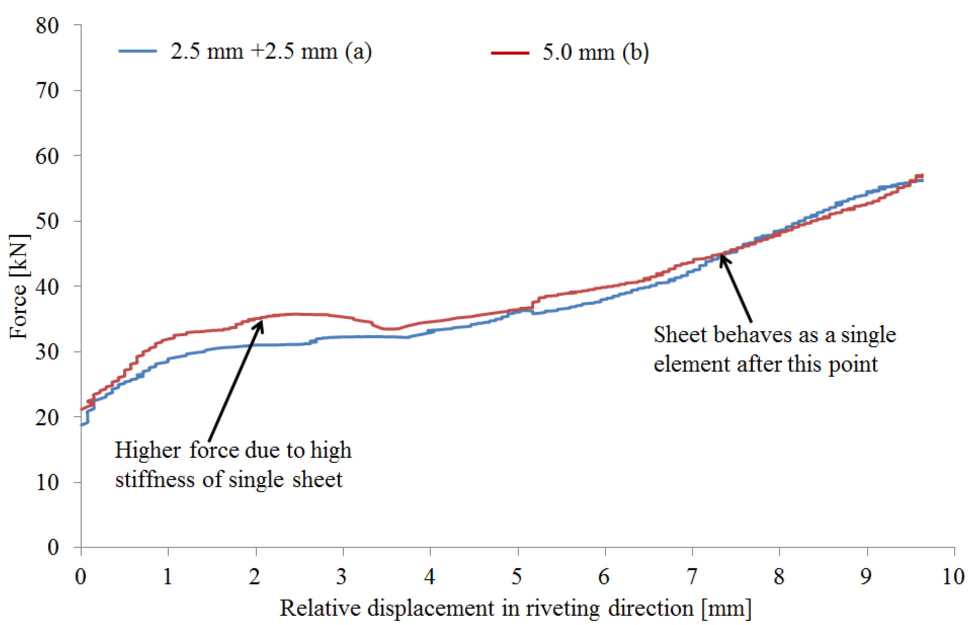

Fig. 5.7.2 Force-displacement curves of (a) double ply and (b) single ply of 5.0 mm joint using an 8 mm 555 HV rivet with a 2.35 mm deep die.

5.7.2 4.0 mm total stack thickness with 555 HV rivet

Cross-sections and the associated force-displacement curves of a 4.0 mm joint using the same die (10 mm diameter and 2.1 mm deep), with rivets of the same length (7.0 mm) and hardness (555 HV) are shown in Figs. 5.7.3 and 4. A significant deviation between the two curves was observed at the initial stages of the process; during the deformation of the material into the die cavity. A single sheet provides a more rigid structure than two single sheets. Thus, the force was high for a single thick sheet joint. Once the material is deformed and contacts the die bottom surface there is no discrimination: the sheets behave as a single element.

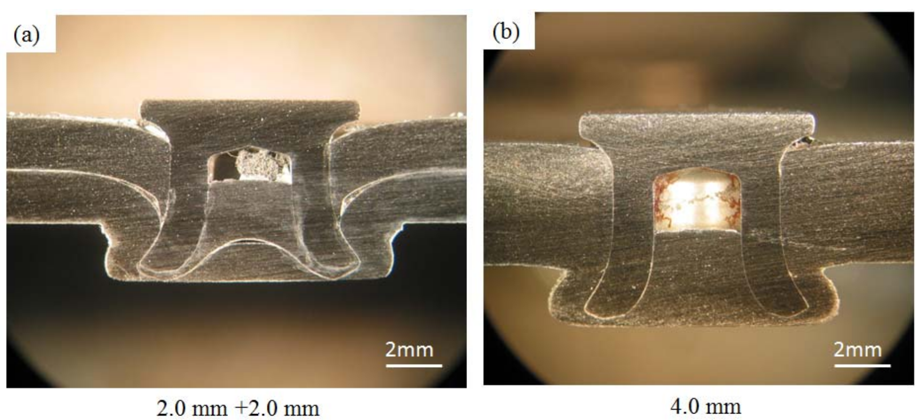

Fig. 5.7.3 Cross-sections of (a) double ply and (b) single ply of 4.0 mm joint using a 7 mm 555 HV rivet with a 2.1 mm deep die.

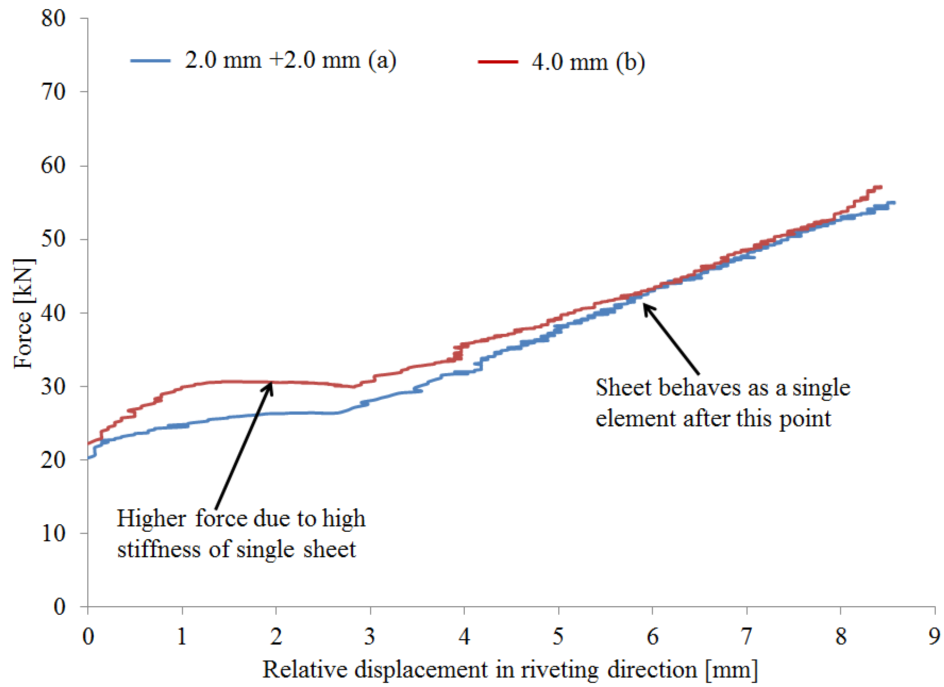

Fig. 5.7.4 Force-displacement curves of (a) double ply and (b) single ply of 4.0 mm joint using a 7 mm 555 HV rivet with a 2.1 mm deep die.

5.7.3 4.0 mm total stack thickness with 480 HV rivet

It is clear from Figs. 5.7.1-4 that a significant deviation in force occurred at the initial stages of the process but the sheets behave as single elements once the material was deformed inside the die cavity and touched the die bottom surface. However, a different behaviour was observed for a joint of total stack thickness of 4.0 mm while using a soft rivet (480 HV) instead of hard rivet (Figs. 5.7.5 and 6). In this case, the deviation in force was observed at all the stages of the process. The force stayed high even after the bottom sheet touched the die bottom surface. After the material was deformed inside the die cavity and touched the die bottom surface, the rivet started to bulge because of the more rigid structure of the single sheet. The bulging of the rivet is clearly visible from the cross-section shown in Fig. 5.7.5b. Hence, the force was always high for the single thick joint. Rivet buckling also occurred at the final stage of the SPR process in the single thick sheet joint, which was represented by the horizontal line after a displacement of 7.60 mm (Fig. 5.7.6).

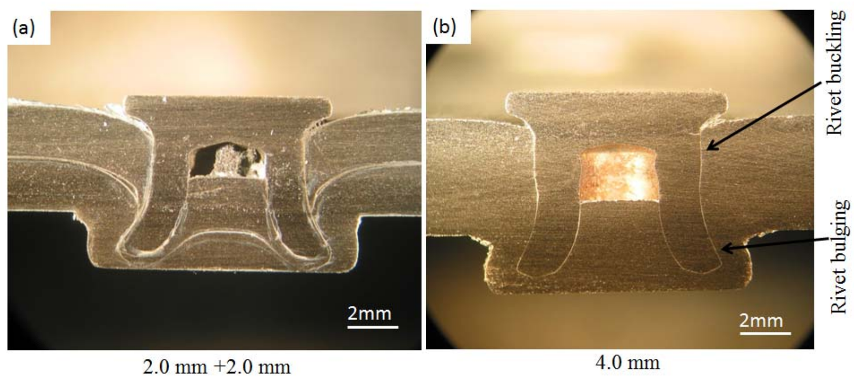

Fig. 5.7.5 Cross-sections of (a) double ply and (b) single ply of 4.0 mm joint using a 7 mm 480 HV rivet with a 2.1 mm deep die.

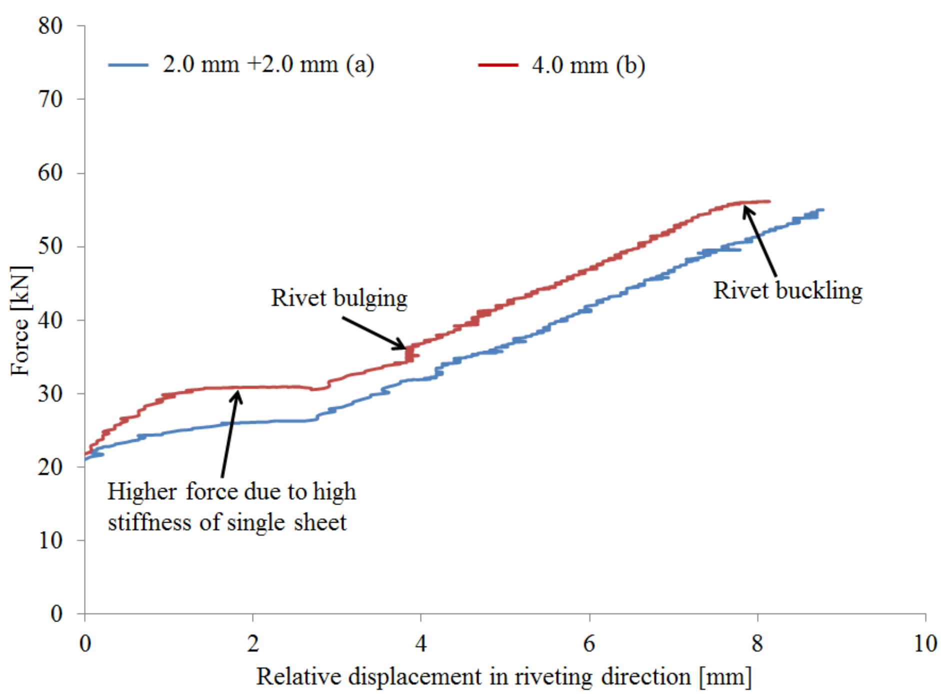

Fig. 5.7.6 Force-displacement curves of (a) double ply and (b) single ply of 4.0 mm joint using a 7 mm 480 HV rivet with a 2.1 mm deep die.

5.7.4 4.0 mm total stack thickness with 410 HV rivet

The force difference was more significant when a soft rivet was used (410 HV rivet in Figs. 5.7.7 & 8). The rivet started to bulge at an earlier stage as the rivet was soft compared with the rigid structure of the single sheet. So, a high force was observed at a low displacement while using a soft rivet in a single sheet of 4.0 mm resulted in severe bulging. Severe rivet buckling also occurred at the final stage, which was represented by the horizontal line after a displacement of 7.20 mm (Fig. 5.7.8).

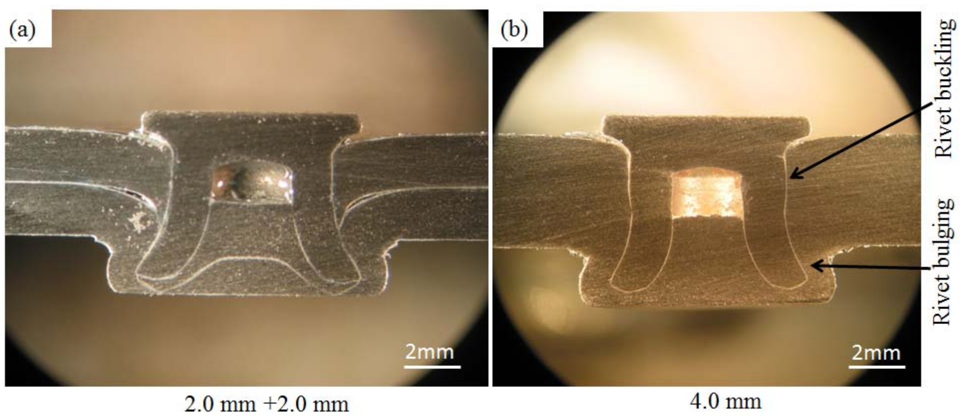

Fig. 5.7.7 Cross-sections of (a) double ply and (b) single ply of 4.0 mm joint using a 7 mm 410 HV rivet with a 2.1 mm deep die.

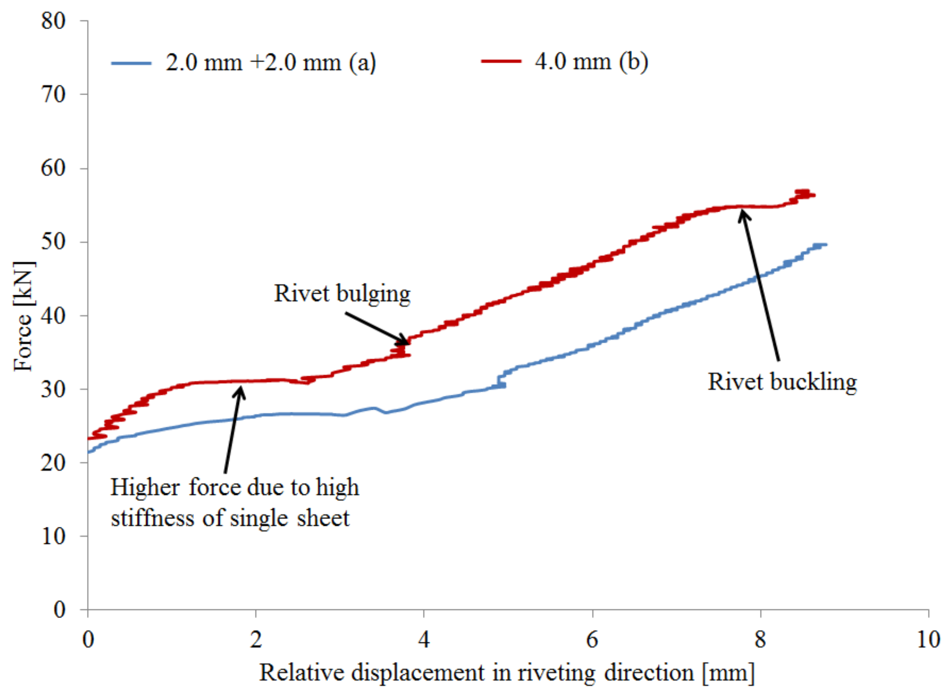

Fig. 5.7.8 Force-displacement curves of (a) double ply and (b) single ply of 4.0 mm joint using a 7 mm 410 HV rivet with a 2.1 mm deep die.

5.8 C-frame deflection

It has been suggested that force-displacement curves could be used as a fingerprint for all joints produced under the same conditions [1, 16, 17, 74]. Such curves have also been used to verify the numerical modelling of the SPR process [76, 82, 133, 167]. However, there was no information available on the C-frame's elastic deflection, which is known to occur [1], and whether this was taken into account in reporting the displacement [16]. It is necessary to deduct the C-frame deflection to characterize the force-displacement curve properly. In order to do so, a flat bottom die was used as the sole insert to measure the C-frame deflection. The pre-clamp pressure was 125 bar for all test conditions. Thus, for measuring the C-frame deflection a pre-clamp pressure was chosen at 125 bar and the riveting punch was run without any specimen or rivet. The displacements were measured for 5 different rivet setting pressures: 156, 176, 201, 223 and 241 bar. A force-displacement curve was produced by using the above data (Figs. 5.8.1 and 2) and an equation was developed for the C-frame used for this experiment. By deducting the displacement of the C-frame (measured from Fig. 5.8.1), a corrected force-displacement curve was produced (Fig. 5.8.3), which was used to characterize the force-displacement curve for the joint. A journal paper was published by the present author on the measuring technique for C-frame deflection [239].

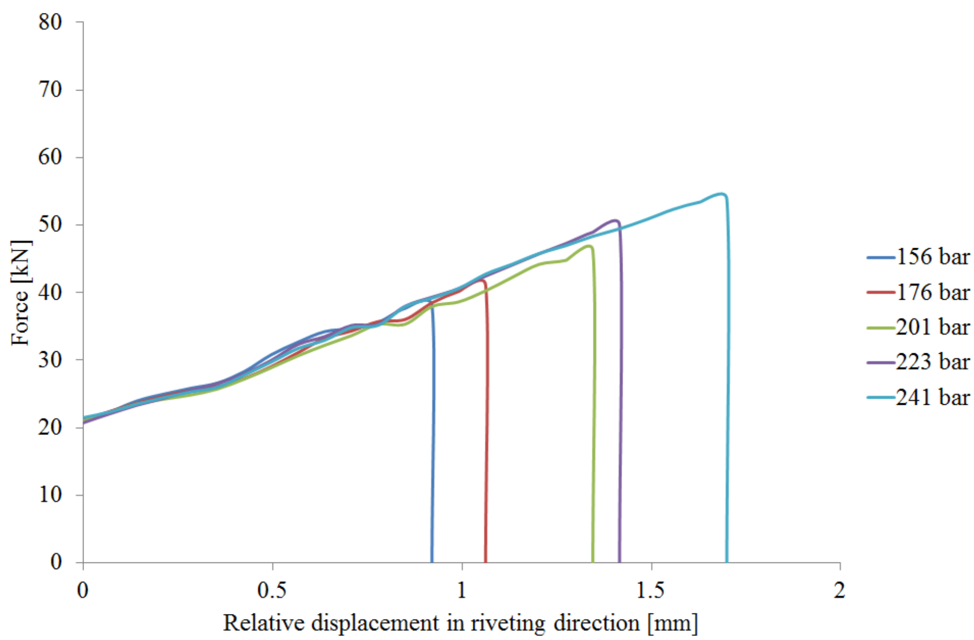

Fig. 5.8.1 Raw data of C-frame deflection at a pre-clamp pressure of 125 bar.

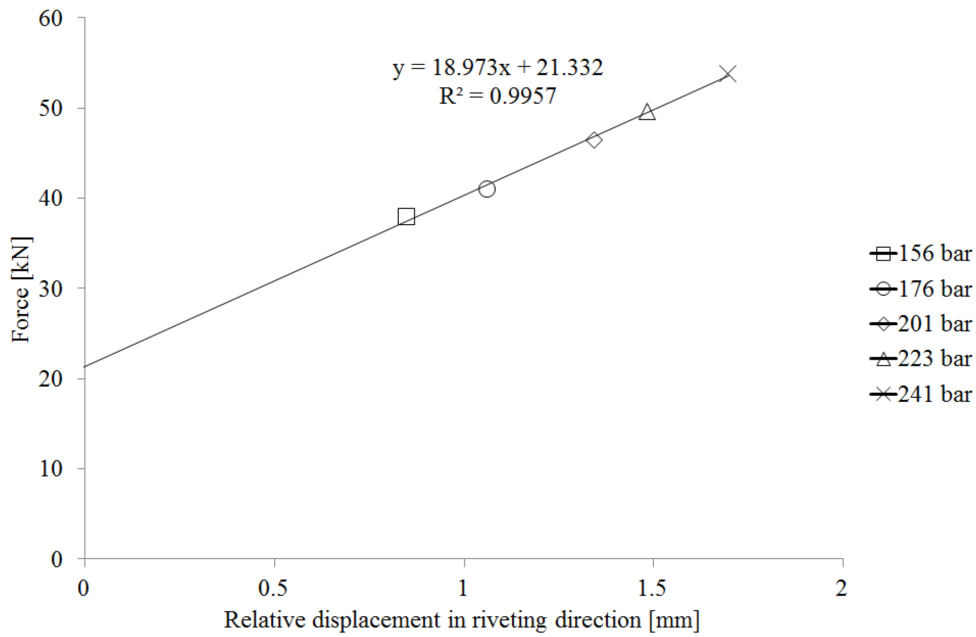

Fig. 5.8.2 C-frame deflection at a pre-clamp pressure of 125 bar.

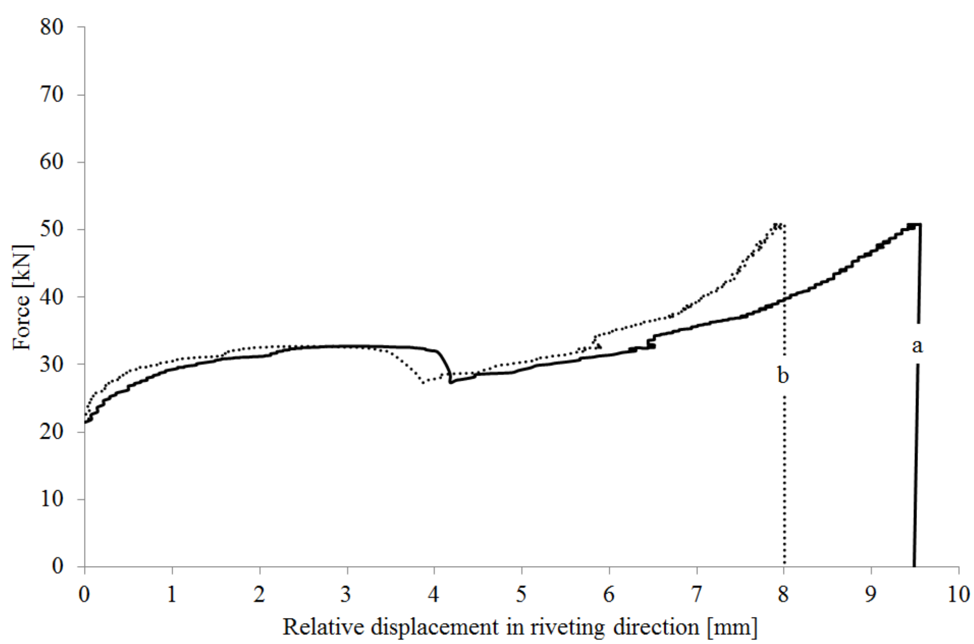

Fig. 5.8.3 Force-displacement curves of 2.5 mm + 2.5 mm G300 with an 8 mm long rivet having a hardness of 555 HV (a) before deducing and (b) after deducing C-frame deflection.

The SPR process involves C-frame deflection, yet no information is available about this elastic deflection in previous studies. King (1997) described in his thesis that C-frame deflection occurred only at the end stage of the SPR process [1]. However, it is clear from Fig.5.8.1 that for different rivet setting pressures, different displacements arose. Hence, and not unsurprisingly, C-frame deflection occurs throughout the SPR process and, also as expected, it exhibits linear behaviour. It is therefore necessary to account for C-frame deflection before characterizing the force-displacement curve of the SPR process. All graphs presented in this report were produced before deducting contributions from the C-frame deflection. However from this point all graphs in this thesis will be presented after deducting the C-frame deflection. It should be noted that C-frame deflection changes with different C-frames, which can affect the forces required in producing the joint, so it is necessary to develop deflection equation for each individual C-frame.

5.9 Characterisation of force-displacement curve

Piercing and flaring are the two main distinctive events involved in SPR joining process. Some researchers described the characteristic curve as having four stages: clamping, piercing, flaring and compression [74, 75, 82]. Hou *et al.* [16] described the curve as comprising rivet edge cutting into the sheet, rivet penetration, filling the die, and formation of interlock by rivet head squeezing. Hoang and co-authors [15] defined the four steps as bending, shearing, spreading and setting. In contrast, Porcaro and co-authors [76] segmented the characteristic curve into three different segments: an elastic part, linear plastic part with hardening, and rising of force due to die reaction.

In this work, the force-displacement curve is also divided into four parts, but with different events occurring compared with those previously reported [15, 16, 74-76, 82]: stage I – bending of sheet and partial filling of die, stage II – piercing of top sheet and sheet bending, stage III – die filling, penetration of rivet in the bottom sheet, stage IV – rivet flaring, thinning of bottom ply and rivet setting

(Fig. 5.9.1). A journal paper on characterising the force-displacement curve was published by the present author [239]. Each part of the curve is described in detail below.

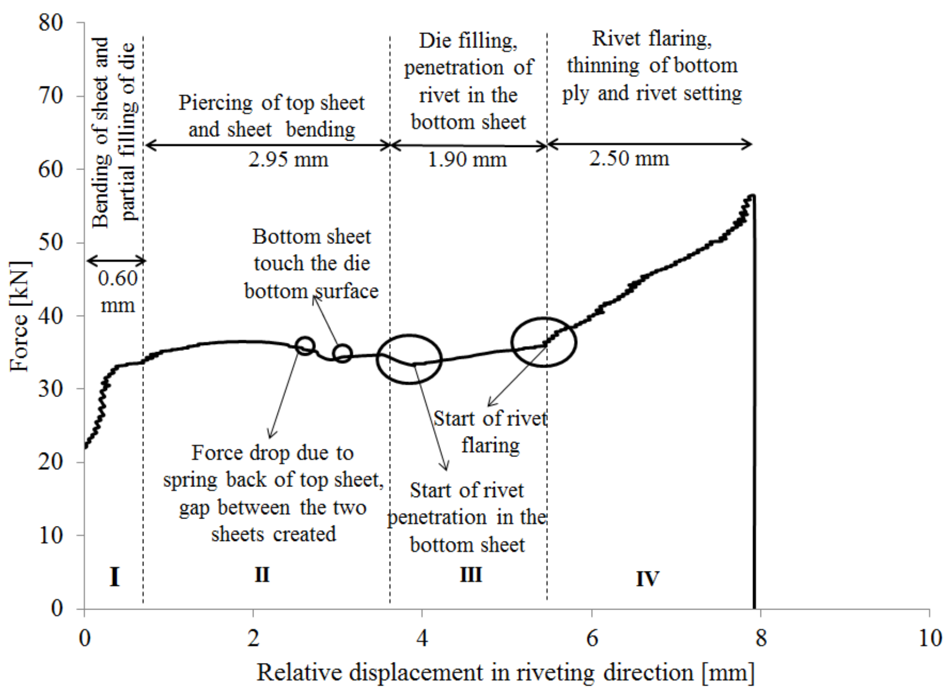

Fig. 5.9.1 Force-displacement curve of 2.5 mm + 2.5 mm sheets (280 HV) joint with an 8 mm long rivet having a hardness of 555 HV.

5.9.1 Stage I – bending of sheet and partial filling of die

During this stage bending of the metal sheet occurs and the die is filled partially by the material. The sheet plastically deforms, but no failure occurs as the stress generated during this period is below the ultimate strength of the material. The thickness of the ply material and the rivet hardness influence this step. The length of this stage decreases with increasing ply material thickness and rivet hardness. An increase in the thickness of material would make the structure more rigid, which would restrict the sheet's ability to bend into the die cavity. This will induce the rivet to pierce the sheet at an early stage, which consequently reduces the length of stage I. An increase in rivet hardness would induce piercing at an early stage, thus reducing the length of stage I. At the beginning of this stage the force increases rapidly, but the gradient reaches a minimum at the end of this stage. The thickness and properties of ply material (e.g. hardness) play a very important role on the force developed in this stage: the thicker and harder the ply materials, the higher are the force.

5.9.2 Stage II – piercing of top sheet and sheet bending

As soon as the force reaches the ultimate strength of the material, ductile failure is initiated in the top sheet and piercing begins. The force is almost constant during this stage for a given total stack thickness and the length of this stage mainly depends on the thickness of the top sheet (Fig. 5.9.1). Other parameters have very little influence on the length of this step (i.e., rivet length and ply material thickness). The bottom sheet touches the die surface in this period, which induces an increase in force (Fig. 5.9.1). In some cases, when the sheets are thin, the bottom sheet touches the die's bottom surface before this stage. The depth of the die is very crucial for this stage, especially for materials which are less ductile. Too deep a die would create a crack at this step (Figs. 5.2.1-6). The crack was created due to excessive bending of the bottom sheet as the sheet was unable to touch the die bottom surface to control the bending. For more ductile materials the depth of the die would increase this step rather than creating a crack (Figs. 5.3.1-3). The force-displacement curve and cross-section of joints during this period are shown in Figs. 5.1.1-10. At the end of this stage the force decreases a little as the resistance force reduces once the top sheet is perforated, the decrease thus indicating the end of piercing of the top sheet (Fig. 5.9.1). It is evident that this decrease would be more visible for a thicker top sheet and a deeper die.

5.9.3 Stage III – die filling, penetration of rivet in the bottom sheet

This step mainly indicates the sheets filling in the die. Once the top sheet is pierced the force rises again as more material flows inside the die cavity. The force increases roughly linearly during this period. As soon as the die fills up completely, material movement without plastic deformation in the riveting direction is no longer possible towards the die. The rivet then starts to penetrate the bottom sheet. Rivet penetration in the bottom sheet is necessary before the rivet starts to flare for an effective mechanical interlock. Thus the length of this stage gives a signature of the penetration of the rivet into the bottom sheet. At the end of this step, the die is completely filled with material, so no more material movement is possible in any direction, but still the rivet is pushed downward because the punch pressure is applied until the pre-set rivet pressure is reached. So a sudden increase in force is observed with flaring, and in some cases bulging of the rivet (Fig. 5.9.1). Rivet bulging occurs when the sheet is too hard compared to the rivet hardness, or when the rivet is too long compared to the joint stack thickness (Figs. 5.7.5-8). The interrupted force-displacement curves and associated joints' cross-sections during this stage are shown in Figs. 5.1.11-18. The shank of the rivet remains straight during this step as the horizontal component of the reaction force (F_H in Fig. 5.9.2) is not sufficient to deform the rivet material. As soon as the horizontal part of the force exceeds the resistance force of the rivet wall, the rivet starts flaring, defining the end of this step. Hence, the properties of the rivet mainly influence this stage. The die recess volume and rivet hardness also influence this stage, with this stage lengthening with greater die volume and higher rivet hardness.

5.9.4 Stage IV – rivet flaring, thinning of bottom ply and rivet setting

During this stage, rivet flaring as well as thinning of the bottom ply continue to occur. This is the most crucial part of the SPR process as mechanical interlocking takes place during this stage by rivet flaring. The mechanical interlock occurs if the rivet penetrates and flares into the bottom sheet, but if flaring occurs between the top and bottom sheet (when the length of stage III is too small) no interlock would form. The force increases with a high gradient, continuously pushing the cylindrical wall of the rivet to flare outwards, which gradually forms the interlock by this outward deformation of the rivet wall (rivet flaring) and compression of the sheets in the die recess and rivet bore. The interrupted force-displacement curves and associated joints' cross-sections during this period are shown in Figs. 5.1.19-26. The force and displacement reach their maxima at the end of this stage. These two parameters can be used to judge the quality of a joint for a given process set-up (rivet length and hardness, total stack thickness and die geometry). The amount of rivet flaring, which is ultimately related to the strength of the joint [136], can be estimated from this step: the longer this step is, the greater is the extent of rivet flaring. The rivet hardness mostly affects this stage: the higher the rivet hardness, the shorter is the length of this step for a given geometry of rivets. The die recess volume together with the joint stack-up design and rivet length also influence this stage.

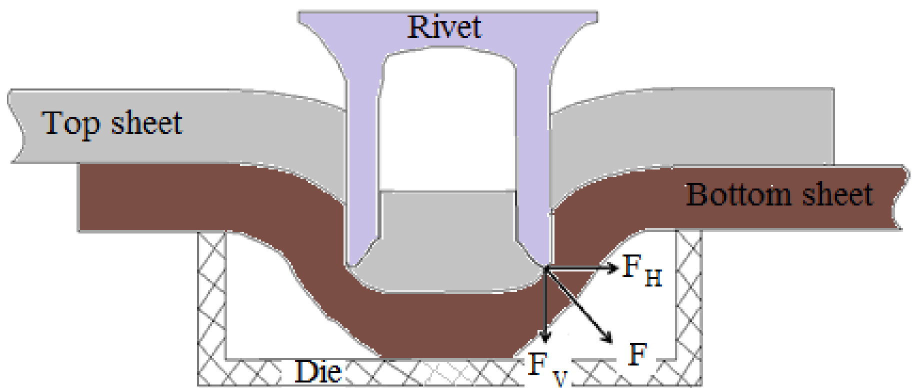

Fig. 5.9.2 Schematic diagram of starting of rivet flaring.

5.9.5 Effect of sheet thickness on the force-displacement curve

Sheet thickness plays a very important role in the different stages of the characteristic curve. As the overall thickness of the ply material increases, a long rivet is needed. So the first effect of stack thickness is on the overall length of the force-displacement curve. This can be seen in Figs. 5.9.3-4 where the total punch displacement was 8, 7 and 6 mm for a joint having a total ply thickness of 5, 4 and 3 mm, respectively.

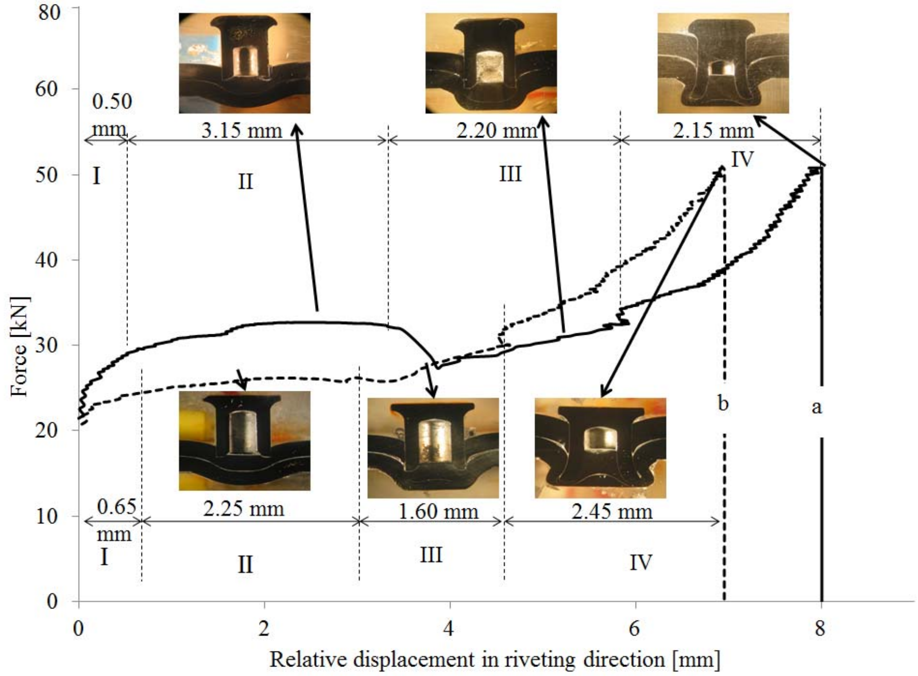

Fig. 5.9.3 Characteristic curves for joints of carbon steel sheets with rivets of 555 HV hardness: (a) 2.5 mm + 2.5 mm sheets + 8 mm long rivet with a 3 mm deep die, and (b) 2.0 mm +2.0 mm sheets + 7 mm long rivet with a 2.5 mm deep die.

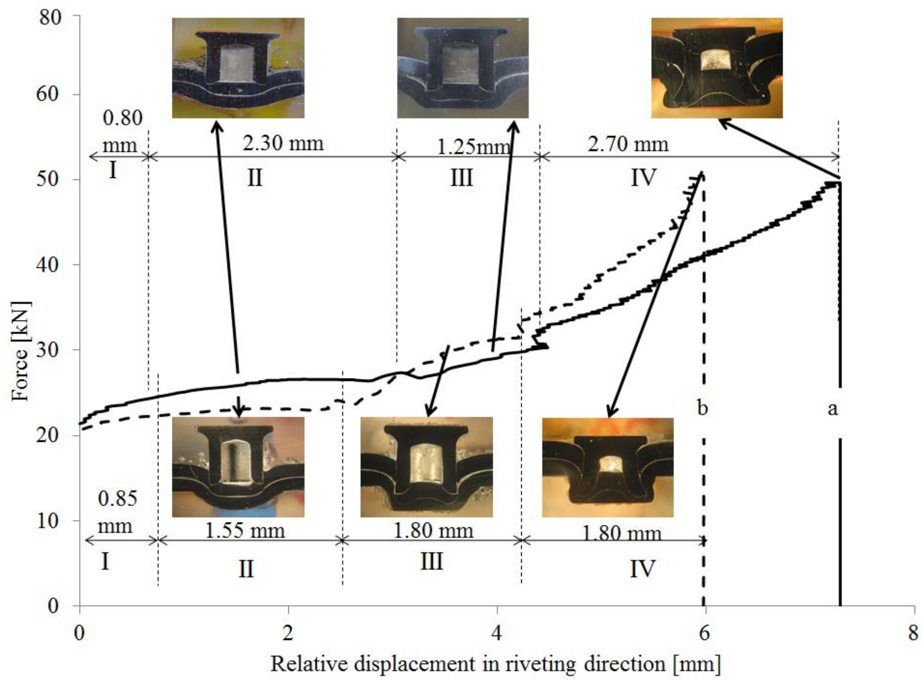

Fig. 5.9.4 Characteristic curves for joints of carbon steel sheets with rivets of 410HV hardness: (a) 2.0 mm + 2.0 mm sheets + 7 mm long rivet, and (b) 1.5 mm + 1.5 mm sheets + 6 mm long rivet.

It is also clear from Figs. 5.9.3-4 that the length of stage I decreases with increasing thickness while using rivets of the same hardness. For a rivet hardness of 555 HV, the length of the first stage is 0.65 mm for a 4 mm stack-up joint, and 0.50 mm for a 5 mm stack-up joint. While, for a 480 HV rivet, this length is 0.85 mm for 3 mm stack-up joint, and 0.80 mm for a 4 mm stack-up joint. The force developed during this stage also depends on the thickness of the top sheet. It can be seen that the force reaches 33 kN, 26 kN and 22 kN for joint stack-up thickness of 5, 4 and 3mm, respectively (Figs. 5.9.3-4). This is due to an increase in the thickness of material making the structure more rigid, which would restrict the sheet's capacity to bend into the die cavity while generating a high force. This would induce piercing at an earlier stage, which consequently reduces the length of stage I.

Stage II is characterized mainly by piercing of the top sheet, so the length of this step depends directly on the thickness of the top sheet. With a 555 HV rivet, the length of this step is 3.15 mm and 2.25 mm for a total joint thickness of 5 and 4mm, respectively (Fig. 5.9.3). With a 410 HV rivet, the length of this step is 2.30 mm for a total joint thickness of 4 mm and reduces to 1.55 mm for a 3 mm thick joint. The length of this step is a bit higher than the thickness of the top material, because bending of the sheet away from the rivet continues during this step. The bottom sheet touches the die bottom surface during this step for a joint thickness of 5 mm and 4 mm, but for the 3 mm thick joint the bottom sheet touches the die surface in the previous stage. This is due to the interplay between the force required to pierce the top sheet and the force required to push the sheet into the die cavity. A decrease in thickness would make the stack more flexible, which means the material cannot generate sufficient reactive force on its own in order for the rivet to pierce the top sheet hence the sheet is pushed down easily into the die cavity. This would cause the bottom sheet to touch the die bottom surface at an earlier stage.

There is no significant effect of ply material thickness on the third and fourth stages of the characteristic curve. The die recess volume mainly affects the third stage, but both the die recess volume and joint stack-up design, or gradient factor (ratio of die recess volume to total ply thickness), affect the fourth stage of the characteristic curve.

5.9.6 Effect of material hardness on the force-displacement curve

Sheet material hardness also plays a very important role in the first two stages of the characteristic curve. As the length of the rivets and the setting pressure are similar the overall length of the curve is equal (Fig. 5.9.5). It is clear from Fig. 5.9.5 that the length of the each stage is also equal. A big deviation in force is observed during stage I: 34 and 28 kN for G450 and G300 steel respectively. The force remains at a high value during stage II as well. The force reached at a value of 36 and 32 kN during stage II for G450 and G300, respectively. No significant effect of material hardness was observed during stages III and IV.

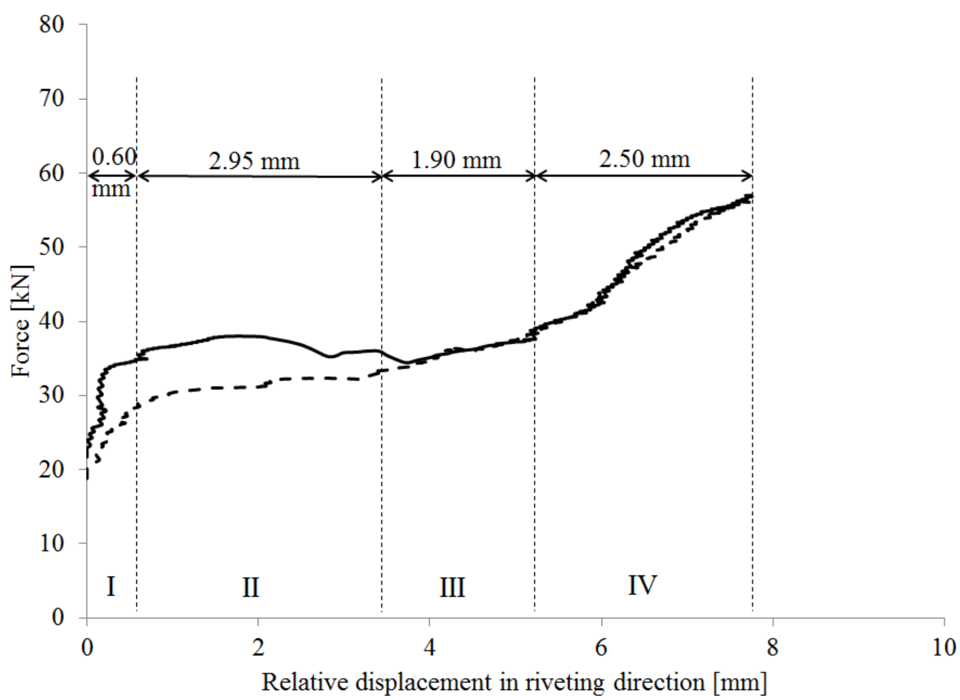

Fig. 5.9.5 Characteristic curves for joints of 2.5 mm + 2.5 mm sheets with 8.0 mm rivets of 555HV hardness: (a) G450 steel, and (b) G300 steel.

5.9.7 Effect of rivet hardness on the force-displacement curve

Rivet hardness plays a very important role in the four different stages of the characteristic curve. Force-displacement curves are shown in Fig. 5.9.6 for joints having the same total ply thickness of 4 mm and produced using the same die, with rivets of the same length but of different hardnesses. It can be seen that the overall length of the curve decreases from 7.3 mm to 7.15 mm then to 6.95 mm with increasing rivet hardness from 410 to 480 then to 555 HV, respectively. This decrease in overall length indicates that the extent of rivet flaring is less for a hard rivet. Likewise, the length of the first stage decreases with an increase in rivet hardness: 0.80, 0.70 and 0.65 mm for 410, 480 and 555 HV, respectively. It is also clear from Fig. 5.9.6 that a harder rivet starts piercing at an earlier stage, but starts flaring later. The slope of the fourth stage of the characteristic curve is steeper for a harder rivet. Other than this change of slope in stage IV, the rivet hardness does not affect the characteristic curve in terms of the magnitude of the force developed during each step of the curve.

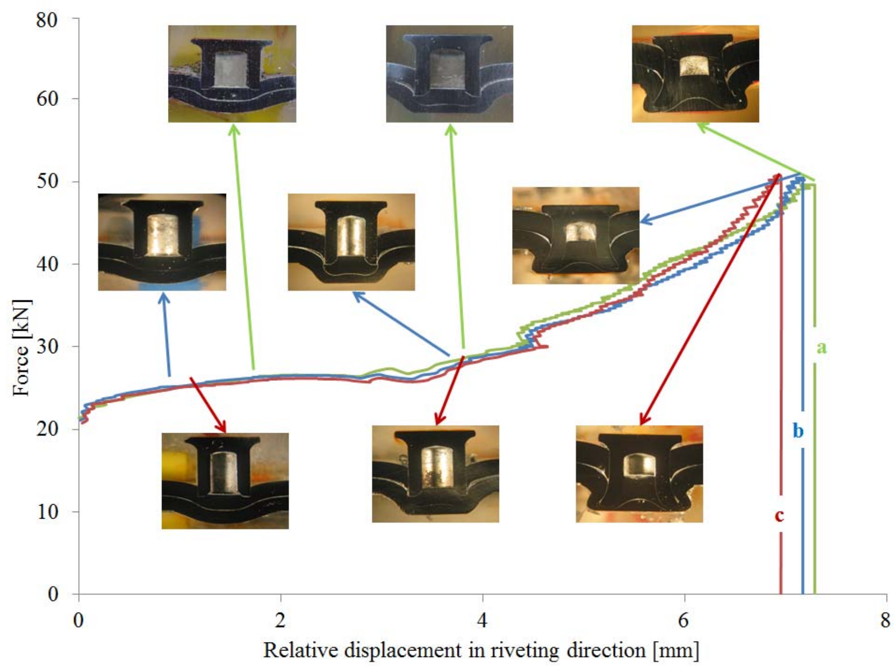

Fig. 5.9.6 Force-displacement curves for joints of 2.0 mm + 2.0 mm carbon steel sheets produced using 7 mm long rivets of different hardnesses: (a) 410 HV (b) 480 HV (c) 555 HV.

5.10 Rivet flaring model

The present study would show that, it is possible to calculate the rivet tail diameter inside a joint without having to cross section a joint. A characteristic curve can be produced by measuring force and displacement directly during riveting. Typically, force, punch displacement, rivet setting pressure and pre-clamp pressure are measured as a function of time. The characteristic curve is produced by plotting the force as a function of displacement relative to the time and position where the rivet just touches the top ply. The detailed process of producing the characteristic force-displacement curve taking into account the elastic deformation of the C-frame is described in Haque et al. 2012 [239]. A force-displacement curve is shown in Fig. 5.10.1 for a SPR process.

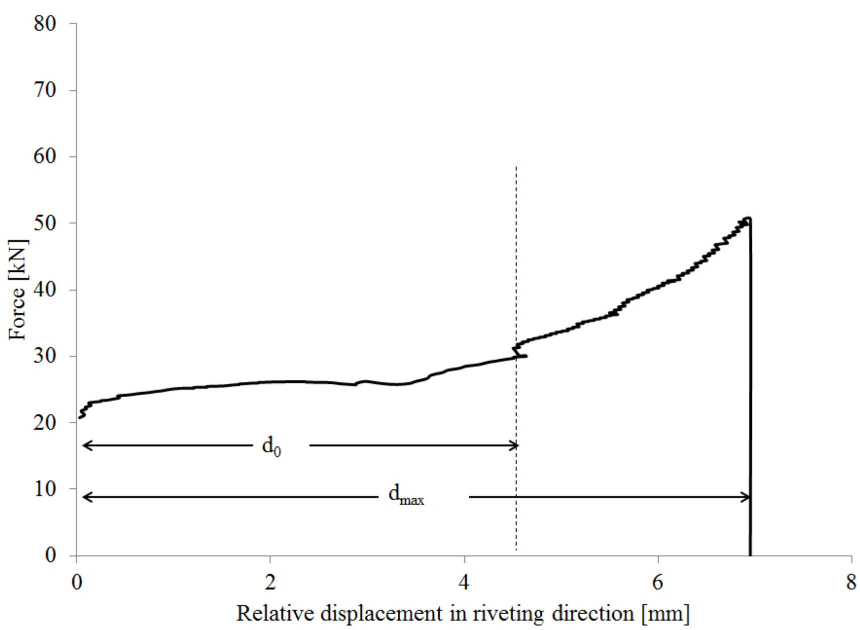

Fig. 5.10.1 Characteristic-curve of 2 mm + 2 mm carbon steel joint with a 7 mm long rivet with a hardness of 555 HV.

During the first stage, bending of the sheet material occurred and the die was partially filled by the material. Plastic deformation occurred, but there was no failure as the ultimate strength of the material was above the stress produced during this period. As soon as the force reached the ultimate strength of the material, ductile failure initiated in the top sheet, i.e., piercing started, which is characterized as the second stage. Again when the bottom sheet touched the die floor, material movement in the riveting direction was no longer possible towards the die, i.e., vertically. The rivet then started to flare because of the reaction force of the die. From the characteristic curve, the displacement of the rivet before flaring (d_0) and the maximum rivet displacement (d_{max}) can be obtained, as shown in Fig. 5.10.1.

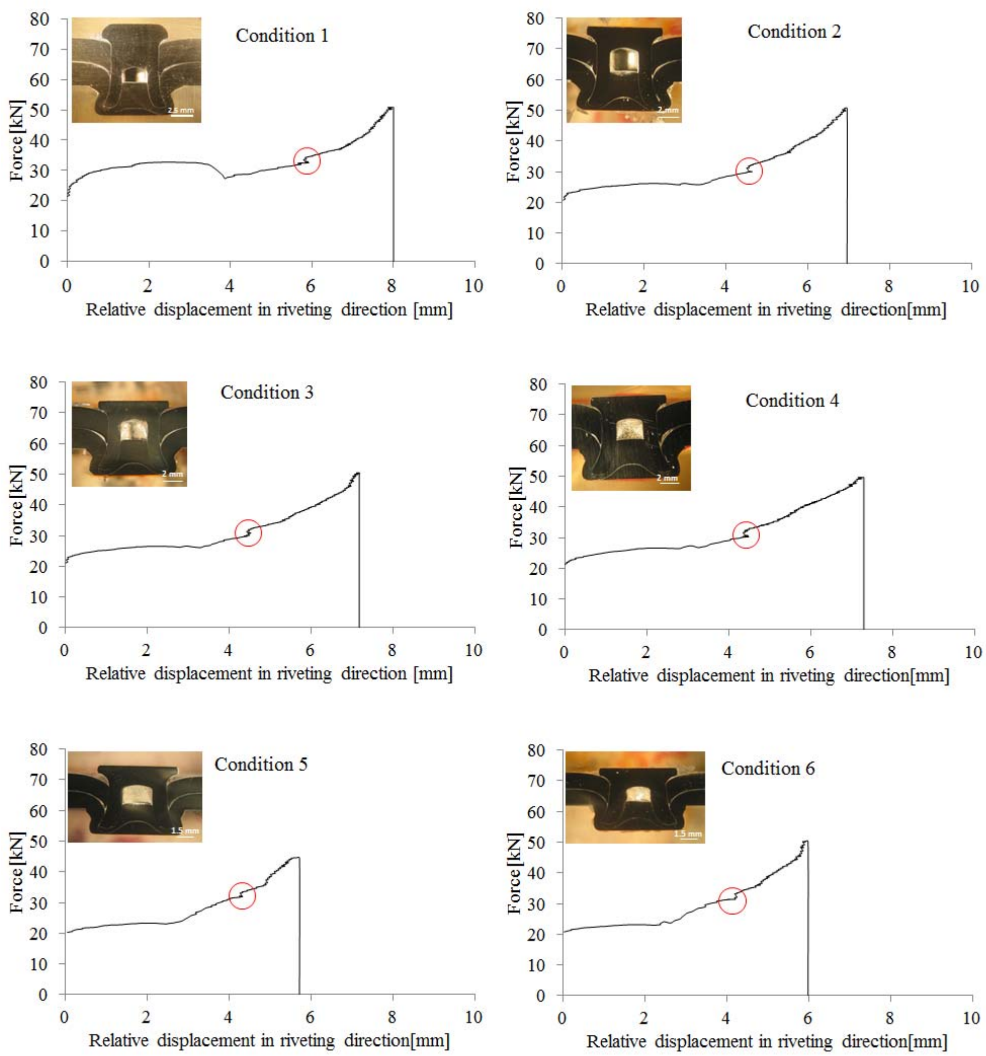

Fig. 5.10.2 Step rise of force for six different conditions (listed in Table 5.10.1); the photograph in each graph depicts the cross-section of the completed SPR joint.

In order to develop a model which can predict the rivet flaring inside a joint, six different completed joints were produced comprising three types of thicknesses of ply material and three different hardnesses of rivet (Fig.5.10.2). These joints were also interrupted at different positions according to Table 5.10.1. The length of the rivet and die were chosen according to the total ply thickness.

Table 5.10.1 Joining parameters (all materials are G300 carbon steel, pre-clamp and rivet setting pressure were 125 and 220 bar, respectively).

<table>
<tr><th colspan="3" rowspan="2">Condition</th><th rowspan="2">Thickness of the joint (top sheet + bottom sheet, mm)</th><th colspan="2">Rivet</th><th colspan="2">Die (flat die profile)</th></tr>
<tr><th>Length (mm)</th><th>Hardness (HV)</th><th>Depth (mm)</th><th>Diameter (mm)</th></tr>
<tr><td rowspan="6">1</td><td>Case</td><td>Interruption distance, mm</td><td rowspan="6">2.5 + 2.5</td><td rowspan="6">8</td><td rowspan="6">555</td><td rowspan="6">3</td><td rowspan="6">10</td></tr>
<tr><td>I</td><td>5.11</td></tr>
<tr><td>II</td><td>6.35</td></tr>
<tr><td>III</td><td>6.71</td></tr>
<tr><td>IV</td><td>7.22</td></tr>
<tr><td>V</td><td>8 (complete joint)</td></tr>
<tr><td rowspan="5">2</td><td>Case</td><td>Interruption distance, mm</td><td rowspan="5">2 + 2</td><td rowspan="5">7</td><td rowspan="5">555</td><td rowspan="5">2.5</td><td rowspan="5">10</td></tr>
<tr><td>I</td><td>3.91</td></tr>
<tr><td>II</td><td>4.68</td></tr>
<tr><td>III</td><td>5.71</td></tr>
<tr><td>IV</td><td>6.95 (complete joint)</td></tr>
<tr><td rowspan="5">3</td><td>Case</td><td>Interruption distance, mm</td><td rowspan="5">2 + 2</td><td rowspan="5">7</td><td rowspan="5">480</td><td rowspan="5">2.5</td><td rowspan="5">10</td></tr>
<tr><td>I</td><td>4.03</td></tr>
<tr><td>II</td><td>4.91</td></tr>
<tr><td>III</td><td>5.69</td></tr>
<tr><td>IV</td><td>7.17 (complete joint)</td></tr>
<tr><td rowspan="5">4</td><td>Case</td><td>Interruption distance, mm</td><td rowspan="5">2 + 2</td><td rowspan="5">7</td><td rowspan="5">410</td><td rowspan="5">2.5</td><td rowspan="5">10</td></tr>
<tr><td>I</td><td>3.82</td></tr>
<tr><td>II</td><td>5.39</td></tr>
<tr><td>III</td><td>6.94</td></tr>
<tr><td>IV</td><td>7.28 (complete joint)</td></tr>
<tr><td colspan="3">5</td><td>1.5 + 1.5</td><td>6</td><td>480</td><td>2.3</td><td>9</td></tr>
<tr><td colspan="3">6</td><td>1.5 + 1.5</td><td>6</td><td>410</td><td>2.3</td><td>9</td></tr>
</table>

5.10.1 Observation on Experimental Results

The cross-sections and related characteristic curves of the above six different conditions are shown in Fig. 5.10.2. It can be observed that for all the conditions, regardless of ply material thickness and rivet length, a sharp and distinctive rise in force occurred in the characteristic curve at a force of 30 kN. It is noted that the shank of the rivet remains straight before this point as the horizontal component of the reaction force is not sufficient to deform the rivet material. As soon as the horizontal force vector F_H exceeds the resistance of the rivet wall, the rivet starts flaring. To examine the above hypothesis, the joints were interrupted at several punch positions according to Table 5.10.1 and force-displacement curves and associated cross-sections for conditions 1-4 are shown in Figs. 5.10.3-6.

5.10.1.1 Condition # 1 in Table 5.10.1

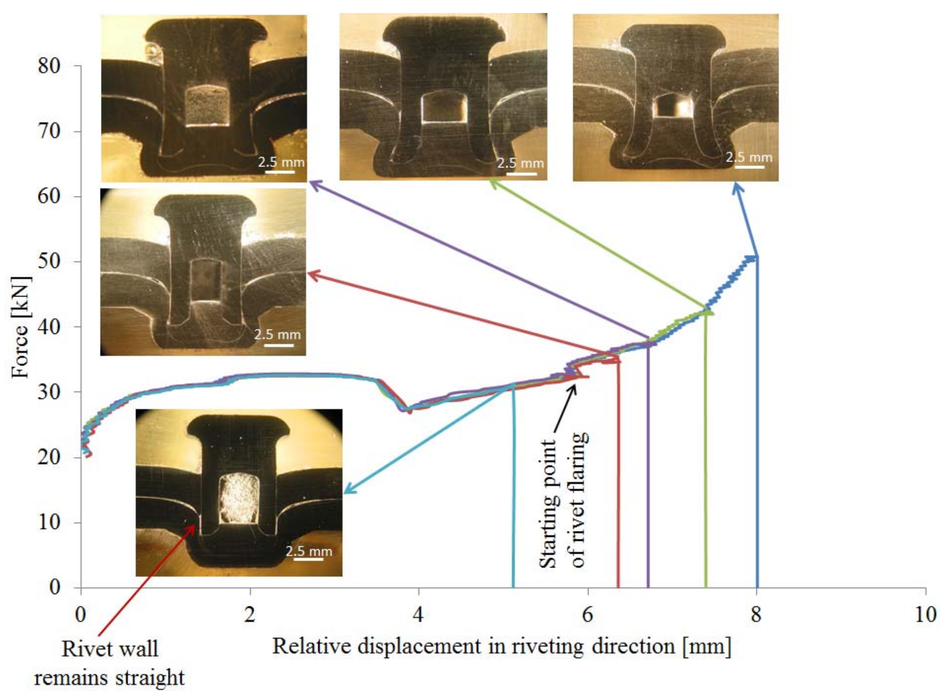

Fig. 5.10.3 Interrupted SPR process curve for different steps of 2.5 mm + 2.5 mm G300 steel joint with 8 mm long rivet of hardness 555 HV.

5.10.1.2 Condition # 2 in Table 5.10.1

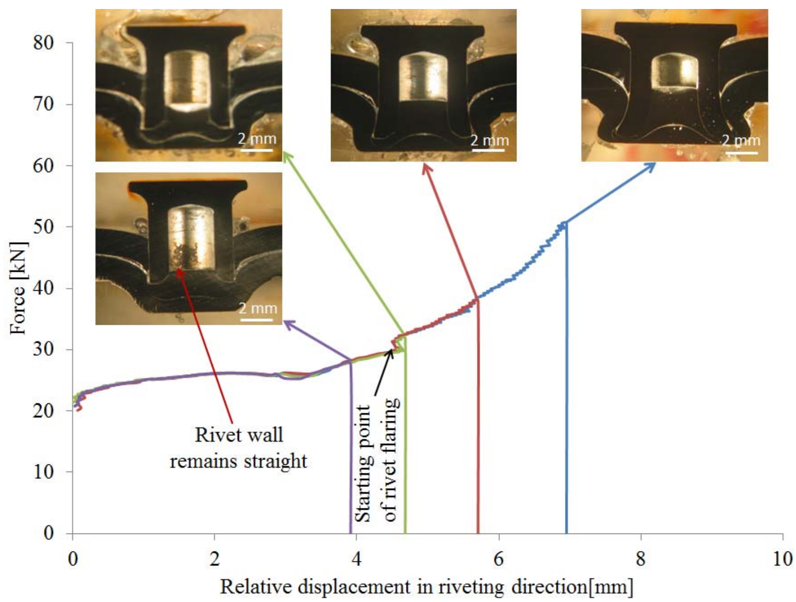

Fig. 5.10.4 Interrupted SPR process curve for different steps of 2.0 mm + 2.0 mm G300 steel joint with 7 mm long rivet of hardness 555 HV.

5.10.1.3 Condition # 3 in Table 5.10.1

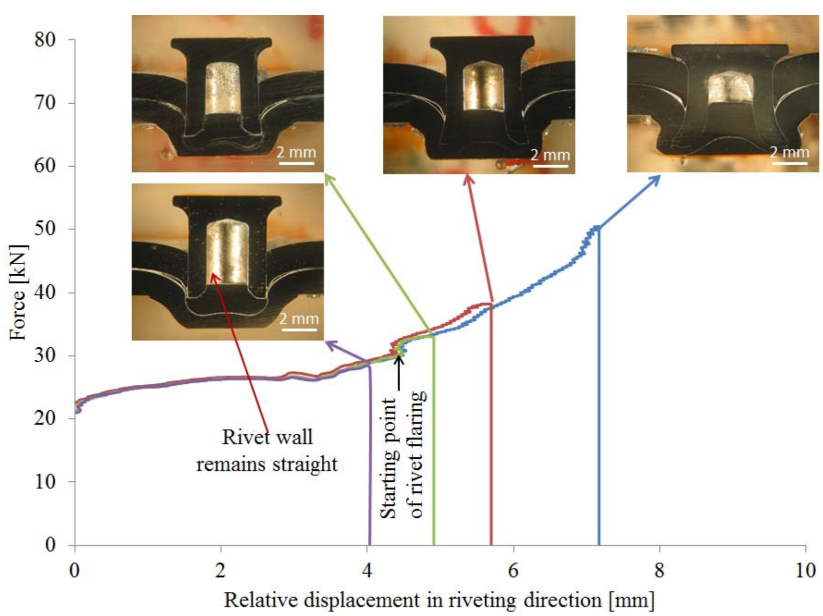

Fig. 5.10.5 Interrupted SPR process curve for different steps of 2.0 mm + 2.0 mm G300 steel joint with 7 mm long rivet of hardness 480 HV.

5.10.1.4 Condition # 4 in Table 5.10.1

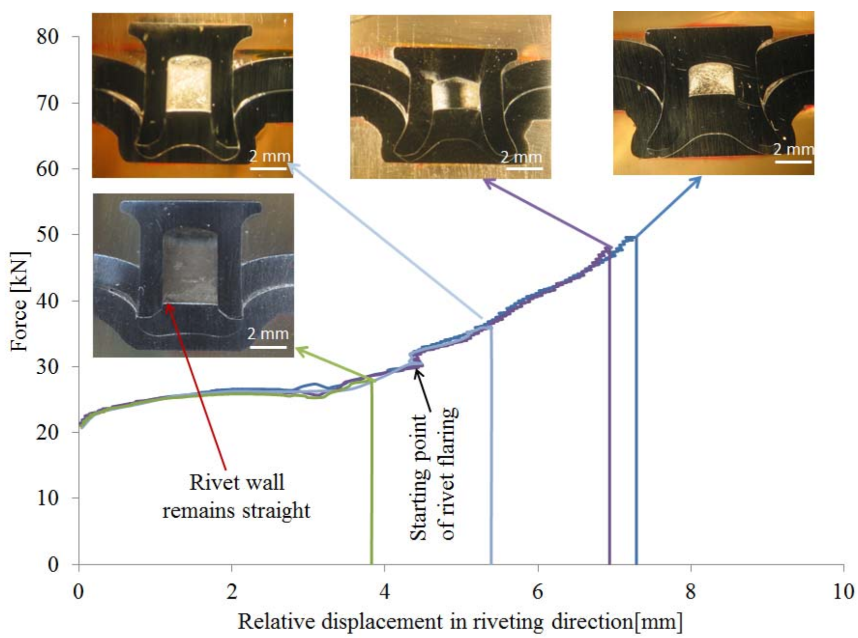

Fig. 5.10.6 Interrupted SPR process curve for different steps of 2.0 mm + 2.0 mm G300 steel joint with 7 mm long rivet of hardness 480 HV.

It is clear from Figs. 5.10.3-6 that the rivets started to flare after a certain value of force was reached. All other joining conditions also followed the same path. Once the start of rivet flaring has been identified, it is necessary to find out the path of the rivet tip. For this, the joints were interrupted at different positions before the completed joints; for example, case I: 5.11 mm, case II: 6.35 mm, case III: 6.71 mm and case IV: 7.22 mm for condition 1 in Table 5.10.1; and the amount of flaring was measured at each interrupted stage. Results showed a linear dependence of the measured rivet flaring upon the displacement in the riveting direction (Fig. 5.10.7). This observation would be used to develop the rivet flaring model in next section.

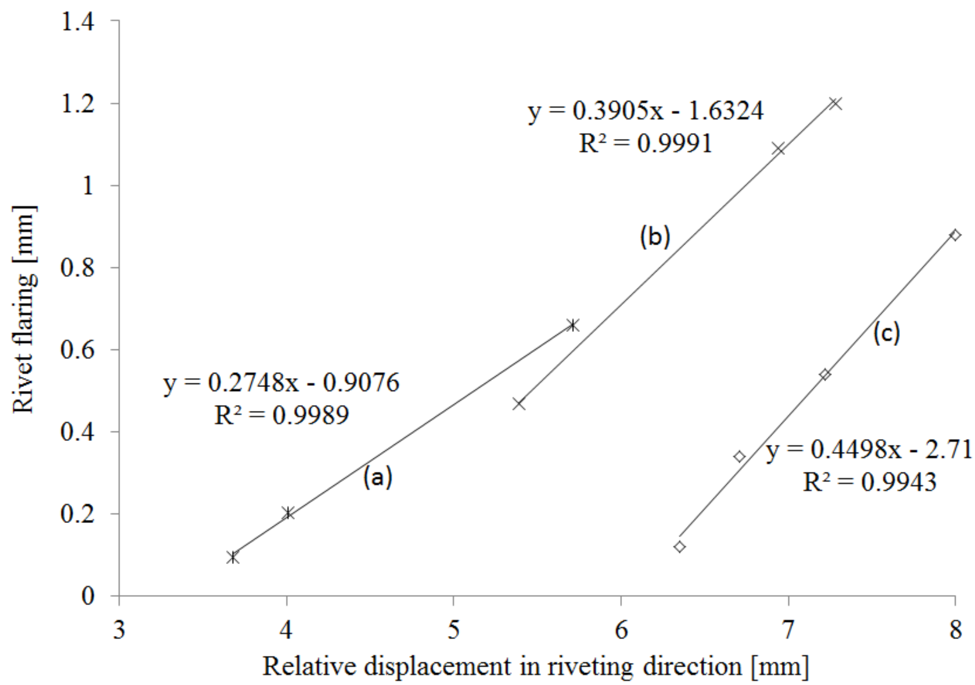

Fig. 5.10.7 Rivet flaring dependence upon rivet displacement for different sheet thicknesses: (a) condition 5: 1.5 + 1.5 mm carbon steel joint, (b) condition 4: 2 + 2 mm carbon steel joint, and (c) condition 1: 2.5 + 2.5 mm carbon steel joint in Table 5.10.1.

5.10.2 Developing the model

It is assumed that the rivet travels a distance d_0 in the vertical direction before it starts to flare because of the reaction force from the die. A schematic of the rivet flaring model is drawn in Fig. 5.10.8. Flaring starts in the OE direction because of the die reaction before reaching point C on line OE after completion of the joint.

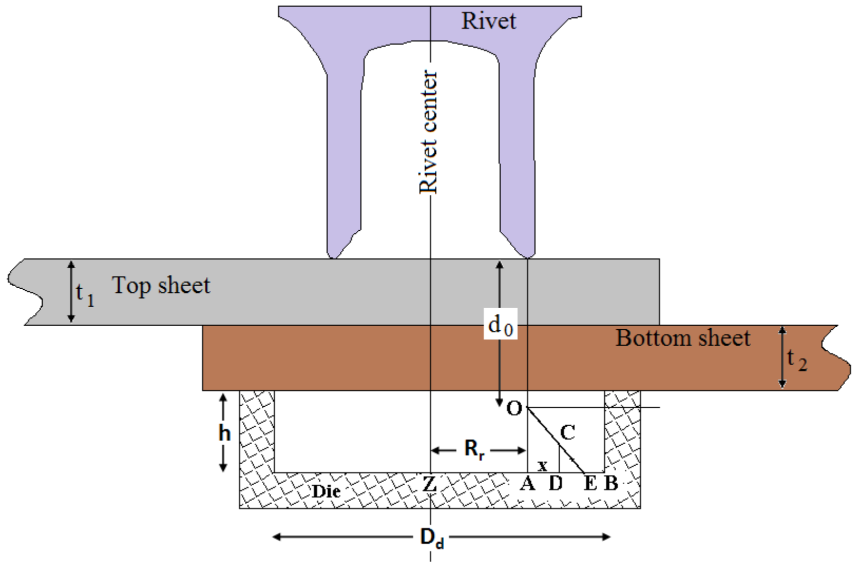

Fig. 5.10.8 Geometrical model of rivet flaring calculation, where x (distance AD) is the rivet flaring.

It is difficult to find the point E on AB because rivet flaring depends on the hardness of the rivet, which determines the angle AOE. Thus point E on AB can be approximated by:

$$AE = C_1 * AB = C_1 * (ZB - ZA) = C_1 * (D_d/2 - R_r) \tag{5.1}$$

where C_1 is a coefficient that depends on the rivet hardness, ZB is the die radius ($D_d/2$) and ZA is the rivet shank radius (R_r).

When the rivet is very hard compared with the sheet material, little or no flaring of the rivet would occur and the rivet tip would move from the point O towards the point A and point E would coincide with point A. Thus the length of line AE would be maximum when E coincides with B, and in that case AE equals AB. So the range of the coefficient for rivet hardness is: $0 \leq C_1 \leq 1$.

Points O, A and E on the triangle OAE can be found thus:

$$OA = (t_1 + t_2 + h - d_0) \tag{5.2}$$

$$OE = \sqrt{OA^2 + AE^2} = \sqrt{(t_1 + t_2 + h - d_0)^2 + (C_1 * (\frac{D_d}{2} - R_r))^2} \tag{5.3}$$

For the path of the rivet tip, it has been assumed that OE is a straight line. Hence,

$$OC = C_2 * (d_{max} - d_0) \tag{5.4}$$

where C_2 is a coefficient that depends on rivet length. C_2, like C_1, ranges from 0 to 1 according to whether the rivet does not flares or flare fully.

It is now possible to calculate rivet flaring (x) from a simple geometrical relation:

$$x = AD = \frac{OC * AE}{OE} \tag{5.5}$$

Substituting values of AE, OE and OC from equations 5.1, 5.3 and 5.4 respectively, equation 5.5 can be rewritten in the following form.

$$x = \frac{C_2 * (d_{max} - d_0) * C_1 * (\frac{D_d}{2} - R_r)}{\sqrt{(t_1 + t_2 + h - d_0)^2 + (C_1 * (\frac{D_d}{2} - R_r))^2}} \tag{5.6}$$

For a given die and rivet, the die diameter (D_d), die depth (h) and rivet radius (R_r) are known. For a given joint, the top sheet thickness (t_1) and bottom sheet thickness (t_2) are also known, and d_{max} and d_o can be obtained from the characteristic force-displacement curve.

5.10.3 Determination of coefficients C_1 and C_2 from interrupted tests

In order to determine the coefficients C_1 and C_2 of equation (5.6) and in particular the assumption of a linear flaring trajectory along OE (Fig. 5.10.8), four different conditions were tested, where the joints were interrupted at different positions as listed in Table 5.10.1. The coefficients were determined empirically and it was found that the calculated values of rivet flaring were very close to the measured values, regardless of rivet hardness and ply material thickness. The details of each case are as follows:

<u>Condition 1</u>: The joints were produced by using 2.5 mm thick carbon steel strips as top and bottom sheet. An 8 mm rivet with a hardness of 555 HV was used to produce each joint. Five different joints were produced with the same specifications: a completed joint and four interrupted joints. Cross-sections and the force-displacement curves are shown in Fig. 5.10.3. It is obvious from Fig. 5.10.3 that for case I no flaring was observed. Geometrical factors identified for condition 1 are summarized in Table 5.10.2. The coefficient for rivet hardness C_1 = 0.43 and coefficient for rivet length C_2 = 0.9 were used and the value of rivet displacement before flaring was identified: d_0 = 5.85 mm. Good agreement was observed between calculated and measured flaring. An example of a calculation for condition 1, case II in Table 5.10.2 is shown below:

$$x = \frac{C_2*(d_{max}-d_0)*C_1*(\frac{D_d}{2}-R_r)}{\sqrt{(t_1+t_2+h-d_0)^2+(C_1*(\frac{D_d}{2}-R_r))^2}} = \frac{0.9*(6.35-5.85)*0.43*(\frac{10}{2}-2.75)}{\sqrt{(2.5+2.5+3-5.85)^2+(0.43*(\frac{10}{2}-2.75))^2}}$$

$= 0.2$

Table 5.10.2 Parameters of selected joints for interruption to conditions 1-4 (all values are in mm).

Condition	Case	Total rivet displacement (d_{max})	Calculated rivet flaring (x)	Measured rivet flaring (x_m)
1	I	5.11	0.00	0.00
	II	6.35	0.2	0.12
	III	6.71	0.34	0.34
	IV	7.22	0.55	0.54
2	I	3.91	0.00	0.00
	II	4.68	0.05	0.12
	III	5.71	0.38	0.35
3	I	4.03	0.00	0.00
	II	4.91	0.17	0.25
	III	5.69	0.47	0.50
4	I	3.82	0.00	0.00
	II	5.39	0.42	0.47
	III	6.94	1.06	1.09

Condition 2: In this condition, ply material thickness was reduced to 2 mm but the rivet hardness maintained at 555 HV. As the thickness of ply materials was reduced, the joints were interrupted at three different positions instead of four as for condition 1. Cross-sections and the force-displacement curves are shown in Fig. 5.10.4. The coefficient for rivet hardness (C_1 = 0.43) was maintained the same as that for condition 1 but the coefficient for rivet length C_2 = 0.67 was used because of the reduction of rivet length and the value of rivet displacement before flaring was identified: d_0 = 4.52 mm. Geometrical factors identified for condition 2 are summarized in Table 5.10.2. Again, good agreement was observed between calculated and measured flaring.

Condition 3: In this condition, ply material thickness and the die were kept the same as those for condition 2 but the hardness of rivet was reduced from 555 to 480 HV. Four different joints were produced: a completed joint and three interrupted joints. Cross-sections and the force-displacement curves are shown in Fig. 5.10.5. The coefficient for rivet length (C_2 = 0.67) was maintained the same as that for condition 2 but the coefficient for rivet hardness C_1 = 0.55 was used because of the reduction of rivet hardness and the value of rivet displacement before flaring was identified: d_0 = 4.44 mm. Geometrical factors identified for condition 3 are summarized in Table 5.10.2.

Condition 4: In this condition, ply material thickness and the die were kept the same as those for conditions 2 and 3 but the hardness of the rivet was further reduced to 410 HV. Again, four different joints were produced: a completed joint and three interrupted joints. Cross-sections and the force-displacement curves are shown in Fig. 5.10.6. Once more, the coefficient for rivet length (C_2 = 0.67) was maintained the same as that for conditions 2 and 3 but the coefficient for rivet hardness C_1 = 0.66 was used because of the reduction of rivet hardness and the value of rivet displacement before flaring was identified: d_0 = 4.35 mm. Geometrical factors identified for condition 4 are summarized in Table 5.10.2. Like the previous three conditions, good agreement was also observed between the calculated and measured flaring.

For the interrupted cases (conditions 1-4), it was observed that the calculated rivet flaring differed considerably from the measured value at the start of rivet flaring (case II in each condition). This difference was minimal for the other cases (case III and IV for condition 1 and case III for conditions 2-4).

5.10.4 Validation of rivet flaring model

After determining the coefficients C_1 and C_2 from the interrupted joints, equation (5.6) was also used to predict rivet flaring for completed joints. In this case, completed joints of conditions 1-4 have been considered and two more conditions were tested. Calculated and measured rivet flaring for completed joints of conditions 1-4 are summarised in Table 5.10.3. A total of three types of thicknesses of ply material and three different hardnesses of rivet were considered. It was found that the calculated values of rivet flaring were very close to the measured values, regardless of rivet hardness and ply material thickness. Case by case details are expressed below:

Condition 5: A 6 mm long 480 HV rivet was used to join two 1.5 mm carbon steel sheets. The cross-section and the force-displacement curve of this joint are shown in Fig. 5.10.2. The geometric factors for condition 5 were: t_1 = 1.5 mm, t_2 = 1.5 mm, h = 2.3 mm, D_d = 9 mm, R_r = 2.5 mm, d_0 = 4.29 mm and d_{max} = 5.71 mm. Coefficient for rivet hardness C_1 = 0.55 was used for the 480 HV rivet and coefficient for rivet length C_2 = 0.6 was used for the 6 mm long rivet. Calculated flaring was determined as x = 0.63 mm and the measured flaring was also found to be 0.66 mm.

Condition 6: Another joint was produced by using a 6 mm rivet of 410 HV and the top and bottom sheets were both 1.5 mm carbon steel, i.e., the same as condition 5 except for the rivet hardness. The cross-section and force-displacement curve of this joint are shown in Fig. 5.10.2. The geometric factors for condition 6 were determined as: t_1 = 1.5 mm, t_2 = 1.5 mm, h = 2.3 mm, D_d = 9 mm, R_r = 2.5 mm, d_0 = 4.21 mm and d_{max} = 5.97 mm. Coefficient for rivet hardness C_1 = 0.66 and coefficient for rivet length C_2 = 0.6 were used. The calculated flaring was determined as x = 0.82 mm and the measured flaring was found to be 0.82 mm.

It was found that the calculated rivet flaring using equation (5.6) was in good agreement with the measured rivet flaring for all completed joints, as summarised in Table 5.10.3. Calculated vs. measured rivet flaring data for conditions 1 to 6 are plotted in Fig. 5.10.9. Hence, this simple formula can successfully predict the rivet flaring without the need to cross-section a joint. The coefficients used in this formula are dependent only on rivet properties (hardness and length). The relationships between these coefficients and rivet properties are shown in Figs. 5.10.10 and 11. It should be noted that coefficient C_1 is valid for a range of rivet hardnesses from 410 HV to 555 HV and coefficient C_2 is valid for a range of rivet lengths from 6 mm to 8 mm, which represent the range of data used to generate the formula for the conditions examined in the present study.

Table 5.10.3 Parameters of completed joints (all values are in mm, except the two coefficients).

Condition	Coefficient for rivet hardness (C_1)	Coefficient for rivet length (C_2)	Rivet displacement before flaring (d_0)	Total rivet displacement (d_{max})	Calculated rivet flaring (x)	Measured rivet flaring (x_m)
1	0.43	0.90	5.85	8.00	0.86	0.88
2	0.43	0.67	4.52	6.95	0.78	0.78
3	0.55	0.67	4.44	7.17	1.02	1.03
4	0.66	0.67	4.35	7.28	1.20	1.20
5	0.55	0.60	4.29	5.71	0.63	0.66
6	0.66	0.60	4.21	5.97	0.82	0.82

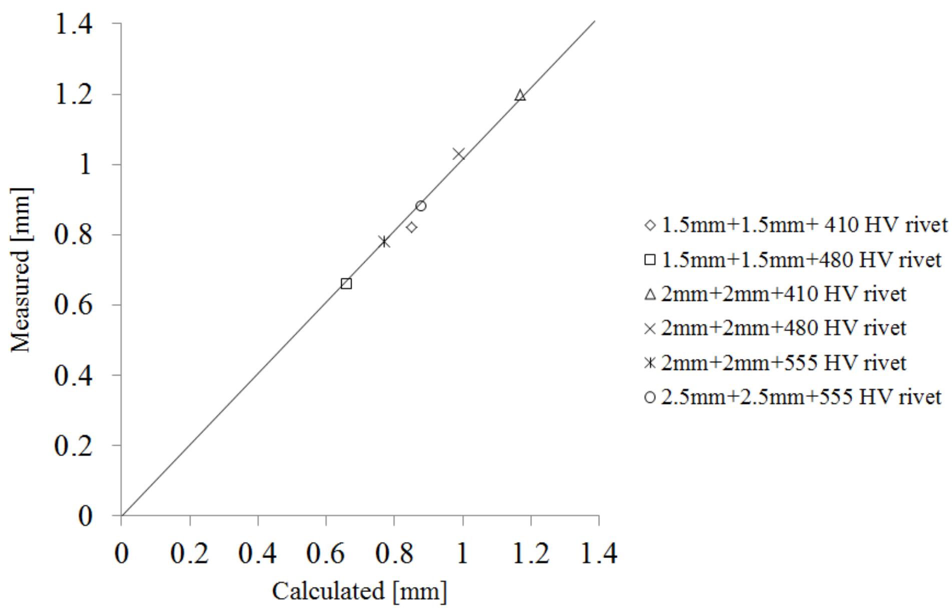

Fig. 5.10.9 Rivet flaring calculated vs. measured for six different conditions in Table 5.10.1.

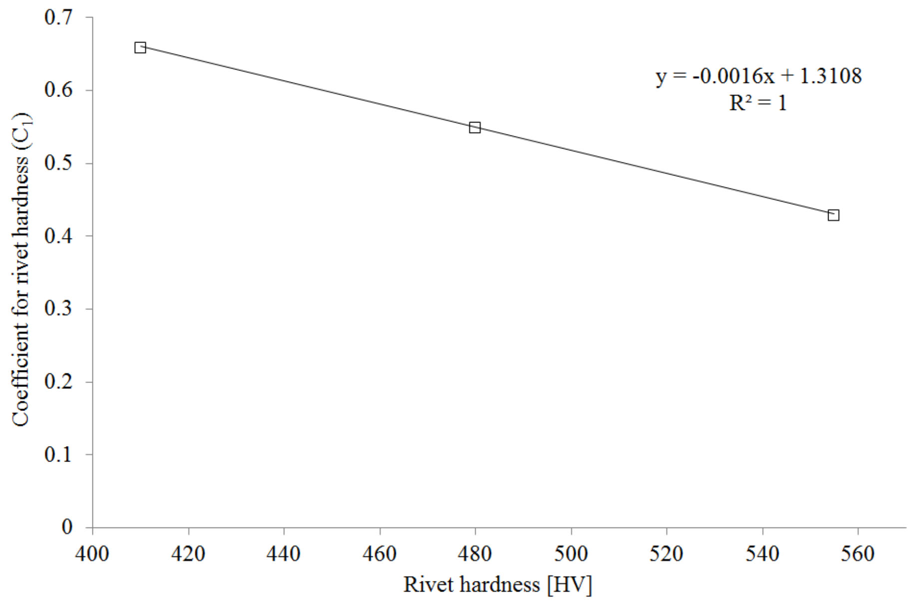

Fig. 5.10.10 Relationship between coefficient C_1 and rivet hardness.

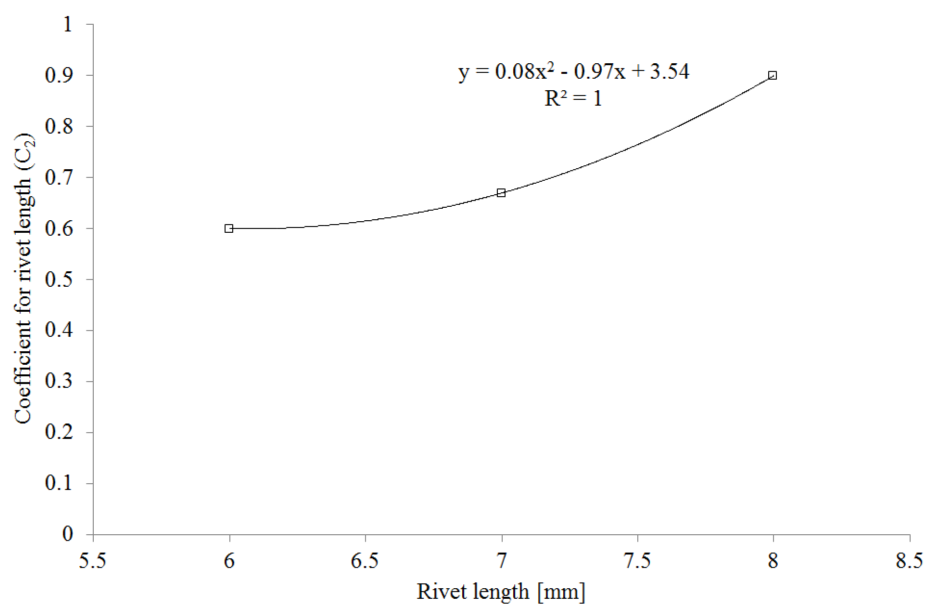

Fig. 5.10.11 Relationship between coefficient C_2 and rivet length.

Due to manufacturing conditions, rivet hardness may vary slightly. This would ultimately affect the rivet hardness coefficient C_1. Assuming a change in rivet hardness of ± 30 HV, the rivet hardness coefficients for the above three rivet hardnesses are summarized in Table 5.10.4. Measured and calculated rivet flaring data are summarized in Table 5.10.5. It is observed that for a change in rivet hardness of ± 30 HV, the above formula still gives a good agreement between the calculated and measured rivet flaring. This means that C_1 is not significantly affected by rivet-to-rivet hardness variation that is likely to occur on a production line. While rivet hardness may vary, in practice, the length of the rivet does not vary much. Hence, no study is included in this thesis about the uncertainties involved in the coefficient for rivet length (C_2).

Table 5.10.4 Coefficient for rivet hardness, C1, obtained by using the formula shown in Fig. 5.10.10.

Rivet hardness (HV)	410 ± 30		480 ± 30		555 ± 30	
Coefficient for rivet hardness (C_1)	380	440	450	510	525	585
	0.71	0.62	0.60	0.50	0.48	0.38

Table 5.10.5 Rivet flaring for the different conditions stated in Table 5.10.1.

Condition	1		2		3		4		5		6	
Coefficient for rivet hardness (C_1)	Max	Min	Max	Min	Max	Min	Max	Min	Max	Min	Max	Min
	0.48	0.38	0.48	0.38	0.60	0.50	0.71	0.62	0.60	0.50	0.71	0.62
Calculated rivet flaring (mm)	Max	Min	Max	Min	Max	Min	Max	Min	Max	Min	Max	Min
	0.94	0.78	0.84	0.70	1.07	0.95	1.25	1.15	0.71	0.66	0.90	0.86
Measured rivet flaring (mm)	0.88		0.78		1.03		1.20		0.66		0.82	

5.10.5 Extended validation of rivet flaring model

After successful prediction of rivet flaring for the above six conditions, equation (5.6) was also used to predict rivet flaring for completed joints to extend its validity for change in process parameters such as sheet materials properties, die depth, rivet setting pressure etc. In order to do so, 8 more conditions were chosen according to Table 5.10.6. The cross-sections and force-displacement curves of these joints are shown in Fig. 5.10.12. It was found that the calculated rivet flaring using equation (5.6) was in good agreement with the measured rivet flaring for all completed joints, as summarised in Table 5.10.7. Calculated vs. measured rivet flaring data for conditions 7 to 14 are plotted in Fig. 5.10.13. Hence, this simple formula can successfully predict the rivet flaring without the need to cross-section a joint.

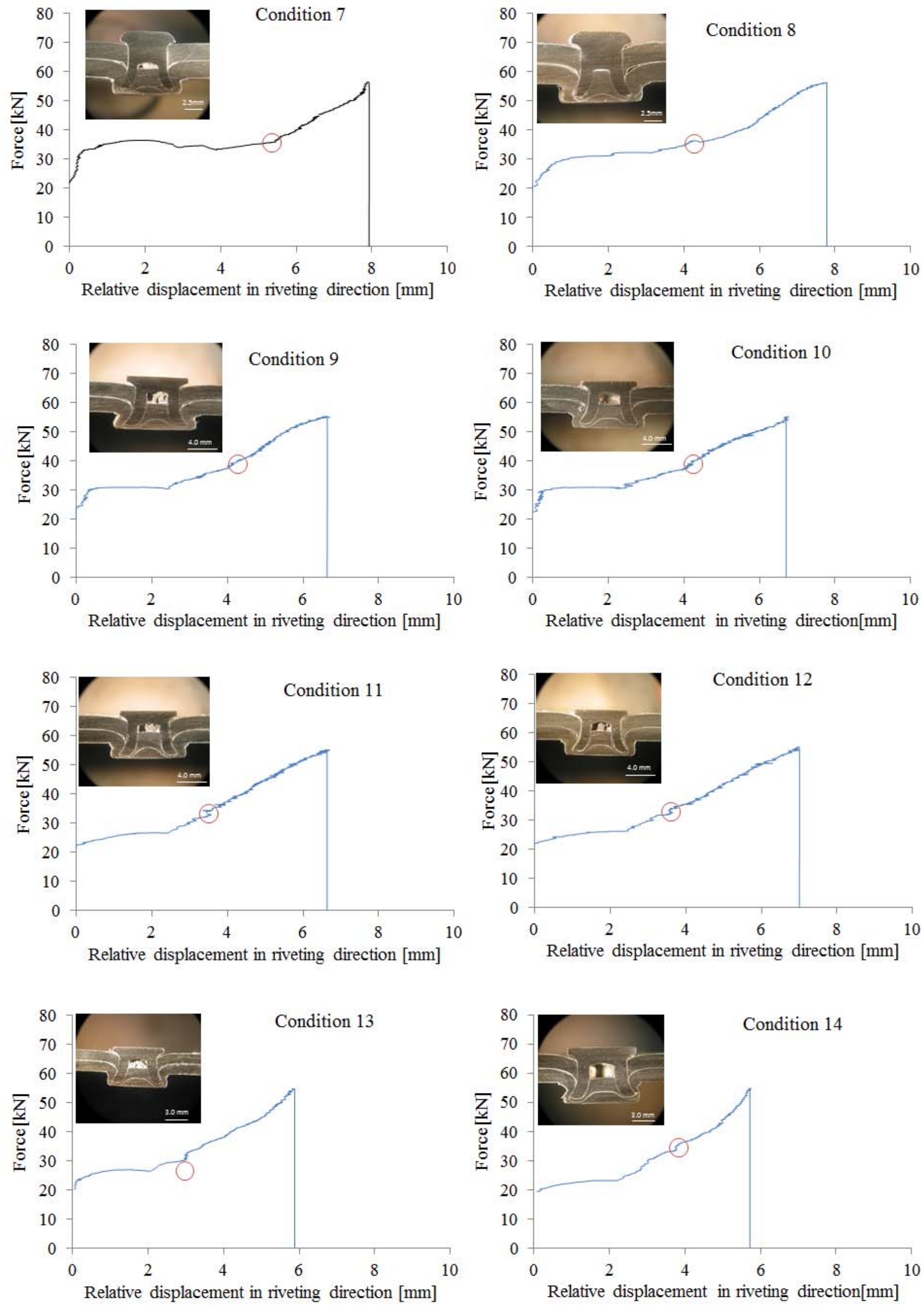

Fig. 5.10.12 Step rise of force for eight different conditions (listed in Table 5.10.6); the photograph in each graph depicts the cross-section of the completed SPR joint.

Table 5.10.6 Joining parameters (pre-clamp and rivet setting pressure were 125 and 250 bar, respectively).

Condition	Materials	Thicknesses of ply materials (mm)	Rivet		Die (flat die profile)	
			Length (mm)	Hardness (HV)	Depth (mm)	Diameter (mm)
7	G450 steel	2.5 +2.5	8	555	2.35	11
8	G300 steel	2.5 +2.5	8	555	2.35	11
9	G450 steel	2.0 +2.0	7	555	2.10	10
10	G450 steel	2.0 +2.0	7	480	2.10	10
11	G300 steel	2.0 +2.0	7	555	2.10	10
12	G300 steel	2.0 +2.0	7	480	2.10	10
13	G450 steel	1.5 +1.5	6	480	2.00	09
14	G300 steel	1.5 +1.5	6	480	2.00	09

Table 5.10.7 Parameters of completed joints (all values are in mm, except the two coefficients).

Condition	Coefficient for rivet hardness (C_1)	Coefficient for rivet length (C_2)	Rivet displacement before flaring (d_0)	Total rivet displacement (d_{max})	Calculated rivet flaring (x)	Measured rivet flaring (x_m)
7	0.43	0.90	5.22	7.95	1.19	1.08
8	0.43	0.90	4.40	7.80	1.13	1.05
9	0.43	0.67	4.10	6.60	0.79	1.02
10	0.66	0.67	4.00	6.70	1.11	1.11
11	0.43	0.67	3.60	6.65	0.80	1.01
12	0.66	0.67	3.50	7.00	1.25	1.11
13	0.66	0.60	3.10	5.90	0.95	0.95
14	0.66	0.60	3.00	5.85	0.90	0.90

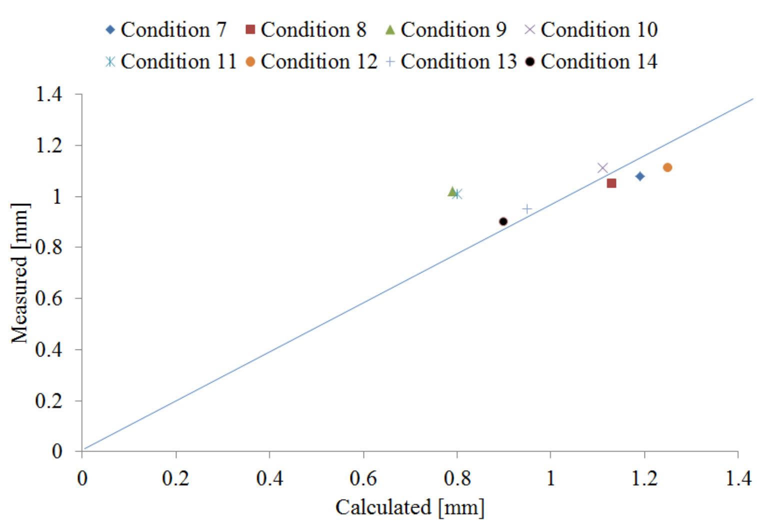

Fig. 5.10.13 Rivet flaring calculated vs. measured for eight different conditions listed in Table 5.10.6.

This chapter presents a simple geometrical method to calculate rivet flaring without the need to cross-section a joint. It is a non-destructive testing method of determining rivet flaring based on the characteristic force-displacement curve. A relationship was established based on ply thickness, nominal die and rivet dimensions, and relative punch displacements at the start and end of rivet flaring as determined by the characteristic force-displacement curve. Equation (5.6) works for a range of materials. Two coefficients were determined empirically as functions of rivet hardness and length. It is believed that coefficient C_1 could be determined experimentally by characterizing the rivet material, which ultimately leads to the design of new high strength rivets.

Equation (5.6) could be improved by considering the path of the rivet tip OE as a parabola rather than a straight line. Considering the simple nature of this equation, reasonably good agreement was achieved between the calculated and measured rivet flaring for interrupted cases. From an industrial viewpoint, interrupted joints are of no interest. Equation (5.6) gives a very good result to determine rivet flaring for a completed joint.

The rivet flaring calculator can be used to improve and optimize an SPR joint for a given material and thickness combination. In practice, it is very easy to pick up the displacement (d_{max}-d_0) and for an operator to decide whether the joint is good or bad in terms of rivet flaring. However, the quality of a SPR joint does not depend solely on rivet flaring; it depends on other factors such as: flaring angle, effective contact length between rivet and tail side material. Some of the factors could be found from the characteristic force-displacement curve. Since rivet flaring is a dominant factor in determining the strength of a SPR joint, the rivet flaring estimator developed in this study could be a very important tool in industrial practice.

5.11 Summary

This chapter has mainly focussed on understanding the physical events involved in the formation of self-pierce riveting joints by characterizing and relating the force-displacement curve to the joint's structure. To do this, the C-frame deflection has been subtracted from the force-displacement curve.

Four stages have been defined and a detailed description of each stage of the force-displacement curve has been provided. A systematic study on the characterization of the SPR process using force-displacement curves has been carried out by interrupting the formation of SPR joints at different rivet positions. Each part of the curve represents a distinctive event in the process. The understanding and knowledge gained from this study could be used for monitoring the industrial SPR process. The following conclusions have been drawn within the range of process parameters studied in this report:

1. C-frame deflection occurs at all stages of the SPR process.
2. The length of the first stage of the characteristic curve decreases with increasing sheet thickness and hardness, and rivet hardness.
3. The force developed in the first stage of the curve is high for a thick and hard joint, due to the increased rigidity of the stack, but the force is not affected by the rivet hardness.
4. The displacement experienced during the second stage depends mainly on the thickness of the top sheet. Other parameters have little influence on this stage.
5. The drop in force just after the completion of piercing of the top sheet is clearly seen when hard or thick material is used as the top sheet, but is not easily detected for thin material.
6. Die geometry significantly changes the third stage of the characteristic curve, with the length of this stage increasing with an increase in die volume. The start of stage III is also affected by die depth, a deeper die delays the starts of stage III. Sometimes a crack also developed especially for less ductile material when a die is too deep. Rivet hardness also influences this stage: the harder the rivet, the longer is this step.

7. The fourth stage of the curve gives an in-sight about the flaring of a rivet inside a joint. A longer fourth stage indicates more flaring and hence a better interlocked joint. An increase in rivet hardness would shorten this stage and reduce the amount of flaring.
8. The maximum force and displacement depends on the joint stack-up design, rivet hardness and length, die recess volume and the total deformed volume of the materials inside the cavity. The total displacement would increase with an increase in ply material thickness and would decrease with a hard rivet.
9. Two key point events of the force-displacement curves were identified, d_0 and d_{max} for start and end of rivet flaring respectively which leads to the development of the rivet flaring model. In practice, it is very easy to pick up the displacement (d_{max}-d_0) and for an operator to determine whether the joint is good or bad in terms of rivet flaring. Two empirical coefficients were defined depending on the rivet hardness and length. No coefficient was considered for the sheet material properties because the material properties are embedded in the force-displacement curve. The developed rivet flaring equation works very well within the range of process parameters studied. This tool is very useful in industrial practice in the preliminary identification of the quality of a joint.

6 RESIDUAL STRESS

Several events occur in the SPR process: a tubular rivet is driven through the top sheet, piercing but not perforating the bottom sheet, accompanied by flaring of the legs in the bottom sheet under the guidance of a suitable die [1]. Rivet as well as sheet materials should have sufficient ductility to deform without cracking. As ply materials increase in hardness, strength or thickness, the ability of a rivet to pierce and deform in a ductile manner becomes more limited, narrowing the operating window in terms of joint quality and performance. Forces for setting the rivet are high, typically 30 to 50 kN. Previous studies [53, 57] have shown that a joint may look good, but micro-computed tomography (CT) confirmed cracking in the same joint. To fully understand the behaviour of SPR joints, it is important to determine how residual stress distribution arises from a riveting process. Residual stresses as high as 1075 MPa have been modelled by Khezri and co-authors [124, 125] but not validated because of a lack of experimental techniques to evaluate these stresses.

The challenges involved with residual stress in SPR, general effects of residual stress on structures are discussed and different techniques for measuring residual stress are discussed in chapter 3. For SPR joints made of high strength steel materials, neutron diffraction is the most appropriate technique among the non-destructive methods.

The purpose of the present study is to evaluate the feasibility of evaluating residual stress in different SPR joints using neutron diffraction at the first stage then optimizing parameters for making meaningful measurements. The present study also discusses residual stress distribution in different SPR joints depending on different joining parameters (ply material's thickness and hardness, rivet hardness, die geometry).

6.1 Feasibility of evaluating residual stress

The feasibility of evaluating residual stress in Self Pierce Riveted (SPR) joints using the neutron diffraction technique was investigated in this study. The main challenge involved dealing with the very small dimensions of SPR joints. Two different joints were examined: aluminium-steel and steel-steel joints. At first, sheet specimens of aluminium and steel were first chosen to ensure that all the diffracted peaks could be determined easily from either the rivet or the bottom sheet, as the diffraction angles for steel and aluminium are different. A riveted joint specimen was produced, as shown in Fig. 4.9.6a (Chapter 4.9), using sheet specimens 150 mm long by 50 mm wide and 5.1 mm thick (3.1 mm aluminium and 2.0 mm steel as top and bottom sheet respectively). Another joint (steel with steel) was produced by keeping the specimen size the same. However, the thickness was reduced to 4.0 mm (2.0 mm carbon steel as top and bottom sheet) by replacing the top aluminium sheet with a 2.0 mm steel sheet (Fig. 4.9.7a). Force and displacement were measured and it was observed that for both conditions all five joints showed high reproducibility during the riveting operation (Fig. 4.9.8). The detailed experimental procedure was explained in chapter 4.9.1. The joint parameters for the purpose of a feasibility test are given in Table 6.1.1. A journal paper on the feasibility test of residual stress evaluation on SPR joints by neutron diffraction from this work was published by the present author [240].

Table 6.1.1 Parameters of selected joints for the feasibility test.

Joint no.	**Total ply thickness**	**Top sheet**	**Bottom sheet**	**Rivet part number** [92]	**Rivet length**	**Rivet shank diameter**	**Steel Rivet hardness**	**Die part number** [119]
68	5.1 mm	3.1 mm Al 6060	2.0 mm G300 steel	PG084 2	8 mm	5 mm	410 Hv	DF1004 3003
78	4 mm	2.0 mm G300 steel	2.0 mm G300 steel	HG074 2	7 mm	5 mm	410 Hv	DF1004 2503

Neutron diffraction measurements were performed on the Strain Scanner named 'Kowari' on the OPAL reactor at the Australian Nuclear Science and Technology

Organisation (ANSTO). A schematic setup of the diffraction experiment is shown in Fig. 4.9.1. As the investigated joint specimen was small, a nominal gauge volume of 0.5x0.5x0.5 mm^3 was used, which is the smallest gauge volume that gave the best compromise between spatial resolution and experimental counting time.

In the first experiment, strain measurements were made along the lines AA, BB and CC, which were at depths of 1 mm, 1.5 mm and 2 mm, respectively, from the surface of the rivet head (Fig. 6.1.1). Strain was also measured along line DD, which was 1 mm up from the un-deformed bottom sheet surface to obtain the behaviour of stress in the steel sheet, and along line EE, which was 2 mm up from the tail (die side) of the joint to obtain the behaviour of material inside the die, as shown in Fig. 6.1.1. The positions of the measurement points taken along those lines and relative to the joint centreline are summarized in Table 6.1.2. It may be noted that all the measurement points along lines AA, BB and CC were within the rivet head, whereas points located at 3 mm and -3 mm on line DD and at 3.5 mm and – 3.5 mm on line EE were within the rivet leg and the rest were located in the steel sheet. A total of 59 points were identified for strain measurement.

The rivets are produced by forging and heat treating to the required hardness level, so residual stress may exist in a new un-used rivet. Therefore, a user reference lattice, d_r, was used instead of the so-called strain free (d_0) reference lattice for the calculation of micro-strain. For the rivet material, d_r was determined from the head of a new unused rivet, and for the steel sheet the reference point was taken at 1 mm from the free corner of a new sheet.

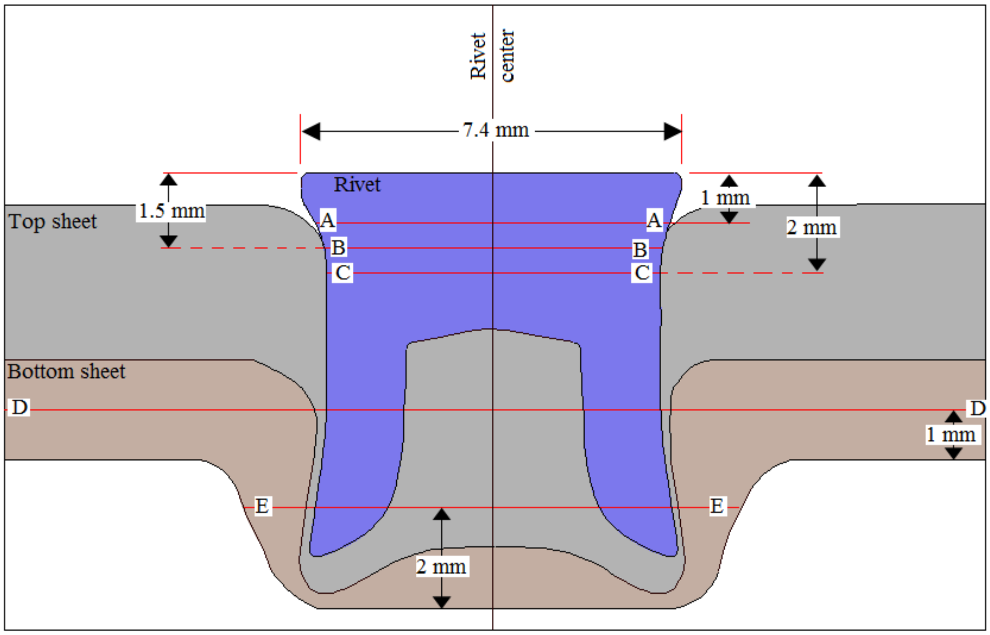

Fig. 6.1.1 Measurement lines for residual stress evaluation in a joint of 3.1 mm Al 6060 + 2.0 mm G300 steel.

Table 6.1.2 Measurement points along lines AA, BB, CC, DD and EE shown in Fig. 6.1.1.

Line	AA, BB and CC	DD	EE
Measurement points (mm) from rivet center shown in Fig. 6.1.1	-3, -2.5, -2, -1.5, -1, -0.5, 0, 0.5, 1, 1.5, 2, 2.5, 3	-9, -7.5, -6, -4.5, -3, 3, 4.5, 6, 7.5, 9	-4, -3.5, -3, -2.5, -2, 2, 2.5, 3, 3.5, 4
Total number of points	13*3 = 39	10	10

Transverse, normal and longitudinal components of micro-strain along the line AA are shown in Fig. 6.1.2. Measurements in six directions of a point are necessary to define the strain tensors completely. Since the principal directions coincide with the coordinate measurement directions, the stress then can be calculated using the following formulae with corresponding expressions for σ_x, σ_y and σ_z in terms of ϵ_x, ϵ_y and ϵ_z [241, 242]:

$$\sigma_x = \frac{E}{(1+\vartheta)(1-2*\vartheta)}\left[(1-\vartheta)*\epsilon_x + \vartheta\left(\epsilon_y + \epsilon_z\right)\right] \tag{6.1}$$

$$\sigma_y = \frac{E}{(1+\vartheta)(1-2*\vartheta)}\left[(1-\vartheta)*\epsilon_y + \vartheta(\epsilon_z + \epsilon_x)\right] \tag{6.2}$$

$$\sigma_z = \frac{E}{(1+\vartheta)(1-2*\vartheta)}\left[(1-\vartheta)*\epsilon_z + \vartheta\left(\epsilon_x + \epsilon_y\right)\right] \tag{6.3}$$

where the diffraction elastic constants are E (elastic modulus with a value of 220 GPa) and ϑ (Poisson's ratio for steel having a value of 0.3).

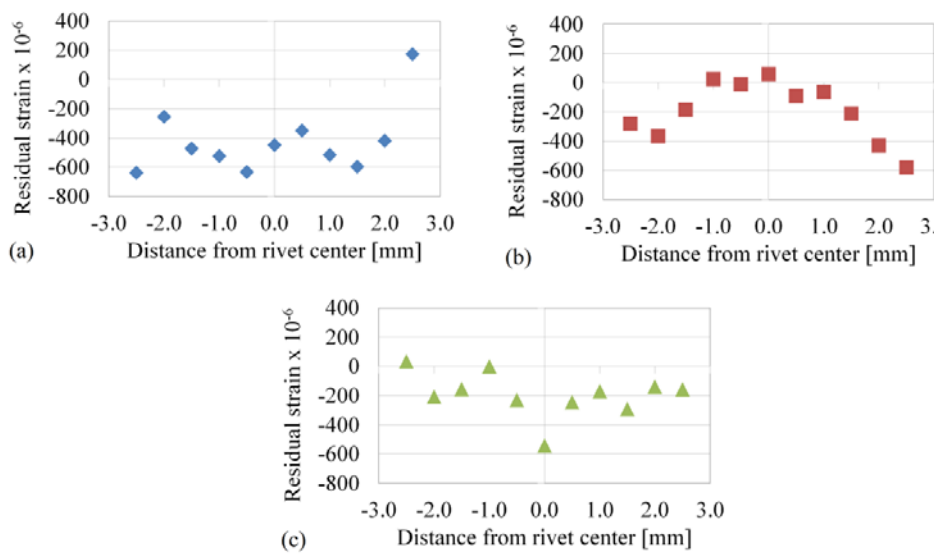

Fig. 6.1.2 Strain profiles along line AA shown in Fig. 6.1.5 (a) transverse (b) normal (c) longitudinal.

In the second experiment, strain measurements were made along lines FF and GG, which were 1 mm and 1.5 mm below the surface of the rivet head (Fig. 6.1.3). Strain was also measured along line HH, which was 1 mm down from the un-deformed top sheet surface, along lines II and JJ, which were 1.5 mm and 1 mm up from the un-deformed bottom sheet surface respectively, and along line KK, which was 1.5 mm up from the tail (die side) of the joint, as shown in Fig. 6.1.3.

The positions of the measurement points taken along those lines and relative to the joint centreline are summarized in Table 6.1.3. It may be noted that all the measurement points along lines FF and GG were within the rivet head, whereas points located at 3.5 mm and -3.5 mm on lines II and KK were within the rivet leg. A total of 69 points were identified for strain measurement. The same procedure was followed for the strain-free lattice reference.

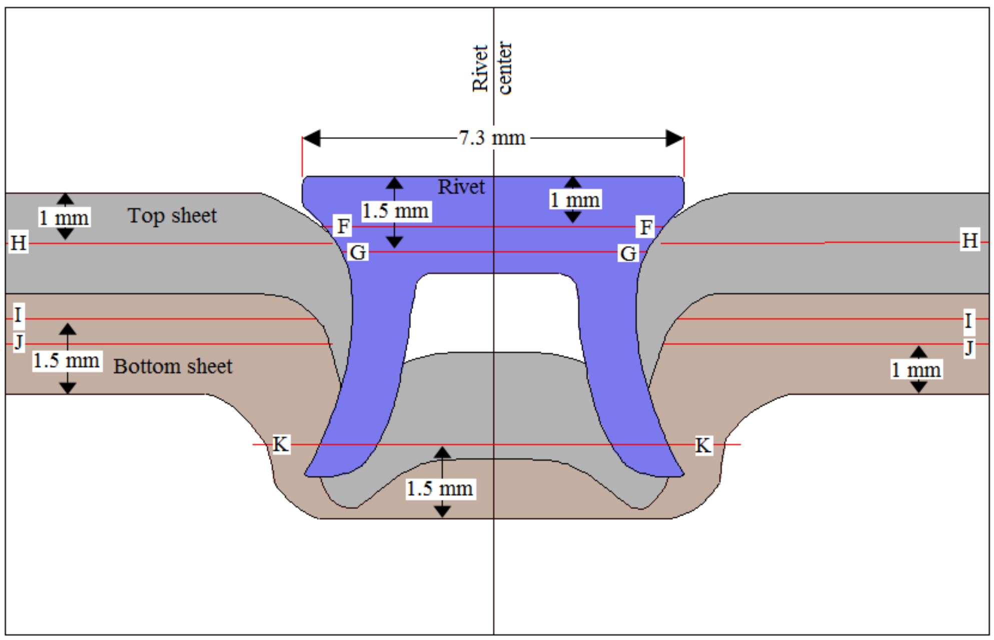

Fig. 6.1.3 Measurement lines for residual stress in a joint of 2.0 mm G300 steel + 2.0 mm G300 steel.

Table 6.1.3 Measurement points along lines FF, GG, HH, II, JJ and KK shown in Fig. 6.1.3.

Line	FF and GG	HH	II	JJ	KK
Measurement points (mm) from rivet centre shown in Fig. 6.1.3	-3, -2.5, -2, -1.5, -1, -0.5, 0, 0.5, 1, 1.5, 2, 2.5, 3	-10, -8.5, -7, -5.5, -4, 4, 5.5, 7, 8.5, 10	-4.5, -3.5, -2.5, -1.5, 1.5, 2.5, 3.5, 4.5	-10, -8.5, -7.0, -5.5, -4.0, -2.5, 2.5, 4.0, 5.5, 7.0, 8.5, 10	-4.0, -3.5, -3.0, -2.5, -2.0,-1.0, 0, 1.0, 2.0, 2.5, 3.0, 3.5, 4.0
Total number of points	13*2 = 26	10	8	12	13

6.1.1 Aluminium-steel joint

The stress components in the rivet head of the aluminium-steel joint are shown in Fig. 6.1.4 (a-c). For the points situated at 3 mm and -3 mm from the rivet axis on lines AA, BB and CC, no diffraction peak was observed, which means that those points were outside the rivet head and situated in the surrounding aluminium sheet. This indicates that a rivet inside a joint can be detected by neutron diffraction. Hence 11 points were considered for stress calculation, excluding the two extreme points at 3 mm and -3 mm on each of the lines AA, BB and CC (Fig. 6.1.1). It was noted with 95% confidence that the uncertainty of calculated stresses was ± 109 MPa. Uncertainty increases as the gauge volume decreases, but the uncertainty could be minimized by increasing the detection time or by using high intensity neutrons. Despite the small dimensions involved here, meaningful results were obtained in this experiment.

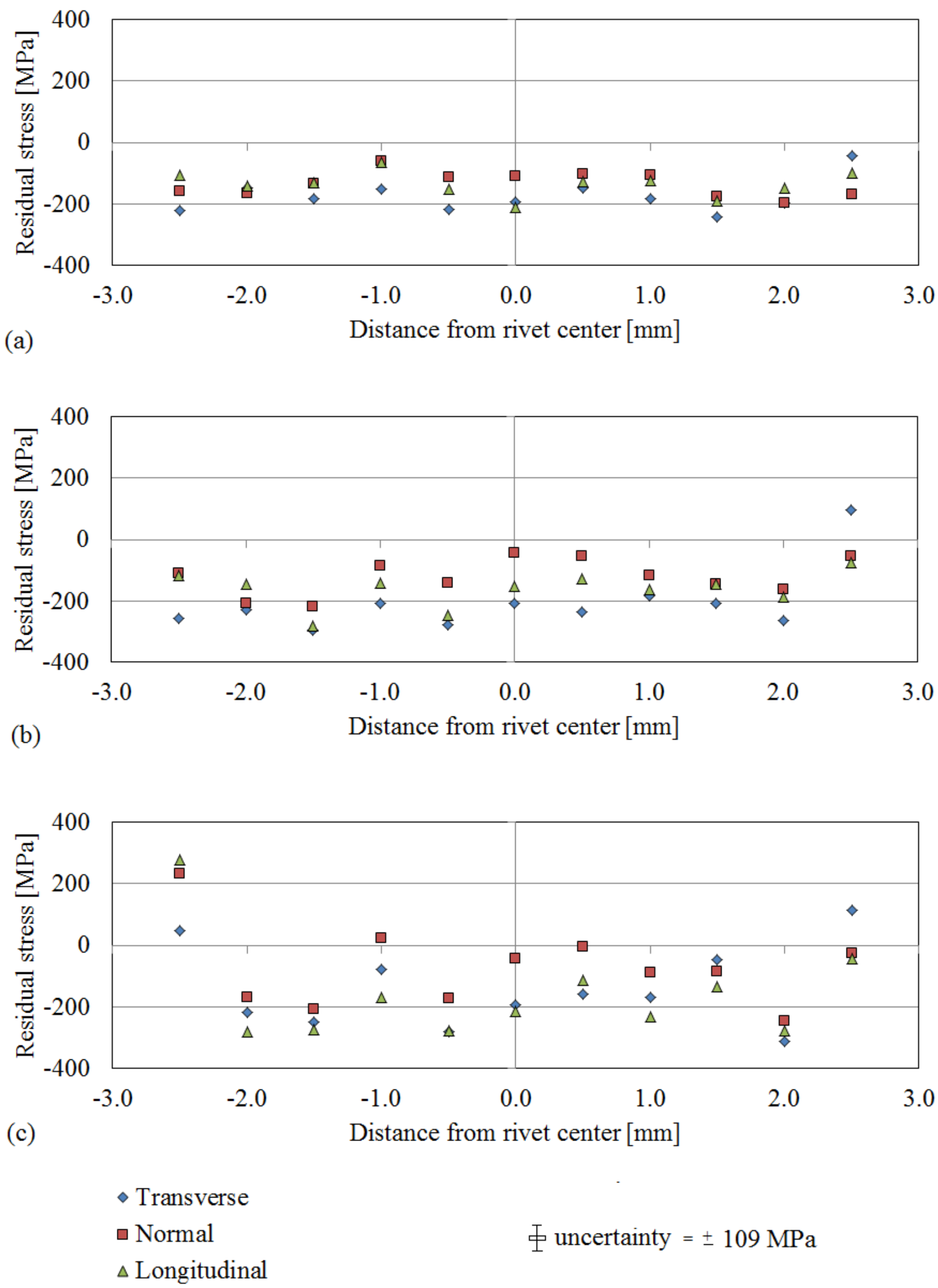

Fig. 6.1.4 Residual stress profiles in the rivet head along lines (a) AA (b) BB (c) CC corresponding to the lines shown in Fig.6.1.1.

It is evident from Fig. 6.1.4 that a compressive residual stress had developed in the rivet head of the aluminium-steel joint. Generally, a normal residual stress near the surface is close to zero. The compressive residual stress on line CC is lower in the normal direction as it is nearer to the inner surface (Fig. 6.1.4c). A tensile trend in the stress profile was found 2.5 mm from the rivet centre. Given that the elastic residual stresses must be balanced, this implies that there could potentially exist a large tensile stress close to the side wall of the rivet head. This pattern of residual tensile stress is in agreement with published modelling data [124]. However, the magnitude of the residual stress depends on the joint parameters, such as rivet hardness and sheet material properties and it would be beneficial to verify the magnitude of the stresses either by simulation or by an alternative test such as synchrotron X-rays or contour methods. The value of the normal stress on line BB (average = -120 ± 60 MPa) falls between that for line AA (average = -136 ± 41 MPa) and line CC (average = -70 ± 120 MPa). The maximum compressive stress in the rivet head was -300 ± 93 MPa, found 1.5 mm from the rivet axis on line BB in the transverse direction (Fig. 6.1.4b).

The stress components in the rivet leg and inside the steel sheet material are shown in Fig. 6.1.5. A substantial change in the magnitude of residual stress 3 mm and -3 mm from the rivet centre on line DD (Fig. 6.1.5a) confirms that these points fell within the rivet leg. The stress was compressive in nature and evaluated to be 550 ± 89 MPa.

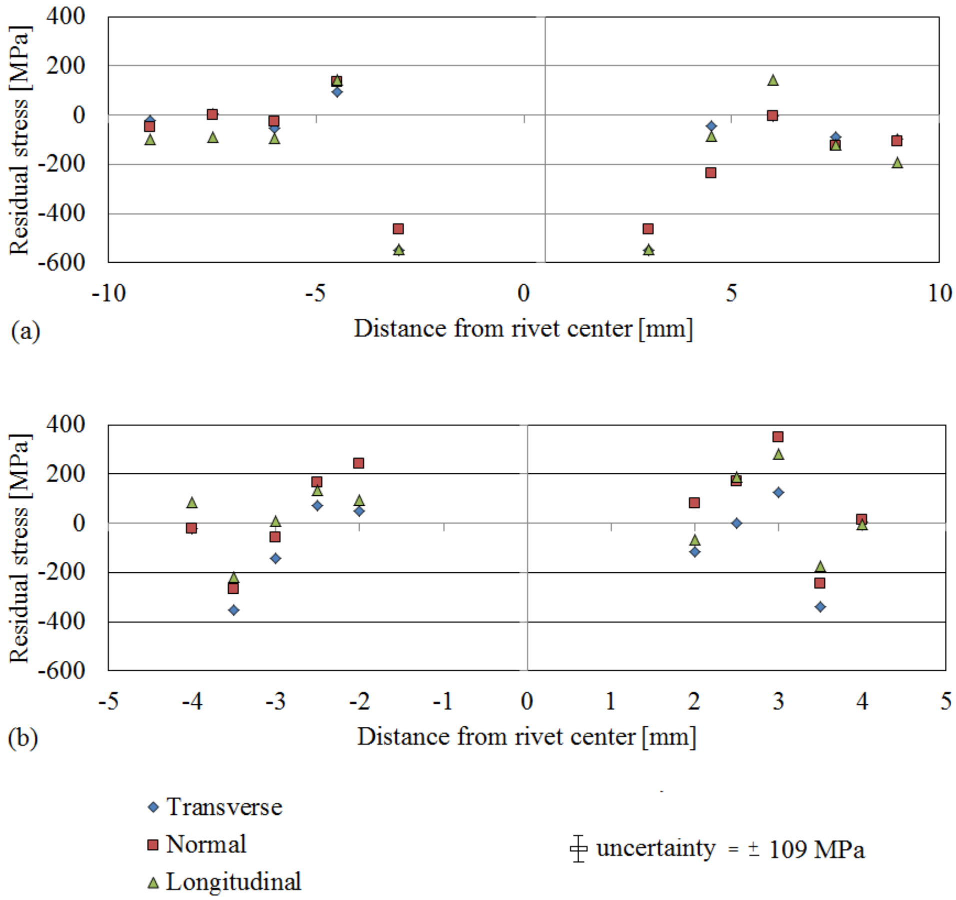

Fig. 6.1.5 Residual stress profiles in rivet legs and surrounding sheet material along lines (a) DD (b) EE corresponding to the lines shown in Fig. 6.1.1.

The stress that developed near the rivet wall was near zero, which is in agreement with the nature of stress balance. The residual stresses that developed 7.5 mm from the rivet centre, which is three times the rivet radius from the rivet axis, were not significant. The tensile stress developed on line DD was related to the surrounding sheet material flowing towards the die. Residual stress evaluated along line EE provides information on the behaviour of the material inside the die (Fig. 6.1.5b). During the riveting operation, as soon as the rivet started flaring, it pushed the bottom sheet toward the die cavity, triggering plastic deformation of the bottom sheet, putting the material in tension during this operation. A tensile condition is observed in this part of the material. On the other hand, at 3.5 mm and – 3.5 mm away from the rivet axis along line EE, a compressive stress of 350 ± 78 MPa was observed, confirming that these points fell within the rivet leg. The sheet material around this point could not move any further due to the restriction from the die, and all the surrounding material enclosed the rivet leg compressively. This is the reason why a compressive stress developed in the rivet leg in this region. It may be noted that the transverse stress near the wall of the rivet leg was close to zero, as expected.

6.1.2 Steel-steel joint

The stress components in the rivet head for the steel-steel joint are shown in Fig. 6.1.6 (a-b) and the stress components in the steel sheet and rivet leg are shown in Fig. 6.1.7 (a-d). A tensile trend of residual stress in the middle of the rivet head was observed for the steel-steel joint, whereas for the aluminium-steel joint the trend was completely compressive. This was due to the indication of a gap under the rivet head (Fig. 4.9.7b). The tensile stress was evaluated to be 300 ± 87 MPa in the middle of the rivet head and the compressive stress reached to -300 ± 69 MPa near the wall of the rivet head. It may be noted that, unlike the aluminium-steel specimen, at 3 mm and -3 mm apart from the rivet axis a diffraction peak was observed for the steel-steel specimen. So it is evident that this diffraction peak comes from the steel sheet. However, the stress values appeared to be too high on line FF (Figs. 6.1.3 and 6.1.6a): this high value of stress might be a result of a combined stress from both rivet head and sheet material. On line GG (Figs. 6.1.3 and 6.1.6b) at 3 mm and -3 mm from the rivet axis, a tensile stress was observed as expected: this is an indication of elongation of sheet material and it flows towards the rivet bore. An equivalent stress comparison, shown in Fig.6.1.8 revealed that the stress in the rivet head was higher for the steel-steel specimen (270 ± 93 MPa), than for the aluminium-steel specimen (160 ± 81 MPa). This means that as the hardness of the ply material increases, the residual stress would increase. It is believed that as the hardness of the ply material increases, residual stress would increase up to a certain limit for a given rivet. Further increase in hardness of the ply material for a given rivet may result in zero residual stress, which would indicate a crack has developed in the rivet inside a joint. Residual stress components on the line HH, which is situated 1 mm below the un-deformed surface of the top sheet, are not significant within the limit of uncertainty and in comparison with the yield strength of material; the values are of the order of 100 MPa (30% of the yield strength of material).

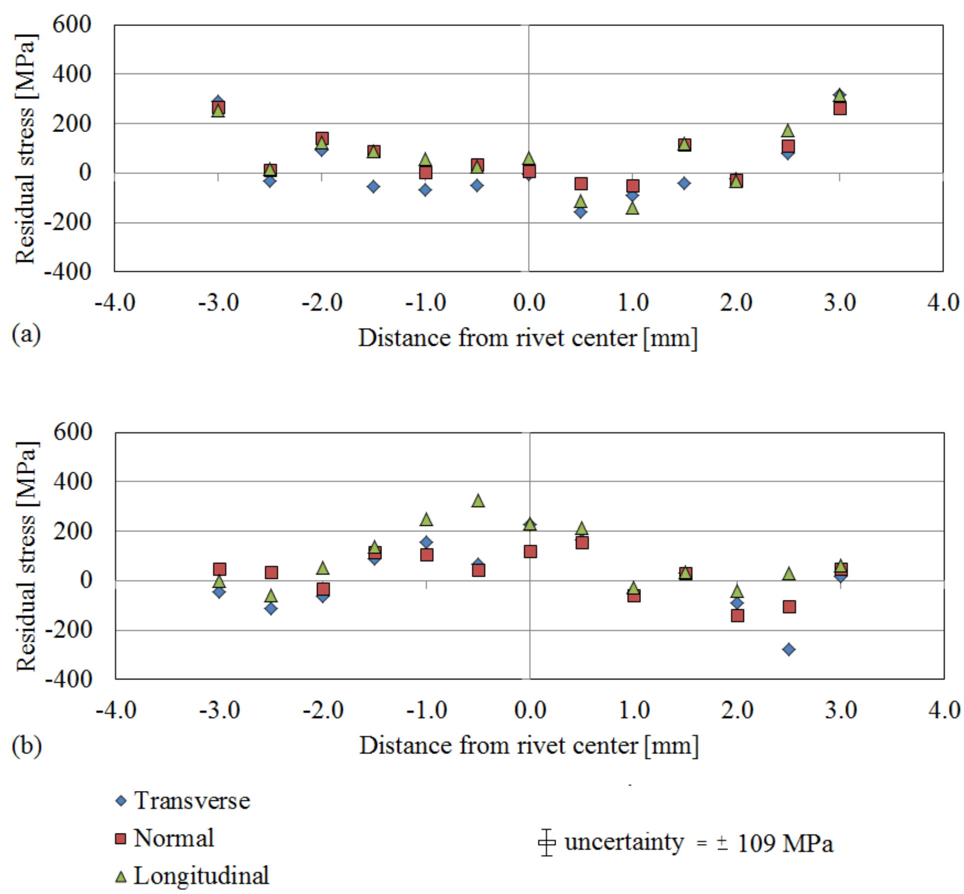

Fig. 6.1.6 Residual stress profiles in the rivet head along lines (a) FF and (b) GG corresponding to the lines shown in Fig. 6.1.3.

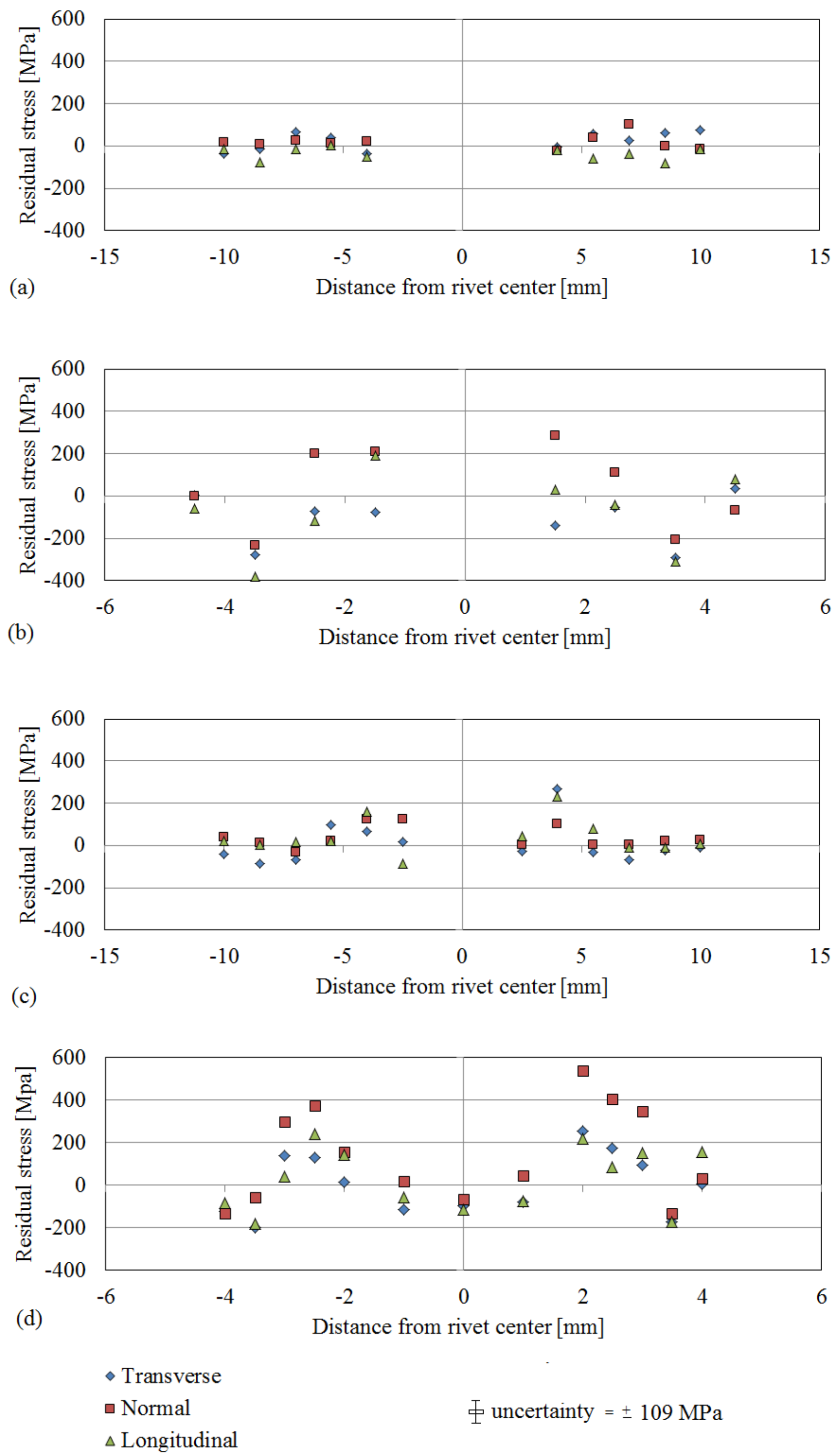

Fig. 6.1.7 Residual stress profiles in the rivet head along lines (a) HH and (b) II (c) JJ (d) KK corresponding to the lines shown in Fig. 6.1.3.

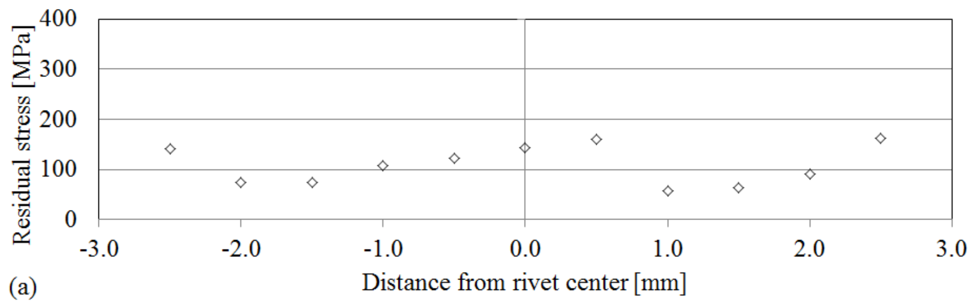

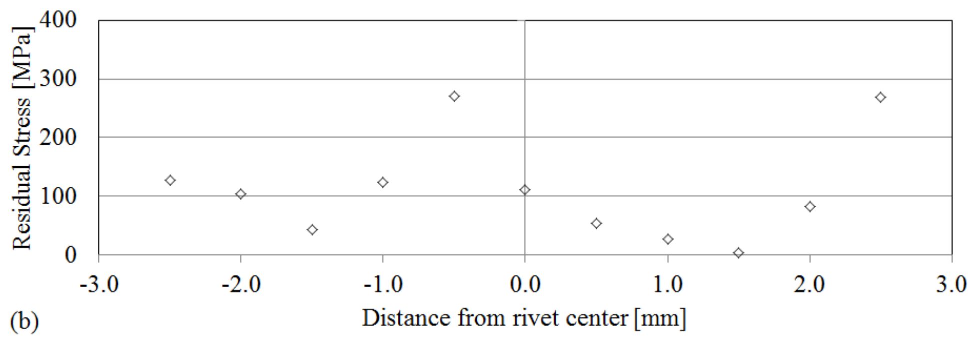

Fig. 6.1.8 Equivalent stress comparison 1.5 mm deep in the rivet head (a) line BB corresponding to Fig.6.1.5 in the aluminium-steel joint (b) line GG corresponding to Fig. 6.1.3 in the steel-steel joint.

A significant big change in the magnitude of residual stress was observed at points 3.5 mm and -3.5 mm on line II from the rivet centre, which confirms that these points were situated in the rivet leg (Fig. 6.1.7b). Other points on this line, such as 1.5, -1.5, 2.5 and -2.5 mm from the rivet centre, are situated inside the gap under the rivet head (Fig. 4.9.7b). The values corresponding to those points may come from the inside wall of the rivet. By observing the raw data it was found that the intensity was low at those points. Residual stress at points 4 mm and -4 mm from the rivet centre on II is a combined stress from different materials.

The information on the behaviour of residual stress in the steel sheet on the die side was found from the evaluations on the line JJ. It can be seen from Fig. 6.1.7c that the stress developed near the rivet wall was near zero, which is in agreement with the nature of stress balance. The equivalent stress profile on line JJ follows the same trend as the stress profile found on line DD (Fig. 6.1.9) since both lines were situated 1 mm up from the un-deformed tail surface and in the middle of the bottom sheet.

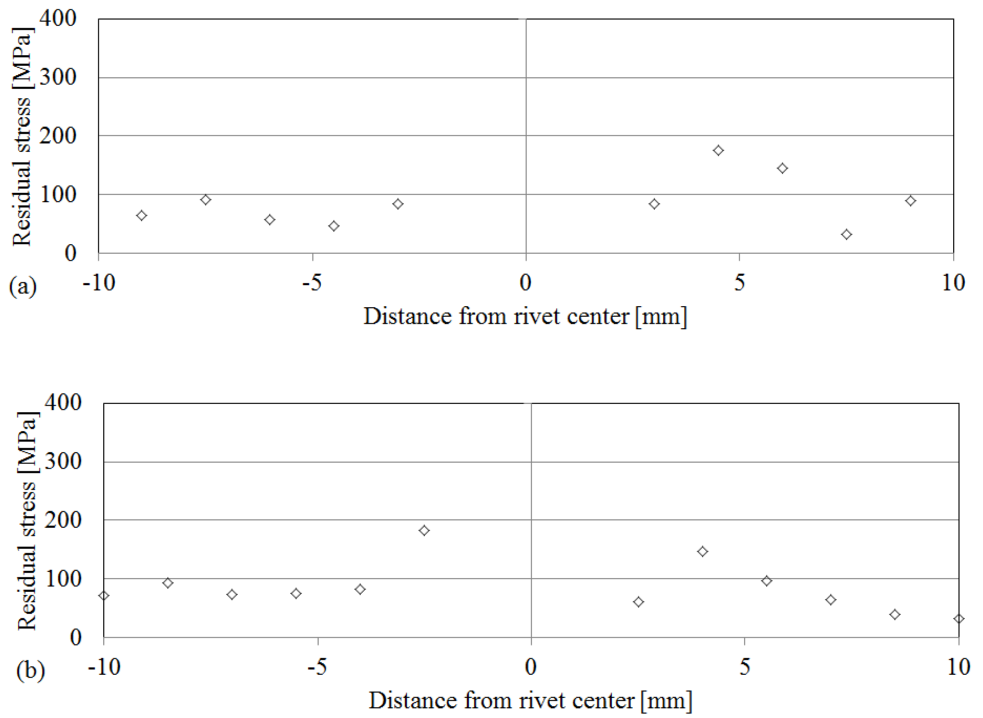

Fig. 6.1.9 Equivalent stress comparison 1.0 mm up from the un-deformed surface of tail side (a) line DD corresponding to Fig. 6.1.1 in the aluminium-steel joint (b) line JJ corresponding to Fig. 6.1.3 in the steel-steel joint.

Residual stress evaluated along line KK at 1.5 mm up from the die wall provides information on the behaviour of the material inside the die (Fig. 6.1.7d). A tensile condition is also observed in this part of the material, as with the aluminium-steel specimen. On the other hand, at 3.5 and –3.5 mm away from the rivet axis along line KK, a compressive stress of 300 ± 97 MPa was observed, confirming that these points fell within the rivet leg.

The feasibility of evaluating residual stress in different riveted joints was examined in this study. The trend of residual stress found in this experiment was consistent with the simulated results reported by authors [130], albeit for other steel joints and thicknesses. It is evident from the residual stress profiles that the neutron diffraction technique can successfully predict the position of the rivet leg after flaring in a joint, without the need to perform a metallography cross-section. This scenario ultimately validates the feasibility of residual stress evaluation using the neutron diffraction technique. Stresses that developed in the rivet bore near the interface between the top and bottom sheets were the largest for both joints and were significant because of the high value of compressive stress. During service, loading of the joint may cause the stress in the rivet to reach the ultimate strength of the material, which would lead to premature failure of the joint. An investigation applying this methodology to the measurement of residual stress for a wider range of joints would be reported later with a view to providing guidance in the optimum design of SPR joining conditions.

6.2 Optimizing the parameters for meaningful evaluation

The feasibility of evaluating residual stress in a riveted joint was examined in the previous chapter. However, it was found that the error bars are quite large when compared with the stress values. It is necessary to develop a relationship between the measurement error with gauge volume and detection time to confirm the limits of this method when applied to such small components.

In principle, to achieve a certain accuracy, it is possible to develop a relationship between measurement time and the gauge volume in particular for a single-phase material with a simple geometry, but this approach could not be applied in this case due to the complex geometry of the specimen, so an experimental approach has been chosen [213]. The relation between time and measurement of d-spacing can be easily calculated, as the error is always related to time [213, 243] , as a function of ($\frac{1}{\sqrt{t}}$). However, it is necessary to check the residual stress profile depending upon the measuring direction, optimize the beam attenuation path-length and the gauge volume. The purpose of this present study is to establish the optimum instrument configuration and experimental procedure that allows evaluation of stress in SPR faster and/or more accurately while at the same time keeping the resolution required for the mm-scale of the problem. A journal paper on the optimizing parameters for meaningful evaluation of residual stress on SPR joints by neutron diffraction from this work was published by the present author [244].

Sheet specimens 150 mm long, 50 mm wide and 2.0 mm thick carbon steel were chosen as top and bottom sheet for the neutron diffraction experiment (details were provided in the experimental setup chapter (chapter 4.9). Joining parameters for this specific study are given in Table 6.2.1. As the investigated joint specimen was small, gauge volumes of 0.5 x 0.5 x 0.5 mm^3 and 1.0 x 1.0 x 1.0 mm^3 were used in order to achieve a good compromise between spatial resolution and experimental counting time. The specimen was accurately positioned (± 100 µm) on the instrument using the software SScanSS [237, 238]. The specimen was first laser scanned to obtain a 3D model, then positioned on the experimental table and aligned using dedicated robotic arms with touch probe. SScanSS was also used to define the measurement points (see experimental procedure) based on the cross-section of the joint through the software as the internal features of the joint are hidden from the laser scan, and to estimate the required counting time depending on the beam path length (Fig. 4.9.1) for a given direction of strain.

Table 6.2.1 Parameters of selected joints.

Specimen	Total ply thickness (mm)	Top sheet thickness (mm)	Bottom sheet thickness (mm)	Rivet			Die	
				Length (mm)	Diameter (mm)	Hardness (HV)	Diameter (mm)	Depth (mm)
Carbon steel	4.0	2.0	2.0	7.0	5.0	410	10	2.5

In order to check the effects of the evaluating side on the residual stress profile, transverse residual strains were measured at 20 points located from -5.0 mm to +5.0 mm relative to the joint axis along line AA, as shown in Fig. 6.2.1a. These points were selected to ensure that the desired gauge volume always fell within the material thickness. The line AA was situated 1 mm below the undeformed surface of the top sheet (Fig. 6.2.1b). At first, transverse strain was measured from the head (rivet) side of the joint along line AA, using 240 s acquisition time per data point, and then the table was rotated 180° in order to measure the strain from the tail (die) side (Fig. 6.2.2). The gauge volume used for this measurement was 1.0 mm^3. It may be noted that to measure the strain from the die side, the acquisition time per data point was increased to 600 s to take into account the longer neutron path length to achieve a resolution of ± 50 µm.

In order to establish the optimum instrument configuration, strains were measured at 30 locations from -7.5 mm to +7.5 mm along line BB situated 1 mm above the undeformed surface of the bottom sheet (Fig. 6.2.1b). Strains were measured twice at each point, using two different gauge volumes of 1.0 mm^3 and 0.125 mm^3) while the acquisition time was varied from 240 s up to 1500 s depending on the gauge volume and measurement location in the longitudinal direction.

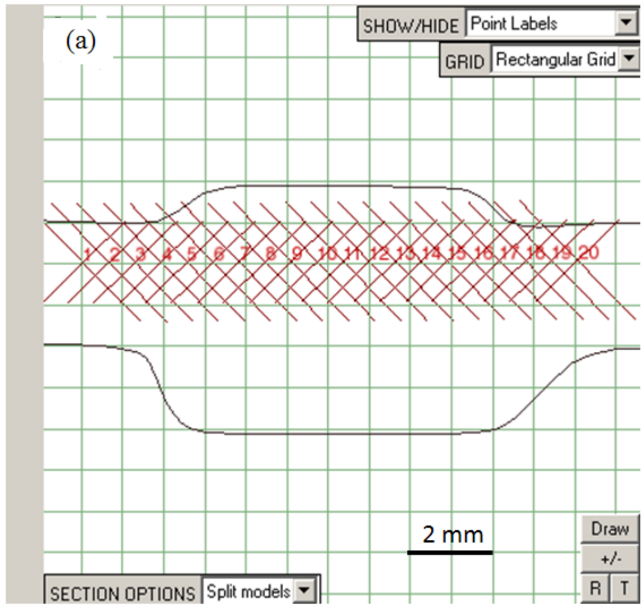

Cross-section of the joint viewed through SScanSS software

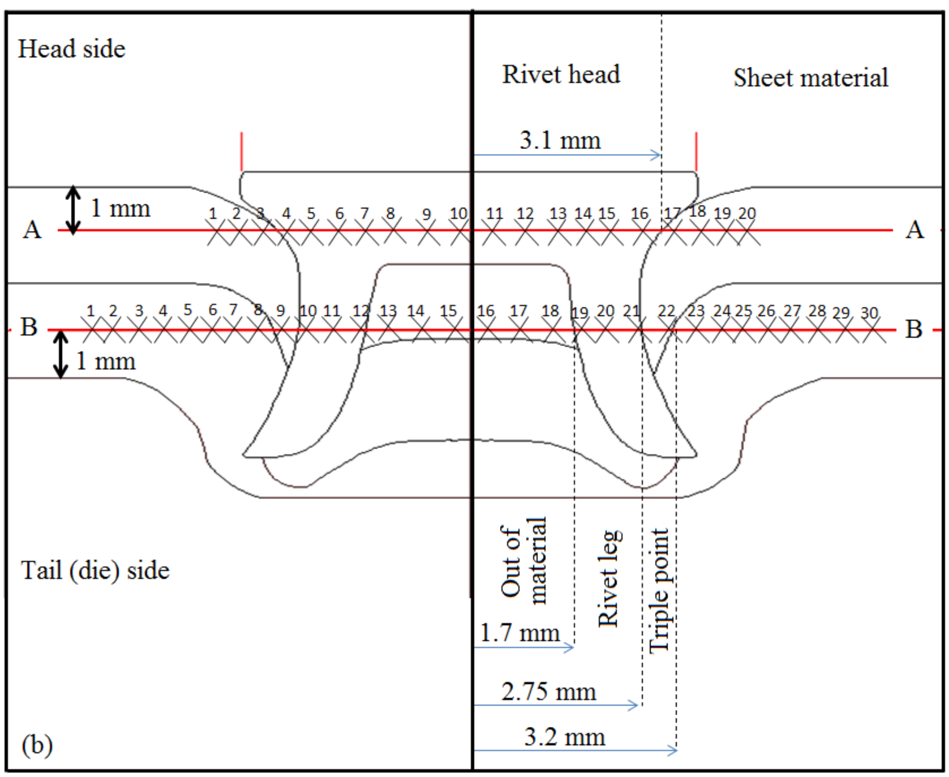

Fig. 6.2.1 (a) Defining the measuring points through the software SScanSS and (b) measurement lines AA and BB for head and die side sheet respectively for residual strains in joint of 2.0 mm + 2.0 mm carbon steel.

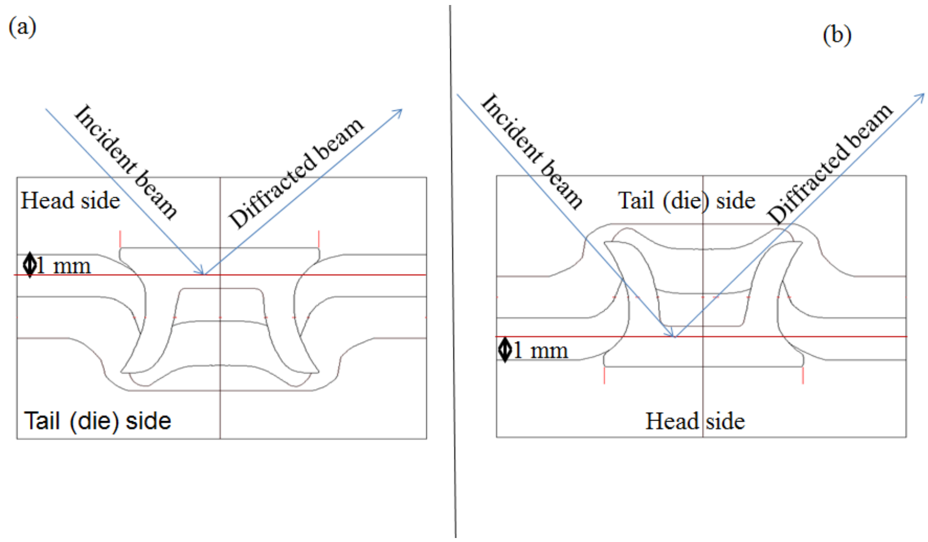

Fig. 6.2.2 Schematic of measurement direction of residual stress evaluated from (a) head side and (b) die side.

Residual stress may exist in a new un-used rivet as they are produced by forging and heat treated to the required hardness level. Therefore, a user reference lattice d_r was used instead of the so-called strain free (d_0) reference lattice for the calculation of micro-strain. For the rivet material, d_r (1.168713 ± 0.000459 Å) was determined from the average of three points (one in the rivet head and two in the rivet leg) of a new unused rivet, and for the steel sheet the reference point d_r (1.167371 ± 6.74x10^{-5} Å) was taken as the average of four points at 1 mm from the four free corners of a new sheet for each gauge volume. The strain and error were determined by the following equations [213, 245]

$$\varepsilon = \frac{d}{d_r} - 1 \tag{6.4}$$

$$\Delta \epsilon = \sqrt{\left[\left\{\left(\frac{\partial \epsilon}{\partial d}\right)\Delta d\right\}^2 + \left\{\left(\frac{\partial \epsilon}{\partial d_r}\right)\Delta d_r\right\}^2\right]} = \sqrt{\left[\left(\frac{\Delta d}{d_r}\right)^2 + \left\{\frac{d * \Delta d_r}{(d_r)^2}\right\}^2\right]} \tag{6.5}$$

where ΔƐ, Δd and Δd_r are measurement errors in strain, lattice spacing and reference lattice spacing respectively.

6.2.1 Measurements along line AA

Neutron path length for the diffraction measurements taken along line AA (Fig. 6.2.1b) was dependent on the measuring side, i.e., from the head side or die side as shown in Fig. 6.2.2. The difference in neutron path length between the two sides was about 7 mm in average, and the maximum neutron path length was found to be 4.5 and 12.95 mm from the head side and die side respectively (Table 6.2.2). The acquisition time of 240 and 600 second for the head and tail side measurements respectively enabled a resolution of ± 50 μm to be achieved (Fig. 6.2.3).

Table 6.2.2 Neutron path length and the acquisition time for a gauge volume of 1.0 mm^3 along the line AA as shown in Fig. 6.2.1b.

Measurement points	Distance from rivet centre (mm)	Measured from head side as shown in Fig. 6.2.2		Measured from tail side as shown in Fig. 6.2.2	
		Neutron path length (mm)	Acquisition time (sec)	Neutron path length (mm)	Acquisition time (sec)
1	-4.915	3.38	240	11.18	600
2	-4.398	3.72		11.21	
3	-3.881	3.76		11.23	
4	-3.364	3.76		11.25	
5	-2.847	3.94		11.30	
6	-2.33	4.15		11.43	
7	-1.813	4.34		11.61	
8	-1.296	4.49		11.97	
9	-0.779	4.54		12.41	
10	-0.262	4.53		12.70	
11	0.262	4.52		12.87	
12	0.779	4.49		12.96	
13	1.296	4.42		12.94	
14	1.813	4.27		12.74	
15	2.33	4.02		12.38	
16	2.847	3.76		11.96	
17	3.364	3.52		11.64	
18	3.881	3.51		11.54	
19	7.398	3.48		11.52	
20	4.915	3.01		11.53	

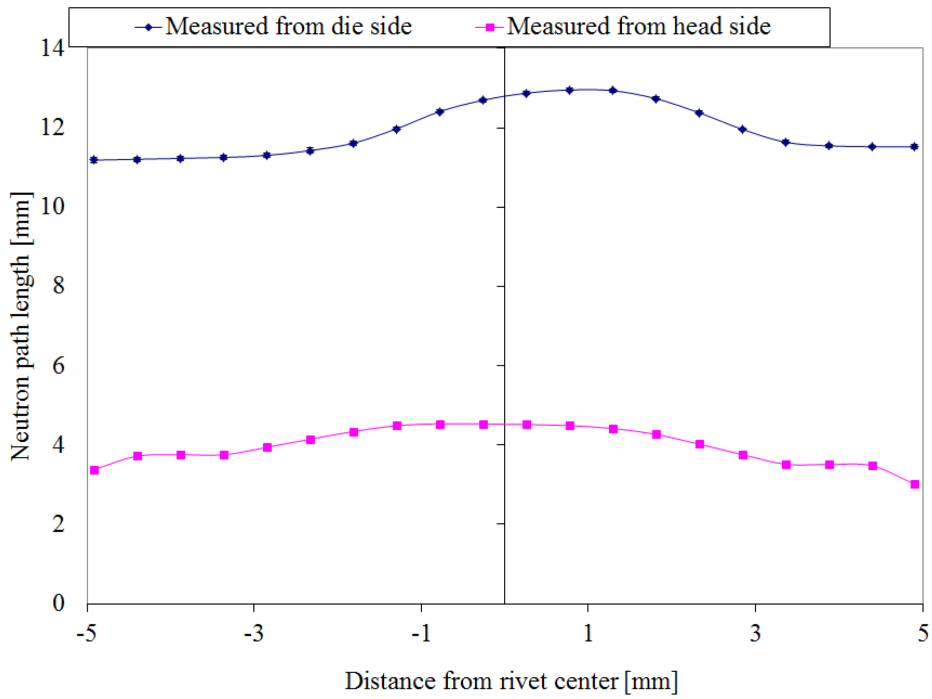

Fig. 6.2.3 Neutron path length distribution along line AA shown in Fig. 6.2.1b depending upon measuring direction.

Strains measured in the transverse direction along line AA were also found to depend on the measuring side (from the head side and die side). As shown in Fig. 6.2.4, the strain profile was symmetrical with respect to the rivet axis when measured from the head side, but not from the die side. The errors (determined by equation 6.5) were in a range of ± 50 µm for both cases. It was expected that points at a distance of 3.1 and -3.1 mm from the rivet axis situated in the top sheet below the rivet head (measurement points 2, 3, 4, 17, 18 and 19 in Fig. 6.2.1b), would be under compression because of the pressure from the rivet head [240]. Compressive strain was indeed observed using data obtained from the head side, but tensile strain was obtained for the same position when using data acquired from the die side (Fig. 6.2.4). This discrepancy, combined with the asymmetric strain profile obtained from the die side, suggest that the alignment might have changed while the sample table was rotated, which could be due to the rotation of the table not being perfectly horizontal, and/or the specimen not being perfectly straight. In any case, this suggests that the specimen's area of interest should be realigned after any rotation of the sample table.

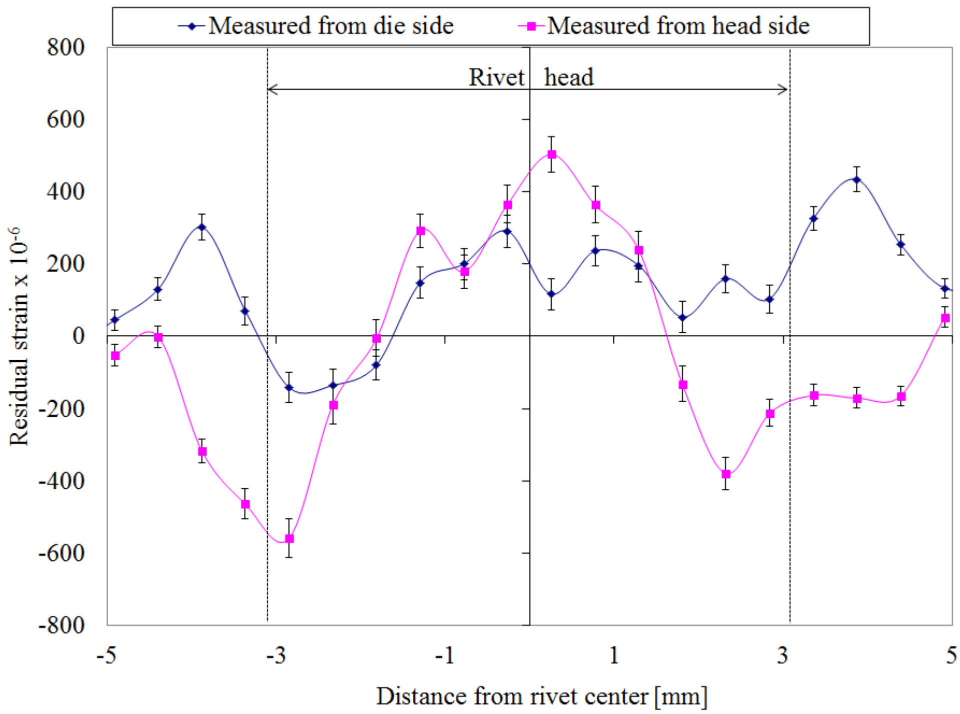

Fig. 6.2.4 Effect of measuring side on the transverse residual strain profile along line AA (shown in Fig. 6.2.1b) using 1.0 mm^3 gauge volume.

Variations in the Full Width Half Maximum (FWHM) and intensity of the neutron diffraction peaks acquired along line AA were also affected by the measuring side, with broader and higher intensity peaks obtained from the die side, by comparison with those obtained from the head side, as shown in Figs. 6.2.5 and 6. The normalized value of FWHM reached 1.4 and 1.8 for the head side and die side measurements respectively. In both cases, peak broadening occurred for the measurement points situated in rivet head. This is due to the different microstructure of the sheet and rivet material (Fig. 6.2.7). Rivet material has a martensitic structure while the sheet material has ferritic structure. Again, peak broadening was high in die side measurement due to the long neutron path. The overall intensity for the die side measurement was found to be high due to the increased acquisition time (Fig. 6.2.6). However, in both measurement directions, the intensity decreased for the measurement points on the rivet head (points 5 to 16 in Fig. 6.2.1b). The intensity for the measurement points on the rivet head was decreased due to two reasons: different microstructure of rivet and longer neutron path length (Table 6.2.2).

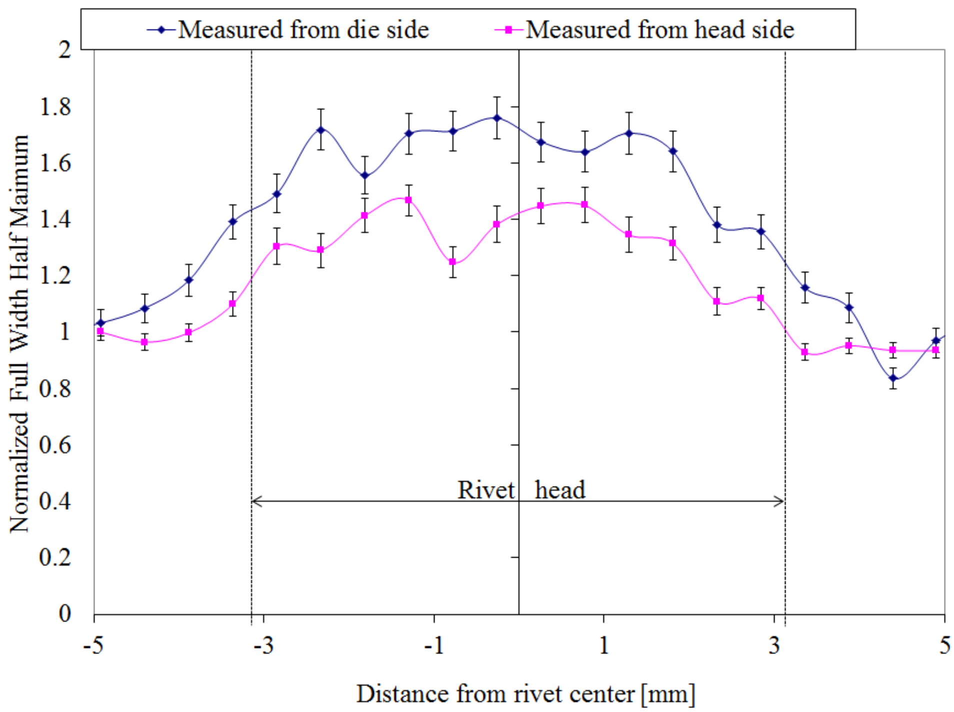

Fig. 6.2.5 Effect of measuring side on Full Width Half Maximum of the neutron peak (transverse) along line AA (shown in Fig. 6.2.1b) depending upon measuring direction using 1.0 mm^3 gauge volume.

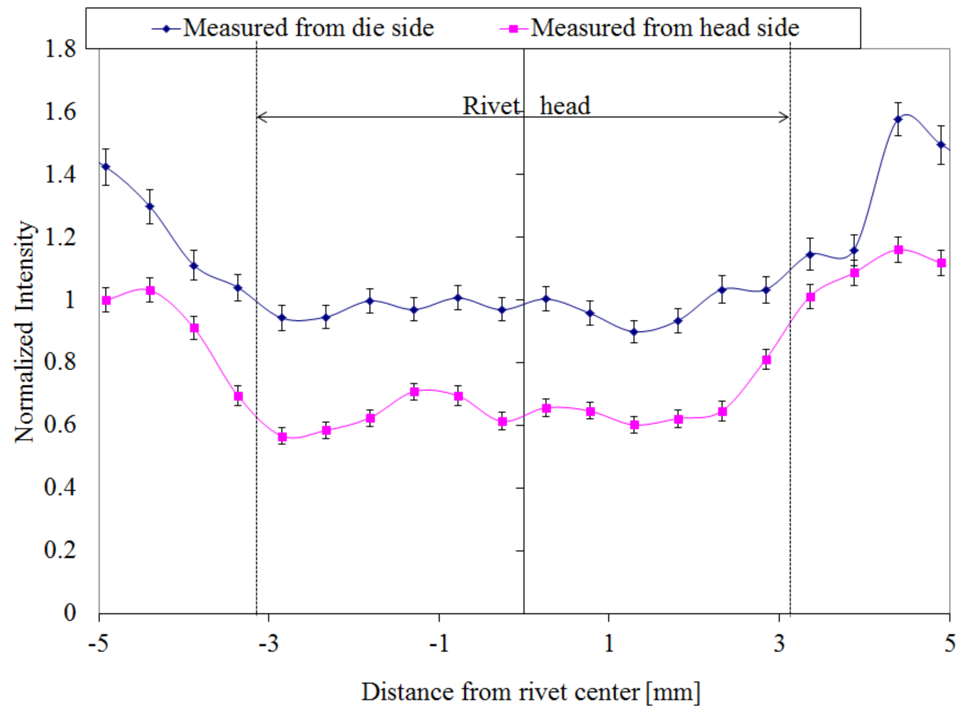

Fig. 6.2.6 Intensity of the neutron peak in transverse direction along line AA (shown in Fig. 6.2.1b) depending upon measuring direction using 1.0 mm^3 gauge volume.

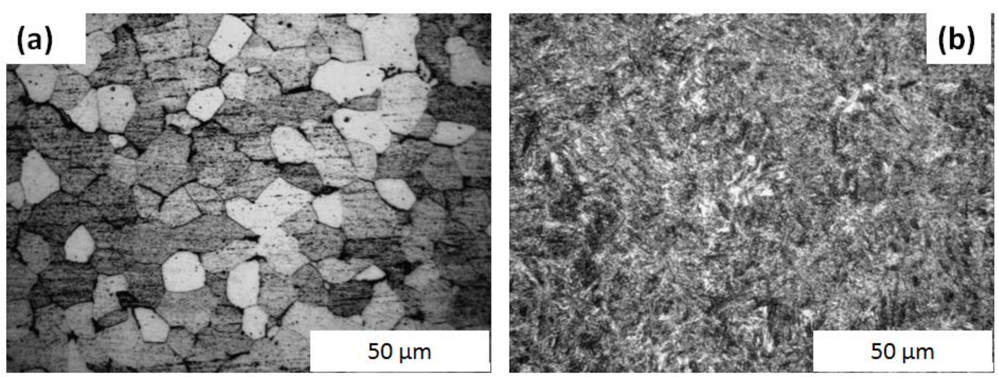

Fig. 6.2.7 Microstructure of (a) sheet material showing a ferritic structure and (b) rivet (as received) material showing a martensitic structure.

However, irrespective of the measuring side, there was an increase in peak broadening with a decrease in peak intensity for measurements taken within the rivet head, which increased the level of uncertainty. Nevertheless, these results were related to microstructural effects. The diffraction peak from the rivet material displayed a slight shift as well as broadening compared to the sheet material, as shown in Fig. 6.2.8, which can be attributed to their differing carbon composition and alloy elements. The rivet was made from 0.35% carbon steel; while the sheet material was composed of 0.28% carbon, 0.1% Phosphorus, 1.6% Manganese and 0.035% Sulphur. The microstructure of the steel rivets is martensitic with a body centred cubic as opposed to tetragonal lattice as no peak splitting was observed in Feα(211) reflection, while the steel sheets have a ferritic microstructure with a body centred cubic lattice (Fig. 6.2.7). Hence, the diffracted peak intensity was less while measuring the strain in the martensitic rivet head [246, 247]. To increase the intensity it is necessary to increase the acquisition time (1.5 and 3 times for 1.0 and 0.125 mm^3 respectively) while the neutron diffraction measurement is conducted in the rivet.

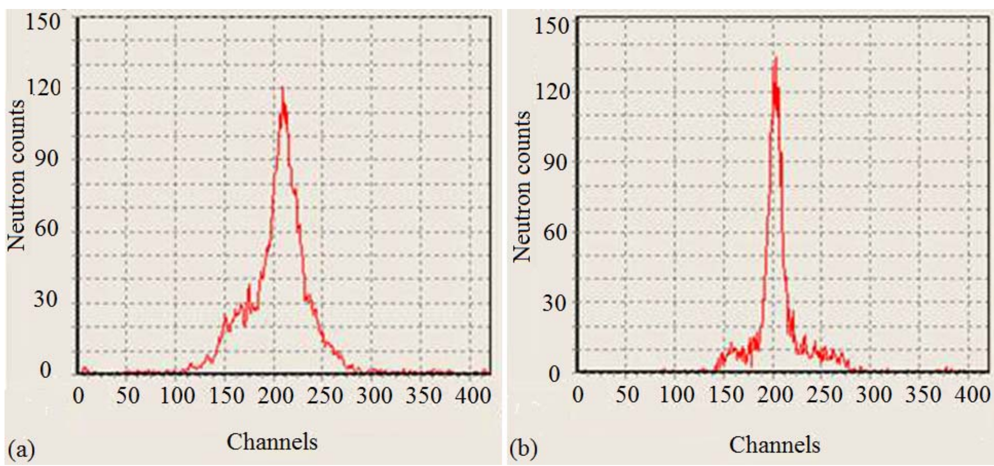

Fig. 6.2.8 Profile of neutron counts showing shift and peak broadening Feα(211) reflection due to different microstructure in (a) rivet and (b) sheet material.

6.2.2 Measurements along line BB

The effect of gauge volume on the strain profile measured along line BB (Fig. 6.2.1b) is shown in Fig. 6.2.9. It should be noted that with 1.0 and 0.125 mm^3 gauge volumes, the acquisition time was 240 and 900 seconds respectively while measuring the strain in the sheet material, and was increased to 600 and 1500 seconds while measuring the strain in the rivet. At first glance, the strain profile measured using 1.0 mm^3 gauge volume seems clear and symmetrical (Fig. 6.2.9). However, it is apparent from Figs. 6.2.1b and 4.9.2.1 that part of the line BB (measurement points 13 to 18 in Fig. 6.2.1b) was out of material (i.e., crossing a void) up to 1.70 mm from the rivet axis. The measurement points located within 1.70 mm from the rivet axis were partially spanning solid material when using the 1.0 mm^3 gauge volume, and completely out of material for the case of 0.125 mm^3 gauge volume. Hence, the result obtained by using 1.0 mm^3 gauge volume was not accurate. The measurement locations (points 10, 11 and 12 in the left side and points 19, 20 and 21 in the right side) situated from 1.70 mm to 2.75 mm are in the rivet leg. However, the measurements were taken at points 1.8, -1.8, 2.3,-2.3, 2.8 and -2.8 mm. So only the locations situated at 2.3 and -2.3 mm (points 11 and 20 in Fig. 6.2.1b) reflect the real measurement for the case of 0.125 mm^3 gauge volume, which was fully immersed within the rivet leg. As for 1.0 mm^3 gauge volume no points were fully situated within the rivet leg, which was why the measurement conducted with 1.0 mm^3 gauge volume was not correct. Likewise, the measurement locations at 2.8 and -2.8 mm from the rivet axis (points 9 and 22) were situated at the triple point and for both cases (1.0 and 0.125 mm^3 gauge volumes) the strain was obtained from a combination of rivet and top and bottom sheets. However, strains measured from 4.0 mm to 7.5 mm (points 1 to 7 and 24 to 30) were completely immersed within the bottom sheet for both gauge volumes. The strain profiles measured from this range (4.0 to 7.5 mm) are shown in Fig. 6.2.10. It is clear from this figure that the trends are similar for both gauge volumes with the 1.0 mm^3 gauge volume data showing a higher magnitude which may be due to the pseudo strain. The other reason of this higher magnitude may be due to the error during the d_0 measurement for 1.0 mm^3 gauge volume, because from the physics point of view the magnitude should be same (magnitude of residual stress does not depends on gauge volume). All else being equal, the bigger gauge volume should give a better statistics in the strain measurement because more material is being sampled.

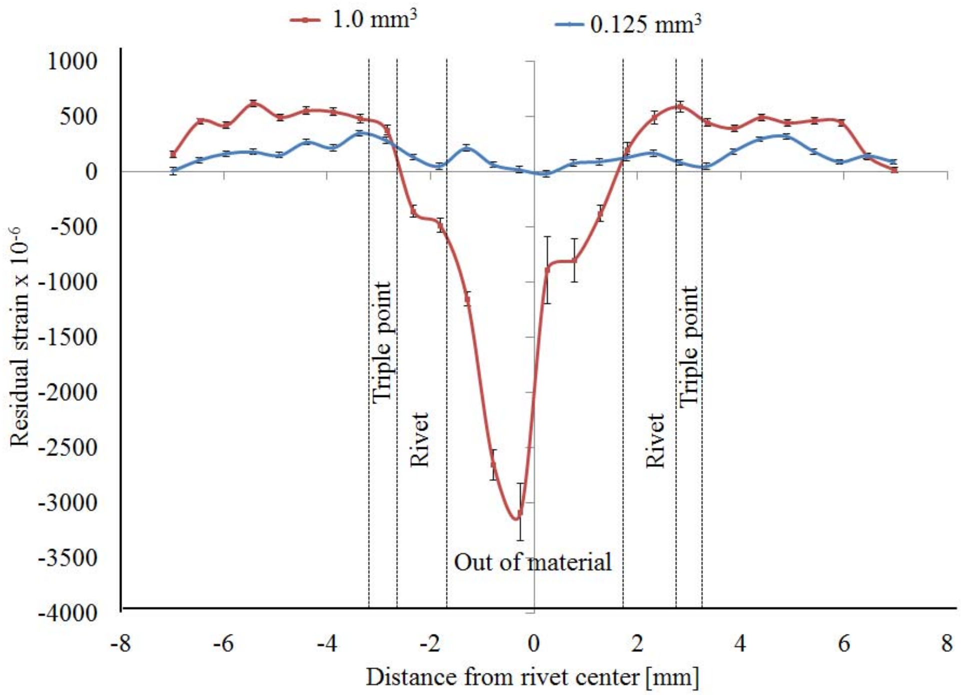

Fig. 6.2.9 Effect of gauge volume on the longitudinal residual strain profile along line BB (shown in Fig. 6.2.1b).

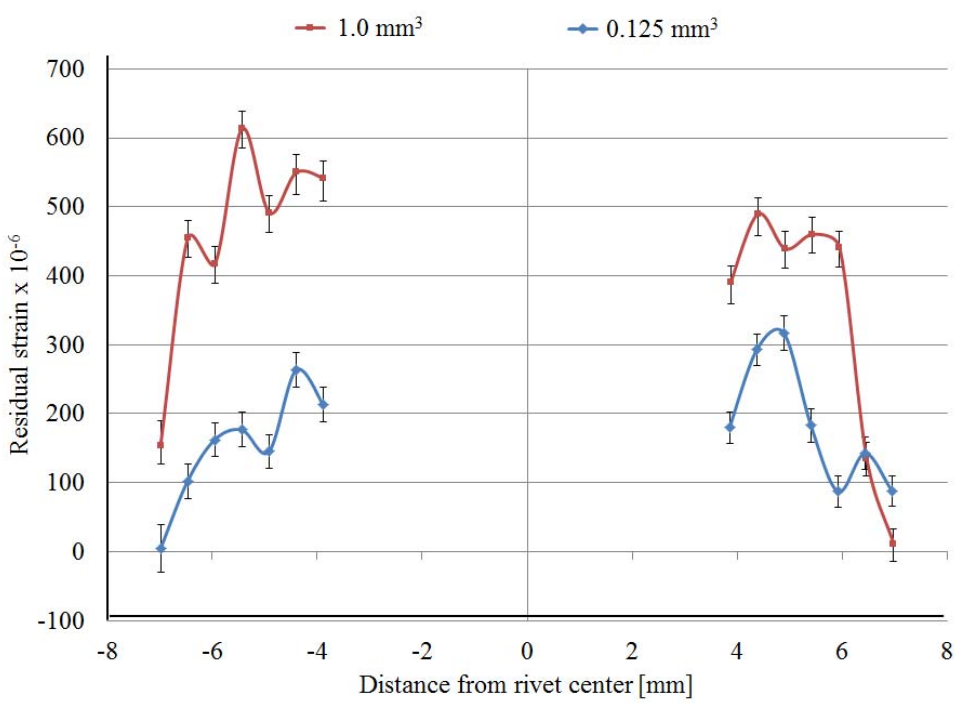

Fig. 6.2.10 Residual strain profile along line BB only on materials shown in Fig. 6.2.1b depending upon gauge volume.

An optimum instrument condition for residual stress evaluation in SPR joints by the neutron diffraction method was developed in this section. It is suggested that the 0.125 mm^3 gauge volume is preferable for the strain measurement in SPR joints. Sufficient acquisition time is necessary to achieve a reasonable measurement uncertainty. At first, the acquisition time should be selected based on the neutron path length of the measurement point. Typically, 240 and 900 seconds are necessary to achieve error (measurement uncertainty) in strain measurement within the range of ± 50 µm in sheet material for 1.0 and 0.125 mm^3 gauge volumes respectively while the neutron path length is around 4.0 mm. The detection time while measuring the d-spacing inside a rivet should be increased to maintain the same measurement error with the same neutron path length due to the different diffraction peaks from martensitic structure of the rivet (the peak position is very close to the d-spacing of the Feα(211) reflection but not the same): 600 and 1500 seconds for 1.0 and 0.125 mm^3 gauge volume respectively. It is also suggested that the realignment should be undertaken if any angular movement of the table occurred. An investigation applying these optimum instrument parameters to the evaluation of residual stress for a wider range of SPR joints is reported in the subsequent sections of this chapter to provide guidance for the optimum design of SPR joining conditions.

6.3 Residual stress in different SPR joints

The feasibility of measuring residual stress in different riveted joints was examined in the previous section and the parameters were optimized to reduce the uncertainties involved and to improve the measurement technique for a meaningful result. Nine different combinations of joints (case A, B to I in Table 6.3.1) comprise types of thickness (5.0, 4.0 and 3.0 mm) and two different hardnesses of material (G300 and G450 carbon steel having hardness of 198 HV and 270 HV respectively) and two forms of rivet hardness (555 and 480 HV) were considered for this study. A flat die was used for each condition with a high die recess volume for the thick joint and low die recess volume for the thin joint. It should be noted that access to the Kowari strain scanner has a limited time frame. Out of the nine different combinations, only seven joints have been fully studied by neutron diffraction while for two joints (D, E) partial strain measurements were undertaken.

Table 6.3.1 Different combinations of joint for residual stress evaluation.

Case no.	Material	Top sheet thickness (mm)	Bottom sheet thickness (mm)	Rivet		Die	
				Length (mm)	Hardness (HV)	Diameter (mm)	Depth (mm)
A	G450 steel	1.5	1.5	6	480	9	2
B	G300 steel						
C	G450 steel	2.5	2.5	8	555	11	2.35
D	G300 steel						
E	G300 steel	2.0	2.0	7	480	10	2.50
F	G450 steel	2.0	2.0	7	555	10	2.10
G					480		
H	G300 steel				555		
I					480		

6.3.A. 1.5 mm + 1.5 mm G450 carbon steel joint with 480 HV rivet

At this stage, a joint was produced by using 1.5 mm thick G450 carbon steel strips as the top material and bottom materials. A 6 mm rivet with a hardness of 480 HV and a flat die (9.0 mm diameter and 2.0 mm deep) were used to produce the joint. The force-displacement curve of this joint was shown previously in Fig. 5.2.5a. Strain measurements were made along lines OO and PP, which were at depths of 0.75 mm and 1.0 mm from the undeformed top sheet surface and the surface of rivet head respectively (Fig. 6.3.1). Strain was also measured along line QQ, which was 0.75 mm up from the undeformed bottom sheet surface to obtain the behaviour of stresses in the steel sheet. To obtain the behaviour of stresses in the rivet, strains were measured along lines RR and SS as shown in Fig. 6.3.1. The positions of the measurement points taken along those lines and relative to the joint centreline are summarized in Table 6.3.2.

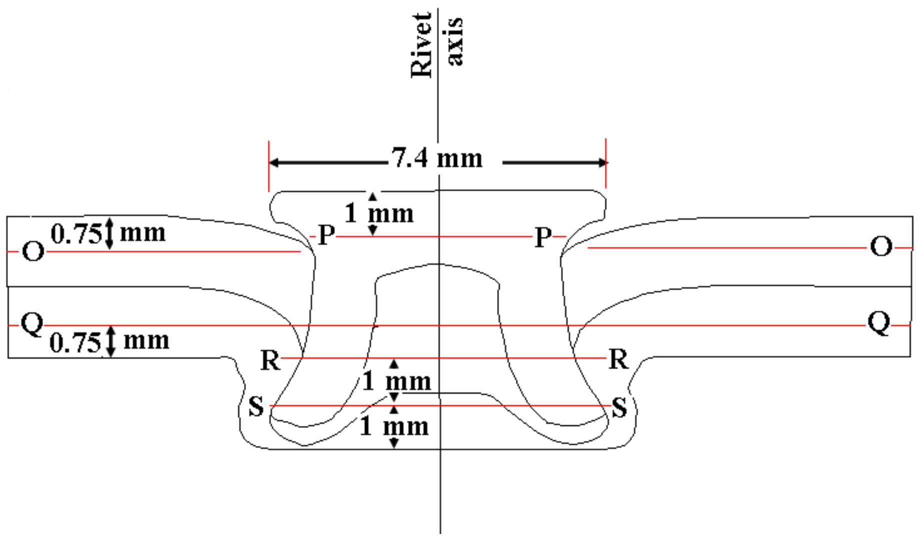

Fig. 6.3.1 Measurement lines for residual stress evaluation in a joint of 1.5 mm G450 + 1.5 mm G450 steel.

Table 6.3.2 Measurement points along lines OO, PP, QQ, RR and SS shown in Fig. 6.3.1.

Line	OO and QQ	PP	RR	SS
Measurement points (mm) from rivet axis shown in Fig. 6.3.1	-8.5, -7.5, -6.5, -5.5, -4.5, 4.5, 5.5, 6.5, 7.5, 8.5	-2.5, -0.5, 0.5, 2.5	-2.5, 2.5	-2.75, 2.75
Total number of points	10*2 = 20	4	2	2

The stresses that were evaluated in the steel sheet along lines OO and QQ are shown in Figs. 6.3.2 & 3. It is clear from Fig. 6.3.2 that the stress components near the joint showed a compressive behaviour at a distance of 4.50 mm from the rivet axis. The stresses that developed far from the joint were not significant. The stress profile looks a bit asymmetric. The force during riveting was not completely vertical due to C-frame deflection. The stress that was developed in the left side was low compared with that in the right side (Fig. 6.3.2). In the right side the stresses were found to be positive, which was counter balanced by the left side of the bottom sheet (Fig. 6.3.3). The minimum stress was observed in the top sheet at -5.5 mm in the transverse direction and the maximum stress was also observed on the top sheet at a displacement of 5.5 mm in the normal direction. The maximum error on calculated residual stresses was ± 22 MPa.

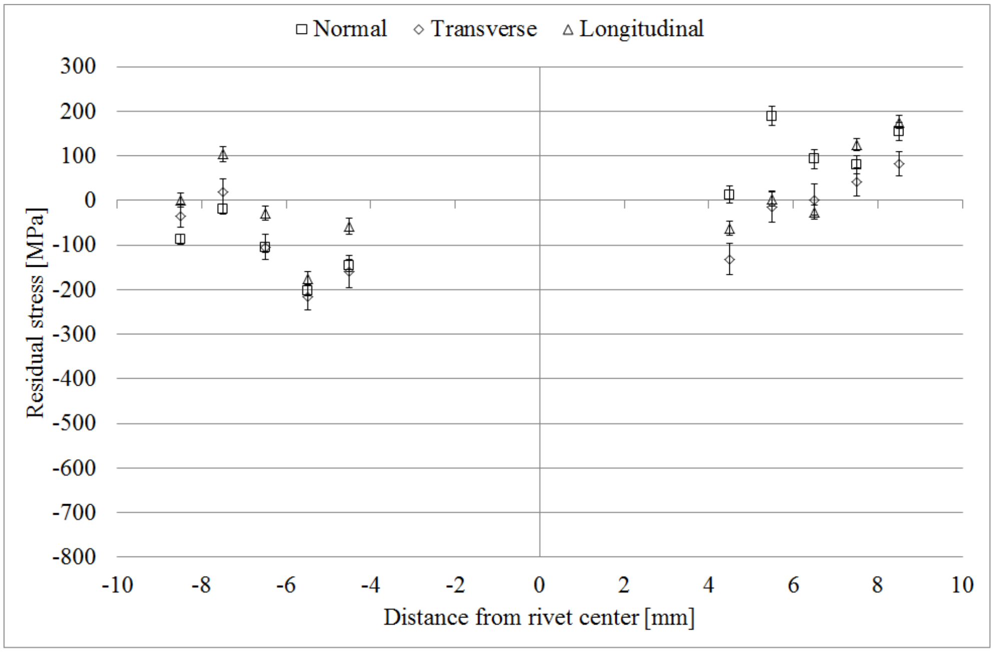

Fig. 6.3.2 Residual stress profiles in top sheet along line OO corresponding to the lines shown in Fig. 6.3.1.

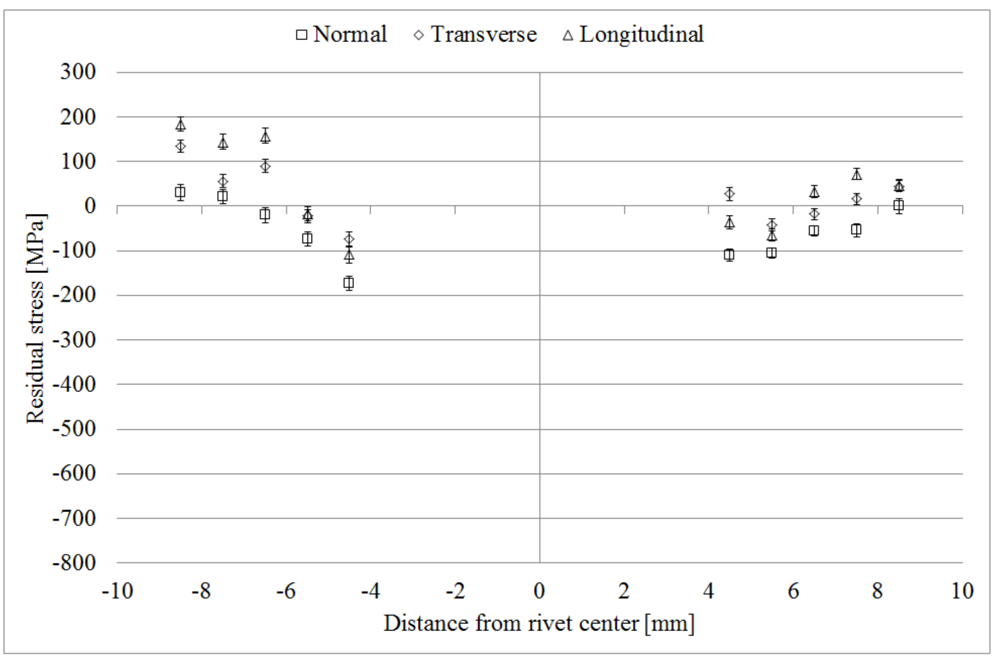

Fig. 6.3.3 Residual stress profiles in bottom sheet along line QQ corresponding to the lines shown in Fig. 6.3.1.

Residual stresses along lines PP, RR and SS were inside the rivet as shown in Fig.6.3.1. The measurement locations (8 points) and the stresses in the rivet are shown in Fig.6.3.4. It was clear that the stresses inside the rivet were determined to be compressive. A huge amount of energy was delivered to a very small volume in the riveting process, welding the rivet and the top and bottom sheets together and causing them to act as a single body. For this reason the stresses observed inside the rivet were compressive and this was counter balanced by the top and bottom sheets. Stresses in the rivet head (measurement locations 3, 4, 5 and 6) were similar in nature and in the order of 650 ± 19 MPa. Stresses determined in the rivet leg were asymmetric. The maximum compressive stress was observed at the left leg of the rivet (measurement location 2) had a value of -753 ± 16 MPa which was measured in the transverse direction. Hardness ratio between rivet (480 HV) and sheet materials (270 HV) plays an important role in the residual stress profile inside the rivet (in this case 480/270 equals 1.78). The higher the ratio is, the lower the magnitude of the residual stress will be.

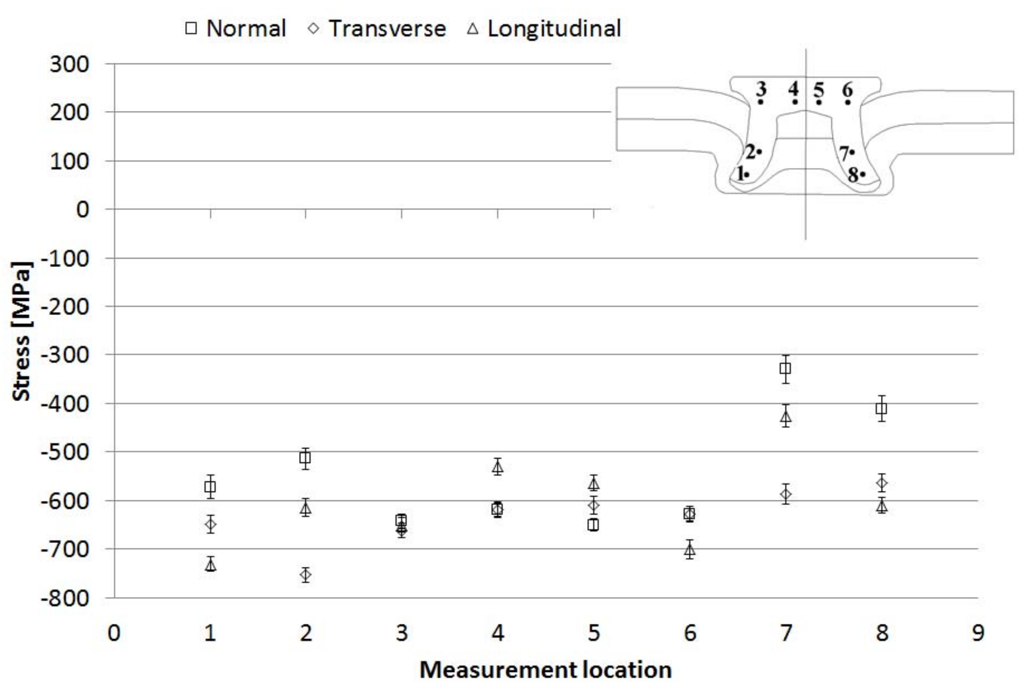

Fig. 6.3.4 Residual stress profiles in rivet on different locations for 1.5 + 1.5 mm G450 carbon steel joint with 480 HV rivet.

6.3.B. 1.5 mm + 1.5 mm G300 steel joint with 480 HV rivet

In this case, the sheet materials were changed by replacing G450 with G300 carbon steel while keeping all other parameters the same as case A in Table 6.3.1. The force-displacement curve of this joint was shown previously in Fig. 5.3.3. Strain measurements were made along lines ÓÓ and P′P′, which were at depths of 0.75 mm and 1.0 mm from the undeformed top sheet surface and the surface of the rivet head respectively (Fig. 6.3.5). Strain was also measured along line Q′Q′, which was 0.75 mm up from the undeformed bottom sheet surface to obtain the behaviour of stress in the steel sheet. To obtain the behaviour of stress in the rivet, strains were measured along lines R′R′ and S′S′ as shown in Fig.6.3.5. The positions of the measurement points taken along those lines and relative to the joint centreline are summarized in Table 6.3.3.

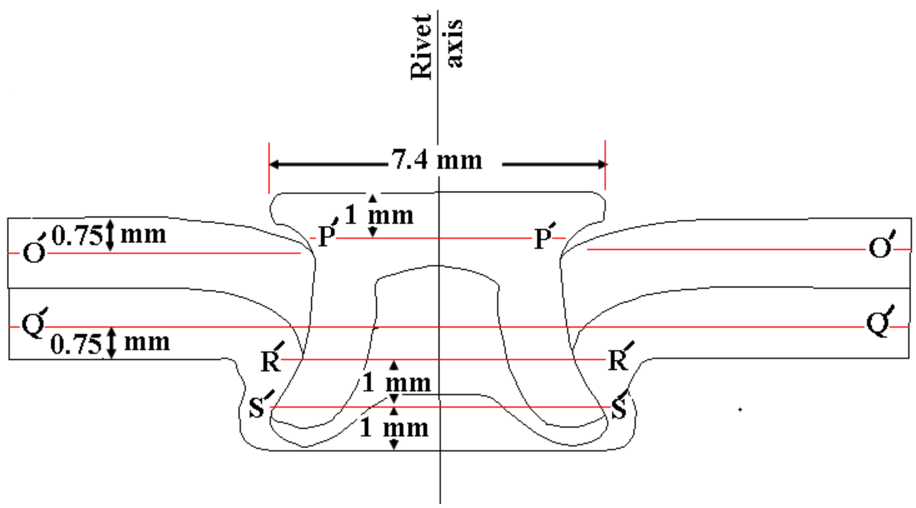

Fig. 6.3.5 Measurement lines for residual stress evaluation in a joint of 1.5 mm G300 + 1.5 mm G300 steel.

Table 6.3.3 Measurement points along lines O′O′, P′P′, Q′Q′, R′R′ and S′S′ shown in Fig. 6.3.5.

Line	**O′O′ and Q′Q′**	**P′P′**	**R′R′**	**S′S′**
Measurement points (mm) from rivet axis shown in Fig. 6.3.5	-8.5, -7.5, -6.5, -5.5, -4.5, 4.5, 5.5, 6.5, 7.5, 8.5	-2.5, -0.5, 0.5, 2.5	-2.5, 2.5	-2.75, 2.75
Total number of points	10*2 = 20	4	2	2

The stresses evaluated in the steel sheet along lines O′O′ and Q′Q′ are shown in Figs. 6.3.6 & 7. It is clear from Fig. 6.3.6 that the stress components near the joint showed a compressive behaviour and the stresses far from the riveting centre were tending to zero. C-frame deflection was negligible due to the soft sheet material. Thus, the stress profile was more symmetric. A similar pattern of residual stress was also observed in the bottom sheet which was along line Q′Q′ (Fig. 6.3.7). The minimum stress was observed on the top sheet at -6.5 mm in the transverse direction and the maximum stress was also observed on top sheet at a displacement of 7.5 mm in the longitudinal direction. The maximum error on calculated residual stresses was ± 16 MPa.

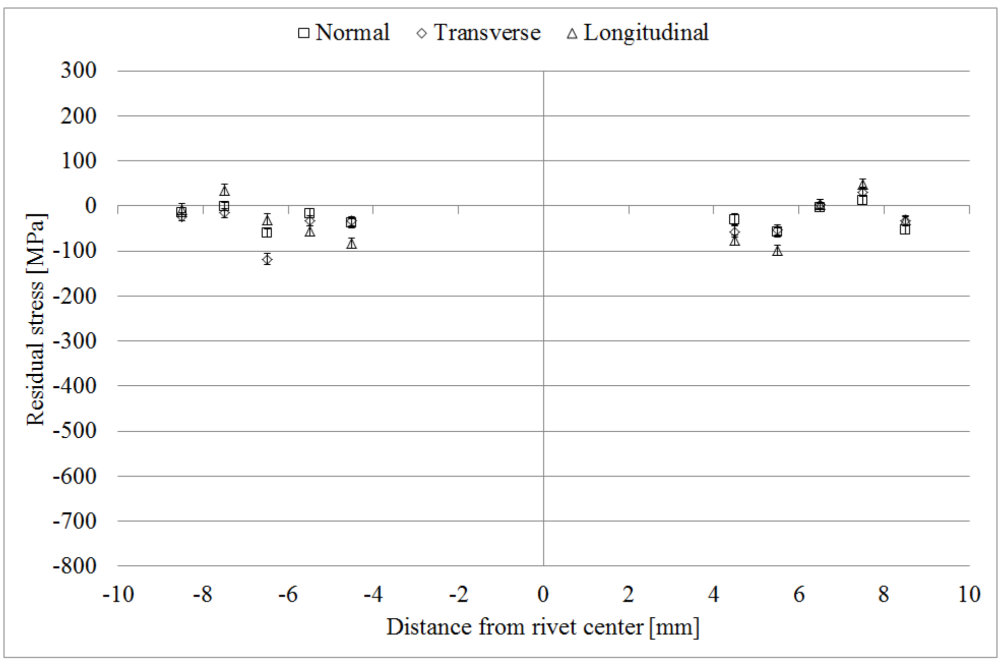

Fig. 6.3.6 Residual stress profiles in top sheet along line O′O′ corresponding to the lines shown in Fig. 6.3.5.

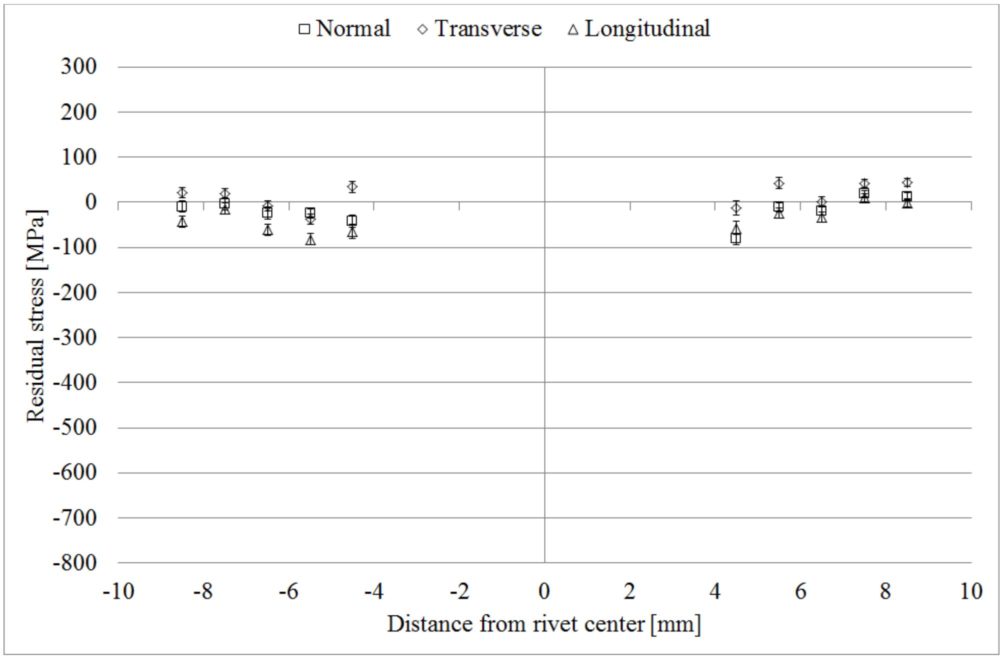

Fig. 6.3.7 Residual stress profiles in bottom sheet along line Q′Q′ corresponding to the lines shown in Fig. 6.3.5.

Residual stresses along lines P′P′, R′R′ and S′S′ were inside the rivet as shown in Fig. 6.3.5. The measurement locations (8 points) and the stress profile in the rivet are shown in Fig. 6.3.8. The stresses inside the rivet were compressive due to the same reason as described previously (the joint behaves as a single body). The stresses on the rivet head (measurement locations 3, 4, 5 and 6) were similar in nature and in the order of 500 MPa. The normal residual stress evaluated at location 3 did not match with the other values of the stresses. It was believed that, this value did not represent the true value and this occurred due to an error during the measurement.

The stresses in the rivet leg were more symmetric compared with the previous condition due to the soft sheet material. The maximum compressive stress was observed at the left leg of the rivet (measurement location 2) in the transverse direction had a value of -630 ± 16 MPa. Due to an increase in hardness ratio between the rivet and the sheet materials (480/198 equals to 2.42) the magnitude of the compressive stress was reduced to a lower value.

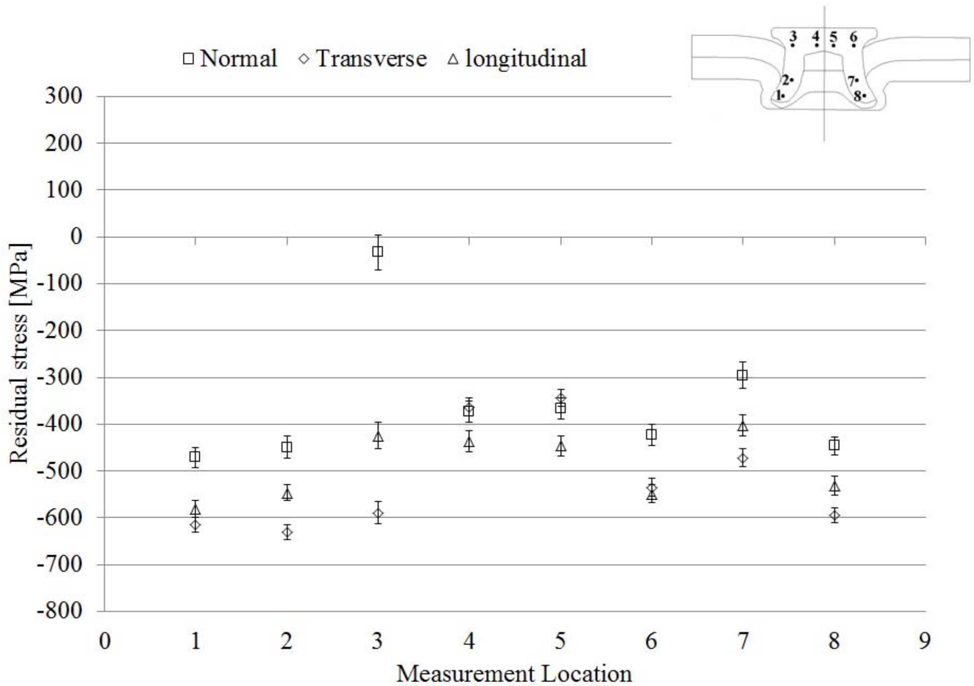

Fig. 6.3.8 Residual stress profiles in rivet on different locations for 1.5 + 1.5 mm G300 carbon steel joint with 480 HV rivet.

6.3.C. 2.5 mm + 2.5 mm G450 steel joint with 555 HV rivet

In this case a joint was produced by increasing the ply material's thickness. A 2.5 mm thick G450 carbon steel strip was used as top and bottom materials (Table 6.3.1). As the thickness was increased a longer rivet was used: 8 mm long rivet with a hardness of 555 HV. Again, a flat die with an increased die recess volume (11.0 mm diameter and 2.35 mm deep) was used to accumulate higher deformation. The force-displacement curve of this joint was shown previously in Fig. 5.4.1. Strain measurements were made along line LL, which was at a depth of 1.25 mm from the undeformed top sheet surface (Fig. 6.3.9). Strain was also measured along line MM, which was 1.25 mm up from the undeformed bottom sheet surface to obtain the behaviour of the stress in the steel sheet. To study the behaviour of the material inside the die, strains were measured along line NN as shown in Fig. 6.3.9. The positions of the measurement points taken along those lines and relative to the joint centreline are summarized in Table 6.3.4.

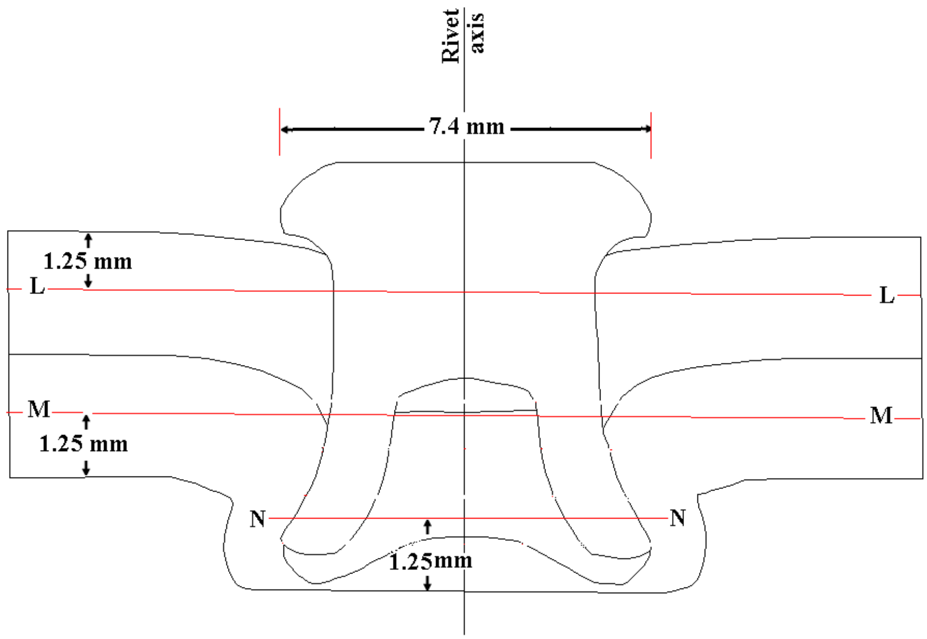

Fig. 6.3.9 Measurement lines for residual stress evaluation in a joint of 2.5 mm G450 + 2.5 mm G450 steel.

Table 6.3.4 Measurement points along lines LL, MM and NN shown in Fig. 6.3.9.

Line	LL	MM	NN
Measurement points (mm) from rivet axis shown in Fig. 6.3.9	-8.5, -7.5, -6.5, -5.5, -4.5, -4.0, -1.5, 0.0, 1.5, 4.0, 4.5, 5.5, 6.5, 7.5, 8.5	-8.5, -7.5, -6.5, -5.5, -4.5, -4.0, -3.5, -2.5, 2.5, 3.5, 4.0, 4.5, 5.5, 6.5, 7.5, 8.5	-3.5, -3.0, -2.0, -1.0, 0.0, 1.0, 2.0, 3.0, 3.5
Total number of points	15	16	9

The stresses evaluated in the steel sheet along lines LL and MM are shown in Figs. 6.3.10 & 11. It is clear from Fig. 6.3.10 that the points -1.5, 0 and 1.5 mm from the rivet axis were on the rivet head and the other points were on the top sheet. The overall stress components on rivet head showed a compressive behaviour with a lower magnitude varying from 23 ± 15 MPa to -225 ± 21 MPa. The stresses on the top sheet were not significant. The minimum stress (-123 ± 14 MPa) was observed on the top sheet at -7.5 mm in the transverse direction and the maximum stress (123 ± 16 MPa) was also observed on the top sheet at a displacement of -6.5 mm in the normal direction. The overall profile of the stress was symmetrical with respect to the rivet centre.

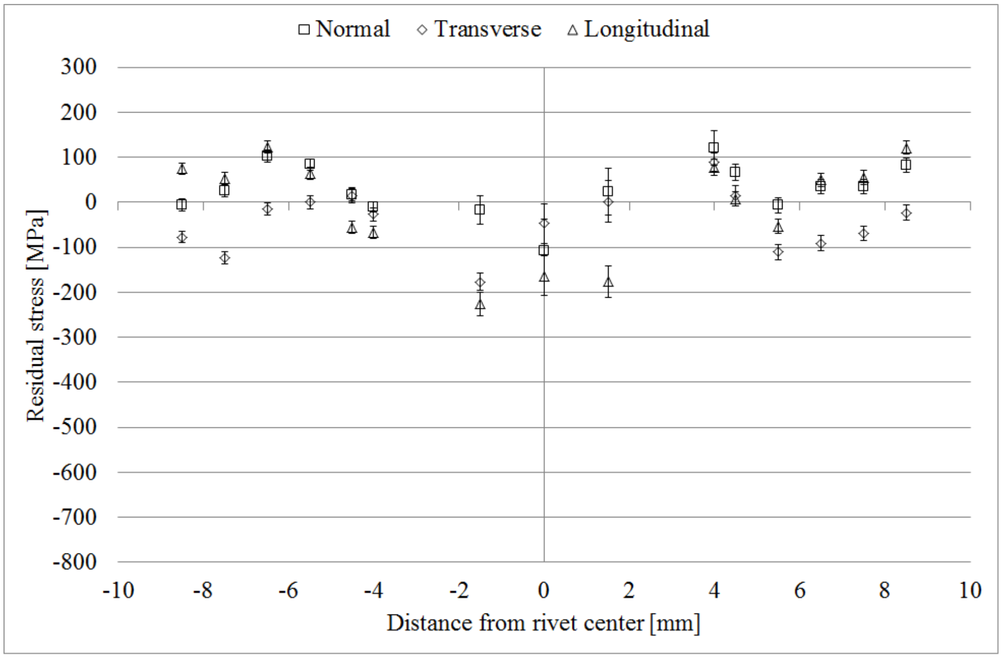

Fig. 6.3.10 Residual stress profiles in top sheet along line LL corresponding to the lines shown in Fig. 6.3.9.

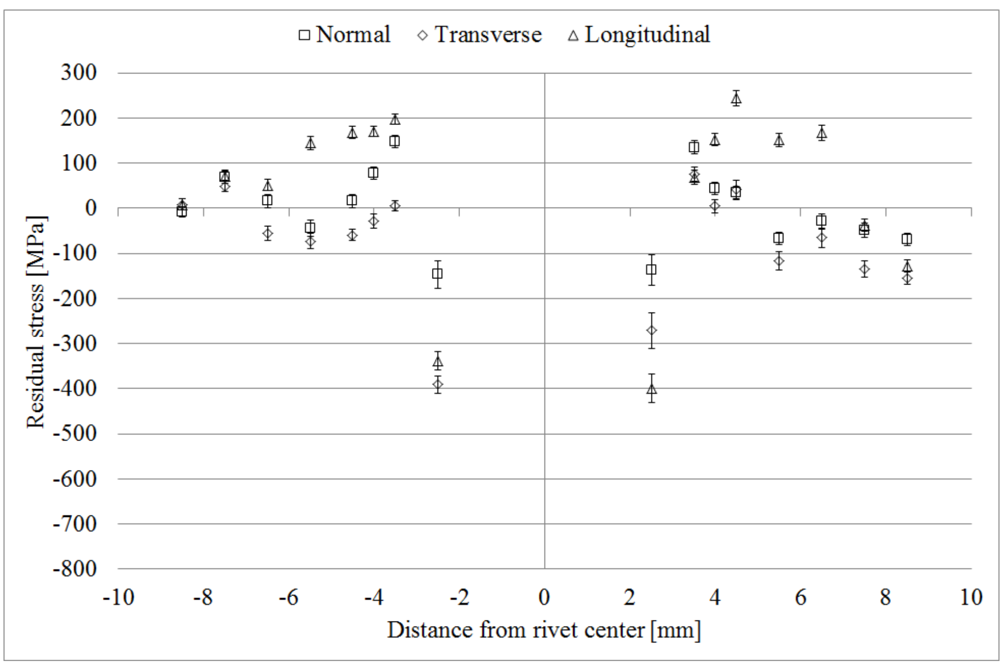

Fig. 6.3.11 Residual stress profiles in bottom sheet along line MM corresponding to the lines shown in Fig. 6.3.9.

It is clear from Fig. 6.3.11 that the points 2.5 and -2.5 mm from the rivet centre were in the rivet leg and the other points were in the bottom sheet. The stress components in the rivet leg showed a compressive behaviour with a higher magnitude compared with the stresses on the rivet head. The magnitude of the compressive stress reached up to -400 ± 23 MPa. Stress values in the bottom sheet were tensile near the joint and tend towards zero far from the rivet centre. The maximum tensile stress went up to a magnitude of 250 ± 12 MPa and the stresses at 6.5 and -6.5 mm from the rivet axis were not significant. It can also be observed from Fig. 6.3.11 that the measurement error in the rivet leg (± 40 MPa) was higher compared with the stresses in the bottom sheet (± 16 MPa). The rivet has a martensitic structure, so it requires more time to achieve required accuracy and intensity during the measurement of the d-spacing on the Feα(211) reflection. On the other hand, the top and bottom sheets have a ferritic structure, in which it is quite easy to detect the diffraction peak. Thus, the residual strain measured in the rivet leg had a large error.

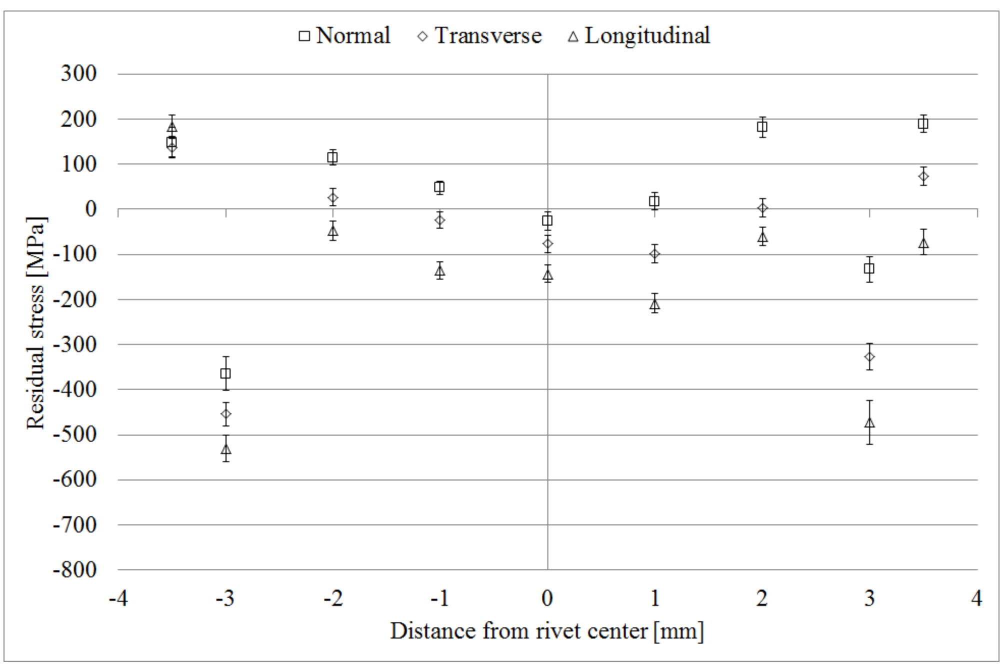

Fig. 6.3.12 Residual stress profiles in bottom sheet along line NN corresponding to the lines shown in Fig. 6.3.9.

The stresses that were measured in the steel sheet along line NN are shown in Fig. 6.3.12. It is clear from Fig. 6.3.12 that the points at 3.0 mm from the rivet centre were in the rivet leg. A high magnitude of compressive stress was observed in the rivet leg. The maximum compressive stress of -530 ± 30 MPa was observed at -3.0 mm from the rivet axis in the longitudinal direction. The stresses in the material showed a symmetric behaviour. It is clear from Fig. 6.3.12 that the normal residual stresses were tensile. During the riveting operation, as soon as the rivet starts flaring, it pushes the material inside the rivet cavity, triggering plastic deformation in the bottom sheet, putting the material in tension in the normal direction. On the other hand, the transverse and longitudinal stresses inside the rivet leg were compressive. However, at a distance of 3.5 and -3.5 mm those stress components (transverse and longitudinal) showed a tensile behaviour. During the bending operation of the SPR process material flows toward the die cavity in a tensile manner. Hence, all the components at a distance of 3.5 and -3.5 mm were in tension. These tensile stresses were counter balanced by the compressive stresses inside the rivet.

Residual stresses at the different locations of the rivet are shown in Fig. 6.3.13. Three points were measured in rivet head and four points were measured on rivet leg. It is clear from Fig. 6.3.13 that the stresses were symmetrical with respect to the rivet axis. The stresses were compressive in nature with a lower magnitude on the rivet head compared with that in the rivet leg. The value of the compressive stress was increased towards the far end of the rivet leg. The highest stresses (-530 ± 21 MPa) were observed at points 1 and 7 which were located at 3.0 mm from the rivet axis and 1.25 mm from the die bottom surface.

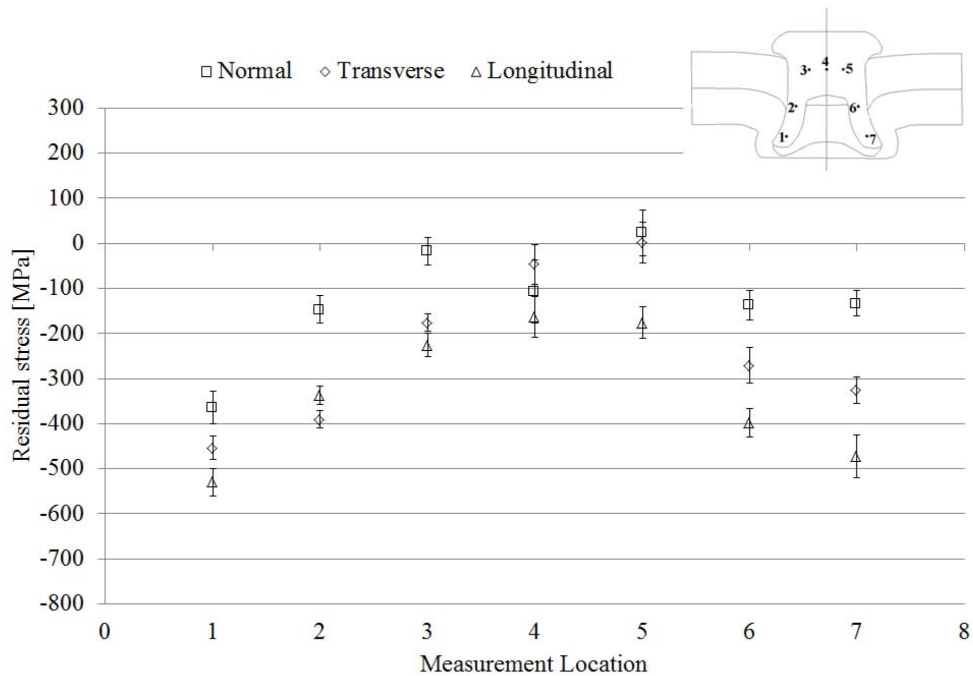

Fig. 6.3.13 Residual stress profiles in rivet on different locations for 2.5 + 2.5 mm G450 carbon steel joint with 555 HV rivet.

6.3.D. 2.5 mm + 2.5 mm G300 steel joint with 555 HV rivet

In this case, a joint was produced by using a G300 steel instead of a G450 carbon steel strip. As the total thickness of the stack was the same as in case C in Table 6.3.1 the same die and rivets were used to produce the joint. The force-displacement curve of this joint was shown previously in Fig. 5.4.1. Strain measurements were made along line L′L′, which was at a depth of 1.25 mm from the undeformed top sheet surface (Fig. 6.3.14). Strain was also measured along line M′M′, which was 1.25 mm up from the undeformed bottom sheet surface to study the behaviour of stress in the steel sheet. To obtain the behaviour of the material inside the die, strains were measured along line N′N′ as shown in Fig. 6.3.14. The position of the measurement points taken along those lines and relative to the joint centreline are summarized in Table 6.3.5. Due to the limitations of beam time, strain was measured only on the right half from the rivet axis.

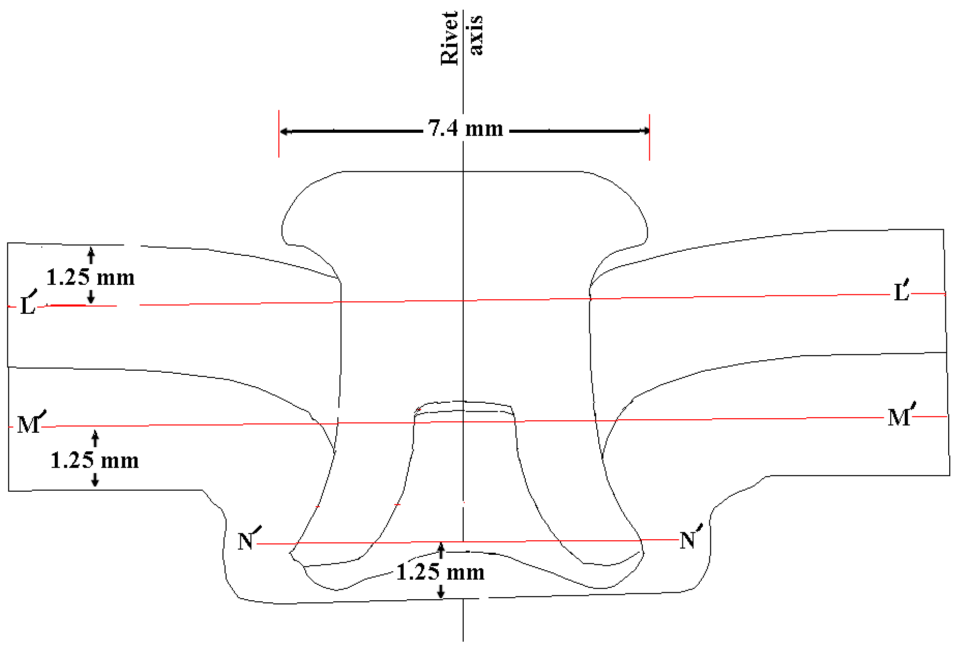

Fig. 6.3.14 Measurement lines for residual stress evaluation in a joint of 2.5 mm G300 + 2.5 mm G300 steel.

Table 6.3.5 Measurement points along lines L′L′, M′M′, and N′N′ shown in Fig. 6.3.14.

Line	L′L′	M′M′	N′N′
Measurement points (mm) from rivet axis shown in Fig. 6.3.14	0.0, 1.5, 5.0, 6.0, 7.0, 8.0	2.0, 5.0, 6.0, 7.0, 8.0	0.0, 1.0, 2.5, 4.0
Total number of points	6	5	4

The stresses evaluated in the steel sheet along lines L′L′ and M′M′ are shown in Figs. 6.3.15 & 16. The points at a distance of 0.0 and 1.5 mm from the rivet axis on line L′L′ are situated on the rivet head and the other points are on the top sheet. It is clear from Fig. 6.3.15 that the stresses inside the rivet head were compressive with a higher magnitude compared with the stresses in steel sheet. The stresses on the top sheet were within the elastic limit of the material.

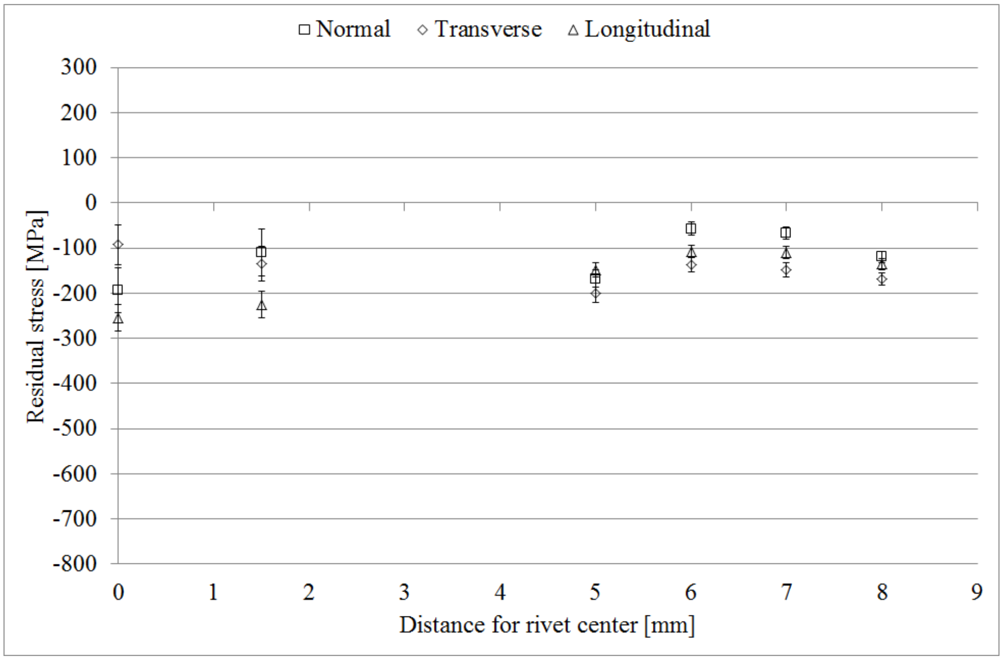

Fig. 6.3.15 Residual stress profiles in top sheet along line L′L′ corresponding to the lines shown in Fig. 6.3.14.

The point 2.0 mm from rivet centre on line M′M′ is in the rivet leg (Fig. 6.3.16). It was clear that the stress in the rivet leg had a higher magnitude compared with the stresses in the bottom sheet. The maximum stress (-431 ± 30 MPa) was observed at 2.0 mm from the rivet axis in the rivet leg. The stresses in the bottom sheet were not significant.

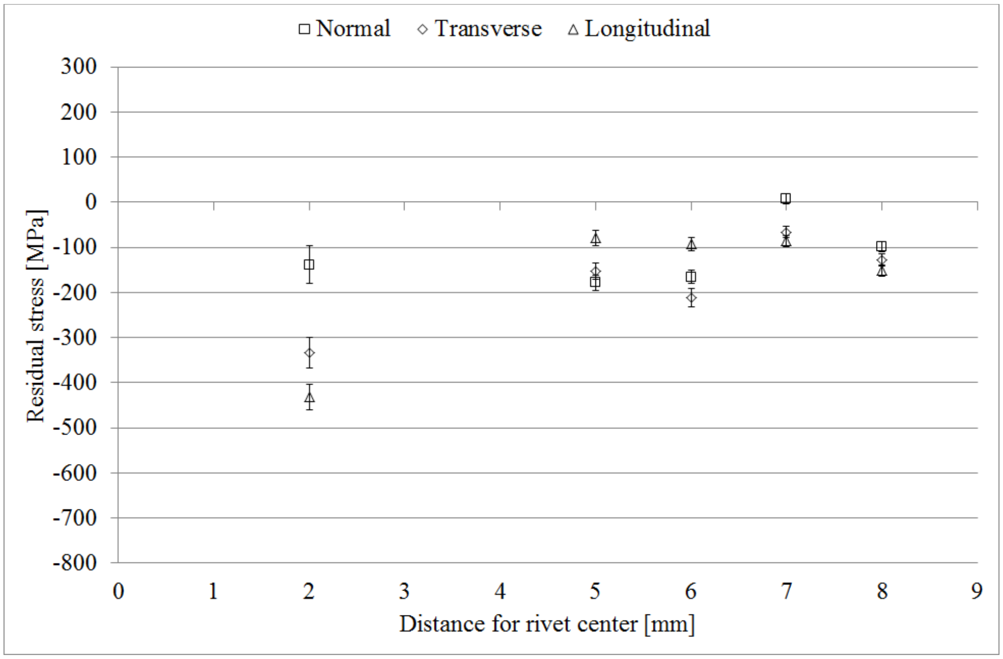

Fig. 6.3.16 Residual stress profiles in bottom sheet along line M′M′ corresponding to the lines shown in Fig. 6.3.14.

The behaviour of the material inside the die was obtained by the stress evaluated along line ŃŃ (Fig. 6.3.17). A high magnitude of compressive stress was observed in the rivet leg at 2.5 mm from the rivet axis. The maximum value of the stress (-317 ± 26 MPa) was found in the longitudinal direction. A high compressive stress (-300 ± 23 MPa) was observed at 0.0 mm from the rivet axis. It could be easily identified from Fig. 6.3.14 that this point (0.0 mm on N′N′ line) was very near to the boundary of the top and bottom sheet. So, the material inside the gauge volume was a mixture of the top and bottom sheets. Due to this reason an unexpected high compressive stress was observed at this point. The stress evaluated at 1.0 mm from rivet centre on line N′N′ was compressive as expected. Surprisingly the stress evaluated at 4.0 mm from rivet centre on line N′N′ was found to be near zero. A tensile stress was expected instead of a zero residual stress. In order to identify the reason, the joint was cross-sectioned after the neutron measurement. A crack was found in the bottom sheet as shown in Fig. 6.3.18 which demonstrated the reason of the zero residual stress at 4.0 mm from the rivet centre.

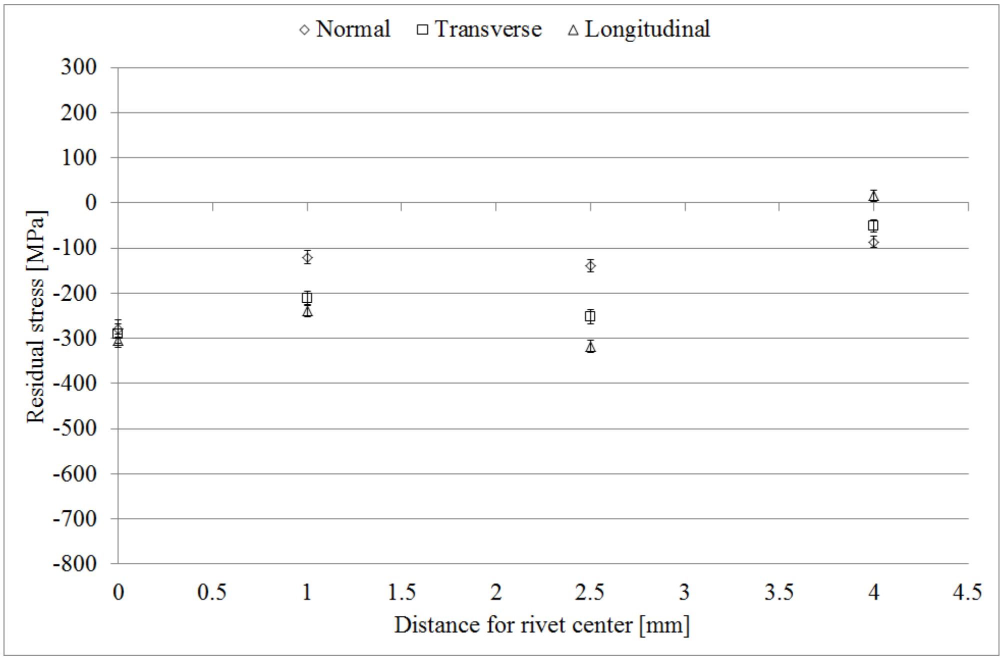

Fig. 6.3.17 Residual stress profiles in bottom sheet along line N′N′ corresponding to the lines shown in Fig. 6.3.14.

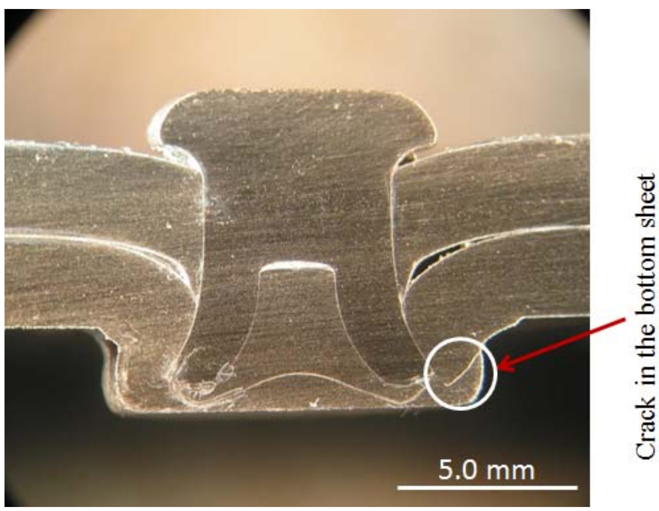

Fig. 6.3.18 Crack observed in the bottom sheet of 2.5 mm + 2.5 mm joint with an 8 mm long rivet with a hardness of 555 HV.

The different locations of the residual stress measurement in the rivet are shown in Fig. 6.3.19. Two points were on the rivet head and four points were in the rivet leg. It was clear that the magnitude of the stress on the rivet head was low. The magnitude of the stress was increased at points 3 and 4 which were positioned in the rivet leg. The highest magnitude of the compressive stress (-438 ± 29 MPa) was observed at point 4 in the longitudinal direction. However, the magnitude started to decrease at points 5 and 6 which indicates a crack was developed inside the rivet. In order to verify this hypothesis the rivet was extracted from joint carefully by inducing no external stress and a crack was observed inside the rivet (Fig. 6.3.20).

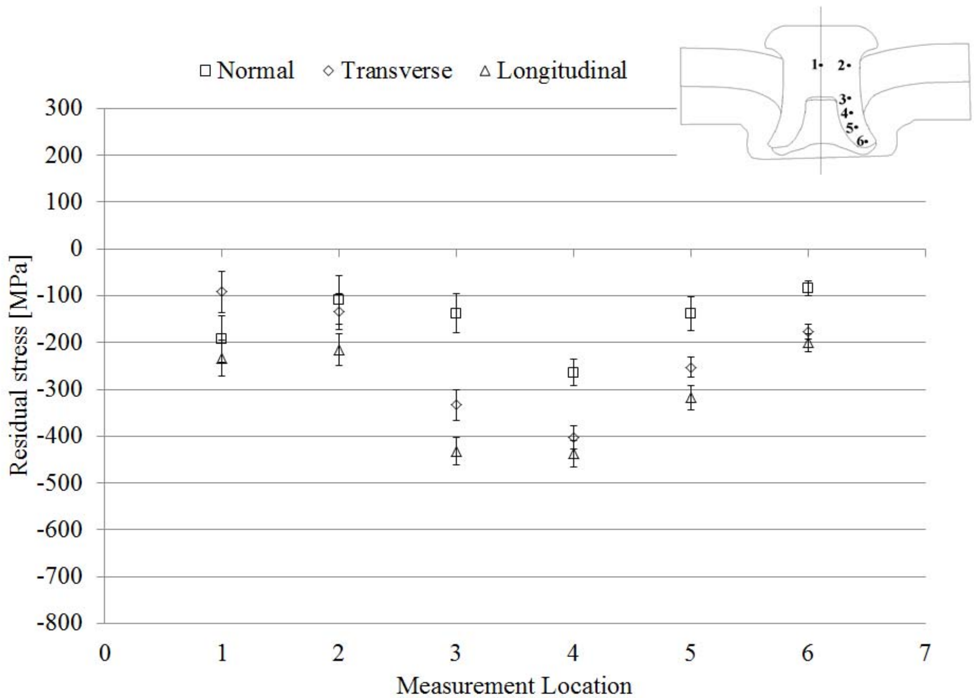

Fig. 6.3.19 Residual stress profiles in rivet on different locations for 2.5 + 2.5 mm G300 carbon steel joint with 555 HV rivet.

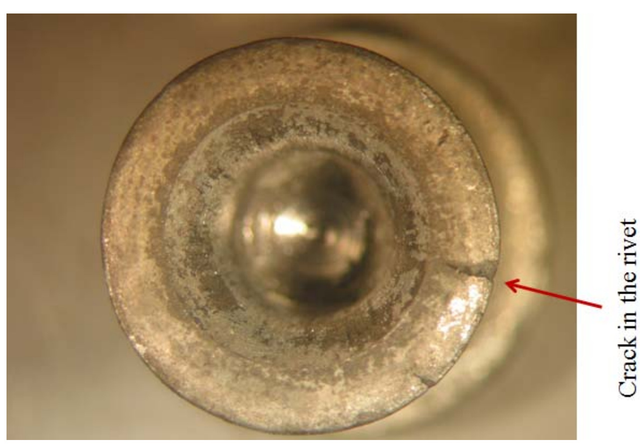

Fig. 6.3.20 Crack in the rivet extracted from 2.5 + 2.5 mm joint with an 8 mm long rivet with a hardness of 555 HV.

6.3.E. 2.0 mm + 2.0 mm G300 steel joint with 480 HV rivet (2.5 mm deep die)

In this case a joint was produced by decreasing the ply material's thickness. A 2.0 mm G300 carbon steel strip was used as the top and bottom sheets. As the total thickness of the stack was reduced to 4.0 mm (2.0 mm at the top and 2.0 mm at the bottom) a 7 mm rivet with a hardness of 480 HV and a flat die (10.0 mm diameter and 2.50 mm deep) were used to produce the joint. The force-displacement curve of this joint was shown previously in Fig. 5.3.2. Strain measurements were made along lines BB and DD, which were at depths of 1.0 mm from the undeformed top sheet surface and 1.0 mm up from the undeformed bottom sheet surface respectively (Fig. 6.3.21). Strain was also measured along line FF (2.0 mm up from the die bottom surface) in order to understand the behaviour of material inside the die cavity. To obtain the stress behaviour inside the rivet head strains were measured along line AA (1.0 mm from the rivet top surface). In order to study the stress profile in the rivet strains were also measured along lines CC, EE, FF and GG which were 4.0, 3.0, 2.0 and 1.0 mm up from the die bottom surface respectively. The positions of the measurement points taken along those lines and relative to the joint centreline are summarized in Table 6.3.6. Again, due to the limitations of the available beam time, strain was measured only on the right half from the rivet axis.

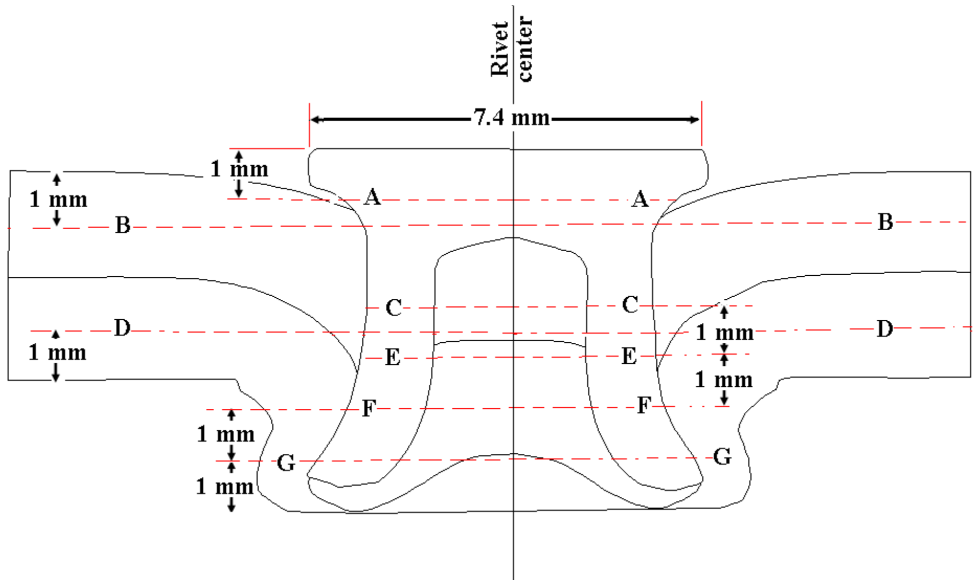

Fig. 6.3.21 Measurement lines for residual stress evaluation in a joint of 2.0 mm G300 + 2.0 mm G300 steel.

Table 6.3.6 Measurement points along lines AA, BB, CC, DD, EE, FF and GG shown in Fig. 6.3.21.

Line	AA	BB and DD	CC	EE	FF	GG
Measurement points (mm) from rivet axis shown in Fig. 6.3.21	0.0, 2.0	5.0, 6.0, 7.0, 8.0	2.0	2.0	0.0, 1.0, 2.5	3.0
Total number of points	2	4*2=8	1	1	3	1

The stresses that were evaluated in the steel sheet along lines BB and DD are shown in Figs. 6.3.22 and 23. It is clear from Fig. 6.3.22 that the stress at 5.0 mm from rivet centre was compressive and the stress that developed at 6.0 mm from the rivet centre was not significant. On the other hand, residual stress in the bottom sheet at 5.0 from the rivet axis was tensile in nature (as expected) and the stresses that were developed beyond 6.0 mm far from the rivet centre were not significant.

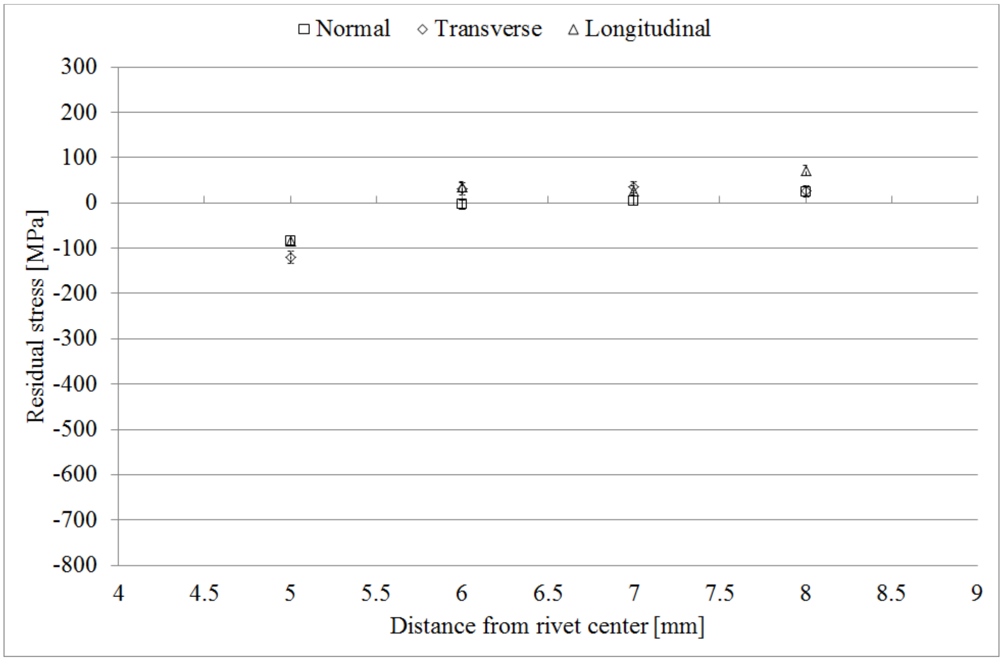

Fig. 6.3.22 Residual stress profiles in top sheet along line BB corresponding to the lines shown in Fig. 6.3.21.

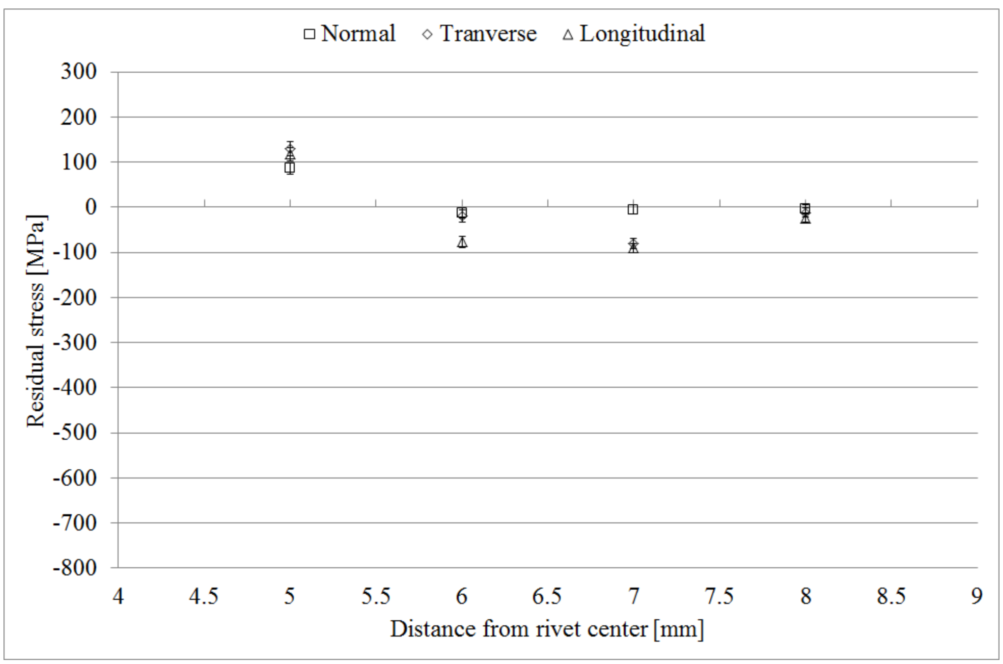

Fig. 6.3.23 Residual stress profiles in bottom sheet along line DD corresponding to the lines shown in Fig. 6.3.21.

To obtain the residual stress inside the die cavity, strains were measured along line FF and the stress profile is shown in Fig. 6.3.24. It should be noted that the point at 2.5 mm from the rivet axis was situated in the rivet leg. The stress in the material showed a compressive behaviour at 0.0 mm. However, a tensile behaviour of stress was observed at 1.0 mm in normal direction. Again, the stress in the rivet leg was compressive according to the expectation.

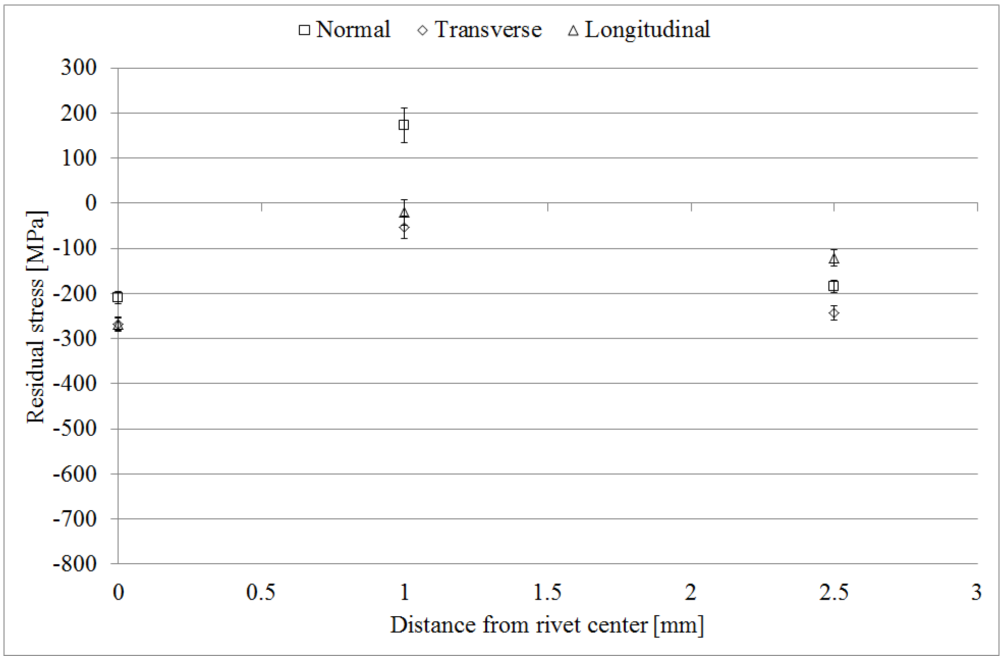

Fig. 6.3.24 Residual stress profiles in bottom sheet along line FF corresponding to the lines shown in Fig. 6.3.21.

Residual stress at different locations in the rivet is shown in Fig. 6.3.25. Two points were in the rivet head and four points were in the rivet leg. It was clear that the stress value in the rivet head was low. The magnitude of residual stress in the rivet leg remained in the order of -200 MPa at points 3, 4 and 5. However, the magnitude was increased at point 6 (3.0 mm from the rivet axis and 1.0 mm from the die bottom surface). Thus, it was easy to conclude that the compressive residual stress increased toward the rivet leg.

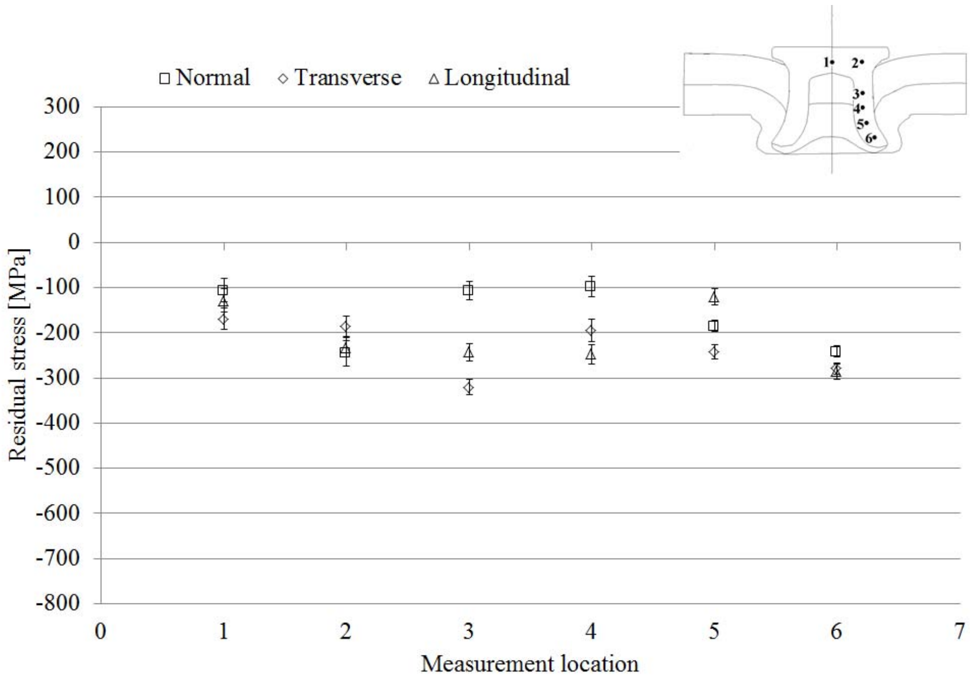

Fig. 6.3.25 Residual stress profiles in rivet on different locations for 2.0 + 2.0 mm G300 carbon steel joint with 480 HV rivet (2.5 mm deep die).

6.3.F. 2.0 mm + 2.0 mm G450 steel joint with 555 HV rivet (2.1 mm deep die)

In this case the die depth was reduced to 2.1 mm from 2.5 mm by keeping the diameter of the die the same as in case E according to Table 6.3.1. The material thickness was kept the same but a different material (G450 instead of G300 carbon steel sheets) was used. A 7 mm rivet was used again as the thickness was unchanged, but the rivet hardness was changed to 555 HV. The force-displacement curve of this joint was shown previously in Fig. 5.2.3a. As the component of interest is rivet the strain was measured at 11 different locations as shown in Fig. 6.3.26. Due to the experience gained in the residual stress evaluation it was easy for the author to align the specimens to measure the strain only inside the rivet. The residual stresses at different locations are shown in Fig. 6.3.26.

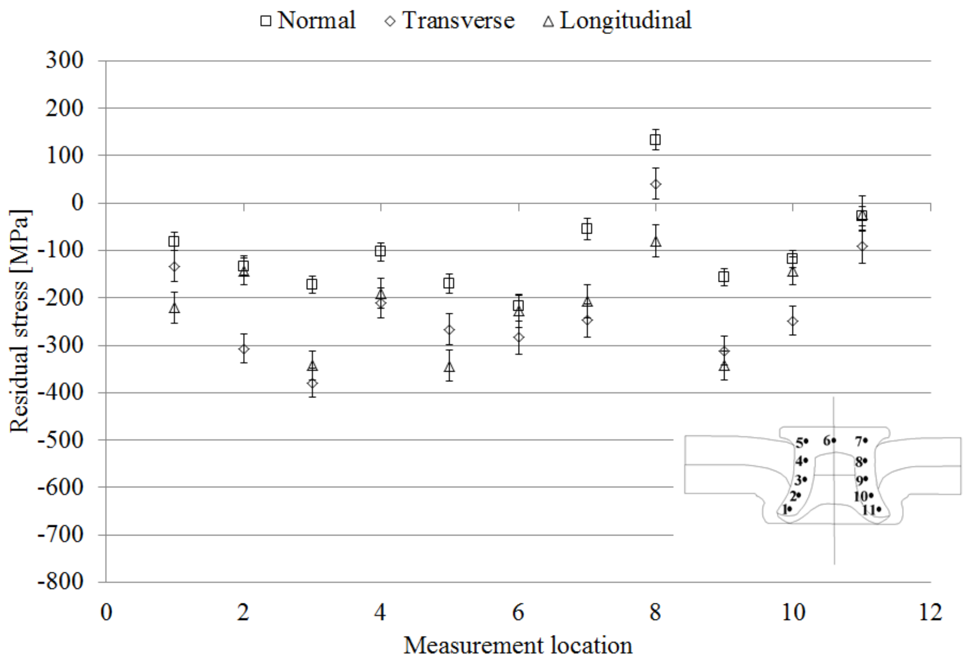

Fig. 6.3.26 Residual stress profiles in the rivet at different locations for a joint of 2.0 + 2.0 mm G450 carbon steel with a 555 HV rivet.

It is clear from Fig. 6.3.26 that the overall residual stress inside the rivet was compressive and the stress profile was approximately symmetric (except for position 8) with respect to the rivet axis. The maximum compressive residual stress was found at point 3 in the rivet leg near to the interface between the top and bottom sheets. The magnitude of the compressive residual stress was -380 ± 41 MPa in the transverse direction. The stress that was evaluated at the corner of the rivet (locations 1 and 11) was close to zero. This value of the stress indicated a crack had developed inside the rivet near those locations. To verify this, the rivet was extracted from the joint and cracks were indeed observed as shown in Fig. 6.3.27.

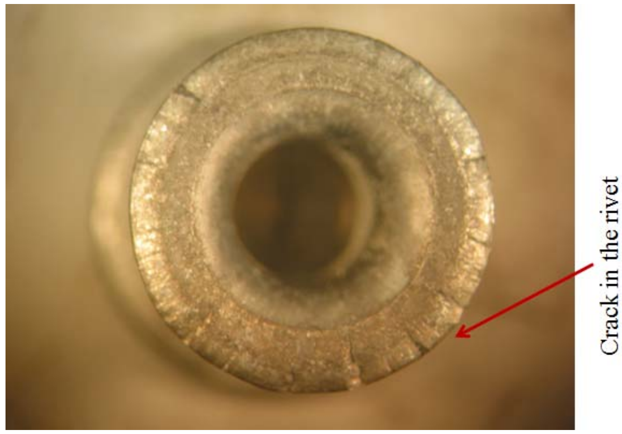

Fig. 6.3.27 Crack in the rivet extracted from 2.0 + 2.0 mm G450 steel joint with a 7 mm long rivet with a hardness of 555 HV.

6.3.G. 2.0 mm + 2.0 mm G450 steel joint with 480 HV rivet (2.1 mm deep die)

To understand the behaviour of residual stress in SPR joints for a change in rivet hardness another joint of 4.0 mm total stack thickness was chosen by keeping all other parameters the same as in case F according to Table 6.3.1. A rivet with a reduced hardness (480 HV) was chosen. The force-displacement curve of this joint was shown in the previous chapter in Fig. 5.2.3b. Again, strain was measured at 11 different locations as shown in Fig. 6.3.28.

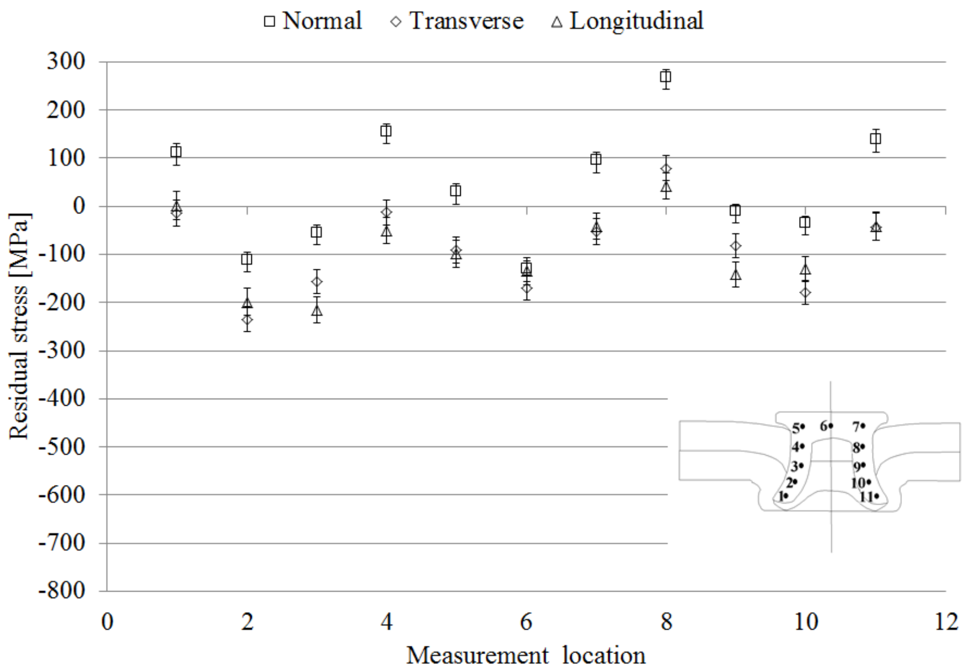

Fig. 6.3.28 Residual stress profiles in rivet on different locations for a joint of 2.0 + 2.0 mm G450 carbon steel with 480 HV rivet.

Only the normal component of the stresses showed a tensile behaviour while the transverse and longitudinal stress components showed a compressive behaviour (Fig. 6.3.28). The magnitude of the compressive stress was in the order of -200 MPa. The maximum value of the compressive residual stress (-235 ± 24 MPa) was observed at location 2 in the transverse direction. Unlike the previous condition, the compressive stresses were lower in magnitude (for a 555 HV rivet stress reached up to a value of -380 ± 41 MPa) due to the soft rivet. Again, stress values at locations 1 and 11 were near to zero due to a crack formed inside the rivet (Fig. 6.3.29). It should be noted that, multiple cracks observed in the case F (Fig. 6.3.27). However, in this case fewer cracks were found (Fig. 6.3.29) due to the soft rivet.

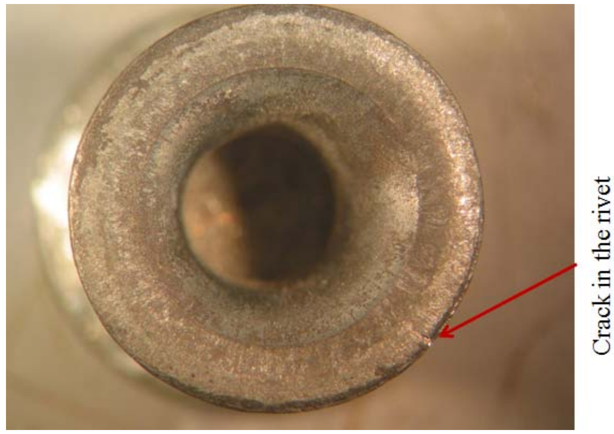

Fig. 6.3.29 Crack in the rivet extracted from 2.0 + 2.0 mm G450 steel joint with a 7 mm long rivet with a hardness of 480 HV.

6.3.H. 2.0 mm + 2.0 mm G300 steel joint with 555 HV rivet (2.1 mm deep die)

To study the residual stress profile in the SPR joint for a soft sheet material, another joint of 4.0 mm total stack thickness was chosen. In this case 2.0 mm G300 carbon steel was used as the top and bottom sheets. A 555 HV rivet was used to produce the joint by keeping the rivet length and the die parameters the same. The force-displacement curve of this joint was shown previously in Fig. 5.3.2. Again, strain was measured at 11 different locations as shown in Fig. 6.3.30, to follow the consistency.

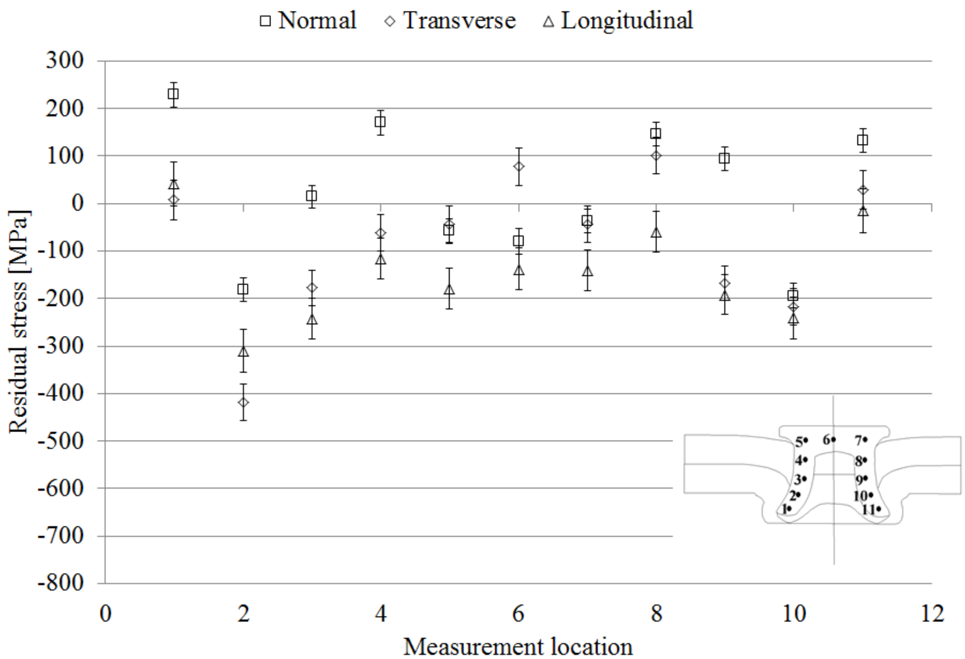

Fig. 6.3.30 Residual stress profiles in rivet on different locations for a joint of 2.0 + 2.0 mm G300 carbon steel with 555 HV rivet.

It is clear from Fig. 6.3.30 that the residual stress inside the rivet was mainly compressive and the stress profile was symmetric with respect to the rivet axis. The magnitude of the compressive residual stress increased towards the rivet leg and away from rivet centre. The maximum compressive residual stress was -420 ± 27 MPa in the transverse direction at location 2. The stress value in longitudinal and transverse directions that was evaluated at the corner of the rivet (locations 1 and 11) was near to zero. This value of stress indicates a crack had formed inside the rivet at those locations and verified by the observation from extracted rivet (Fig. 6.3.31). It should be noted that the number of cracks in the rivet leg again increased compared with the case G in Table 6.3.1 because of the hard rivet.

Crack in the rivet

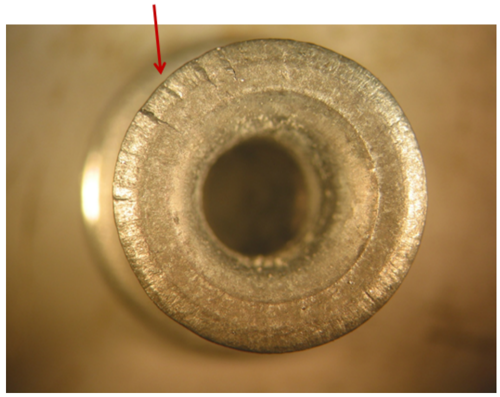

Fig. 6.3.31 Crack in the rivet extracted from 2.0 mm + 2.0 mm G300 steel joint with a 7 mm long rivet with a hardness of 555 HV.

6.3.I. 2.0 mm + 2.0 mm G300 steel joint with 480 HV rivet (2.1 mm deep die)

The effect of rivet hardness on the residual stress profile in soft steel sheets was investigated in this condition. All parameters were kept the same except the rivet hardness. A rivet with a hardness of 480 HV was chosen. The force-displacement curve of this joint was shown in the previous chapter in Fig. 5.3.2. To follow the consistency of the experiment, strain was measured again at 11 different locations as shown in Fig. 6.3.32.

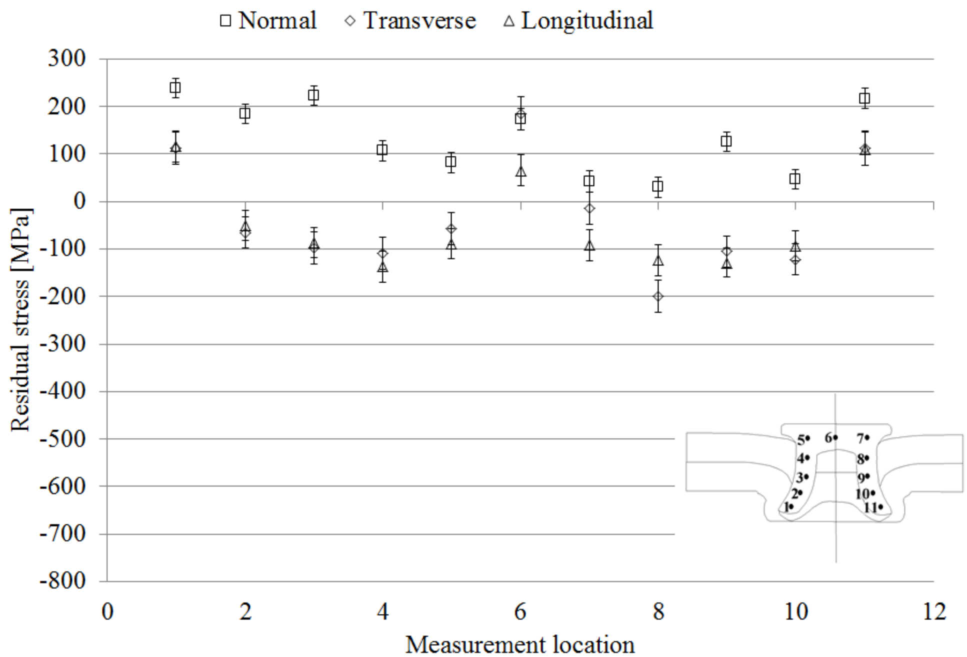

Fig. 6.3.32 Residual stress profiles in rivet on different locations for a joint of 2.0 + 2.0 mm G300 carbon steel with 480 HV rivet.

Residual stress observed in Fig. 6.3.32 was symmetric with respect to the rivet axis. It was also clear that the normal stress components were tensile in nature and compressive residual stresses found in the transverse and longitudinal directions. At the beginning, the magnitude of the compressive residual stresses increased towards the rivet leg. Stresses at locations 2, 3, 4 and 8, 9, 10 are almost in the same order of -100 MPa. Maximum compressive stress was -200 ± 23 MPa in the transverse direction at location 8. The stress components at locations 1 and 11 were tensile. As a soft rivet was used in this case a large rivet flaring was occurred (rivet flaring was 1.11 mm in Table 5.8). Due to this reason a tensile residual stress was observed at the far end of the rivet leg.

Unlike the previous three conditions (cases F, G and H in Table 6.3.1, all of them are 4.0 mm joint), stress components at locations 1 and 11 are found to be tensile. In the previous conditions the stress components at the same locations found to be zero (Fig. 6.3.30). This means that no crack should be observed in the rivet leg. The rivet was extracted from the joint and no crack was found in the extracted rivet (Fig. 6.3.33).

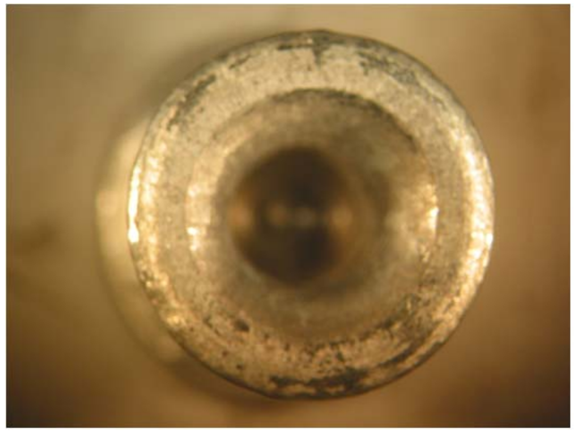

Fig. 6.3.33 No crack in the rivet extracted from 2.0 mm + 2.0 mm G300 steel joint with a 7 mm long rivet with a hardness of 480 HV.

6.4 Effect of ply materials' hardness on residual stress profile

Ply materials' hardness plays a very important role on the residual stress profile in different SPR joints. Two different hardnesses of material consisting of three different thicknesses were chosen to investigate the effect of materials' hardness on the residual stress profile.

6.4.1 3 mm (1.5 mm + 1.5 mm) stack thickness

In order to investigate the effect of ply material's hardness on the residual stress profile, at first, two joints of 3.0 mm total thickness were produced by two different materials (G450 and G300 carbon steel) by keeping all other parameters the same. The length of the rivet was 6.0 mm (480 HV). In addition, a flat die (9.0 mm diameter and 2.0 mm deep) was used to produce the joints. Transverse residual stresses (for normal and longitudinal stress see Appendix B) were measured at 8 different locations inside the rivet as shown in Fig. 6.4.1. The force-displacement curves of these joints were shown in the previous chapter in Fig. 5.4.3 (inset of Fig. 6.4.1).

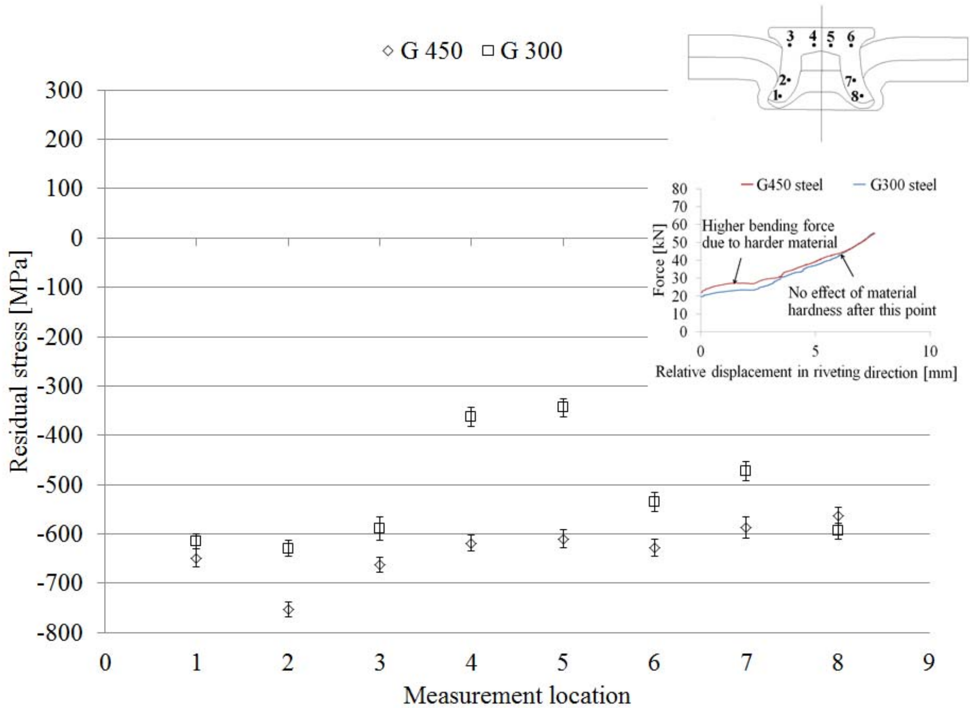

Fig. 6.4.1 Transverse residual stress profile depending on material hardness of 1.5 mm + 1.5 mm joint.

It is clear from Fig. 6.4.1 that the magnitudes of the residual stress at locations 1 and 8 were similar for both joints. In the previous chapter (Chapter 5.4), it was observed that after a certain displacement, the two curves became identical: the role of the material was insignificant (Fig. 5.4.3). Due to this reason, the magnitude of the residual stress was also similar at the corner of the rivet leg. The residual stresses in the rivet leg varied about 100 MPa depending on the material hardness at locations 2 and 7. High compressive stresses were observed for the hard material. This high compressive stresses can be related to the high force required while producing the joint. A significant deviation in the residual stress was observed in the middle of the rivet head at locations 4 and 5 in Fig. 6.4.1. The magnitude of the compressive stresses was -350 ± 23 MPa for the soft sheet material. It was believed that this residual stress in the rivet head originated during the piercing stage of the riveting process. It is clear from Fig. 5.4.3 a high force was required during the piercing stage for the hard sheet. Due to this reason, the magnitude of residual stresses was high in the rivet head for hard material.

6.4.2 4 mm (2.0 mm + 2.0 mm) stack thickness

To investigate the effect of ply material's hardness on residual stress profile further for a thicker joint, two joints of 4.0 mm total thickness were produced by two different materials (G450 and G300 carbon steel) by keeping all other parameters the same. As the joint thickness was increased, a long rivet (7.0 mm long and hardness of 555 HV) was used to produce those joints. A flat die with increased die recess volume (10.0 mm diameter and 2.1 mm deep) was used to produce the joints. The force-displacement curves of these joints were shown in the previous chapter (Chapter 5.4) in Fig. 5.4.2. Transverse residual stresses (for normal and longitudinal stress see Appendix B) were measured at 11 different locations inside the rivet as shown in Fig. 6.4.2.

It is clear from Fig. 6.4.2 that the magnitude of the residual stresses in the rivet leg (locations 1-4 and 8-11) varied in the order of 100 MPa depending on material hardness. The harder the ply materials are the higher the compressive stresses in the rivet leg will be. However, the value of the stresses on the rivet head (measurement locations 5-7) changed more significantly due to a change in material hardness. The stresses were 150 MPa higher in magnitude for the soft materials due to the lower force required during the piercing stage.

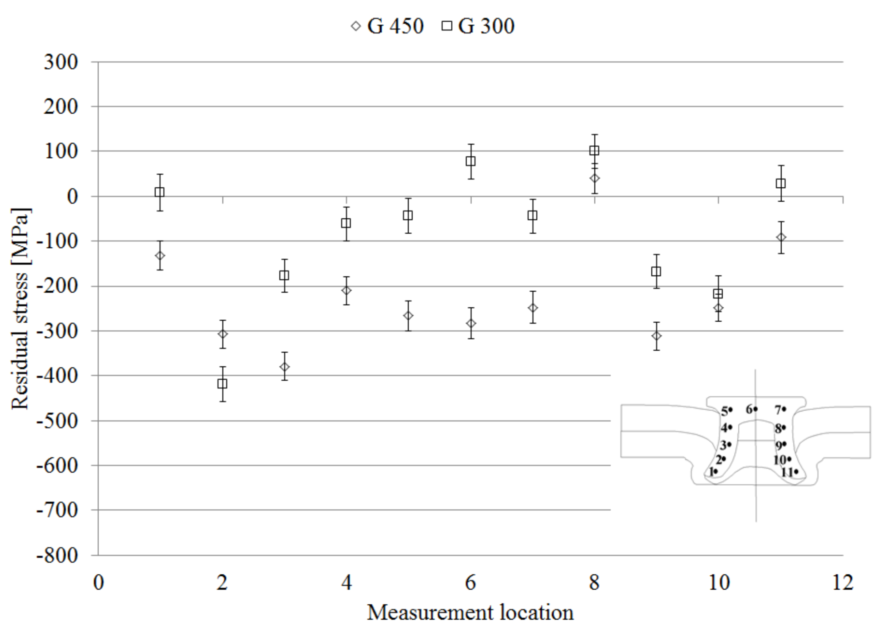

Fig. 6.4.2 Transverse residual stress profile depending on material hardness of 2.0 mm + 2.0 mm joint.

6.4.3 5 mm (2.5 mm + 2.5 mm) stack thickness

To investigate the effect of ply material's hardness on residual stress profile for a much thicker joint, two joints of 5.0 mm total thickness were produced by two different materials (G450 and G300 carbon steel) by keeping all other parameters the same. As the joint thickness was increased again, a long rivet (8.0 mm, 555 HV) was used to produce those joints. In addition, a flat die with increased die recess volume (11.0 mm diameter and 2.35 mm deep) was used. The force-displacement curves of these joints were shown in the previous chapter in Fig. 5.4.1. Transverse residual stresses (for normal and longitudinal stress see Appendix B) were measured at 4 different locations inside the rivet (2 locations were on the rivet head and another 2 locations were in the rivet leg) as shown in Fig. 6.4.3.

Unlike the previous two conditions the magnitude of the residual stresses inside the rivet leg (locations 3 and 4) was high for the softer material. In order to find the reason, the joints were cross-sectioned after the residual stress measurement. The cross-sections of these joints are shown in Fig. 6.4.4. A gap under the rivet head was observed for the G450 sheet while there was no gap for the G300 steel sheet. The material inside the rivet bore was packed for G300 steel, which puts more compressive pressure on rivet leg. For this reason, high compressive stress was observed in G300 steel joint.

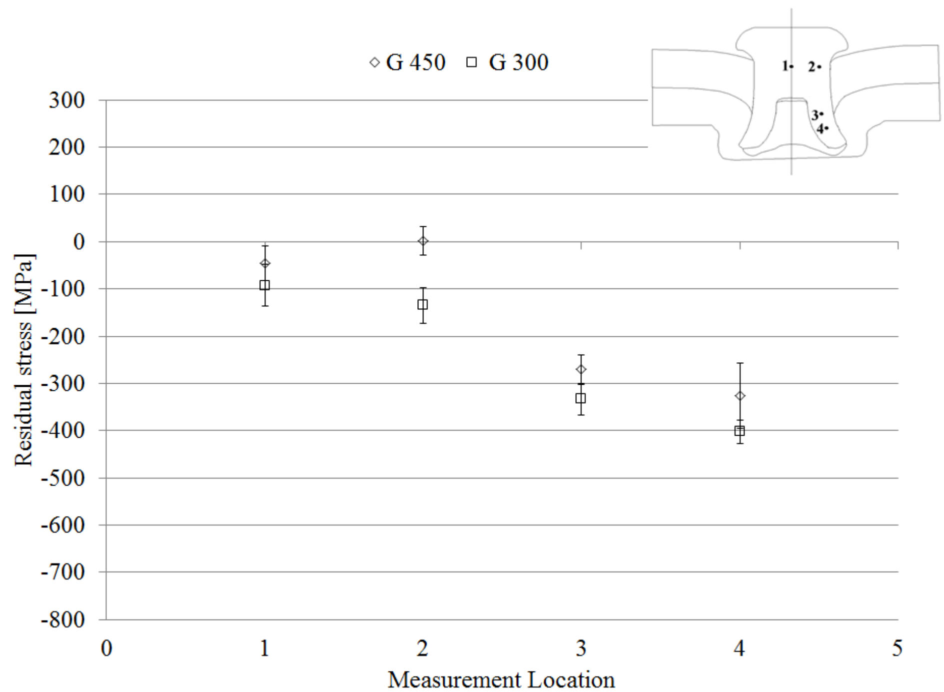

Fig. 6.4.3 Transverse residual stress profile depending on material hardness of 2.5 mm + 2.5 mm joint.

It is clear from Fig. 6.4.3 that no significant change in the residual stress profile on the rivet head was observed due to a change in material hardness. On the other hand, significant change in the residual stress profile was observed in the previous two conditions. A strong rivet was used to produce this joint and the rivet head was much thicker compared with the rivet leg (Fig. 6.4.4). Due to this reason, high energy required for developing a high residual stress inside the rivet head. Thus, the stresses that developed at locations 1 and 2 were negligible.

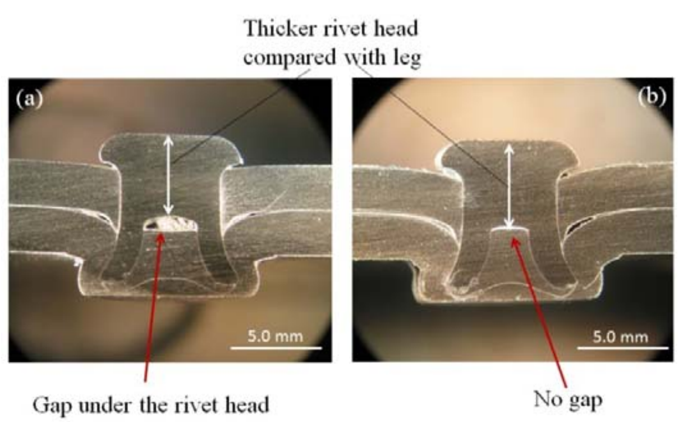

Fig. 6.4.4 Cross- sections of riveted joint of 5.0 mm stack thickness (a) G450 and (b) G300 carbon steel.

6.5 Effect of ply materials' thickness on residual stress profile

Ply materials' thickness also plays a very important role on the residual stress profile in SPR joints. Three different thicknesses were considered to study the effect of material thickness on residual stress profile. The study also considered two different materials (G450 and G300 carbon steel). Due to the similar nature of the results, only joints for G450 carbon steel are shown here (for G300 steel joints see Appendix B).

6.5.1 5.0 mm vs. 4.0 mm with 555 HV rivet

To investigate the effect of materials' thickness on residual stress at first, two different stack thicknesses of 5.0 mm and 4.0 mm were considered. A 555 HV rivet with a length of 8.0 and 7.0 mm was used to produce 5.0 mm stack and 4.0 mm stack joints respectively. The die geometry was also different for those joints. A big die (flat die, 11.0 mm diameter and 2.35 mm deep) was used for 5.0 mm joint and a comparatively smaller die (flat die, 10.0 mm diameter and 2.1 mm deep) was used for 4.0 mm joint. The force-displacement curves for these joints are shown in Fig. 5.5.1. Stresses were measured at 7 different locations and the corresponding residual stresses are also shown in Fig. 6.5.1.

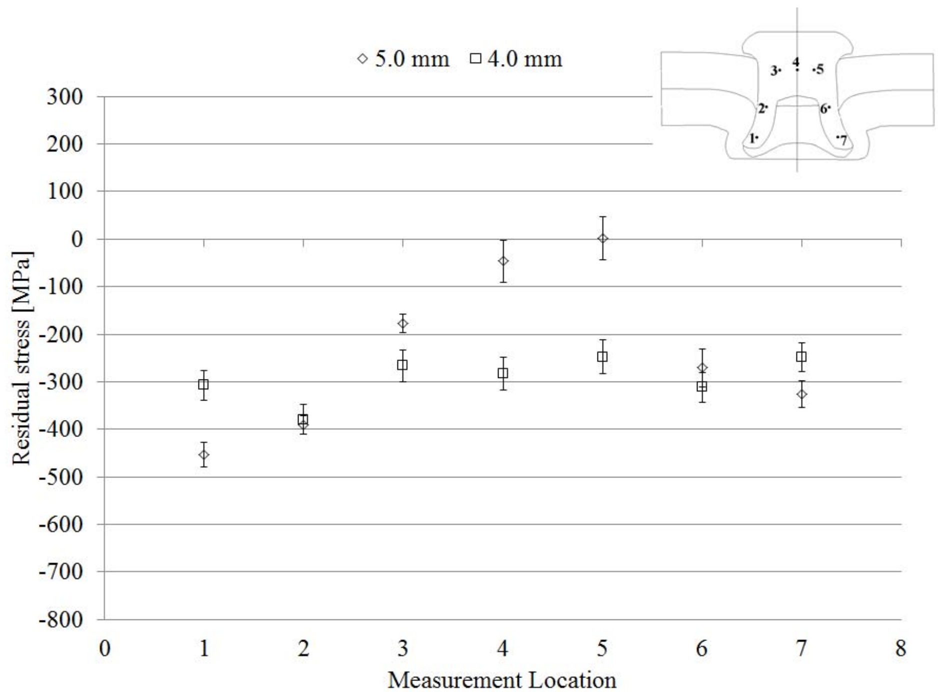

Fig. 6.5.1 Transverse residual stress profile depending on the material thickness of G450 steel joint with 555 HV rivet.

It is clear from Fig. 6.5.1 that the residual stresses on the rivet head (locations 3, 4 and 5) were negligible for the 5.0 joint whereas stresses had a magnitude in the order of -275 MPa for the 4.0 mm joint. It is also clear from Fig. 6.5.2 that a thick rivet head was used for the 5.0 joint. Due to this, stresses that were developed inside the rivet head were not significant for the 5.0 mm joint. It can be observed from Fig. 6.5.1 that the residual stresses were more compressive toward the rivet leg for the 5.0 mm joint.

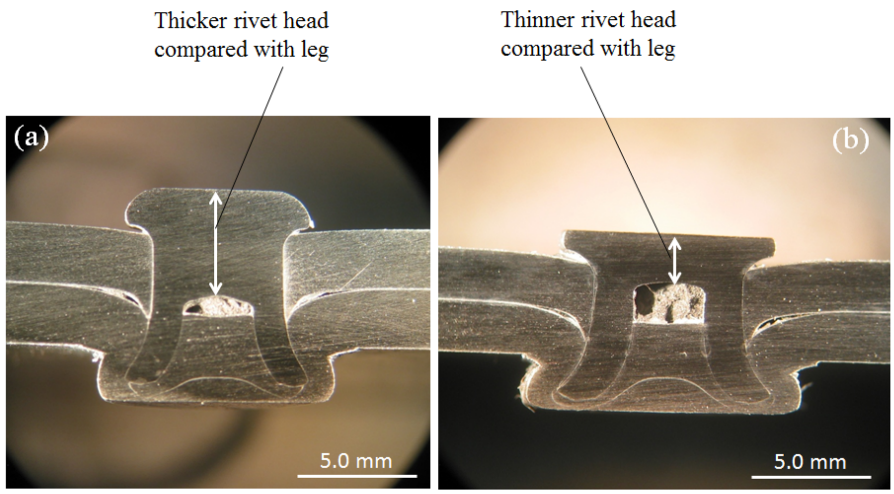

Fig. 6.5.2 Cross- sections of riveted joint of G450 steel (a) 5.0 and (b) 4.0 mm.

6.5.2 4.0 mm vs. 3.0 mm with 480 HV rivet

To investigate the effect of materials thickness on the residual stress profile, joints of two different stack thicknesses (4.0 and 3.0 mm) were considered. A 480 HV rivet with a length of 7.0 and 6.0 mm was used to produce the 4.0 and 3.0 mm joints respectively. The geometry of the die was also different for those joints. A big die (flat die, 10.0 mm diameter and 2.1 mm deep) was used for the 4.0 mm joint and a comparatively smaller die (flat die, 9.0 mm diameter and 2.0 mm deep) was used for the 3.0 mm joint. The force-displacement curves for these joints are shown in Fig. 5.5.3. Stresses were measured at 7 different locations and the corresponding residual stresses are shown in Fig. 6.5.3.

It is clear from Fig. 6.5.3 that a distinctive change in residual stress profile occurred due to a change in the material thickness. A high value of compressive stress was observed for the thin joint. Even in the rivet head residual stress was highly compressive, reached to a value of -650 ± 26 MPa, for the thin joint. This high value of residual stress could be related with high gradient of force during the flaring period of the SPR process for the thin joint (Fig. 5.5.3).

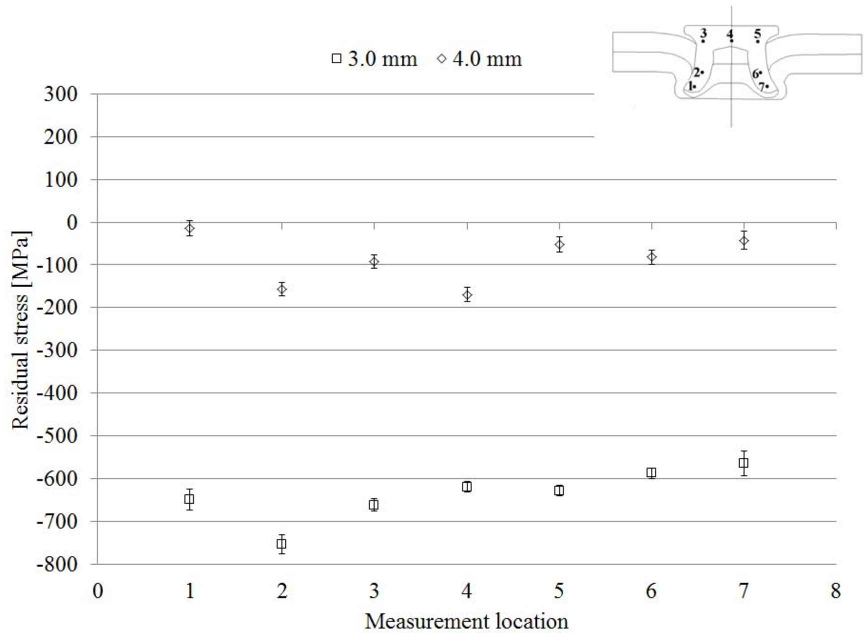

Fig. 6.5.3 Transverse residual stress profile depending on material thickness of G450 steel joint with 480 HV rivet.

6.6 Effect of rivet hardness on residual stress profile

Rivet hardness plays a very important role on the residual stress profile in SPR joints. Two different hardnesses of rivet (555 and 480 HV) were considered along with two different hardnesses of material (G450 and G300 carbon steel) for this study.

6.6.1 G450 steel

To investigate the effect of rivet hardness on residual stress profile at first, a joint of G450 steel sheet with total stack thickness of 4.0 mm was considered. A 7.0 mm long rivet was used to produce the joints with two different hardnesses of rivet (555 and 480 HV). The same die was used due to the same total thickness (flat die, 10.0 mm diameter and 2.1 mm deep). Stresses were measured at 11 different locations and the corresponding residual stresses are also shown in Fig. 6.6.1. The force-displacement curves for these joints are shown in Fig. 5.6.3 (inset of Fig. 6.6.1).

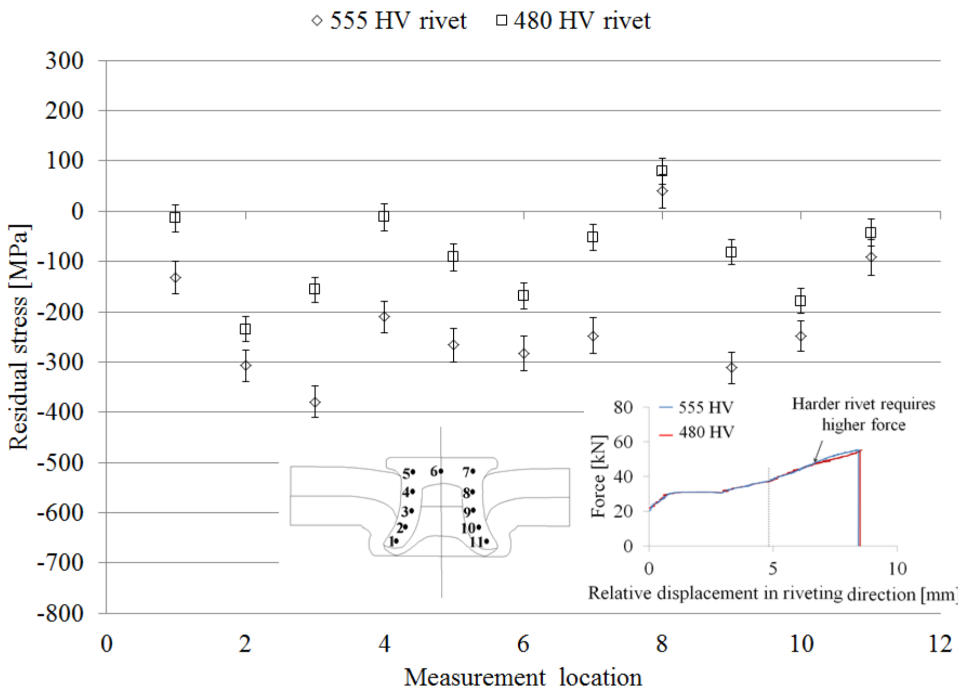

Fig. 6.6.1 Transverse residual stress profile depending on rivet hardness of G450 steel joint.

It is clear from Fig. 6.6.1 that the trend of residual stress was similar for both the hard and soft rivets. The average magnitude difference was 150 MPa and high compressive stresses were observed for the hard rivet. High compressive stresses were observed for hard rivet even on the rivet head (locations 5, 6 and 7). This high value of residual stress could be related with the high gradient of the force during the flaring period of the SPR process for the 555 HV riveted joint (Fig. 5.6.3).

6.6.2 G300 steel

Residual stress was further evaluated in a soft material (G300 steel) in order to understand the effect of rivet hardness on residual stress profile. A 7.0 mm long rivet was used to produce the joints with two different hardnesses of the rivet (555 and 480 HV). The same die was used due to the same total thickness (flat die, 10.0 mm diameter and 2.1 mm deep). Stresses were measured at 11 different locations and the corresponding residual stresses are also shown in Fig. 6.6.2. The force-displacement curves for these joints are shown in Fig. 5.6.2 (inset of Fig. 6.6.2).

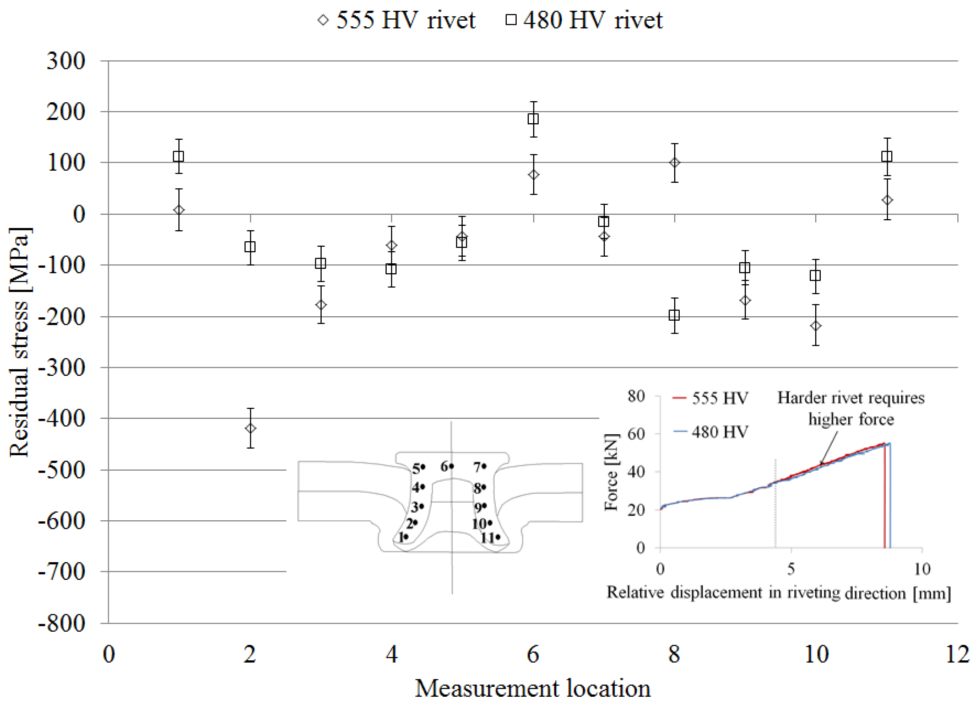

Fig. 6.6.2 Transverse residual stress profile depending on rivet hardness of G300 steel joint.

It is clear from Fig. 6.6.2 that the trend of residual stress was similar for both the hard and the soft rivet except the two extreme positions (locations 1 and 11). At locations 1 and 11 the magnitude of the residual stress was zero for the hard rivet which indicates a crack was formed inside the rivet. An extracted rivet from the joint confirmed the crack (Fig. 6.3.31). However, for the soft rivet these locations showed a tensile behaviour of residual stress indicated no crack was formed inside rivet which was verified by the extracted rivet (Fig. 6.3.33). For the case of the hard rivet, the magnitude of the residual stress (-420 ± 52 MPa) was highest (20% of the yield strength) at location 2, which was -380 ± 79 MPa in difference with the soft rivet at the same location. On the rivet head (locations 5, 6 and 7) stresses were almost similar within the uncertainty during measurement. In the rivet leg compressive stresses were high for the hard rivet which can be related with high gradient of force during flaring period of the SPR process for the 555 HV riveted joint (Fig. 5.6.2).

6.7 Summary

Residual stress measurement was conducted at three different phases. At first a reproducibility and feasibility test was carried out. It was found that the neutron diffraction technique can successfully predict the position of the rivet leg inside a joint.

After the successful completion of the feasibility test by neutron diffraction, another investigation was carried out to optimize the parameters for meaningful evaluation of residual stress by minimizing the measurement errors involved in this technique. An optimum instrument condition was suggested for the residual stress measurement in SPR joints by neutron diffraction. Typically, 240 and 900 seconds are necessary to achieve error (measurement uncertainty) within the range of ± 50 µm in sheet material for 1.0 and 0.125 mm^3 gauge volumes respectively while the neutron path length is around 4.0 mm.

The third phase of the residual stress investigation was conducted to evaluate stress in a family of SPR joints comprising nine different joints by applying the optimum instrument condition. The behaviours of the sheet material and the rivet inside a joint were investigated by studying the residual stress profile. The effects of different process parameters on the residual profiles are discussed. The high stress was observed for thin and hard joints due to the high force-gradient during the riveting process. A symmetric residual stress profile was observed for SPR joints of soft materials due to a negligible effect of the C-frame deflection. It was observed that neutron diffraction can also detect a crack inside a joint. The dependency of residual stress profile on rivet hardness is also discussed. It was evident that the magnitude of residual stress increased with increase in rivet hardness to a certain limit. Then a zero residual stress was observed due to cracking.

7 STATIC STRENGTH OF SPR JOINTS

7.1 Introduction

The strength of a SPR joint is primarily determined by the interlock between a rivet shank and sheet materials [109, 136]. This strength depends on many factors such as width of a specimen, thickness and properties of sheets, die specifications (die profile, diameter and depth) and rivet properties (diameter, length and hardness) [59, 69, 75, 79, 122, 168]. The strength also depends on the loading conditions, for example, cross-tension and lap-shear [84, 137, 149, 179]. It was found that cross-tension always gave a lower strength compared with lap-shear. In order to predict the strength of a SPR joint, Jonsson [248], Porcaro et al. [179, 203] used finite element simulation as a tool, while Sun and Khaleel [136] and He [171] proposed an analytical approach to predict the strength. Those analytical methods, used to predict the strength of a SPR joint, required some geometrical dimensions which can be obtained by physically measuring the cross-section of a joint. Most of the previous research conducted either in lap-shear or cross-tension loading condition. Sun and Khaleel [136] mentioned joint strength under coach-peel and lap-shear condition can be related to its cross-tension strength. However, this relationship formula is unavailable in the open literature. In order to obtain the strength of a specific SPR joint one needs to examine both loading conditions.

In this study the effect of different process parameters (ply material properties, rivet hardness and die dimensions) on the static strength of a SPR joint in cross-tension and lap-shear loading conditions was investigated systematically. The aim was to establish a relationship between SPR process parameters (force-displacement) and joint strength by using the rivet flaring model (Chapter 5.10) and to develop a correlation between the strengths in two loading conditions (lap-shear and cross-tension) based on the tensile resistance formulae presented in Euro-code 9 [172] for different failure modes.

7.2 Approach

Nine different combinations of joints (cases A to I in Table 7.2.1) comprised of three types of thicknesses (5.0, 4.0 and 3.0 mm) and two different hardnesses of material (G300 and G450 carbon steel with hardness of 198 HV and 270 HV respectively), and two values of rivet hardness (555 and 480 HV) were considered for this study. Three different lengths of rivet were used depending on the joint total thickness: 6, 7 and 8 mm long rivet for 3, 4 and 5 mm joint respectively. A die with a flat profile was used for all conditions but with a high die recess volume for the thick joint and a low die recess volume for the thin joint. Five single point joint specimens were produced for each joining configuration (cross-tension and lap-shear) as described in Figs 4.10.1 and 3. The detailed experimental procedure was described in chapter 4.10. The effective length of the rivet in the bottom sheet (t_{eff}) and the deformed rivet diameter (D_t) were measured by metallographic cross-sections (Figs 7.2.1 and 2.3.1).

Table 7.2.1 Summary of different joining combinations for static strength analysis.

<table>
<tr><th colspan="2">Case no.</th><th>A</th><th>B</th><th>C</th><th>D</th><th>E</th><th>F</th><th>G</th><th>H</th><th>I</th></tr>
<tr><td colspan="2">Material</td><td>G450 steel</td><td colspan="2">G300 steel</td><td colspan="2">G450 steel</td><td colspan="2">G300 steel</td><td>G450 steel</td><td>G300 steel</td></tr>
<tr><td colspan="2">Thickness of the joint (Top sheet + bottom sheet, mm)</td><td colspan="3">2.5 + 2.5</td><td colspan="4">2.0 + 2.0</td><td colspan="2">1.5 +1.5</td></tr>
<tr><td rowspan="2">Rivet</td><td>Length (mm)</td><td colspan="3">8</td><td colspan="4">7</td><td colspan="2">6</td></tr>
<tr><td>Hardness (HV)</td><td colspan="4">555</td><td>480</td><td>555</td><td>480</td><td colspan="2">480</td></tr>
<tr><td rowspan="2">Flat die</td><td>Diameter (mm)</td><td colspan="2">11</td><td colspan="5">10</td><td colspan="2">9</td></tr>
<tr><td>Depth (mm)</td><td colspan="2">2.35</td><td>3.00</td><td colspan="4">2.10</td><td colspan="2">2.00</td></tr>
<tr><td colspan="2">**Equivalent joint condition in Tables 5.10.1, 3, 6 and 7</td><td>7</td><td>8</td><td>1</td><td>9</td><td>10</td><td>11</td><td>12</td><td>13</td><td>14</td></tr>
<tr><td colspan="2">Effective length of rivet in bottom sheet, t_{eff} (mm)</td><td>3.2</td><td>3.04</td><td>3.68</td><td>2.66</td><td>2.44</td><td>2.73</td><td>2.73</td><td>2.25</td><td>2.25</td></tr>
<tr><td colspan="2">Deformed rivet diameter, D_t (mm)</td><td>7.66</td><td>7.6</td><td>7.26</td><td>7.54</td><td>7.72</td><td>7.52</td><td>7.72</td><td>7.4</td><td>7.4</td></tr>
</table>

** Equivalent joint means they produced under same condition with the same process parameters

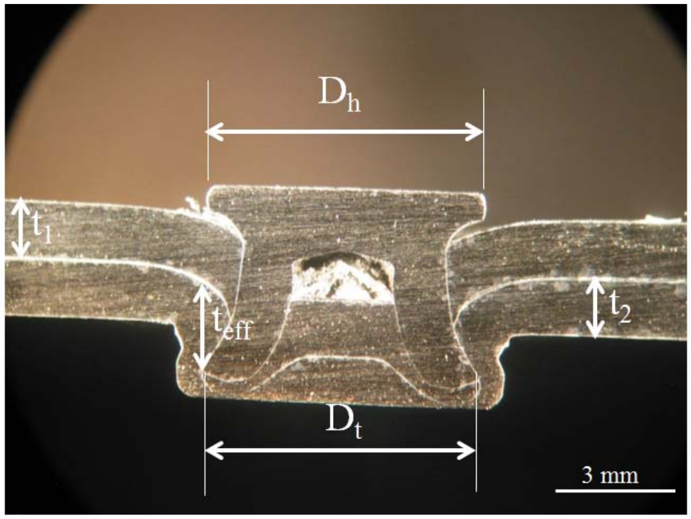

t_1 = Top sheet thickness, t_2 = Bottom sheet thickness
D_t = Deformed rivet diameter, D_h = Rivet head diameter
t_{eff}= Effective length of rivet in bottom sheet

Fig. 7.2.1 Cross-section of a riveted joint showing the different quality parameters.

In this chapter, the results obtained for both cross-tension and lap-shear tests using all of the above conditions are reported first. The effect of ply materials properties is also discussed. The effect of rivet hardness on the joint strength is also reported and finally, the effect of die depth on the energy required before the failure of a joint is analysed. The extension of the rivet flaring model presented in chapter 5.10 to estimate the strength of a riveted joint is examined in chapter 7.8. In the last section of this chapter, the relationship between cross-tension and lap-shear in terms of maximum force needed to initiate failure is developed.

All data reported in the subsequent sections are average and standard deviation values calculated from five repeats.

7.3 Cross-tension and Lap-shear test results

Two types of failure modes were observed here:

- *Failure mode 1: Pull-out of the rivet from the bottom sheet (Fig. 7.3.1)*
- *Failure mode 2: Tilting and pull-out of the rivet from the bottom sheet and further pull-out of the rivet head from the top sheet (Fig. 7.3.2)*

Fig. 7.3.1 Rivet pull-out (failure mode 1) from the bottom sheet for cross-tension test.

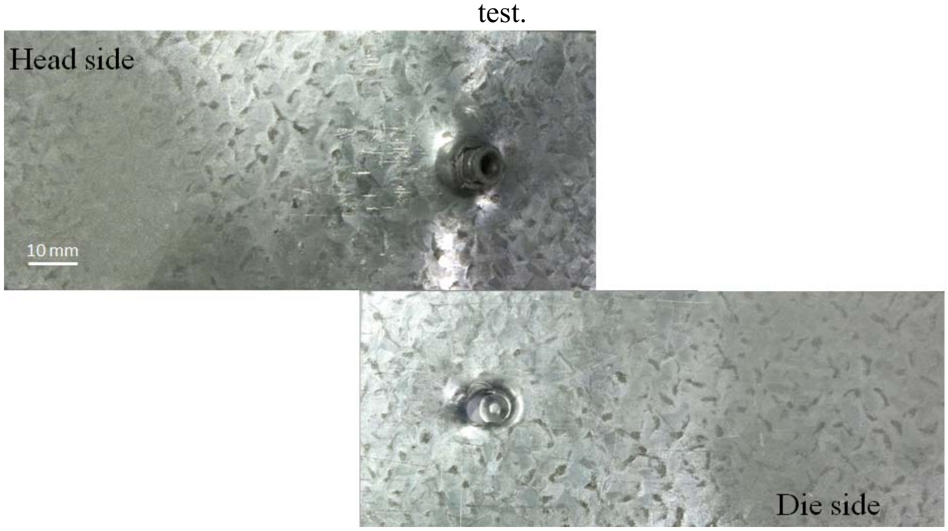

Fig. 7.3.2 Tilting and pull-out of rivet from bottom sheet with additional rivet head pull-out from top sheet (failure mode 2) for lap-shear test.

The cross-tension test repeatedly showed pull-out of the rivet from the bottom sheet (failure mode 1). However, for thick joints, rivet failure also occurred in addition to the pull-out of the rivet from the bottom sheet (Fig. 7.3.3). Failure mode 2 was always encountered in the lap-shear test. Unlike the cross-tension condition, rivet failure (Fig. 7.3.4) only occurred for thick and hard joints (2.5 mm thick G450 carbon steel).

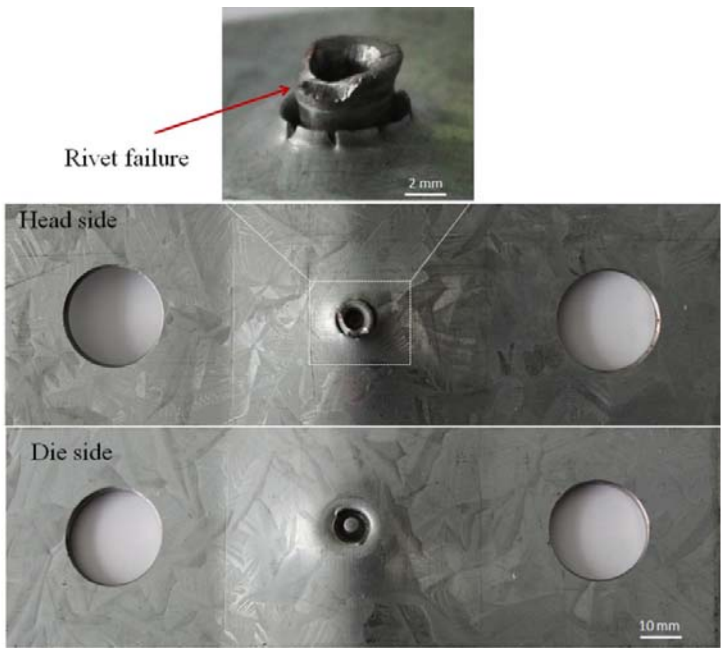

Fig. 7.3.3 Rivet failure + pull-out of rivet from the bottom sheet (failure mode 1) for cross-tension test of thick sheet material (2.5 mm).

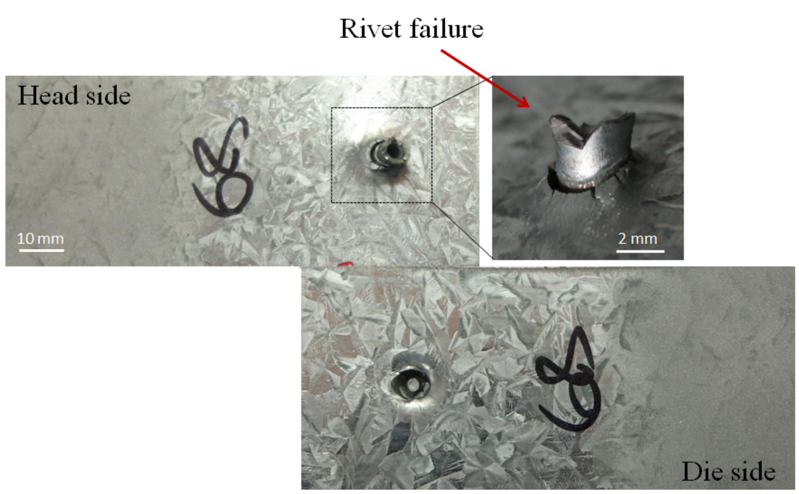

Fig. 7.3.4 Rivet failure + tilting and pull-out of rivet from bottom sheet with additional rivet head pull-out from top sheet (failure mode 2) for lap-shear test of thick and hard sheet material (2.5 mm G450 carbon steel).

Test results of the two extreme conditions, Case A (harder and thickest joint) and Case I (softer and thinnest joint) of Table 7.2.1 are presented below to demonstrate the reproducibility and general behaviour of the SPR joints. The results of cases B to H in Table 7.2.1 are presented in Appendix C.

Case A: 2.5 mm + 2.5 mm G450 carbon steel joint with 555 HV rivet

These joints were produced by 8 mm long rivets and a flat die (11.0 mm diameter and 2.35 mm deep). The results obtained for cross-tension and lap-shear tests are summarized in Table 7.2.1.A below. Force-displacement curves of the cross-tension and lap-shear tests are shown in Fig. 7.3.5.

Table 7.2.1.A The features of cross-tension and lap-shear tests for case A in Table 7.2.1.

Cross-Tension	Lap-Shear
Failure mode 1 + rivet failure	Failure mode 2 + rivet failure
Maximum force : 11.16 ± 0.61 kN	Maximum force : 17.9 ± 0.73 kN
Displacement at maximum force : 12.45 ± 0.55 mm	Displacement at maximum force : 4.34 ± 0.15 mm
Energy (area under the curve) : 92.50 ± 0.90 kN-mm	Energy (area under the curve) : 126.23 ± 0.77 kN-mm

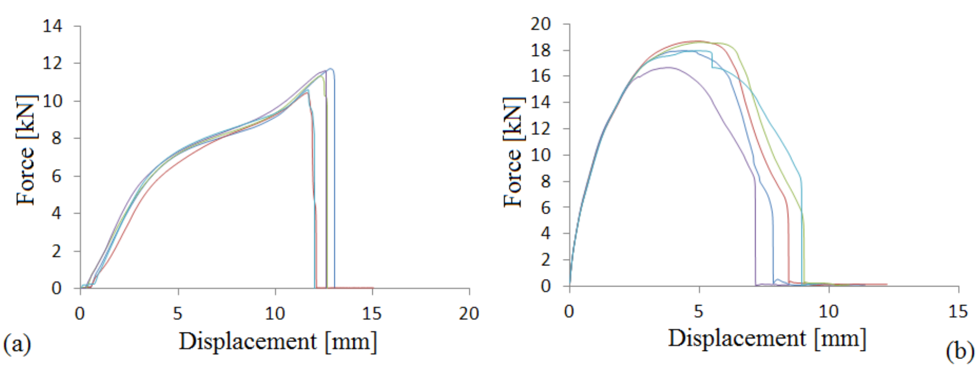

Fig. 7.3.5 Force-displacement curves of 2.5 + 2.5 mm G450 carbon steel sheet joints (a) cross-tension and (b) lap-shear test for the case A in table 7.2.1.

Case I: 1.5 mm + 1.5 mm G300 carbon steel joint with 480 HV rivet

Compared to the above Case A, the sheet materials were changed by replacing the 2.5 mm G450 with the 1.5 mm G300 carbon steel. A similar flat die was used with a low die recess volume (9.0 mm diameter and 2.00 mm deep) and the rivet length was reduced to 6 mm due to the thin sheets. The results obtained for the cross-tension and lap-shear tests are summarized in Table 7.2.1.I below. Force-displacement curves of the cross-section and lap-shear tests are shown in Fig. 7.3.6.

Table 7.2.1.I The features of cross-tension and lap-shear tests for case I in Table 7.2.1

Cross-Tension	**Lap-Shear**
Failure mode 1	Failure mode 2
Maximum force :4.69 ± 0.13 kN	Maximum force : 8.33 ± 0.82 kN
Displacement at maximum force : 13.98 ± 1.14 mm	Displacement at maximum force : 2.56 ± 0.02 mm
Energy (area under the curve) : 38.03 ± 1.02 kN-mm	Energy (area under the curve) : 41.13 ± 0.88 kN-mm

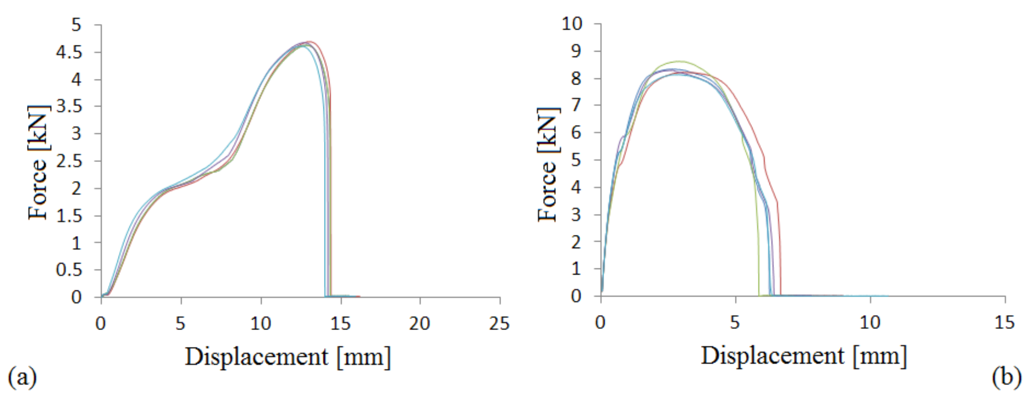

Fig. 7.3.6 Force-displacement curves of 1.5 + 1.5 mm G300 carbon steel sheet joints with 480 HV rivet (a) cross-tension and (b) lap-shear test for the case I in table 7.2.1.

It was clear that the force-displacement curves from all cross-tension tests showed similar patterns whereby three distinctive stages occurred for all conditions. For example, the force-displacement curve of the 1.5 + 1.5 mm G300 carbon steel joint (Fig. 7.3.7) shows that during the first stage, the force increased linearly with the displacement indicating that bending of the sheet materials occurred elastically. It should be noted that, the five curves in Fig. 7.3.6 showed reproducible behaviour. Hence, the curve presented in Fig. 7.3.7 is the median curve in terms of the maximum force among the five curves shown in Fig. 7.3.6 and all the graphs presented in the subsequent sections follow the same criterion. In the middle stage, plastic bending of the materials occurred and the slope of the curve was reduced. Hence, the force increased with a much lower gradient. Finally, the force started to increase again with a higher gradient due to the resistance to plastic deformation from the sheet material surrounding the rivet leg. In this case, the flared portion of the rivet tail sheared through the effective length of rivet in the bottom sheet (Figs. 7.2.1 and 2.3.1) and the joint failed by the pull-out of the rivet from the bottom sheet. It is necessary to mention that the maximum force that is needed to cause failure is dependent on the effective length of rivet in the bottom sheet (t_{eff}) and the deformed rivet diameter (D_t). Lap–shear test results also showed a similar pattern of force-displacement curves for each condition.

However, the maximum force was always higher in lap-shear than in the cross-tension loading condition for the same joint while the total displacement was larger in cross-tension than in lap-shear. This is typically shown in Fig. 7.3.8.

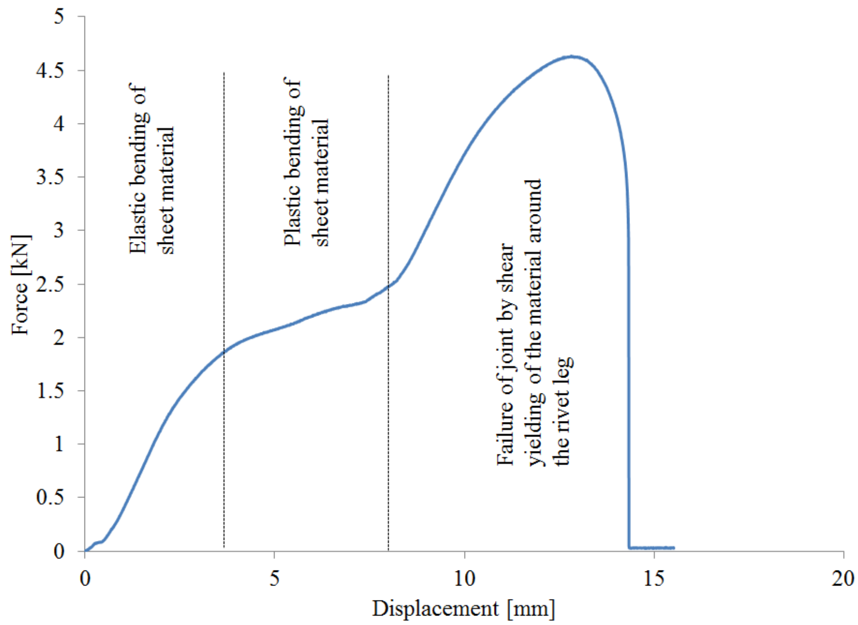

Fig. 7.3.7 Median force-displacement curve of a cross-tension test for 1.5 + 1.5 mm G300 carbon steel joint showing the three distinctive stages.

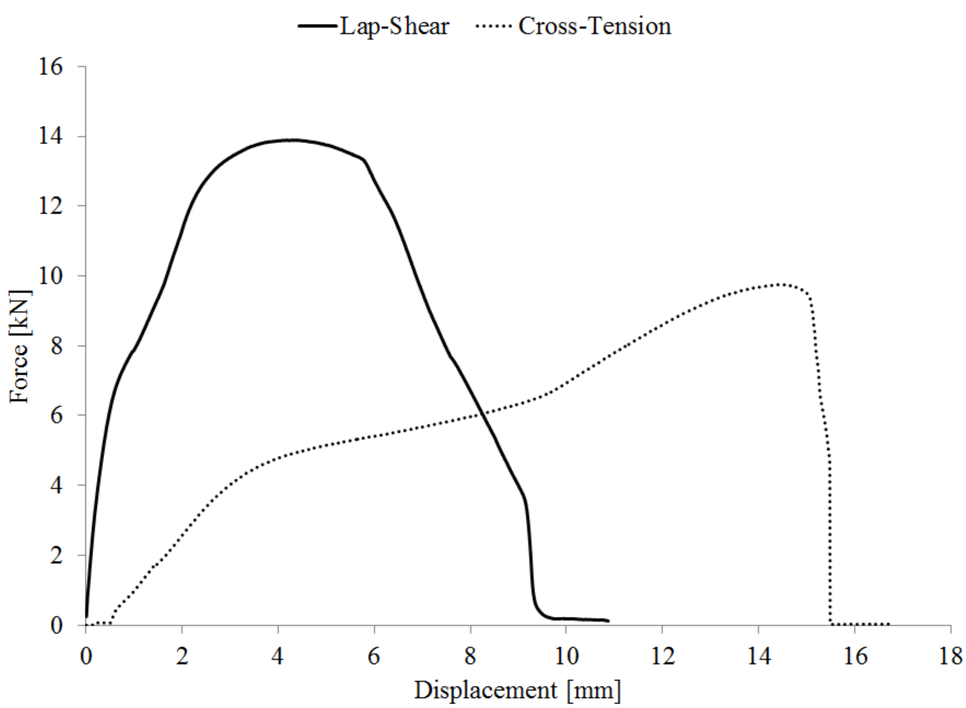

Fig. 7.3.8 Effect of loading condition on force-displacement curves of 2.5 + 2.5 mm G300 carbon steel joint.

In general, it was observed that the strength of a SPR joint was highly dependent on the mode of loading: higher strength was always observed in lap-shear than in cross-tension. However, in both conditions (lap-shear and cross-tension) the strength of a joint was greatly dependent on the hardness and thickness of the sheet materials. The harder and thicker a ply material, the higher is the strength of a joint in terms of both maximum force and energy. The key points for each condition of Table 7.2.1 are summarized in Table 7.3.1.

Table 7.3.1 Failure mode, maximum force and absorbed energy for different cross-tension and lap-shear test conditions of Table 7.2.1.

Case no.		Failure mode	Maximum force (kN)	Displacement at maximum force (mm)	Energy absorbed before failure (kN-mm)
A	Cross-tension	Mode 1 + rivet failure	11.16 ± 0.61	12.45 ± 0.55	92.50 ± 0.90
	Lap-shear	Mode 2 + rivet failure	17.90 ± 0.73	4.34 ± 0.15	126.23 ± 0.77
B	Cross-tension	Mode 1 + rivet failure	10.34 ± 1.04	15.66 ± 0.48	97.31 ± 1.20
	Lap-shear	Mode 2	12.90 ± 0.53	4.07 ± 0.10	98.27 ± 0.95
C	Cross-tension	Mode 1 + rivet failure	11.33 ± 1.02	16.67 ± 0.62	125.46 ± 1.41
	Lap-shear	Mode 2	14.17 ± 0.83	3.99 ± 0.12	105.11 ± 1.33
D	Cross-tension	Mode 1	9.78 ± 0.64	15.52 ± 0.64	89.09 ± 0.88
	Lap-shear	Mode 2	14.28 ± 0.14	3.99 ± 0.09	102.33 ± 0.22
E	Cross-tension	Mode 1	9.76 ± 0.24	16.76 ± 0.37	97.19 ± 0.52
	Lap-shear	Mode 2	14.35 ± 0.81	3.99 ± 0.07	91.53 ± 1.05
F	Cross-tension	Mode 1	7.97 ± 0.70	17.22 ± 0.49	83.14 ± 1.13
	Lap-shear	Mode 2	11.36 ± 0.31	3.53 ± 0.11	82.31 ± 0.85
G	Cross-tension	Mode 1	7.32 ± 0.22	15.92 ± 0.34	73.37 ± 0.59
	Lap-shear	Mode 2	10.73 ±0.63	3.53 ± 0.06	77.51 ± 1.03
H	Cross-tension	Mode 1	6.84 ± 0.94	14.23 ± 0.04	56.29 ± 1.31
	Lap-shear	Mode 2	10.54 ± 0.71	3.25 ± 0.02	69.10 ± 1.23
I	Cross-tension	Mode 1	4.69 ± 0.13	13.98 ± 1.14	38.03 ± 1.02
	Lap-shear	Mode 2	8.33 ± 0.82	2.56 ± 0.02	41.13 ± 0.88

7.4 Effect of ply materials' properties on joint strength

7.4.1 Cross-tension test

The strength of SPR joints is highly dependent on the properties of sheet materials. The force-displacement curves for the cross-tension tests of 4.0 mm joints with a 555 HV rivet are shown in Fig. 7.4.1. Two different materials were used for this examination: G450 and G300 carbon steel. It was clear that the maximum force was high for the harder material due to a higher rigidity and yield strength of the ply materials. The maximum force was found to be 22% higher (9.78 kN) for G450 than G300 carbon steel joint (7.97 kN) while the maximum displacement was greater for the softer material due to higher ductility. As a result, the energies required to fail the joints were 89 and 82 kN-mm for the harder and softer materials respectively. It is apparent from Fig. 7.4.1 that initially the two joints behaved very similarly due to their identical thickness. However, after a displacement of 2.90 mm the force started to increase with a higher gradient for the harder material.

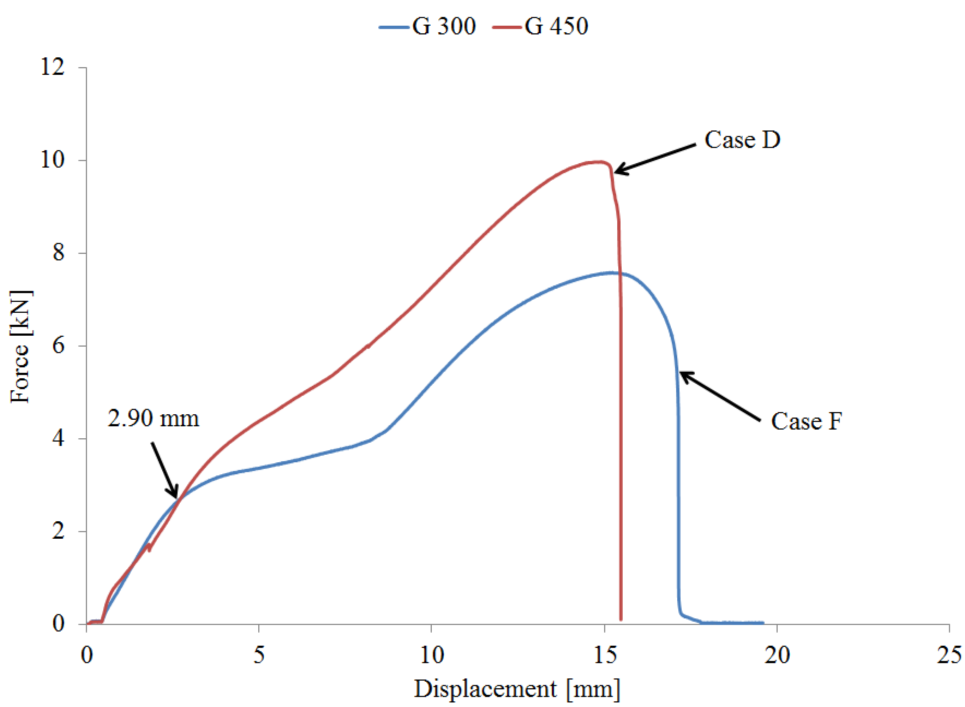

FIg. 7.4.1 Force versus displacement curves for cross-tension tests of a 2.0 + 2.0 mm joint showing different gradients due to material properties.

The failure mode for the above cross-tension tests was rivet tail pull-out from the bottom sheet (failure mode 1) and in this case the flared portion of the rivet tail sheared through the effective length of the rivet in the bottom sheet (t_{eff} in Fig. 7.2.1). Hence, the maximum force needed to cause a failure was highly dependent on the shear yield strength of the ply material. Other factors such as the effective length of rivet in the bottom sheet and the deformed rivet diameter (t_{eff} and D_t in Fig. 7.2.1) also affected the strength of a SPR joint. Fig. 7.4.2 shows the effect of material properties on the static strength of a SPR joint for three different thicknesses.

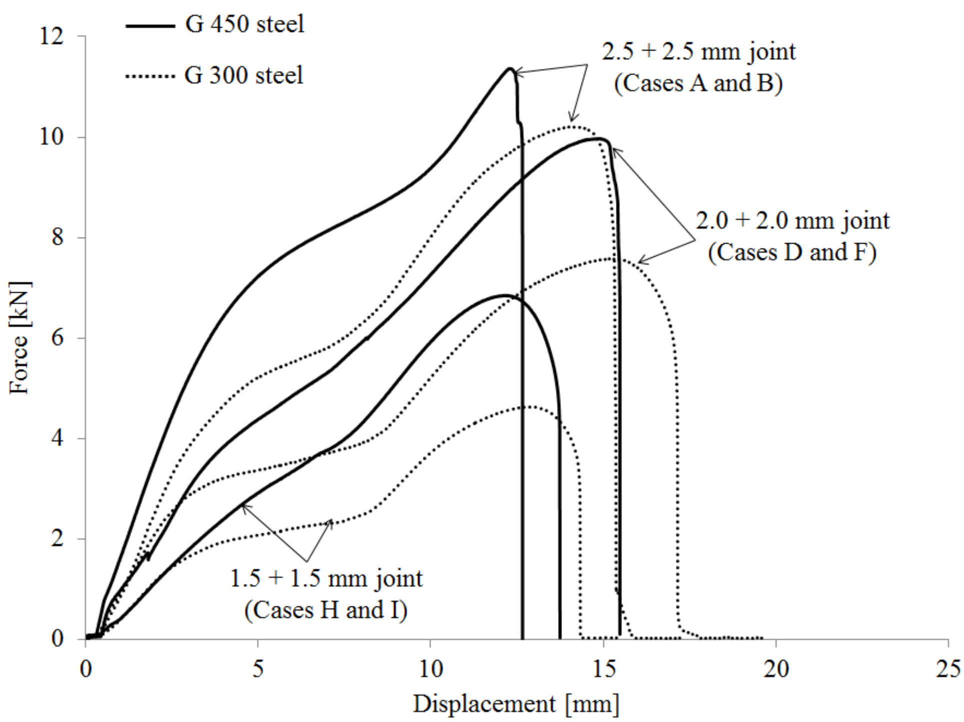

FIg. 7.4.2 Force versus displacement curves showing the effect of material grade and thickness on cross-tension static strength

It can be observed from Fig. 7.4.2 that for a 50% increment in the yield strength of the material the maximum force was increased by 8%, 22% and 45% for 5.0, 4.0 and 3.0 mm thick SPR joints. The effective length of the rivet in the bottom sheet (t_{eff} = 2.25 mm in Fig.7.2.1 and Table 7.2.1) and the deformed rivet diameter (Dt = 7.4 mm) for a 3.0 mm joint were found to be same for both joints (G300 and G450). Due to this reason, the joint strength increased with the rate of increase in the yield strength of the ply materials. However, in the 4.0 mm joint, the effective length of the rivet in the bottom sheet was less for the G450 joint (t_{eff} = 2.66 and 2.73 for the G450 and G300 joints respectively, Table 7.2.1) while the deformed rivet diameter was the same (D_t = 7.50 mm). As a result, the strength of the joint for G450 carbon steel did not increase proportionately with the yield strength. For 5.0 mm joints, the failure mode was different for the G450 joint (rivet failure observed additionally with failure mode 1), which is why the joint strength was not increased equitably with the increase in yield strength.

7.4.2 Lap-shear test

In the lap-shear condition, the strength of a joint depends also on the properties of ply materials. A force-displacement curve of 2.0 + 2.0 mm joints for the two different materials are shown in Fig. 7.4.3. The maximum force for the G450 (14.28 kN) was found to be 26% higher compared with the G300 carbon steel joint (11.36 kN).

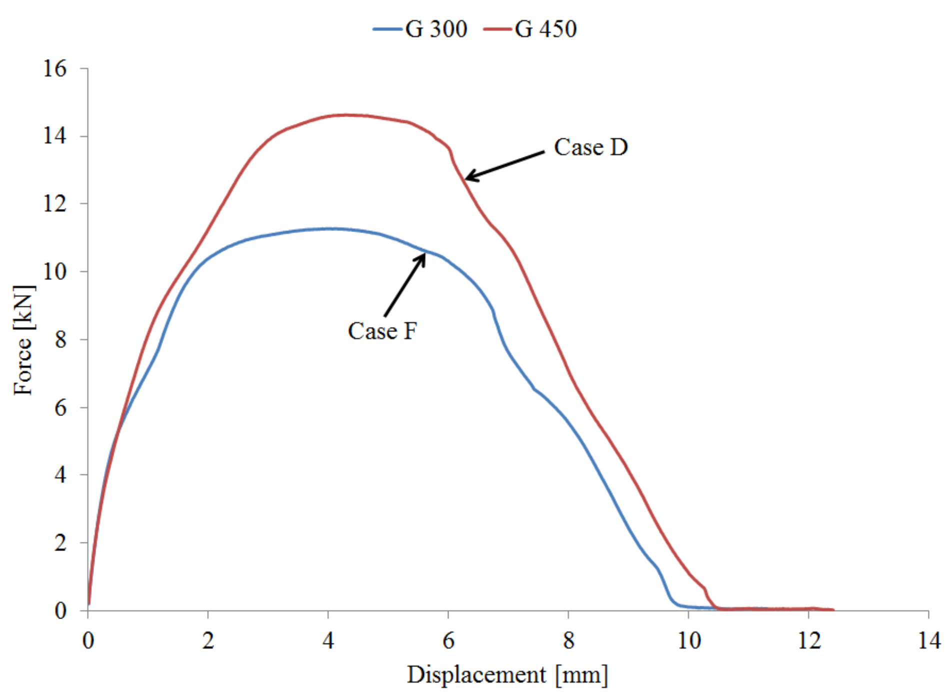

FIg. 7.4.3 Force versus displacement curves showing the effect of material hardness for lap-shear test of a 2.0 + 2.0 mm joint.

The average energies required before failure of the joints were 102 and 82 kN-mm for G450 and G300 carbon steel sheet respectively, and the failure mode for both the joints was tilting and pull-out of the rivet from the bottom sheet and further pull-out of the rivet head from the top sheet (failure mode 2). Initially the two joints behaved similarly due to the tilting of the rivet and the resistance energy was mainly from the rivet. However, the two joints started to separate at 0.50 mm displacement when pull out of the rivet initiated with shearing of the material. Like the cross-tension, the effective length of the rivet in the bottom sheet and the deformed rivet diameter also affected the strength of a riveted joint in lap-shear loading condition. Fig. 7.4.4 shows the effect of material properties on the lap-shear static strength of SPR joints of three different thicknesses.

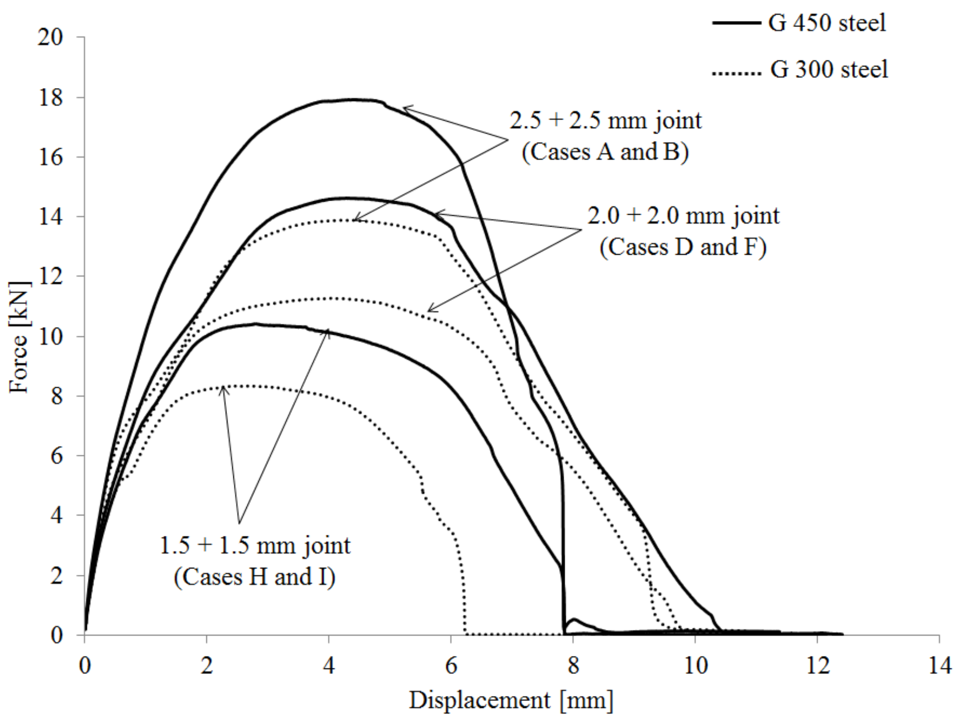

FIg. 7.4.4 Force versus displacement curves showing the effect of material grade and thickness on lap-shear static strength.

The increase in maximum force due to material properties was found to be similar for all different thicknesses (Fig. 7.4.4). Like the cross-tension condition, the effective length of the rivet in the bottom sheet (t_{eff}) was not the only crucial factor for lap-shear loading condition; the deformed rivet diameter (D_t) was also another crucial factor. In general, it was observed that the effective material thickness (t_{eff}) was high when the deformed rivet diameter (D_t) was low. The energy was mainly dependent on the deformed rivet diameter and the pull out strength was mainly characterized by the effective material thickness. As a combination of the three factors (effective length of the rivet in the bottom sheet, the deformed rivet diameter and material properties) the increase in maximum force was about 30% for the above riveting condition.

7.5 Effect of ply materials' thickness on joint strength

7.5.1 Cross-tension test

A joint strength is dependent on the thickness of the ply materials for the cross-tension test. The force-displacement curves of various joint stacks for G300 carbon steel joints are shown in Fig. 7.5.1 (for G450 carbon steel see Appendix C).

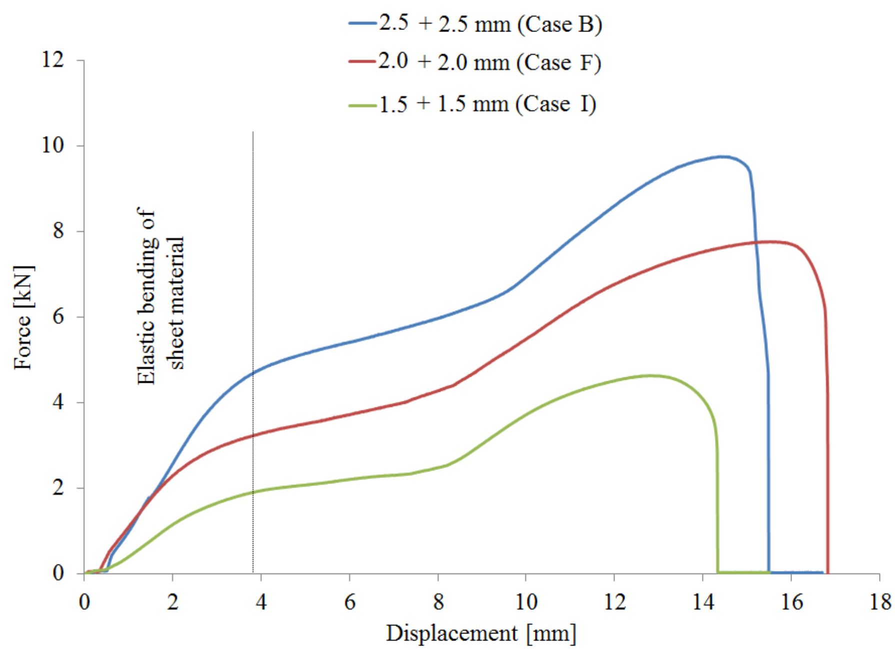

Fig. 7.5.1 Force versus displacement curves showing the effect of material thickness on the cross-tension static strength of G300 carbon steel joints.

It is clear from Fig. 7.5.1 that the displacement for elastic bending for each case was similar due to the same material. However, the plastic bending and yielding of material varied for different thicknesses due to stiffness. The maximum forces were 10.34, 7.97 and 4.69 kN for 5.0, 4.0 and 3.0 mm joints respectively (Table 7.3.1). An increase in joint thickness needed a longer rivet to be used which ultimately affects the quality of a joint such as deformed rivet diameter and also the effective length of the rivet in the bottom sheet. Thus, for a 33% and 67% increase in thickness (from 3.0 to 4.0 and 5.0 mm) the maximum force increased by 70% and 120% respectively. The displacements before complete failure were

14.3, 16.8 and 15.5 mm for 3.0, 4.0 and 5.0 mm joints respectively. The displacement for the 5.0 mm joint was low due to a different failure mode (rivet failure observed additionally with the pull-out of the rivet as shown in Fig. 7.3.3).

7.5.2 Lap- shear test

The joint strength in the lap-shear condition also depended on the thickness of the ply materials. The force-displacement curves of G300 carbon steel for various ply material thicknesses are shown in Fig. 7.5.2 (for G450 carbon steel, see Appendix C).

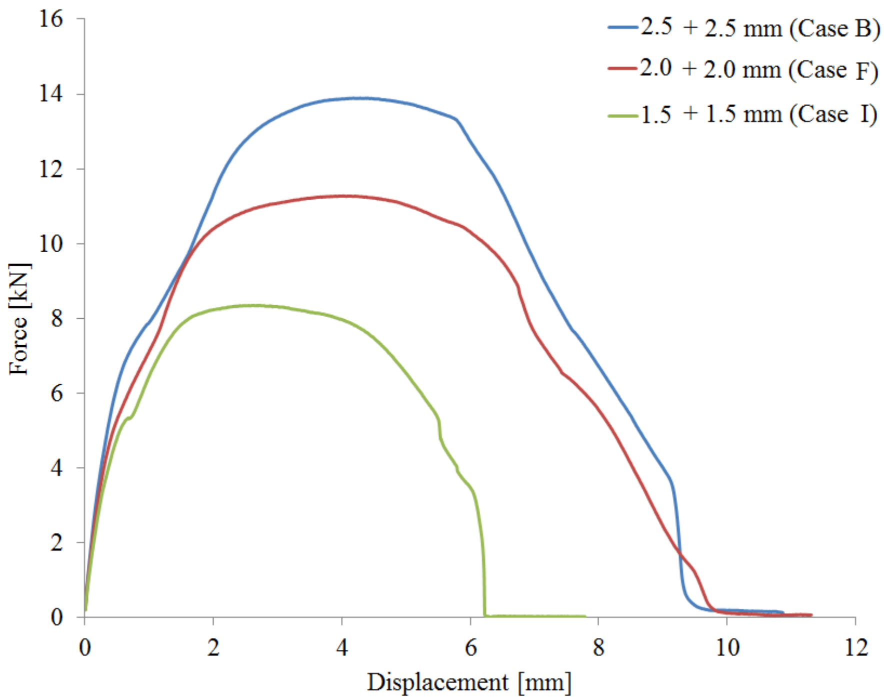

Fig. 7.5.2 Force versus displacement curves showing the effect of material thickness on the lap-shear static strength of G300 carbon steeljoints.

It is clear from Fig. 7.5.2 that the maximum force increased with the increase in joint thickness. The forces were 14.2, 11.3 and 8.3 kN for 5.0, 4.0 and 3.0 mm joints respectively. The joint strengths increased by 35% and 70% for a increases in thickness of 33% and 66% respectively. All the above joints showed similar failure mode. Thus the force increased proportionately with an increase in thickness.

7.6 Effect of rivet hardness on joint strength

7.6.1 Cross-tension test

Force-displacement curves for the cross-tension test of 2.0 + 2.0 mm G450 carbon steel sheet are shown in Fig. 7.6.1 (same graph for G300 carbon steel, see Appendix C).

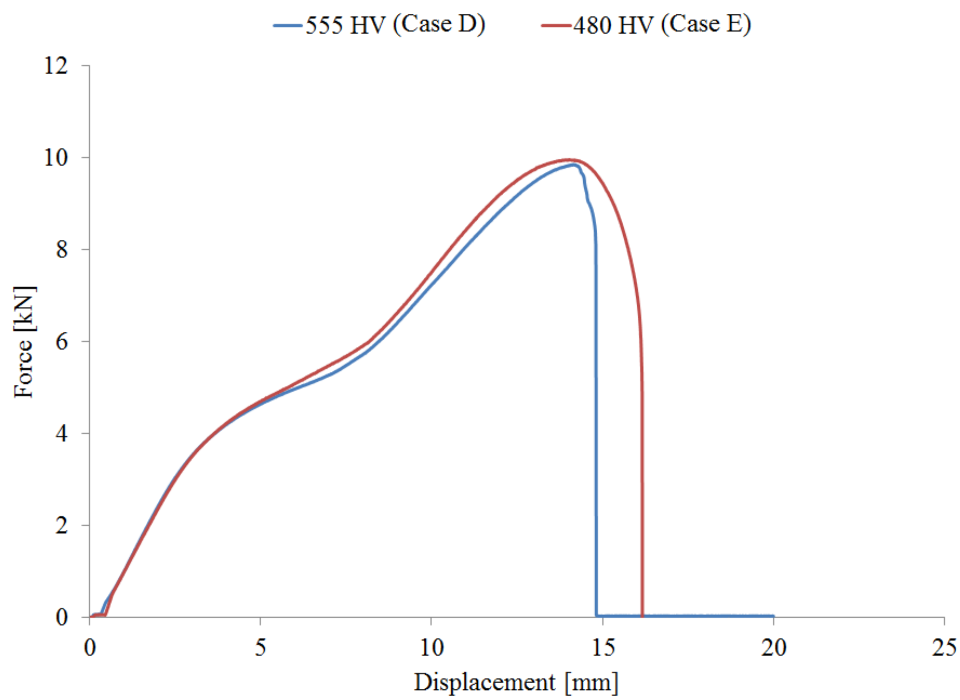

Fig. 7.6.1 Force-displacement curves for a 2.0 + 2.0 G450 carbon steel sheet joint in cross-tension condition.

It was clear that the two joints behaved identically during the elastic bending of the sheet material. However, a small increase in the force was observed for the joint with the softer rivet. This was due to the higher deformed rivet diameter (D_t = 7.72 and 7.54 mm for 480 and 555 HV rivet respectively, Table 7.2.1). The failure mode for both joints was rivet pull out from the bottom sheet (failure mode 1), which occurred mainly by shear failure of the material. Therefore, rivet hardness (for the range of HV examined) does not appear to be a critical factor for joint peel strength.

7.6.2 Lap-shear test

Force- displacement curves for the lap-shear condition of 2.0 + 2.0 mm G450 carbon steel sheet are shown in Fig. 7.6.2 (same graph for G300 carbon steel, see Appendix C). It is evident from Fig.7.6.2 that the maximum force was higher for the harder rivet (14.35 and 14.28 kN for 555 and 480 HV rivets respectively, Table 7.3.1). In the lap-shear condition initially the energy was absorbed by the rivet while tilting of rivet occurred, so it was easy to deform the sheet material for the harder rivet. Initially the force was high for the same amount of displacement for the softer rivet. However, the effective length of the rivet in the bottom sheet (t_{eff} = 2.66 and 2.44 mm for G450 and G300 joint respectively, Table 7.2.1) was higher for the 555 HV rivet and due to this aspect, the maximum force was also high. Though the hardness of the rivet was increased by 15%, the maximum force was increased by only 0.4%. It can be concluded that the rivet hardness (within the range of HV examined) played an insignificant role in terms of the joint strength.

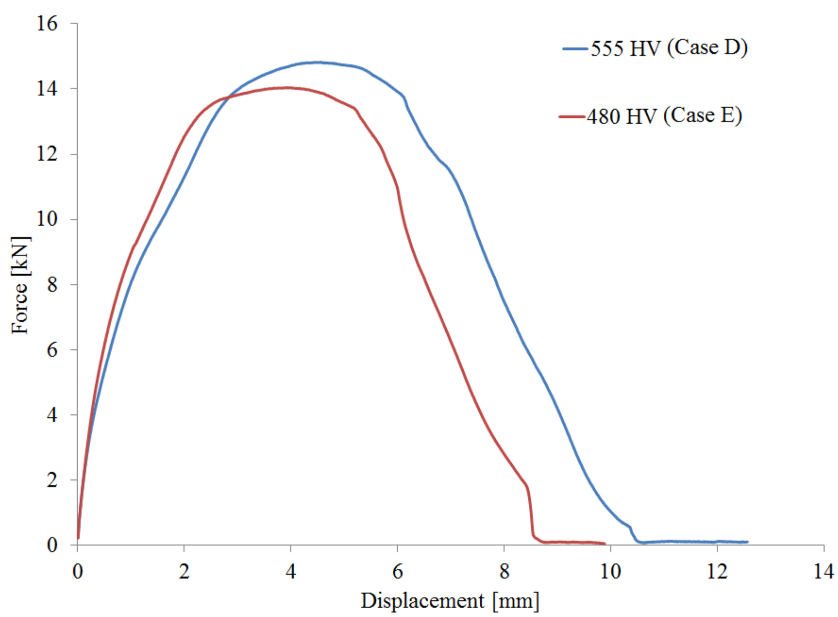

Fig. 7.6.2 Joint strength depending on rivet hardness for a 2.0 + 2.0 mm G450 carbon steel sheet joint in lap-shear condition.

7.7 Effect of die depth on joint strength

7.7.1 Cross-tension test

Die depth plays an important role on the effective material thickness (t_{eff}) of a SPR joint which ultimately leads to a high force for the static condition. Force-displacement curves for the cross-tension condition of 2.5 + 2.5 mm G300 carbon steel joints are shown in Fig. 7.7.1. It was clear that the force was high (11.33 kN) for the 3.0 mm deep die and low (10.34 kN) for the 2.35 mm deep die. This was mainly due to the effective material thickness (t_{eff} = 3.68 and 3.04 mm for the 3.0 and 2.35 mm deep dies respectively, Table 7.2.1). Thus, a deep die should be used if possible. However, it was observed that a deep die can also lead to cracking of hard material with low elongation (see chapter 5.2). So, extreme care should be taken when selecting a proper die for a given set of riveting parameters (ply material thickness and hardness, rivet length and hardness).

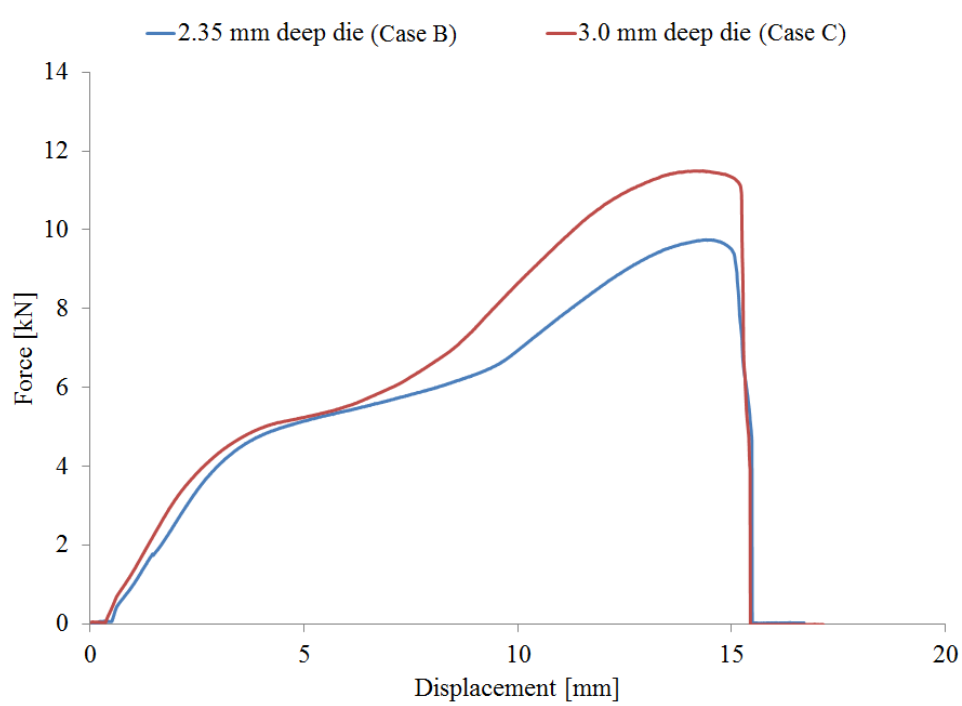

Fig. 7.7.1 Force versus displacement curves showing the effect of die depth on joint strength for the cross-tension test of 2.5 + 2.5 mm G300 carbon steel sheet.

7.7.2 Lap-shear test

The force-displacement curves for the lap-shear condition of 2.5 + 2.5 mm G300 carbon steel joints with different die depths are shown in Fig. 7.7.2. Like the cross-tension condition, the force was also high for the 3.0 mm deep die in this condition. Though the deformed rivet diameter was higher for the 2.35 mm deep die (D_t = 7.6 and 7.26 mm for the 2.35 and 3.0 mm deep dies respectively, Table 7.2.1), the force recorded was lower due to the lower effective material thickness (t_{eff} = 3.04 mm). From this result, it is possible to conclude that the effective material thickness should be included as a quality parameter for a riveted joint whereas most literature had reported only the deformed rivet diameter as a quality parameter [69, 91, 122, 136].

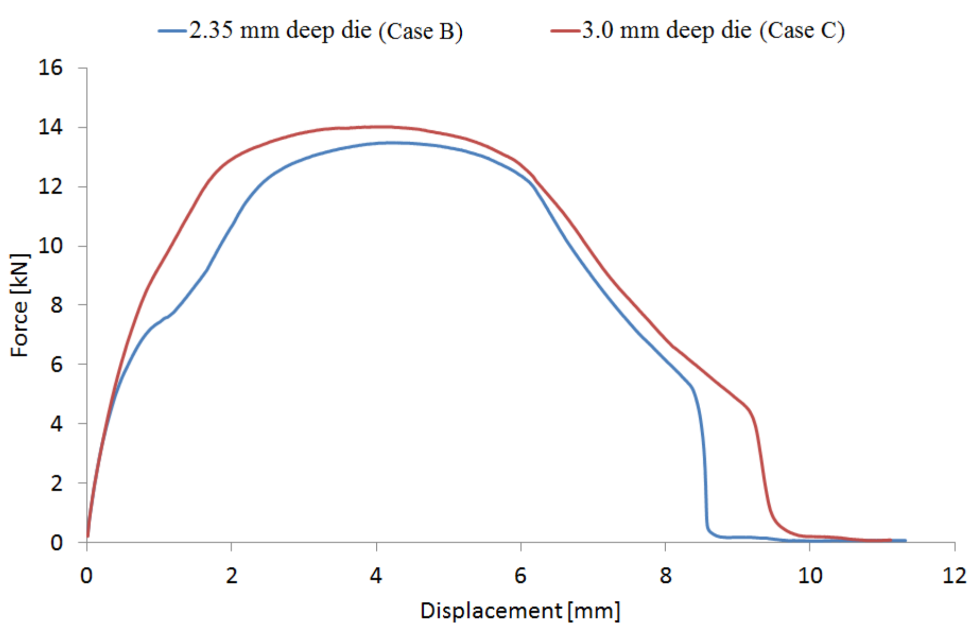

Fig. 7.7.2 Force versus displacement curves showing the effect of die depth on joint strength for the lap-shear test of 2.5 + 2.5 mm G300 carbon steel sheet.

7.8 Extension of rivet flaring model to joint strength estimator

A rivet flaring model was developed in chapter 5.10, where it was shown that the deformed rivet diameter (D_t) can be calculated by using an empirical equation (equation 5.6). Three different inputs were taken in that equation. Firstly, two empirical coefficients depending on rivet hardness and length, secondly, physical geometrical parameters such as thickness of the top and bottom sheets, rivet diameter and die parameters (diameter and depth) and finally, relative punch displacement before (d_0) and after flaring (d_{max}) from the characteristic force-displacement curve (Fig. 5.10.1) were used. It was observed that the rivet flaring model can successfully predict the rivet flaring (deformed rivet diameter) albeit the simple nature of that equation.

It was clear from the previous section (chapter 7.5) that the joint strength under cross-tension directly depends on the material thickness. Sun and Khaleel [136] studied the rivet joint and proposed an empirical equation to estimate the static strength of joint assuming that the rivet periphery was under perfect axisymmetric loading just before the failure. They also assumed that sufficient interlock was achieved during the riveting process. Equation (7.1) is their proposed equation for rivet tail pull out.

$$F_{CT} \approx 0.7\eta_t\beta_t t_{eff}\pi D_t\sigma_t \tag{7.1}$$

where F_{CT} is the joint strength for tail pull-out failure. D_t is the deformed rivet diameter and t_{eff} is effective length of the rivet in the bottom sheet. η_t is the empirical coefficient of material degradation due to the piercing process for the tail side (η_t = 0.6 if the elongation is >9% and η_t = 0.5 for materials having elongation <9%). β_t is an empirical coefficient of the sheet bending induced thickness reduction for the tail side materials (β_t=1 for t_2>1.5 mm and $\beta_t \cong$0.8 for $t_2 \leq$1.5 mm, see Fig. 7.2.1). σ_t is the yield strength of the sheet material.

The above equation can be useful for the preliminary design of the joint parameters, by which the strength of a joint can be predicted. It should be noted that the above strength estimator highly depends on the measurements of very small dimensions of deformed rivet diameter (Dt) and effective material thickness (t_{eff}) as shown in Fig. 7.2.1. Accurate sectioning and adequate specimen preparation are also required to get precise measurements. A small error on any of the above in the process of measurement can lead to a very big error on the estimation of the joint strength. For the tail pull out strength in equation 7.1, two factors are unknown unless the rivet cross section is available: t_{eff} and D_t. The purpose of this study is to eliminate the need for having a cross-section of a joint to measure these geometrical values. Since the riveting process requires no piercing through the bottom sheet, the deformed rivet diameter (D_t) and the effective material thickness (t_{eff}) can be approximated by the following equations with the help of the rivet flaring model, provided good interlock has been achieved:

$$D_t = 2 \times (R_r + x) \tag{7.2}$$

$$t_{eff} = t_2 + \frac{h-x}{2} \tag{7.3}$$

where R_r is the undeformed rivet shank radius and x is the rivet flaring calculated by using equation 5.6 in section 5.10. t_2 is the bottom sheet thickness and h is the depth of the die (see Figs. 7.2.1 and 5.10.8).

Substituting values of D_t and t_{eff} from equations 7.2 and 7.3 respectively, equation 7.1 can be rewritten in the following form.

$$F_{CT} \approx 0.7\eta_t\beta_t \times \left(t_2 + \frac{h-x}{2}\right)\pi \times 2 \times (R_r + x) \times \sigma_t \tag{7.4}$$

For a given die and rivet, die depth (h) and rivet radius (R_r) are known. For a given joint, the top sheet thickness (t_1) and bottom sheet thickness (t_2) are also known, and rivet flaring (x) can be calculated by equation 5.6. Thus equation 7.4 eliminates the need for experimental measurements.

Nine different experimental cases were considered to demonstrate and validate the above strength estimator, comprising two different hardnesses of materials and rivet, three types of thicknesses of materials and four levels of die depths (Table 7.2.1). In this experiment the same value of the empirical coefficients for material thickness (β_t) and degradation due to the piercing process (η_t) were used from Sun and Khaleel [136] as the materials are of similar elongation and thickness. The rivet radius (Rr = 2.75 mm) was the same for all experiments. An example calculation of joint strength for case A in Table 7.2.1 is given below and the calculated joint strengths for all the cases are summarized in Table 7.8.1.

Case A: The yield strength of the material was σ_t = 450 MPa. The geometrical factors were: R_r = 2.75 mm, h = 2.35 mm, t_2 = 2.5mm and rivet flaring (x = 1.19 mm, from condition 7 in Table 5.10.7) as determined by equation 5.6. Equation 7.4 produces

$$F_{CT} = 0.7\eta_t\beta_t \times \left(t_2 + \frac{h-x}{2}\right)\pi \times 2 \times (R_r + x) \times \sigma_t = 0.7 \times 0.5 \times 1 \times$$
$$\left(2.5 + \frac{2.35-1.19}{2}\right) \times 3.14 \times 2 \times (2.75 + 1.19) \times 450 = 12{,}002N = 12.08\ kN$$

The experimentally measured joint strength was found to be 11.16 ± 0.61 kN.

Table 7.8.1 Joint strengths for all cases in Table 7.2.1

Case no.	Yield strength of bottom sheet, σ_t (MPa)	Die depth, h (mm)	Bottom sheet thickness, t_2 (mm)	**Rivet flaring, x (mm)	Calculated joint strength, F_{CT} (kN)	Measured joint strength (kN)
A	450	2.35	2.5	1.19	12.08	11.16 ± 0.61
B	300	2.35	2.5	1.13	9.54	10.34 ± 1.04
C	300	3.00	2.5	0.86	10.19	11.33 ± 1.02
D	450	2.10	2.0	0.79	9.29	9.78 ± 0.64
E	450	2.10	2.0	1.11	9.52	9.76 ± 0.24
F	300	2.10	2.0	0.80	7.44	7.97 ± 0.70
G	300	2.10	2.0	1.25	7.67	7.32 ± 0.22
H	450	2.00	1.5	0.95	5.92	6.84 ± 0.94
I	300	2.00	1.5	0.90	4.73	4.69 ± 0.13

** The value of rivet flaring was taken from Tables 5.10.3 and 7.

Considering the simple nature of equations 5.6 and 7.4, a reasonably good correlation was obtained between experimental and predicted strengths. A comparison between the calculated and measured joint strengths is shown in Fig. 7.8.1.

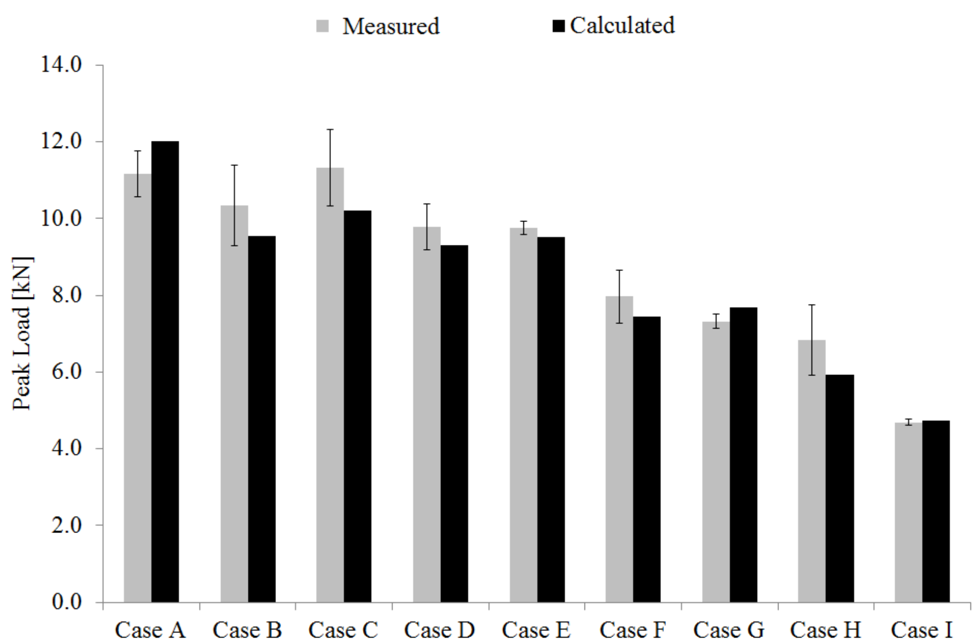

Fig. 7.8.1 Comparison of calculated and average measured joint strength in cross-tension loading condition.

It was observed that almost all of the calculated joint strengths fall within 10% of the respective measured joint strength. This joint strength estimator highly depends on the rivet flaring model and estimation of effective rivet thickness (t_{eff}). The rivet flaring model could be improved by considering the path of the rivet tip as a parabola rather than a straight line, as discussed in chapter 5.10. It is believed that the effective rivet thickness (t_{eff}) could be estimated from the characteristic force-displacement curve by identifying the exact point when the rivet finishes the piercing of the top sheet. However, the above estimator was simple in nature and could be used as a very important tool in industrial practice.

7.9 Relation between cross-tension and lap-shear condition

In the previous chapter an analytical method to calculate the strength of the cross-tension loading condition was developed. However, the joint strength depends on other loading conditions such as lap-shear. The lap–shear loading condition is heavily used in industrial practice along with the cross-tension condition to demonstrate the strength of a riveted joint. Sun and khaleel [136] mentioned joint strength under the lap-shear condition can be connected to its cross-tension strength but the relationship between these loading conditions was not published. In general, it is well known that the strength of a joint under the lap-shear condition is generally higher than that for the cross-tension condition. The purpose of this study is to develop a relationship between the above two loading conditions.

7.9.1 Developing the relation

SPR is a cold forming process and Eurocode 9 allows the design of cold-formed joints to be assessed by theoretical models [172]. However, no recommendations were available for self-piercing riveting in the Eurocode 9 (prEN1999-1-4). The design formula was only available for blind rivets. Considering the similarity of the failure mode (tail pull-out), two equations were proposed. For the cross-tension loading condition (failure mode 1), the equation was developed based on the pull-out resistance and for the lap-shear loading condition (failure mode 2), the equation was developed based on the bearing resistance of the rivet. The equations are as follows:

$$F_{CT} = \alpha_{CT} \times \sigma \times \sqrt{D_t \times t_{eff}^3} \tag{7.5}$$

$$F_{LS} = \alpha_{LS} \times \sigma \times D_t \times t_{eff} \tag{7.6}$$

where F_{CT} and F_{LS} are the maximum force for the cross-tension and lap-shear loading conditions respectively. σ is the yield strength of the material. D_t and t_{eff} are the deformed rivet diameter and the effective length of the rivet in the bottom sheet respectively. α_{CT} and α_{LS} are the empirical coefficients for the cross-tension and lap-shear conditions respectively.

By dividing equation 7.6 with equation 7.5 the expression for the maximum force for the lap-shear condition becomes:

$$F_{LS} = \left(\frac{\alpha_{LS}}{\alpha_{CT}} \times \sqrt{\frac{D_t}{t_{eff}}}\right) \times F_{CT} \tag{7.7}$$

The relationship between the cross-tension and lap-shear conditions was developed through the equation 7.7. For a given joint, the deformed rivet diameter (D_t) and the effective length of the rivet in the bottom sheet (t_{eff}) are known. If the empirical coefficients α_{CT} and α_{LS} are also known, then the strength measurement is needed only in one condition and the strength for the other condition can be calculated by equation 7.7.

7.9.2 Determination of coefficients α_{CT} and α_{LS}

The coefficient α_{CT} was found from equation 7.5 by replacing F_{CT} with the experimentally obtained values for the cross-tension condition and the coefficient for the lap-shear condition (α_{LS}) was found from equation 7.6 by using the experimental F_{LS} values. Four different joining conditions were considered to determine the above coefficients, comprising two types of hardness of materials and two levels of rivet hardness (cases D, E, F and G in Table 7.2.1). The calculation of the constants for the cross-tension and the lap-shear is shown below and the values for different cases are summarized in Table 7.9.1.

<u>Case D:</u> The yield strength of the material was 450 MPa. The geometrical factors were: x = 0.79 mm (condition 9 in Table 5.10.7) and t_{eff} = 2.66 mm. The experimentally obtained forces were: F_{CT}=9.78 ± 0.64 kN and F_{LS}= 14.28 ± 0.14 kN. Equations 7.2, 7.5 and 7.6 produced the α_{CT1} and α_{LS1} as follows:

Deformed rivet diameter D_t= 2 x (R_r + x) = 2 x (2.75 + 0.79) = 7.08

Constant for cross-tension, $\alpha_{CT} = \dfrac{F_{CT}}{\sigma\times\sqrt{D_t t_{eff}^3}}$

$$= \frac{9.78\times10^3}{(450\times10^6)\times\sqrt{(7.08\times10^{-3})\times(2.66\times10^{-3})^3}} = 1.89$$

Constant for lap-shear, $\alpha_{LS} = \dfrac{F_{LS}}{\sigma\times D_t\times t_{eff}}$

$$= \frac{14.28\times10^3}{(450\times10^6)\times7.08\times10^{-3}\times2.66\times10^{-3}} = 1.69$$

Table 7.9.1 Constants for cross-tension and lap-shear loading for the different cases in Table 7.2.1

Case no.	Yield strength of bottom sheet, σ_t (MPa)	**Rivet flaring, x, (mm)	Deformed rivet diameter, D_t (mm)	Effective length of rivet in bottom sheet, t_{eff} (mm)	Constant for cross-tension, α_{CT}	Constant for lap-shear, α_{LS}
D	450	0.79	7.08	2.66	1.89	1.69
E	450	1.11	7.72	2.50	1.98	1.66
F	300	0.80	7.10	2.65	2.31	2.01
G	300	1.25	8.00	2.43	2.28	1.84

** The value of rivet flaring was taken from Table 5.10.7.

The coefficients for the cross-tension (α_{CT}) and lap-shear (α_{LS}) conditions were determined by the average of the above calculated coefficients.

Coefficient for cross-tension, $\alpha_{CT} = 2.11 \pm 0.21$

Coefficient for cross-tension, $\alpha_{LS} = 1.80 \pm 0.16$

7.9.3 Prediction of strength for lap-shear condition by equation 7.7

The coefficients α_{CT} and α_{LS} from the experimental measurement were needed to verify equation 7.7. Five different joining conditions were considered sufficient to validate equation 7.7, comprising two values of thickness and hardness of materials, and with two different values of hardness of the rivet (cases A, B, C, H and I in Table 7.2.1). The calculations for case A is shown below and the experimental and calculated joint strengths for all the conditions are summarized in Table 7.9.2. The strengths for cases D-G in Table 7.2.1 were back calculated again by using the coefficients α_{CT} and α_{LS}.

<u>Case A:</u> The geometrical factors were: x =1.19 mm (condition 7 in Table 5.10.7) and t_{eff} = 3.08 mm. The experimentally obtained force for the cross-tension condition was: F_{CT}=11.16 ± 0.61 kN. Equations 7.7 becomes

$$F_{LS} = \left(\frac{\alpha_{LS}}{\alpha_{CT}} \times \sqrt{\frac{D_t}{t_{eff}}}\right) \times F_{CT} = \left(\frac{(1.80 \pm\ 0.16)}{(2.11 \pm\ 0.21)} \times \sqrt{\frac{7.88}{3.08}}\right) \times (11.16)$$

$$= 15.18 \pm 0.82$$

The experimentally measured joint strength for the lap-shear condition was found to be 17.90 ± 0.73 kN.

Table 7.9.2 Lap-shear joint strength for different cases in Table 7.2.1

Case no.	****Rivet flaring, x, (mm)**	**Deformed rivet diameter, D_t (mm)**	**Effective length of rivet in bottom sheet calculated by equation 7.3, t_{eff} (mm)**	**Calculated joint strength (kN)**	**Measured joint strength (kN)**
A	1.19	7.88	3.04	15.18 ± 0.82	17.90 ± 0.73
B	1.13	7.76	3.11	13.89 ± 1.38	12.90 ± 0.53
C	0.86	7.22	3.57	13.70 ± 1.23	14.17 ± 0.83
D	0.79	7.08	2.66	13.6 ± 0.30	14.28 ± 0.14
E	1.11	7.72	2.50	14.6 ± 1.30	14.3 ± 0.81
F	0.80	7.10	2.65	11.1 ± 0.53	11.36 ± 0.31
G	1.25	8.00	2.43	11.3 ± 0.92	10.73 ± 0.63
H	0.95	7.40	2.03	11.12 ± 1.52	10.54 ± 0.71
I	0.90	7.40	2.05	7.52 ± 0.21	8.33 ± 0.82

** The value of rivet flaring was taken from Tables 5.10.3 and 7.

It was observed that the equation 7.7 gives a reasonable prediction of strength for the lap-shear condition. A comparison between the predicted and experimented strengths for the lap-shear condition is shown in Fig. 7.9.1.

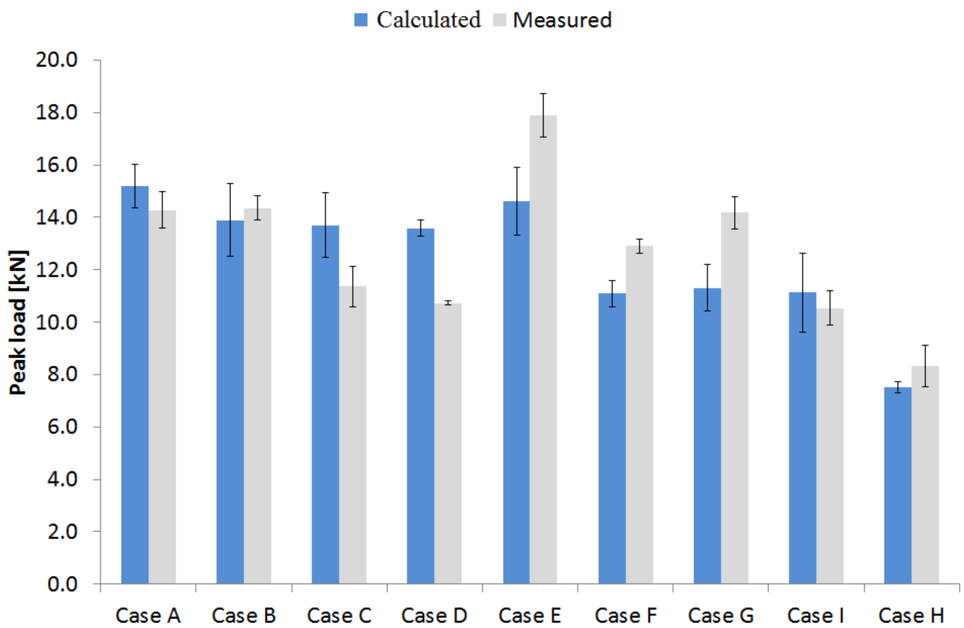

Fig. 7.9.1 Comparison between predicted and measured joint strengths for the lap-shear loading conditions for the nine different cases as tabulated in Tables 7.9.1 and 2.

It is clear from Fig. 7.9.1 that the equation 7.7 relates the joint strength between lap-shear and cross-tension with less than 8% error. Case E showed a significant discrepancy between the predicted and measured strengths. It should be noted that the failure mode in the lap-shear condition for case E was different from the other eight cases. The failure mode was tilting and pull-out of the rivet from the bottom sheet and pull-out of the rivet head from the top sheet (failure mode 2) for cases B-I as tabulated in Table 7.2.1. However, for 'case E' rivet failure occurred additionally with the failure mode 2. Thus, a big difference between the calculated and measured strengths was observed for this case. Discrepancy also observed for cases C, D, F and G due to the averaging of the co-efficient for lap-shear condition (α_{LS}). It should be noted that while determining the coefficients for the cross-tension and lap-shear conditions, the joints were chosen with 2.0 mm thick sheet. However, equation 7.7 was validated for completely different thickness combinations. This demonstrates the scenario that the coefficients are not dependent on the material thickness. The coefficients were also independent of material properties. However, the coefficients (α_{CT} and α_{LS}) were strictly related to the parameters studied in this investigation (rivet and die geometry) and cannot be generalized. Still, the developed relationship between the cross-tension and lap-shear conditions represents a useful reference to be considered for further studies especially for different rivet and die geometries.

7.10 Summary

A systematic investigation was conducted on the static strength of a single point SPR joint in the cross-tension and lap-shear loading conditions depending on different process parameters. The failure mode depends on the loading condition. Rivet pull-out was the main failure mode in cross-tension and rivet pull-out with tilting of rivet was the main failure mode for lap-shear loading. Additionally, rivet failures tend to occur for thick and hard sheet material in both loading conditions. The joint strength increases non-proportionally with increased hardness and thickness of materials for all loading conditions as other factors like rivet flaring and effective length of the rivet in the bottom sheet (t_{eff}) also influence the joint strength. The depth of the die plays a significant role in the deformation behaviour of the material. As a result, the effective length of the rivet in the bottom sheet (t_{eff}) was high for a die with a high depth which ultimately increases the joint strength.

The extension of the rivet flaring model (equation 7.4) can be used effectively to predict the joint strength in cross-tension loading and the joint strength under lap-shear loading. Equation 7.7 successfully links the joint strength with the characteristic force-displacement curve. The developed relationship represents a useful reference to be considered for further studies especially for different rivet and die geometries.

8 DISCUSSION AND GUIDANCE FOR INDUSTRY

A series of interrupted tests was conducted in this project to understand the deformation behaviour of the rivet and sheet material in the SPR process. The results of interrupted tests confirm that the force-displacement curve can be segmented in four stages: stage I – bending of the sheet and partial filling of the die, stage II – piercing of the top sheet and sheet bending, stage III – die filling, penetration of the rivet into the bottom sheet, stage IV – rivet flaring, thinning of the bottom ply and rivet setting (Fig. 5.9.1).

Different process parameters have significant impact on the different stages. The thickness and hardness of the sheet materials have the most significant influence on stage I of the characteristic force-displacement curve. Stage II mainly depends on the thickness of the top sheet. The force is almost constant during this stage. Die depth is also crucial. A deeper die may introduce an early drop in force which indicates a crack (Figs. 5.2.1-6). This information is very useful for the industry for choosing an optimum die.

Stage III provides information about penetration of the rivet in the bottom sheet (t_{eff} in Fig. 2.3.1). A good SPR joint should have sufficient rivet penetration in the bottom sheet. The rivet wall remains straight during this stage (Figs. 5.1.1-16). At the end of this stage a sudden rise in force indicates the start of rivet flaring. An early rise in force indicates rivet bulging (Figs. 5.7.5-8). A too early rise in force would indicate that the rivet had flared in between the top and bottom sheets. If a short rivet is used no rise in force would be observed. The industry may use this information to choose the optimum rivet parameters (hardness and length) and die geometry.

The amount of rivet flaring, which is ultimately related to the strength of the joint, can be estimated from stage IV: the longer this step is, the greater is the extent of rivet flaring (Chapter 5.10). The path of the rivet tip during flaring can be considered as a straight line (Fig. 5.10.7). The rivet hardness and geometry of the rivet tip mostly affects this stage: the higher the rivet hardness, the shorter is the length of this step for a given geometry of the rivet. This information can be used to develop new rivet geometry.

The thinning of the bottom ply occurs in stage IV. A long stage IV denotes more thinning of the bottom sheet. A good joint should have minimum bottom thickness (b in Fig. 2.3.1). The interrupted test shows that the thinning of the bottom ply follows the geometry of the rivet tip. This information is useful while designing the new rivet.

A rivet flaring model is developed in chapter 5.10. A very good correlation exists between the experimental and the predicted rivet flaring (Figs. 5.10.9 and 5.10.13). In practice, it is very easy to pick up the displacement (d_{max}-d_0) and for an operator to determine whether the joint is good or bad in terms of rivet flaring. Two empirical coefficients were defined depending on the rivet hardness and length. No coefficient was considered for the sheet material properties because the material properties are embedded in the force-displacement curve. This equation (equation 5.6) can be used as a good tool to predict rivet flaring without the need for a metallographic cross-section. The rivet flaring calculator can also be used to improve and optimize an SPR joint for a given material and thickness combination in industrial practice. The empirical coefficients used in this equation may provide useful guidance to design new rivets. Again, this force-displacement curve can be used not only for the validation of FEM model but also can used along with FEM model to predict and optimize the SPR process.

High compressive residual stress is observed in the rivet leg for hard material (Chapter 6.4). A significant deviation in compressive stress occurred in the rivet head due to change in hardness of the material. Residual stress in the rivet head also depends on the web thickness (W in Fig. 2.3.1) of the rivet (Figs. 6.5.1-2). This information is useful for designing a new rivet. The dependency of the residual stress profile on rivet hardness was discussed in chapter 6.6. High residual stress was observed in both the rivet head and the leg for harder rivets (Figs. 6.6.1-2). Multiple cracks were observed in harder rivets and fewer cracks were observed in softer rivets while joining 2 + 2 mm G450 steel (Figs. 6.3.27 and

6.3.29). No crack was observed in a 480 HV rivet for joining of 2 + 2 mm G300 steel, whereas a 555 HV rivet showed cracks (Figs. 6.3.31 and 6.3.33). So it is necessary to use softer rivets provided the hardness of the rivet is sufficient to pierce the top sheet. This information is useful for industry while choosing the hardness of the rivet for a given combination of materials.

The effects of material properties and thickness are discussed in chapters 7.4 and 7.5. It is clear that the joint strength increased with an increase in hardness and thickness of sheet materials in both the cross-tension and the lap-shear loading conditions (Figs. 7.4.2 and 7.4.4). The joint strength also increased with the increase in die depth (figs. 7.7.1-2). However, a deep die may create a crack in the joint as discussed in chapter 5.2. Hence, the die depth should be chosen as deep as possible unless it leads to cracking in the rivets or sheets. The industry can use this information to optimize the die for a given combination of material. From chapter 7.3 it is observed that the rivet hardness does not have a direct influence on the joint static strength (Figs. 7.6.1-2). However, from chapter 6.6 it is clear that a harder rivet may experience a number of cracks inside the rivet for a given combination of materials compared with a soft rivet. These cracks may have significant impact on the fatigue strength of the SPR joints. So, a softer rivet should be used in the application of SPR where ever possible.

The extension of the rivet flaring model can predict the joint strength within 10% error as discussed in chapter 7.8 (Fig. 7.8.1). The prediction of the deformed rivet diameter is made by equation 7.2, which is dependent on the accuracy of the rivet flaring model. Another simple prediction of effective rivet thickness (t_{eff} in Fig. 2.3.1) is determined empirically. It is believed that most of the error comes from the prediction of effective rivet thickness. However, despite the simple relationship the model can predict the joint strength with minimum error.

A relationship between the lap-shear and cross-tension loading conditions is developed in chapter 7.9. The joint strength in the lap-shear condition is predicted from the joint strength in the cross-tension loading condition. The empirical relationship is developed from the design formula proposed in Eurocode 9 [172] and it was observed that the predicted joint strengths are within 8% error. This formula can be used by industry to assess the joint strength preliminarily, which will save a lot of effort required to measure the strength in the lap-shear loading condition.

9 CONCLUSIONS AND FURTHER WORK

The project has shown that the deformation characteristics of the rivet and sheet materials can be evaluated from the force-displacement curve. The main objectives of this thesis were:

- To investigate the effect of different riveting process parameters on the deformation behaviour of the SPR process by examining the force-displacement curve.
- To examine the residual stress distribution in the rivet and surrounding sheet material for a range of joints produced by changing the material thickness and hardness, rivet hardness and die geometry.
- To examine the joint strength in static loading conditions based on several different process variables.
- To develop a technique to predict the rivet flaring without the need for cross-section metallography and to develop a relationship between the different loading conditions for static strength.

9.1 Deformation behaviour by characterizing the riveting process

The characterization of the riveting process is examined by a series of interrupted tests. The deformation behaviour of the rivet and material is understood by analysing the force-displacement curve and by examining each interrupted joint by standard optical microscopy and quantitative metallography. The following conclusions are made within the process parameters studied in this report:

- ➢ Any change in process parameter leaves a fingerprint on the characteristic force-displacement curve.
- ➢ C-frame deflection occurs in all stages of the riveting process.

- The length of the first stage of the force-displacement curve shows the stiffness of the stack and this length decreases with the increase in material hardness and thickness. An increase in rivet hardness also decreases the length of this stage. However, the force developed in this stage is independent of the rivet hardness.
- The force remains constant during the piercing stage of the riveting process for a given combination of materials. The force level changes with the material's hardness and thickness. A high force level is experienced for a hard and thick joint. Sometimes an increase in force is observed when the bottom sheet touches the die bottom surface during this stage. The touch point of the bottom sheet surface mainly depends on the material's thickness and die depth. Again, depending on the joint combination, a drop in force is experienced during this stage due to the spring-back of top sheet; a gap is created between the two sheets due to the different bending force experienced by two different sheets.
- The displacement experienced during the piercing stage depends mainly on the thickness of the top sheet and other parameters have a little influence.
- A rapid drop in force is observed at the end of the piercing stage when hard or thick material is used as the top sheet, but is not easily detected for thin material. Sometimes the bottom sheet touched the die bottom surface at the same time when the rivet completes the piercing of the bottom sheet depending on the material properties and die geometry. For these cases, no drop in force is observed at the end of the piercing stage of the riveting process.
- Die geometry significantly changes the stage III of the characteristic curve, with the length of this stage increasing with an increase in die volume. The starting of stage III is also affected by die depth, a deeper die delays the start of stage III. Sometimes cracks also developed especially for less ductile material when the die is too deep to initiate the third stage. Rivet hardness also influences this stage: the harder the rivet, the longer is this step which results in less flaring and small bottom thickness.

- The final stage of the curve gives an idea about the flaring of the rivet inside the joint. A longer fourth stage indicates more flaring and hence a better interlocked joint. An increase in rivet hardness would shorten this stage and reduce the amount of flaring.
- The prediction of rivet flaring is possible without the need for metallographic cross-sections of joints by using equation 5.6. This equation relates the fourth and final stage of the characteristic force-displacement curve to the rivet flaring.
- The overall total displacement of the characteristic curve is directly related with material thickness and rivet length. The maximum force is dependent on the pre-set rivet-setting pressure and also on the joint design parameters.

9.2 Residual stress

The residual stress examination was conducted in three different stages. For the first stage, a reproducibility and feasibility test was conducted. The next stage of the experiment was optimizing parameters for making meaningful evaluations of residual stress. The final stage of the experiment was to evaluate the residual stress profile in different SPR joints using the optimum condition developed in the previous stage. The aim of the final stage of the residual stress evaluation was to examine the effect of material hardness and thickness, and rivet hardness on the residual stress profile. The following conclusions can be drawn from the residual stress examination:

- The neutron diffraction technique successfully evaluates the position of the rivet leg after flaring in a joint, without the need to cross-section. This ultimately validates the feasibility of the residual stress evaluation.
- Stresses in the sheet material adjacent to the rivet wall and at a distance of three times the rivet radius from the rivet axis were not significant.
- Typically, 240 and 900 seconds acquisition times were necessary to achieve error (measurement uncertainty) within the range of ±50 μm in

sheet material for 1.0 and 0.125 mm^3 gauge volume respectively, while the neutron path length was around 4.0 mm.

- The detection time while evaluating the d-spacing inside a rivet should be increased to maintain the same measurement error with the same neutron path length due to the different diffraction peaks from the tetragonal material of the rivet (the peak is very close to the d-spacing 211 but not the same): 600 and 1500 seconds for 1.0 and 0.125 mm^3 gauge volume respectively.
- The magnitude of the compressive residual stress in the rivet was high for hard material. On the other hand, the magnitude of the stress was low for thick sheet material. This is attributed to the low gradient of force during the final stage of the force-displacement curve.
- An increase in rivet hardness results in an increase in the magnitude of the residual stress. However, residual stress towards the rivet leg increases up to a certain limit. When a zero residual stress is observed, this indicates a crack has developed inside the rivet. The hypothesis is verified by the extracted rivet. Multiple cracks were observed for a hard rivet in hard sheet materials joints. The number of cracks decrease for the hard rivet in soft material, and no crack was observed for a soft rivet in a soft material. The use of a soft rivet is suggested wherever possible.
- The residual stress profile is more symmetrical when a soft material is joined by SPR due to the negligible effect of the C-frame deflection.
- Residual stress in the rivet head depends on the web thickness of the rivet. The greater the web thickness of the rivet, the lesser the magnitude of the residual stress on the rivet head.
- The deformation behaviour of the material flow inside the die cavity can be examined by the residual stress profile. A tensile residual stress was observed in the material inside the joint button.

9.3 Static strength

The following conclusions are drawn from the static strength experiment:

- First of all the static strength depends on the loading condition. The strength was much higher in the lap-shear compared with the cross-tension loading condition.
- The failure mode also depends on the loading condition. Rivet pull-out was the main failure mode in cross-tension, and rivet pull-out with tilting of rivet was the main failure mode for lap-shear loading. Additionally, rivet failures tend to occur for thick and hard sheet material in both loading conditions.
- In each loading condition, the joint strength increases with increased hardness and thickness of materials. However, the increase in strength does not have a linear relationship with the hardness and thickness of materials. Other factors like rivet flaring and effective length of the rivet in the bottom sheet (t_{eff}) also influence the joint strength.
- The effect of rivet hardness on the static strength of the joint in both loading conditions was not significant. However, for the hard rivet high residual stress was observed and cracks also developed in the rivet, which may influence the fatigue strength of the joint.
- The depth of the die plays a significant role in the deformation behaviour of the material. As a result, the effective length of the rivet in the bottom sheet (t_{eff}) was high for a deeper die which ultimately increases the joint strength.
- The extension of the rivet flaring model (equation 7.4) can be used effectively to predict the joint strength in cross-tension loading. Despite the simple nature, the equation can predict the joint strength within 10% error.
- A relationship is developed to predict the joint strength under lap-shear strength from its strength in cross-tension with less than 8% error (equation 7.7). The developed relationship represents a useful reference to be considered for further studies especially for different rivet and die geometries.

9.4 Further research

Based on the knowledge developed during this study the following principal areas of work could be explored:

- Further analysis of the deformation behaviour of the SPR process for dissimilar materials by interrupted tests.
- Additional study of the rivet flaring model for a wider range of SPR joints including dissimilar materials such as aluminium and magnesium. The model can be extended beyond 2-ply joints for 3 and 4-ply joints.
- Throughout this project the spatial resolution of the residual stress evaluation was limited and the gauge volume was also limited to 0.125 mm^3, so residual stress evaluation was only possible for joints produced with thick walled rivets (1.1 mm), but in practice, a wide range of thin walled rivets (0.5 mm) are also used, which requires less force and less energy during production. So, a key area of research is to develop a suitable technique to measure the residual stress in thin as well as thick walled rivets. Another area of research could be the use of these results to validate FEA and then use FEM to predict residual stress in thin walled rivets.
- Further examination of residual stress in a variety of SPR joints with different measurement techniques (for example, measuring six co-ordinate strain by neutron diffraction and Contour) to develop a stress map instead of point measurement. A finite element model may also be developed for the stress mapping.
- Further development of equation 7.4 to predict the joint strength for a family of rivet joints with different materials. It is believed that the accuracy of the equation could be increased by accurate prediction of effective rivet thickness in the bottom sheet (t_{eff}) from the force-displacement curve.
- The joint strength of a SPR joint under the coach-peel loading condition is related with its cross-tension strength. However, the relation is unknown.

A potential area of research is to develop a relationship between cross-tension and the coach-peel loading condition.

- Investigation on the effect of residual stress on the dynamic and fatigue behaviour of the SPR joints.

10 REFERENCES

1. King, R.P., *Analysis and quality monitoring of a self-pierce riveting process*, in *PhD Thesis* 1997, University of Hertfordshire: Hertfordshire, UK.
2. Blacket, S., *Self-Pierce Riveting Technology. A Joining Solution for Light Metals*, in *Proceedings of the 1st International Light Metals Technology Conference, Brisbane, Qld, Australia, September,* . 2003. p. 383-388.
3. Barnes, T.A. and I.R. Pashby, *Joining techniques for aluminium spaceframes used in automobiles: Part II -- adhesive bonding and mechanical fasteners.* Journal of Materials Processing Technology, 2000. **99**(1-3): p. 72-79.
4. Briskham, P., N. Blundell, L. Han, R. Hewitt, and K. Young, *Comparison of self-pierce riveting, resistance spot welding and spot friction joining for aluminium automotive sheet.* SAE International, 2006. **2006-01-0774**.
5. Voelkner, W., *Present and future developments of metal forming: selected examples.* Journal of Materials Processing Technology, 2000. **106**(1-3): p. 236-242.
6. Barnes, T.A. and I.R. Pashby, *Joining techniques for aluminium spaceframes used in automobiles: Part I -- solid and liquid phase welding.* Journal of Materials Processing Technology, 2000. **99**(1-3): p. 62-71.
7. Varis, J., *Economics of clinched joint compared to riveted joint and example of applying calculations to a volume product.* Journal of Materials Processing Technology, 2006. **172**(1): p. 130-138.
8. Varis, J.P., *The suitability of clinching as a joining method for high-strength structural steel.* Journal of Materials Processing Technology, 2003. **132**(1-3): p. 242-249.
9. Lee, C.-J., J.-Y. Kim, S.-K. Lee, D.-C. Ko, and B.-M. Kim, *Design of mechanical clinching tools for joining of aluminium alloy sheets.* Materials & Design, 2010. **31**(4): p. 1854-1861.
10. Jaguar, *Jaguar world monthly*, in *Jaguar world monthly*. January, 2006, , Kelsey Publishing Ltd, UK.

11. Mortimer, J., *Jaguar uses castings, extrusions to reduce parts count in new sports car.* Assembly Automation, 2006. **26**(2): p. 115-120.
12. Carney, D., *Advanced metals gaining momentum.* Automotive Engineering International, 2008. **116**(8): p. 44-47.
13. Howard, R.M. and S.P. Sunday, *The Corrosion Performance of Steel Self-Piercing Rivets When Used with Aluminum Components.* SAE International, 1983. **SAE-831816**.
14. He, X., I. Pearson, and K. Young, *Self-pierce riveting for sheet materials: State of the art.* Journal of Materials Processing Technology, 2008. **199**: p. 27–36.
15. Hoang, N.H., R. Porcaro, M. Langseth, and A.G. Hanssen, *Self-piercing riveting connections using aluminium rivets.* International Journal of Solids and Structures, 2010. **47**: p. 427–439.
16. Hou, W., E. Mangialardi, S.J. Hu, P.C. Wang, and R. Menassa, *Characterization for quality monitoring of a self-piercing riveting process.* In: Proceedings of the Sheet Metal Welding conference XI, Sterling Heights, MI, 2004.
17. Cai, W., P.C. Wang, and W. Yang, *Assembly dimensional prediction for self-piercing riveted aluminum panels.* International Journal of Machine Tools & Manufacture, 2005. **45**: p. 695–704.
18. John, M., *Jaguar uses X350 car to pioneer use of self-piercing rivets.* Industrial Robot, 2001. **28**(3): p. 192.
19. LaPensee, M.L., *Self-Pierce Riveting Technology: A Joining Solution for Light Metals.* Light Metal Age, 2003. **61**(9-10): p. 32-35.
20. Anon, *Self-piercing rivets attach can handle.* Eng. Mater. Design 19 (12), 46, 1975.
21. Anon, *Self-piercing riveted overcame impossible joining problems.* Eureka Transfers Technol. 10, 15, 1990.
22. Moss, S. and M. Mahendran. *Structural behaviour of self-piercing riveted connections in steel framed housing*. in *Sixteenth International Specialty Conference on Cold-Formed Steel Structures: Recent Research and Developments in Cold-Formed Steel Design and Construction; Orlando,*

FL; United States; 17 October 2002 through 18 October 2002; Code 63263. 2002.

23. *Henrob group: www.henrob.co.uk*.
24. Mahendran, M., S. Pilcher, and T. Connely. *Strength of self piercing riveted connections*. in *5th International Conference on Advances in Steel Structures, ICASS 2007;* . 2007. Singapore, 5 December 2007 through 7 December 2007.
25. Moss, S.R. and M. Mahendran, *Structural behaviour of self-piercing riveted connections in G300 and G550 thin sheet steels*. Advances in Structures, Vols 1 and 2, ed. G.J. Hancock, et al. 2003. 275-280.
26. Moroni, F. and A. Pirondi, *Technology of Rivet: Adhesive Joints*, in *Hybrid Adhesive Joints*. 2011, Springer. p. 79-108.
27. Hill, H. *Introduction to the self-pierce riveting process and equipment*. in *IBEC'94 Body Assembly and Manufacture, vol. 8, Warren, pp. 1–9.* 1994.
28. Blacket, S. *The self pierce riveting process comes of age*. in *the Materials in Welding and Joining Conference. Published by Institute of Metals and Materials Australasia Ltd., pp. 149–154.* 1995.
29. Doo, R., *Automotive body construction using self-piercing rivets.* Automotive Manufacturing International, Sterling Publications International Ltd., 1993.
30. Jaguar, *Jaguar world monthly,* , in *Jaguar world monthly* December,2005, , Kelsey Publishing Ltd, UK.
31. Matsumura, Y., T. Misaki, T. Yoshida, T. Kondo, A. Sakuma, M. Maeda, Y. Yoshihara, K. Fukumoto, Y. Sugiura, and A. Okumura, *Development of application technology of aluminum roof.* Mitsubishi Motors, Technical Review, 2006. **18**: p. 68-74.
32. Tong, Y. and L. Qu, *Recent patents in riveting and applications.* Recent Patents on Engineering, 2009. **3**(3): p. 220-227.
33. Han, L., M. Thornton, and M. Shergold, *A comparison of the mechanical behaviour of self-piercing riveted and resistance spot welded aluminium sheets for the automotive industry.* Materials & Design, 2010. **31**(3): p. 1457-1467.

34. Rahman, M.M., R.A. Bakar, M.M. Noor, M.R.M. Rejab, and M.S.M. Sani, *Fatigue Life Prediction of Spot-Welded Structures: A Finite Element Analysis Approach.* European Journal of Scientific Research, 2008. **22**(3): p. 444-456.
35. Litherland, H. *Self-piercing riveting for aluminium applications.* in *In: Proceedings of the Seventh International Conference INALCO'98, Cambridge, April 15–17, pp. 135–147*. 1998.
36. Thomas, W. *Enhancement of aluminium alloy surfaces by using mechanical insert*. in *n: Proceedings of the Seventh International Conference INALCO'98, Cambridge, April 15–17, pp. 135–147. 1998.* 1998.
37. Emhart. *web reference*. Available from: www.emhart.com.
38. Bollohoff fastenings Ltd: www. boellhoff.de.
39. Dilthey, U. and L. Stein, *Multimaterial car body design: challenge for welding and joining.* Science & Technology of Welding & Joining, 2006. **11**(2): p. 135-142.
40. Mortimer, J., *Rivet technology rules for Jaguar.* Automotive Engineer (London), 2004. **29**(3): p. 14.
41. TWI. *web reference*. Available from: www.twi.co.uk.
42. Cheraghi, S., *Effect of variations in the riveting process on the quality of riveted joints.* The International Journal of Advanced Manufacturing Technology, 2008. **39**(11-12): p. 1144-1155.
43. Larsson, J. *Clinch-joining–a cost effective joining technique for BIW Assembly*. in *Proceedings of the International Conference on Body engineering, advanced technologies and processes, Warren, Michigan, USA*. 1994.
44. Bokhari, N., *Self-piercing riveting - process and equipment.* Welding and Metal Fabrication, 1995. **63**(5).
45. Sunday, S.P., *Self-Piercing Rivets for Aluminum Components*, in *SAE Technical Paper 830526, 1983, doi:10.4271/830526*. 1983.
46. Monday, D., *Joining Through thick and thin* Feb, 2008Appliance Design: Australia, http://www.appliancedesign.com.

47. Bonde, N. and S. Grange-Jansson. *Self-piercing riveting in high strength steel- a way to increase fatigue life*. in *Advanced Technologies & Process. IBEC, pp 16-20*. 1996.

48. Profast. *web reference*. Available from: www.profast.com.au.

49. Wang, J.W., Z.X. Liu, Y. Shang, A.L. Liu, M.X. Wang, R.N. Sun, and P.-C. Wang, *Self-Piercing Riveting of Wrought Magnesium AZ31 Sheets.* Journal of Manufacturing Science & Engineering, 2011. **133**(3): p. 031009-1-031009-9.

50. Liu, Z.X., P.C. Wang, and J.W. Wang, *Investigation to self-piercing riveting of wrought magnesium AZ31 sheets.* Advanced Materials Research, 2012. **472-475**: p. 1188-1191.

51. R. Neugebauer, S.D., C. Kraus *Comparison of Dieless Clinching and Dieless Rivet Clinching of Magnesium* in *7th International conference on magnesium alloys and their applications, Dresden, Germany, Wiley-VCH; 2006. p. 1069-75*, K. KU, Editor. 2006.

52. Easton, M., A. Beer, M. Barnett, C. Davies, G. Dunlop, Y. Durandet, S. Blacket, T. Hilditch, and P. Beggs, *Magnesium alloy applications in automotive structures.* JOM Journal of the Minerals, Metals and Materials Society, 2008. **60**(11): p. 57-62.

53. Durandet, Y., B. Dempster, W. Song, and M. Brandt, *Examination of rivets performance for LSPR joining*. 2008, CAST Report 2008 421.

54. Durandet, Y., R. Deam, A. Beer, W. Song, and S. Blacket, *Laser assisted self-pierce riveting of AZ31 magnesium alloy strips.* Materials and Design, 2010. **31**(3): p. S13-S16.

55. Durandet, Y., W. Song, S. Blacket, and M. Brandt. *Spot joining of magnesium using thermally enhanced self-piercing riveting technology*. in *Proceedings of the 3rd International Conference on Light metals technology (LMT). Quebec, Canada: Saint- Sauveur; 2007. p. 141–6*. 2007.

56. Durandet, Y., R. Deam, A. Beer, W. Song, R. Clegg, and S. Blacket, *Joining of AZ31 magnesium alloy strips by laser assisted self-pierce riveting*, in *Kainer KU, editor. 8th International conference on magnesium*

alloys and their applications. Weimar, Germany: Wiley-VCH Books; 2009. 2009.

57. Durandet, Y., W. Song, B. Dempster, R. Clegg, and A. Beer, *LSPR Joining Technical Summary Report (3rd Year Review CAST3)*. 2008, CAST Report 2008 434.
58. Lou, M., Y. Li, Y. Li, and G. Chen, *Behavior and quality evaluation of electroplastic self-piercing riveting of aluminum alloy and advanced high strength steel.* Journal of Manufacturing Science and Engineering, Transactions of the ASME, 2013. **135**(1).
59. Wang, B., C. Hao, and J. Zhang, *A New Self-Piercing Riveting Process and Strength Evaluation.* Journal of Manufacturing Science and Engineering, 2006. **128**: p. 580-587.
60. Hahn, O., R. Neugebauer, G. Leuschen, C. Kraus, and R. Mauermann, *Research in Impulse Joining of Self Pierce Riveting*, in *3rd International Conference on High Speed Forming – 2008*. 2008: Dortmund, Germany.
61. Neugebauer, R., R. Mauermann, and R. Grützner, *Combination of hydroforming and joining.* Steel Research International, 2005. **76**(12): p. 939-944.
62. Fiore, V., F. Alagna, G. Di Bella, and A. Valenza, *On the mechanical behavior of BFRP to aluminum AA6086 mixed joints.* Composites Part B: Engineering, 2013. **48**: p. 79-87.
63. Fratini, L. and V.F. Ruisi, *Self-piercing riveting for aluminium alloys-composites hybrid joints.* International Journal of Advanced Manufacturing Technology, 2009. **43**(1/2): p. 61-66.
64. Di Franco, G., L. Fratini, and A. Pasta, *Analysis of the mechanical performance of hybrid (SPR/bonded) single-lap joints between CFRP panels and aluminum blanks.* International Journal of Adhesion and Adhesives, 2013. **41**(0): p. 24-32.
65. Hahn, O. and T.M. Wibbeke, *Application of low-heat hybrid joining technologies for the joining of thin-walled sheet materials.* Welding and Cutting, 2005. **4**(4): p. 208-214.

66. Ueda, M., S. Miyake, H. Hasegawa, and Y. Hirano, *Instantaneous mechanical fastening of quasi-isotropic CFRP laminates by a self-piercing rivet.* Composite Structures, 2012. **94**(11): p. 3388-3393.

67. Han, L., *Mechanical behaviour of self-piercing riveted aluminium joints*. 2003, PhD thesis, University of Hertfordshire, UK.

68. Xu, Y., *Characterization of Self-piercing Riveted joint*, in *Engineering Science*. 2005, PhD Dissertation,The University of Toledo.

69. Xu, Y., *Effects of factors on physical attributes of self-piercing riveted joints.* Science & Technology of Welding & Joining, 2006. **11**(6): p. 666-671.

70. Han, L. and A. Chrysanthou, *Evaluation of quality and behaviour of self-piercing riveted aluminium to high strength low alloy sheets with different surface coatings.* Materials and Design 2008. **29**: p. 458-468.

71. Andersson, R., P. Jonason, and T. Pettersson, *Self-Pierce Riveting Through 3 Sheet Metal Combinations* in *THE 14TH INTERNATIONAL ESAFORM CONFERENCE ON MATERIAL FORMING: ESAFORM 2011 Date: 27–29 April 2011 Location: Belfast, (United Kingdom)*. 2011.

72. Tileli, F., J.M. O'Sullivan, Y.K. Chen, J. Andrew, and K. Denham, *Dynamic response of self-pierce riveted joints*, in *Proceedings of the 15th National Conference on Manufacturing Research, pp. 3–7*. 1999.

73. Agrawal, H., W. Li, S. Bollimunta, K. Potty, and A. Blows, *Fatigue life of self-piercing rivets (SPR) in car body.* SAE technical paper series 2003-01-914, 2003.

74. Atzeni, E., R. Ippolito, and L. Settineri, *Experimental and numerical appraisal of self-piercing riveting.* CIRP Annals - Manufacturing Technology, 2009. **58**(1): p. 17-20.

75. Atzeni, E., R. Ippolito, and L. Settineri, *Experimental and numerical investigation on self-piercing riveting*, in *SME technical paper TP05PUB94*. 2010, Politecnico di Torino: Turin, Italy.

76. Porcaro, R., A.G. Hanssen, M. Langseth, and A. Aalberg, *Self-piercing riveting process: An experimental and numerical investigation.* Journal of Materials Processing Technology, 2006. **171**: p. 10–20.

77. Hanssen, A.G., L. Olovsson, R. Porcaro, and M. Langseth, *A large-scale finite element point-connector model for self-piercing rivet connections.* European Journal of Mechanics - A/Solids, 2010. **29**(4): p. 484-495.

78. King, R.P., J.M. Osullivan, D. Spurgeon, and P. Bentley, *Setting load requirements and fastening strength in the self-pierce riveting process*. Advances in Manufacturing Technology Ix, ed. D. Stockton and C. Wainwright. 1995. 57-61.

79. Kim, D.-W., J. Xu, W. Li, and D. Blake, *Force characteristics of self-piercing riveting.* Proceedings of the Institution of Mechanical Engineers, Part B: Journal of Engineering Manufacture, 2006. **220**(8): p. 1259-1266.

80. Casalino, G., *DOE Analysis of the Effects of Geometrical Parameters on the Self-Piercing Riveting of Aluminium Alloy AA6060T4.* Key Engineering Materials, 2011. **473**(1): p. 733-738.

81. Mucha, J., *A study of quality parameters and behaviour of self-piercing riveted aluminium sheets with different joining conditions.* Strojniski Vestnik/Journal of Mechanical Engineering, 2011. **57**(4): p. 323-333.

82. Cacko, R., *Review of different material separation criteria in numerical modeling of the self-piercing riveting process - SPR.* Archives of Civil and Mechanical Engineering, 2008. **8**(2): p. 21-30.

83. He, X.C., J.N. He, J.H. Ke, J.K. Xie, and Y.F. Ding, *Quality evaluation and strength reliability prediction of self-pierce riveted joints.* Hunan Daxue Xuebao/Journal of Hunan University Natural Sciences, 2010. **37**(SUPPL. 1): p. 1-4.

84. He, X., Y. Hu, B. Xing, Y. Ding, and K. Zeng, *Numerical simulation and online window monitoring of SPR process*. 2013. p. 1765-1768.

85. He, X., F. Gu, and A. Ball, *A process monitoring method for self-piercing riveting.* Advanced Science Letters, 2012. **14**(1): p. 394-397.

86. Stepinski, T. *Assessing Quality of Self-piercing Rivets Using Ultrasound*. in *Proceeding of the 9th European Conference on NDT, Berlin, Sept 25-29, 2006*. 2006. Citeseer.

87. Hewitt, R., *ADVANCED BODY JOINING*. 2007, Closure report on Premium Automotive Research and Development Programme, The University of Warwick, UK.

88. Johnson, P., J.D. Cullen, A.I. Al-Shamma'A, and A. Shaw, *Online visual inspection of self-piercing riveting to determine the quality of the mechanical interlock.* Journal of Physics: Conference Series, 2007. **76**(1).

89. Johnson, P., J.D. Cullen, L. Sharples, A. Shaw, and A.I. Al-Shamma'a, *Online visual measurement of self-pierce riveting systems to help determine the quality of the mechanical interlock.* Measurement: Journal of the International Measurement Confederation, 2009. **42**(5): p. 661-667.

90. Sadowski, T. and M. Knec, *Application of DIC technique for monitoring of deformation process of SPR hybrid joints.* Archives of Metallurgy and Materials, 2013. **58**(1): p. 119-125.

91. Fu, M. and P.K. Mallick, *Effect of process variables on the static and fatigue properties of self-piercing riveted joints in aluminum alloy 5754.* Society of Automotive Engineers, 2001(SAE Paper No. 2001-01-0825).

92. Henrob, *Henrob rivet information.* 'Henrob rivet information'- Internal communication with Henrob, 2001.

93. Henrob, *Product information - Rivet joint optimisation criteria for Henrob Self Pierce rivets in steel.* Henrob Internal Report 2009.

94. Westgate, S.A., R. Doo, F. Liebrecht, S. Braeunling, T. Mattsson, and K.O. Strömberg, *The development of lightweight self-piercing riveting equipment.* SAE Technical Papers Code 90814, 2001.

95. Varis, J.P. and J. Lepisto, *A simple testing-based procedure and simulation of the clinching process using finite element analysis for establishing clinching parameters.* Thin-Walled Structures, 2003. **41**(8): p. 691-709.

96. Sjöström, E., J. Gårdstam, and R. Trinick, *Development of martensitic stainless steel rivets for applications of self piercing riveting of stainless steel sheets*. 2004, Swedish Institute for Metals Research, IM-2004-536.

97. J.Gårdstam, *Simulation and verification of strength of self pierced rivet joints of stainless sheet steels*. 2004, Swedish Institute for Metals Research, IM-2004-547.

98. Jin, Z. and P.K. Mallick. *Enhancement of fatigue life of self-piercing riveted joints by coining*. in *ASME 2002 International Mechanical Engineering Congress and Exposition, IMECE2002; New Orleans, LA;*

United States; 17 November 2002 through 22 November 2002; Code 82313. 2002.

99. Huang, H., D. Du, B.H. Chang, B. Sui, and Q. Chen, *Distortion analysis for self-piercing riveting of aluminium alloy sheets.* Science and Technology of Welding and joining, 2007. **12**(1): p. 73-78.

100. Liu, R. and X. Dang. *Mechanical behaviour of self-piercing riveted two-layer joints with different surface treatment*. in *Proceedings 2011 International Conference on Mechatronic Science, Electric Engineering and Computer, MEC 2011 , art. no. 6025562 , pp. 703-706* 2011.

101. Henrob, *Self-Piercing Riveting Joint Data –Hydraulic Pre-Clamp Process Users Guide.* 2002. **Rivet Joint Data (Hydraulic) Users Guide Issue 3**.

102. Sui, B., D. Du, B.H. Chang, H. Huang, and L. Wang, *Simulation and analysis of self-piercing riveting process in aluminum sheets.* Cailiao Kexue yu Gongyi/Material Science and Technology, 2007. **15**(5): p. 713-717.

103. Kaščák, L., E. Spišák, and J. Mucha, *Evaluation of properties of joints made by clinching and self-piercing riveting methods.* Acta Metallurgica Slovaca, 2012. **18**(4): p. 172-180.

104. Xu, J., X. He, Y. Tang, Y. Ding, Y. Hu, and K. Zeng, *Microstructure and mechanical properties analysis of AL-5052 self-pierce riveting joint in material application engineering*. 2013. p. 173-176.

105. Han, L., K.W. Young, A. Chrysanthou, and J.M. O'Sullivan, *The Effect of Pre-Straining on the Mechanical Behaviour of Self-Piercing Riveted Aluminium Alloy Sheets.* Advanced Materials Research, 2005. **6**(1): p. 157-162.

106. Wood, P.K.C., C.A. Schley, M. Buckley, B. Walker, and T. Dutton. *Modelling self-piercing riveted joint failures in automotive crash structures*. in *Proceedings of 10th Int. LS-DYNA Users' Conference, 2008-06-08 - 2008-06-10, Detroit, Michigan*. 2008.

107. Han, L., K.W. Young, A. Chrysanthou, and J.M. O'Sullivan, *The effect of pre-straining on the mechanical behaviour of self-piercing riveted aluminium alloy sheets.* Materials and Design, 2006. **27**(10): p. 1108-1113.

108. Madasamy, C., O. Faruque, T. Tyan, and R. Thomas. *Static and impact behavior of self-pierced rivet connections in aluminum*. in *2001 ASME International Mechanical Engineering Congress and Exposition; New York, NY; United States; 11 November 2001 through 16 November 2001; Code 62034*. 2001.

109. Sun, X. and M.A. Khaleel, *Performance optimization of self-piercing rivets through analytical rivet strength estimation.* Journal of Manufacturing Processes, 2005. **7**(1): p. 83-93.

110. Mori, K., Y. Abe, and T. Kato, *Mechanism of superiority of fatigue strength for aluminium alloy sheets joined by mechanical clinching and self-pierce riveting.* Journal of Materials Processing Technology, 2012. **212**(9): p. 1900-1905.

111. Li, D., L. Han, M. Thornton, and M. Shergold, *Influence of rivet to sheet edge distance on fatigue strength of self-piercing riveted aluminium joints.* Materials Science and Engineering A, 2012. **558**: p. 242-252.

112. Han, L., K.W. Young, R. Hewitt, M.R. Alkahari, and A. Chrysanthou, *Effect of sheet material coatings on quality and strength of self-piercing riveted joints.* SAE Technical Papers, 2006 SAE World Congress; Detroit, MI; United States; 3 April 2006 through 6 April 2006; Code 90162, 2006.

113. Liu, R., Y. Chu, X. Dang, and X. Wang, *Connection strength of self-piercing riveted with different surface treatment.* Information (Japan), 2012. **15**(12 A): p. 5403-5410.

114. Han, L., A. Chrysanthou, and J.M. O'Sullivan, *Fretting behaviour of self-piercing riveted aluminium alloy joints under different interfacial conditions.* Materials and Design, 2006. **27**: p. 200–208.

115. Wake, R., *Riveting ride to a greener world*, in *manufacturer's monthly, march 2010, http://www.manmonthly.com.au*. 2010: Australia.

116. Hahn, O., G. Meschut, and A. Peetz, *Mechanical properties of punch-riveted and adhesive-bonded aluminium sheets.* Schweissen und Schneiden/Welding and Cutting, 1999. **51**(7): p. E130-E134.

117. Hahn, O. and T.M. Wibbeke, *Application of low-heat hybrid joining technologies for the joining of thin-walled sheet materials.* Welding and Cutting, 2004. **4 (2004), No. 4**.

118. He, X., B. Xing, Y. Ding, Y. Hu, and K. Zeng, *Strength and energy absorption of self-piercing riveted joints*. 2013. p. 1783-1786.

119. Henrob, *Dies.* Internal communication with Henrob, 2009.

120. Gårdstam, J., *Simulation of self piercing riveting of the austenitic stainless sheet steel EN 1.4301 in 1+1 mm sheet thickness*. 2003, Master's thesis, Swedish Institute for Metals Research, IM-2003-114.

121. Mori, K., T. Kato, Y. Abe, and Y. Ravshanbek, *Plastic Joining of Ultra High Strength Steel and Aluminium Alloy Sheets by Self Piercing Rivet.* CIRP Annals - Manufacturing Technology, 2006. **55**(1): p. 283-286.

122. Pickin, C.G., K. Young, and I. Tuersley, *Joining of lightweight sandwich sheets to aluminium using self-pierce riveting.* Materials and Design, 2007. **28**: p. 2361-2365.

123. Gardstam, J., *Simulation of mechanical joining for automotive applications* in *Licentiate thesis, Department of mechanics*. 2006, Royal Institute of Technology,Sweden: Stockholm.

124. Khezri, R. and A. Melander, *New technology for self piercing riveting of TRIP800 in 1+1 and 1+2mm sheet thickness*. 2003, Swedish Institute for Metal Research report, IM-2003-545.

125. Khezri, R. and A. Melander, *Simulation of self piercing riveting of TRIP800 sheet steel in 1+1mm thickness*. 2003, Swedish Institute for Metals Research, IM-2003-515.

126. Fayolle, S., P.O. Bouchard, and K. Mocellin, *Joining and Mechanical Strength of Selfpiercing Riveted Structure - Numerical Modeling and Experimental Validation*, in *Experimental Analysis of Nano and Engineering Materials and Structures*, E.E. Gdoutos, Editor. 2007, Springer Netherlands. p. 813-814.

127. Taylor, G., *Self-pierce riveting in automotive assembly*, in *Proceedings of the 30th ISATA Materials for Energy Efficient Vehicles Conference, Florence, Italy, June 16–19,pp. 229–240,* . 1997.

128. Masters, I., X. Fan, R. Roy, and D. Williams, *Modelling distortion induced in an assembly by the self piercing rivet process.* Proceedings of the Institution of Mechanical Engineers Part B-Journal of Engineering Manufacture, 2012. **226**(B2): p. 300-312.

129. Leijon, G., *Strain controlled fatigue testing of two high strength austenitic stainless steels- HyTens 800 and HyTens 1000*. 2004, Swedish Institute for Metals Research, IM-2004-509.

130. J.Gårdstam, *Simulation of self piercing riveting of high strength austenitic stainless steel in 1 and 2 mm sheet thickness*. 2004, Swedish Institute for Metals Research, IM-2004-537.

131. Abe, Y., T. Kato, and K. Mori, *Joinability of aluminium alloy and mild steel sheets by self piercing rivet.* Journal of Materials Processing Technology, 2006. **177**: p. 417–421.

132. Abe, Y., T. Kato, and K. Mori, *Self-piercing riveting of high tensile strength steel and aluminium alloy sheets using conventional rivet and die.* Journal of Materials Processing Technology, 2009. **209**: p. 3914–3922.

133. Bouchard, P.O., T. Laurenta, and L. Tollier, *Numerical modeling of self-pierce riveting—From riveting process modeling down to structural analysis.* Journal of Materials Processing Technology, 2008. **202**: p. 290-300.

134. Chenot, J.-L., P.-O. Bouchard, E. Massoni, K. Mocellin, and P. Lasne, *Finite Element Modeling and Optimization of Mechanical Joining Technology.* AIP Conference Proceedings, 2011. **1353**(1): p. 1247-1252.

135. Huang, Z.C., Z.J. Zhou, and W. Huang, *Mechanical Behaviors of Self-Piercing Riveting Joining Dissimilar Sheets.* Advanced Materials Research, 2010. **97**(1): p. 3932-3935.

136. Sun, X. and M.A. Khaleel, *Strength estimation of self-piercing rivets using lower bound limit load analysis.* Science and Technology of Welding and joining, 2005. **10**(5): p. 624-635.

137. Han, L., A. Chrysanthou, and K.W. Young, *Mechanical behaviour of self-piercing riveted multi-layer joints under different specimen configurations.* Materials and Design, 2007. **28**: p. 2024–2033.

138. Han, L., M. Thornton, R. Hewitt, A. Chrysanthou, and M. Shergold. *Process feasibility analysis of self-pierce riveting high strength low alloy steel*. in *ASME 2010 10th Biennial Conference on Engineering Systems Design and Analysis, ESDA2010; Istanbul; Turkey; 12 July 2010 through 14 July 2010; Code 84828*. 2010.

139. He, X., B. Xing, K. Zeng, F. Gu, and A. Ball, *Numerical and experimental investigations of self-piercing riveting.* International Journal of Advanced Manufacturing Technology, 2013: p. 1-7.

140. Li, D., L. Han, M. Thornton, and M. Shergold, *Influence of edge distance on quality and static behaviour of self-piercing riveted aluminium joints.* Materials & Design, 2012. **34**: p. 22-31.

141. Mucha, J. and W. Witkowski, *The experimental analysis of the double joint type change effect on the joint destruction process in uniaxial shearing test.* Thin-Walled Structures, 2013. **66**(0): p. 39-49.

142. Iyer, K., F.L. Brittman, S.J. Hu, P.C. Wang, D.B. Hayden, and S.P. Marin. *Fatigue and fretting of self-piercing riveted joints*. in *ASME International Mechanical Engineering Congress and Exposition, Proceedings , pp. 401-415, November 17-22, New Orleans, Louisiana, USA*. 2002.

143. Bijju, M., *Failure analysis of self-piercing riveted joint under different loading conditions using finite element method*, in *Department of Mechanical Engineering*. 2008, Wichita State University: USA.

144. Lim, B.K., *Analysis of fatigue life of SPR(Self-Piercing Riveting) jointed various specimens using FEM.* Materials Science Forum, 2008. **580-582**: p. 617-620.

145. Iyer, K., S.J. Hu, F.L. Brittman, P.C. Wang, D.B. Hayden, and S.P. Marin, *Fatigue of single- and double-rivet self-piercing riveted lap joints.* Fatigue & Fracture of Engineering Materials & Structures, 2005. **28**: p. 997-1007.

146. Di Franco, G., L. Fratini, A. Pasta, and V.F. Ruisi, *On the self-piercing riveting of aluminium blanks and carbon fibre composite panels.* International Journal of Material Forming, 2013. **6**(1): p. 137-144.

147. Franco, G.D., L. Fratini, and A. Pasta, *Influence of the distance between rivets in self-piercing riveting bonded joints made of carbon fiber panels and AA2024 blanks.* Materials and Design, 2011. **35**(1): p. 342-349.

148. Zhou, M., S.J. Hu, and H. Zhang, *Critical Specimen Sizes for Tensile-Shear Testing of Steel Sheets.* Welding Journal (Miami, Fla), 1999. **78**(9): p. 305s-313s.

149. Lennon, R., R. Pedreschi, and B.P. Sinha, *Comparative study of some mechanical connections in cold formed steel.* Construction and Building Materials, 1999. **13**(3): p. 109-116.

150. Han, L., A. Chrysanthou, K.W. Young, and J.M. O'Sullivan, *Characterization of fretting fatigue in self-piercing riveted aluminium alloy sheets.* Fatigue and Fracture of Engineering Materials and Structures, 2006. **29**(8): p. 646-654.

151. Wood, P.K.C., C.A. Schley, M.A. Williams, and A. Rusinek, *A model to describe the high rate performance of self-piercing riveted joints in sheet aluminium.* Materials & Design, 2011. **32**(4): p. 2246-2259.

152. Sun, X. and M.A. Khaleel, *Dynamic strength evaluations for self-piercing rivets and resistance spot welds joining similar and dissimilar metals.* International Journal of Impact Engineering, 2007. **34**: p. 1668–1682.

153. Han, L., Y.K. Chen, A. Chrysanthou, and J.M. O'Sullivan, *Self-Pierce Riveting: A New Way for Joining Structures.* ASME Conference Proceedings, 2002. **2002**(46571b): p. 123-127.

154. Chen, Y.K., L. Han, A. Chrysanthou, and J.M. O'Sullivan, *Fretting wear in self-piercing riveted aluminium alloy sheet.* Wear, 2003. **255**(7-12): p. 1463-1470.

155. Ruijun, L. and D. Xiangwen. *Weight analysis on parameters of self-pierce riveting*. in *2011 International Conference on Consumer Electronics, Communications and Networks, CECNet 2011; XianNing; China; 16 April 2011 through 18 April 2011; Category numberCFP1153N-DVD; Code 85030*. 2011.

156. Fu, M. and P.K. Mallick, *Fatigue of self-piercing riveted joints in aluminum alloy 6111.* International Journal of Fatigue, 2003. **25**: p. 183–189.

157. Settineri, L., E. Atzeni, and R. Ippolito, *Self piercing riveting for metal-polymer joints.* International Journal of Materials Forming, 2010. **3**(0 suppl.): p. 995-998.

158. Franco, G.D., L. Fratini, A. Pasta, and A. Ruisi, *On the self-piercing riveting of aluminium blanks and carbon fibre composite panels.*

International Journal of Materials Forming, 2010. **3**(0 suppl.): p. 1035-1038.

159. Franco, G.D., L. Fratini, and A. Pasta, *Fatigue behaviour of self-piercing riveting of aluminium blanks and carbon fibre composite panels.* Proceedings of the Institution of Mechanical Engineers, Part L: Journal of Materials: Design and Applications, 2012. **226**(3): p. 230-241.

160. Calabrese, L., L. Bonaccorsi, E. Proverbio, G. Di Bella, and C. Borsellino, *Durability on alternate immersion test of self-piercing riveting aluminium joint.* Materials and Design, 2013. **46**: p. 849-856.

161. Khanna, S.K., X. Long, S. Krishnamoorthy, and H.N. Agrawal, *Fatigue properties and failure characterisation of self-piercing riveted 6111 aluminium sheet joints.* Science and Technology of Welding and Joining, 2006. **11**(5): p. 544-549.

162. Fagerberg, D., *Prediction of fatigue strength of shear loaded self-piercing rivet joints with different gaps and cracks*, in *Master's thesis, Swedish Institute for Metals Research, IM-2002-031,* . 2002.

163. Krause, A.R. and R.A. Chernenkoff, *A comparative study of the fatigue behavior of spot welded and mechanically fastened aluminum joints.* SAE Technical Papers, SAE International Congress and Exposition; Detroit, MI; United States; 27 February 1995 through 2 March 1995; Code 90411, 1995.

164. Porcaro, R., M. Langseth, S. Weyer, and H. Hooputra, *An experimental and numerical investigation on self-piercing riveting.* International Journal of Material Forming, 2008. **1**(SUPPL. 1): p. 1307-1310.

165. Hoang, N.H., O.S. Hopperstad, M. Langseth, and I. Westermann, *Failure of aluminium self-piercing rivets: An experimental and numerical study.* Materials and Design, 2013. **49**: p. 323-335.

166. Porcaro, R., A.G. Hanssen, M. Langseth, and A. Aalberg, *The behaviour of a self-piercing riveted connection under quasi-static loading conditions.* International Journal of Solids and Structures, 2006. **43**(17): p. 5110-5131.

167. Porcaro, R., A.G. Hanssen, M. Langseth, and A. Aalberg, *An experimental investigation on the behaviour of self-piercing riveted connections in*

aluminium alloy AA6060. International Journal of Crashworthiness, 2006. **11**(5): p. 397-417.

168. Li, B. and A. Fatemi, *An experimental investigation of deformation and fatigue behavior of coach peel riveted joints.* International Journal of Fatigue, 2006. **28**: p. 9-18.
169. Eckstein, J., E. Roos, K. Roll, M. Ruther, and M. Seidenfuß. *Experimental and numerical investigations to extend the process limits in Self-Pierce Riveting*. in *10TH ESAFORM CONFERENCE ON MATERIAL FORMING; Zaragoza; Spain; 18 April 2006 through 20 April 2006*. 2007.
170. He, X., *Coefficient of variation and its application to strength prediction of self-piercing riveted joints.* Scientific Research and Essays, 2011. **6**(34): p. 6850-6855.
171. He, X., *An approximate method via coefficient of variation for strength prediction of self-piercing riveted joints.* Applied Mechanics and Materials, 2010. **26-28**: p. 334-339.
172. CEN, prEN1999-1-4, Eurocode 9 : Design of aluminium structures, Part: 1–4: Supplementary rules for cold-formed sheeting (stage 34), 2004(May).
173. Haberkorn, G., E.W. Blumcke, and K. Thoma, *Investigation of a self piercing riveted joint with a focus on dynamic loads.* Materialprufung, 2006. **48**(10): p. 486-492.
174. Sun, X., E.V. Stephens, and M.A. Khaleel, *Fatigue behaviors of self-piercing rivets joining similar and dissimilar sheet metals.* International Journal of Fatigue, 2007. **29**: p. 370–386.
175. Lee, M.H., H.Y. Kim, and S.I. Oh, *Crushing test of double hat-shaped members of dissimilar materials with adhesively bonded and self-piercing riveted joining methods.* Thin-Walled Structures, 2006. **44**(4): p. 381-386.
176. Hahn, O., G. Meschut, and A.P. Paderborn, *Mechanical properties of punch-riveted and adhesive-bonded aluminium sheet.* Welding and Cutting, 1999. **51 (1999) No. 7**.
177. Sadowski, T., T. Balawender, R. Śliwa, P. Golewskp, and M. Kneć, *Modern hybrid joints in aerospace: Modelling and testing.* Archives of Metallurgy and Materials, 2013. **58**(1): p. 163-169.

178. Sadowski, T. and E. Zarzeka-Raczkowska, *Hybrid adhesive bonded and riveted joints - Influence of rivet geometrical layout on strength of joints.* Archives of Metallurgy and Materials, 2012. **57**(4): p. 1127-1135.

179. Porcaro, R., M. Langseth, A.G. Hanssen, H. Zhao, S. Weyer, and H. Hooputra, *Crashworthiness of self-piercing riveted connections.* International Journal of Impact Engineering, 2008. **35**(11): p. 1251-1266.

180. Presz, W. and R. Cacko, *Influence of Micro-Rivet Manufacturing Process on Quality of Micro-Joint.* AIP Conference Proceedings, 2011. **1353**(1): p. 541-546.

181. Han, L., K. Young, R. Hewitt, A. Chrysanthou, and J.M. O'Sullivan. *Fatigue failure modes in self-piercing riveted aluminium alloy joints*. in *Proceedings of the 7th Biennial Conference on Engineering Systems Design and Analysis - 2004; Manchester; United Kingdom; 19 July 2004 through 22 July 2004; Code 63942*. 2004.

182. Wester, C., *Prediction of fatigue strength of peel loaded self-piercing rivet joints with different gaps and cracks, M.Sc. Thesis*. 2003, Swedish Institute for Metals Research, IM-2003-139.

183. He, X. and S.O. Oyadiji, *Three dimensional FEA of torsional free vibration of bonded beams*. Integrating Dynamics, Condition Monitoring and Control for the 21st Century - Dymac 99, ed. A.G. Starr, et al. 1999, Leiden: A a Balkema Publishers. 481-487.

184. He, X. *Influence of sheet material characteristics on the torsional free vibration of single lap-jointed cantilevered spr joints*. 2009. Zhangjiajie, Hunan.

185. He, X., B. Dong, and X. Zhu. *Free vibration characteristics of hybrid SPR beams*. in *2nd International Symposium on Computational Mechanics, ISCM II, and the 12th International Conference on the Enhancement and Promotion of Computational Methods in Engineering and Science, EPMESC XII; Hong Kong, Macau; China; 30 November 2009 through 3 December 2009*. 2010. AIP Conference Proceedings Volume 1233, Issue PART 1, 2010, Pages 678-683.

186. He, X., X. Zhu, and B. Dong. *Transverse free vibration analysis of hybrid SPR steel joints*. in *Proceedings of the 2010 International Conference on*

Mechanical, Industrial, and Manufacturing Technologies, MIMT 2010, Pages 389-394. 2010.

187. He, X., F. Gu, and A. Ball, *Recent development in finite element analysis of self-piercing riveted joints.* International Journal of Advanced Manufacturing Technology, 2012. **58**(5-8): p. 643-649.
188. Hoang, N.H., A.G. Hanssen, M. Langseth, and R. Porcaro, *Structural behaviour of aluminium self-piercing riveted joints: An experimental and numerical investigation.* International Journal of Solids and Structures, 2012. **49**(23-24): p. 3211-3223.
189. Hoang, N.H., M. Langseth, R. Porcaro, and A.G. Hanssen, *The effect of the riveting process and aging on the mechanical behaviour of an aluminium self-piercing riveted connection.* European Journal of Mechanics, A/Solids, 2011. **30**(5): p. 619-630.
190. Han, S.L., Y.W. Wu, Q.L. Zeng, and Y. Gao. *Numerical analysis of self-pierce riveting of AZ31 magnesium alloy sheets*. in *11th International Conference on Numerical Methods in Industrial Forming Processes, NUMIFORM 2013*. 2013. Shenyang.
191. Cacko, R. and P. Czyżewski, *Verification of numerical modeling of the SPR joint by experimental stack-up*, in *Proceedings of the Computer Methods in Materials Science 7(1):124–130*. 2007.
192. Tang, D.X., B. Barthelemy, and H. Yuan. *Self-Pierced Rivet (SPR) modeling in aluminum structure crash analysis*. in *ASME 2002 International Mechanical Engineering Congress and Exposition, IMECE2002; New Orleans, LA; United States; 17 November 2002 through 22 November 2002; Code 82313*. 2002.
193. Krishnappa, U.S., *Numerical investigation of self-piercing riveted dual layer joint*. 2008, Master's thesis, Wichita State University, USA.
194. Khezri, R., E. Sjostrom, and A. Melander, *Simulation of self piercing riveting of the DP600 sheet steel in thickness 1+2 and 2+2 mm and of DP800 in thickness 1+1mm,* . 2001, Swedish Institute for Metals Research, IM-2001-537.

195. Malender, A., *Finite element simulation of self piercing riveting of DP600-development of simulation procedure*. 2000, Swedish Institute for Metals Research, IM-2000-528.

196. Westerberg, C., *Finite Element Simulation of Crash Testing of Self-Piercing Rivet Joints, Peel Specimen*, in *Master's thesis, Division of Structural Mechanics, Lund University, Sweden*. 2002.

197. Khezri, R., E. Sjostrom, and A. Melander, *Self-piercing riveting of high strength steel*. 2000, Swedish Institute for Metals Research, IM-2000-554.

198. Qu, S.G. and W.J. Deng. *Finite element simulation of the self-piercing riveting process*. in *2008 ASME International Mechanical Engineering Congress and Exposition, IMECE 2008; Boston, MA; United States; 31 October 2008 through 6 November 2008; Code 76723*. 2009.

199. J.Gårdstam, A. Melander, U. Persson, E. Sjöström, G. Leijon, L. Pazienza, R. Ritzén, E. Schedin, V. Sorel, and R. Trinick, *Development of self piercing riveting technology for stainless sheet steels – an executive summary report*. 2004, Swedish Institute for Metals Research, IM-2004-120.

200. Casalino, G., A. Rotondo, and A. Ludovico, *On the numerical modelling of the multiphysics self piercing riveting process based on the finite element technique.* Advances in Engineering Software, 2008. **39**(9): p. 787-795.

201. Neugebauer, R., M. Rössinger, M. Wahl, F. Schulz, A. Eckert, and W. Schützle, *Predicting Dimensional Accuracy of Mechanically Joined Car Body Assemblies.* Key Engineering Materials, 2011. **473**(1): p. 973-980.

202. Chenot, J.L., P.O. Bouchard, Y. Chastel, and E. Massoni, *Finite element simulation of forming, joining and strength of sheet components.* Key Engineering Materials, 2007. **344**: p. 21-28.

203. Porcaro, R., A.G. Hanssen, A. Aalberg, and M. Langseth, *Joining of aluminium using self-piercing riveting: Testing, modelling and analysis.* International Journal of Crashworthiness, 2004. **9**(2): p. 141-154.

204. Chukwuemeka, O.J., I.O. Kingsley, and E. Chinonye, *Analysis of strength of self pierce riveted aluminium plate using finite element method* in

Department of mechanical engineering. 2008, Blekinge Institute of Technology: Sweden.

205. Khezri, R. and M. Larsson, *Fatigue properties of self-piercing riveted joints of steel sheets with different thicknesses in shear and peel loading*. 2004, Swedish Institute for Metals Research, IM-2004-567.
206. Melander, A., J. Linder, R. Khezri, and J. Hellstrom, *Finite element simulation of the self piercing riveting process and the fatigue performance of the riveted joint*. 2000, Swedish Institute for Metals Research, IM-2000-736.
207. Melander, A. and R. Khezri, *Simulation of self piercing riveting of the steel TRIP800 in 1 and 2mm thicknesses*. 2002, Swedish Institute for Metals Research, IM-2002-551.
208. Melander, A., *The effect of coefficient of friction on the result from simulations*. 2002, Swedish Institute for Metals Research, IM-2002-532.
209. Persson, U., *Optimisation of heat treatment of semi austenitic precipitation hardenable (17-7PH) and martensitic (VAL2AV) stainless steel for self piercing rivets*. 2004, Swedish Institute for Metals Research, IM-2004-809.
210. Blundell, N., L. Han, R. Hewitt, and K. WilliamYoung. *A Comparative Study between Self Pierce Riveting and Spot Friction Joining*. in *JSAE Annual congress*. 2005.
211. Sun, X., E.V. Stephens, M.A. Khaleel, H. Shao, and M. Kimchi, *Resistance spot welding of aluminum alloy to steel with transition material - From process to performance - Part I: Experimental study.* Welding Journal (Miami, Fla), 2004. **83**(6): p. 188-S-195-S.
212. Mortimer, J., *Jaguar "Roadmap" rethinks self-piercing technology.* Industrial Robot, 2005. **32**(3): p. 209-213.
213. Hutchings, M.T., P.J. Withers, T.M. Holden, and T. Lorentzen, *Introduction to the characterization of residual stress by neutron diffraction*, ed. M.T. Hutchings. 2005, Boca Raton, FL: Boca Raton, FL : Taylor & Francis.
214. Withers, P.J. and H.K.D.H. Bhadeshia, *Residual stress. Part 2 – Nature and origins.* Materials Science & Technology, 2001. **17**(4): p. 366-375.

215. Charitidis, C.A., D.A. Dragatogiannis, E.P. Koumoulos, and I.A. Kartsonakis, *Residual stress and deformation mechanism of friction stir welded aluminum alloys by nanoindentation.* Materials Science and Engineering A, 2012. **540**: p. 226-234.

216. Bahadur, A., B.R. Kumar, A.S. Kumar, G.G. Sarkar, and J.S. Rao, *Development and comparison of residual stress measurement on welds by various methods.* Materials Science & Technology, 2004. **20**(2): p. 261-269.

217. Jang, C., P.-Y. Cho, M. Kim, S.-J. Oh, and J.-S. Yang, *Effect of microstructure and residual stress on fatigue crack growth of stainless steel narrow gap welds.* Materials and Design, 2010. **31**: p. 1862-1870.

218. Chang, K.-H., G.-C. Jang, Y.-E. Shin, J.-G. Han, and J.-M. Kim, *The behavior of welded joint in steel pipe members under monotonic cyclic loading.* International Journal of Pressure Vessels and Piping, 2006. **83**: p. 846-852.

219. Withers, P.J., M. Turski, L. Edwards, P.J. Bouchard, and D.J. Buttle, *Recent advances in residual stress measurement.* International Journal of Pressure Vessels and Piping, 2008. **85**(3): p. 118-127.

220. Withers, P.J. and H.K.D.H. Bhadeshia, *Residual stress. Part 1 – Measurement techniques.* Materials Science & Technology, 2001. **17**(4): p. 355-365.

221. O’Dowd, N.P., K.M. Nikbin, H.Y. Lee, R.C. Wimpory, and F.R. Biglari, *Stress Intensity Factors Due to Residual Stresses in T-Plate Welds.* ASME, 2004. **126**: p. 432-437.

222. Webster, G.A. and R.C. Wimpory, *Non-destructive measurement of residual stress by neutron diffraction.* Materials Processing Technology, 2001. **117**: p. 395-399.

223. Staron, P., U. Cihak, H. Clemens, M. Stockinger, F.S. Bayraktar, M. Kocak, and A. Schreyer, *Diffraction based residual stress analysis applied to aircraft industry.* Advanced Engineering Material, 2007. **9**(8): p. 627-638.

224. Prime, M.B., T. Gnaupel-Herold, J.A. Baumann, R.J. Lederich, D.M. Bowden, and R.J. Sebring, *Residual stress measurements in a thick,*

dissimilar aluminium alloy friction stir weld. Acta Materialia, 2006. **54**: p. 4013-4021.

225. Paradowska, A.M., J.W.H. Price, T.R. Finlayson, and U. Lienert, *Residual stress distribution in steel butt welds measured using neutron and synchrotron diffraction.* Journal of Physics: Condensed Matter, 2009. **21**(12).

226. Prime, M.B., *Cross-Sectional Mapping of Residual Stresses by Measuring the Surface Contour After a Cut.* Journal of Engineering Materials and Technology, 2001. **123**(2): p. 162-168.

227. Prime, M.B. and R.L. Martineau, *Mapping Residual Stresses after Foreign Object Damage Using the Contour Method.* Materials Science Forum, 2002. **404**(1): p. 521-526.

228. Prime, M., R. Sebring, J. Edwards, D. Hughes, and P. Webster, *Laser surface-contouring and spline data-smoothing for residual stress measurement.* Experimental Mechanics, 2004. **44**(2): p. 176-184.

229. Zhang, Y., S. Ganguly, L. Edwards, and M.E. Fitzpatrick, *Cross-sectional mapping of residual stresses in a VPPA weld using the contour method.* Acta Materialia, 2004. **52**(17): p. 5225-5232.

230. Hacini, L., N. Van Lê, and P. Bocher, *Evaluation of Residual Stresses Induced by Robotized Hammer Peening by the Contour Method.* Experimental Mechanics, 2009. **49**(6): p. 775-783.

231. Bueckner, H.F., *The propagation of cracks and the energy of elastic deformation* Trans. ASME, 1958. **80**: p. 435-440.

232. DeWald, A. and M. Hill, *Multi-Axial Contour Method for Mapping Residual Stresses in Continuously Processed Bodies.* Experimental Mechanics, 2006. **46**(4): p. 473-490.

233. Hill, M.R., *Determination of residual stress based on the estimation of eigenstrain*, in *PhD thesis, Stanford University, USA*. 1996.

234. Kartal, M.E., C.D.M. Liljedahl, S. Gungor, L. Edwards, and M.E. Fitzpatrick, *Determination of the profile of the complete residual stress tensor in a VPPA weld using the multi-axial contour method.* Acta Materialia, 2008. **56**(16): p. 4417-4428.

235. *ASM Handbook Volume 9, Metallography and Microstructures.* ASM International, Materials Park, OH, 2004.

236. Kirstein, O., U. Garbe, and V. Luzin, *Kowari - OPAL's new stress diffractometer for the engineering community: Capabilities and first results*. 2010. p. 86-91.

237. James, J.A., J.R. Santisteban, L. Edwards, and M.R. Daymond, *A virtual laboratory for neutron and synchrotron strain scanning.* Physica B: Condensed Matter, 2004. **350**(1-3).

238. James, J.A. and L. Edwards, *Application of robot kinematics methods to the simulation and control of neutron beam line positioning systems.* Nuclear Instruments and Methods in Physics Research Section A, 2007. **571**(3): p. 709-718.

239. Haque, R., J.H. Beynon, and Y. Durandet, *Characterisation of force-displacement curve in self-pierce riveting.* Science and Technology of Welding and joining, 2012. **17**(6): p. 476-488.

240. Haque, R., J.H. Beynon, Y. Durandet, O. Kirstein, and S. Blacket, *Feasibility of measuring residual stress profile in different self-pierce riveted joints.* Science & Technology of Welding & Joining, 2012. **17**(1): p. 60-68.

241. Doyle, E.D., Y.C. Wong, and M.I. Ripley, *Residual stress evaluation in martensitic stainless steel as a function of gas quenching pressure using thermal neutrons.* Physica B, 2006. **385-386**: p. 897-899.

242. Wimpory, R., P. May, N. O'Dowd, G. Webster, D. Smith, and E. Kingston, *Measurement of residual stresses in T-plate weldments.* Journal of Strain Analysis for Engineering Design, 2003. **38**(4): p. 349-365.

243. Withers, P.J., *Depth capabilities of neutron and synchrotron diffraction strain measurement instruments. I. The maximum feasible path length.* Journal of Applied Crystallography, 2004. **37**(4): p. 596-606.

244. Haque, R., Y. Durandet, Y.C. Wong, A. Paradowska, J.H. Beynon, and S. Blacket, *Optimising parameters for meaningful measurement of residual strain by neutron diffraction in self-pierce riveted joints.* Science and Technology of Welding and Joining, 2013. **18**(6): p. 492-499.

245. Taylor, J.R., *An introduction to error analysis : the study of uncertainties in physical measurements*. 1982: Mill Valley, Calif : University Science Books.

246. Woo, W., V.T. Em, E.Y. Kim, S.H. Han, Y.S. Han, and S.H. Choi, *Stress-strain relationship between ferrite and martensite in a dual-phase steel studied by in situ neutron diffraction and crystal plasticity theories.* Acta Materialia, 2012. **60**(20): p. 6972-6981.

247. Filippone, R., J. Root, P. Jacques, and S. Yue, *The influence of martensite on line broadening in neutron diffraction spectra of a DP steel.* ISIJ International, 2002. **42**(3): p. 304-309.

248. Jonsson, M., *Crash simulation of self-piercing rivet joints with different gaps and cracks*, in *Master's thesis, Swedish Institute for Metals Research, IM-2002-029,* . 2002.

List of publications

1. R. Haque, J. H. Beynon, Y. Durandet, O. Kirstein and S. Blacket: 'Feasibility of measuring residual stress profile in different self-pierce riveted joints', Science and Technology of Welding and Joining, 2012, Vol 17, No 1, pp 60-68.

2. Rezwanul Haque, John Beynon, Oliver Kirstein, Yat Choy Wong, Yvonne Durandet: 'Evaluation of residual stress in SPR joint by neutron diffraction', Advanced Materials Research, Vol. 409 (2012) pp 575-580

3. R. Haque, J. H. Beynon, Y. Durandet: "Characterisation of force–displacement curve in self-pierce riveting", Science and Technology of Welding and Joining, 2012, Vol 17, No 6, pp 476-488.

4. R. Haque, Y. Durandet, Y. C. Wong, A. Paradowska, J. H. Beynon and S. Blacket: Optimizing the parameters for meaningful measurement of residual strain by neutron diffraction in Self-Pierce Riveted joints', Science and Technology of Welding and Joining, 2013, Vol 18, No 6, pp 492-499.

Appendix A

Cross-sections and force-displacement curves of condition 2 in Table 5.1.1

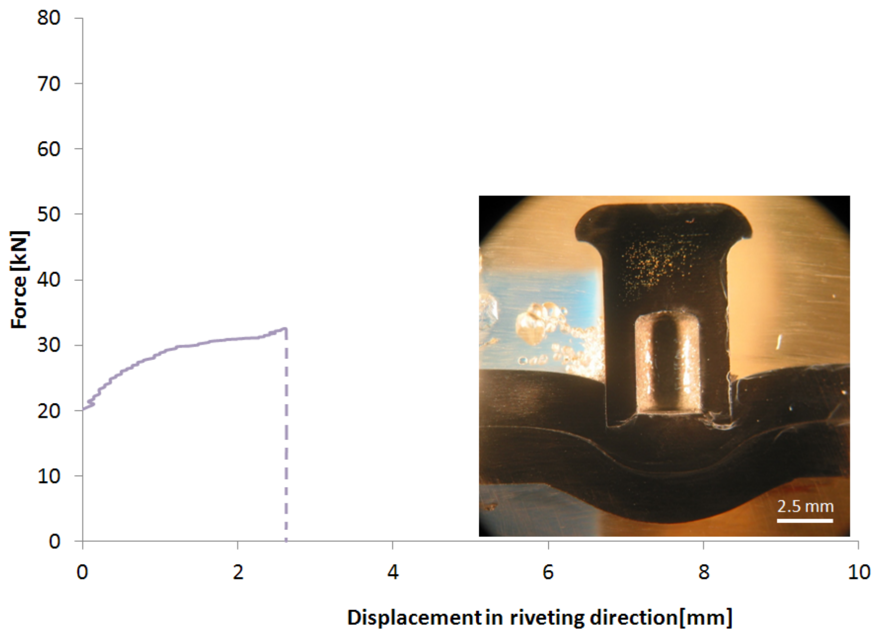

Fig. A.1 Force-displacement curve and cross-section of 2.5 + 2.5 mm G300 steel sheet with 8 mm long rivet of hardness of 555 HV and interrupted at 2.60 mm

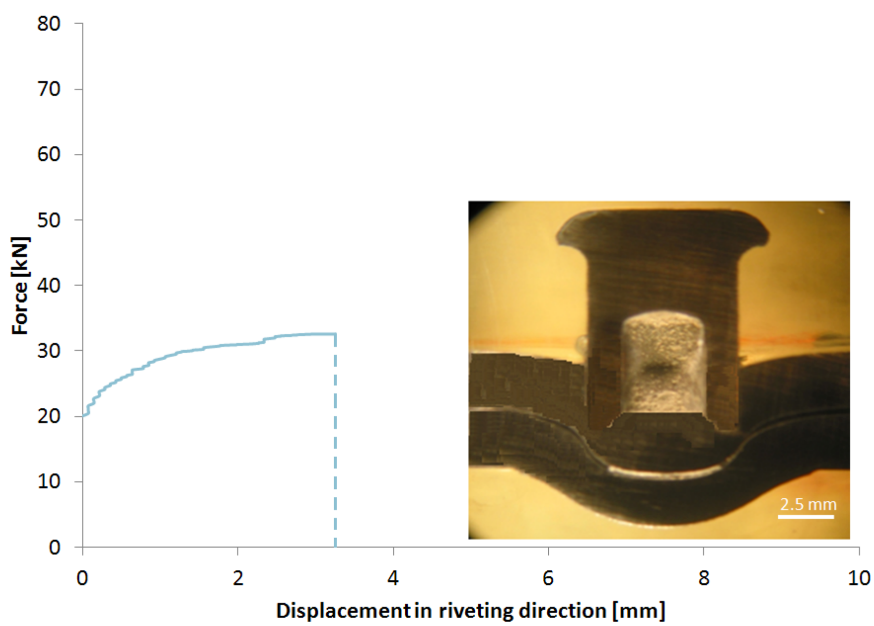

Fig. A.2 Force-displacement curve and cross-section of 2.5 + 2.5 mm G300 steel sheet with 8 mm long rivet of hardness of 555 HV and interrupted at 3.25 mm

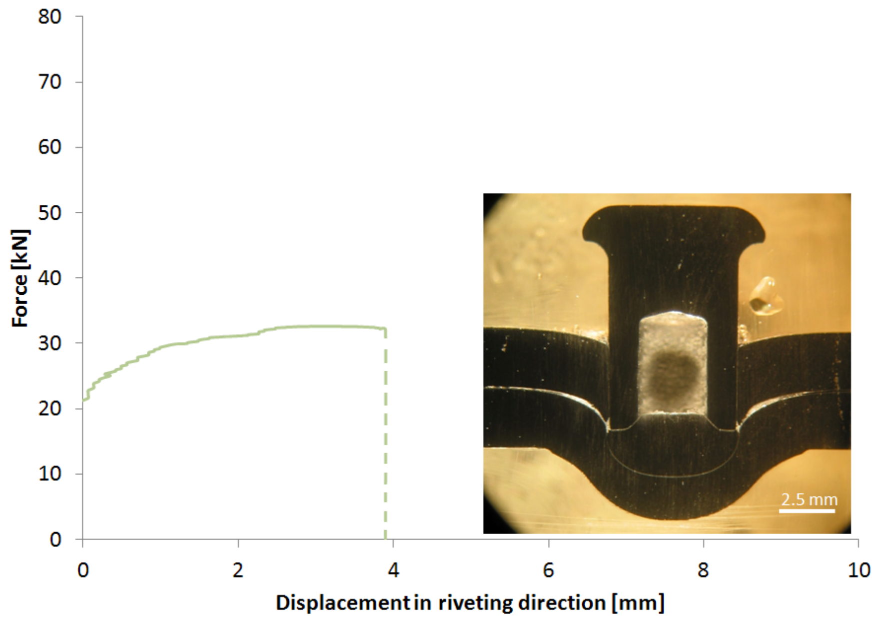

Fig. A.3 Force-displacement curve and cross-section of 2.5 + 2.5 mm G300 steel sheet with 8 mm long rivet of hardness of 555 HV and interrupted at 3.90 mm

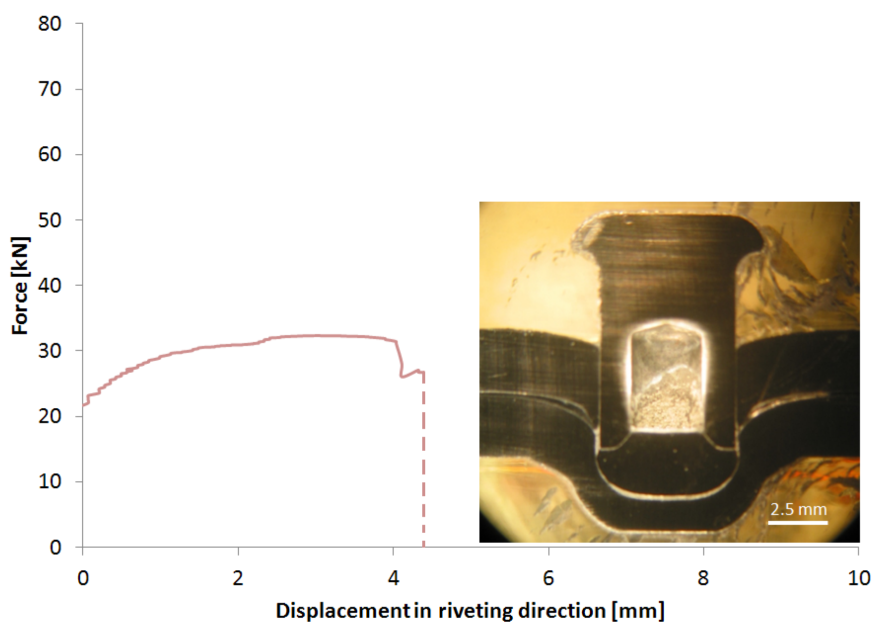

Fig. A.4 Force-displacement curve and cross-section of 2.5 + 2.5 mm G300 steel sheet with 8 mm long rivet of hardness of 555 HV and interrupted at 4.40 mm

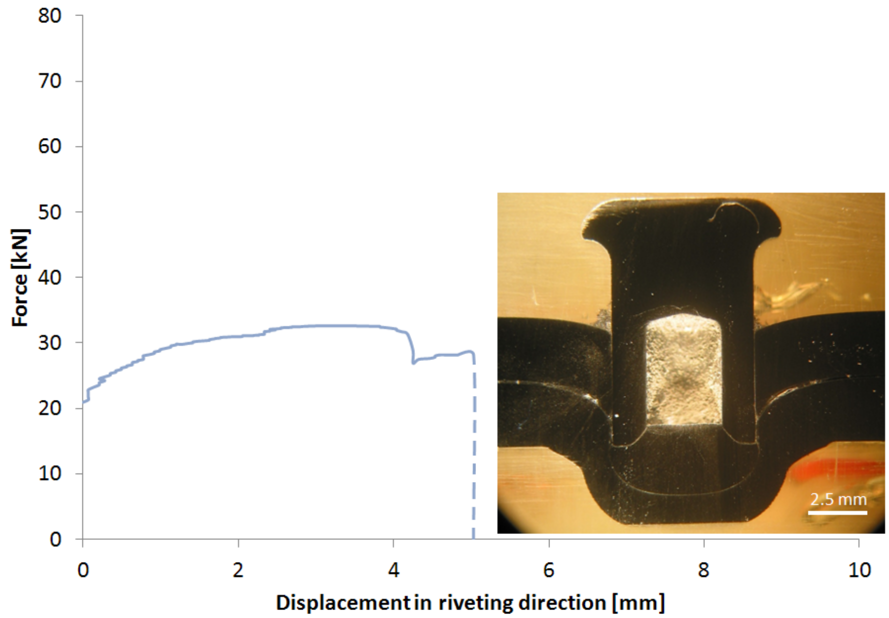

Fig. A.5 Force-displacement curve and cross-section of 2.5 + 2.5 mm G300 steel sheet with 8 mm long rivet of hardness of 555 HV and interrupted at 5.00 mm

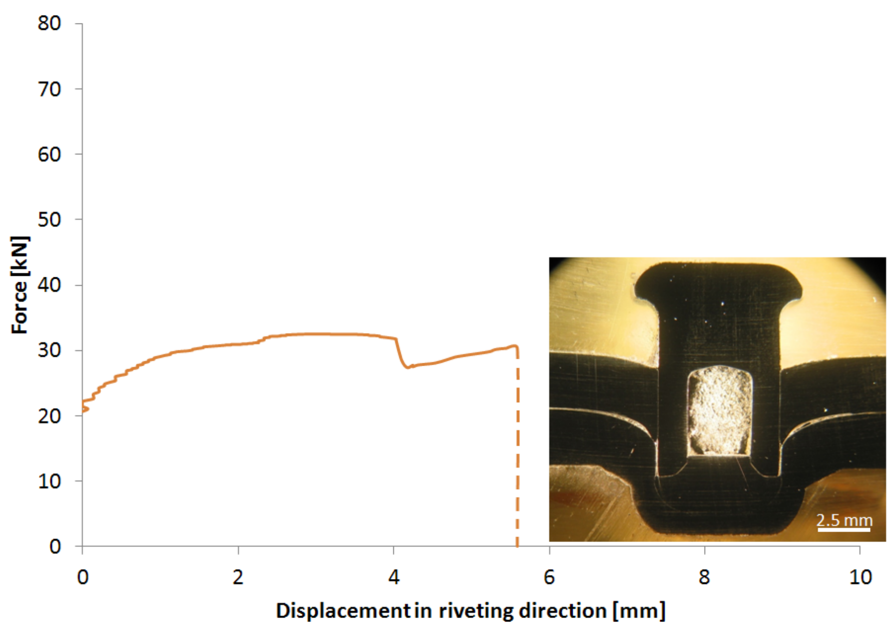

Fig. A.6 Force-displacement curve and cross-section of 2.5 + 2.5 mm G300 steel sheet with 8 mm long rivet of hardness of 555 HV and interrupted at 5.60 mm

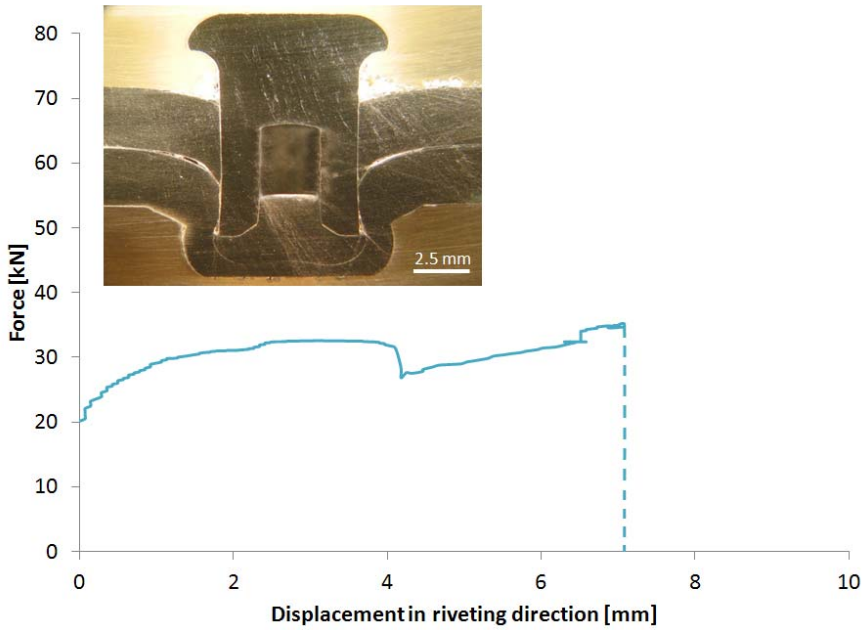

Fig. A.7 Force-displacement curve and cross-section of 2.5 + 2.5 mm G300 steel sheet with 8 mm long rivet of hardness of 555 HV and interrupted at 7.10 mm

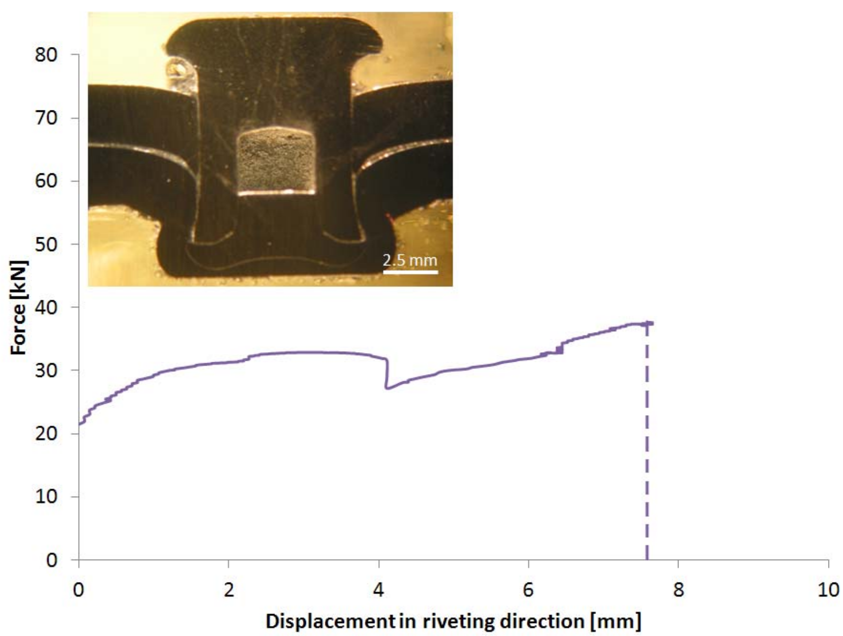

Fig. A. 8 Force-displacement curve and cross-section of 2.5 + 2.5 mm G300 steel sheet with 8 mm long rivet of hardness of 555 HV and interrupted at 7.60 mm

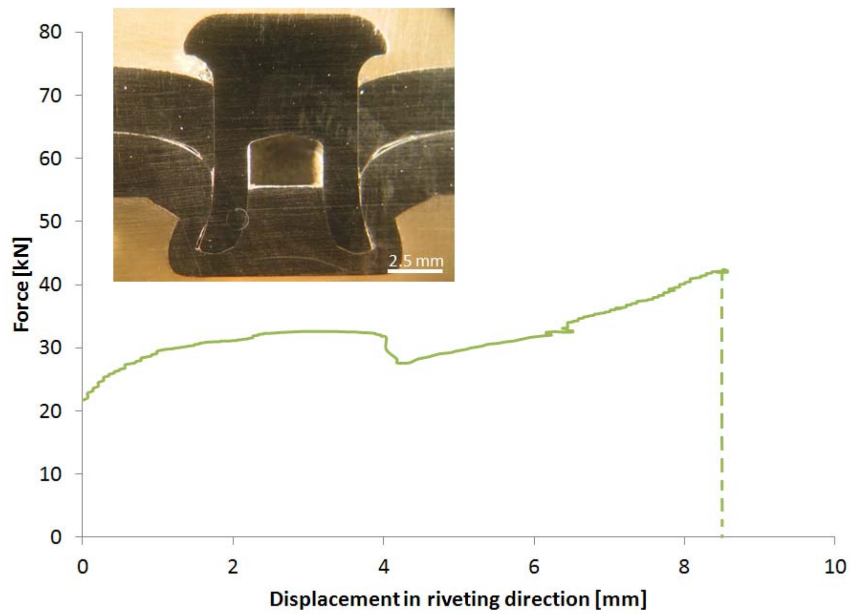

Fig. A. 9 Force-displacement curve and cross-section of 2.5 + 2.5 mm G300 steel sheet with 8 mm long rivet of hardness of 555 HV and interrupted at 8.50 mm

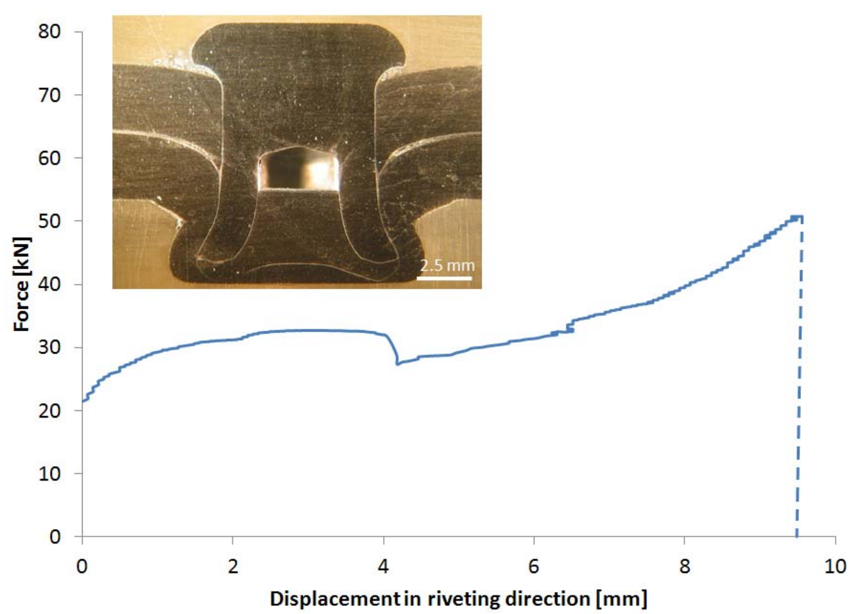

Fig. A.10 Force-displacement curve and cross-section of 2.5 + 2.5 mm G300 steel sheet with 8 mm long rivet of hardness of 555 HV and interrupted at 9.50 mm (complete joint)

Cross-sections and force-displacement curves of condition 3 in Table 5.1.1

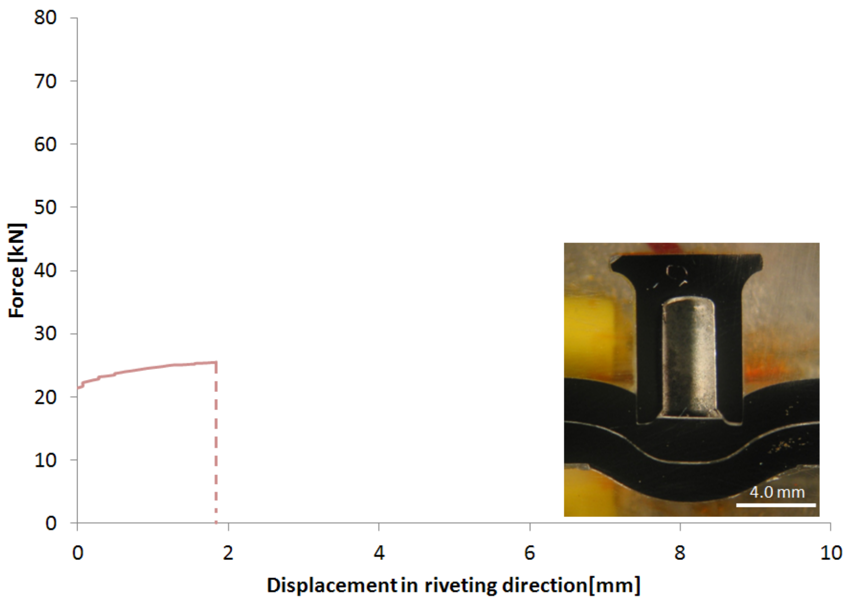

Fig. A.11 Force-displacement curve and cross-section of 2.0 + 2.0 mm G300 steel sheet with 7 mm long rivet of hardness of 555 HV and interrupted at1.85 mm

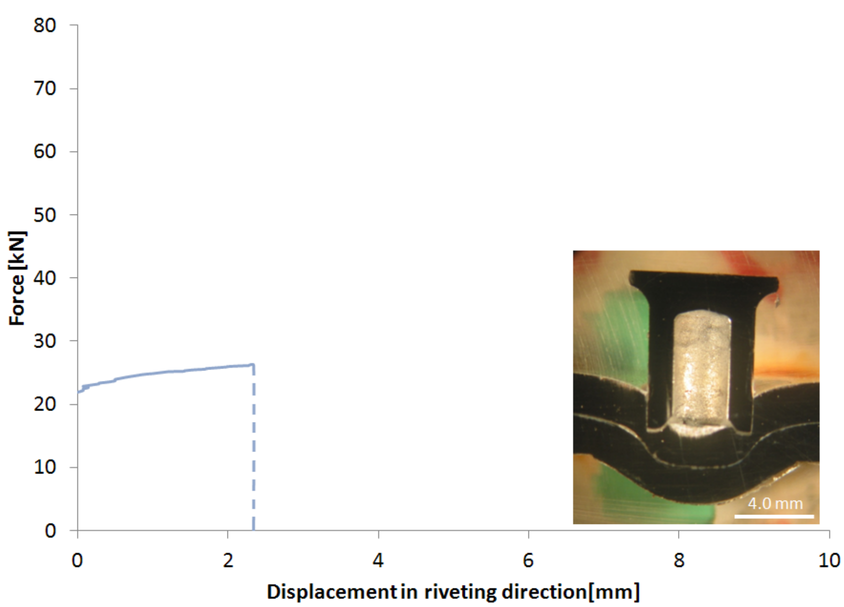

Fig. A. 12 Force-displacement curve and cross-section of 2.0 + 2.0 mm G300 steel sheet with 7 mm long rivet of hardness of 555 HV and interrupted at 2.35 mm

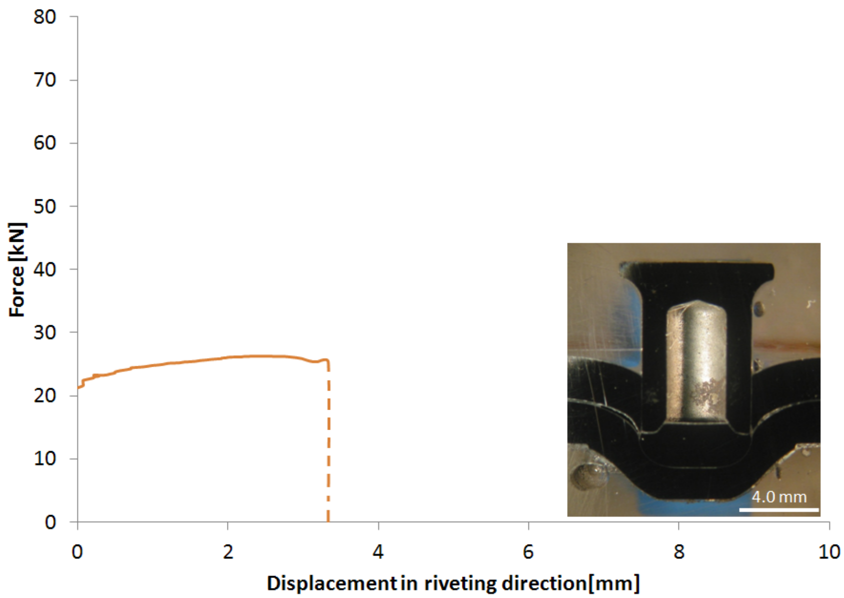

Fig. A.13 Force-displacement curve and cross-section of 2.0 + 2.0 mm G300 steel sheet with 7 mm long rivet of hardness of 555 HV and interrupted at 3.35 mm

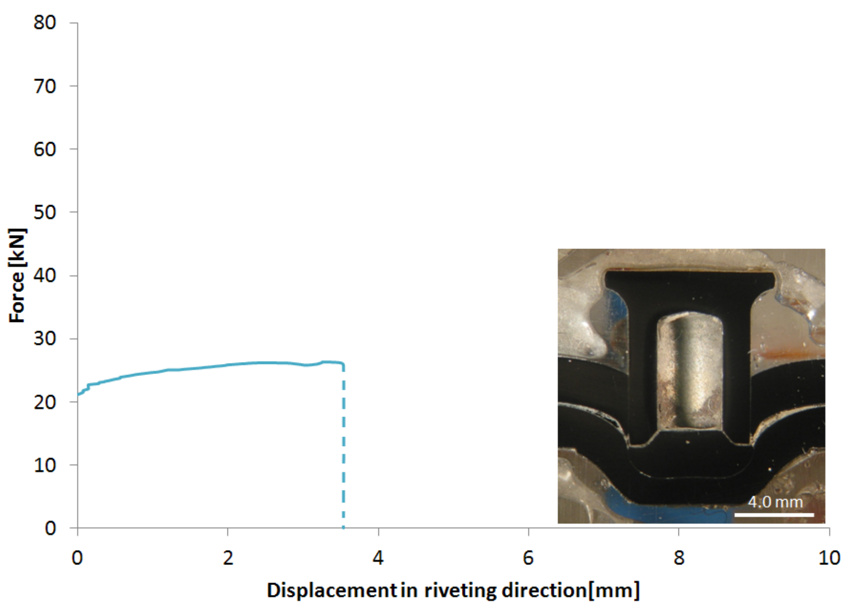

Fig. A. 14 Force-displacement curve and cross-section of 2.0 + 2.0 mm G300 steel sheet with 7 mm long rivet of hardness of 555 HV and interrupted at 3.55 mm

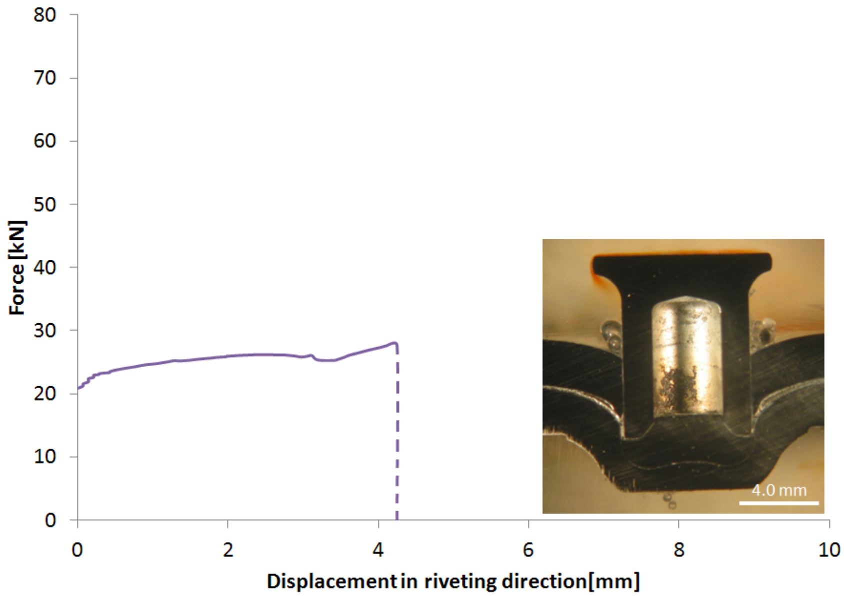

Fig. A.15 Force-displacement curve and cross-section of 2.0 + 2.0 mm G300 steel sheet with 7 mm long rivet of hardness of 555 HV and interrupted at 4.25 mm

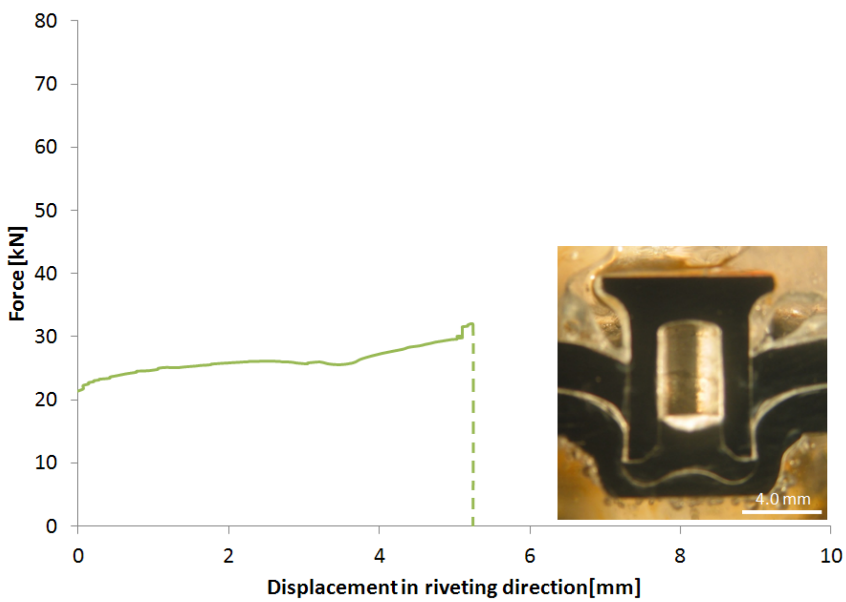

Fig. A.16 Force-displacement curve and cross-section of 2.0 + 2.0 mm G300 steel sheet with 7 mm long rivet of hardness of 555 HV and interrupted at 5.25 mm

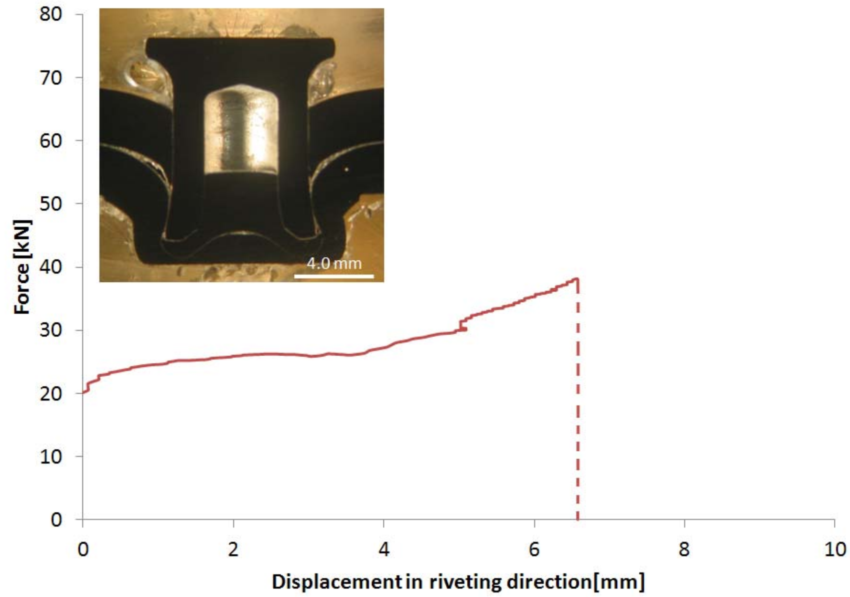

Fig. A. 17 Force-displacement curve and cross-section of 2.0 + 2.0 mm G300 steel sheet with 7 mm long rivet of hardness of 555 HV and interrupted at 6.60 mm

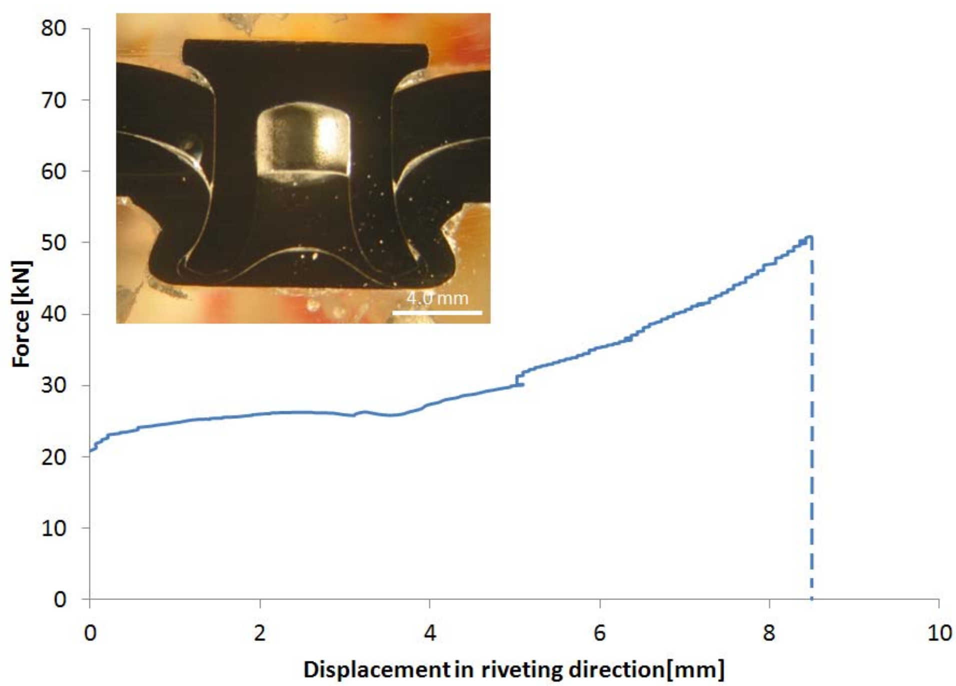

Fig. A.18 Force-displacement curve and cross-section of 2.0 + 2.0 mm G300 steel sheet with 7 mm long rivet of hardness of 555 HV and interrupted at 8.50 mm (complete joint)

Cross-sections and force-displacement curves of condition 4 in Table 5.1.1

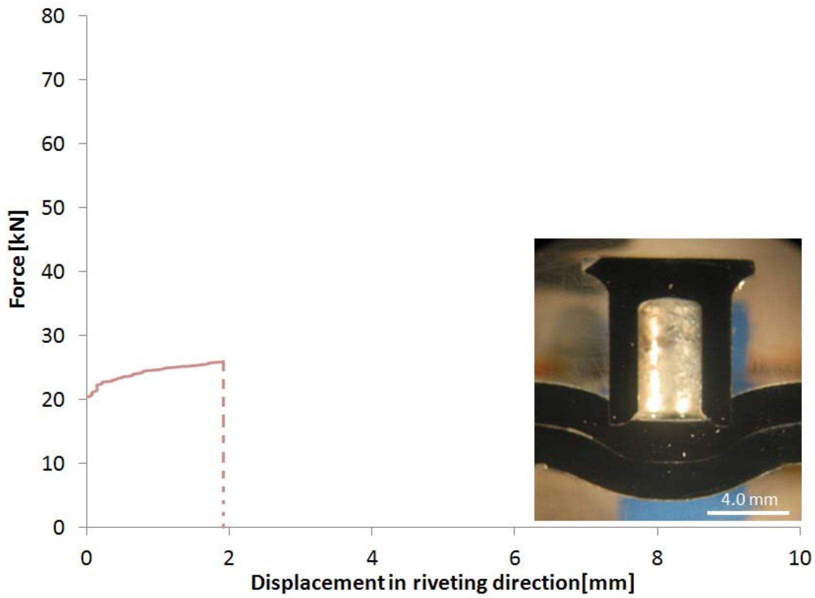

Fig. A.19 Force-displacement curve and cross-section of 2.0 + 2.0 mm G300 steel sheet with 7 mm long rivet of hardness of 480 HV and interrupted at 1.90 mm

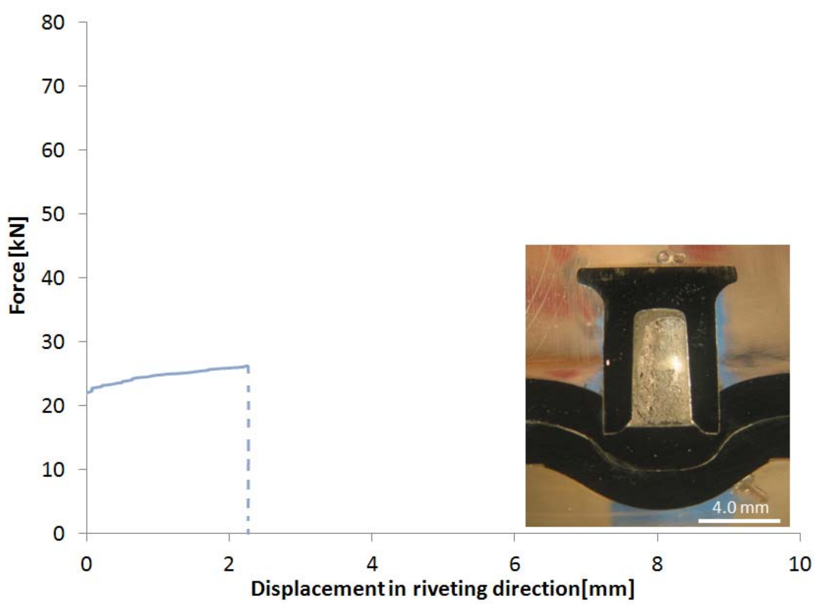

Fig. A.20 Force-displacement curve and cross-section of 2.0 + 2.0 mm G300 steel sheet with 7 mm long rivet of hardness of 480 HV and interrupted at 2.25 mm

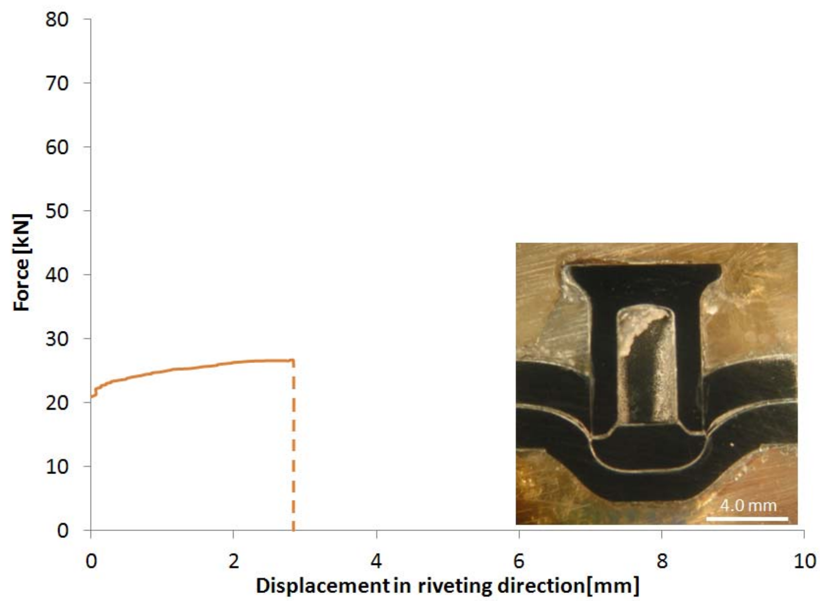

Fig. A.21 Force-displacement curve and cross-section of 2.0 + 2.0 mm G300 steel sheet with 7 mm long rivet of hardness of 480 HV and interrupted at 2.85 mm

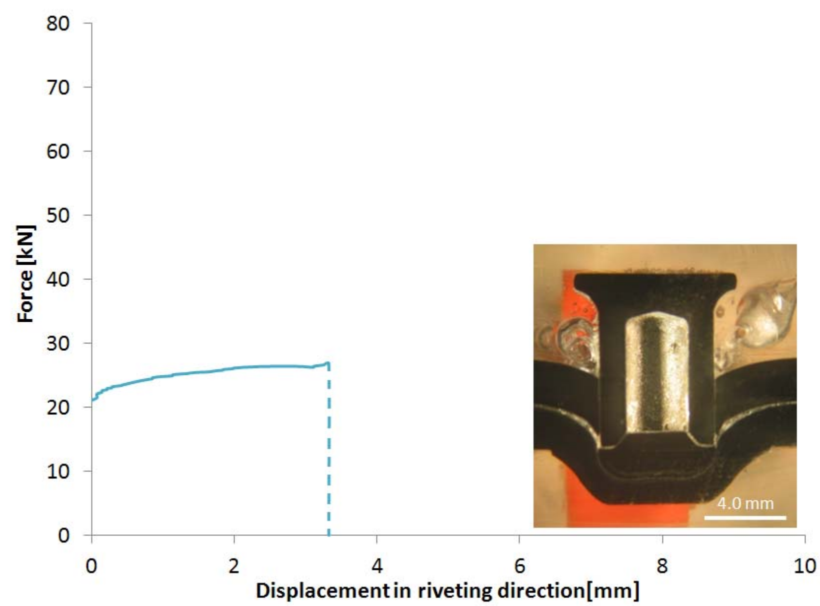

Fig. A.22 Force-displacement curve and cross-section of 2.0 + 2.0 mm G300 steel sheet with 7 mm long rivet of hardness of 480 HV and interrupted at 3.30 mm

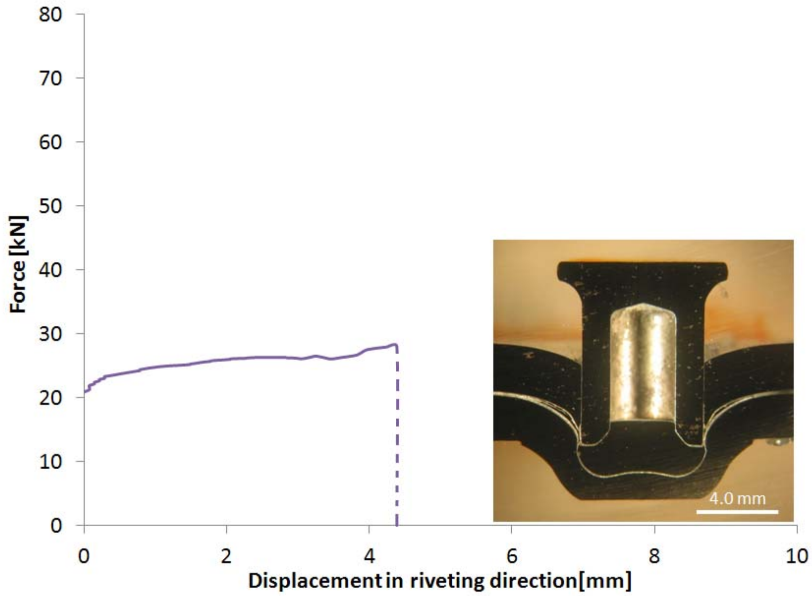

Fig. A.23 Force-displacement curve and cross-section of 2.0 + 2.0 mm G300 steel sheet with 7 mm long rivet of hardness of 480 HV and interrupted at 4.40 mm

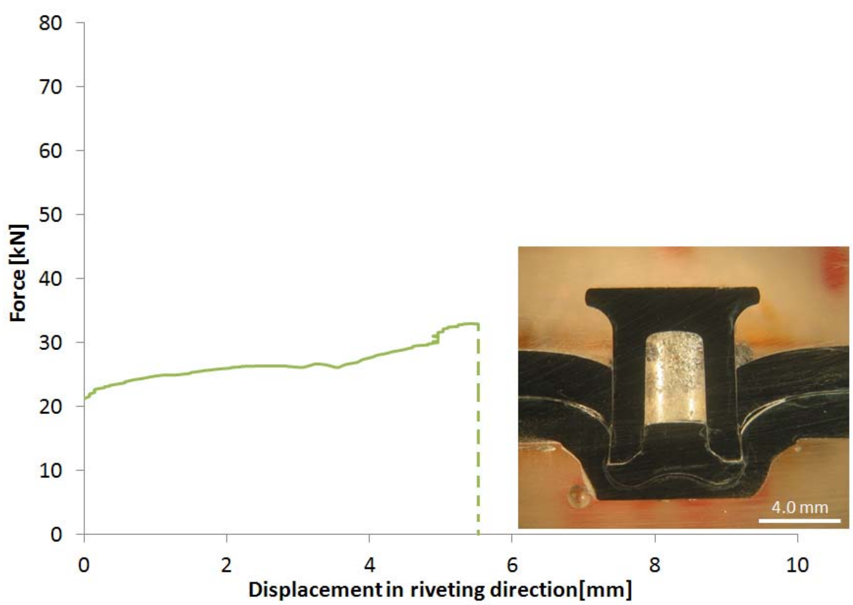

Fig. A.24 Force-displacement curve and cross-section of 2.0 + 2.0 mm G300 steel sheet with 7 mm long rivet of hardness of 480 HV and interrupted at 5.50 mm

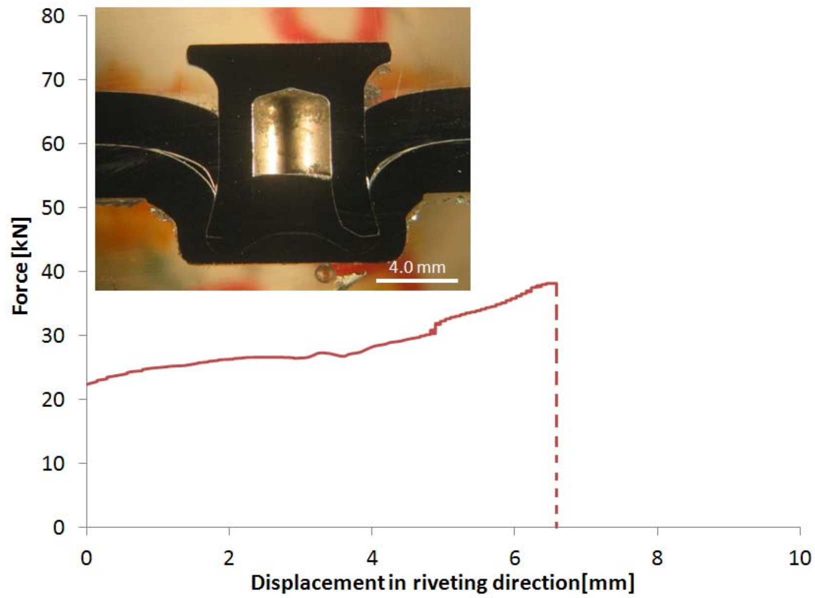

Fig. A.25 Force-displacement curve and cross-section of 2.0 + 2.0 mm G300 steel sheet with 7 mm long rivet of hardness of 480 HV and interrupted at 6.60 mm

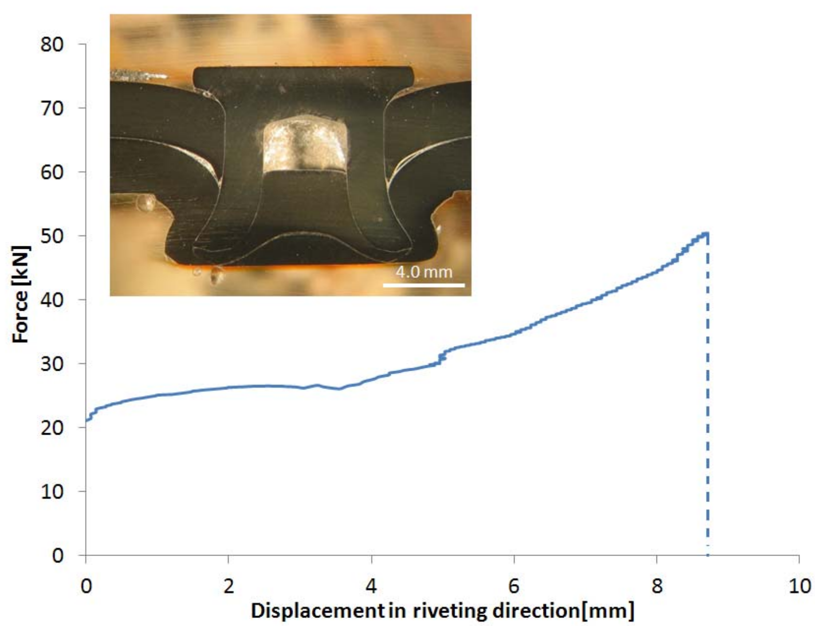

Fig. A.26 Force-displacement curve and cross-section of 2.0 + 2.0 mm G300 steel sheet with 7 mm long rivet of hardness of 480 HV and interrupted at 8.70 mm (complete joint)

Cross-sections and force-displacement curves of condition 5 in Table 5.1.1

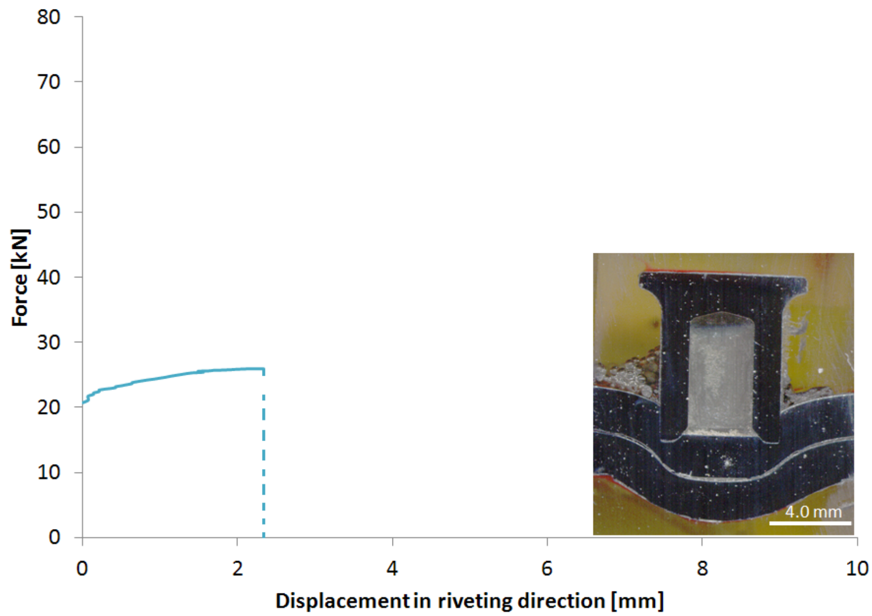

Fig. A 27 Force-displacement curve and cross-section of 2.0 + 2.0 mm G300 steel sheet with 7 mm long rivet of hardness of 410 HV and interrupted at 2.30 mm

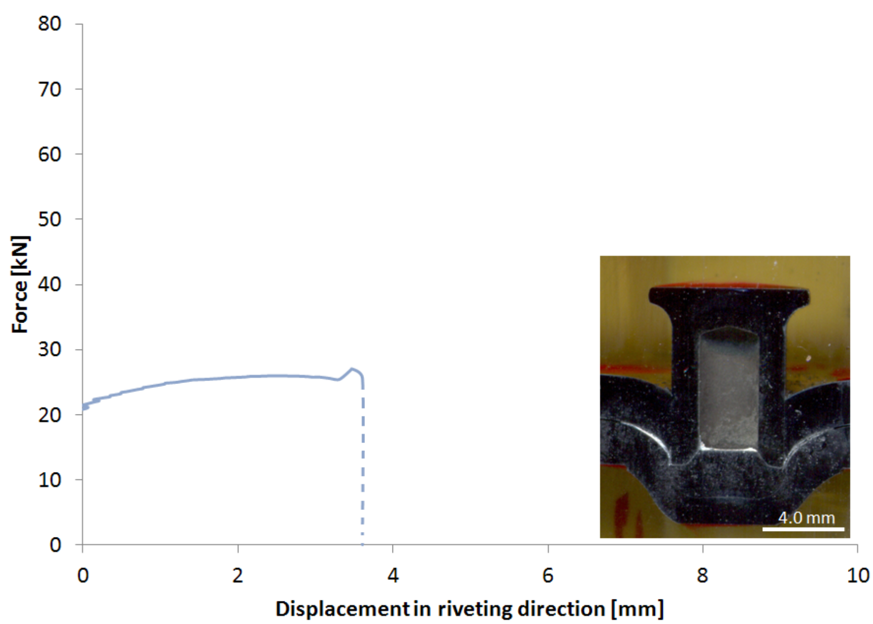

Fig. A.28 Force-displacement curve and cross-section of 2.0 + 2.0 mm G300 steel sheet with 7 mm long rivet of hardness of 410 HV and interrupted at 3.60 mm

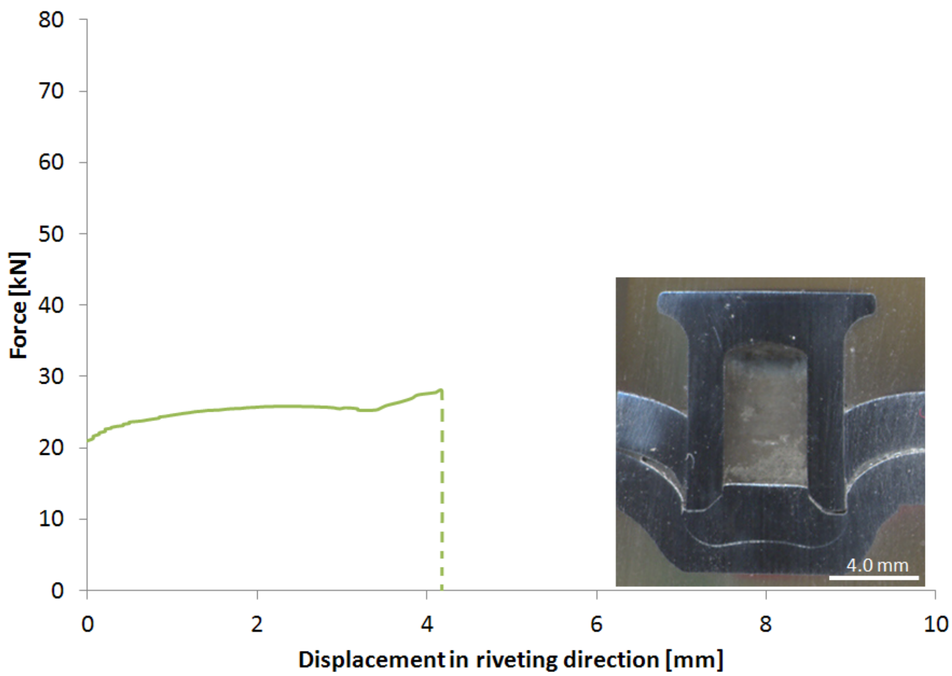

Fig. A.29 Force-displacement curve and cross-section of 2.0 + 2.0 mm G300 steel sheet with 7 mm long rivet of hardness of 410 HV and interrupted at 4.20 mm

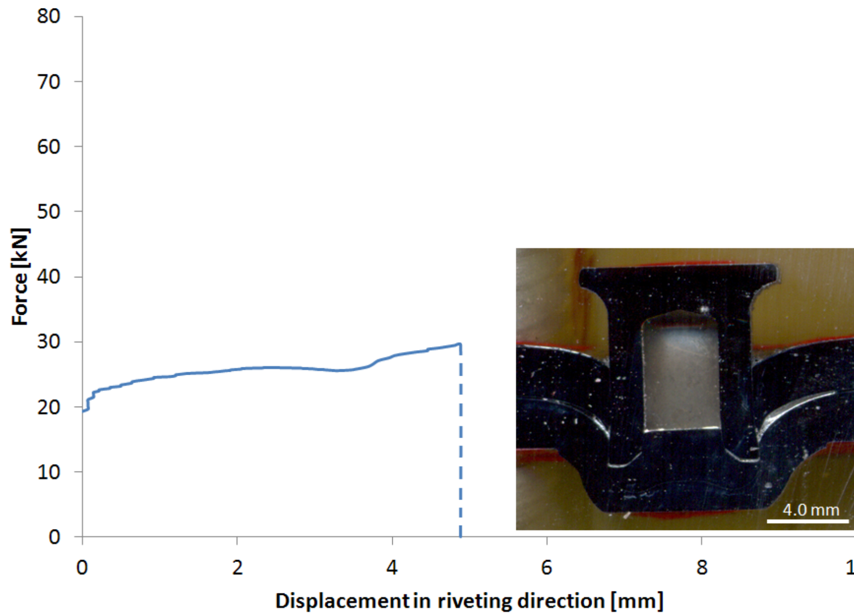

Fig. A.30 Force-displacement curve and cross-section of 2.0 + 2.0 mm G300 steel sheet with 7 mm long rivet of hardness of 410 HV and interrupted at 4.90 mm

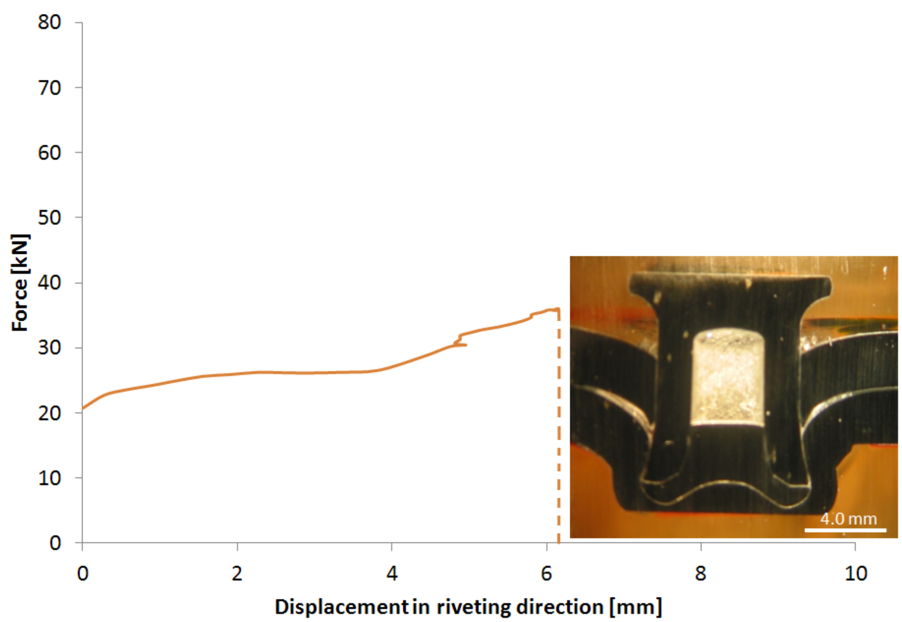

Fig. A.31 Force-displacement curve and cross-section of 2.0 + 2.0 mm G300 steel sheet with 7 mm long rivet of hardness of 410 HV and interrupted at 6.15 mm

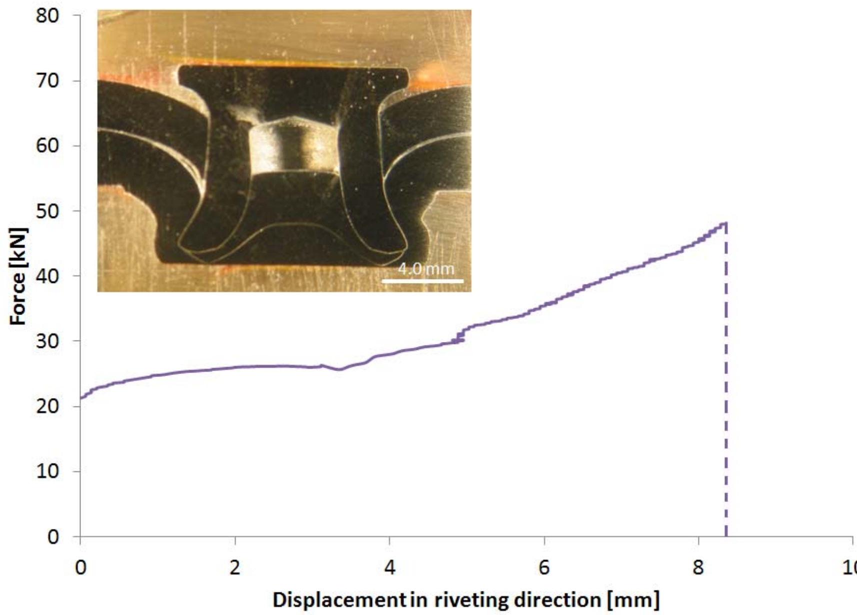

Fig. A.32 Force-displacement curve and cross-section of 2.0 + 2.0 mm G300 steel sheet with 7 mm long rivet of hardness of 410 HV and interrupted at 8.35 mm

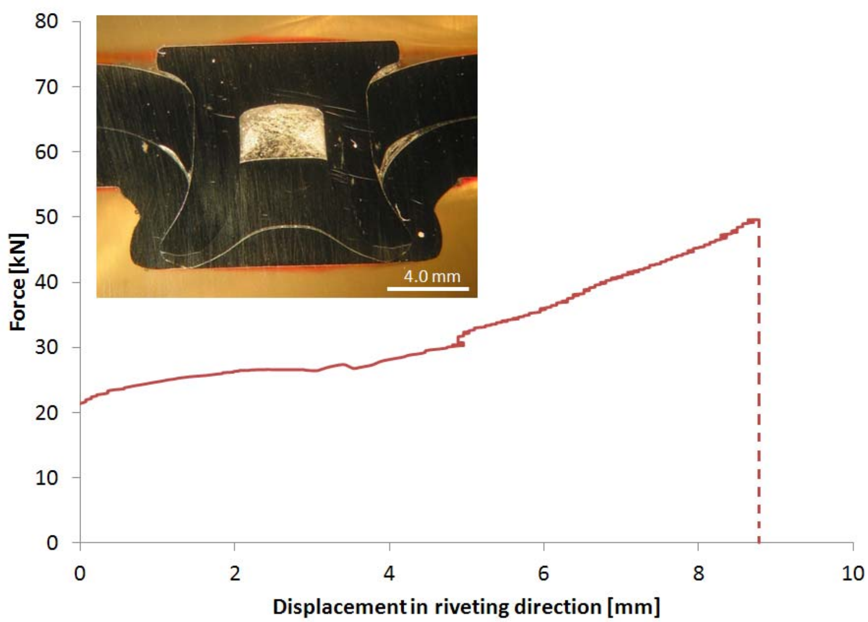

Fig. A 33 Force-displacement curve and cross-section of 2.0 + 2.0 mm G300 steel sheet with 7 mm long rivet of hardness of 410 HV and interrupted at 8.80 mm (complete joint)

Cross-sections and force-displacement curves of condition 6 in Table 5.1.1

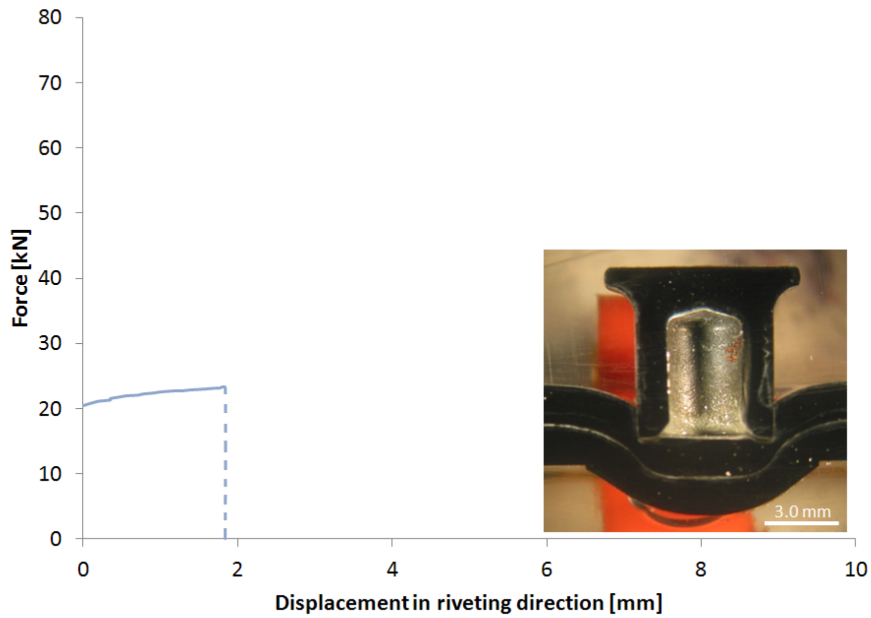

Fig. A.34 Force-displacement curve and cross-section of 1.5 + 1.5 mm G300 steel sheet with 6 mm long rivet of hardness of 480 HV and interrupted at 1.85 mm

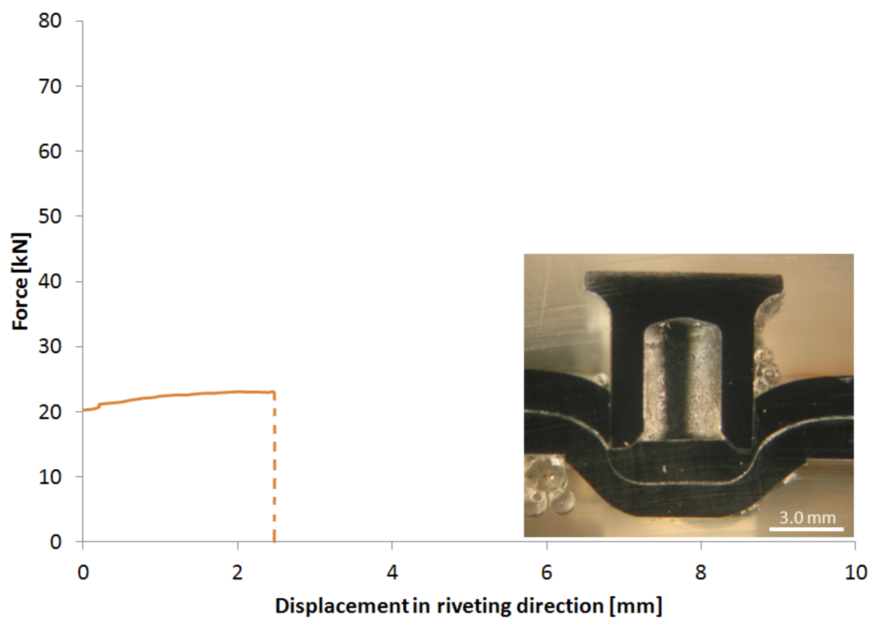

Fig. A.35 Force-displacement curve and cross-section of 1.5 + 1.5 mm G300 steel sheet with 6 mm long rivet of hardness of 480 HV and interrupted at 2.50 mm

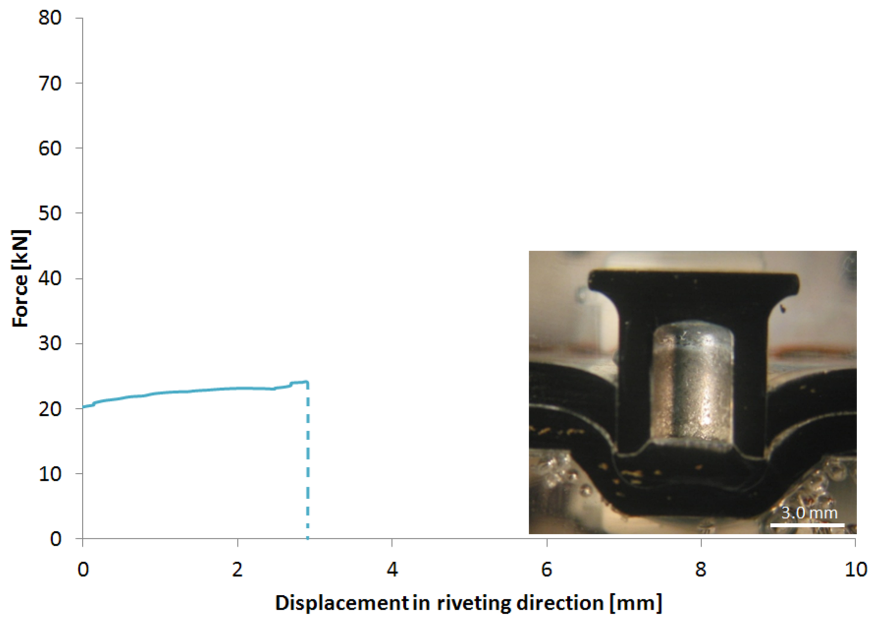

Fig. A. 36 Force-displacement curve and cross-section of 1.5 + 1.5 mm G300 steel sheet with 6 mm long rivet of hardness of 480 HV and interrupted at 2.90 mm

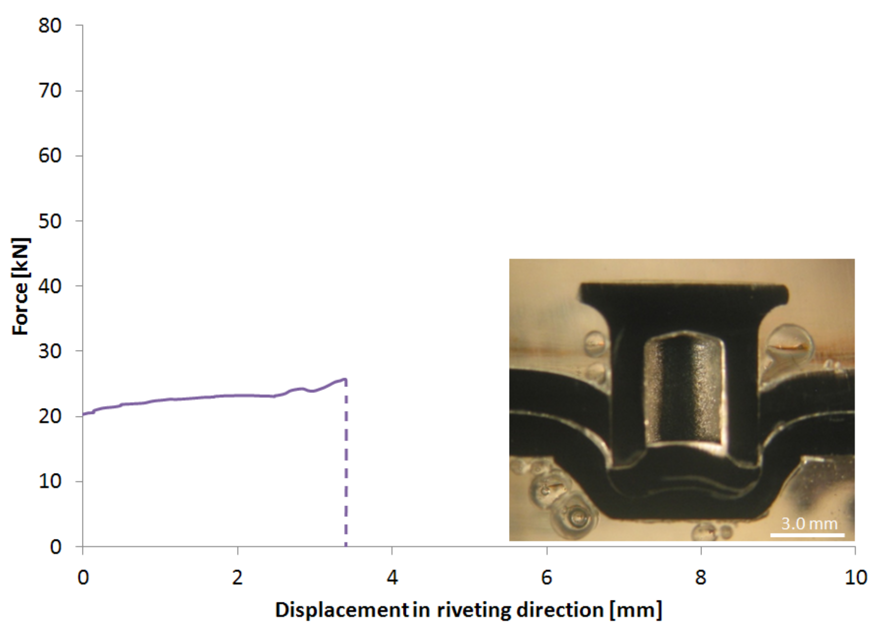

Fig. A. 37 Force-displacement curve and cross-section of 1.5 + 1.5 mm G300 steel sheet with 6 mm long rivet of hardness of 480 HV and interrupted at 3.40 mm

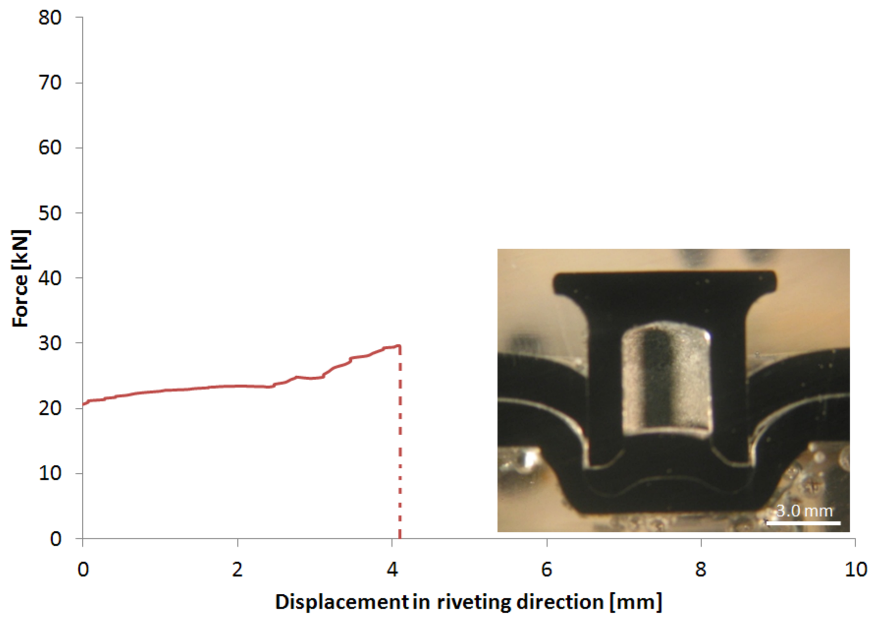

Fig. A. 38 Force-displacement curve and cross-section of 1.5 + 1.5 mm G300 steel sheet with 6 mm long rivet of hardness of 480 HV and interrupted at 4.10 mm

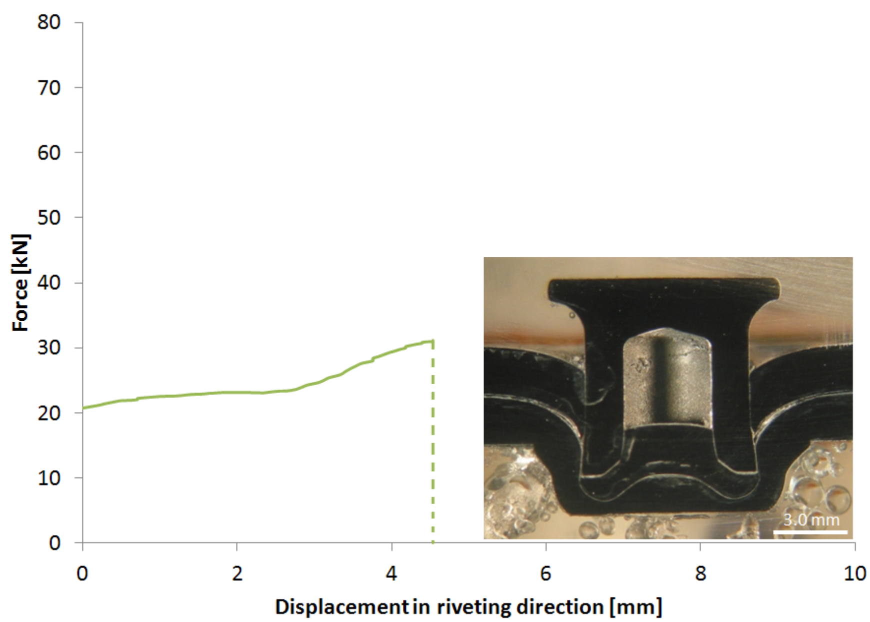

Fig. A.39 Force-displacement curve and cross-section of 1.5 + 1.5 mm G300 steel sheet with 6 mm long rivet of hardness of 480 HV and interrupted at 4.50 mm

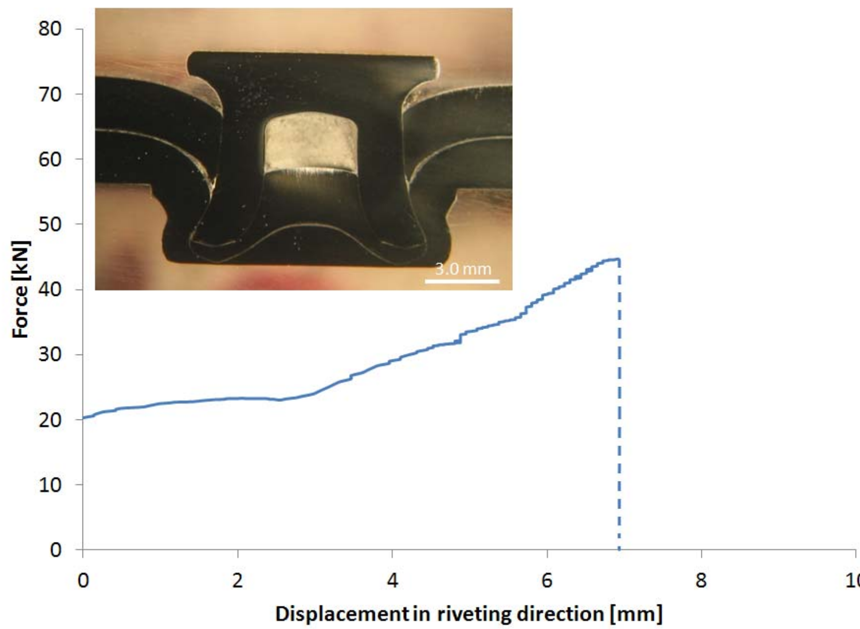

Fig. A.40 Force-displacement curve and cross-section of 1.5 + 1.5 mm G300 steel sheet with 6 mm long rivet of hardness of 480 HV and interrupted at 6.95 mm (complete joint)

Cross-sections and force-displacement curves of condition 7 in Table 5.1.1

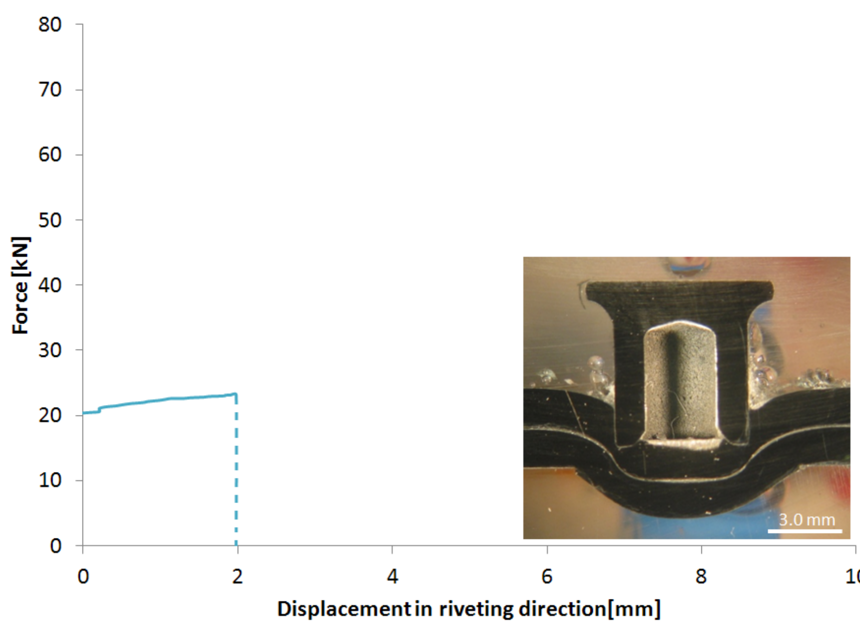

Fig. A.41 Force-displacement curve and cross-section of 1.5 + 1.5 mm G300 steel sheet with 6 mm long rivet of hardness of 410 HV and interrupted at 2.00 mm

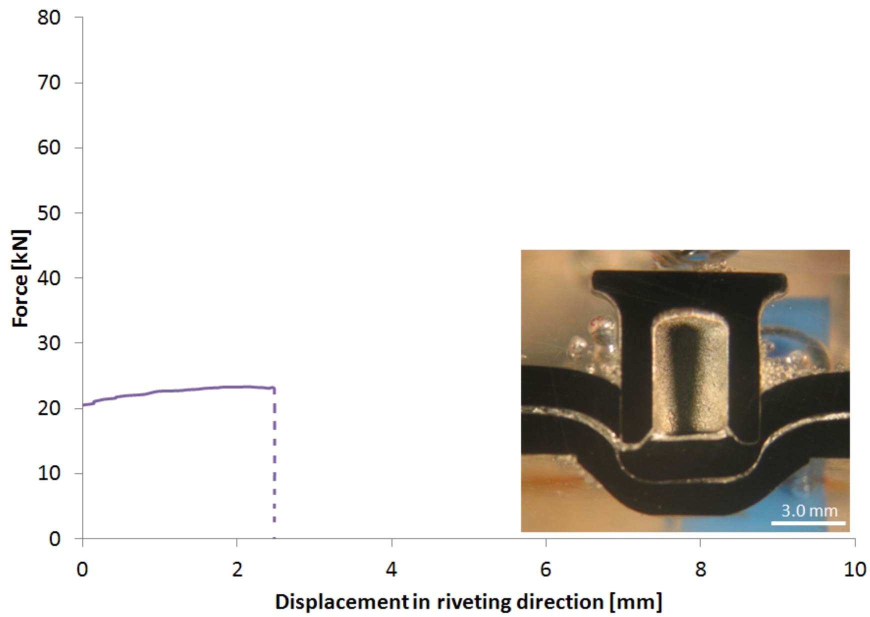

Fig. A. 42 Force-displacement curve and cross-section of 1.5 + 1.5 mm G300 steel sheet with 6 mm long rivet of hardness of 410 HV and interrupted at 2.50 mm

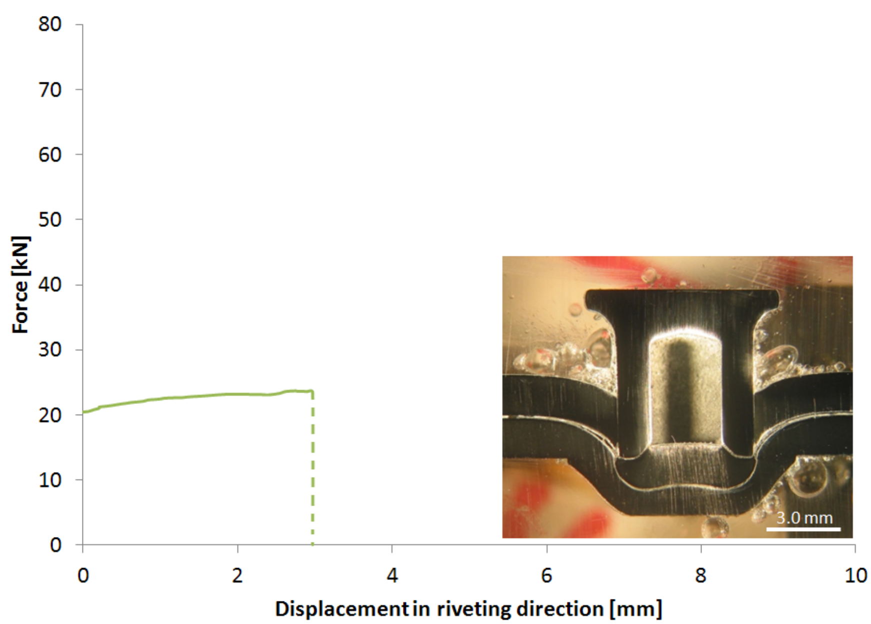

Fig. A.43 Force-displacement curve and cross-section of 1.5 + 1.5 mm G300 steel sheet with 6 mm long rivet of hardness of 410 HV and interrupted at 2.95 mm

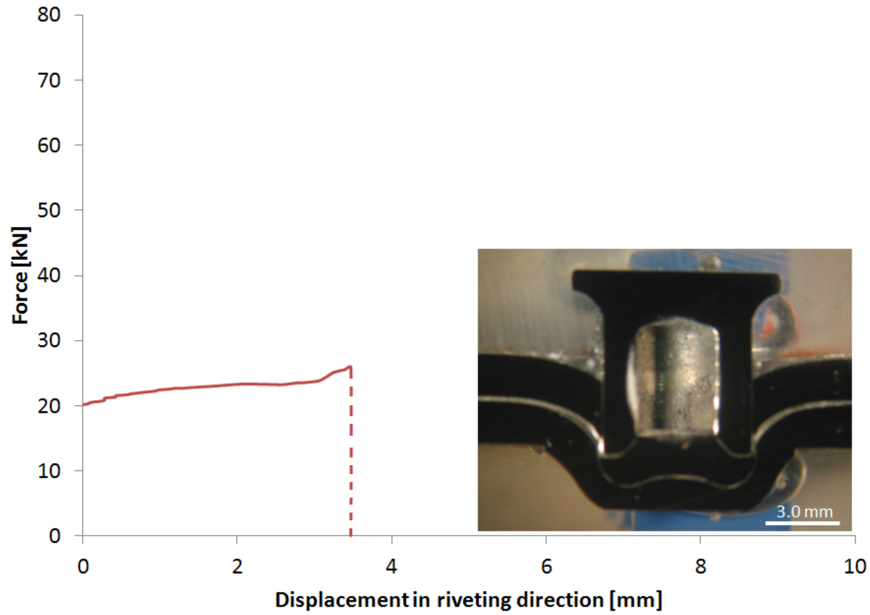

Fig. A.44 Force-displacement curve and cross-section of 1.5 + 1.5 mm G300 steel sheet with 6 mm long rivet of hardness of 410 HV and interrupted at 3.45 mm

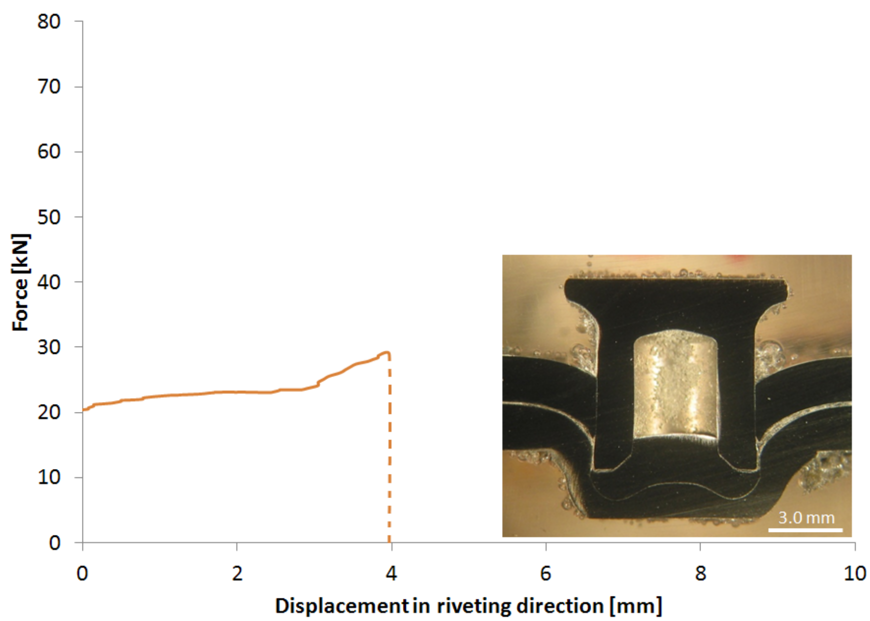

Fig. A. 45 Force-displacement curve and cross-section of 1.5 + 1.5 mm G300 steel sheet with 6 mm long rivet of hardness of 410 HV and interrupted at 3.95 mm

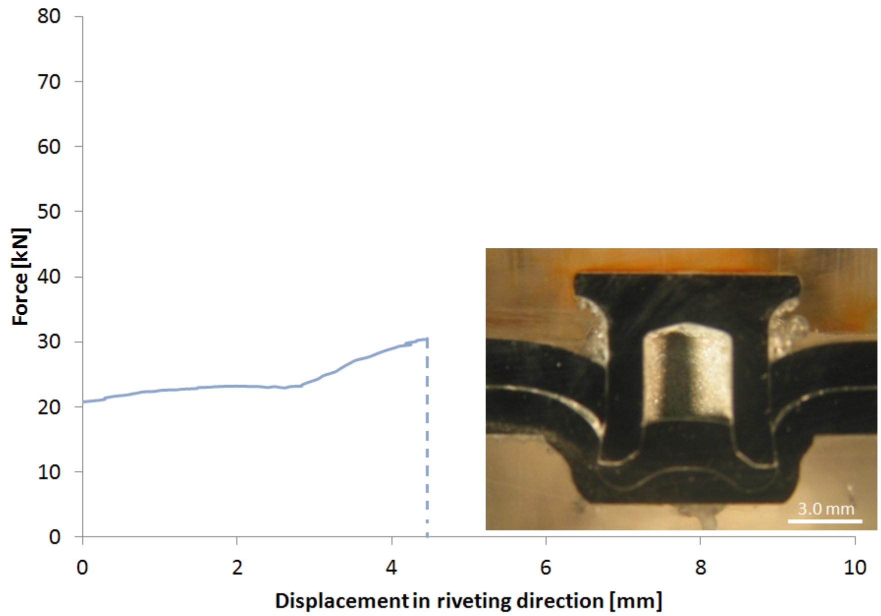

Fig. A.46 Force-displacement curve and cross-section of 1.5 + 1.5 mm G300 steel sheet with 6 mm long rivet of hardness of 410 HV and interrupted at 4.45 mm

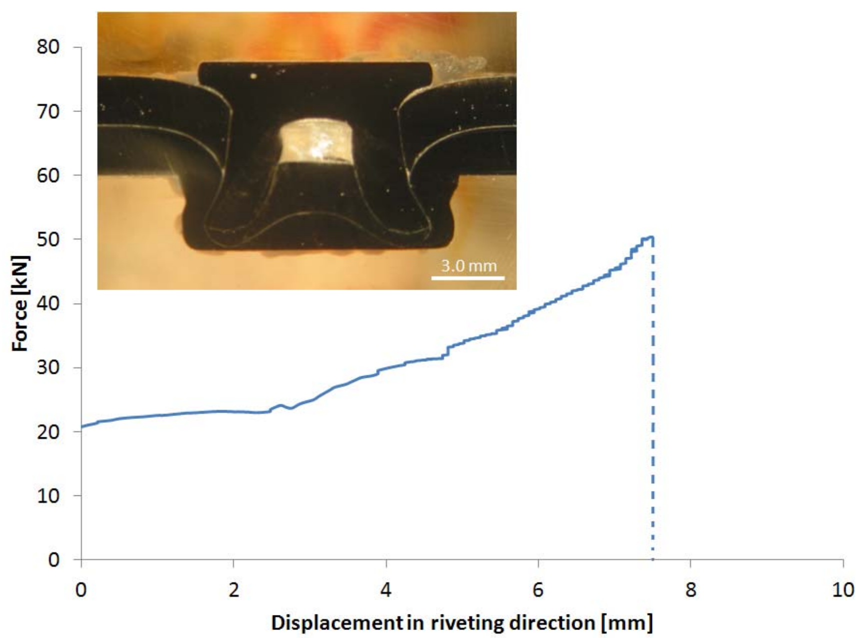

Fig. A.47 Force-displacement curve and cross-section of 1.5 + 1.5 mm G300 steel sheet with 6 mm long rivet of hardness of 410 HV and interrupted at 7.50 mm (complete joint)

Appendix B

Effect of material hardness on residual stress profile as discussed in chapter 6.4

3 mm (1.5 mm + 1.5 mm) stack thickness

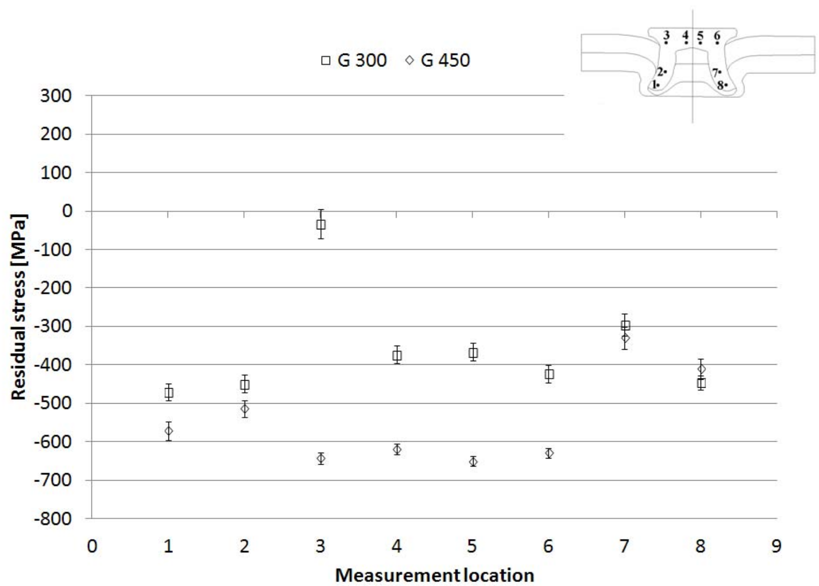

Fig. B.1 Normal residual stress profile depending on material hardness of 1.5 mm + 1.5 mm joint

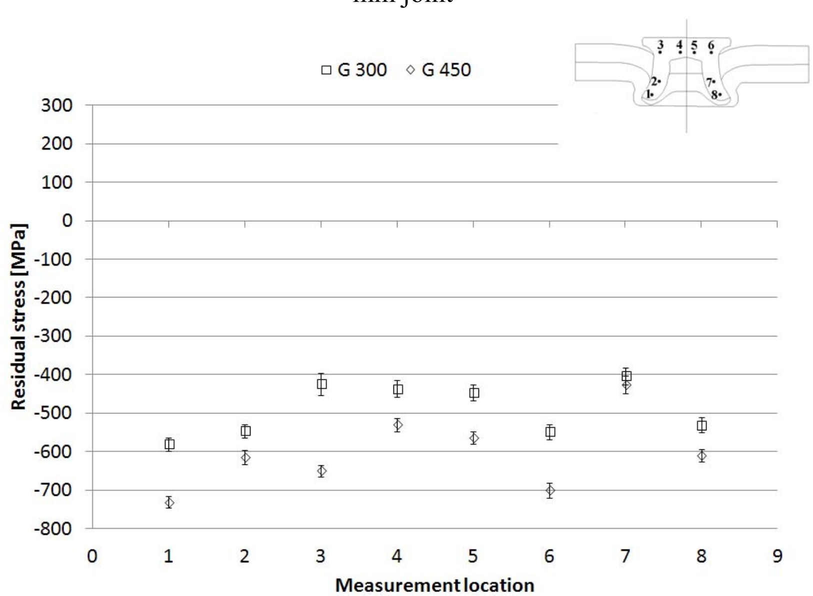

Fig. B.2 Longitudinal residual stress profile depending on material hardness of 1.5 mm + 1.5 mm joint

4 mm (2.0 mm + 2.0 mm) stack thickness with 555 HV rivet

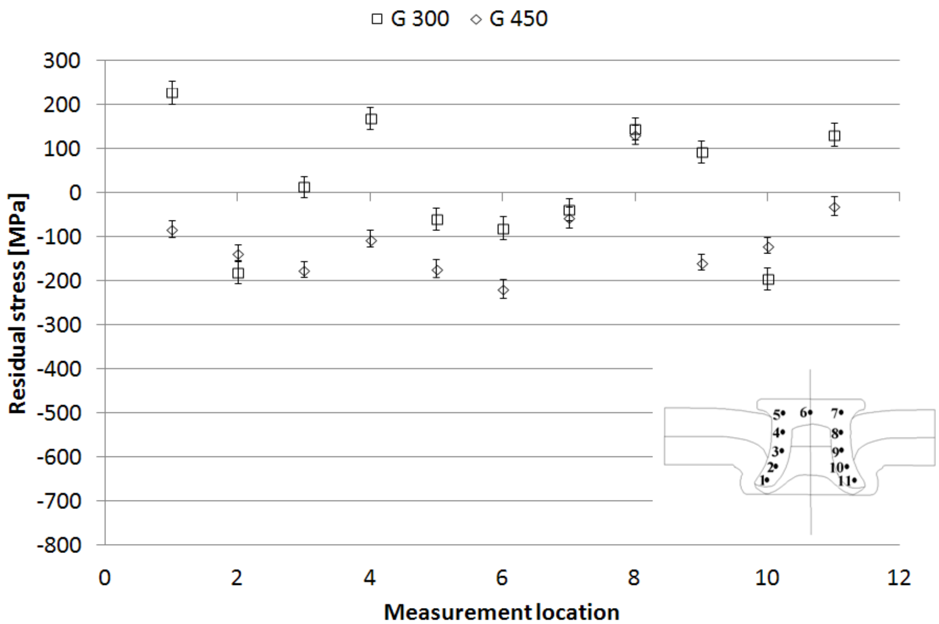

Fig. B.3 Normal residual stress profile depending on material hardness of 2.0 mm + 2.0 mm joint with 555 HV rivet

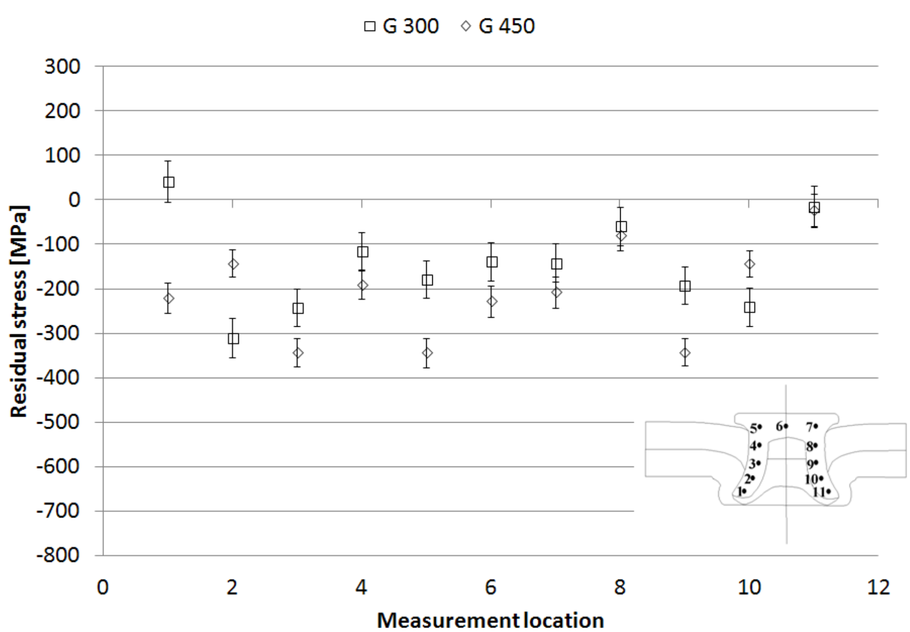

Fig. B.4 Longitudinal residual stress profile depending on material hardness of 2.0 mm + 2.0 mm joint with 555 HV rivet

4 mm (2.0 mm + 2.0 mm) stack thickness with 480 HV rivet

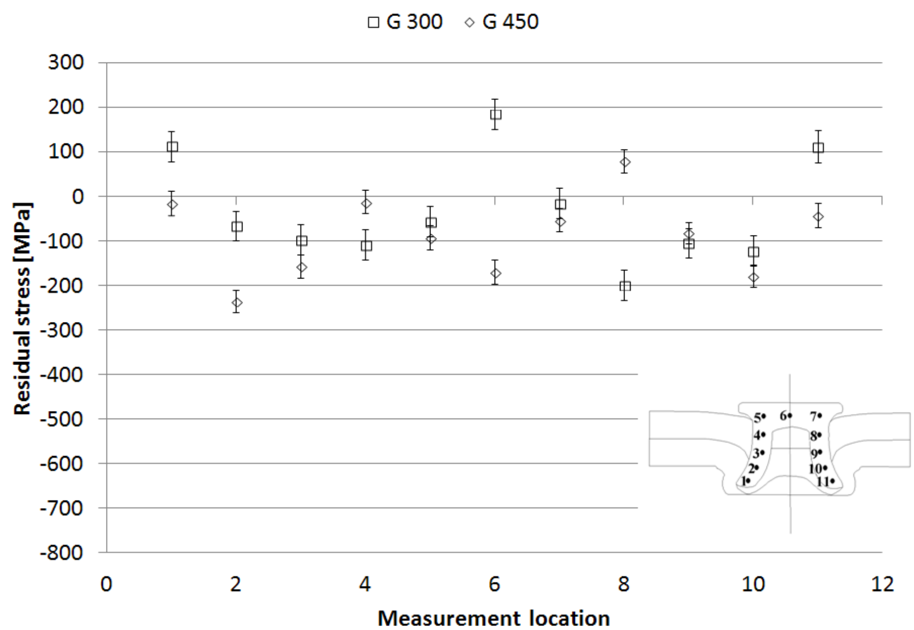

Fig. B.5 Transverse residual stress profile depending on material hardness of 2.0 mm + 2.0 mm joint with 480 HV rivet

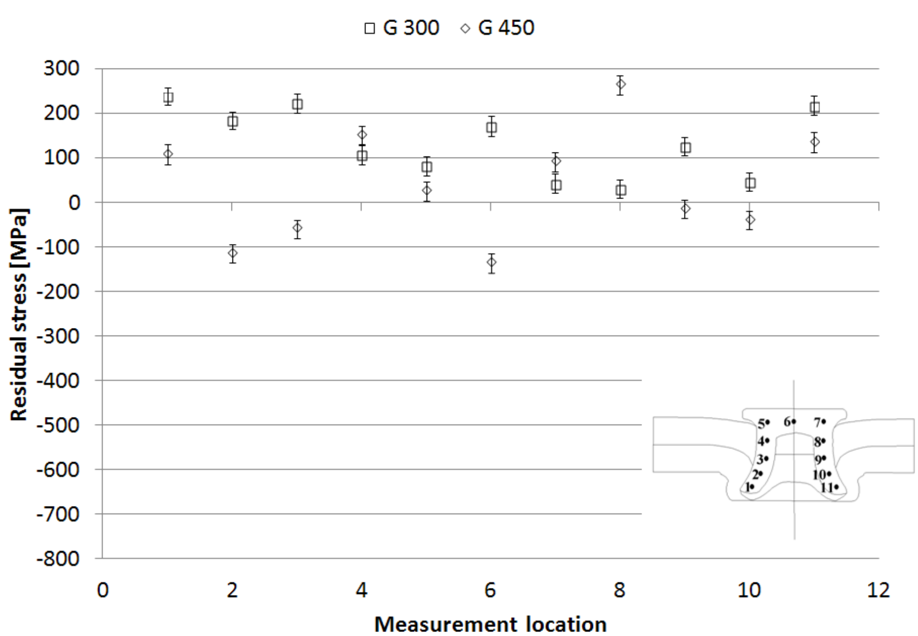

Fig. B.6 Normal residual stress profile depending on material hardness of 2.0 mm + 2.0 mm joint with 480 HV rivet

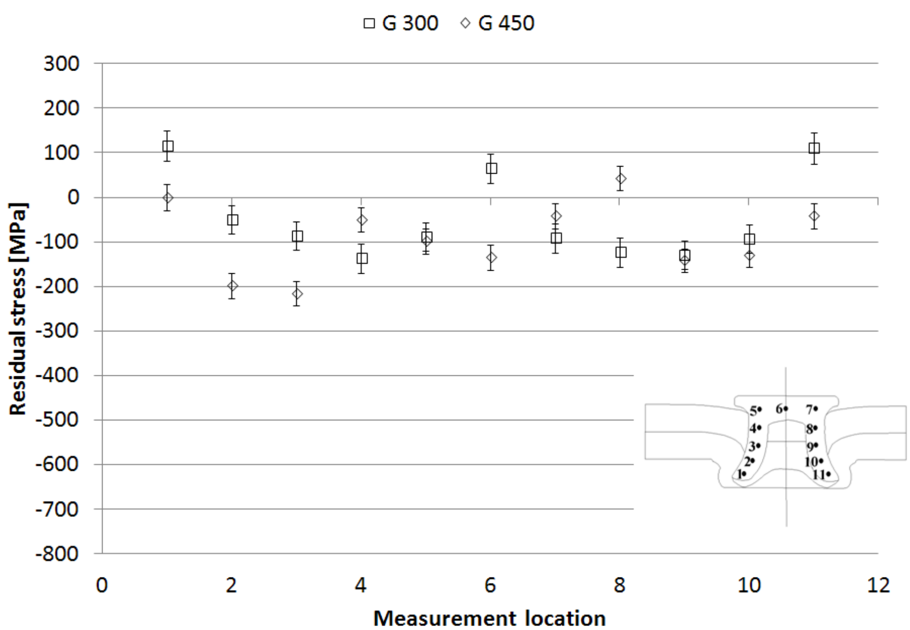

Fig. B.7 Longitudinal residual stress profile depending on material hardness of 2.0 mm + 2.0 mm joint with 480 HV rivet

5 mm (2.5 mm + 2.5 mm) stack thickness with 555 HV rivet

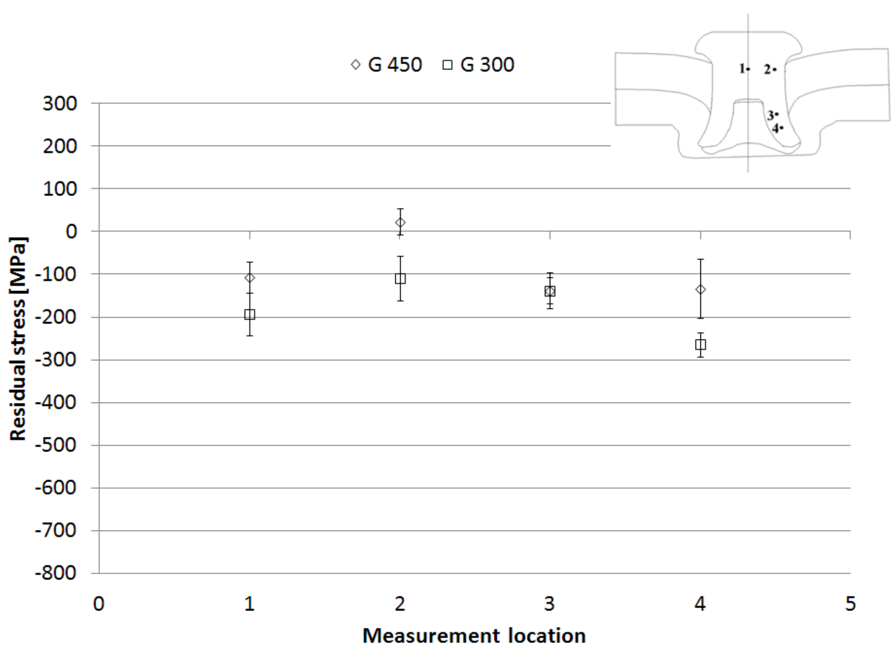

Fig. B.8 Normal residual stress profile depending on material hardness of 2.5 mm + 2.5 mm joint with 555 HV rivet

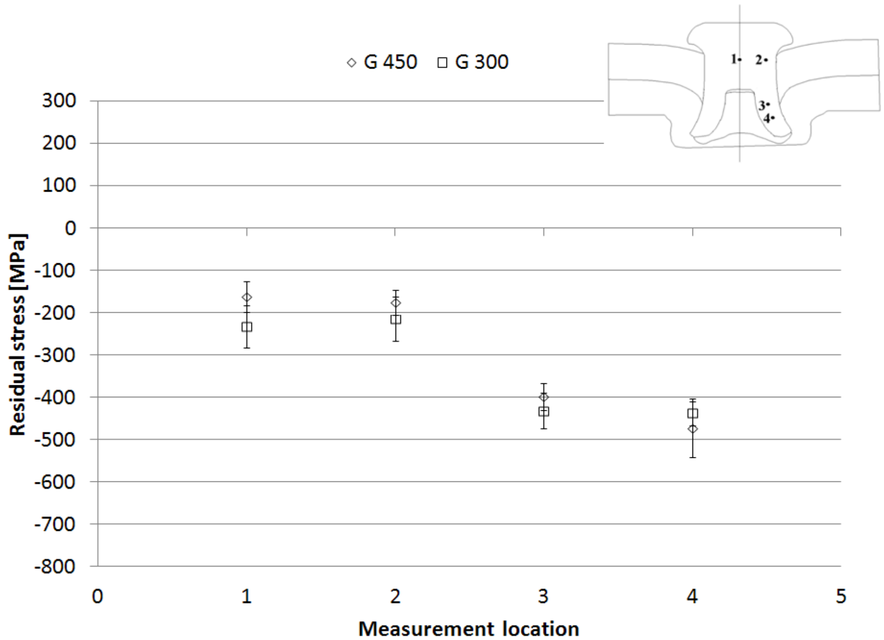

Fig. B.9 Longitudinal residual stress profile depending on material hardness of 2.5 mm + 2.5 mm joint with 555 HV rivet

Effect of material thickness on residual stress profile as discussed in chapter 6.5

5.0 mm vs. 4.0 mm with 555 HV rivet

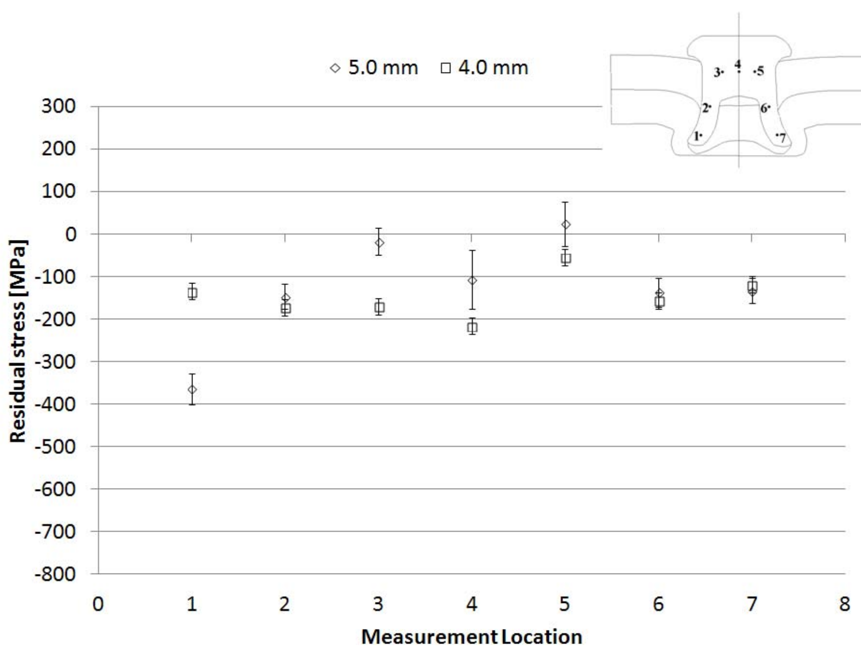

Fig. B.10 Normal residual stress profile depending on the material thickness of G450 steel joint with 555 HV rivet

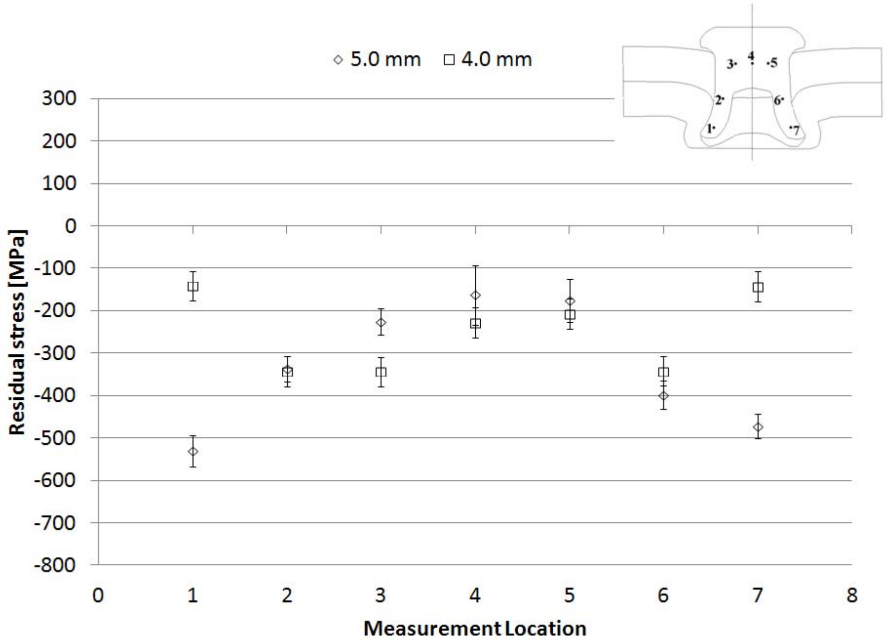

Fig. B.11 Longitudinal residual stress profile depending on the material thickness of G450 steel joint with 555 HV rivet

4.0 mm vs. 3.0 mm with 555 HV rivet

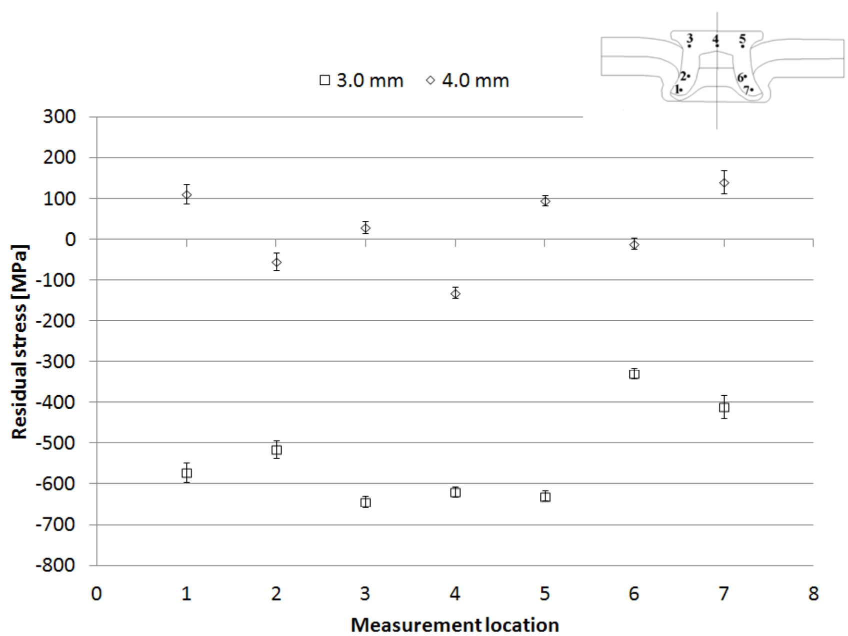

Fig. B.12 Normal residual stress profile depending on the material thickness of G450 steel joint with 480 HV rivet

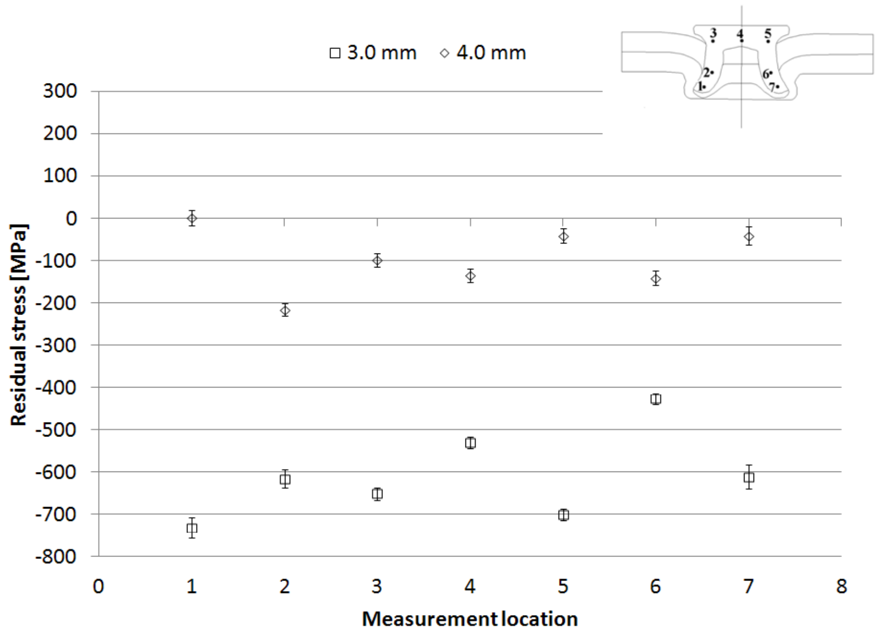

Fig. B.13 Longitudinal residual stress profile depending on the material thickness of G450 steel joint with 480 HV rivet

Appendix C

Cross-tension and Lap-shear test results of chapter 7.3

Case B in Table 7.2.1: 2.5 mm + 2.5 mm G300 carbon steel joint with 555 HV rivet

In this case, the sheet materials were changed by replacing G450 with G300 carbon steel while keeping all other parameters the same as in case A in Table 7.2.1. The results obtained for cross-tension and lap-shear tests are summarized in Table A.7.2.1.B and the force-displacement curves are shown in Fig. A.7.3.B.

Table A.7.2.1.B The features of cross-tension and lap-shear tests for case B in Table 7.2.1.

Cross-Tension	Lap-Shear
Failure mode 1 + rivet failure	Failure mode 2
Maximum force : 10.34 ± 1.04 kN	Maximum force : 12.9 ± 0.53 kN
Displacement at maximum force : 15.66 ± 0.48 mm	Displacement at maximum force : 4.07 ± 0.1 mm
Energy (area under the curve) : 97.31 ± 1.20 kN-mm	Energy (area under the curve) : 98.27 ± 0.95 kN-mm

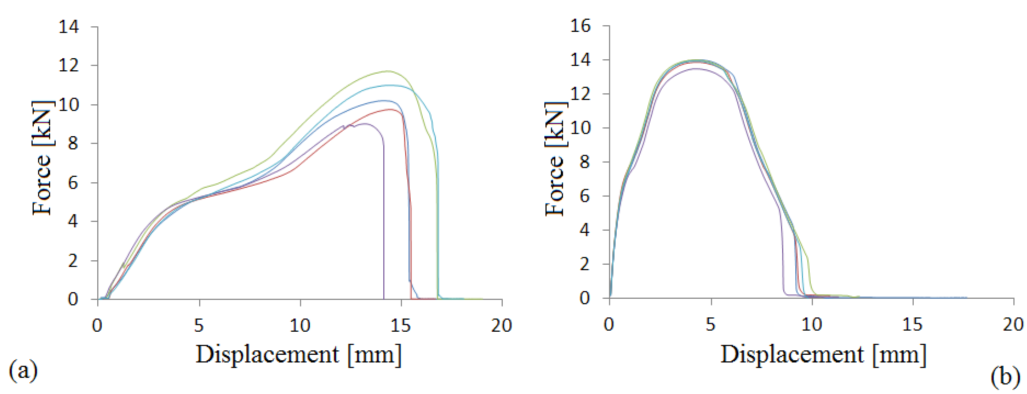

Fig. A.7.3.B Force-displacement curves of 2.5 + 2.5 mm G300 carbon steel sheet joints (a) cross-tension and (b) lap-shear test for the case B in table 7.2.1.

Case C in Table 7.2.1: 2.5 mm + 2.5 mm G300 carbon steel joint with 555 HV rivet (3.0 mm deep die)

In this instance, the die depth was increased to 3.0 mm by decreasing the diameter to 10.0 mm. The results obtained for cross-tension and lap-shear tests are summarized in Table A.7.2.1.C and the force-displacement curves are shown in Fig. A.7.3.C.

Table A.7.2.1.C The features of cross-tension and lap-shear tests for case C in Table 7.2.1.

Cross-Tension	**Lap-Shear**
Failure mode 1 + rivet failure	Failure mode 2
Maximum force : 11.33 ± 1.02 kN	Maximum force : 14.17 ± 0.83 kN
Displacement at maximum force : 16.67 ± 0.62 mm	Displacement at maximum force : 3.99 ± 0.12 mm
Energy (area under the curve) : 125.46 ± 1.41 kN-mm	Energy (area under the curve) : 105.11 ± 1.33 kN-mm

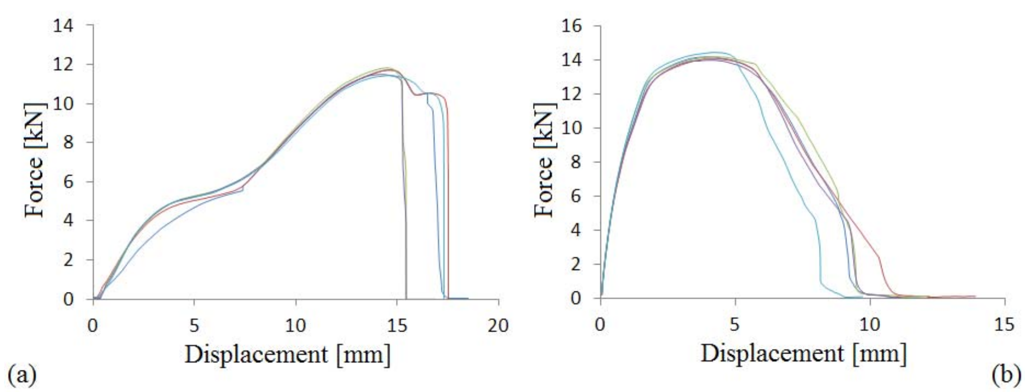

Fig. A.7.3.C Force-displacement curves of 2.5 + 2.5 mm G300 carbon steel sheet joints with a deeper die (a) cross-tension and (b) lap-shear test for the case C in table 7.2.1.

Case D in Table 7.2.1: 2.0 mm + 2.0 mm G450 carbon steel joint with 555 HV rivet

The thickness of the ply materials' was reduced to 2.0 mm in this case. The length of the rivet was reduced to 7.0 mm due to reduced thickness. The rivet hardness (555 HV) was the same as in the previous cases A, B and C in Table 7.2.1. The die dimension was changed to incorporate with reduced volume. A flat die (10.0 mm diameter and 2.1 mm deep) was used again. The results obtained for cross-tension and lap-shear tests are summarized in Table A.7.2.1.D and force-displacement curves are shown in Fig. A.7.3.D.

Table A.7.2.1.D The features of cross-tension and lap-shear tests for case D in Table 7.2.1.

Cross-Tension	**Lap- Shear**
Failure mode 1	Failure mode 2
Maximum force : 9.78 ± 0.64 kN	Maximum force : 14.28 ± 0.14 kN
Displacement at maximum force : 15.52 ± 0.64 mm	Displacement at maximum force : 3.99 ± 0.09 mm
Energy (area under the curve) : 89.09 ± 0.88 kN-mm	Energy (area under the curve) : 102.33 ± 0.22 kN-mm

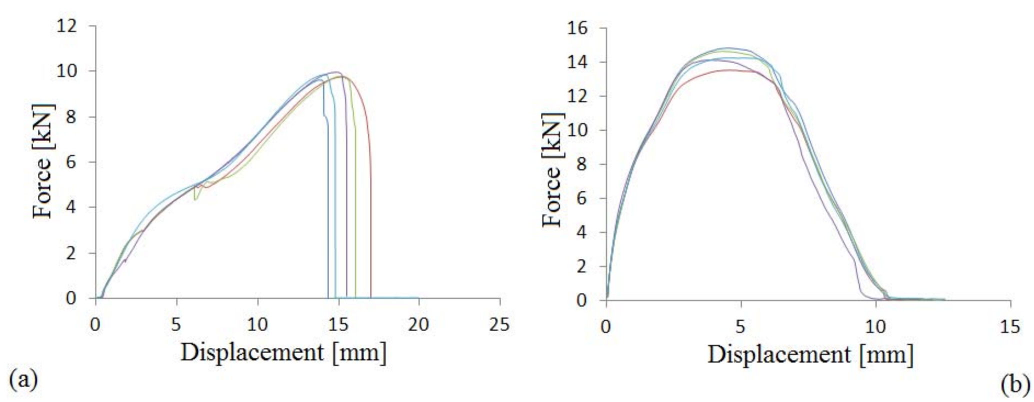

Fig. A.7.3.D Force-displacement curves of 2.0 + 2.0 mm G450 carbon steel sheet joints with 555 HV rivet (a) cross-tension and (b) lap-shear test for the case D in Table 7.2.1.

Case E in Table 7.2.1: 2.0 mm + 2.0 mm G450 carbon steel joint with 480 HV rivet

To understand the effect of rivet hardness on the static strength of SPR joints, another joint of 4.0 mm total stack thickness was produced using a rivet with 480 HV while keeping all other parameters the same as in case D (Table 7.2.1). The results obtained for cross-tension and lap-shear tests are summarized in Table A.7.2.1.E below. Force-displacement curves of the cross-section and lap-shear tests are shown in Fig. A.7.3.E.

Table A.7.2.1.E The features of cross-tension and lap-shear tests for case E in Table 7.2.1.

Cross-Tension	**Lap-Shear**
Failure mode 1	Failure mode 2
Maximum force : 9.76 ± 0.24 kN	Maximum force : 14.35 ± 0.81 kN
Displacement at maximum force : 16.76 ± 0.37 mm	Displacement at maximum force : 3.99 ± 0.07 mm
Energy (area under the curve) : 97.19 ± 0.52 kN-mm	Energy (area under the curve) : 91.53 ± 1.05 kN-mm

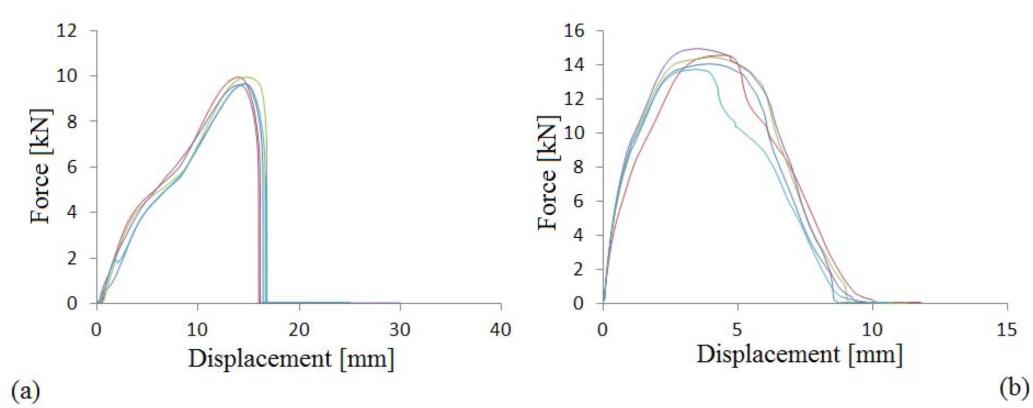

Fig. A.7.3.E Force-displacement curves of 2.0 + 2.0 mm G450 carbon steel sheet joints with 480 HV rivet (a) cross-tension and (b) lap-shear test for the case E in table 7.2.1.

Case F in Table 7.2.1: 2.0 mm + 2.0 mm G300 carbon steel joint with 555 HV rivet

To determine the effect of material properties another joint of 4.0 mm total stack thickness was produced by keeping all parameters the same as case D except the materials (G300 used instead of G450 The results obtained for cross-tension and lap-shear tests are summarized in Table A.7.2.1.F and force-displacement curves are shown in Fig. A.7.3.F.

Table A.7.2.1.F The features of cross-tension and lap-shear tests for case F in Table 7.2.1.

Cross-Tension	**Lap-Shear**
Failure mode 1	Failure mode 2
Maximum force :7.97 ± 0.70 kN	Maximum force : 11.36 ± 0.31 kN
Displacement at maximum force : 17.22 ± 0.49 mm	Displacement at maximum force : 3.53 ± 0.11 mm
Energy (area under the curve) : 83.14 ± 1.13 kN-mm	Energy (area under the curve) : 82.31 ± 0.85 kN-mm

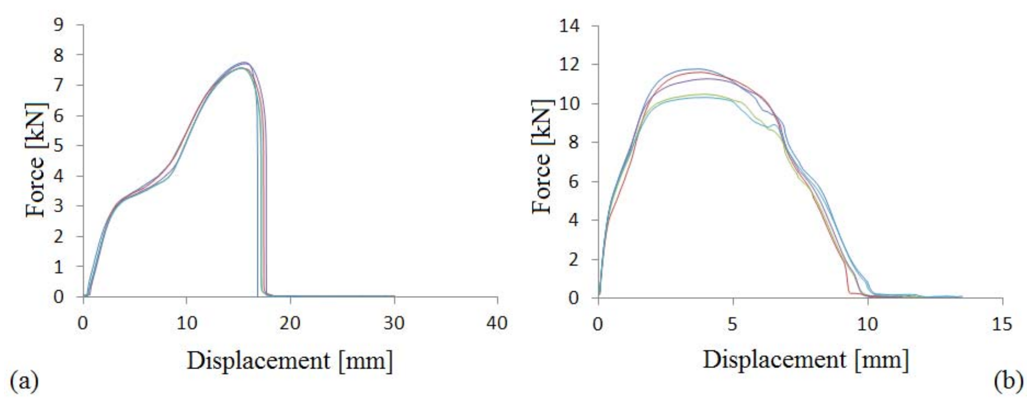

Fig. A.7.3.F Force-displacement curve of 2.0 + 2.0 mm G300 carbon steel sheet joints with 555 HV rivet (a) cross-tension and (b) lap-shear test for the case F in table 7.2.1.

Case G in Table 7.2.1: 2.0 mm + 2.0 mm G300 carbon steel joint with 480 HV rivet

All parameters were kept the same as in case F, except the rivet hardness. The rivet chosen had a hardness of 480 HV. The results obtained for cross-tension and lap-shear tests are summarized in Table A.7.2.1.G and force-displacement curves are shown in Fig. A.7.3.G.

Table A.7.2.1.G The features of cross-tension and lap-shear tests for case G in Table 7.2.1.

Cross-Tension	**Lap-Shear**
Failure mode 1	Failure mode 2
Maximum force :7.32 ± 0.22 kN	Maximum force : 10.73 ± 0.63 kN
Displacement at maximum force : 15.92 ± 0.34 mm	Displacement at maximum force : 3.53 ± 0.06 mm
Energy (area under the curve) : 73.37 ± 0.59 kN-mm	Energy (area under the curve) : 77.51 ± 1.03 kN-mm

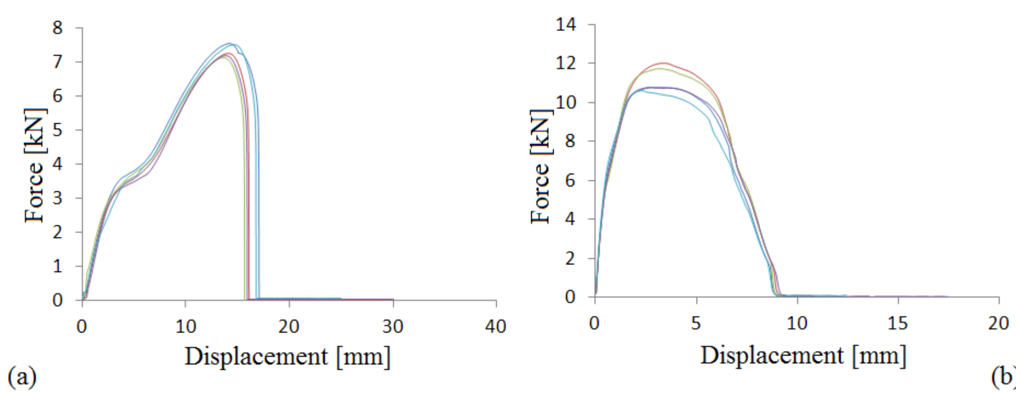

Fig. A.7.3.G Force-displacement curve of 2.0 + 2.0 mm G300 carbon steel sheet joints with 480 HV rivet (a) cross-tension and (b) lap-shear test for the case G in table 7.2.1.

Case H in Table 7.2.1: 1.5 mm + 1.5 mm G450 carbon steel joint with 480 HV rivet

The thickness of the ply materials was reduced further to 1.5 mm in this case. The length of the rivet was reduced again to 6.0 mm due to thickness reduction of the joint. The rivet hardness was kept the same (480 HV). Again, a flat die with changed dimension (9.0 mm in diameter and 2.0 mm deep) was used to incorporate with the reduced volume. The results obtained for cross-tension and lap-shear tests are summarized in Table A.7.2.1.H and force-displacement curves are shown in Fig. A.7.3.H.

Table A.7.2.1.H The features of cross-tension and lap-shear tests for case H in Table 7.2.1.

Cross-Tension	**Lap-Shear**
Failure mode 1	Failure mode 2
Maximum force :6.84 ± 0.94 kN	Maximum force : 10.54 ± 0.71 kN
Displacement at maximum force : 14.23 ± 0.04 mm	Displacement at maximum force : 3.25 ± 0.02 mm
Energy (area under the curve) : 56.29 ± 1.31 kN-mm	Energy (area under the curve) : 69.10 ± 1.23 kN-mm

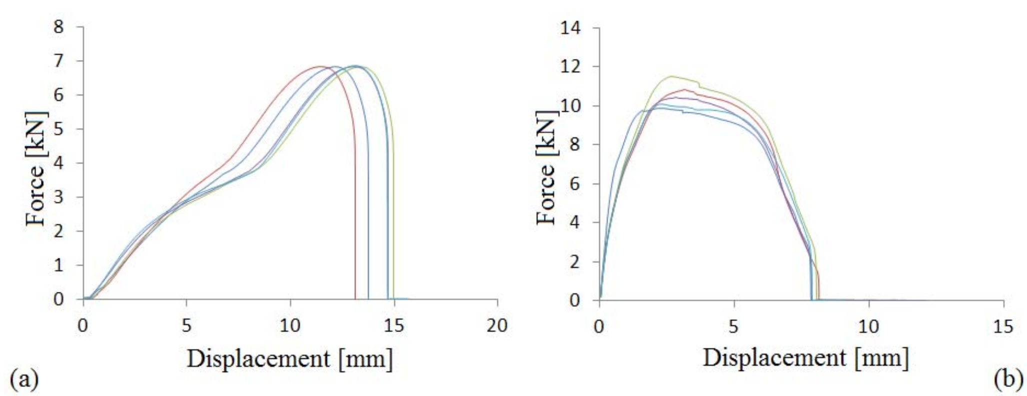

Fig. A.7.3.H Force-displacement curves of 1.5 + 1.5 mm G450 carbon steel sheet joints with 480 HV rivet (a) cross-tension and (b) lap-shear test for the case H in table 7.2.1.

Effect of sheet material's thickness on joint strength for cross-tension loading

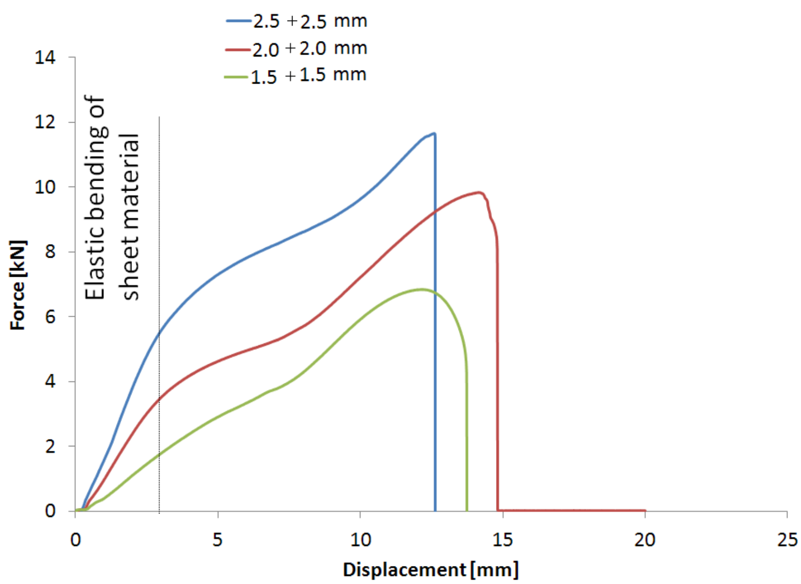

Fig. C.1 Effect of material thickness on the static strength of a joint for G450 carbon steel in cross-tension condition

Effect of sheet material's thickness on joint strength for lap-shear loading

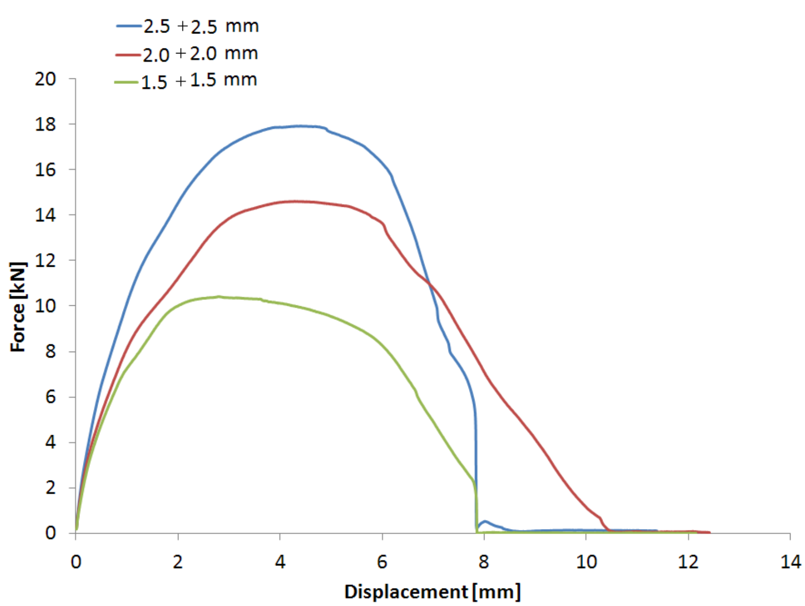

Fig. C.2 Effect of material thickness on the static strength of a joint for G450 carbon steel in lap-shear condition

Effect of rivet hardness on joint strength for cross-tension loading

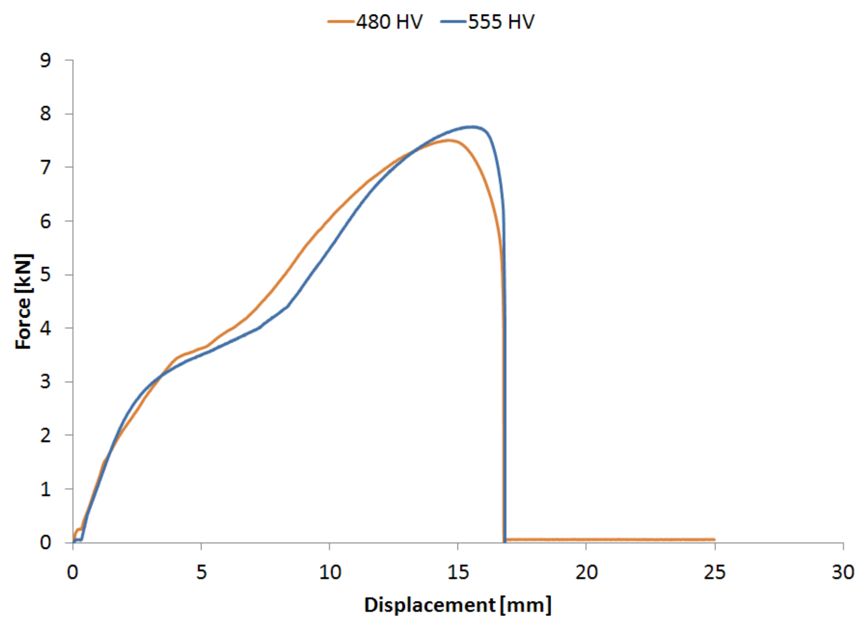

Fig. C.3 Joint strength depending on rivet hardness for a 2.0 +2.0 G300 carbon steel sheet joint in cross-tension condition

Effect of rivet hardness on joint strength for lap-shear loading

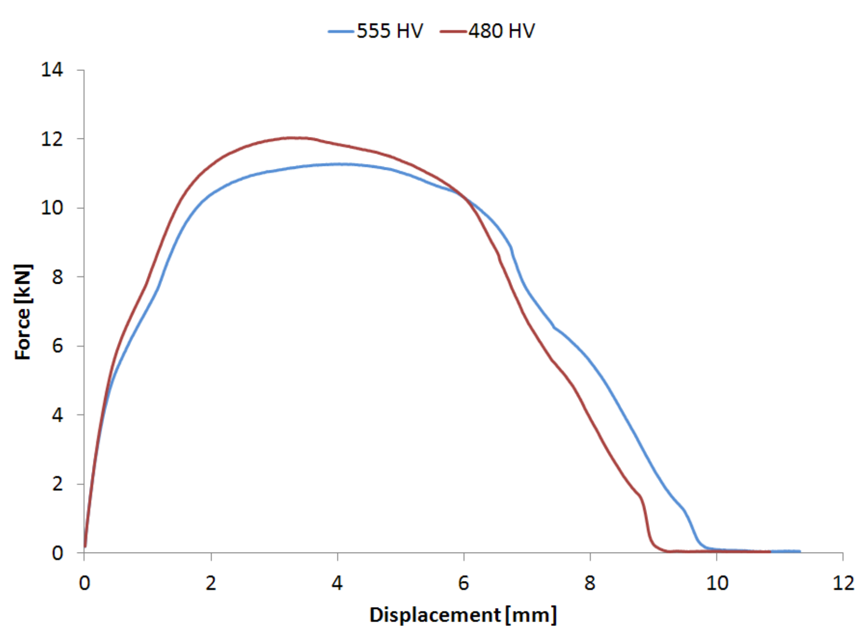

Fig. C.4 Joint strength depending on rivet hardness for a 2.0 +2.0 G300 carbon steel sheet joint in lap-shear condition